

## Major Report

# The Large Hadron–Electron Collider at the HL-LHC

P Agostini<sup>1</sup>, H Aksakal<sup>2</sup>, S Alekhin<sup>3,4</sup>, P P Allport<sup>5</sup>,  
N Andari<sup>6</sup>, K D J Andre<sup>7,8</sup>, D Angal-Kalinin<sup>9,10</sup>,  
S Antusch<sup>11</sup>, L Aperio Bella<sup>12</sup>, L Apolinario<sup>13</sup>,  
R Apsimon<sup>10,14</sup>, A Apyan<sup>15</sup>, G Arduini<sup>8</sup>, V Ari<sup>16</sup>,  
A Armbruster<sup>8</sup>, N Armesto<sup>1</sup>, B Auchmann<sup>8</sup>,  
K Aulenbacher<sup>17,18</sup>, G Azuelos<sup>19</sup>, S Backovic<sup>20</sup>,  
I Bailey<sup>10,14</sup>, S Bailey<sup>21</sup>, F Balli<sup>6</sup>, S Behera<sup>22</sup>, O Behnke<sup>23</sup>,  
I Ben-Zvi<sup>24</sup>, M Benedikt<sup>8</sup>, J Bernauer<sup>25,26</sup>, S Bertolucci<sup>8,27</sup>,  
S S Biswal<sup>28</sup>, J Blümlein<sup>23</sup>, A Bogacz<sup>29</sup>, M Bonvini<sup>30</sup>,  
M Boonekamp<sup>31</sup>, F Bordry<sup>8</sup>, G R Boroun<sup>32</sup>, L Bottura<sup>8</sup>,  
S Bousson<sup>6</sup>, A O Bouzas<sup>33</sup>, C Bracco<sup>8</sup>, J Bracinik<sup>5</sup>,  
D Britzger<sup>34,\*</sup>, S J Brodsky<sup>35</sup>, C Bruni<sup>6</sup>, O Brüning<sup>8,\*</sup>,  
H Burkhardt<sup>8</sup>, O Cakir<sup>16</sup>, R Calaga<sup>8</sup>, A Caldwell<sup>34</sup>,  
A Caliskan<sup>36</sup>, S Camarda<sup>8</sup>, N C Catalan-Lasheras<sup>8</sup>,  
K Cassou<sup>37</sup>, J Cepila<sup>38</sup>, V Cetinkaya<sup>39</sup>, V Chetvertkova<sup>8</sup>,  
B Cole<sup>40</sup>, B Coleppa<sup>41</sup>, A Cooper-Sarkar<sup>21</sup>, E Cormier<sup>42</sup>,  
A S Cornell<sup>43</sup>, R Corsini<sup>8</sup>, E Cruz-Alaniz<sup>7</sup>, J Currie<sup>44</sup>,  
D Curtin<sup>45</sup>, M D’Onofrio<sup>7</sup>, J Dainton<sup>14</sup>, E Daly<sup>29</sup>, A Das<sup>46</sup>,  
S P Das<sup>47</sup>, L Dassa<sup>8</sup>, J de Blas<sup>44</sup>, L Delle Rose<sup>48</sup>,  
H Denizli<sup>49</sup>, K S Deshpande<sup>50</sup>, D Douglas<sup>29</sup>, L Duarte<sup>51</sup>,  
K Dupraz<sup>37,52</sup>, S Dutta<sup>53</sup>, A V Efremov<sup>54</sup>, R Eichhorn<sup>55</sup>,  
K J Eskola<sup>56</sup>, E G Ferreira<sup>1</sup>, O Fischer<sup>57</sup>,  
O Flores-Sánchez<sup>58</sup>, S Forte<sup>59,60</sup>, A Gaddi<sup>8</sup>, J Gao<sup>61</sup>,  
T Gehrman<sup>62</sup>, A Gehrman-De Ridder<sup>62,63</sup>, F Gerigk<sup>8</sup>,  
A Gilbert<sup>64</sup>, F Giuli<sup>65</sup>, A Glazov<sup>23</sup>, N Glover<sup>44</sup>,  
R M Godbole<sup>66</sup>, B Goddard<sup>8</sup>, V Gonçalves<sup>67</sup>,  
G A Gonzalez-Sprinberg<sup>51</sup>, A Goyal<sup>68</sup>, J Grames<sup>29</sup>,  
E Granados<sup>8</sup>, A Grassellino<sup>69</sup>, Y O Gunaydin<sup>2</sup>, Y C Guo<sup>70</sup>,  
V Guzey<sup>71</sup>, C Gwenlan<sup>21</sup>, A Hammad<sup>11</sup>, C C Han<sup>72,73</sup>,  
L Harland-Lang<sup>21</sup>, F Haug<sup>8</sup>, F Hautmann<sup>21</sup>, D Hayden<sup>74</sup>,  
J Hessler<sup>34</sup>, I Helenius<sup>56</sup>, J Henry<sup>29</sup>,  
J Hernandez-Sanchez<sup>58</sup>, H Hesari<sup>75</sup>, T J Hobbs<sup>76</sup>, N Hod<sup>77</sup>,

\*Authors to whom any correspondence should be addressed.



Original content from this work may be used under the terms of the [Creative Commons Attribution 4.0 licence](https://creativecommons.org/licenses/by/4.0/). Any further distribution of this work must maintain attribution to the author(s) and the title of the work, journal citation and DOI.

G H Hoffstaetter<sup>55</sup>, B Holzer<sup>8</sup>, C G Honorato<sup>58</sup>,  
 B Hounsell<sup>7,10,37</sup>, N Hu<sup>37</sup>, F Hug<sup>17,18</sup>, A Huss<sup>8,44</sup>,  
 A Hutton<sup>29</sup>, R Islam<sup>22,78</sup>, S Iwamoto<sup>79</sup>, S Jana<sup>57</sup>,  
 M Jansova<sup>80</sup>, E Jensen<sup>8</sup>, T Jones<sup>7</sup>, J M Jowett<sup>8</sup>,  
 W Kaabi<sup>37</sup>, M Kado<sup>30</sup>, D A Kalinin<sup>9,10</sup>, H Karadeniz<sup>81</sup>,  
 S Kawaguchi<sup>82</sup>, U Kaya<sup>83</sup>, R A Khalek<sup>84</sup>, H Khanpour<sup>75,85</sup>,  
 A Kilic<sup>86</sup>, M Klein<sup>7,\*</sup>, U Klein<sup>7</sup>, S Kluth<sup>34</sup>, M Köksal<sup>87</sup>,  
 F Kocak<sup>86</sup>, M Korostelev<sup>21</sup>, P Kostka<sup>7</sup>, M Krelina<sup>88</sup>,  
 J Kretzschmar<sup>7</sup>, S Kuday<sup>89</sup>, G Kulipanov<sup>90</sup>, M Kumar<sup>91</sup>,  
 M Kuze<sup>82</sup>, T Lappi<sup>56</sup>, F Larios<sup>33</sup>, A Latina<sup>8</sup>, P Laycock<sup>24</sup>,  
 G Lei<sup>92</sup>, E Levitchev<sup>90</sup>, S Levonian<sup>23</sup>, A Levy<sup>93</sup>, R Li<sup>94,95</sup>,  
 X Li<sup>61</sup>, H Liang<sup>61</sup>, V Litvinenko<sup>24,25</sup>, M Liu<sup>70</sup>, T Liu<sup>96</sup>,  
 W Liu<sup>97</sup>, Y Liu<sup>98</sup>, S Liuti<sup>99</sup>, E Lobodzinska<sup>23</sup>,  
 D Longuevergne<sup>37</sup>, X Luo<sup>100</sup>, W Ma<sup>61</sup>, M Machado<sup>101</sup>,  
 S Mandal<sup>102</sup>, H Mäntysaari<sup>56,103</sup>, F Marhauser<sup>29</sup>,  
 C Marquet<sup>104</sup>, A Martens<sup>37</sup>, R Martin<sup>8</sup>, S Marzani<sup>105,106</sup>,  
 J McFayden<sup>8</sup>, P McIntosh<sup>9</sup>, B Mellado<sup>91</sup>, F Meot<sup>55</sup>,  
 A Milanese<sup>8</sup>, J G Milhano<sup>13</sup>, B Militsyn<sup>9,10</sup>, M Mitra<sup>107</sup>,  
 S Moch<sup>23</sup>, M Mohammadi Najafabadi<sup>75</sup>, S Mondal<sup>103</sup>,  
 S Moretti<sup>108</sup>, T Morgan<sup>44</sup>, A Morreale<sup>25</sup>, P Nadolsky<sup>76</sup>,  
 F Navarra<sup>109</sup>, Z Nergiz<sup>110</sup>, P Newman<sup>5</sup>, J Niehues<sup>44</sup>,  
 E A Nissen<sup>8</sup>, M Nowakowski<sup>111</sup>, N Okada<sup>112</sup>, G Olivier<sup>37</sup>,  
 F Olness<sup>76</sup>, G Olry<sup>37</sup>, J A Osborne<sup>8</sup>, A Ozansoy<sup>16</sup>,  
 R Pan<sup>94,95</sup>, B Parker<sup>24</sup>, M Patra<sup>113</sup>, H Paukkunen<sup>56</sup>,  
 Y Peinaud<sup>37</sup>, D Pellegrini<sup>8</sup>, G Perez-Segurana<sup>10,14</sup>,  
 D Perini<sup>8</sup>, L Perrot<sup>37</sup>, N Pietralla<sup>114</sup>, E Pilicer<sup>86</sup>, B Pire<sup>104</sup>,  
 J Pires<sup>13</sup>, R Placakyte<sup>115</sup>, M Poelker<sup>29</sup>, R Polifka<sup>116</sup>,  
 A Polini<sup>117</sup>, P Poulou<sup>22</sup>, G Pownall<sup>21</sup>, Y A Pupkov<sup>90</sup>,  
 F S Queiroz<sup>118</sup>, K Rabbertz<sup>119</sup>, V Radescu<sup>120</sup>,  
 R Rahaman<sup>121</sup>, S K Rai<sup>107</sup>, N Raicevic<sup>122</sup>, P Ratoff<sup>10,14</sup>,  
 A Rashed<sup>123</sup>, D Raut<sup>124</sup>, S Raychaudhuri<sup>113</sup>, J Repond<sup>125</sup>,  
 A H Rezaeian<sup>126,127</sup>, R Rimmer<sup>29</sup>, L Rinolfi<sup>8</sup>, J Rojo<sup>84</sup>,  
 A Rosado<sup>58</sup>, X Ruan<sup>91</sup>, S Russenschuck<sup>8</sup>, M Sahin<sup>128</sup>,  
 C A Salgado<sup>1</sup>, O A Sampayo<sup>129</sup>, K Satendra<sup>22</sup>,  
 N Satyanarayan<sup>130</sup>, B Schenke<sup>24</sup>, K Schirm<sup>8</sup>, H Schopper<sup>8</sup>,  
 M Schott<sup>18</sup>, D Schulte<sup>8</sup>, C Schwanenberger<sup>23</sup>, T Sekine<sup>82</sup>,  
 A Senol<sup>49</sup>, A Seryi<sup>29</sup>, S Setiniyaz<sup>10,14</sup>, L Shang<sup>131</sup>,  
 X Shen<sup>94,95</sup>, N Shipman<sup>8</sup>, N Sinha<sup>132</sup>, W Slominski<sup>133</sup>,  
 S Smith<sup>9,10</sup>, C Solans<sup>8</sup>, M Song<sup>134</sup>, H Spiesberger<sup>18</sup>,  
 J Stanyard<sup>8</sup>, A Starostenko<sup>90</sup>, A Stasto<sup>135</sup>, A Stocchi<sup>37</sup>,  
 M Strikman<sup>135</sup>, M J Stuart<sup>8</sup>, S Sultansoy<sup>83</sup>, H Sun<sup>100</sup>,  
 M Sutton<sup>136</sup>, L Szymanowski<sup>137</sup>, I Tapan<sup>86</sup>,  
 D Tapia-Takaki<sup>138</sup>, M Tanaka<sup>82</sup>, Y Tang<sup>139</sup>, A T Tasci<sup>140</sup>,  
 A T Ten-Kate<sup>8</sup>, P Thonet<sup>8</sup>, R Tomas-Garcia<sup>8</sup>,  
 D Tommasini<sup>8</sup>, D Trbojevic<sup>24,55</sup>, M Trott<sup>141</sup>, I Tsurin<sup>7</sup>,



**A Tudora<sup>8</sup>, I Turk Cakir<sup>81</sup>, K Tywoniuk<sup>142</sup>, C Vallerand<sup>37</sup>,  
 A Valloni<sup>8</sup>, D Verney<sup>37</sup>, E Vilella<sup>7</sup>, D Walker<sup>44</sup>, S Wallon<sup>37</sup>,  
 B Wang<sup>94,95</sup>, K Wang<sup>94,95</sup>, K Wang<sup>143</sup>, X Wang<sup>100</sup>,  
 Z S Wang<sup>144</sup>, H Wei<sup>145</sup>, C Welsch<sup>7,10</sup>, G Willering<sup>8</sup>,  
 P H Williams<sup>9,10</sup>, D Wollmann<sup>8</sup>, C Xiaohao<sup>12</sup>, T Xu<sup>146</sup>,  
 C E Yaguna<sup>147</sup>, Y Yamaguchi<sup>82</sup>, Y Yamazaki<sup>148</sup>, H Yang<sup>149</sup>,  
 A Yilmaz<sup>81</sup>, P Yock<sup>150</sup>, C X Yue<sup>70</sup>, S G Zadeh<sup>151</sup>,  
 O Zenaiev<sup>8</sup>, C Zhang<sup>152</sup>, J Zhang<sup>153</sup>, R Zhang<sup>61</sup>, Z Zhang<sup>37</sup>,  
 G Zhu<sup>94,95</sup>, S Zhu<sup>131</sup>, F Zimmermann<sup>8</sup>, F Zomer<sup>37</sup>,  
 J Zurita<sup>154,155</sup> and P Zurita<sup>156</sup>**

<sup>1</sup> Universidade de Santiago de Compostela (USC), Santiago de Compostela, Spain

<sup>2</sup> Kahramanmaras Sutcu Imam University, Kahramanmaras, Turkey

<sup>3</sup> Universität Hamburg, Hamburg, Germany

<sup>4</sup> Institute of High Energy Physics (IHEP), Protvino, Russia

<sup>5</sup> University of Birmingham, Birmingham, United Kingdom

<sup>6</sup> Université Paris-Saclay, Saint-Aubin, France

<sup>7</sup> University of Liverpool, Liverpool, United Kingdom

<sup>8</sup> European Organization for Nuclear Research (CERN), Genève, Switzerland

<sup>9</sup> Science and Technology Facilities Council (STFC)—Daresbury Laboratory, Daresbury, United Kingdom

<sup>10</sup> Cockcroft Institute of Accelerator Science and Technology, Daresbury, United Kingdom

<sup>11</sup> Universität Basel, Basel, Switzerland

<sup>12</sup> Chinese Academy of Sciences—Institute of High Energy Physics (IHEP), Beijing, People's Republic of China

<sup>13</sup> Laboratório de Instrumentação e Física Experimental de Partículas (LIP), Lisbon, Portugal

<sup>14</sup> University of Lancaster, Lancaster, United Kingdom

<sup>15</sup> A Alikhanian National Laboratory (AANL), Yerevan, Armenia

<sup>16</sup> Ankara University, Ankara, Turkey

<sup>17</sup> Johannes Gutenberg University Mainz (JGU)—PRISMA Cluster of Excellence, Mainz, Germany

<sup>18</sup> Johannes Gutenberg-Universität Mainz (JGU), Mainz, Germany

<sup>19</sup> Université de Montréal, Montreal, Canada

<sup>20</sup> University of Montenegro, Podgorica, Montenegro

<sup>21</sup> University of Oxford, Oxford, United Kingdom

<sup>22</sup> Department of Physics, Indian Institute of Technology, Guwahati, Assam, India

<sup>23</sup> Deutsches Elektronen-Synchrotron (DESY), Hamburg, Germany

<sup>24</sup> Brookhaven National Laboratory (BNL), Upton, United States of America

<sup>25</sup> Stony Brook University, Stony Brook, United States of America

<sup>26</sup> BNL Research Center, RIKEN, Upton, NY, United States of America

<sup>27</sup> Università di Bologna, Bologna, Italy

<sup>28</sup> Ravenshaw University, Cuttack, India

<sup>29</sup> Thomas Jefferson National Accelerator Facility (Jefferson Lab), Newport News, United States of America

<sup>30</sup> Istituto Nazionale di Fisica Nucleare (INFN)—Sezione di Roma, Rome, Italy

<sup>31</sup> Commissariat à l'Énergie Atomique (CEA)—Institut de Recherche sur les Lois Fondamentales de l'Univers (IRFU), Gif-sur-Yvette, France

<sup>32</sup> Razi University, Kermanshah, Iran

<sup>33</sup> Centro de Investigación y de Estudios Avanzados (CINVESTAV), Mérida, Mexico

- <sup>34</sup> Max-Planck-Institut für Physik, Munich, Germany  
<sup>35</sup> SLAC National Accelerator Laboratory, Menlo Park, United States of America  
<sup>36</sup> Gumushane University, Gumushane, Turkey  
<sup>37</sup> Université Paris-Saclay, CNRS/IN2P3, IJCLab, Orsay, France  
<sup>38</sup> Faculty of Nuclear Sciences and Physical Engineering, Czech Technical University in Prague, Prague, Czech Republic  
<sup>39</sup> Kutahya Dumlupinar University, Kutahya, Turkey  
<sup>40</sup> Columbia University, New York, United States of America  
<sup>41</sup> Indian Institute of Technology (IIT), Gandhinagar, India  
<sup>42</sup> Laboratoire Photonique, Numérique et Nanosciences (LP2N), IOGS-CNRS-Université Bordeaux, Talence, France  
<sup>43</sup> University of Johannesburg (UJ), Johannesburg, South Africa  
<sup>44</sup> Institute for Particle Physics Phenomenology, Durham University, Durham, United Kingdom  
<sup>45</sup> University of Toronto, Toronto, Canada  
<sup>46</sup> Osaka University, Osaka, Japan  
<sup>47</sup> Universidad de los Andes, Santiago, Columbia  
<sup>48</sup> Istituto Nazionale di Fisica Nucleare (INFN)—Sezione di Firenze, Firenze, Italy  
<sup>49</sup> Bolu Abant İzzet Baysal University, Bolu, Turkey  
<sup>50</sup> University of Maryland, College Park, United States of America  
<sup>51</sup> Universidad de la Republica—Instituto de Física Facultad de Ciencias (IFFC), Montevideo, Uruguay  
<sup>52</sup> Université Paris-Sud, Orsay, France  
<sup>53</sup> Sri Guru Tegh Badadur Khalsa College, Delhi, India  
<sup>54</sup> Joint Institute for Nuclear Research (JINR), Dubna, Russia  
<sup>55</sup> Cornell University, Ithaca, United States of America  
<sup>56</sup> University of Jyväskylä, Jyväskylä, Finland  
<sup>57</sup> Max-Planck-Institut für Kernphysik, Heidelberg, Germany  
<sup>58</sup> Benemerita Universidad Autónoma de Puebla (BUAP), Puebla, Mexico  
<sup>59</sup> Università degli Studi di Milano, Milano, Italy  
<sup>60</sup> Istituto Nazionale di Fisica Nucleare (INFN)—Sezione di Milano, Milano, Italy  
<sup>61</sup> University of Science and Technology of China (USTC), Hefei, People's Republic of China  
<sup>62</sup> Department of Physics, Universität Zürich, Zurich, Switzerland  
<sup>63</sup> Institute for Theoretical Physics, ETH, Zurich, Switzerland  
<sup>64</sup> Northwestern University, Evanston, United States of America  
<sup>65</sup> University of Rome Tor Vergata and INFN, Sezione di Roma 2, Rome, Italy  
<sup>66</sup> Indian Institute of Science (IISc), Bangalore, India  
<sup>67</sup> Universidade Federal de Pelotas (UFPEL), Pelotas, Brazil  
<sup>68</sup> University of Delhi, Delhi, India  
<sup>69</sup> Fermi National Accelerator Laboratory (FNAL), Batavia, United States of America  
<sup>70</sup> Liaoning Normal University (LNNU), Dalian, People's Republic of China  
<sup>71</sup> Petersburg Nuclear Physics Institute (PNPI), Petersburg, Russia  
<sup>72</sup> University of Tokyo, Tokyo, Japan  
<sup>73</sup> Kavli Institute for the Physics and Mathematics of the Universe (KIPMU), Kashiwa, Japan  
<sup>74</sup> Michigan State University, East Lansing, United States of America  
<sup>75</sup> Institute for Research in Fundamental Sciences (IPM), Tehran, Iran  
<sup>76</sup> Southern Methodist University, Dallas, United States of America  
<sup>77</sup> Weizmann Institute of Science, Rehovot, Israel  
<sup>78</sup> Department of Physics, Mathabhanga College, Cooch Behar, West Bengal, India  
<sup>79</sup> Università degli Studi di Padova, Padua, Italy

- 80 Université de Strasbourg, Strasbourg, France  
81 Giresun University, Giresun, Turkey  
82 Tokyo Institute of Technology, Tokyo, Japan  
83 TOBB University of Economic and Technology (TOBB ETU), Ankara, Turkey  
84 Vrije University, Amsterdam, The Netherlands  
85 University of Science and Technology of Mazandaran, Behshahr, Iran  
86 Uludag University, Bursa, Turkey  
87 Sivas Cumhuriyet University, Sivas, Turkey  
88 Universidad Tecnica Federico Santa Maria, Valparaiso, Chile  
89 Istanbul Aydin University, Istanbul, Turkey  
90 Siberian Branch of Russian Academy of Science—Budker Institute of Nuclear Physics (BINP), Novosibirsk, Russia  
91 University of the Witwatersrand, Johannesburg, South Africa  
92 Tsinghua University, Beijing, People’s Republic of China  
93 Tel-Aviv University, Tel Aviv, Israel  
94 Zhejiang Institute of Modern Physics (ZIMP), Hangzhou, People’s Republic of China  
95 Zhejiang University (ZJU), Hangzhou, People’s Republic of China  
96 Xiamen University (XMU), Xiamen, People’s Republic of China  
97 University College London, London, United Kingdom  
98 Henan Institute of Science and Technology (HIST), Xinxiang, People’s Republic of China  
99 University of Virginia, Charlottesville, United States of America  
100 Dalian University of Technology (DLUT), Dalian, People’s Republic of China  
101 Universidade Federal do Rio Grande do Sul (UFRGS), Porto Alegre, Brazil  
102 Institut de Física Corpuscular—CSIC/Universitat de València, Paterna (Valencia), Spain  
103 University of Helsinki, Helsinki, Finland  
104 CPHT, CNRS, Ecole Polytechnique, I. P. Paris, France  
105 University Genova, Genova, Italy  
106 Istituto Nazionale di Fisica Nucleare (INFN)—Sezione di Genova, Genova, Italy  
107 Harish-Chandra Research Institute (HRI), Allahabad, India  
108 University of Southampton, Southampton, United Kingdom  
109 Universidade de São Paulo (USP), São Paulo, Brazil  
110 Nigde Omer Halisdemir University, Nigde, Turkey  
111 Universidad de los Andes, Carrera, Colombia  
112 The University of Alabama, Tuscaloosa, United States of America  
113 Tata Institute of Fundamental Research (TIFR), Mumbai, India  
114 Technische Universität Darmstadt, Darmstadt, Germany  
115 Homeday GmbH Berlin, Berlin, Germany  
116 Charles University, Prague, Czech Republic  
117 Istituto Nazionale di Fisica Nucleare (INFN)—Sezione di Bologna, Bologna, Italy  
118 Univ. Federal do Rio Grande do Norte, Natal, Brazil  
119 Karlsruher Institut für Technologie (KIT), Karlsruhe, Germany  
120 IBM Deutschland RnD, GmbH, Urbar, Germany  
121 Indian Institute of Science Education and Research (IISER), Kolkata, India  
122 University of Montenegro, Podgorica, Yugoslavia  
123 Shippensburg University of Pennsylvania, Shippensburg, PA, United States of America  
124 University of Delaware, Newark, United States of America  
125 Argonne National Laboratory, Argonne, United States of America  
126 Oracle, San Fransisco, United States of America

- <sup>127</sup> Applied AI Center of Excellence, San Francisco, United States of America  
<sup>128</sup> Usak University, Usak, Turkey  
<sup>129</sup> National University of Mar del Plata, Mar del Plata, Argentina  
<sup>130</sup> Oklahoma State University (OSU), Stillwater, United States of America  
<sup>131</sup> Peking University (PKU), Beijing, People's Republic of China  
<sup>132</sup> Institute of Mathematical Sciences (IMSc), Chennai, India  
<sup>133</sup> Jagiellonian University, Cracow, Poland  
<sup>134</sup> Anhui University (AHU), Hefei, People's Republic of China  
<sup>135</sup> Pennsylvania State University (PSU), University Park, United States of America  
<sup>136</sup> University of Sussex, Sussex, United Kingdom  
<sup>137</sup> Narodowe Centrum Badań Jądrowych (NCBJ), Warsaw, Poland  
<sup>138</sup> Kansas State University, Manhattan, United States of America  
<sup>139</sup> Korea Institute for Advanced Study (KIAS), Cheongryangri-dong, Republic of Korea  
<sup>140</sup> Kastamonu University, Kastamonu, Turkey  
<sup>141</sup> Københavns Universitet—Niels Bohr Institutet (NBI), Copenhagen, Denmark  
<sup>142</sup> University of Bergen, Bergen, Norway  
<sup>143</sup> Wuhan University of Technology, Wuhan, People's Republic of China  
<sup>144</sup> Asia Pacific Center for Theoretical Physics (APCTP), Pohang, Korea  
<sup>145</sup> University of California (UC), Riverside, United States of America  
<sup>146</sup> Hebrew University of Jerusalem—Racah Institute of Physics, Jerusalem, Israel  
<sup>147</sup> Universidad Pedagógica y Tecnológica de Colombia, Tunja, Colombia  
<sup>148</sup> Kobe University, Kobe, Japan  
<sup>149</sup> Lawrence Berkeley National Laboratory (LBNL), Berkeley, United States of America  
<sup>150</sup> University of Auckland, Auckland, New Zealand  
<sup>151</sup> Universität Rostock, Rostock, Germany  
<sup>152</sup> National Center for Theoretical Sciences (NCTS), Hsinchu, Taiwan  
<sup>153</sup> Nankai University (NKU), Tianjin, People's Republic of China  
<sup>154</sup> Karlsruher Institut für Technologie (KIT)—Institut für Theoretische Teilchenphysik (TTP), Karlsruhe, Germany  
<sup>155</sup> Karlsruher Institut für Technologie (KIT)—Institut für Kernphysik (IKP), Karlsruhe, Germany  
<sup>156</sup> Universität Regensburg, Regensburg, Germany

E-mail: [britzger@mpp.mpg.de](mailto:britzger@mpp.mpg.de), [oliver.bruning@cern.ch](mailto:oliver.bruning@cern.ch) and [mklein@hep.ph.liv.ac.uk](mailto:mklein@hep.ph.liv.ac.uk)

Received 15 October 2020, revised 4 December 2020

Accepted for publication 31 March 2021

Published 20 December 2021



CrossMark

### Abstract

The Large Hadron–Electron Collider (LHeC) is designed to move the field of deep inelastic scattering (DIS) to the energy and intensity frontier of particle physics. Exploiting energy-recovery technology, it collides a novel, intense electron beam with a proton or ion beam from the High-Luminosity Large Hadron Collider (HL-LHC). The accelerator and interaction region are designed for concurrent electron–proton and proton–proton operations. This

report represents an update to the LHeC's conceptual design report (CDR), published in 2012. It comprises new results on the parton structure of the proton and heavier nuclei, QCD dynamics, and electroweak and top-quark physics. It is shown how the LHeC will open a new chapter of nuclear particle physics by extending the accessible kinematic range of lepton–nucleus scattering by several orders of magnitude. Due to its enhanced luminosity and large energy and the cleanliness of the final hadronic states, the LHeC has a strong Higgs physics programme and its own discovery potential for new physics. Building on the 2012 CDR, this report contains a detailed updated design for the energy-recovery electron linac (ERL), including a new lattice, magnet and superconducting radio-frequency technology, and further components. Challenges of energy recovery are described, and the lower-energy, high-current, three-turn ERL facility, PERLE at Orsay, is presented, which uses the LHeC characteristics serving as a development facility for the design and operation of the LHeC. An updated detector design is presented corresponding to the acceptance, resolution, and calibration goals that arise from the Higgs and parton-density-function physics programmes. This paper also presents novel results for the Future Circular Collider in electron–hadron (FCC-eh) mode, which utilises the same ERL technology to further extend the reach of DIS to even higher centre-of-mass energies.

Keywords: deep-inelastic scattering, high-lumi LHC, QCD, Higgs, top and electroweak physics, nuclear physics, beyond Standard Model, energy-recovery-linac, accelerator physics

(Some figures may appear in colour only in the online journal)

## Contents

Preface	13
1. Introduction	15
1.1. The context	15
1.1.1. Particle physics—at the frontier of fundamental science	15
1.1.2. Deep inelastic scattering and HERA	16
1.2. This paper	17
1.2.1. The LHeC physics programme	17
1.2.2. The accelerator	20
1.2.3. PERLE	21
1.2.4. The detector	22
1.3. Outline	22
2. LHeC configuration and parameters	23
2.1. Introduction	23
2.2. Cost estimates, default configuration, and staging	24
2.3. Configuration parameters	25
2.4. Luminosity	26
2.4.1. Electron–proton collisions	27
2.4.2. Electron–ion collisions	29
2.5. Linac parameters	29

2.6. Operational schedule	30
3. Parton distributions—resolving the substructure of the proton	32
3.1. Introduction	32
3.1.1. Partons in deep inelastic scattering	32
3.1.2. Fit methodology and HERA PDFs	34
3.2. Simulated LHeC data	37
3.2.1. Inclusive neutral- and charged-current cross-sections	37
3.2.2. Heavy quark structure functions	40
3.3. Parton distributions from the LHeC	42
3.3.1. Procedure and assumptions	42
3.3.2. Valence quarks	44
3.3.3. Light sea quarks	46
3.3.4. Strange quark	47
3.3.5. Heavy quarks	50
3.3.6. The gluon PDF	52
3.3.7. Luminosity and beam-charge dependence of LHeC PDFs	54
3.3.8. Use of weak interactions to probe the proton structure	55
3.3.9. Parton–parton luminosities	60
3.4. The 3D structure of the proton	62
4. Exploration of quantum chromodynamics	69
4.1. Determination of the strong coupling constant	69
4.1.1. Strong coupling due to inclusive jet cross-sections	70
4.1.2. Pinning down $\alpha_s$ using inclusive and jet LHeC data	74
4.1.3. Strong coupling from other processes	78
4.2. Discovery of new strong interaction dynamics at small $x$	79
4.2.1. Resummation at small $x$	80
4.2.2. Disentangling nonlinear QCD dynamics at the LHeC	83
4.2.2.1. Analysis settings	83
4.2.2.2. Results and discussion	85
4.2.2.3. Summary	87
4.2.3. Small $x$ and the longitudinal structure function $F_L$	88
4.2.3.1. DIS cross-section and the challenge of accessing $F_L$	88
4.2.3.2. Parton evolution at low $x$	89
4.2.3.3. Kinematics of Higgs production at the HL-LHC	90
4.2.3.4. Indications for resummation in H1 $F_L$ data	91
4.2.3.5. The longitudinal structure function at the LHeC	91
4.2.4. Associated jet final states at low $x$	94
4.2.5. Relation to ultra-high-energy neutrino and astroparticle physics	95
4.3. Diffractive deep inelastic scattering at the LHeC	98
4.3.1. Introduction and formalism	98
4.3.2. Pseudodata for the reduced cross-section	104
4.3.3. Potential to constrain diffractive PDFs at the LHeC	105
4.3.4. Hadronic final states in diffraction and hard rapidity gap processes	107
4.4. Theoretical developments	109
4.4.1. Prospects for higher-order pQCD in DIS	109

4.4.2.	Theoretical concepts for the light cone	111
4.4.2.1.	Intrinsic heavy-quark phenomena	111
4.4.2.2.	Light-front holography and superconformal algebra	112
4.4.2.3.	Light-front holography and recent theoretical advances	112
4.4.2.4.	The QCD running coupling at all scales based on light-front holography	113
4.4.2.5.	Superconformal algebra and hadron physics with LHeC data	113
5.	Electroweak and top quark physics	114
5.1.	Electroweak physics with inclusive DIS data	115
5.1.1.	Electroweak effects in inclusive NC and CC DIS cross sections	115
5.1.2.	Methodology of a combined EW and QCD fit	117
5.1.3.	Weak boson masses $M_W$ and $M_Z$	117
5.1.4.	Further mass determinations	119
5.1.5.	Weak neutral-current couplings	120
5.1.6.	The neutral-current $\rho_{NC}$ and $\kappa_{NC}$ parameters	121
5.1.7.	The effective weak mixing angle $\sin^2 \theta_W^{\text{eff},\ell}$	122
5.1.8.	Electroweak effects in charged-current scattering	125
5.1.9.	Conclusions	125
5.2.	Direct $W$ and $Z$ production and anomalous triple gauge couplings	126
5.2.1.	Direct $W$ and $Z$ production	126
5.2.2.	Anomalous triple gauge couplings	127
5.3.	Top quark physics	130
5.3.1.	$Wtq$ couplings	130
5.3.2.	Top quark polarisation	132
5.3.3.	Top- $\gamma$ and top- $Z$ couplings	132
5.3.4.	Top-Higgs coupling	133
5.3.5.	Top quark PDF and the running of $\alpha_s$	134
5.3.6.	FCNC top quark couplings	134
5.3.7.	Summary of top quark physics	136
6.	Nuclear particle physics with electron-ion scattering at the LHeC	138
6.1.	Introduction	138
6.2.	Nuclear parton densities	140
6.2.1.	Pseudodata	141
6.2.2.	Nuclear gluon PDFs in a global-fit context	142
6.2.3.	nPDFs from DIS on a single nucleus	145
6.3.	Nuclear diffraction	149
6.3.1.	Exclusive vector meson diffraction	150
6.3.2.	Inclusive diffraction on nuclei	155
6.4.	New dynamics at small $x$ with nuclear targets	157
6.5.	Collective effects in dense environments—the ‘ridge’	159
6.6.	Novel QCD nuclear phenomena at the LHeC	159
7.	Higgs physics with the LHeC	162
7.1.	Introduction	162
7.2.	Higgs production in deep inelastic scattering	162



7.2.1.	Kinematics of Higgs production	163
7.2.2.	Cross-sections and rates	164
7.3.	Higgs signal-strength measurements	167
7.3.1.	Higgs decay into bottom and charm quarks	168
7.3.2.	Higgs decay into $WW$	174
7.3.3.	Accessing further decay channels	176
7.3.4.	Systematic and theoretical errors	177
7.4.	Higgs coupling analyses	179
7.5.	Measuring the top-quark–Higgs Yukawa coupling	182
7.6.	Higgs decay into invisible particles	185
8.	Searches for physics beyond the Standard Model	188
8.1.	Introduction	188
8.2.	Extensions of the SM Higgs sector	188
8.2.1.	Modifications of the top–Higgs interaction	189
8.2.2.	Charged scalars	189
8.2.3.	Neutral scalars	190
8.2.4.	Modifications of Higgs self-couplings	191
8.2.5.	Exotic Higgs boson decays	192
8.3.	Searches for supersymmetry	192
8.3.1.	Search for the SUSY electroweak sector: prompt signatures	193
8.3.2.	Search for the SUSY electroweak sector: long-lived particles	194
8.3.3.	Signatures that violate R-parity	195
8.4.	Feebly interacting particles	196
8.4.1.	Searches for heavy neutrinos	196
8.4.2.	Fermion triplets in a type-III seesaw	197
8.4.3.	Dark photons	198
8.4.4.	Axion-like particles	200
8.5.	Anomalous gauge couplings	201
8.5.1.	Radiation amplitude zero	202
8.6.	Theories with heavy resonance and contact interaction	202
8.6.1.	Leptoquarks	203
8.6.2.	$Z'$ -mediated charged-lepton-flavour violation	203
8.6.3.	Vector-like quarks	204
8.6.4.	Excited fermions ( $\nu^*$ , $e^*$ , and $u^*$ )	205
8.6.5.	Colour octet leptons	205
8.6.6.	Quark substructure and contact interactions	206
8.7.	Summary and conclusions	207
9.	Influence of the LHeC on physics at the HL-LHC	208
9.1.	Precision electroweak measurements at the HL-LHC	208
9.1.1.	The effective weak mixing angle	208
9.1.2.	The $W$ -boson mass	210
9.1.3.	Impact on electroweak precision tests	212
9.2.	Higgs physics	214
9.2.1.	Impact of LHeC data on Higgs cross-section predictions at the LHC	214

9.2.2.	Higgs couplings from a simultaneous analysis of pp and ep collision data	217
9.3.	Further precision SM measurements at the HL-LHC	219
9.4.	High-mass searches at the LHC	223
9.4.1.	Supersymmetric particles produced by the strong interaction	223
9.4.2.	Contact interactions	224
9.5.	PDFs, the HL-LHC, and the LHeC	225
9.5.1.	PDF prospects of the HL-LHC and the LHeC	225
9.5.2.	Parton luminosities at the HL-LHC	225
9.5.3.	PDF sensitivity: comparing the HL-LHC and the LHeC	226
9.6.	Impact of new small-x dynamics on hadron collider physics	227
9.7.	Heavy ion physics with eA input	229
10.	The electron-energy-recovery linac	233
10.1.	Introduction—design goals	233
10.2.	The ERL configuration of the LHeC	236
10.2.1.	Baseline design—lattice architecture	236
10.2.1.1.	Linac configuration and multipass optics	237
10.2.1.2.	Recirculating arc-emittance-preserving optics	238
10.2.1.3.	Spreaders and recombiners	240
10.2.1.4.	Alternative design of the spreader/recombiner	240
10.2.1.5.	IR bypasses	243
10.2.1.6.	Synchrotron radiation effects—emittance dilution	244
10.2.2.	30 GeV ERL options	247
10.2.3.	Component summary	248
10.3.	Electron–ion collisions	249
10.4.	Beam–beam interactions	250
10.4.1.	Effect on the electron beam	250
10.4.2.	Effect on the proton beam	252
10.5.	Arc magnets	252
10.5.1.	Dipole magnets	253
10.5.2.	Quadrupole magnets	253
10.5.2.1.	Quadrupoles for recirculator arcs	253
10.5.2.2.	Quadrupoles for the two 8.1 GeV linacs	254
10.6.	LINAC and superconducting RF system	254
10.6.1.	Choice of frequency	256
10.6.2.	Component summary	257
10.6.3.	Cavity cryomodule	259
10.6.4.	Electron sources and injectors	264
10.6.4.1.	Specification of the electron source	264
10.6.4.2.	The LHeC unpolarised injector	265
10.6.4.3.	Polarised electron source for ERL	266
10.6.4.4.	Lasers as electron sources	267
10.6.5.	Positrons	267
10.6.5.1.	Physics and intensity considerations	267
10.6.5.2.	Positron sources	269

10.6.5.3. Approaches for LHeC positrons	270
10.6.6. Compensation for synchrotron radiation losses	271
10.6.7. LINAC configuration and infrastructure	272
10.7. Interaction region	272
10.7.1. Layout	273
10.7.2. Proton optics	275
10.7.3. Electron optics	282
10.7.3.1. Improved electron lattice	285
10.7.4. Interaction-region magnet design	291
10.7.4.1. Triplet magnet design	291
10.7.4.2. Normal conducting magnet design	294
10.8. Civil engineering	294
10.8.1. Placement and geology	295
10.8.2. Underground infrastructure	296
10.8.3. Construction methods	298
10.8.4. Civil engineering for the FCC-eh	299
10.8.5. Cost estimates	301
10.8.6. Spoil management	301
11. The technology of ERL and PERLE	301
11.1. Energy-recovery linac technology—status and prospects	303
11.1.1. ERL applications	303
11.1.2. Challenges	303
11.1.2.1. Space charge	303
11.1.2.2. Beam breakup instability	304
11.1.2.3. Coherent synchrotron radiation	304
11.1.2.4. Microbunching instability	304
11.1.2.5. Halo	304
11.1.2.6. RF transients	305
11.1.2.7. Wakefields and the interaction of the beam with the environment	305
11.1.2.8. Multiturn, common transport	305
11.1.3. ERL landscape	306
11.2. The ERL facility, PERLE	307
11.2.1. Configuration	308
11.2.2. Importance of PERLE for the LHeC	308
11.2.3. PERLE layout and beam parameters	309
11.2.4. PERLE lattice	309
11.2.5. The site	311
11.2.6. Building PERLE in stages	312
11.2.7. Concluding remarks	313
12. Experimentation at the LHeC	313
12.1. Introduction	313
12.2. Overview of the main detector elements	316
12.3. Inner tracking	316
12.3.1. Overview and performance	317

12.3.2. Silicon technology choice	321
12.4. Calorimetry	323
12.5. Muon detector	326
12.6. Forward and backward detectors	328
12.6.1. Zero-degree (neutron) calorimeter	329
12.6.1.1. Physics requirement for forward neutron and $\pi^0$ production measurement	329
12.6.1.2. ZDC location	330
12.6.1.3. Radiation requirement for the ZDC	331
12.6.1.4. Possible calorimeter design	331
12.7. Detector installation and infrastructure	331
12.8. Detector design for a low-energy FCC-eh	336
13. Conclusions	337
Acknowledgments	340
Appendix A. Statement of the International Advisory Committee	340
A.1. Report by the IAC on the LHeC to the DG of CERN	341
A.2. Main developments 2014–2019	341
A.3. Mandate of the International Advisory Committee	342
A.4. Members of the Committee	343
Appendix B. Membership of coordination	343
B.1. Coordinating group	343
B.2. Physics convenors	343
References	344

## Preface

This paper represents the updated design study for the Large Hadron–Electron Collider (LHeC), a TeV-energy-scale electron–hadron (*eh*) collider which may come into operation during the third decade of the lifetime of the Large Hadron Collider (LHC) at the European Council for Nuclear Research (CERN). It is an account, accompanied by numerous papers in the literature, of many years of study and development, guided by an International Advisory Committee (IAC) which was charged by the CERN Directorate with advising on the direction of energy-frontier electron–hadron physics at CERN. At the end of 2019, the IAC summarised its observations and recommendations in a brief report to the Director General of CERN, which is reproduced here as an appendix.

This paper outlines a unique, far-reaching physics programme for the study of deep inelastic scattering (DIS), a design concept for a new generation collider–detector, together with a novel configuration of an intense, high-energy electron beam. This study builds on the previous, detailed LHeC conceptual design report (CDR), which was published eight years ago [1]. It surpasses the initial study in the following essential characteristics: (i) the depth of the physics programme, mainly owing to insights obtained using the LHC, and (ii) the expected luminosity, which will enable a novel Higgs facility to be built and the opportunity to search for and discover new physics to be strengthened. It builds on the recent and forthcoming progress in modern technology, due to major advances, in particular, in superconducting radio frequency (RF) technology and also in new detector techniques.

In contrast to the situation in 2012, a decision has now been taken to configure the LHeC in an electron linac–proton or nucleus–ring configuration, which leaves the ring–ring option [1, 2] as a backup. In the  $ep$  configuration, a high instantaneous luminosity of about  $10^{34} \text{ cm}^{-2} \text{ s}^{-1}$  may be achieved using an electron accelerator built as an energy-recovery linac (ERL) and also because the brightness of the LHC exceeds early expectations by far (not least because of the upgrade of the LHC to its high-luminosity version, the HL-LHC) [3, 4]. For  $e\text{Pb}$  collisions, the corresponding per-nucleon instantaneous luminosity would be about  $10^{33} \text{ cm}^{-2} \text{ s}^{-1}$ . The LHeC is designed to be compatible with concurrent operation with the LHC. It thus represents a unique opportunity to advance particle physics by building on the singular investments that CERN and its global partners have made in the LHC facility.

Since the 2012 document, significant experience with multiturn ERL design, construction, and operation has been gained with the CBETA accelerator (Cornell-Brookhaven ERL Test Accelerator), which has an accelerated and energy-recovered beam in all of its four turns [5, 6]. Extending far beyond the CDR, a configuration has recently been designed for a low-energy ERL facility, known as PERLE [7], which is moving ahead to construction at Orsay by an international collaboration. The major parameters of PERLE have been taken from the LHeC, such as the three-turn configuration, the source, the 801.58 MHz frequency, and the cavity-cryomodule technology, in order to make PERLE a suitable facility for the development of LHeC ERL technology and to accumulate operating experience prior to, and later, in parallel with, the LHeC. In addition, the PERLE facility has a striking low-energy physics programme and industrial applications and will be an enabler for ERL technology as the first facility to operate in the 10 MW power regime.

While the 2012 CDR focussed the physics discussion on the genuine physics of DIS far beyond those of the Hadron–Electron Ring Accelerator (HERA), a new focus arose through the challenges and opportunities posed by the HL-LHC. It has been demonstrated that DIS at the LHeC can play a crucial role in sustaining and enriching the LHC programme, which is a consequence of the results obtained at the LHC, i.e. the discovery of the Higgs boson, the non-observation of supersymmetry (SUSY) or other non-Standard Model (SM) exotic particles and, not least, the unexpected realisation of the huge potential of the LHC for discovery through precision measurements in the strong and electroweak sectors. Thus, it was felt that this is an appropriate time to summarise the last seven years of LHeC development, in support of the current discussions on the future of particle physics, especially at the energy frontier. For both the LHeC [8–10] and PERLE [11], documents have been submitted for consideration as part of the European Strategy for Particle Physics update.

The LHeC is a once-in-our-lifetime opportunity for substantial progress in particle physics. It comprises (with a linac shorter than the pioneering two-mile linac at SLAC) a most ambitious and exciting physics programme, the introduction of novel accelerator technology, and the complete exploitation of the unique values of, and spending on, the LHC. This work probably requires less courage than that of Pief Panofsky and colleagues half a century ago. Last but not least, one may consider the fact that the power the LHeC would have needed without the energy-recovery technique would have been beyond 1 GW if the electron beam were to be dumped at the injection energy. This is, therefore, a significant step towards green accelerator technology, a major general desire and a requirement of our times. This paper aims to substantiate these statements in the various following chapters.

Oliver Brüning (CERN) and Max Klein (University of Liverpool)

## 1. Introduction

### 1.1. The context

1.1.1. *Particle physics—at the frontier of fundamental science.* Despite its striking success, the Standard Model (SM) has been recognised to have major deficiencies. These may be summarised in various ways. Some major questions can be condensed, as follows:

- **Higgs boson.** Is the electroweak scale stabilised by new particles, interactions, and symmetries? Is the Higgs boson discovered in 2012 the Standard Model Higgs boson, and what is its potential? Do more Higgs bosons exist as predicted, for example, by supersymmetric theories?
- **Elementary particles.** The SM has 61 identified particles: 12 leptons, 36 quarks and anti-quarks, 12 mediators, and 1 Higgs boson. Are these too many or too few? Do right-handed neutrinos exist? Why are there three families? What makes leptons and quarks different? Do leptoquarks (LQs) exist, and is there a deeper substructure?
- **Strong interactions.** What are the true parton dynamics and structure inside the proton, inside other hadrons and inside nuclei—at different levels of resolution? How is confinement explained, and how do partons hadronise? How can the many-body dynamics of the quark-gluon plasma (QGP) state be described in terms of the elementary fields of quantum chromodynamics (QCD)? What is the meaning of the anti-de Sitter/conformal field theory (AdS/CFT) correspondence and of supersymmetry in strong interactions? Do axions, odderons, and instantons exist?
- **Grand Unified Theory (GUT).** Is there a genuine, grand unification of interactions at high-energy scales, and would this include gravitation? What is the correct value of the strong coupling constant? Is lattice theory correct in this respect? Is the proton stable?
- **Neutrinos.** Do Majorana or/and sterile neutrinos exist, and is there charge conjugation-parity (CP) violation in the neutrino sector?
- **Dark matter.** Is dark matter composed of elementary particles or has it another origin? Do hidden or dark sectors exist in nature, and would they be accessible to accelerator experiments?

These and other open problems are known, and they have been persistent questions in particle physics. They are intimately related, and any future strategic programme should not be confined to only one or a few of these. The field of particle physics is far from being understood, despite the phenomenological success of the  $SU_L(2) \times U(1) \times SU_c(3)$  gauge field theory known as the SM. Certain attempts to declare its demise not only contradict the experience gained from a series of past revolutions in science, but are indeed contrary to the incomplete status of particle physics as sketched above. The question is not why to end particle physics but how to proceed. The answer is not hidden in philosophy, but requires new, better, and affordable experiments. Indeed, the situation is unique, as expressed by Guido Altarelli a few years ago: *it is now less unconceivable that no new physics will show up at the LHC... We expected complexity and instead we have found a maximum of simplicity. The possibility that the Standard Model holds well beyond the electroweak scale must now be seriously considered* [12]. This is reminiscent of the time before 1969, prior to anything like a SM, when gauge theory was just for theorists, while a series of new accelerators, such as the two-mile electron linac at Stanford or the Super Proton Synchrotron (SPS) at CERN, were planned, which resulted in a complete change of the paradigm of particle physics.

Ingenious theoretical hypotheses, such as those for the existence of extra dimensions, for SUSY, un-particles, or the embedding in higher gauge groups such as E8, are a strong motivation to rigorously develop high-energy physics further. In this endeavour, a substantial increase in precision, the conservation of diversity of projects, and an extension of kinematic coverage are necessities, and will most likely turn out to be of fundamental importance. The strategic question in this context, therefore, is not just which new collider should be built next, as one often hears, but how we may best challenge the current and incomplete knowledge. A realistic step to progress comprises a new  $e^+e^-$  collider, perhaps built in Asia, and complementing the LHC with an electron ERL to synchronously provide  $ep$  and  $pp$  collisions at the LHC, the topic of this paper.

One may call these machines first-technology generation colliders, as their technology has been proven to basically work [13]. Beyond the present time, there is a long-term future reaching to the year 2050 and far beyond, for a second, further generation of hadron, lepton, and electron–hadron colliders. CERN has recently published a design study for a Future Circular  $hh$ ,  $eh$  and  $e^+e^-$  Collider (FCC) complex [14–16], which would provide a corresponding basis. For electron–hadron scattering, this study opens a new horizon with the FCC-eh, a  $\sim 3$  TeV centre-of-mass system (cms) energy collider which is also considered in this paper, mostly for comparison with the LHeC. A proposal similar to that of the FCC is also being developed in China [17, 18].

A new collider for CERN at the  $\mathcal{O}(10^{10})$  CHF level of cost should have the potential to change the paradigm of particle physics with direct, high-energy discoveries in the 10 TeV mass range. This may only be achieved if the FCC-hh includes an  $eh$  experiment. The FCC-hh/eh complex allows access to physics at several hundred TeV, assisted by a qualitatively new level of QCD/DIS. A prime, very fundamental goal of the FCC-pp is the clarification of the Higgs vacuum potential. This collider therefore has an overriding justification beyond the unknown prospects of finding new physics, which is nowadays called ‘exotics’. It accesses rare Higgs boson decays, high energy scales and, when combined with  $ep$ , it measures the SM Higgs couplings to a precision of less than one percent. There is a huge, fundamental programme of electroweak and strong interactions, flavour, and heavy ions for FCC-hh to explore. This represents CERN’s unique opportunity to build on the ongoing LHC programme for many decades ahead. The size of the FCC-hh requires this to be established as a global enterprise. The HL-LHC and the LHeC can be understood as very important steps towards this major new facility, both in terms of physics and technology. This report outlines a roadmap for realising a next-generation energy-frontier electron–hadron collider as part of this programme, which would maximally exploit and support the LHC.

*1.1.2. Deep inelastic scattering and HERA.* The field of deep inelastic lepton–hadron scattering (DIS) [19] was born with the discovery [20, 21] of partons [22, 23] about 50 years ago. It readily contributed fundamental insights, for example, to the development of QCD, by confirming fractional quark charges and asymptotic freedom, and by the spectacular finding that the weak isospin charge of the right-handed electron was zero [24] which established the Glashow–Weinberg–Salam ‘Model of Leptons’ [25] as the basis of the united electroweak theory. The quest to reach higher energies in accelerator-based particle physics led to generations of colliders, of which HERA [26] is, so far, the only electron–proton example.

HERA collided electrons (and positrons) with energies of  $E_e = 27.6$  GeV on protons with energies of  $E_p = 920$  GeV, achieving a centre-of-mass energy  $\sqrt{s} = 2\sqrt{E_e E_p}$  of about 0.3 TeV. It therefore extended the kinematic range covered by fixed-target experiments by two orders of magnitude in Bjorken  $x$  and in four-momentum transfer squared,  $Q^2$ , with its limit  $Q_{\max}^2 = s$ .



HERA was built in less than a decade, and it operated for 16 years. Together with the Tevatron and the Large Electron–Positron (LEP) collider, HERA was pivotal to the development of the Standard Model.

HERA had a unique collider physics programme and success [27]. It established QCD as the correct description of proton substructure and parton dynamics down to  $10^{-19}$  m. It demonstrated that electroweak theory holds in the newly accessed range, especially by the measurement of neutral and charged current (CC)  $ep$  scattering cross-sections beyond  $Q^2 \sim M_{W,Z}^2$  and the proof of electroweak interference at high scales through the measurement of the interference structure functions  $F_2^{\gamma Z}$  and  $xF_3^{\gamma Z}$ . The HERA collider has provided the core basis of the physics of parton distributions, not only by determining the gluon, valence, light and heavy sea quark momentum distributions over a significantly extended range, but also by supporting the foundation of the theory of unintegrated, diffractive, photon and neutron parton distribution functions (PDFs) through a series of corresponding measurements. It discovered the rise of the parton distributions towards small momentum fractions,  $x$ , supporting early QCD expectations about the asymptotic behaviour of the structure functions [28]. Like the Tevatron, the LEP, and the Stanford Linear Collider (SLC), which explored Fermi-scale energies of a few hundred GeV, determined by the vacuum expectation value of the Higgs field,  $v = 1/\sqrt{\sqrt{2}G_F} = 2M_W/g \simeq 246$  GeV, HERA also showed that no supersymmetric or other exotic particle with reasonable couplings exists at the Fermi energy scale.

HERA established electron–proton scattering as an integral part of modern high-energy particle physics. It demonstrated the richness of DIS physics, and the feasibility of constructing and operating energy-frontier  $ep$  colliders. What did we learn that can be used in the next, higher-energy  $ep$  collider design? Perhaps there arose three lessons about:

- *The need for higher energy*, for three reasons: (i) to make CCs a real, precision part of  $ep$  physics, for instance, for the complete unfolding of the flavour composition of the sea and valence quarks; (ii) to produce more massive particles (Higgs, top, exotics) with favourable cross-sections, and (iii) to discover or disprove the existence of gluon saturation, for which one needs to measure at a lower  $x \propto Q^2/s$ , i.e. a higher  $s$  than HERA had available;
- *The need for much higher luminosity*: for almost the first ten years, HERA provided just a hundred  $\text{pb}^{-1}$ . As a consequence, HERA could not accurately access the high- $x$  region, and it was inefficient and lacked statistics with which to resolve puzzling event fluctuations;
- *The complexity of the interaction region* that occurred when a bent electron beam caused synchrotron radiation, while an opposing proton beam generated a significant halo background through beam–gas and beam–wall proton–ion interactions.

Based on these and further lessons, a first LHeC paper was published in 2006 [29]. The LHeC design was then intensely developed, and a comprehensive CDR appeared in 2012 [1]. This has now been pursued much further, while still recognising that the LHC is the only existing base that can realise a TeV energy scale electron–hadron collider in the accessible future. It offers highly energetic, intense hadron beams, a long-term perspective, and a unique infrastructure and expertise, i.e. everything required for an innovative energy-frontier DIS physics and accelerator programme.

## 1.2. This paper

**1.2.1. The LHeC physics programme.** This paper presents a design concept for the LHeC, using a 50 GeV electron beam to be scattered off by the LHC hadron beams (proton and ion)

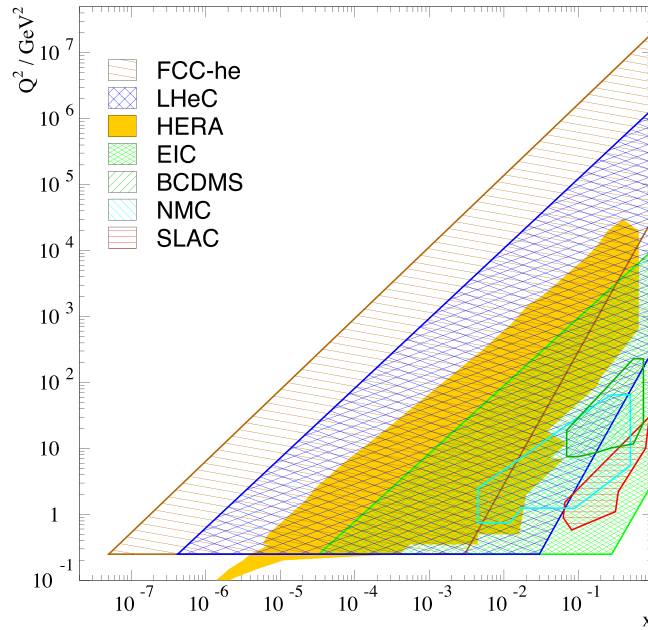


**Figure 1.** Coverage of the kinematic plane in deep inelastic lepton–proton scattering by some initial fixed-target experiments using electrons (SLAC) and muons (NMC and BCDMS experiments), and by the  $ep$  colliders: the Electron–Ion Collider (EIC) (green), HERA (yellow), the LHeC (blue) and the FCC-he (brown). Here, the low  $Q^2$  region for the colliders is limited to about  $0.2 \text{ GeV}^2$ , which is roughly covered by the central detectors, and perhaps using low-energy electron-beam data. Electron taggers may extend this to even lower values of  $Q^2$ . The high  $Q^2$  limit at fixed  $x$  is given by the line of inelasticity  $y = 1$ . Approximate limitations of acceptance at medium  $x$  and low  $Q^2$  are illustrated using polar-angle limits of  $\eta = -\ln \tan \theta/2$  of 4, 5, 6 for the EIC, LHeC, and FCC-he, respectively. These lines are given by  $x = \exp \eta \cdot \sqrt{Q^2}/(2E_p)$ , and can be moved to larger  $x$  when  $E_p$  is reduced to less than the nominal values.

in a concurrent operating mode<sup>157</sup>. Its main characteristics are presented in section 2. The instantaneous luminosity is designed to be  $10^{34} \text{ cm}^{-2} \text{ s}^{-1}$ , exceeding that of HERA (which achieved a few times  $10^{31} \text{ cm}^{-2} \text{ s}^{-1}$ ) by a factor of several hundred. The kinematic range is nominally extended by a factor of about 15, but in fact, by a larger amount, because of the hugely increased luminosity which is available for exploring the maximum  $Q^2$  and large  $x \leq 1$  regions, which were major deficiencies at HERA. The coverage of the  $Q^2, x$  plane available to previous and future DIS experiments is illustrated in figure 1.

The LHeC will provide a major extension of the DIS kinematic range, as required by the physics programme at the energy frontier. For the LHC, the  $ep/A$  detector would be a substantial new experiment, allowing a number of significant themes to be explored, with significant

<sup>157</sup> In 2012, the CDR used 60 GeV of beam energy. Recent considerations of cost, effort, and synchrotron radiation effects led to a preference for a small reduction in the energy. Various physics studies presented here still used 60 GeV. While high energy is indeed important for BSM, top, and Higgs physics, the basic conclusions remain valid even if the eventual energy choice is somewhat smaller than that previously considered. This is discussed further below. A decision on the energy would clearly be accompanied by approval.

discovery potential. These are presented in quite some detail in the seven chapters of this paper dedicated to physics:

- Based on the unique hadron beams of the LHC and employing a point-like probe, the LHeC would represent the world's cleanest high-resolution microscope for exploring the substructure of, and dynamics inside, matter, which may be dubbed 'the Hubble telescope for the smallest dimensions'. The first chapter on physics, section 3, is devoted to the measurement of parton distributions using the LHeC; it also presents the potential for resolving the proton structure in 3D.
- Section 4 is devoted to a deep exploration of QCD. A key deliverable of the LHeC is the clarification of the parton interaction dynamics at small Bjorken  $x$ , in the new regime of very high parton densities but small couplings, which HERA discovered, but was unable to clarify because its energy was limited. It is first shown that the LHeC can measure  $\alpha_s$  to per-mille accuracy, followed by various studies that illustrate the unique potential of the LHeC for pinning down the dynamics at small  $x$ . This chapter also covers the seminal potential for diffractive DIS to be developed. It concludes with brief presentations of the theoretical developments in perturbative QCD (pQCD) and of the novel physics on the light cone.
- The maximum  $Q^2$  exceeds the  $Z$  and  $W$  boson mass values (squared) by two orders of magnitude. The LHeC, supported by variations of beam parameters and high luminosity, thus offers a unique potential to test the electroweak SM in the spacelike region with unprecedented precision. The high  $ep$  cms energy will lead to the copious production of single top-quarks, about  $2 \times 10^6$  single top and  $5 \times 10^4$   $t\bar{t}$  events. Top-quark production could not be observed at HERA but will thus become a central theme of precision and discovery physics for the LHeC. In particular, the top-quark momentum fraction inside the proton, and the top-quark couplings to the photon or the  $W$  boson, and possible flavour-changing neutral current (FCNC) interactions can be studied in a uniquely clean environment (section 5).
- In lepton-nucleus collision mode, the LHeC extends the kinematic range of eA scattering by nearly four orders of magnitude compared to existing fixed target data. It will thus completely transform nuclear particle physics by resolving the hitherto hidden parton dynamics and substructure in nuclei and clarifying the QCD basis for the collective dynamics observed in QGP phenomena (section 6).
- The clean DIS final state in neutral and CC scattering and the high integrated luminosity will enable a high-precision Higgs physics programme to take place at the LHeC. The Higgs production cross-section is comparable to that of Higgs-strahlung at  $e^+e^-$ . This opens the extra possibility of independently testing the Higgs sector of the SM, in particular, with high-precision insight into the  $H-WW/ZZ$  and  $H-bb/cc$  couplings (section 7).
- As a new, unique, luminous TeV-scale collider, the LHeC offers an outstanding opportunity to discover new physics, such as in the exotic Higgs, dark matter, heavy neutrino, and QCD areas (section 8).
- With concurrent  $ep$  and  $pp$  operation, the LHeC will transform the LHC into a three-beam twin collider of greatly improved potential, as outlined in section 9. Through ultra-precise strong and electroweak measurements, the  $ep$  experiment will make the HL-LHC complex a much more powerful search and measurement laboratory than the current facility based on  $pp$  only. The joint  $pp/ep$  LHC facility, together with a novel  $e^+e^-$  collider, will represent a major step forward in the study of the SM Higgs boson, leading far beyond the

HL-LHC. The combination of  $pp$  and  $ep$  results, as illustrated for PDFs, will lead to new insights, especially compared to its single  $pp$  and  $ep$  components.

The development of particle physics, the future of CERN, the exploitation of the singular LHC investments, and the culture of accelerator art, all make the LHeC a unique project of great interest. It is challenging in terms of technology, affordable given budgetary constraints, and it may still be realised in the two decades of the currently projected LHC lifetime.

**1.2.2. The accelerator.** The LHeC provides an intense, high-energy electron beam for use in collisions with the LHC beam. It represents the highest-energy application of ERL technology, which is increasingly recognised as one of the major pilot technologies for the development of particle physics, because it utilises and stimulates superconducting RF technology progress and increases intensity, while keeping the power consumption low.

The LHeC's instantaneous luminosity is determined by the integrated luminosity goal of  $\mathcal{O}(1) \text{ ab}^{-1}$ , due to various physics reasons. The electron beam energy is chosen to achieve collision energies of the order of TeV cms, enabling competitive searches and precision Higgs boson measurements. A cost–physics–energy evaluation is presented here, which points to the choice of  $E_e \simeq 50 \text{ GeV}$  as the new default value, which was previously 60 GeV [1]. The wall-plug power has been constrained to 100 MW. Two superconducting linacs about 900 m long, which are placed opposite to each other, accelerate passing electrons by 8.3 GeV each. This leads to a final electron-beam energy of about 50 GeV in a three-turn racetrack ERL configuration.

To measure at very low  $Q^2$  and determine the longitudinal structure function  $F_L$  (see below), the electron-beam energy may be reduced to a minimum of about 10 GeV. To maximise the acceptance at large Bjorken  $x$ , the proton-beam energy  $E_p$  may be reduced to 1 TeV. This determines a minimum cms energy of 200 GeV, less than HERA's 319 GeV. If the ERL were to be combined in the more distant future with the double-energy High-Energy LHC (HE-LHC) [30], the proton-beam energy  $E_p$  could reach 14 TeV and the cms energy could be increased to 1.7 TeV. This is extended to 3.5 TeV for the FCC-eh, which has a 50 TeV proton energy beam. We thus have a unique, exciting prospect for future DIS  $ep$  scattering at CERN, with energies covering a range from less than HERA's energy to the few TeV region, at hugely increased luminosity, and based on much more sophisticated experimental techniques than those available at the time of HERA.

A spectacular extension of the kinematic range is expected for deep inelastic lepton–nucleus scattering, which was not pursued at HERA. Currently, the highest-energy lepton–nucleus collision data are obtained from fixed-target muon–nucleus experiments, such as the NMC and COMPASS experiments, with a maximum cms energy of about 20 GeV, which permits a maximum  $Q^2$  of 400 GeV<sup>2</sup>. This will be extended by the EIC at Brookhaven National Laboratory (BNL) to about  $10^4 \text{ GeV}^2$ . The corresponding numbers for  $e\text{Pb}$  scattering at the LHeC and FCC-eh are  $\sqrt{s} \simeq 0.74 \text{ (2.2) TeV}$  and  $Q_{\text{max}}^2 = 0.54 \text{ (4.6)} \times 10^6 \text{ GeV}^2$ , respectively. The kinematic range in  $eA$  scattering will thus be extended through the LHeC (FCC-eh) by three (four) orders of magnitude, compared to the current status. This will thoroughly alter the understanding of parton and collective dynamics inside nuclei.

The ERL beam configuration is located inside the LHC ring but outside its tunnel, which minimises any interference with the main hadron beam infrastructure. The electron accelerator may thus be built in a way that is mostly independent of the operational status of the proton machine. The length of the ERL has a configuration that is a fraction  $1/n$  of the LHC's circumference, as required for the  $e$  and  $p$  matching of bunch patterns. Here, the return arcs count as two single half rings. The chosen electron-beam energy of 50 GeV leads, for  $n = 5$ , to a

circumference  $U$  of 5.4 km for the electron racetrack<sup>158</sup>. A three-pass ERL configuration was also adopted for the FCC-eh, although it maintained the original 60 GeV as the default, leading to a 9 km circumference.

For the LHC, the ERL will be tangential to IP2. According to current plans, IP2 is allocated to the ALICE experiment detector with a programme extending up until LS4, the first long shutdown following the three-year pause of the LHC operation for the upgrade of the luminosity performance and detectors. There are plans for a new heavy-ion detector to move into IP2. The LS4 shutdown is currently scheduled to begin in 2031, with a certain likelihood of being postponed to 2032 or later, as recent events appear to have delayed the start of Long Shutdown 3 (LS3) and extended its duration to three years.

For FCC-eh the preferred position is interaction point  $L$ , mostly for geological reasons, and the time of operation fully depends on the progress of FCC-hh, beginning at the earliest in the late 2040s if CERN starts construction of the hadron collider directly after the LHC.

The LHeC operation is transparent to LHC collider experiments owing to the low lepton bunch charge and resulting small beam–beam tune shift experienced by the protons. The LHeC is thus designed to run simultaneously with  $pp$  (or  $pA$  or  $AA$ ) collisions with a dedicated final operation over a few years.

This paper presents the design of the LHeC in considerable detail (section 10), i.e. the optics and lattice, components, magnets, as well as the designs of the linac and interaction regions along with special topics, such as the prospects for electron–ion scattering, positron–proton operation and a novel study of beam–beam interaction effects. With the more ambitious luminosity goal, a new lattice adapted to 50 GeV, with progress on the IR design, a novel analysis of the civil engineering works and especially, the production and successful test [31] of the first SC cavity at the newly chosen default frequency of 801.58 MHz, this report extends considerably beyond the initial CDR. This holds especially since several LHeC institutes have recently embarked on the development of ERL technology with a low energy facility, PERLE, to be built at the Irène Joliot-Curie (IJC) Laboratory at Orsay.

**1.2.3. PERLE.** Great progress has been made in the development of superconducting, high-gradient cavities with quality factors,  $Q_0$ , beyond  $10^{10}$ . This will enable the exploitation of ERLs in high-energy physics colliders, of which the LHeC is a prime example, while proposals have also been made for future  $e^+e^-$  colliders [32, 33] and for proton-beam cooling with an ERL tangential to eRHIC. The status and challenges of ERLs are summarised in section 11, which also presents the design, status, and prospects for the ERL development facility PERLE. The major parameters of PERLE have been taken from the LHeC, such as the three-turn configuration, source, frequency and cavity-cryomodule technology, in order to make PERLE a suitable facility for the development of LHeC ERL technology and to accumulate operational experience prior to, and later in parallel with, the LHeC.

An international collaboration has been established to build PERLE at Orsay. With design goals of 500 MeV of electron energy obtained in three passes through two cryomodes, and of 20 mA, corresponding to a 500 nC charge at a 40 MHz bunch frequency, PERLE is set to become the first ERL facility to operate at a power of 10 MW. Following its CDR [7] and the submission of a paper for the European strategy [11], work has started on the construction of a first dressed cavity and to release a technical design report (TDR) by 2021/22. Besides its value to accelerator and ERL technology, PERLE is also of importance for pursuing a low-energy physics programme, see [7], and for several possible industrial applications. It also serves as

<sup>158</sup> The circumference may eventually be chosen may be 6.8 km, the length of the SPS, which would relax certain parameters and also facilitate a possible energy upgrade.



a local hub for the education of accelerator physicists at a place, previously called the Linear Accelerator Laboratory (LAL), which has long been at the forefront of accelerator design and operation.

There are a number of related ERL projects, as characterised in section 11. The realisation of the ERL for the LHeC at CERN represents a unique opportunity not only for physics and technology but also for the next and current generations of accelerator physicists, engineers, and technicians to realise an ambitious collider project while the plans for the subsequent very expensive machines take shape. Similarly, this holds for a new generation of detector experts. As the design for the upgrade of the general-purpose detectors (GPDs) at the LHC is reaching completion, questions are increasingly being posed about new opportunities for collider detector construction, so as not to lose the expertise nor the infrastructure for building trackers, calorimeters, and so on. The LHeC offers the opportunity for novel  $4\pi$  particle physics detector design, construction, and operation. As a linac–ring collider, it may require a detector smaller than the CMS experiment and larger than H1 and ZEUS.

*1.2.4. The detector.* Section 12, on the topic of the detector, relies to a large extent on the very detailed write-up of the kinematics, design considerations, and realisation of a detector for the LHeC presented in the CDR [1]. In the previous report, one can find detailed studies not only of the central detector and its magnets, a central solenoid for momentum measurements, and an extended dipole for ensuring head-on  $ep$  collisions, but also of the forward ( $p$  and  $n$ ) and backward ( $e$  and  $\gamma$ ) tagging devices. The work on the detector presented here was focussed on the optimisation of the performance and on the scaling of the design towards higher proton-beam energies. It presents a new, consistent design and summaries of the essential characteristics in support of the many physics analyses that this paper entails.

The most demanding performance requirements arise from the  $ep$  Higgs measurement programme, in particular, the large acceptance and high precision desirable for heavy flavour (HF) tagging and the requirement to resolve the hadronic final state. This has been influenced by both the rapidity acceptance extensions and the technology progress of the HL-LHC detector upgrades. A key example, also discussed, is high-voltage CMOS (HV-CMOS) silicon technology, for which the LHeC is an ideal application due to the very limited radiation level as compared to that of  $pp$  colliders.

Therefore, we have now completed two design studies: previously, a design for a rather conventional detector with limited cost, and here, for a more ambitious device. Both of these designs appear feasible, which is also true for the installation. This paper presents a brief description of the installation of the LHeC detector at IP2, with the intention that it may proceed within two years, including the dismantling of the the resident detector. This calls for modularity and the pre-mounting of detector elements on the surface, as was also done for CMS. The LHeC detector collaboration, to be established with the approval of the project, will eventually refine the design of the detector according to its understanding and technical capabilities.

### 1.3. Outline

This paper is organised as follows. To provide a brief overview, section 2 summarises the LHeC characteristics. Section 3 presents the physics of the LHeC as seen as a microscope for measuring PDFs and exploring the 3D structure of the proton. Section 4 describes further means of exploring QCD, especially low- $x$  dynamics, together with two sections on QCD theory developments. Section 5 describes the electroweak and top-quark physics potential of the LHeC. Section 6 presents the seminal nuclear particle physics potential of the LHeC due to

luminous electron–ion scattering, exploring a hitherto unexplored kinematic territory. Section 7 presents a detailed analysis of the opportunity to examine precision SM Higgs boson physics with charged and neutral current (NC)  $ep$  scattering. Section 8 is a description of the salient opportunities to discover physics beyond the SM with the LHeC, including non-SM Higgs physics, right-handed neutrinos, physics of the dark sector, heavy resonances, and exotic substructure phenomena. Section 9 describes the interplay of  $ep$  and  $pp$  physics, i.e. the necessity to have the LHeC to fully exploit the potential of the LHC facility, e.g. through the large increase of electroweak precision measurements, the considerable extension of search ranges, and the joint  $ep$  and  $pp$  Higgs physics potential. Section 10 presents an update of the design of the electron accelerator, with many novel results, such as those for the lattice and interaction region, updated parameters for  $ep$  and  $eA$  scattering, new specifications of components, updates to the electron source, and so on. This chapter also presents the encouraging results for the first LHeC 801.58 MHz cavity. Section 11 is first devoted to the status and challenges of energy-recovery-based accelerators, and second, to a description of the PERLE facility between its CDR and a forthcoming TDR. Section 12 provides an update on the detector studies working towards an optimum configuration in terms of acceptance and performance. Section 13 presents a summary of this paper, including a timeline for realising the LHeC to operate with the LHC. An appendix presents the statement of the International Advisory Committee on its evaluation of the project, together with recommendations about how to proceed. It also contains an account of the members of the LHeC organisation, i.e. the coordination group and finally the list of physics working group convenors.

## 2. LHeC configuration and parameters

### 2.1. Introduction

The CDR of the LHeC was published in 2012 [1]. The default CDR configuration uses a 60 GeV electron beam derived from a racetrack, three-turn, intense ERL achieving a cms energy of  $\sqrt{s} = 1.3$  TeV, where  $s = 4E_p E_e$  is determined by the electron and proton beam energies,  $E_e$  and  $E_p$ . In 2012, the Higgs boson,  $H$ , was discovered, which has become a central topic of current and future high-energy physics. The Higgs production cross-section in charged current (CC) deep inelastic scattering (DIS) at the LHeC is roughly 100 fb. So far, the Large Hadron Collider has not led to the discovery of any exotic phenomena. This makes it necessary to pursue  $pp$  and also  $ep$  searches with the highest achievable precision, in order to access the maximum range of phase space and possibly rare channels. The DIS cross-section at large values of  $x$  behaves roughly according to  $(1-x)^3/Q^4$ , demanding very high luminosities to explore the unknown regions of Bjorken  $x$  near 1 and very high  $Q^2$ , the negative four-momentum transfer squared between the electron and the proton. For the current update of the LHeC design, this has set a luminosity goal about an order of magnitude higher than the  $10^{33} \text{ cm}^{-2} \text{ s}^{-1}$  that was adopted for the CDR. As a result, the potential arises, as described subsequently in this paper, to transform the LHC into a high-precision electroweak, Higgs, and top-quark physics facility.

The  $ep$  Higgs production cross-section approximately increases with  $E_e$ . New physics may be related to the heaviest known elementary particle, i.e. the top quark, the  $ep$  production cross-section of which increases more than linearly with  $E_e$  in the LHeC kinematic range, since that range is not very far from the  $t\bar{t}$  threshold. Searches for heavy neutrinos, SUSY particles, etc., are more promising at higher energies. The region of DIS and pQCD requires that  $Q^2$  be larger than  $M_p^2 \simeq 1 \text{ GeV}^2$ . DIS access to very low Bjorken  $x$  requires high energies because  $x = Q^2/s$ ; for inelasticity,  $y = 1$ . In DIS, one needs  $Q^2 > M_p^2 \simeq 1 \text{ GeV}^2$ . Physics therefore



requires a maximally large energy. However, cost and effort impose realistic limits, such that doubling the HERA electron beam energy of about 27 GeV appears to yield a reasonable and affordable target value.

In the CDR [1] the default electron energy chosen was 60 GeV. This can be achieved with an ERL circumference of 1/3 of that of the LHC. Recently, the cost was estimated in quite some detail [34] and also compared with the costs of other accelerator projects. Aiming at cost optimisation and providing an option for staged installation, the cost estimate led to the definition of a new default configuration of  $E_e = 50$  GeV, with the option of starting in an initial phase with a beam energy of  $E_e = 30$  GeV and a circumference of 5.4 km, which is 1/5 of the LHC length. Reducing  $E_e$  is also advantageous for mastering the synchrotron radiation challenges in the interaction region. Naturally, the  $E_e$  decision has not been taken yet. This paper comprises studies with different energy configurations, mainly  $E_e = 50$  and  $E_e = 60$  GeV, which have similar centre-of-mass energy values of 1.2 and 1.3 TeV, respectively.

At beam energies of up to about 60 GeV, the ERL cost is dominated by the cost of the superconducting RF technology of the linacs, which scales approximately linearly with the beam energy. Above this energy the return arcs represent the main contribution to the cost and are no longer linear with the ERL cost scaling. Given the nonlinear dependence of the cost on  $E_e$  for energies larger than about 60 GeV, significantly larger electron-beam energy values could only be justified by overriding arguments, such as the existence of leptoquarks (LQs)<sup>159</sup>. Higher values of  $\sqrt{s}$  are also provided with enlarged proton beam energies by the high-energy LHC ( $E_p = 13.5$  TeV) [30] and the FCC-hh [16] with  $E_p$  values between 20 and possibly 75 TeV, depending on the dipole magnet technology.

## 2.2. Cost estimates, default configuration, and staging

In 2018 a detailed cost estimate was carried out [34], following the guidance and practice of CERN accelerator studies. The assumptions were also compared with the cost of the European XFEL at DESY. The result was that for the 60 GeV configuration, about half of the total cost was due to the two superconducting (SC) linacs. The cost of the arcs decreases more than linearly with decreasing energy, at about  $\propto E^4$  for synchrotron radiation losses and  $\propto E^3$  when emittance dilution must be avoided [35]. It was therefore considered that a new default of 50 GeV should be set, with a circumference of 1/5 of that of the LHC, see section 2.3, compared to 1/3 for 60 GeV. Furthermore, an initial phase at 30 GeV was considered within the 1/5 configuration, but with only partially equipped linacs. The HERA electron beam energy was 27 GeV. The main results, taken from [34], are reproduced in table 1.

The choice of 50 GeV at 1/5 of the LHC circumference, as displayed, has a total cost of 1075 MCHF for the initial 30 GeV configuration, and an additional upgrade cost to 50 GeV of 296 MCHF. If one restricted the LHeC to a non-upgradeable 30 GeV-only configuration, one would, still in a triple-racetrack configuration, arrive at a roughly 1 km-long structure with two linacs about 500 m long, probably in a single-linac-tunnel configuration. The cost of this version of the LHeC is roughly 800 MCHF, i.e. about half the estimated cost of the 60 GeV option. However, this would essentially reduce the LHeC to a QCD and electroweak machine,

<sup>159</sup> If these existed with a mass of, say  $M = 1.5$  TeV, this would require (for the LHC with  $E_p = 7$  TeV) that  $E_e$  is larger than 90 GeV, and the associated funding. LQs would be produced by  $ep$  fusion and appear as resonances, much like the  $Z$  boson in  $e^+e^-$  and would therefore fix  $E_e$  (given a certain  $E_p$ , which exceeds 7 TeV at the FCC). The genuine DIS kinematics, however, is spacelike, with a negative exchanged four-momentum squared  $q^2 = -Q^2$ , which implies that the choice of energies is less constrained than in an  $e^+e^-$  collider that is intended for the study of the  $Z$  or  $H$  bosons.

**Table 1.** Summary of cost estimates, in millions of Swiss francs (MCHF). Reproduced with permission from [34]. The 60 GeV configuration is built with a 9 km triple racetrack configuration, as described in the CDR [1]. It is taken as the default configuration for the FCC-eh, with an additional civil engineering cost of 40 MCHF due to the larger depth at point  $L$  (FCC) as compared to IP2 (LHC). Both the 30 and the 50 GeV options assume a 5.4 km configuration, i.e. the 30 GeV option is assumed to be the first stage of the LHeC and upgradeable to 50 GeV ERL. Whenever a choice was to be made on estimates, the conservative number was chosen in [34].

Component	CDR 2012 (60 GeV)	Stage 1 (30 GeV)	Default (50 GeV)
Superconducting radio-frequency (SRF) system	805	402	670
SRF research and development (R+D) and prototyping	31	31	31
Injector	40	40	40
Arc magnets and vacuum	215	103	103
SC interaction region (IR) magnets	105	105	105
Source and dump system	5	5	5
Cryogenic infrastructure	100	41	69
General infrastructure and installation	69	58	58
Civil engineering	386	289	289
<b>Total cost</b>	<b>1756</b>	<b>1075</b>	<b>1371</b>

still very powerful, but requiring substantial losses from its Higgs, top, and beyond the standard model (BSM) programmes.

A detailed study was made of the cost of the civil engineering, which is also discussed subsequently. This included a comparison between the 1/3 and 1/5 LHC circumference versions and the FCC-eh. The results are illustrated in figure 2. They show that the civil engineering cost for the 1/5 version is about a quarter of the total cost. The reduction from 1/3 to 1/5 saves about 100 MCHF.

The choice of the final energy will be made later. It depends not only on a budget but also on the future development of particle physics at large. For example, it may turn out that for some years into the future, the community may not acquire funding of the order of several tens of billion Swiss francs required to build any of the  $e^+e^-$  colliders currently considered. In this case, the only way to substantially improve on Higgs measurements beyond the scope of the HL-LHC would be to use the high-energy (50–60 GeV), high-luminosity ( $\int L = 1 \text{ ab}^{-1}$ ) LHeC. Obviously, physics and cost are intimately related. Based on such considerations, but also taking into account technical constraints resulting from the amount of synchrotron radiation losses in the interaction region and the arcs, we have chosen 50 GeV in a 1/5 of U(LHC) configuration as the new default. This saves about 400 MCHF as compared to the CDR configuration.

If the LHeC ERL were built, it could later be transferred, with some reconfiguration and upgrades, to the FCC, to serve as the FCC-eh. The FCC-eh has its own location,  $L$ , for the ERL, which requires a new accelerator tunnel. It has been decided to keep the 60 GeV configuration for the FCC, as described in the recently published CDR of the FCC [16]. The LHeC ERL configuration may also be used as a top-up injector for the  $Z$  and possibly  $WW$  phases of the FCC-e, should the FCC-ee indeed precede the FCC-hh/eh phase.

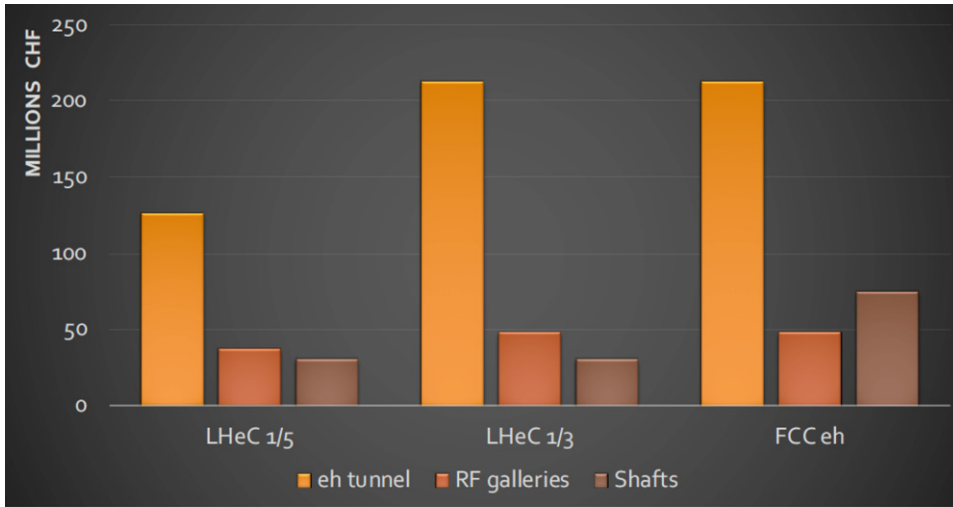


**Figure 2.** Cost estimates for the civil engineering work for the tunnel, rf galleries, and shafts for the LHeC at 1/5 of the LHC circumference (left), at 1/3 (middle), and for the FCC-eh (right). The unit costs and percentages are consistent with FCC and Compact Linear Collider (CLIC) unit prices. The estimates are considered reliable to 30%. The cost estimates include: site investigations: 2%, preliminary design, tender documents, and project changes: 12%, and the contractors' profits: 3%. Surface site work is not included, which is required for LHeC for IP2.

### 2.3. Configuration parameters

A possible transition from the 60 GeV to the 50 GeV configuration of the LHeC was already envisaged in 2018, as considered in the paper submitted for the European strategy [9]. The machine layout shown in that paper is reproduced in figure 3. It is a rough sketch, illustrating the reduction from a 60 GeV to a 50 GeV configuration, which not only results in a reduction of capital costs, as discussed above, but also of effort.

The ERL configuration has recently been revisited [35], considering its dependence on the electron-beam energy. After applying a dimensional scaling which preserves the emittance dilution, the results obtained are summarised in table 2.

The 1/5 configuration is chosen as the new LHeC default, while the CDR for the LHeC from 2012 and the recent CDR for FCC-eh used the 1/3 configuration. The energy and configuration may be decided as physics, cost, and effort dictate, once a decision is taken.

### 2.4. Luminosity

The luminosity  $L$  of the LHeC in its linac–ring configuration is determined by

$$L = \frac{N_e N_p n_p f_{\text{rev}} \gamma_p}{4\pi \epsilon_p \beta^*} \cdot \prod_{i=1}^3 H_i, \quad (2.1)$$

where  $N_{e(p)}$  is the number of electrons (protons) per bunch,  $n_p$  is the number of proton bunches in the LHC,  $f_{\text{rev}}$  is the revolution frequency in the LHC (the bunch spacing in a batch is given by  $\Delta$ , equal to 25 ns for protons in the LHC) and  $\gamma_p$  is the relativistic factor  $E_p/M_p$  of the proton beam. Furthermore,  $\epsilon_p$  denotes the normalised proton transverse beam emittance and  $\beta^*$  denotes the proton beta function at the interaction point (IP), assumed to be equal in

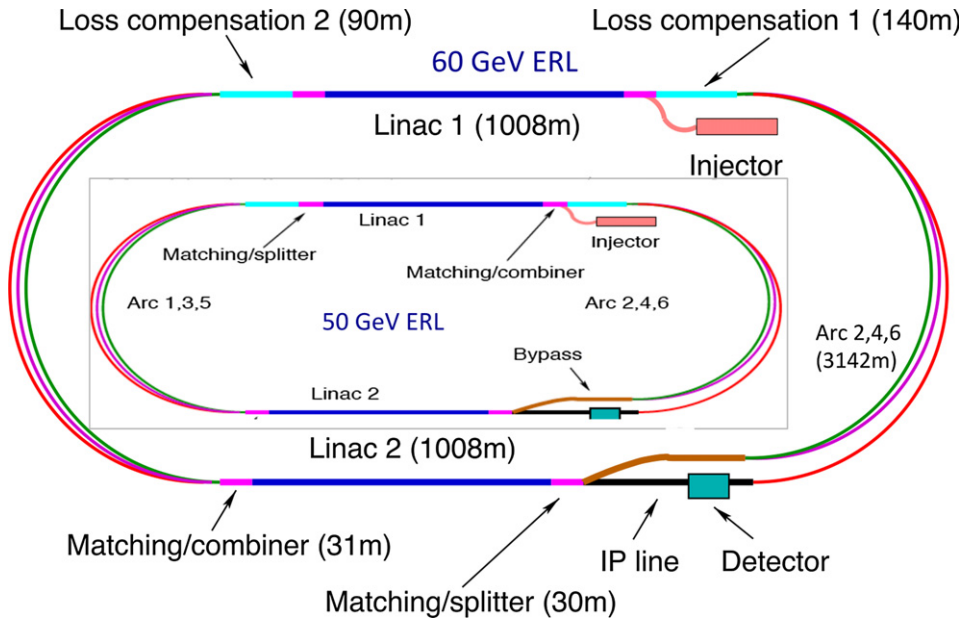


**Figure 3.** Schematic view of the three-turn LHeC configuration with two oppositely positioned electron linacs and three arcs housed in the same tunnel. Two configurations are shown: outer: default  $E_e = 60$  GeV with linacs about 1 km long with a 1 km arc radius, leading to an ERL circumference of about 9 km, or  $1/3$  of the LHC length. Inner: sketch for  $E_e = 50$  GeV with linacs about 0.8 km long with a 0.55 km arc radius, leading to an ERL circumference of 5.4 km, or  $1/5$  of the LHC length, which is smaller than the size of the SPS. The  $1/5$  circumference configuration is flexible: it offers the possibility of staging the project as physics funds dictate by using only partially equipped linacs, and it also permits an upgrade to somewhat higher energies if one permits increased synchrotron power losses and operation at higher gradients. Reproduced from [9]. © IOP Publishing Ltd. CC BY 3.0.

$x$  and  $y$ . The luminosity is moderated by the hourglass factor,  $H_1 = H_{\text{geo}} \simeq 0.9$ , the pinch, or beam–beam correction factor,  $H_2 = H_{\text{b-b}} \simeq 1.3$ , and the filling factor  $H_3 = H_{\text{coll}} \simeq 0.8$ , should an ion clearing gap be required in the electron beam. This justifies taking the product of these factors. As the product is close to unity, the factors are not listed in the subsequent tables, for simplicity.

The electron-beam current is given by

$$I_e = eN_e f, \quad (2.2)$$

where  $f$  is the bunch frequency  $1/\Delta$ . The current of the LHeC is limited by the charge delivery of the source. In the new default design, we have  $I_e = 20$  mA, which results from a charge of 500 pC for a bunch frequency of 40 MHz. One of the tasks of the PERLE facility is to investigate the stability of the three-turn ERL configuration in view of the challenge that each cavity has to accommodate a sixfold current due to the simultaneous acceleration and deceleration of bunches, each at three different beam energies.

**2.4.1. Electron–proton collisions.** The design parameters of the luminosity were recently provided in a note describing the FCC-eh configuration [36], including the LHeC. Table 3 rep-

**Table 2.** Scaling of the electron-beam energy, linac, and further accelerator element dimensions for choices of the total circumference in units  $1/n$  of the LHC circumference. For comparison, the CERN SPS has a circumference of 6.9 km, only somewhat larger than  $1/4$  of that of the LHC.

Parameter	Unit	LHeC option			
		1/3 LHC	1/4 LHC	1/5 LHC	1/6 LHC
Circumference	m	9000	6750	5332	4500
Arc radius	$m \cdot 2\pi$	1058	737	536	427
Linac length	$m \cdot 2$	1025	909	829	758
Spreader and recombiner length	$m \cdot 4$	76	76	76	76
Electron energy	GeV	61.1	54.2	49.1	45.2

**Table 3.** Summary of luminosity parameter values for the LHeC and FCC-eh. Left: CDR from 2012; middle: LHeC in three stages: an initial run, possibly during run 5 of the LHC, 50 GeV operation during run 6 (both of these operations are concurrent with the LHC), and a final, dedicated, stand-alone  $ep$  phase; right: FCC-eh with 20 and 50 TeV proton beams in synchronous operation.

Parameter	Unit	LHeC				FCC-eh	
		CDR	Run 5	Run 6	Dedicated	$E_p = 20$ TeV	$E_p = 50$ TeV
$E_e$	GeV	60	30	50	50	60	60
$N_p$	$10^{11}$	1.7	2.2	2.2	2.2	1	1
$\epsilon_p$	$\mu\text{m}$	3.7	2.5	2.5	2.5	2.2	2.2
$I_e$	mA	6.4	15	20	50	20	20
$N_e$	$10^9$	1	2.3	3.1	7.8	3.1	3.1
$\beta^*$	cm	10	10	7	7	12	15
Luminosity	$10^{33} \text{ cm}^{-2} \text{ s}^{-1}$	1	5	9	23	8	15

resents an update that also includes the initial 30 GeV configuration and the lower-energy version of the FCC-hh based on the LHC magnets<sup>160</sup>. For the LHeC, as noted above, we assume  $E_e = 50$  GeV, while for the FCC-eh, we retain 60 GeV. Since the source limits the electron current, the peak luminosity may be taken not to depend on  $E_e$ . Studies of the interaction region design presented in this paper show that we can be confident of reaching a  $\beta^*$  of 10 cm, but it will be a challenge to reach even smaller values. Similarly, it will be quite a challenge to operate with a current much beyond 20 mA. That has nevertheless been considered [37] for a possible dedicated LHeC operating mode for a few years following the  $pp$  operation programme.

The peak luminosity values exceed those of HERA by 2–3 orders of magnitude. The operation of HERA in its first, extended running period, 1992–2000, provided an integrated

<sup>160</sup> As of today, the low-energy FCC-pp collider uses a 6 T LHC magnet in a 100 km tunnel. If, in the coming decades, high field magnets become available based on High Temperature Superconductor (HTS) technology, then a 20 TeV proton beam energy may even be achievable in the LHC tunnel. To this extent, the low-energy FCC considered here and an HTS-based HE-LHC would be comparable options in terms of their energy reach.

**Table 4.** Baseline parameters of future electron–ion collider configurations based on the electron ERL, in concurrent  $eA$  and AA operational modes with the LHC and the two versions of a future hadron collider at CERN. Following the established convention in this field, the luminosity quoted at the start of a fill is the *electron–nucleon* luminosity, which is a factor of  $A$  larger than the usual (i.e. electron–nucleus) luminosity.

Parameter	Unit	LHeC	FCC-eh	FCC-eh
			( $E_p = 20$ TeV)	( $E_p = 50$ TeV)
Ion energy $E_{Pb}$	PeV	0.574	1.64	4.1
Ion energy/nucleon $E_{Pb}/A$	TeV	2.76	7.88	19.7
Electron-beam energy $E_e$	GeV	50	60	60
Electron–nucleon cms energy $\sqrt{s_{eN}}$	TeV	0.74	1.4	2.2
Bunch spacing	ns	50	100	100
Number of bunches		1200	2072	2072
Ions per bunch	$10^8$	1.8	1.8	1.8
Normalised emittance $\epsilon_n$	$\mu\text{m}$	1.5	1.5	1.5
Electrons per bunch	$10^9$	6.2	6.2	6.2
Electron current	mA	20	20	20
IP beta function $\beta_A^*$	cm	10	10	15
$e$ – $N$ luminosity	$10^{32} \text{ cm}^{-2} \text{ s}^{-1}$	7	14	35

luminosity of about  $0.1 \text{ fb}^{-1}$  for the collider experiments H1 and ZEUS. This may now be expected to be taken or produced in a day of initial LHeC operation.

**2.4.2. Electron–ion collisions.** The design parameters and luminosity were also provided recently [36] for collisions between electrons and lead nuclei (fully stripped  $^{208}\text{Pb}^{82+}$  ions). Table 4 is an update of the numbers presented in that paper, for consistency with the Run 6 LHeC configuration in table 3 and with the addition of parameters corresponding to the  $E_p = 20$  TeV FCC-hh configuration. A further discussion of this operating mode and motivations for the parameter choices in this table are provided in section 10.3.

One can expect the average luminosity during fills to be about 50% of the peak in table 4, and we assume an overall operational efficiency of 50%; in this case, a year of  $eA$  operation, possibly composed of combined shorter periods of operation, would have the potential to provide an integrated data set of about 5 (25)  $\text{fb}^{-1}$  for the LHeC (FCC-eh), respectively. This exceeds the HERA electron–proton luminosity value by about tenfold for the LHeC, and much more than that at FCC-eh, while the fixed-target nuclear DIS experimental kinematics is extended by 3–4 orders of magnitude. These energy-frontier electron–ion configurations therefore have the unique potential to radically modify our present view of nuclear structure and parton dynamics. This is discussed in section 6.

## 2.5. Linac parameters

Our brief summary of the main LHeC characteristics concludes here with a table of the main ERL parameters for the new default electron energy of 50 GeV, table 5, which are discussed in detail in section 8.

**Table 5.** Basic LHeC ERL characteristics for the default configuration using two linacs located opposite each other in a racetrack 5.4 km long. Each linac is passed three times for acceleration and three times for deceleration.

Parameter	Unit	Value
Frequency	MHz	801.58
Bunch charge	pC	499
Bunch spacing	ns	24.95
Electron current	mA	20
Injector energy	MeV	500
Gradient	MV m <sup>-1</sup>	19.73
Cavity length, active	m	0.918
Cavity length, flange-to-flange	m	1.5
Cavities per cryomodule		4
Length of cryomodule	m	7
Acceleration per cryomodule	MeV	72.45
Total number of cryomodules		112
Acceleration energy per pass	GeV	8.1

## 2.6. Operational schedule

The LHeC parameters are determined to be compatible with a parasitic operation with the nominal HL-LHC proton-proton operation. This implies limiting the electron bunch current to sufficiently small values, so that the proton beam-beam parameter remains small enough to be negligible for the proton beam dynamics.

Assuming a ten-year construction period for the LHeC after approval of the project and a required installation window of two years for the LHeC detector, the earliest realistic operational period for the LHeC coincides with the LHC Run 5 period in 2032 and with a detector installation during LS4, which is currently scheduled for 2030 and would need to be extended by one year to 2031. The baseline HL-LHC operational mode assumes 160 days of proton operation, 20 days of ion operation and 20 days of machine development time for the Run 4 period, amounting to a total of 200 operational days per year. After the Run 4 period, the operational plan of the HL-LHC does not include ion operation at present, and assumes 190 days for proton operation. The HL-LHC project assumes an overall machine efficiency of 54% (the fraction of scheduled operational time spent in physics production), and we assume that the ERL does not contribute to significant additional downtime for the operation. Assuming an initial 15 mA of electron-beam current, a  $\beta^*$  of 10 cm and HL-LHC proton-beam parameters, the LHeC reaches a peak luminosity of  $0.5 \times 10^{34} \text{ cm}^{-2} \text{ s}^{-1}$ . Assuming further a proton-beam lifetime of 16.7 h, a proton fill length of 11.7 h, and an average proton beam turnaround time of 4 h, in this configuration, the LHeC can reach in this configuration an annual integrated luminosity of  $20 \text{ fb}^{-1}$ .

For an evaluation of the physics potential, it is important to note that the initial Run 5 *ep* operational period may accumulate about  $50 \text{ fb}^{-1}$  of integrated luminosity. This is a hundred times the value that H1 (or ZEUS) accumulated over a HERA lifetime of 15 years. As one may expect (for details, see section 3), such a huge DIS luminosity is ample for pursuing basically the complete QCD programme. In particular, the LHeC would deliver on time for the HL-LHC



**Table 6.** LHeC performance levels during different operational modes.

Parameter	Unit	Run 5 period	Run 6 period	Dedicated
Brightness $N_p/(\gamma\epsilon_p)$	$10^{17} \text{ m}^{-1}$	2.2/2.5	2.2/2.5	2.2/2.5
Electron-beam current	mA	15	25	50?
Proton $\beta^*$	m	0.1	0.7	0.7
Peak luminosity	$10^{34} \text{ cm}^{-2} \text{ s}^{-1}$	0.5	1.2	2.4
Proton-beam lifetime	h	16.7	16.7	100
Fill duration	h	11.7	11.7	21
Turnaround time	h	4	4	3
Overall efficiency	%	54	54	60
Physics time/year	Days	160	180	185
Annual integrated luminosity	$\text{fb}^{-1}$	20	50	180

precision analyses the external, precise PDFs and with just a fraction of the  $50 \text{ fb}^{-1}$ , the secrets of low- $x$  parton dynamics would unfold. The higher  $ep$  luminosity is necessary for ultimate precision and for the top, BSM, and Higgs programmes of the LHeC to be of competitive value.

For the Run 6 period of the HL-LHC (the last of the HL-LHC operational periods), we assume that the number of machine development sessions for the LHC can be suppressed, providing an increase in the operational time for physics production from 190 days to 200 days per year. Furthermore, we assume that the electron-beam parameters can be pushed slightly further. Assuming that  $\beta^*$  can be reduced to 7 cm, with an electron-beam current of up to 25 mA and nominal HL-LHC proton beam parameters, the LHeC would reach a peak performance of  $1.2 \times 10^{34} \text{ cm}^{-2} \text{ s}^{-1}$  and an annual integrated luminosity of  $50 \text{ fb}^{-1}$ . This would add up to an integrated luminosity of a few hundred  $\text{fb}^{-1}$ , a strong basis for top, BSM, and Higgs physics at the LHeC.

Beyond the HL-LHC exploitation period, the electron-beam parameters could be further pushed in dedicated  $ep$  operation, when the requirement of parasitic operation on the HL-LHC proton–proton operation may no longer be imposed. The proton-beam lifetime without proton–proton collisions would be significantly larger than in the HL-LHC configuration. In the following we assume a proton-beam lifetime of 100 h and a proton-beam efficiency of 60% without proton–proton beam collisions. The electron-beam current in this configuration would only be limited by the electron beam dynamics and the SRF beam-current limit. Assuming electron-beam currents of up to 50 mA, the LHeC would reach a peak luminosity of  $2.4 \times 10^{34} \text{ cm}^{-2} \text{ s}^{-1}$  and an annual integrated luminosity of up to  $180 \text{ fb}^{-1}$ . Table 6 summarises the LHeC configurations over these three periods of operation.

Depending on the years available for a dedicated final operation (or through an extension of the  $pp$  LHC run, currently not planned but interesting for collecting 4 instead of 3  $\text{ab}^{-1}$  in order to, for example, observe di-Higgs production at the LHC), a total luminosity of 1  $\text{ab}^{-1}$  could be available for the LHeC. This would double the precision of Higgs couplings measured in  $ep$ , as compared to the default HL-LHC run period with  $ep$  added as described. It would also significantly enlarge the potential to observe or/and quantify rare and NP phenomena. Obviously such considerations are subject to the grand developments at CERN. A period with most interesting physics and on-site operation activity could be particularly welcome to narrow the possible large time gap between the LHC and its grand successor, the FCC-hh. One may,

however, be interested in closing down the LHC on time. It is thus important for the LHeC project to recognise its particular value as an asset of the HL-LHC and on its own, even with less than the ultimate luminosity, albeit with values that could only have been dreamt of at HERA.

### 3. Parton distributions—resolving the substructure of the proton

#### 3.1. Introduction

Since the discovery of quarks in the famous  $ep \rightarrow eX$  scattering experiment at Stanford [20, 21], the DIS process has been established as the most reliable method for resolving the substructure of the proton, and was immediately recognised as such, not least by Feynman [19]. Since that time, a series of electron, muon, and neutrino DIS experiments has validated the quark–parton model (QPM) and promoted the development of QCD. A new quality of this physics was realised by HERA, the first electron–proton collider built, which extended the kinematic range in momentum transfer squared to  $Q_{\text{max}}^2 = s \simeq 10^5 \text{ GeV}^2$ , for  $s = 4E_e E_p$ . Seen from today’s perspective, largely influenced by the LHC, it is necessary to advance to a further level in these investigations, with higher energies and much greater luminosity than HERA could achieve. This is a major motivation for building the LHeC, with an extension of the  $Q^2$  and  $1/x$  ranges by more than an order of magnitude and increase the luminosity by a factor of almost a thousand. It may be the case that QCD breaks down or be embedded in a higher gauge symmetry, or unconfined colour might be observed; these phenomena would raise a series of fundamental questions about the theory of QCD [38] and highlight the importance of a precision DIS programme using the LHeC.

This chapter is mainly devoted to an exploration of the seminal potential of the LHeC to resolve the substructure of the proton in an unprecedented range, with the first ever complete and coherent measurement of the full set of PDFs in one experiment. The precise and consistent determination of PDFs to high orders of pQCD is crucial for the interpretation of LHC physics, i.e. its precision electroweak and Higgs measurements, as well as an exploration of the high-mass region where new physics may occur when the HL-LHC operates. Extra constraints on PDFs also arise from  $pp$  scattering, as discussed in a later chapter. Conceptually, however, the LHeC provides the singular opportunity to completely separate the PDF determination from proton–proton physics. This approach is not only more precise for the PDFs, but it is theoretically more accurate, and enables incisive tests of QCD by confronting independent predictions with LHC (and later FCC) measurements, as well as providing an indispensable basis for reliable interpretations of searches for new physics.

While the resolution of the longitudinal, collinear structure of the proton is key to the physics programme of the LHeC (and the LHC), the  $ep$  collider provides further fundamental insights into the structure of the proton, such as semi-inclusive measurements of jets and vector mesons. In particular, deeply virtual Compton scattering (DVCS), a process established at HERA, will also shed light on the transverse structure of the proton in a new kinematic range. This is presented at the end of this chapter.

**3.1.1. Partons in deep inelastic scattering.** PDFs  $xf(x, Q^2)$  represent a probabilistic view of hadron substructure at a given distance,  $1/\sqrt{Q^2}$ . They depend on the parton type  $f = (q_i, g)$  for quarks  $q_i$  of flavour  $i$  and gluons  $g$ , and must be determined by experiment, most suitably DIS, since perturbative QCD does not prescribe the parton density at a given momentum fraction, Bjorken  $x$ . PDFs are also important because they determine the Drell–Yan (DY) hadron–hadron scattering processes, which are supposedly universal through the QCD

factorisation theorem [39].<sup>161</sup> The PDF programme of the LHeC has unprecedented reach for the following reasons:

- For the first time it will completely resolve the partonic structure of the proton (and nuclei), i.e. it will determine the  $u_v, d_v, u, d, s, c, b$ , and gluon momentum distributions through NC and CC cross-sections as well as direct heavy-quark PDF measurements, performed over a huge kinematic range of DIS from  $x = 10^{-6}$  to 0.9 and from  $Q^2 > 1$  to  $10^6$  GeV<sup>2</sup>. The LHeC will explore the strange density and the momentum fraction carried by top quarks [41], which was impossible at HERA.
- Very high luminosity and unprecedented precision, due to both new detector technology and the redundant evaluation of event kinematics from the leptonic and hadronic final states, will lead to extremely high PDF precision.
- The LHeC has high energy, and the weak probes ( $W, Z$ ) dominate the interaction at larger  $Q^2$ , which permits the up and down sea and valence quark distributions to be resolved over the full range of  $x$ . Thus, no additional data will be required<sup>162</sup>; i.e. there will be no influence from higher twists, nuclear uncertainties, or data inconsistencies, which are main sources of uncertainty in the current so-called global PDF determinations.

While PDFs are nowadays often merely seen as a tool for interpreting LHC data, in fact, what is really involved is a new understanding of strong interaction dynamics and a deeper resolution of substructure extending into hitherto uncovered phase-space regions, in particular, the small  $x$  region (by virtue of the very high energy  $s$  and the very small spatial dimension ( $1/\sqrt{Q^2}$ )) and the  $x \rightarrow 1$  region (owing to the high luminosity and energy). The quark parton model (QPM) is not sufficiently tested, despite decades of DIS and other experiments, and neither is QCD fully developed in these kinematic regimes.

Examples of issues of fundamental interest for the LHeC to resolve are: (i) the long-awaited resolution of the behaviour of  $d/u$  near the kinematic limit ( $x \rightarrow 1$ ); (ii) the flavour democracy of the light quark sea (is  $d \simeq u \simeq s$ ?); (iii) the existence of quark-level charge-symmetry [42]; (iv) the behaviour of the ratio  $\bar{d}/\bar{u}$  at small  $x$ ; (v) the turn-on and the values of heavy-quark PDFs; (vi) the value of the strong coupling constant and (vii) the question of the dynamics (linear or nonlinear) at small  $x$ , where the gluon and quark densities increase.

The gluon distribution is of special further interest because the gluon self-interaction prescribes all visible mass, the gluon–gluon fusion process dominates Higgs production at hadron colliders (the LHC and the FCC), and because its large- $x$  behaviour, essentially unknown today, affects the predictions of BSM cross-sections at the LHC.

The LHeC may be understood to be an extension of HERA to a considerable extent. It has the reach in  $x \propto 1/s$  to resolve the question of new strong interaction dynamics at small  $x$ , and it accesses high  $Q^2$ , much larger than  $M_{W,Z}^2$ , with huge luminosity, to make accurate use of weak NC and CC cross-sections in DIS PDF physics for the first time. QCD analyses of HERA data are still ongoing. For obvious reasons, no quantitative analysis of LHC-related PDF physics is possible without relying on the HERA data, and often on its QCD analyses. These are introduced briefly in the next section. Albeit with certain assumptions and limited

<sup>161</sup> In his referee report on the LHeC CDR in 2012, Guido Altarelli noted with respect to the factorisation theorem in QCD for hadron colliders that: ‘many people still advance doubts. Actually, this question could be studied experimentally, in that the LHeC, with its improved precision, could put bounds on the allowed amount of possible factorisation violations (e.g., by measuring in DIS the gluon at large  $x$  and then comparing with jet production at large  $p_T$  in hadron colliders).’ This question was also addressed in a previous LHeC paper [40].

<sup>162</sup> The LHeC may be operated at basically HERA energies and collect an fb<sup>-1</sup> of luminosity for cross-checks and to maximise high  $x$  and medium  $Q^2$  acceptance, see section 3.2.

luminosity, HERA completely changed the field of PDF physics as compared to the times of solely fixed-target data (see reference [43]), and it pioneered the era of high-density parton physics at small  $x$ .

**3.1.2. Fit methodology and HERA PDFs.** The methodology of PDF determinations with HERA data was developed over decades by the H1 and ZEUS collaborations [27, 44, 45], in close contact with many theorists. It has essentially been adopted with suitable modifications for the LHeC PDF prospect study, as detailed subsequently.

HERAPDF fits use information from both  $e^\pm p$  NC and CC scattering, exclusively from the  $ep$  collider experiments, H1 and ZEUS, up to high  $Q^2 = 30\,000\text{ GeV}^2$  and down to about  $x = 5 \times 10^{-5}$ . The precision of the HERA combined data is better than 1.5% over the  $Q^2$  range of  $3 < Q^2 < 500\text{ GeV}^2$  and remains below 3% up to  $Q^2 = 3000\text{ GeV}^2$ . The precision for large  $x > 0.5$  is rather poor due to limited luminosity and high- $x$  acceptance limitations at medium  $Q^2$ .

The QCD analysis is performed at leading order (LO), next-to-leading order (NLO), and next-to-next-to-leading order (NNLO) within the  $xFitter$  framework [44, 46, 47]; the latest version is the HERAPDF2.0 family [45]. The Dokshitzer-Gribov-Lipatov-Altarelli-Parisi (DGLAP) evolution of the PDFs, as well as the light-quark coefficient functions, are calculated using QCDNUM [48, 49]. The contributions of heavy quarks are calculated using the general-mass variable-flavour-number scheme given in references [49, 50]. The experimental uncertainties are determined using the Hessian method, imposing a  $\chi^2 + 1$  criterion. This is usually impossible in global fits over rather incoherent data sets originating from different processes and experiments, but has been a major advantage of the solely HERA-based QCD analyses.

In the HERAPDF analysis, as well as subsequently in the LHeC study, the starting scale is chosen to be  $Q_0^2 = 1.9\text{ GeV}^2$ , such that it is less than the charm mass,  $m_c^2$ . The data are restricted to  $Q_{\min}^2 \geq 3.5\text{ GeV}^2$  in order to stay in the DIS kinematic range. The forward hadron final-state acceptance introduces a lower  $W$  cut, which removes the region that is otherwise potentially sensitive to higher twist effects [51]. The strong coupling constant is set to  $\alpha_s(M_Z) = 0.118$ .<sup>163</sup> All these assumptions are varied in the evaluation of model uncertainties for the resulting fit. These variations would essentially have no significant effect in the case of the LHeC, as the sensitivity to the quark masses, for example, would be hugely improved with respect to HERA,  $\alpha_s$  would be known to 1–2 per mille, and the kinematic range of the data would be significantly extended.

In HERAPDF fits, the quark distributions at the initial  $Q_0^2$  are represented by the generic form

$$xq_i(x) = A_i x^{B_i} (1-x)^{C_i} P_i(x), \quad (3.1)$$

where  $i$  specifies the flavour of the quark distribution and  $P_i(x) = (1 + D_i x + E_i x^2)$ . The inclusive NC and CC cross-sections determine four independent quark distributions, which are essentially the sums of the up and down quark and antiquark densities. These may be decomposed into any other four distributions of up and down quarks using an ad-hoc assumption about the fraction of strange to anti-down quarks, which has a minimal numerical effect on the PDFs, apart from that on  $x_s$  itself. The parameterised quark distributions,  $xq_i$ , are chosen to be

<sup>163</sup> The strong coupling constant cannot be reliably determined from the inclusive HERA data alone. DIS results, including fixed-target data, have provided values which tend to be lower [52] than the value chosen here; for a discussion, see reference [53]. As is further presented in detail in section 4.1, the LHeC reaches a sensitivity to  $\alpha_s$  at the per-mille level based on inclusive and jet data, as well as their combination.

the valence quark distributions ( $xu_v, xd_v$ ) and the light antiquark distributions ( $x\bar{u}, x\bar{d}$ ). This has also been adopted for the LHeC.

The parameters  $A_{u_v}$  and  $A_{d_v}$  are fixed using the quark-counting rule. The normalisation and slope parameters,  $A$  and  $B$ , of  $\bar{u}$  and  $\bar{d}$  are set equal, such that  $x\bar{u} = x\bar{d}$  at  $x \rightarrow 0$ , a crucial assumption which the LHeC can validate. The strange quark PDF  $x\bar{s}$  is set as a fixed fraction  $r_s = 0.67$  of  $x\bar{d}$ . This fraction is varied during the determination of model uncertainties. By default it is assumed that  $x_s = x\bar{s}$  and that the  $u$  and  $d$  sea quarks and antiquarks also have the same distributions. These assumptions will be resolved by the LHeC and their uncertainties will essentially be eliminated, see section 3.3.4. The  $D$  and  $E$  parameters are used only if required by the data, following a  $\chi^2$  saturation procedure [44]. For HERAPDF2.0 this leads to two non-zero parameters,  $E_{u_v}$  and  $D_{\bar{u}}$ .

The gluon distribution is parameterised differently:

$$xg(x) = A_g x^{B_g} (1-x)^{C_g} - A'_g x^{B'_g} (1-x)^{C'_g}. \quad (3.2)$$

The normalisation parameter  $A_g$  is calculated using the momentum sum rule. Variations of the PDFs were also considered with  $A'_g = 0$ , which had been the default choice for earlier HERA data fits. The appearance of this second term may be understood as originating from a poorly constrained behaviour of  $xg(x, Q^2)$  at small  $x$ . In fact,  $xg$  resembles a valence-quark distribution at  $Q^2 \simeq Q_0^2$ . The much-extended  $Q^2$  range of the LHeC at a given small  $x$  and the access to much smaller  $x$  values than those probed at HERA will certainly enable this behaviour to be clarified. Since  $C'_g$  had also been set to a large value, that second term in equation (3.2) has a negligible effect on the resulting PDF uncertainties. Consequently  $A'_g$  is set to zero in the LHeC study.

Alternative parameterisations are used in the evaluation of the parameterisation uncertainty. These variations include: the introduction of extra parameters  $D, E$  for each quark distribution, the removal of primed gluon parameters, and the relaxation of assumptions about the low- $x$  sea. These fits provide alternative extracted PDFs with a similar fit quality. The maximum deviation from the central PDF at each value of  $x$  is taken as an envelope and added in quadrature to the experimental and model uncertainties to give the total uncertainty. As for the model uncertainties, the extended range and improved precision of the LHeC data may well be expected to render such variations negligible.

The results of the HERA PDF analysis [45] are shown in figure 4 for the HERA-PDF2.0NNLO PDF set, displaying the experimental, model, and parameterisation uncertainties separately. The structure of the proton is seen to depend on the resolution  $\propto 1/\sqrt{Q^2}$  with which it is probed. At a  $Q^2$  of about 1–2 GeV<sup>2</sup>, corresponding to 0.2 fm, the parton contents may be decomposed, as shown in figure 4 (top). The gluon distribution at  $Q^2 \simeq 2$  GeV<sup>2</sup> has a valence-like shape, i.e. at very low  $x$ , the momentum is carried by sea quarks (see figure 4 (top)). At medium  $x \sim 0.05$  the gluon density dominates, compared to all quark densities. At the largest values of  $x$ , above 0.3, the proton structure is dominated by the up and down valence quarks. This picture evolves such that below  $10^{-16}$  m, for  $x \leq 0.1$ , the gluon density also dominates over the sea-quark density, see figure 4 (bottom). The valence quark distributions are rather insensitive to the resolution, which reflects their non-singlet transformation behaviour in QCD.

The HERAPDF set differs from other PDF sets in that: (i) it represents a fit to a consistent data set with small correlated systematic uncertainties; (ii) it uses data from a proton target only, such that no heavy-target corrections are needed and the assumption of strong isospin invariance,  $d_{\text{proton}} = u_{\text{neutron}}$ , is not required; (iii) a large  $x, Q^2$  region is covered, such that no regions where higher twist effects are important are included in the analysis.

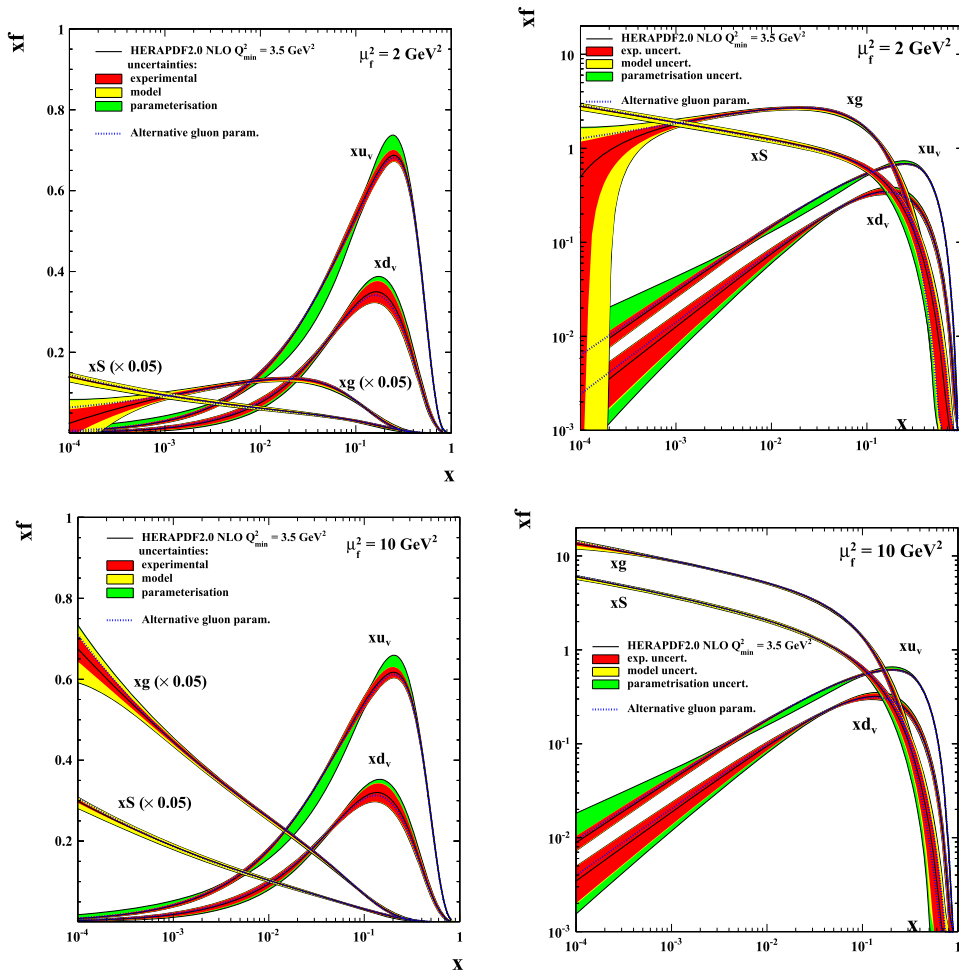


**Figure 4.** Parton distributions as determined by the QCD fit to the combined H1 and ZEUS data at  $Q^2 = 1.9 \text{ GeV}^2$  (top) and at  $Q^2 = 10 \text{ GeV}^2$  (bottom). The colour coding represents the experimental, model, and parameterisation uncertainties separately. Here  $xS = 2x(\bar{u} + \bar{d})$  denotes the total sea-quark density. Note that  $xg$  and  $xS$  are scaled by  $1/20$  in the left-hand-side plots with a linear  $y$  scale.

The limitations of HERA PDFs are also known: (i) the data are limited in statistics, such that the region  $x > 0.5$  is poorly constrained; (ii) the energy is limited, such that the very low  $x$  region below  $x \simeq 10^{-4}$  is not accessed, or not reliably accessed; (iii) the limits of luminosity and energy imply that the potential of the flavour resolution through weak interactions in NC and CC, while remarkable, can not be utilised accurately and  $\alpha_s$  cannot be determined alongside PDFs in solely inclusive fits; (iv) the strange-quark density was not accessed by H1 and ZEUS, and only initial measurements of  $xc$  and  $xb$  could be performed. The strong success compared to the fixed-target PDF situation before HERA was, however, most remarkable. The thorough clarification of parton dynamics and the establishment of a precision PDF basis for the LHC and later hadron colliders, however, make a next-generation, high-energy and -luminosity  $ep$  collider a necessity.



The PDF potential of the LHeC is presented next. This study closely follows the first extended analysis, as developed for the CDR and subsequently detailed in reference [54]. The main differences compared to that analysis result from the choice of the linac–ring LHeC configuration, with a preference for  $e^-p$  of high polarisation (and much less  $e^+p$ ), combined with an order-of-magnitude enhancement in the luminosity and developments of the apparatus design.

### 3.2. Simulated LHeC data

**3.2.1. Inclusive neutral- and charged-current cross-sections.** In order to estimate the uncertainties in the PDFs obtained from the LHeC, several sets of LHeC inclusive NC/CC DIS data with a full set of uncertainties have been simulated and are described in the following. The systematic uncertainties of the DIS cross-sections have a number of sources, which can be classified as correlated and uncorrelated across bin boundaries. For the NC case, the uncorrelated sources (apart from event statistics) are a global efficiency uncertainty, due, for example, to tracking or electron identification errors, as well as uncertainties due to photo-production background, calorimeter noise, and radiative corrections. The correlated uncertainties result from imperfect electromagnetic and hadronic energy-scale and angle calibrations. In the classic  $ep$  kinematic reconstruction methods used here, the scattered electron energy  $E'_e$  and the polar electron angle  $\theta_e$ , complemented by the energy of the hadronic final state  $E_h$ , can be employed to determine  $Q^2$  and  $x$  in a redundant way.

Briefly,  $Q^2$  is best determined from the electron kinematics, and  $x$  is calculated from  $y = Q^2/sx$ . At large  $y$ , the inelasticity is best measured using the electron energy,  $y_e \simeq 1 - E'_e/E_e$ . At low  $y$ , the relation  $y_h = E_h \sin^2(\theta_h/2)/E_e$  can be used to provide a measurement of the inelasticity from the hadronic final-state energy  $E_h$  and the angle  $\theta_h$ . This results in an uncertainty of  $\delta y_h/y_h \simeq \delta E_h/E_h$ , which is determined by the  $E_h$  calibration uncertainty to a good approximation.

Various refined methods have been proposed for determining the DIS kinematics, such as the double-angle method [55], which is commonly used to calibrate the electromagnetic energy scale, or the so-called  $\Sigma$  method [56], which exhibits reduced sensitivity to QED radiative corrections (see a discussion in reference [57]). For an estimate of the cross-section uncertainty the electron method ( $Q_e^2, y_e$ ) is used at large  $y$ , while at low  $y$ , we use  $Q_h^2, y_h$ , which is transparent and accurate to better than a factor of two. In much of the phase space, moreover, it is the uncorrelated efficiency or further specific errors, rather than the kinematic correlations, which dominate the cross-section measurement precision.

The assumptions used in the simulation of the pseudodata are summarised in table 7. The procedure was gauged using full H1 Monte Carlo (MC) simulations, and the assumptions correspond to H1's achievements with an improvement of, at most, a factor of two. Using a numerical procedure developed in reference [58], the scale uncertainties are transformed into kinematics-dependent correlated cross-section uncertainties caused by imperfect measurements of  $E'_e, \theta_e$ , and  $E_h$ .

These data uncertainties were imposed for all data sets, NC and CC, as subsequently listed and described.

The design of the LHeC assumes that it operates with the LHC in the high-luminosity phase, following LS4 at the earliest. As detailed in section 2, it is assumed that there will be an initial phase, during which, the LHeC may collect  $50 \text{ fb}^{-1}$  of data. This may begin with a sample of  $5 \text{ fb}^{-1}$ . Such values are very high when compared with HERA, corresponding to, respectively,



**Table 7.** Assumptions about the sizes of uncertainties from various sources used in the simulation of the NC cross-sections. The top three are uncertainties in the calibrations, which are included to provide correlated systematic cross-section errors. The lower three values are uncertainties in the cross-sections caused by various sources.

Source of uncertainty	Uncertainty
Scattered electron energy scale $\Delta E'_e/E'_e$	0.1%
Scattered electron polar angle	0.1 mrad
Hadronic energy scale $\Delta E_h/E_h$	0.5%
Radiative corrections	0.3%
Photoproduction background (for $y > 0.5$ )	1%
Global efficiency error	0.5%

**Table 8.** Summary of the characteristic parameters of the data sets used to simulate NC and CC  $e^\pm$  cross-section data, for a lepton beam energy of  $E_e = 50$  GeV. Sets D1–D4 are for  $E_p = 7$  TeV and  $e^-p$  scattering, with varying assumptions for the integrated luminosity and the electron-beam polarisation. The data set D1 corresponds to possibly the first year of LHeC data, and ten times the amount of luminosity that H1/ZEUS collected in their lifetimes. The data set D5 is a low  $E_p$  energy run, which is essential to extend the acceptance at large  $x$  and medium  $Q^2$ . The D6 and D7 sets are for smaller amounts of positron data. Finally, D8 and D9 are for high-energy  $e^-p$  scattering with positive helicity, which is important for electroweak NC physics. These variations of the data used are subsequently studied for their effects on the PDF determinations.

Parameter	Unit	Data set								
		D1	D2	D3	D4	D5	D6	D7	D8	D9
Proton-beam energy	TeV	7	7	7	7	1	7	7	7	7
Lepton charge		-1	-1	-1	-1	-1	+1	+1	-1	-1
Longitudinal lepton polarisation		-0.8	-0.8	0	-0.8	0	0	0	+0.8	+0.8
Integrated luminosity	fb <sup>-1</sup>	5	50	50	1000	1	1	10	10	50

a hundred and ten times the integrated luminosity that H1 (ZEUS) collected in their lifetime of about 15 years. The total luminosity may come close to 1 ab<sup>-1</sup>.

The bulk of the data is assumed to be acquired from electrons, possibly at a large negative helicity  $P_e$ , because this configuration maximises the number of Higgs bosons that one can produce at the LHeC:  $e^-$  couples to  $W^-$ , which primarily interacts with an up quark; the CC cross-section is proportional to  $(1 - P_e)$ . However, for electroweak physics there is a strong interest in varying the polarisation and charge<sup>164</sup>. It was considered that the  $e^+p$  luminosity may reach 1 fb<sup>-1</sup>, while ten times that amount has been simulated for sensitivity studies. A dataset has also been produced with reduced proton beam energy, as that enlarges the acceptance of larger  $x$  at smaller  $Q^2$ . The full list of simulated sets is provided in table 8.

The highest energies obviously give access to the smallest  $x$  at a given  $Q^2$ , and to the maximum  $Q^2$  for a fixed  $x$ . This is illustrated by the kinematic plane, iso-energy, and iso-angle lines, see figure 5. It is instructive to see how the variation of the proton-beam energy changes the kinematics considerably and enables additional coverage of various regions. This is clear

<sup>164</sup>With a linac source, the generation of an intense positron beam is very challenging, and it will not be able to compete with the electron intensity. This is discussed in the accelerator chapter.

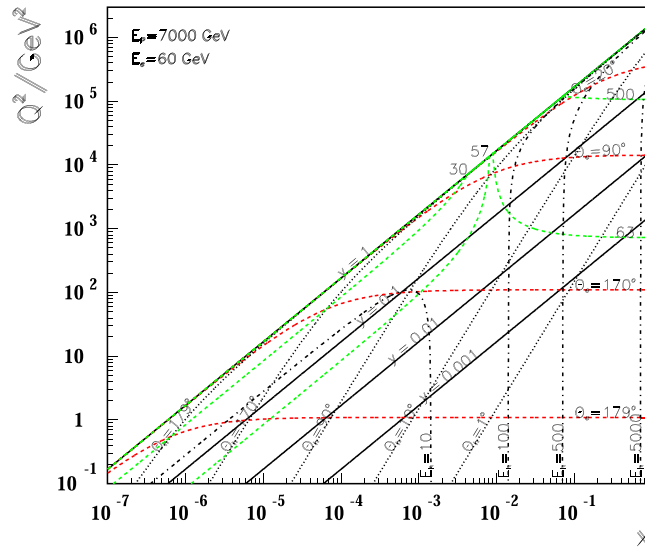


**Figure 5.** Kinematic plane covered by the maximum beam energies at the LHeC. Red dashes: lines of constant scattered electron polar angle. Note that low  $Q^2$  is measured with electrons scattered into the backward region and the highest  $Q^2$  is reached with Rutherford backscattering; black dots: lines of constant angle of the hadronic final state; black solid: lines of constant inelasticity  $y = Q^2/sx$ ; green dashes: lines of constant scattered electron energy  $E'_e$ . Most of the central region is covered by what is termed the kinematic peak, where  $E'_e \simeq E_e$ . The small- $x$  region is accessed using small energies  $E'_e$  below  $E_e$ , while electrons detected in the forward direction and at high- $Q^2$  carry TeV energies; black dashed-dotted: lines of constant hadronic final state energy  $E_h$ . Note that the very forward, large- $x$  region also sees very high hadronic energy deposits.

from figure 6 which shows that the kinematic plane determines the approximate minimum energies the LHeC could operate with. One may note striking changes related to kinematics (see reference [58]); for example, one can see that the line of  $\theta_e = 179^\circ$  now corresponds to  $Q^2 \simeq 0.1 \text{ GeV}^2$ , which is due to a reduction in  $E_e$ , compared to  $1 \text{ GeV}^2$  in the maximum energy case, see figure 5. Similarly, by comparing the two figures one finds that the lower  $Q^2$ , larger  $x$  region becomes easier to access with lower energies, in this case, solely owing to the reduction of  $E_p$  from 7 to 1 TeV. It is worth noting that the LHeC, when operating at these low energies, would permit a complete repetition of the HERA programme within a short period of special data taking.

The coverage of the kinematic plane is illustrated by a plot of the  $x, Q^2$  bin centres of the data points used in simulations, see figure 7 [59]. The full coverage at the highest Bjorken  $x$ , i.e. very close to  $x = 1$ , is enabled by the high luminosity of the LHeC. This was impossible to achieve with HERA as the NC/CC DIS cross-sections decrease proportionally to some power of  $(1 - x)$  when  $x$  approaches 1, as has long been established by Regge counting [60–62].

It has been a prime goal, extending beyond previous PDF studies, to understand the importance of these varying data-collection conditions for measuring PDFs with the LHeC. This holds true, in particular, for the question about what can be expected from an initial, lower-luminosity LHeC operating period, which is of the highest interest for the LHC analyses during the HL-LHC phase. Some special data sets of reduced electron energy have also been produced

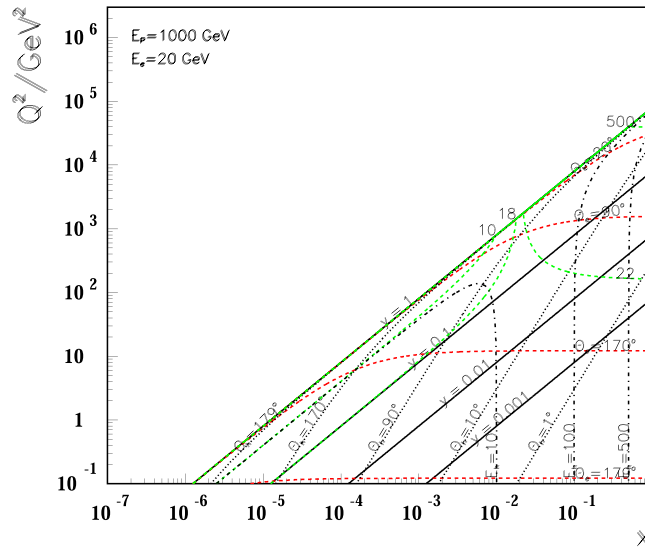


**Figure 6.** Kinematic plane covered by the minimum beam energies at LHeC. The meaning of the curves is the same as in the previous figure. This coverage is very similar to that of HERA, as the energies are about the same.

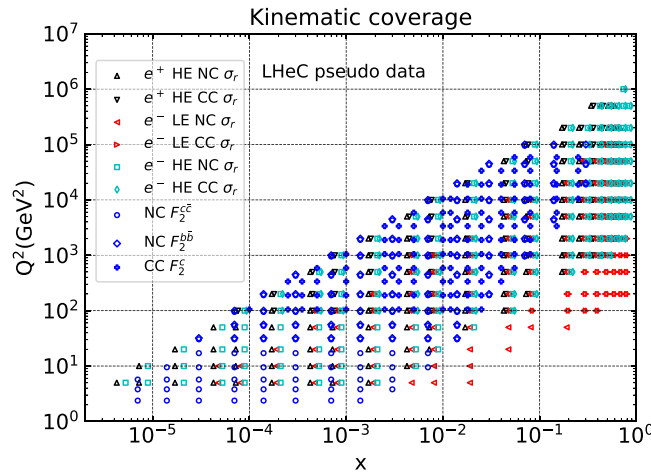


**Figure 7.** Illustration of the  $x, Q^2$  values of simulated cross-section and heavy quark density data used in LHeC studies. The red points illustrate the gain in acceptance towards large values of  $x$  at fixed  $Q^2$  when  $E_p$  is reduced; see the text. Reproduced from [59]. CC BY 4.0.

in order to evaluate the potential for measuring  $F_L$ , see section 4.2.3. These data sets have not been included in the bulk PDF analyses presented subsequently in this chapter.

**3.2.2. Heavy quark structure functions.** The LHeC is the ideal environment for the determination of the strange, charm, and bottom density distributions, which is necessary for a

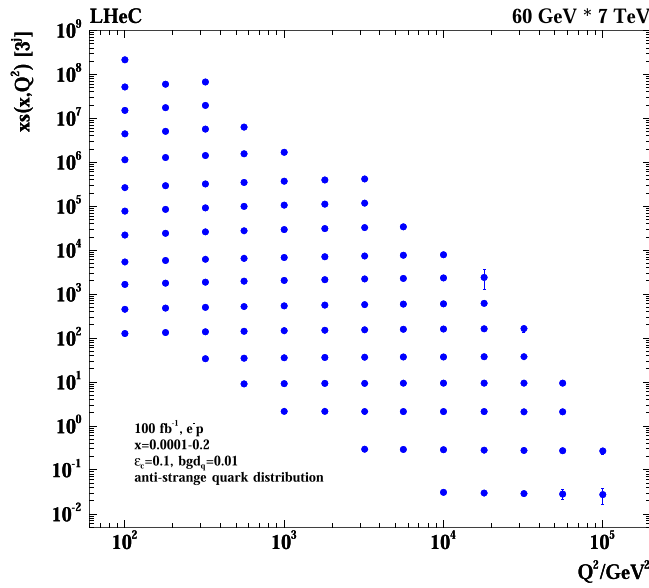


**Figure 8.** Simulation of the measurement of the (anti)-strange quark distribution,  $x\bar{s}(x, Q^2)$ , in CC  $e^-p$  scattering through the  $t$ -channel reaction  $W^- \bar{s} \rightarrow c$ . The vertical error bars indicate the full systematic and statistical uncertainties added in quadrature, but are mostly smaller than the marker size. The  $x$  range covered extends from  $10^{-4}$  (top left bin), determined by the CC trigger threshold, conservatively assumed to be at  $Q^2 = 100 \text{ GeV}^2$ , to  $x \simeq 0.2$  (bottom right) determined by the forward tagging acceptance limits, which could be further extended by lowering  $E_p$ .

comprehensive unfolding of the parton contents and dynamics in protons and nuclei. With charm-tagging techniques one can directly access  $x\bar{s}$  in CC or  $x\bar{c}$  in NC DIS, while with bottom tagging, one has access to  $x\bar{b}$  in NC DIS. The inner silicon detectors have a typical resolution of  $10 \mu\text{m}$ , which is much smaller than the typical charm and bottom decay lengths of several hundred  $\mu\text{m}$ . In addition, the transverse extension of the beam spot of only  $(7 \mu\text{m})^2$  is comparably small. The experimental challenges, then, are the beam-pipe radius, dealing with strong synchrotron radiation effects at the LHeC, and the forward tagging acceptance, which are similar to the HL-LHC challenges, albeit much easier due to the absence of pile-up in  $ep$  (see e.g. [63] for a brief discussion). Very sophisticated techniques (not discussed here) are being developed at the LHC in order to identify bottom production through jets [64].

A simulation of the measurement of the anti-strange density at the LHeC was performed using impact parameter tagging in  $ep$  CC scattering, see figure 8. The measurements of the charm and beauty structure functions using  $c$  and  $b$  tagging were simulated for NC DIS (see figures 9 and 10). The results served as inputs for the PDF study subsequently presented.

For this simulation, the charm and beauty tagging efficiencies are assumed to be 10% and 60%, respectively. These values are derived from HF tagging techniques at HERA and by the ATLAS collaboration. Backgrounds arise from light-quark jets in the charm analysis, or charm background in the beauty analysis. The light-quark jet background is assumed to be reducible to the per cent level, and the charm-quark jet background is assumed to be 10%. The background contaminations, as well as the tagging efficiencies, primarily affect the statistical uncertainty of the measurement, which for the assumed  $100 \text{ fb}^{-1}$  is only relevant in some edges of the phase space, as the figures illustrate for all three distributions.

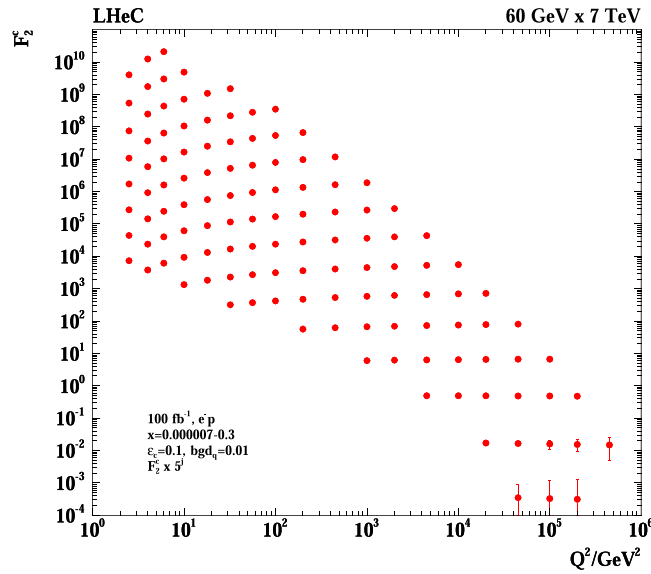


**Figure 9.** Simulation of the measurement of the charm quark distribution expressed as  $F_2^c = e_c^2 x(c + \bar{c})$  in NC  $e^-p$  scattering. The vertical error bars indicate the full systematic and statistical uncertainties added in quadrature, but are mostly smaller than the marker size. The minimum  $x$  (left top bin) is at  $7 \times 10^{-6}$ , and the data extend to  $x = 0.3$  (right bottom bin). The simulation uses a massless scheme and is only indicative near the threshold, although the uncertainties entering the QCD PDF analysis are consistently estimated.

In addition, an uncorrelated systematic uncertainty of 3% is assumed in the simulated strange and beauty quark measurements, while for charm, a 2% error is used. These errors determine the measurement uncertainties over almost the full kinematic range. At higher  $Q^2$  and  $x$ , these increase, for example, to 10%, 5%, and 7% for  $xs$ ,  $xc$ , and  $xb$ , respectively, at  $x \simeq 0.1$  and  $Q^2 \simeq 10^5$  GeV<sup>2</sup>. As specified in the figures, the  $x$  and  $Q^2$  ranges of these measurements extend over three, five, and four orders of magnitude for  $s$ ,  $c$  and  $b$ . The coverage of very high  $Q^2$  values, far beyond  $M_Z^2$ , permits us to determine the  $c$  and  $b$  densities probed in  $\gamma Z$  interference interactions for the first time. At HERA,  $xs$  was not directly accessible, while pioneering measurements of  $xc$  and  $xb$  could be performed [65], albeit over a smaller range and less precisely than will be achieved with the LHeC. These measurements, as discussed below and in much detail in the 2012 LHeC CDR [1], are of vital importance for the development of QCD and for the interpretation of precision LHC data.

### 3.3. Parton distributions from the LHeC

**3.3.1. Procedure and assumptions.** In this section, PDF constraints from the simulation of LHeC inclusive NC and CC cross-section measurements and heavy quark densities are investigated. The analysis closely follows the one for HERA presented above.

The expectations for PDFs for the ‘LHeC inclusive’ dataset, corresponding to a combination of the datasets D4, D5, D6, and D9, are presented, see table 8. These datasets have the highest sensitivity to general aspects of PDF phenomenology. Since the data will be recorded concurrently with the HL-LHC operation, they will only become available after the end of

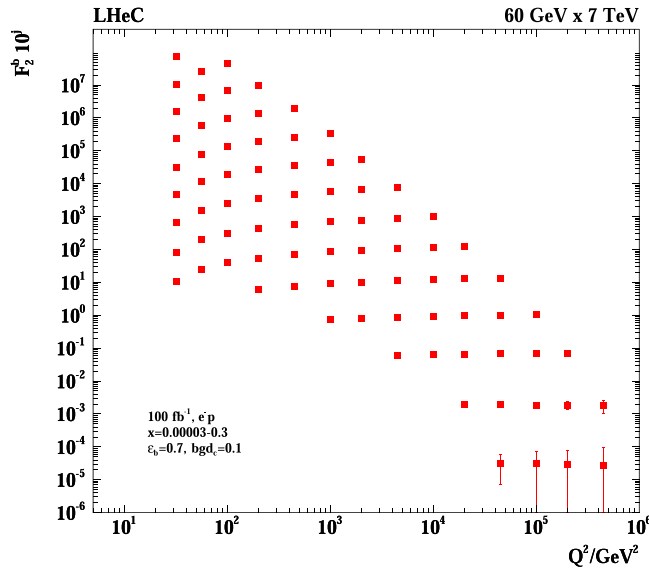


**Figure 10.** Simulation of the measurement of the bottom quark distribution expressed as  $F_2^b = e_b^2 x(b + \bar{b})$  in NC  $e^-p$  scattering. The vertical error bars indicate the full systematic and statistical uncertainties added in quadrature, but are mostly smaller than the marker size. The minimum  $x$  (top left bin) is at  $3 \times 10^{-5}$ , and the data extend to  $x = 0.3$  (bottom right bin). The simulation uses a massless scheme and is only indicative near the threshold, although the uncertainties entering the QCD PDF analysis are consistently estimated.

the HL-LHC. Therefore, these PDFs will be valuable for the re-analysis or re-interpretation of (HL-)LHC data, and for further future hadron colliders.

In order that LHeC can be useful during the lifetime of the HL-LHC, it is very desirable that the LHeC can deliver PDFs of transformative precision in a short timescale. Therefore, in this study particular attention is paid to PDF constraints that can be extracted from the first  $50 \text{ fb}^{-1}$  of electron–proton data, which corresponds to the first three years of LHeC operation. The dataset is labelled D2 in table 8 and also referred to as ‘LHeC first run’ in the following.

Even the data recorded during the initial weeks of data taking will be highly valuable and will impose new PDF constraints. This is because the initial instantaneous luminosity will already be comparably high and the kinematic range largely extended in comparison to the HERA data. These initial analyses will provide the starting point for the LHeC PDF programme. It may be recalled that the HERA I data period (1992–2000) provided just  $0.1 \text{ fb}^{-1}$  of data, which was ample for discovering the increases of  $F_2$  and  $xg$  towards small  $x$  at low  $Q^2$ , and even today, these data form the most important ingredient of the combined legacy HERA data [45]. The data sets in table 8 comprise D1, with  $5 \text{ fb}^{-1}$ , still ten times the amount that H1 or ZEUS collected in 15 years, and D3, which resembles D2, but has the electron polarisation set to zero.

Additional dedicated studies of the impact of  $s$ ,  $c$ ,  $b$  data on the PDFs are then also presented, based on  $10 \text{ fb}^{-1}$  of  $e^-p$  simulated data. Further important PDF constraints that would be provided by the measurements of  $F_L$  and jets are not considered in the present study. These remarks are significant in that they mean one has to be cautious when comparing the LHeC

PDF potential with some global fits:  $F_L$  will resolve the low- $x$  nonlinear parton interaction issue (see section 4.2.3), and jets are important to pin down the gluon density behaviour at large  $x$  as well as to provide a precision measurement of  $\alpha_s$  (see section 4.1).

To assess the importance of different operating conditions, the impacts of datasets with differing amounts of integrated luminosity (D1 vs D4), with and without positrons (D6 vs D7), and with different polarisation states for the leptons (D3 vs D8) are also considered.

In the following, PDF fits are presented that make use of the simulated data and NLO QCD predictions. Fits were performed using NNLO QCD as a cross-check. The analysis closely follows the HERAPDF procedure (cf section 3.1.2 and reference [45]). The parametric functions in equations (3.1) and (3.2) are used, and the parameterised PDFs are the valence distributions  $xu_v$  and  $xd_v$ , the gluon distribution  $xg$ , and the  $x\bar{U}$  and  $x\bar{D}$  distributions, using  $x\bar{U} = x\bar{u}$  and  $x\bar{D} = x\bar{d} + x\bar{s}$ . In total the following 14 parameters are free for the nominal fits:  $B_g, C_g, D_g, B_{uv}, C_{uv}, E_{uv}, B_{dv}, C_{dv}, A_{\bar{U}}, B_{\bar{U}}, C_{\bar{U}}, A_{\bar{D}}, B_{\bar{D}}, C_{\bar{D}}$ . These fit parameters are similar to HERAPDF2.0, although, to some extent, more flexible due to the stronger constraints provided by the LHeC. Note that the  $B$  parameters for  $u_v$  and  $d_v$ , and the  $A$  and  $B$  parameters for  $\bar{U}$  and  $\bar{D}$  are fitted independently, such that the up and down valence and sea quark distributions are uncorrelated in the analysis, whereas for HERAPDF2.0  $x\bar{u} \rightarrow x\bar{d}$  as  $x \rightarrow 0$  is imposed. The other main difference is that no negative gluon term has been included, i.e.  $A'_g = 0$  but  $D_g \neq 0$ .

This ansatz is natural to the extent that the NC and CC inclusive cross-sections determine the sums of the up and down quark distributions and their antiquark distributions as four independent sets of PDFs, which may be transformed to the ones chosen if one assumes that  $u_v = U - \bar{U}$  and  $d_v = D - \bar{D}$ , i.e. the equality of anti- and sea-quark distributions of a given flavour. For the majority of the QCD fits presented here, the strange quark distribution at  $Q_0^2$  is assumed to be a constant fraction of  $\bar{D}$ ,  $x\bar{s} = f_s x\bar{D}$  with  $f_s = 0.4$  as for HERAPDF, while this assumption is relaxed for the fits including simulated  $s, c, b$  data.

Note that the prospects presented here are illustrations for a different era of PDF physics, which will be richer and deeper than one may be able to simulate now. For instance, without real data one cannot determine the actual parameterisation needed for the PDFs. In particular the low  $x$  kinematic region is, so far, unexplored; the simulated data rely on a simple extrapolation of current PDFs, and no reliable data or model are available that provide constraints on this region<sup>165</sup>. The LHeC data explores new corners of phase space with high precision, and therefore it will have great potential, much larger than HERA had, to determine the parameterisation. As another example, with the LHeC data, one will be able to directly derive relations for how the valence quarks are determined with a set of NC and CC cross-section data in a redundant way, since the gluon distribution at small  $x$  can be determined from the  $Q^2$  derivative of  $F_2$  and from a measurement of  $F_L$ . The question of the optimal gluon parameterisation may then be settled by analysing these constraints and not by assuming some specific behaviour of a given fit.

Furthermore, the precise direct determinations of  $s, c$  and  $b$  densities with measurements of the impact parameters of their decays will take the treatment of HFs in PDF analyses to a new level. The need for the phenomenological introduction of the  $f_s$  factor will disappear, and the debate about the value of fixed and variable HF schemes will be settled.

<sup>165</sup> It is expected that real LHeC data and also the inclusion of further information, such as  $F_L$ , will certainly lead to a quite different optimal parameterisation ansatz than that used in this analysis. It has been confirmed that with a more relaxed set of parameters, very similar results are obtained for the PDF uncertainties, which justifies the size of the prospective PDF uncertainties.



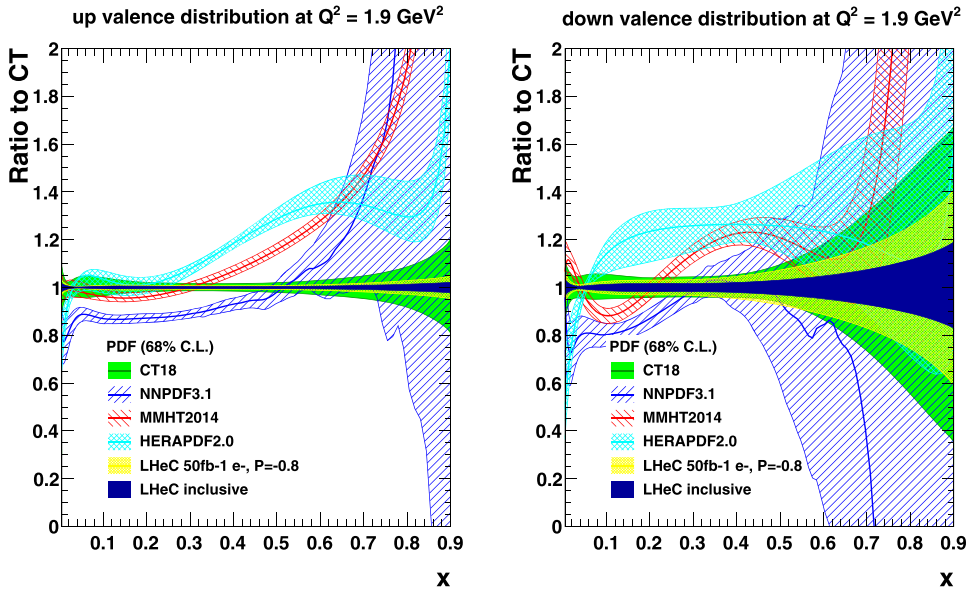


**Figure 11.** Valence quark distributions at  $Q^2 = 1.9 \text{ GeV}^2$  as a function of  $x$ , displayed as a ratio to the CT18 PDF set. Reproduced with permission from [68]. The yellow band corresponds to the ‘LHeC first run’ PDFs (D2), while the dark blue band shows the final ‘LHeC inclusive’ PDFs based on the data sets (D4, D5, D6, and D9), as described in section 3.3.1. For the purpose of more clearly illustrating the improvement in the uncertainties, the central values of the LHeC PDFs have been scaled to the CT18 PDF, which is itself displayed by the green band.

**3.3.2. Valence quarks.** From the first measurements of DIS physics, it was proposed to identify partons with quarks and to consider the proton as consisting of valence quarks together with ‘an indefinite number’ of  $(q\bar{q})$  pairs [66]. Fifty years later, basic questions are still unanswered about the behaviour of valence quarks, such as the  $d_v/u_v$  ratio at large  $x$ , and PDF fits struggle to resolve the flavour composition and interaction dynamics of the sea. The LHeC is the machine best suited to resolving these challenges.

The precision that can be expected for the valence quark distributions from the LHeC is illustrated in figure 11 and compared to a selection of recent PDF sets. Today, the precision of the valence quark distributions, particularly at large  $x$ , is fairly limited, as can be derived from the figure. This is due to the limited integrated luminosity of the HERA data, challenging systematics that rise proportionally to  $1/(1-x)$ , and to uncertainties attributed to nuclear corrections. At lower values of  $x$  the valence quark distributions are very small compared to the sea quarks and cannot easily be separated from them.

Today, the  $u$  valence distribution is known with higher precision than the  $d$  valence, since it enters the calculation of  $F_2$  with a fourfold higher weight because of the different electric charges of the quarks. Nevertheless, a substantial improvement in  $d_v$  due to the LHeC is also visible, because the relative weight of  $d_v$  to  $u_v$  changes favourably towards the down quark due to the influence of weak NC and CC interactions at high  $Q^2$ , where the LHeC provides very accurate data. The strong constraints on the highest  $x$  valence distributions are due to the very high integrated luminosity. Note that even though the HL-LHC has a high integrated luminosity, the highest  $x$  values attained there are only accessible as convolutions with partons at lower  $x$ , and those can therefore not be well constrained.

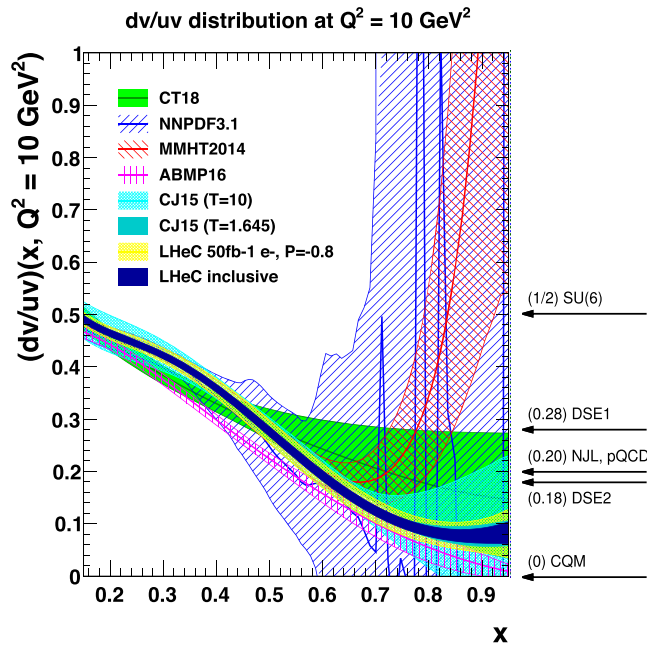


**Figure 12.** The  $d_v/u_v$  distribution at  $Q^2 = 10 \text{ GeV}^2$  as a function of  $x$ . The yellow band corresponds to the ‘LHeC first run’ PDFs (D2), while the dark blue shows the final ‘LHeC inclusive’ result. Both LHeC PDFs shown are scaled to the central value of CJ15.

Note that the ‘LHeC first run’ PDF, shown by the yellow band in figure 11, includes only electron, i.e. no positron, data. In fact, access to valence quarks at low  $x$  can be obtained from the  $e^\pm p$  cross-section differences. As has already been illustrated in the CDR from 2012 [1] the sum of  $2u_v + d_v$  may be measured directly with the NC  $\gamma Z$  interference structure function  $x F_3^{\gamma Z}$  down to  $x \simeq 10^{-4}$  with very good precision. Thus, the LHeC will have direct access to the valence quarks at small  $x$ . This also tests the assumption of the equality of sea- and antiquark densities, which, if different, would cause  $x F_3^{\gamma Z}$  to increase towards small  $x$ .

As is evident from figure 11 there are striking differences and even contradictions between the estimates of the uncertainties of the parton distributions between the various fit groups. This is due to different fit technologies but also a result of different data choices and assumptions about the  $d/u$  ratio. Such major uncertainties would be resolved by the LHeC.

The precise determinations of the valence quark distributions at large  $x$  have strong implications for physics at the HL-LHC, in particular for BSM searches. The precise determination of the valence quarks will resolve the long-standing mystery of the behaviour of the  $d/u$  ratio at large  $x$ , see figure 12. As exemplarily shown in figure 12, there are currently conflicting theoretical pictures for the central value of the  $d/u$  ratio, although the large uncertainty bands of the different PDF sets mainly overlap. As of today, the constraints from the data are statistically inconclusive and also suffer from large uncertainties due to the use of DIS data on nuclear targets.

**3.3.3. Light sea quarks.** Our current knowledge about antiquark distributions is fairly poor; uncertainties are very large at smaller values of  $x$  and also at the highest  $x$ . In particular, at low  $x$ , the sizes of the antiquark PDFs are large and they contribute significantly to precision SM

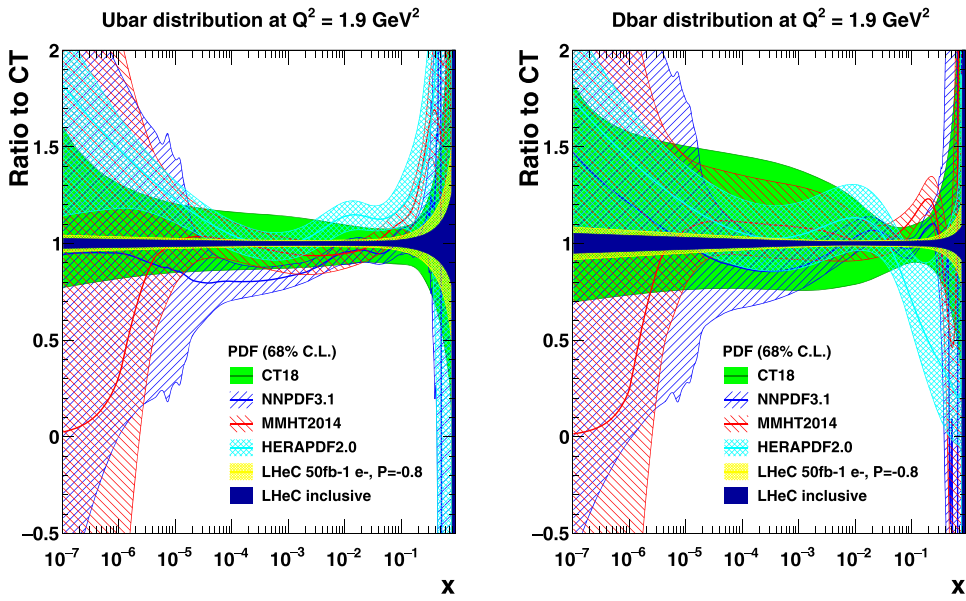


**Figure 13.** Sea quark distributions at  $Q^2 = 1.9 \text{ GeV}^2$  as a function of  $x$ , displayed as the ratio to the CT18 PDF set. The yellow band corresponds to the ‘LHeC first run’ PDFs (D2), while the dark blue band shows the final ‘LHeC inclusive’ PDFs (D4, D5, D6, and D9), as described in the text. Both LHeC PDFs shown are scaled to the central value of CT18.

measurements at the HL-LHC. At high  $x$ , sea and valence quark densities need to be properly distinguished and accurately measured for reliable BSM searches at high mass.

Our knowledge about antiquark PDFs will be completely changed by the LHeC data. Precise constraints are obtained with inclusive NC/CC DIS data despite the relaxation of any assumptions in the fit ansatz that would force  $\bar{u} \rightarrow \bar{d}$  as  $x \rightarrow 0$ , as is the case for other PDF determinations today. At smaller  $Q^2$  in DIS, one essentially measures  $F_2 \propto 4\bar{U} + \bar{D}$ . Thus, at HERA, with limited precision at high  $Q^2$ , it was not possible to resolve the two parts, and neither will that be possible at any other lower-energy  $ep$  collider which cannot reach small  $x$ . In contrast, at the LHeC, the CC DIS cross-sections will be measured very well, even at  $x$  values less than  $10^{-4}$ , and, in addition, there are strong weak-current contributions to the NC cross-section that probe the flavour composition differently than the photon exchange does. This enables the distinction of  $\bar{U}$  and  $\bar{D}$  at the LHeC.

The distributions of  $\bar{U}$  and  $\bar{D}$  for the PDFs from the first run and the ‘LHeC inclusive data’ are shown in figures 13 and 14 for  $Q^2 = 1.9 \text{ GeV}^2$  and  $Q^2 = 10^4 \text{ GeV}^2$ , respectively, and compared to current PDF analyses. One observes a striking increase in precision for both  $\bar{U}$  and  $\bar{D}$  which persists from low to high scales. The relative uncertainty is large at high  $x$  ( $x \gtrsim 0.5$ ). However, in that region, the sea-quark contributions are already very tiny. In the high- $x$  region, one can observe the value of the full LHeC data sample fitted to the initial one, while the uncertainties below  $x \simeq 0.1$  for both the small and the full data sets are comparable and of very small size.

**3.3.4. Strange quark.** The determination of the strange PDF has generated significant controversy in the literature for more than a decade. Fixed-target neutrino DIS measurements [68–72] typically prefer a strange PDF that is roughly half of the up and down sea distributions;

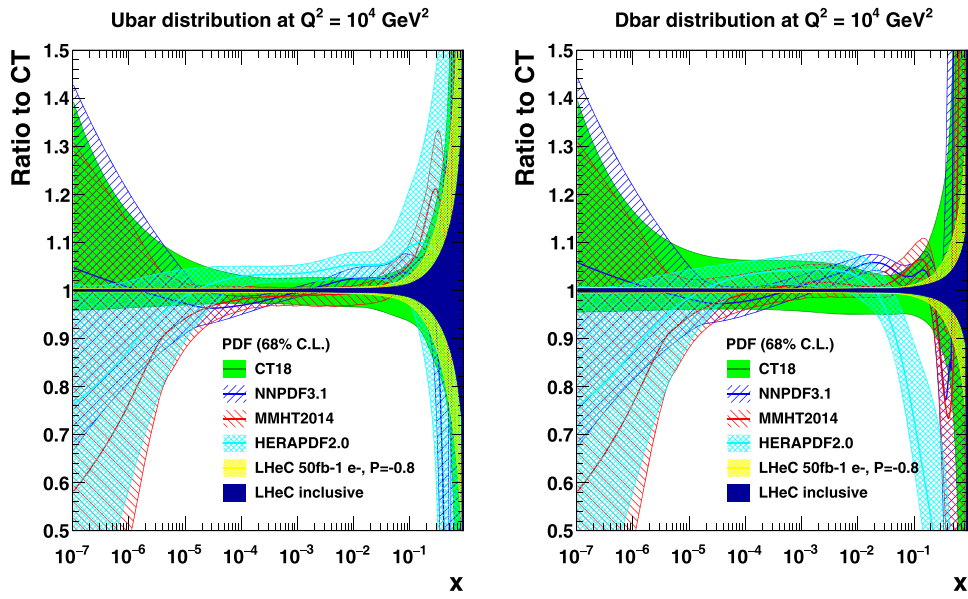


**Figure 14.** Sea quark distributions at  $Q^2 = 10^4 \text{ GeV}^2$  as a function of  $x$ , displayed as the ratio to the CT18 PDF set. The yellow band corresponds to the ‘LHeC first run’ PDFs (D2), while the dark blue band shows the final ‘LHeC inclusive’ PDFs (D4, D5, D6, and D9), as described in the text. Both LHeC PDFs shown are scaled to the central value of CT18.

$\kappa = (s + \bar{s})/(\bar{u} + \bar{d}) \sim 0.5$  Recent measurements made by the LHC [73–76] and from related studies [77, 78] suggest a larger strange-quark distribution, that may potentially be even larger than those of the up and down sea quarks. The  $x$  dependence of  $x\bar{s}$  is essentially unknown, and it may differ from that of  $x\bar{d}$  or  $x(\bar{u} + \bar{d})$  by more than a normalisation factor. A recent paper ascribes the strange enhancement to a suppression of the anti-down distribution related to suspected parameterisation effects and the behaviour of the ratio  $d/u$  for  $x \rightarrow 1$  [79]. Apparently, a direct measurement of  $x\bar{s}(x, Q^2)$  and the resolution of the complete light-quark structure of the proton is required, which is a fundamental goal of the LHeC.

The precise knowledge of the strange quark PDF is of high relevance, since it provides a significant contribution to *standard candle* measurements at the HL-LHC, such as  $W/Z$  production, and it imposes a significant uncertainty on the  $W$  mass measurements at the LHC. The question of light-sea flavour ‘democracy’ is of principal relevance for QCD and the parton model. For the first time, as has been presented in section 3.2.2,  $x\bar{s}(x, Q^2)$  will be accurately measured, namely through the charm tagging  $W_s \rightarrow c$  reaction in CC  $e^-p$  scattering at the LHeC. The inclusion of the CC charm data in the PDF analysis will settle the question of how strange the strange quark distribution really is<sup>166</sup>. This prospect has been analysed within the LHeC fit framework introduced here and also studied in detail in a profiling analysis using *xFitter*. Both analyses yield rather compatible results and are presented in the following.

In the standard LHeC fit studies, the parameterised PDFs are the four quark distributions  $xu_v$ ,  $xd_v$ ,  $x\bar{U}$ ,  $x\bar{D}$  and  $xg$  (constituting a  $4 + 1$  parameterisation), as the inclusive NC and CC data only determine the sums of the up and down quark and antiquark distributions,

<sup>166</sup> The provision of positron–proton data will enable very interesting tests of charge symmetry, i.e., it will allow us to search for a difference between the strange and anti-strange quark densities. This has not been studied in this paper.

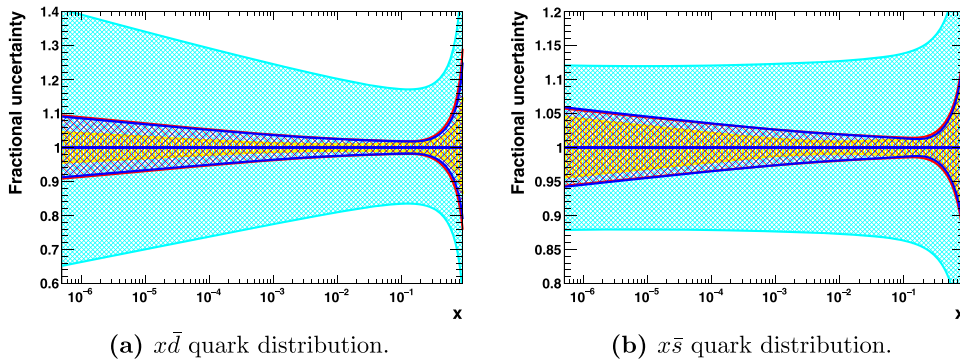


**Figure 15.** PDF uncertainties at  $Q^2 = 1.9 \text{ GeV}^2$  as a function of  $x$  for the  $\bar{d}$  and  $\bar{s}$  distributions. The yellow band represents the uncertainties of the nominal ‘LHeC inclusive’ PDF, which was obtained from a  $4 + 1$  PDF fit. Using the same dataset, the results of the more flexible  $5 + 1$  fit (see text) are displayed as a cyan band. The red band displays the results when an LHeC measurement of the  $\bar{s}$  quark density is also included. When, as a further step, LHeC measurements of  $F_2^c$  and  $F_2^b$  are also included, the PDF fit yields the uncertainties displayed by the blue band.

as discussed previously. The strange-quark PDF is then assumed to be a constant fraction of  $x\bar{d}$ .

With the strange-quark data available, the LHeC PDF fit parameterisations can be extended to include  $x\bar{s}$ , parameterised as  $A_s x^{B_s} (1-x)^{C_s}$ .<sup>167</sup> For the fits presented in the following,  $\bar{d}$  and  $\bar{s}$  are now treated separately, and therefore a total of five quark distributions are parameterised ( $xu_v$ ,  $xd_v$ ,  $x\bar{u}$ ,  $x\bar{d}$ ,  $x\bar{s}$ ) as well as  $g$ . This provides a  $5 + 1$  parameterisation, and the total number of free parameters in the PDF fit then becomes 17.

The results for the  $5 + 1$  PDF fits are shown in figure 15, where fits to inclusive NC/CC DIS data are displayed for reference (for both the  $4 + 1$  and  $5 + 1$  ansatzes) and the fits where, in addition, strange density measurements and even further measurements of  $F_2^{c,b}$  are considered. As expected, the uncertainties of the  $5 + 1$  fit to the inclusive DIS data, especially for the  $\bar{d}$  and  $\bar{s}$  distributions (cf figure 15), become substantially larger in comparison to the respective  $4 + 1$  fit, since the  $\bar{d}$  and  $\bar{s}$  distributions are now treated separately. This demonstrates that the inclusive DIS data alone do not have the flavour-separating power to determine the individual distributions very precisely.

When an LHeC measurement of the  $\bar{s}$  quark density based on  $10 \text{ fb}^{-1}$  of  $e^-p$  data is included, the uncertainties in the  $\bar{d}$  and  $\bar{s}$  PDFs become significantly smaller. By chance, those uncertainties are then comparable to those of the  $4 + 1$  fit, in which  $x\bar{s}$  is linked to  $x\bar{d}$  by a constant fraction.

The constraints from a measurement of charm quark production cross-sections in CC DIS have also been studied in a profiling analysis using *xFitter* [80]. The treatment of heavy quark production in higher order pQCD is extensively discussed in this paper. At leading-order QCD, the subprocess under consideration is  $Ws \rightarrow c$ , where  $s$  represents an intrinsic strange quark. Figure 16 displays the tight constraints obtained for the strange PDF when using the LHeC pseudo-data for the CC charm production channel. The results of this profiling analysis, both

<sup>167</sup> It is worth mentioning that the  $W, Z$  data [73] essentially only determine the moment of  $x\bar{s}$  at  $x \sim 0.02$ , and not the  $x$ -dependence. Therefore, in analyses of HERA and ATLAS data, such as reference [78], no determination of the relevant parameter,  $B_s$ , is attempted, which is instead set equal to  $B_{\bar{d}}$ . The kinematic dependence of  $x\bar{s}$  is basically not determined by the LHC data, but the hint that the strange quark density is unsuppressed has been persistent.

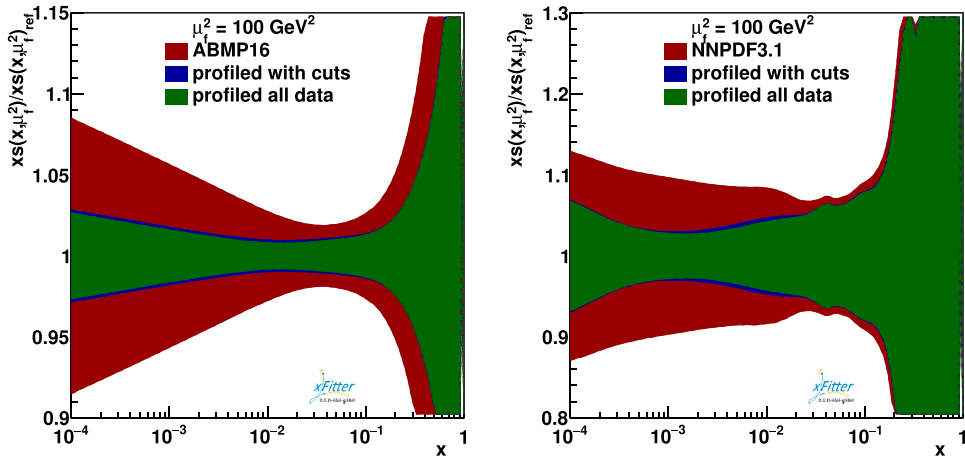


**Figure 16.** Constraints on the strange-quark PDF  $x_s$  using simulated data for CC production of charm quarks at the LHeC, from a profiling study [80] using the ABMP16 (left) and the NNPDF3.1 (right) PDF sets. The red band displays the nominal PDF uncertainties, and the green and blue bands show the improved uncertainties due to the LHeC strange quark data.

those based on the [52] and NNPDF3.1 PDF sets and those of the direct fit presented above, are very similar, reaching a precision of about 3%–5% for  $x$  less than  $\simeq 0.01$ .

In a variation of the study described in [80], a large reduction in uncertainties was already observed when the input data were restricted to the kinematic range in which the differences between the different HF schemes (variable flavour number schemes (VFNSs) and fixed flavour number schemes (FFNSs)) were less than the current PDF uncertainties. This further indicates that the PDF constraints are stable and independent of the particular heavy-flavour scheme.

It may thus be concluded that the LHeC, through high luminosity, high energy, and precise kinematic reconstruction, will be able to solve a long-standing question about the role of the strange-quark density in the proton, and its integration into a consistent QCD treatment of parton dynamics.

**3.3.5. Heavy quarks.** One of the unsolved mysteries of the SM is the existence of three generations of quarks and leptons. The strongly interacting fermion sector contains a total of six quarks with masses that differ by up to five orders of magnitude. This hierarchy of masses is, on the one hand, a challenge to explain, but on the other hand, it offers a unique opportunity to explore dynamics at a variety of different scales and thus develop different facets of the strong interaction. While the light quarks at low scales are non-perturbative and couple strongly, the heavier quarks (charm, bottom, and top) are separated from the soft sea by their masses and can thus serve as a suitable additional probe for the soft part of QCD.

There are a number of deep and unresolved questions that can be posed in the context of the proton structure: what is the individual contribution of the different quark flavours to the structure functions? Are heavy quarks, such as the charm and bottom quarks, radiatively generated, or is there also an intrinsic heavy-quark component in the proton? To what extent do the universality and factorisation theorems work in the presence of heavy quarks? It is therefore imperative to be able to perform precise measurements of each individual quark flavour



and their contribution to the proton structure. The LHeC is the ideal place for these investigations, because it will resolve the complete composition of the proton flavour by flavour. In particular, as shown in section 3.2.2, the LHeC provides data for  $F_2^c$  and  $F_2^b$  that extend over nearly five and six orders of magnitude in  $x$  and  $Q^2$ , respectively. These are obtained through charm and beauty tagging with high precision in NC  $ep$  scattering. A thorough PDF analysis of the LHeC data can thus be based on the inclusive NC/CC cross-sections and tagged  $s$ ,  $c$ ,  $b$  data. In addition, one may use DIS jets, used here for the  $\alpha_s$  prospective study (section 4.1) and low-energy data, and analysed here to resolve the low- $x$  dynamics with a precision measurement of  $F_L$  (section 4.2.3). The current studies in this chapter must therefore be understood to be indicative only, as we have not yet performed a comprehensive analysis using all these data<sup>168</sup>.

The production of heavy quarks (charm and bottom) at HERA was an especially interesting process, as the quark mass introduced a new scale ( $m = m_{c,b}$ ) that was neither heavy nor light (see e.g. reviews [81, 82]). In fact, the treatment of heavy-quark mass effects is essential in PDF fits that include data from fixed-target to collider energies and thus require the computation of physical cross-sections over a large range of perturbative scales  $\mu^2$ . As these scales pass through (or close to) the thresholds for charm, bottom, and eventually top quarks, precise computations demand the incorporation of heavy-quark mass effects close to the threshold  $\mu^2 \sim m^2$  and the resummation of collinear logarithms  $\ln(\mu^2/m^2)$  at scales far above the threshold, i.e.  $\mu^2 \gg m^2$ . The first problem can be dealt with through the use of massive matrix elements for the generation of heavy quark–antiquark pairs, while keeping a fixed number of parton densities (fixed flavour number schemes, FFNSs). On the other hand, the proper treatment of resummation is achieved through the use of variable flavour number schemes (VFNSs), which deal with an increasing number of massless parton species, evolved through standard DGLAP, when the scale is increased above heavy-quark mass thresholds. At present, calculations involving heavy quarks in DIS in different schemes (generalised-mass VFNSs) with different numbers of active flavours participating in DGLAP evolution are combined to derive an expression for the coefficient functions which is valid both close to the threshold and far above it. Such multiscale problems are particularly difficult, and numerous techniques have been developed to cope with this challenging problem [51, 83–91]. Additional complications, see e.g. reference [92], arise when the possibility of a non-perturbative origin of heavy quark distributions is allowed above the heavy quark mass threshold—intrinsic HF. The ABMP16 analysis [52] underlines that the available DIS data are compatible with an FFNS treatment, assuming that the heavy quarks are generated in the final state.

At the LHeC, as illustrated in figures 9 and 10, the large polar-angle acceptance and the high centre-of-mass energy allow heavy-quark physics to be investigated from below the threshold to almost  $10^6$  GeV<sup>2</sup>. The extended reach in comparison to HERA is dramatic. This permits the comprehensive exploration of the *asymptotic* high-energy limit where  $m_{c,b}^2/Q^2 \rightarrow 0$ , as well as the low-energy *decoupling* region  $m_{c,b}^2/Q^2 \sim 1$ .

For the PDF determination, the tagged charm and bottom data will have obvious and direct impacts on the determination of  $xc$  and  $xb$  and the clarification of their appropriate theoretical treatment. In addition, however, a remarkable improvement is achieved in the determination of the gluon density, see figure 17. The determination of  $xg$  will be discussed in much more detail in the following section.

<sup>168</sup> This is to be considered when one compares the precision of the inclusive PDF fits with that of the so-called global analyses, for example regarding the behaviour of  $xg$  at large  $x$ .



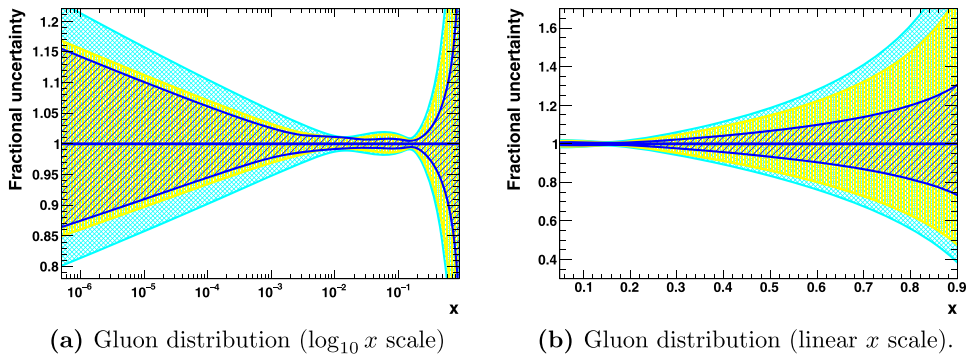


**Figure 17.** PDF uncertainties at  $Q^2 = 1.9 \text{ GeV}^2$  as a function of  $x$  to illustrate the constraints due to additional heavy-quark-sensitive measurements at the LHeC. The gluon distribution is displayed using logarithmic and linear scales. The yellow band illustrates the uncertainty of the nominal ‘LHeC inclusive’ PDF obtained from a  $4 + 1$  PDF fit. From the same dataset, the results of the more flexible  $5 + 1$  fit (see text) are displayed as a cyan band. When LHeC measurements of  $F_2^c$  and  $F_2^b$  are also included, the PDF fits yield the uncertainties displayed by the blue band.

These channels will also strongly improve the determination of the charm and bottom quark masses and bring their uncertainties down to about  $\delta m_{c(b)} \simeq 3(10) \text{ MeV}$  [1].<sup>169</sup> These accuracies and precisions are crucial in order to eliminate the corresponding model uncertainties in the PDF fit. Precision tagged charm and bottom data are also essential for the determination of the  $W$ -boson mass in  $pp$ , and the extraction of the Higgs  $\rightarrow c\bar{c}$  and  $b\bar{b}$  couplings in  $ep$ , as discussed further below.

**3.3.6. The gluon PDF.** The LHeC, with hugely increased precision and an extended DIS kinematic range, in other words, the most appropriate process for exploring  $xg(x, Q^2)$ , can pin down the gluon distribution much more accurately than it is known today. This can primarily be attributed to the huge kinematic range and high precision of the measurement of  $\partial F_2 / \partial \ln Q^2$ , which at small  $x$  is closely related to a direct measurement of  $xg$ . The precision determination of the quark distributions discussed previously also strongly constrains  $xg$ . Further sensitivity originates from the high- $y$  part of the NC cross-section, which is controlled by the longitudinal structure function, as discussed in section 4.2.3.

The gluon distribution, as obtained from the fit to the LHeC inclusive NC/CC data, is shown in figure 18. The determination of  $xg$  will be radically improved by the LHeC NC and CC precision data, which provide constraints on  $\partial F_2 / \partial \ln Q^2$  down to very low  $x$  values,  $\gtrsim 10^{-5}$ , and also at large values,  $x \leq 0.8$ .

At less than  $x \simeq 5 \times 10^{-4}$ , the HERA data provide almost no constraints, due to the kinematic limits, and therefore the gluon is currently not well known at lower  $x$ . This can be seen in all modern PDF sets. With the LHeC, a precision of a few per cent at small  $x$  will be achieved down to about  $10^{-5}$ . This should resolve the question of nonlinear parton interactions at small  $x$  (cf section 4.2). It also has direct implications for the LHC (and even more so for the FCC): with the extension of the pseudorapidity range to about 4 at the HL-LHC by ATLAS and CMS,

<sup>169</sup> Such precision demands the availability of calculations with higher orders in pQCD, and those computations are already ongoing [93–95]. Note that in PDF fits, the heavy quark mass is an effective parameter that has to be related to the pole mass; see e.g., reference [96] and references therein.

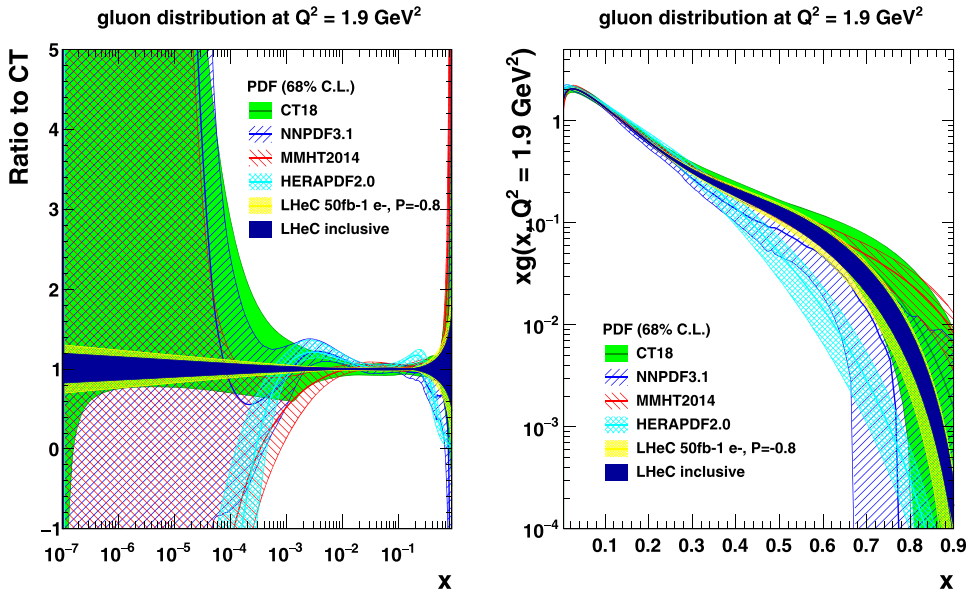


**Figure 18.** Gluon distribution at  $Q^2 = 1.9 \text{ GeV}^2$  as a function of  $x$ . Left: the distribution is displayed as the ratio to the CT18 PDF set and highlights the low- $x$  region. Right: the distribution is shown on a linear  $x$  scale and highlights the high- $x$  region. The yellow band corresponds to the ‘LHeC first run’ PDFs (D2), while the dark blue band shows the ‘LHeC inclusive’ PDFs (D4, D5, D6, and D9), as described in the text. Both LHeC PDFs are shown scaled to the central value of CT18.

Higgs physics will become small- $x$  physics, for which  $xg$  must be known very accurately, since  $gg \rightarrow H$  is the dominant production mechanism.

At large  $x$ , i.e. at values greater than 0.3, the gluon distribution becomes very small. In this region, the uncertainty in  $xg$  is very large, and the gluon distributions from several PDF groups differ substantially. The limited experimental constraints are partially due to the small luminosity at HERA, while the uncertainties in jet measurements are also non-negligible. In addition, at high  $x$  the valence quarks dominate, the non-singlet evolution of which is insensitive to the gluon distribution. At the LHeC, the very large luminosity provides NC and CC data that accurately access the highest values of  $x$ , disentangling the sea from the dominant valence part. The gluon distribution at high  $x$  is then largely constrained by the momentum sum rule, which at the LHeC (and FCC-eh) profits from the seminal coverage from  $x$  near 1 down to very small values of  $x$ . The resulting tiny uncertainties in the high- $x$  quark and gluon PDFs, as illustrated in the figures, are of great importance for BSM searches in hadron–hadron collisions at high energy scales, as illustrated in this paper. If the LHeC were to establish nonlinear parton interactions at small  $x$ , this would also be reflected in high- $x$  PDFs. Furthermore, tests of the factorisation theorem can be performed and electroweak effects can be measured to unprecedented precision jointly with PDFs (see also section 5.1).

The analysis presented here has not made use of the additional information that is provided at the LHeC in the measurements of  $F_2^{c,b}$  (see section 3.3.5) or  $F_L$ . The large- $x$  situation can be expected to further improve with the use of LHeC jet data, providing further direct constraints at large  $x$  which, however, have not yet been studied in comparable detail.

The LHeC is the ideal laboratory for resolving all the unknowns of the gluon density, which is the origin of all the visible mass in the Universe and one of the particular secrets of particle physics, since gluons cannot be directly observed but are confined inside hadrons. It is obvious that resolving this puzzle is an energy-frontier DIS task and goal, which also includes electron-ion scattering since the gluons inside heavy matter are known even less. Therefore, the special importance of this part of high-energy PDF physics is not primarily related to the smallness of the uncertainties; rather, it is about a consistent understanding and resolution of QCD at all regions of the spatial and momentum dimensions that the LHeC will explore.

**3.3.7. Luminosity and beam-charge dependence of LHeC PDFs.** It is informative to study the transition of the PDF uncertainties from the ‘LHeC first run’ PDFs, which only exploit a single electron–proton dataset, D2, through to the ‘LHeC final inclusive’ PDFs, which make use of the full datasets D4, D5, D6, and D9, as listed in table 8, i.e. including high-luminosity data (D4), small sets of low-energy ( $E_p = 1$  TeV) and positron data (D5 and D6), together with  $10 \text{ fb}^{-1}$  of opposite helicity data (D9). Various intermediate PDF fits are performed using subsets of the data in order to quantify the influence of the beam parameters on the precision of the various PDFs. All fits use the same standard  $4 + 1$  fit parameterisation and exclude the use of  $s, c, b$  data, the effect of which was evaluated previously. The fits neither include the low-electron-energy data sets generated for the  $F_L$  analysis (see section 4.2.3), nor any jet  $ep$  data. The emphasis is on the development of the  $u_v, d_v$ , total sea and  $xg$  uncertainties.

A first study, figure 19, shows the influence of the integrated luminosity. This compares four cases, three with luminosity increasing from 5, to 50, to  $1000 \text{ fb}^{-1}$ . These assumptions, according to the luminosity scenarios presented elsewhere, correspond to year one (D1), the initial three years (D2) and the maximum attainable integrated luminosity (D4). The fourth case is represented by what is known as the LHeC inclusive fit. One can observe a number of features. For example, the initial  $5 \text{ fb}^{-1}$  (yellow in figure 19), i.e. ten times the amount that either H1 or ZEUS collected over its lifetime (albeit with different beam parameters), leads (i) to an extension of the HERA range to low and higher  $x$ , (ii) to high precision at small  $x$ , for example, of the sea quark density of 5% below  $x = 10^{-5}$ , or (iii) also of 5% for  $u_v$  at very high  $x = 0.8$ . With  $50 \text{ fb}^{-1}$  the down-valence distribution is measured to a precision of within 20% at  $x = 0.8$ , an improvement of about a factor of two, compared to the  $5 \text{ fb}^{-1}$  case, and a major improvement on what is currently known about  $x d_v$  at large  $x$  (compare with figure 11). The very high luminosity, taken here to be  $1 \text{ ab}^{-1}$ , leads to the next level of high precision, for example, better than 2% below  $x = 10^{-5}$  for the total sea. The full data set further improves the situation, especially the case for  $x d_v$  and the gluon at high  $x$ . The valence quark improvement is mostly linked to the positron data, while the gluon improvement is related to the extension of the lever arm towards small values of  $Q^2$  as the reduction of  $E_p$  extends the acceptance at large  $x$ . The visible improvement through the final inclusive fit is probably related to the increased precision at high  $x$ , as there is a momentum sum rule correlation over the full range of  $x$ . In comparison to the analogous HERA fit, it becomes clear that the vast majority of the gain is already present in the first  $5\text{--}50 \text{ fb}^{-1}$ .

The second study presented here concerns the impact on the PDF uncertainties when additional positron data of different luminosities are added to a baseline fit of  $50 \text{ fb}^{-1}$  of  $e^-p$  data, the ‘LHeC first run’ dataset. The results are illustrated in figure 20. It can be observed that the addition of the positron data does bring benefits, which, however, are not striking in their effect on the PDFs considered here. A notable improvement is obtained for the  $d$ -valence PDF, primarily due to the sensitivity gained via the CC cross-section of the positron data. The benefit of the precise access to NC and CC weak interactions by the LHeC is clearer when one

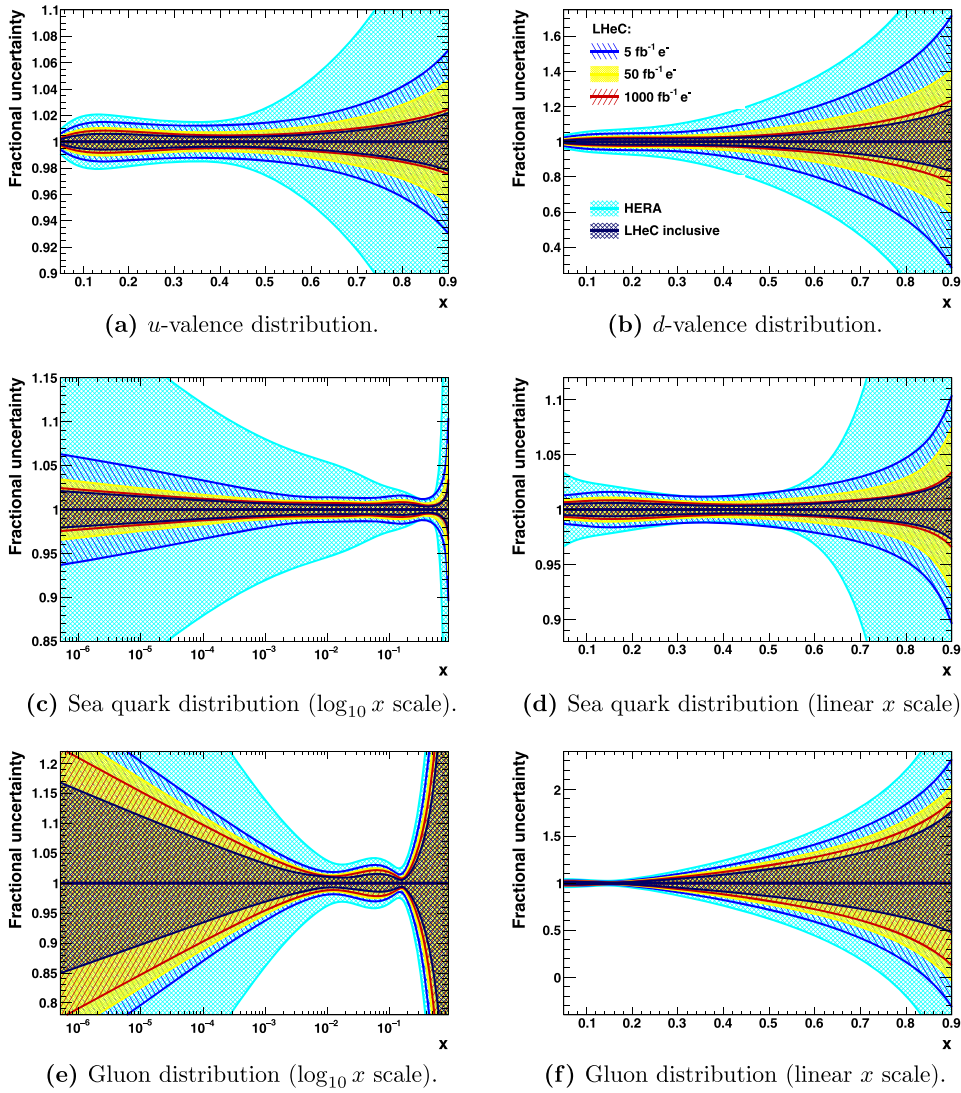


**Figure 19.** PDF distributions at  $Q^2 = 1.9 \text{ GeV}^2$  as a function of  $x$ , illustrating the impact of different amounts of integrated luminosity. The blue, yellow, and red bands correspond to LHeC PDFs using electron-only NC and CC inclusive measurements with 5, 50, and  $1000 \text{ fb}^{-1}$  (datasets D1, D2, and D4), respectively. The yellow band is therefore equivalent to the ‘LHeC first run’ PDF. For reference, the dark blue band shows the results of the final ‘LHeC inclusive’ PDF. For comparison, the cyan band represents an identical PDF fit using HERA’s combined inclusive NC and CC data [45], restricted solely to the experimental uncertainties. Note that this, unlike the LHeC band, extends everywhere beyond the narrow limits of the  $y$  scale of the plots.

studies the cross-sections and their impact on the PDFs. This is illustrated in the following section.

**3.3.8. Use of weak interactions to probe the proton structure.** It had long been suggested that the weak interactions should be used to probe the proton structure in DIS [97]. The

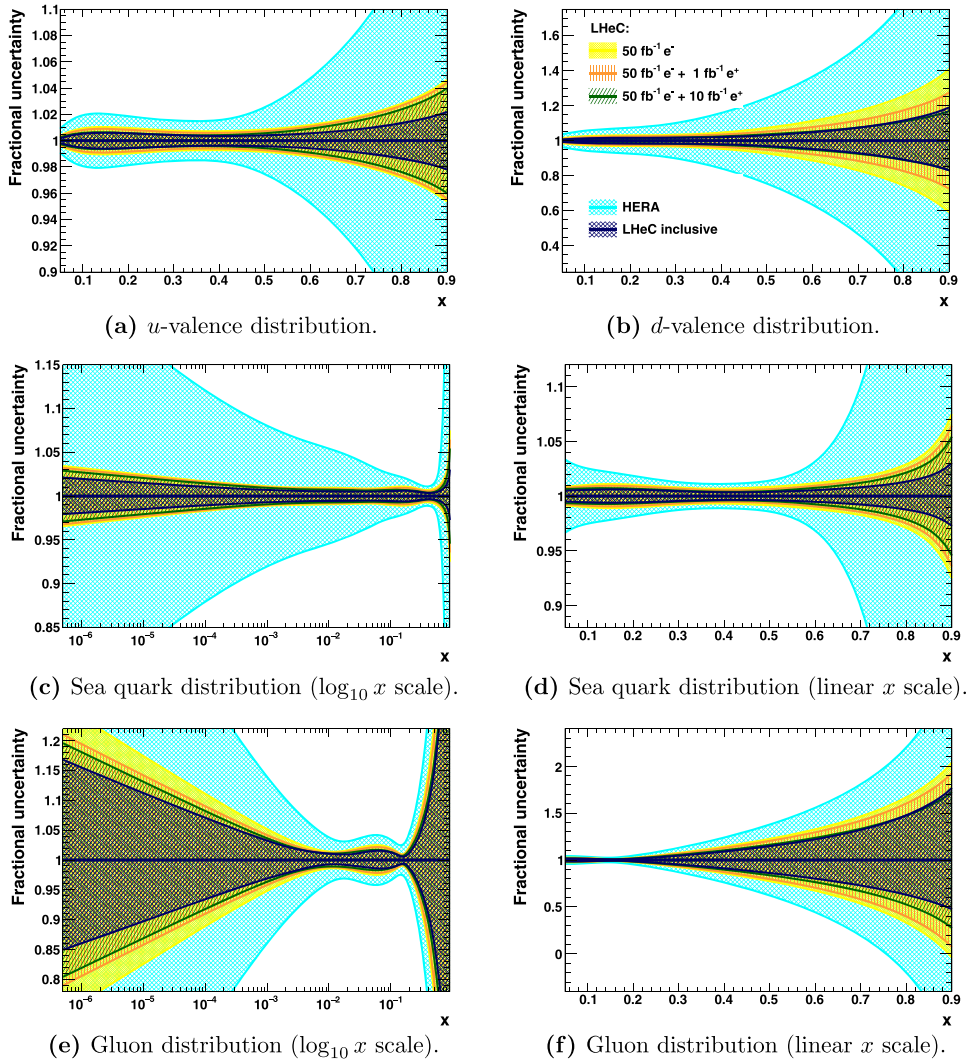


**Figure 20.** PDF distributions at  $Q^2 = 1.9 \text{ GeV}^2$  as a function of  $x$ , illustrating the impact of including positron data. The yellow (‘LHeC first run’), dark blue (‘LHeC final inclusive’), and cyan bands (HERA data) are as in figure 19. The orange band corresponds to a fit with  $1 \text{ fb}^{-1}$  of inclusive NC and CC positron–proton data, in addition to  $50 \text{ fb}^{-1}$  of electron–proton data (D2 and D6), while the green band is similar, but with  $10 \text{ fb}^{-1}$  of positron–proton data (D2 and D7).

first important steps in this direction were pursued with HERA, especially by the measurements of the polarisation and beam-charge asymmetries in NC  $ep$  scattering made by H1 and ZEUS [45]. This area of research will become a focus at the LHeC, because the  $Q^2$  range is extended by two to three orders of magnitude beyond the weak scale  $Q^2 \simeq M_{W,Z}^2$ , with hugely increased luminosity. In section 5.1 below, the emphasis is on accessing the electroweak theory parameters at a new level of sensitivity. Here, we illustrate the importance of using the  $Z$  and  $W$  exchanges to pin down the parton contents of the proton. This has been implicit for the



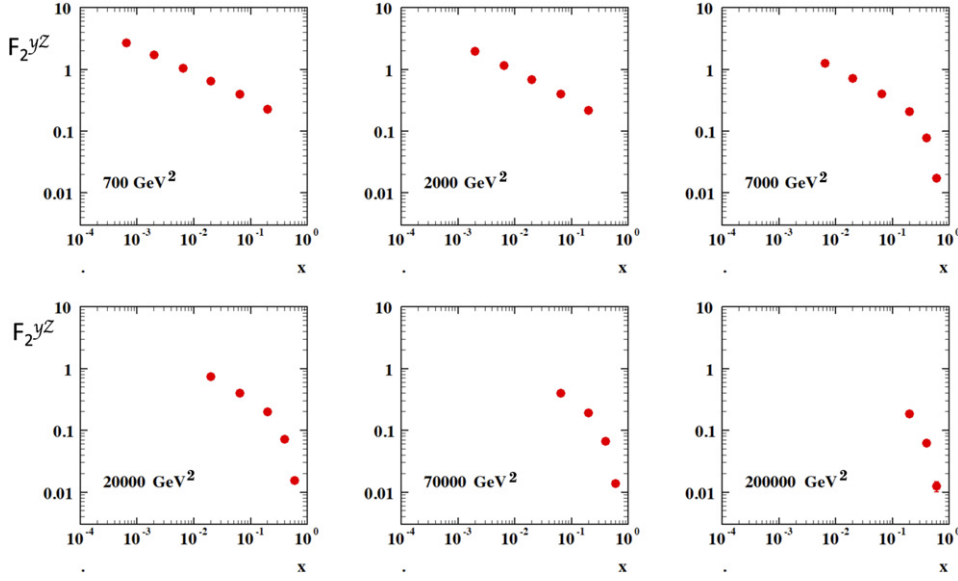


**Figure 21.** Prospective measurement of the photon– $Z$  interference structure function  $F_2^{\gamma Z}(x, Q^2)$  at the LHeC using polarised electron beams of helicity  $\pm 0.8$  and an integrated luminosity of  $10 \text{ fb}^{-1}$  for each state. The uncertainties are statistical only.

QCD fits presented above, yet it only emerges clearly when one directly considers the cross-sections, their asymmetries with respect to beam charge and polarisation, and certain kinematic limits.

Parity violation is accessed in NC DIS through a variation of the lepton-beam helicity,  $P$ , as can be deduced from [97]

$$\frac{\sigma_{\text{r,NC}}^{\pm}(P_R) - \sigma_{\text{r,NC}}^{\pm}(P_L)}{P_R - P_L} = \mp \kappa_Z g_A^e F_2^{\gamma Z} - (\kappa_Z g_A^e)^2 \frac{Y_-}{Y_+} x F_3^Z \quad (3.3)$$

where  $\sigma_{\text{r,NC}}$  denotes the double differential NC scattering cross-section scaled by  $Q^4 x / 2\pi\alpha^2 Y_+$ . Here  $\kappa_Z$  is of the order of  $Q^2/M_Z^2$ ,  $F_2^{\gamma Z} = 2x \sum Q_q g_V^q (q - \bar{q})$  and the NC vector couplings are determined by  $g_V^f = I_{3,L}^f - 2Q_f \sin^2 \theta_W$ , where  $Q_f$  is the electric charge and  $I_{3,L}^f$  the left-handed weak isospin charge of the fermion  $f = e, q$ , which also determines the axial vector couplings  $g_A^f$ , with  $g_A^e = -1/2$ . At the LHeC (unlike FCC-eh) the second term in equation (3.3) is suppressed with respect to the first one, as it results from a pure  $Z$  exchange and because the  $Y$  factor is small,  $\propto y$ , since  $Y_{\mp} = (1 \mp (1-y)^2)$ .

For the approximate value of the weak mixing angle  $\sin^2 \theta_W = \frac{1}{4}$ , one obtains  $g_V^e = 0$ ,  $g_V^u = 1/6$  and  $g_V^d = -1/3$ . Consequently, one may write (to a good approximation)

$$F_2^{\gamma Z}(x, Q^2) = 2x \sum_q Q_q g_V^q (q - \bar{q}) \simeq x \frac{2}{9} [U + \bar{U} + D + \bar{D}]. \quad (3.4)$$

The beam helicity asymmetry therefore determines the total sea. A simulation is shown in figure 21 for integrated luminosities of  $10 \text{ fb}^{-1}$  and helicities of  $P = \pm 0.8$ .

Apparently, this asymmetry will provide a very precise measurement of the total sea. The combination of up and down quarks accessed using  $F_2^{\gamma Z}$  (equation (3.4)) is different from that

provided by the known function

$$F_2(x, Q^2) = 2x \sum_q Q_q^2 (q - \bar{q}) = x \frac{1}{9} [4(U + \bar{U}) + D + \bar{D}] \quad (3.5)$$

because of the difference between the photon and  $Z$  boson couplings to quarks. Following equation (3.3), the beam polarisation asymmetry

$$A^\pm = \frac{\sigma_{\text{NC}}^\pm(P_R) - \sigma_{\text{NC}}^\pm(P_L)}{\sigma_{\text{NC}}^\pm(P_R) + \sigma_{\text{NC}}^\pm(P_L)} \simeq \mp (P_L - P_R) \kappa_Z g_A^e \frac{F_2^{\gamma Z}}{F_2} \quad (3.6)$$

measures the  $F_2$  structure function ratio to a very good approximation. The different compositions of the up and down quark contributions to  $F_2^{\gamma Z}$  and  $F_2$ , see above, indicate that the weak NC interactions will assist in separating the up and down quark distributions that HERA had to link together by setting  $B_d = B_u$ .

Inserting  $P_L = -P_R = -P$  and considering the large  $x$  limit, one observes that the asymmetry measures the  $d/u$  ratio of the valence quark distributions according to

$$A^\pm \simeq \pm \kappa_Z P \frac{1 + d_v/u_v}{4 + d_v/u_v}. \quad (3.7)$$

This quantity will be accessible with very high precision, as figure 21 illustrates, which is one reason (besides the CC cross-sections) why the  $d/u$  ratio turns out to be so highly constrained by the LHeC (see figure 12).

A further interesting quantity is the the lepton-beam charge asymmetry, which is given by

$$\sigma_{\text{r,NC}}^+(P_1) - \sigma_{\text{r,NC}}^-(P_2) = \kappa_Z a_e \left[ - (P_1 + P_2) F_2^{\gamma Z} - \frac{Y_-}{Y_+} \left( 2x F_3^{\gamma Z} + \kappa_Z a_e (P_1 - P_2) x F_3^Z \right) \right] \quad (3.8)$$

neglecting the terms  $\propto g_V^e$ . For zero polarisation this directly provides a parity-conserving measurement of the structure function

$$xF_3^{\gamma Z}(x, Q^2) = 2x \sum_q Q_q g_A^q (q - \bar{q}) = \frac{2}{3}x (U - \bar{U}) + \frac{1}{3}x (D - \bar{D}). \quad (3.9)$$

The appearance of this function in weak NC DIS resembles that of  $xW^3$  in CC, or fixed-target neutrino-nucleon scattering, and allows one to resolve the flavour contents of the proton. The function  $xF_3^{\gamma Z}$  was first measured by the BCDMS collaboration in  $\mu^\pm C$  scattering [98] at the SPS.

The HERA result is shown in figure 22. It covers the range from about  $x = 0.05$  to  $x = 0.6$  with a typical statistical precision of 10%. Assuming that the sea and antiquark densities are equal, such as  $u_s = \bar{u}$  or  $d_s = \bar{d}$ ,  $xF_3^{\gamma Z}$  is given by  $x/3(2u_v + d_v)$ . This function therefore accesses valence quarks down to small values of  $x$  where their densities become much smaller than those of the sea quarks. Since the  $Q^2$  evolution of the non-singlet valence quark distributions is very weak, it has been customary to project the various charge asymmetry measurements to some low value of  $Q^2$  and present the measurement as the  $x$  dependence of  $xF_3^{\gamma Z}$ .

If, however, there were differences between the sea and antiquarks, for example, if  $s \neq \bar{s}$ , one would expect a rise of  $xF_3^{\gamma Z}$  towards low  $x$ . This may be a cause for the undershoot of the QCD fit below the HERA data near  $x \simeq 0.01$ , see figure 22, are not yet precise enough.



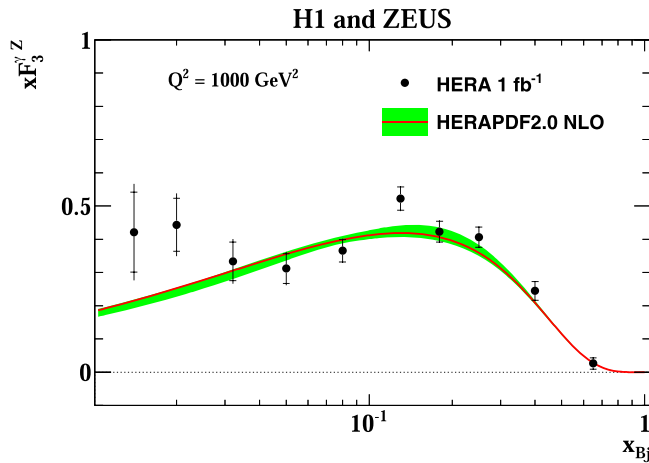


**Figure 22.** Combination of H1 and ZEUS measurements of the structure function  $x F_3^{\gamma Z}(x, Q^2)$  as a function of  $x$  projected to a fixed  $Q^2$  value of 2000 GeV<sup>2</sup>. Reproduced with permission from [45]. The inner error bar represents the statistical uncertainty.

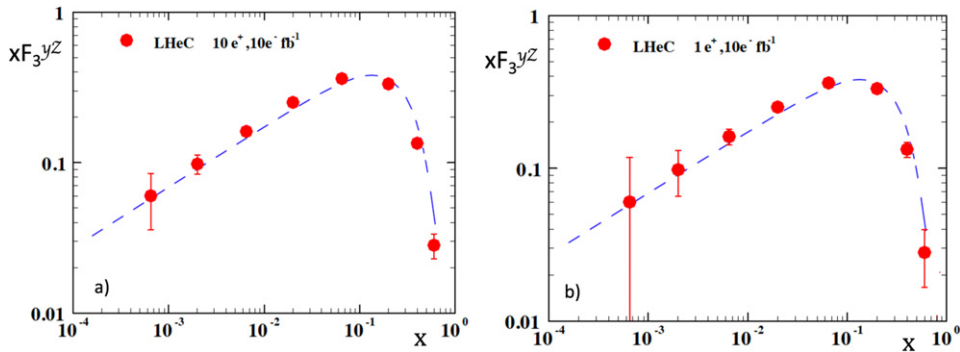


**Figure 23.** Prospective measurement of the photon– $Z$  interference structure function  $x F_3^{\gamma Z}(x, Q^2)$  at the LHeC, projected to a fixed  $Q^2$  value of 2000 GeV<sup>2</sup>. The results correspond to a cross-section charge asymmetry for an unpolarised  $e^-p$  beam with 10 fb<sup>-1</sup> of luminosity combined with unpolarised  $e^+p$  beams of (a) 10 fb<sup>-1</sup> (left) and (b) 1 fb<sup>-1</sup> (right). The error bars represent the statistical uncertainty. The curve is drawn to guide the eye. It is possible that the measurement will discover an increase in  $x F_3^{\gamma Z}$  towards low  $x$  if there are hitherto unknown differences between sea and antiquark densities (see the text).

However, it is apparent that, besides providing constraints on the valence-quark densities, this measurement indeed has the potential to discover a new anti-symmetry in the quark sea.

Such a discovery would be enabled by the LHeC as illustrated in figure 23, with an extension of the kinematic range by an order of magnitude towards small  $x$  and a much-increased precision in the medium- $x$  region. The simulation is performed for 10 and 1 fb<sup>-1</sup> of  $e^+p$  luminosity. Obviously, it would be very desirable to reach high values of integrated luminosity in positron–proton scattering as well.

Finally, it is of interest to consider the role of precisely measured cross-sections in CC scattering. The coupling of the  $W$  boson to quarks is flavour-dependent, resulting in the relations

$$\sigma_{r,CC}^+ = (1 + P)[x\bar{U} + (1 - y)^2 xD], \quad (3.10)$$

$$\sigma_{r,CC}^- = (1 - P)[xU + (1 - y)^2 x\bar{D}]. \quad (3.11)$$

Here,  $\sigma_{r,CC}$  is the double differential CC DIS cross-section scaled by a factor of  $2\pi x \cdot (M_W^2 + Q^2)^2 / (G_F M_W^2)^2$  with the Fermi constant  $G_F$  and the  $W$  boson mass  $M_W$ . The positron beam at the LHeC will most likely be unpolarised,  $P = 0$ . The maximum rate of  $e^-p$  is achieved with large negative polarisation. In the valence-quark approximation, the  $e^+p$  CC cross-section is proportional to  $(1 - y)^2 x d_v$  while  $\sigma_{r,CC}^- \propto u_v$ . This provides direct, independent measurements of  $d_v$  and  $u_v$ , as already illustrated in the LHeC CDR [1].

Inclusive NC and CC DIS accesses four combinations of parton distributions, as is obvious from equation (3.10) for CC above and from the NC relation

$$\sigma_{r,NC}^\pm \simeq [c_u(U + \bar{U}) + c_d(D + \bar{D})] + \kappa_Z[d_u(U - \bar{U}) + d_d(D - \bar{D})]$$

with

$$c_{u,d} = Q_{u,d}^2 + \kappa_Z(-g_V^e \mp P g_A^e) Q_{u,d} g_V^{u,d} \quad \text{and} \quad d_{u,d} = \pm g_A^e g_A^{u,d} Q_{u,d}, \quad (3.12)$$

restricted to photon and  $\gamma Z$  interference contributions. These four PDF combinations are complemented by the  $s, c, b$  measurements introduced previously. The parton contents can therefore be completely resolved, which was impossible at HERA.

It is the high-energy and high-luminosity access to DIS, the high-precision NC/CC, and the tagged heavy-quark measurement programme, which make the LHeC an environment uniquely suited to uncovering the secrets of parton structure and dynamics. This will establish a new level with possible discoveries of strong-interaction physics and also provide the necessary basis for precision electroweak and Higgs measurements at the LHC, massively extending the range of BSM searches and reliably interpreting NP signals in hadron-hadron scattering at the LHC.

**3.3.9. Parton-parton luminosities.** The energy frontier in accelerator particle physics is represented by the LHC, with a cms energy of  $\sqrt{s} = 2E_p \simeq 14$  TeV, and the prospect of a future circular hadron collider, the FCC-hh, which will reach energies of up to  $\sqrt{s} = 100$  TeV. Proton-proton collider reactions are characterised by DY scattering [99]. To leading order, the double differential DY scattering cross-section [100] for the NC reaction  $pp \rightarrow (\gamma, Z)X \rightarrow e^+e^-X$  and the CC reaction  $pp \rightarrow W^\pm X \rightarrow e\nu X$  can be written as

$$\frac{d^2\sigma}{dM dy} = \frac{4\pi\alpha^2(M)}{9} \cdot 2M \cdot P(M) \cdot \Phi(x_1, x_2, M^2) \text{ (nb GeV}^{-1}\text{)}. \quad (3.13)$$

Here,  $M$  is the mass of the  $e^+e^-$ ,  $e^+\nu$ , and  $e^-\bar{\nu}$  systems for the NC and CC processes, respectively, and  $y$  is the boson rapidity. The cross-section implicitly depends on the Bjorken  $x$  values of the incoming quark  $q$  and its antiquark  $\bar{q}$ , which are related to the rapidity  $y$  as follows:

$$x_1 = \sqrt{\tau} e^y \quad x_2 = \sqrt{\tau} e^{-y} \quad \tau = \frac{M^2}{s}. \quad (3.14)$$

For the NC process, the cross-section is the sum of the contributions of the photon and  $Z$  exchanges as well as an interference term. In the case of photon exchange, the propagator term  $P(M)$  and the parton distribution term  $\Phi$  are given by

$$P_\gamma(M) = \frac{1}{M^4} \quad \Phi_\gamma = \sum_q Q_q^2 F_{q\bar{q}} \quad (3.15)$$

$$F_{q\bar{q}} = x_1 x_2 \cdot [q(x_1, M^2) \bar{q}(x_2, M^2) + \bar{q}(x_1, M^2) q(x_2, M^2)]. \quad (3.16)$$

The corresponding formulae for the  $\gamma Z$  interference term read as follows:

$$P_{\gamma Z} = \frac{\kappa_Z g_V^e (M^2 - M_Z^2)}{M^2 [(M^2 - M_Z^2)^2 + (\Gamma_Z M_Z)^2]} \quad \Phi_{\gamma Z} = \sum_q 2Q_q g_V^q F_{q\bar{q}}. \quad (3.17)$$

The interference contribution is small, as it is proportional to the vector coupling of the electron  $g_V^e$ . One also sees in equation (3.17) that the interference cross-section contribution changes sign from plus to minus as the mass increases and passes  $M_Z$ . The expressions for  $P$  and  $\Phi$  for the pure  $Z$  exchange part are

$$P_Z = \frac{\kappa_Z^2 (g_V^{e^2} + g_A^{e^2})}{(M^2 - M_Z^2)^2 + (\Gamma_Z M_Z)^2} \quad \Phi_Z = \sum_q (g_V^{q^2} + g_A^{q^2}) F_{q\bar{q}}. \quad (3.18)$$

For the CC cross-section, the propagator term is

$$P_W = \frac{\kappa_W^2}{(M^2 - M_W^2)^2 + (\Gamma_W M_W)^2} \quad (3.19)$$

and the charge-dependent parton distribution forms are

$$\begin{aligned} \Phi_{W^+} = x_1 x_2 [ & V_{ud}^2 (u_1 \bar{d}_2 + u_2 \bar{d}_1) + V_{cs}^2 (c_1 \bar{s}_2 + c_2 \bar{s}_1) \\ & + V_{us}^2 (u_1 \bar{s}_2 + u_2 \bar{s}_1) + V_{cd}^2 (c_1 \bar{d}_2 + c_2 \bar{d}_1) ] \end{aligned} \quad (3.20)$$

$$\begin{aligned} \Phi_{W^-} = x_1 x_2 [ & V_{ud}^2 (\bar{u}_1 d_2 + \bar{u}_2 d_1) + V_{cs}^2 (\bar{c}_1 s_2 + \bar{c}_2 s_1) \\ & + V_{us}^2 (\bar{u}_1 s_2 + \bar{u}_2 s_1) + V_{cd}^2 (\bar{c}_1 d_2 + \bar{c}_2 d_1) ], \end{aligned} \quad (3.21)$$

with  $\kappa_W = 1/(4 \sin^2 \Theta)$  and  $q_i = q_i(x, M^2)$  and the Cabibbo-Kobayashi-Maskawa (CKM) matrix elements  $V_{ij}$ . The expressions given here are valid in the QPM. At higher-order pQCD, DY scattering also includes quark–gluon and gluon–gluon contributions. Certain production channels are sensitive to specific parton–parton reactions; Higgs production, for example, originates predominantly from gluon–gluon fusion. Based on the factorisation theorem [39] a further testing ground was therefore opened for PDFs, and much of the current PDF analysis aims to constrain parton distributions using DY scattering measurements and semi-inclusive production processes such as top, jet, and charm production at the LHC. An account of this field is provided below, including a study of how LHeC would add to the ‘global’ PDF knowledge at the time of the HL-LHC.

There are drawbacks to the use of DY and other hadron collider data for the PDF determination, and advantages for  $ep$  scattering: (i) DIS has the ability to prescribe the reaction type and the kinematics ( $x, Q^2$ ) through the reconstruction of just the leptonic vertex; (ii) there is no colour reconnection, and for the lepton vertex, no hadronisation effects that disturb the theoretical description; (iii) the most precise LHC data, i.e. those for  $W$  and  $Z$  production, are located

at a fixed equivalent  $Q^2 = M_{W,Z}^2$  and represent a snapshot at a fixed scale, which in DIS at the LHeC will vary by more than five orders of magnitude<sup>170</sup>.

There are further difficulties inherent in the use of LHC data for PDF determinations, such as hadronisation corrections and data incompatibilities. For example, the most recent CT18 [67] global PDF analysis had to arrange for a separate set (CT18A), because the standard fit would not respond well to the most precise ATLAS  $W, Z$  data taken at a centre of mass energy of 7 TeV. The intent to include all data can only be realised with the introduction of so-called  $\chi^2$  tolerance criteria, which fundamentally affect the meaning of the quoted PDF uncertainties.

Conceptually, the LHeC enables us to change this approach completely. Instead of trying to use all previous and current PDF-sensitive data, to which one nowadays has no alternative, it replaces these by pure  $ep$  collider DIS data. This will bring order back into the PDF field: parton distributions will be completely resolved, using a single process extending over nearly six orders of magnitude and calculated from NLO pQCD up to probably even N<sup>4</sup>LO (see section 4.4.1). These PDFs will be applicable for (i) identifying new dynamics and symmetries; (ii) testing factorisation; (iii) confronting other PDF analyses at that time; (iv) performing high-precision Higgs and electroweak analyses, and (v) interpreting any peculiar HL-LHC signals of BSM physics using that independent PDF. It has been customary, as is obvious from equations (3.15), (3.20), and (3.21), to express the usefulness of various PDF determinations and prospects for the LHC, and similarly the FCC, with four so-called parton luminosities, which are defined as

$$L_{ab}(M_X) = \int dx_a dx_b \sum_q F_{ab} \delta(M_X^2 - sx_a x_b) \quad (3.22)$$

where  $F_{ab}$  for  $(a, b) = (q\bar{q})$  is defined in equation (3.15) and  $(a, b)$  could also be  $(g, q)$ ,  $(g, \bar{q})$  and  $(gg)$ , without a sum over quarks in the latter case. The expectations for the quark- and gluon-related four-parton luminosities are presented in figure 24. The LHeC provides very precise parton luminosity predictions in the complete range of  $M_X$  up to the high-mass edge of the search range at the LHC. This eliminates the currently sizeable PDF uncertainty of precision electroweak measurements at the LHC, as, for example, for the anticipated measurement of  $M_W$  to within an uncertainty of  $10^{-4}$ , see below. One may also notice that the gluon–gluon luminosity (top left in figure 24) is at a per cent level for the Higgs mass  $M_X = M_H \simeq 125$  GeV. This is evaluated further in the chapter on Higgs physics with the LHeC.

### 3.4. The 3D structure of the proton

As is evident from the discussion in the previous sections, the LHeC machine will be able to measure collinear PDFs with unprecedented accuracy in its extended range of  $x$  and  $Q^2$ . Thus, it will provide a new insight into the details of the one-dimensional structure of the proton and nuclei, including novel phenomena at low  $x$ . In addition to collinear dynamics, the LHeC opens a new window into proton and nuclear structure by allowing a precise investigation of the partonic structure in more than just one dimension of the longitudinal momentum. Precision DIS thus gives access to multidimensional aspects of hadron structure. This can be achieved by accurately measuring processes with more exclusive final states, such as the production of

<sup>170</sup>This is mitigated by measurements of DY scattering at low masses, which are, however, less precise. At high masses,  $M = \sqrt{sx_1x_2} \gg M_{W,Z}$ , one soon reaches the region where NP may occur, i.e. the difficulty arises of separating unknown physics from the uncertainty of the quark and gluon densities at large  $x$ . High-mass DY searches often are performed at the edge of the data statistics, i.e. they cannot really be guided by the data, but lack reliable guidance for the behaviour of the SM background around and beyond a (non-)resonant effect they would like to discover.

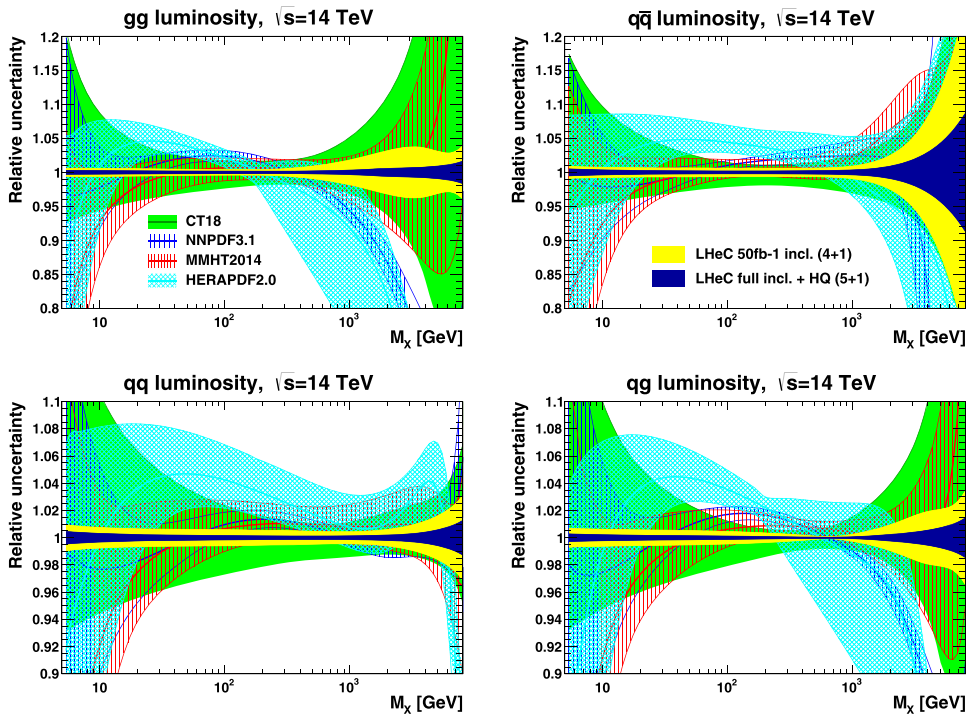


**Figure 24.** Uncertainty bands for parton luminosities as a function of the mass  $M_X = \sqrt{s x_1 x_2}$  for LHC energies. The yellow band corresponds to the ‘LHeC first run’ PDFs (D2), while the dark blue band shows a fit to the LHeC inclusive data sets (D4, D5, D6, and D9) in table 8 together with the simulated HF  $s, c, b$  data with a five-quark distribution parameterisation as described in the text. Both LHeC PDFs shown are scaled to the central value of CT18.

jets, the semi-inclusive production of hadrons, and exclusive processes—in particular, the elastic diffractive production of vector mesons and DVCS that were explored in the 2012 LHeC CDR [1]. These processes have the potential to provide information not only on the longitudinal distribution of partons in the proton or nucleus, but also on the dependence of the parton distribution on transverse momenta and momentum transfer. Therefore, future high-precision DIS machines, such as the LHeC or the Electron–Ion Collider (EIC) in the US [101], open a unique window into the details of the 3D structure of hadrons. Note that the measurement of these processes requires a detector with large acceptance,  $|\eta| < 4$ , see e.g. [1, 102]. The current LHeC central detector design covers  $|\eta| \lesssim 4.5$ , see section 12.

The most general quantity that can be defined in QCD that would contain very detailed information about the partonic content of the hadron is the Wigner distribution [103]. This function  $W(x, \mathbf{k}, \mathbf{b})$  is a 1 + 4-dimensional function. One can think of it as the ‘mother’ or ‘master’ parton distribution, from which lower-dimensional distributions can be obtained. In the definition of the Wigner function,  $\mathbf{k}$  is the transverse momentum of the parton and  $\mathbf{b}$  is the two-dimensional impact parameter, which can be defined as a Fourier conjugate to the momentum transfer of the process. The other, lower-dimensional parton distributions can be obtained by integrating out different variables. Thus, transverse-momentum-dependent (TMD) parton distributions (or unintegrated PDFs)  $f_{\text{TMD}}(x, \mathbf{k})$  can be obtained by integrating out the impact parameter  $\mathbf{b}$  in the Wigner function, while the generalised parton densities (GPD),  $f_{\text{GPD}}(x, \mathbf{b})$ ,

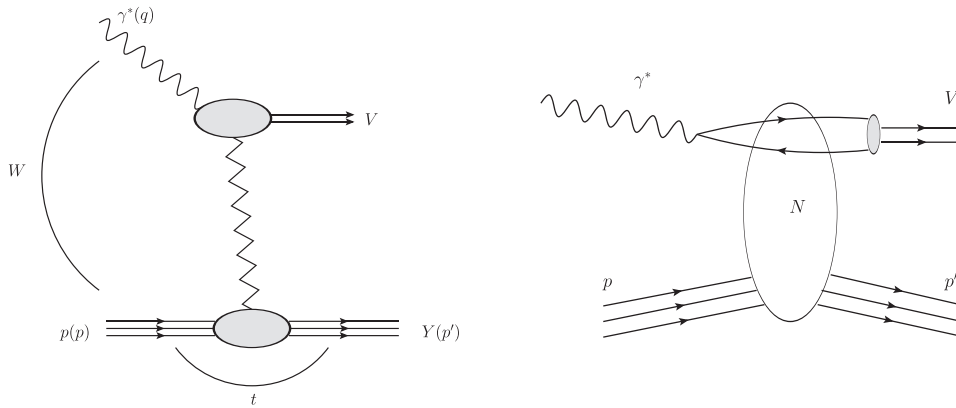


**Figure 25.** Left: Diagram of the quasi-elastic production of the vector meson. Right: Schematic illustration of the same process, quasi-elastic vector-meson production, within the framework of the dipole picture. Reproduced from [110]. CC BY 4.0. The initial virtual photon fluctuates into a quark–antiquark pair which then scatters off the hadronic target and forms the vector meson. The details of the hadronic interaction of the dipole with the target are encoded in the dipole amplitude  $N$ .

can be obtained from the Wigner function through the integration over the transverse momentum  $\mathbf{k}$ . In the regime of small  $x$ , or high energy, a suitable formalism is that of the dipole picture [104–109], where the fundamental quantity that contains the details of the partonic distribution is the dipole amplitude  $N(x, \mathbf{r}, \mathbf{b})$ . This object contains the dependence on the impact parameter  $\mathbf{b}$  as well as another transverse size  $\mathbf{r}$ , the dipole size, which can be related to the transverse momentum of the parton  $\mathbf{k}$  through a Fourier transform. The important feature of the dipole amplitude is that it should obey the unitarity limit  $N \leq 1$ . The dipole amplitude  $N$  within this formalism can be roughly interpreted as a Wigner function in the high-energy limit, as it contains information about the spatial distribution of the partons in addition to the dependence on the longitudinal momentum fraction  $x$ .

Detailed simulations of elastic  $J/\psi$  vector-meson production were performed for the LHeC kinematic region and beyond [1], using the formalism of the dipole picture. This particular process is shown in figure 25, left plot. The proton is elastically scattered with a momentum transfer  $t$ , and a vector meson is produced, which is separated from the final-state proton by a rapidity gap. The measurement of the  $t$  slope of this process is of particular importance, since it can be directly related to the impact parameter distribution and is thus sensitive to the transverse variation of the partonic density in the target. The first instance of such an analysis, in the context of elastic scattering, was performed by Amaldi and Schubert [111], where it was demonstrated that the Fourier transform of the elastic cross-section yields access to the impact parameter profile of the scattering amplitude. This method can be used in the context of vector-meson scattering in DIS, where the transverse distribution of partons in the perturbative regime can be extracted through the appropriate Fourier transform [112]. The additional advantage of studying diffractive vector-meson production is the fact that the partonic distributions can be studied as a function of the hard scale given in this process by the mass of the vector meson  $M_V^2$  in the photoproduction case or  $Q^2$  (or more precisely a combination of  $Q^2$  and  $M_V^2$ ) in the case of the diffractive DIS production of vector mesons, as well as the energy  $W$  of the photon–proton system available in the process, which is closely related to  $x$ .



The differential cross-section for elastic vector-meson production can be expressed in the following form:

$$\frac{d\sigma^{\gamma^* p \rightarrow J/\psi p}}{dt} = \frac{1}{16\pi} |\mathcal{A}(x, Q, \Delta)|^2, \quad (3.23)$$

where the amplitude for the process of elastic diffractive vector meson production in the high-energy limit, in the dipole picture, is given by

$$\mathcal{A}(x, Q, \Delta) = \sum_{h\bar{h}} \int d^2\mathbf{r} \int dz \Psi_{h\bar{h}}^*(z, \mathbf{r}, Q) \mathcal{N}(x, \mathbf{r}, \Delta) \Psi_{h\bar{h}}^V(z, \mathbf{r}). \quad (3.24)$$

In the above formula,  $\Psi_{h\bar{h}}^*(z, \mathbf{r}, Q)$  is the photon wave function that describes the splitting of the virtual photon  $\gamma^*$  into a  $q\bar{q}$  pair. This wave function can be calculated in perturbative QCD. The function  $\Psi_{h\bar{h}}^V(z, \mathbf{r})$  is the wave function of the vector meson. Finally,  $\mathcal{N}(x, \mathbf{r}, \Delta)$  is the dipole amplitude that contains all the information about the interaction of the quark–antiquark dipole with the target. The formula (3.24) can be interpreted as the process of fluctuation of the virtual photon into a  $q\bar{q}$  pair, which subsequently interacts with the target through the dipole amplitude  $\mathcal{N}$  and then forms the vector meson given by the amplitude  $\Psi^V$ , see figure 25, right plot. The two integrations in the defining equation (3.24) are performed over the dipole size, denoted by  $\mathbf{r}$ , and  $z$ , which is the longitudinal momentum fraction of the photon carried by the quark. The scattering amplitude depends on the value of the momentum transfer  $\Delta$ , which is related to the Mandelstam variable  $t = -\Delta^2$ . The sum is performed over the helicity states of the quark and antiquark.

The dipole amplitude  $\mathcal{N}(x, \mathbf{r}, \Delta)$  can be related to the dipole amplitude in coordinate space through the appropriate Fourier transform

$$N(x, \mathbf{r}, \mathbf{b}) = \int d^2\Delta e^{i\Delta \cdot \mathbf{b}} \mathcal{N}(x, \mathbf{r}, \Delta). \quad (3.25)$$

We stress that here,  $\mathbf{r}$  and  $\mathbf{b}$  are two different transverse sizes. The dipole size  $\mathbf{r}$  is conjugate to the transverse momentum of the partons  $\mathbf{k}$ , whereas the impact parameter is roughly the distance from the centre of the scattering target to the centre of mass of the quark–antiquark dipole and is related to the Fourier conjugate variable, the momentum transfer  $\Delta$ .

The dipole amplitude  $N(x, \mathbf{r}, \mathbf{b})$  contains rich information about the dynamics of the hadronic interaction. It is a five-dimensional function that depends on the longitudinal momentum fraction and two two-dimensional coordinates. The dependence on the longitudinal momentum fraction is obviously related to the evolution of the process with the centre-of-mass energy, while the dependence on  $\mathbf{b}$  provides information about the spatial distribution of the partons in the target. The dipole amplitude is related to the distribution of gluons in impact-parameter space. The dipole amplitude has the useful property that its value should be bounded from above by the unitarity requirement  $N \leq 1$ . The complicated dependence on energy, dipole size, and impact parameter of this amplitude can provide a unique insight into the dynamics of QCD, and on the approach to the dense partonic regime. Besides, from equations (3.23)–(3.25) it is evident that the information about the spatial distribution of impact parameter  $\mathbf{b}$  is related through the Fourier transform to the dependence of the cross-section on the momentum transfer  $t = -\Delta^2$ .

To see how the details of the distribution, and in particular the approach to unitarity, can be studied through the VM elastic production, calculations based on the dipole model were performed [113], and extended to energies that can be reached at the LHeC as well as the FCC-eh. The parameterisations used in the calculation were the so-called IP-Sat [114, 115]

and b-CGC [116] models. In both cases the impact parameter dependence has to be modelled phenomenologically. In the IP-Sat model the dipole amplitude has the following form

$$N(x, \mathbf{r}, \mathbf{b}) = 1 - \exp \left[ -\frac{\pi^2 r^2}{2N_c} \alpha_s(\mu^2) xg(x, \mu^2) T_G(b) \right], \quad (3.26)$$

where  $xg(x, \mu^2)$  is the collinear gluon density, evolved using LO DGLAP (without quarks), from an initial scale  $\mu_0^2$  up to the scale  $\mu^2$  set by the dipole size  $\mu^2 = \frac{4}{r^2} + \mu_0^2$ . Here,  $\alpha_s(\mu^2)$  is the strong coupling. The parameterisation of the gluon density at the initial scale  $\mu_0^2$  is given by

$$xg(x, \mu_0^2) = A_g x^{-\lambda_g} (1-x)^{5.6}, \quad (3.27)$$

and the impact parameter profile for the gluon is given by

$$T_G(b) = \frac{1}{2\pi B_G} \exp(-b^2/2B_G). \quad (3.28)$$

An alternative parameterisation is given by the b-CGC model [116], which has the form

$$N(x, \mathbf{r}, \mathbf{b}) = \begin{cases} N_0 \left( \frac{rQ_s}{2} \right)^{2\gamma_{\text{eff}}} & \text{for } rQ_s \leq 2, \\ 1 - \exp(-\mathcal{A} \ln^2(\mathcal{B}rQ_s)) & \text{for } rQ_s > 2. \end{cases} \quad (3.29)$$

Here the effective anomalous dimension  $\gamma_{\text{eff}}$  and the saturation scale  $Q_s$  of the proton explicitly depend on the impact parameter and are defined as

$$\gamma_{\text{eff}} = \gamma_s + \frac{1}{\kappa\lambda \ln 1/x} \ln \left( \frac{2}{rQ_s} \right),$$

$$Q_s(x, b) = \left( \frac{x_0}{x} \right)^{\lambda/2} \exp \left[ -\frac{b^2}{4\gamma_s B_{\text{CGC}}} \right] \text{ GeV}, \quad (3.30)$$

where  $\kappa = \chi''(\gamma_s)/\chi'(\gamma_s)$  and  $\chi(\gamma)$  is the leading logarithmic Balitsky, Fadin, Kuraev, and Lipatov (BFKL) kernel eigenvalue function [117]. The parameters  $\mathcal{A}$  and  $\mathcal{B}$  in equation (3.29) are uniquely determined from the match of the dipole amplitude and its logarithmic derivatives at the limiting value of  $rQ_s = 2$ . The b-CGC model is constructed by smoothly interpolating between two analytically known limiting cases [116], namely the solution of the BFKL equation in the vicinity of the saturation line for small dipole sizes  $r < 2/Q_s$  and the solution of the BK equation deep inside the saturation region for large dipole sizes  $r > 2/Q_s$ .

The parameters  $\mu_0, A_g, \lambda_g$  of the IP-Sat model and  $N_0, \gamma_s, x_0, \lambda$  of the b-CGC model were fitted to obtain the best description of the inclusive data for the structure function  $F_2$  at HERA. The slope parameters  $B_g$  and  $B_{\text{CGC}}$ , which control the  $b$ -dependence in both models, were fitted to obtain the best description of elastic diffractive  $J/\psi$  production, in particular, its  $t$ -dependence, at small values of  $t$ .

In figures 26 and 27 we show the simulated differential cross-section  $d\sigma/dt$  as a function of  $|t|$  and study its variation with energy, virtuality, and its model dependence. First, in figure 26 we show the differential cross-section as a function of  $t$  for a fixed energy of  $W = 1$  TeV for the case of the photoproduction of  $J/\psi$  (left plot) and for the case of DIS with  $Q^2 = 10$  GeV<sup>2</sup> (right plot). The energy  $W$  corresponds to the LHeC kinematics. There are three different calculations in each plot, corresponding to the IP-Sat model, the b-CGC model, and the 1-Pomeron approximation. The last of these is obtained by keeping just the first non-trivial term in the expansion of

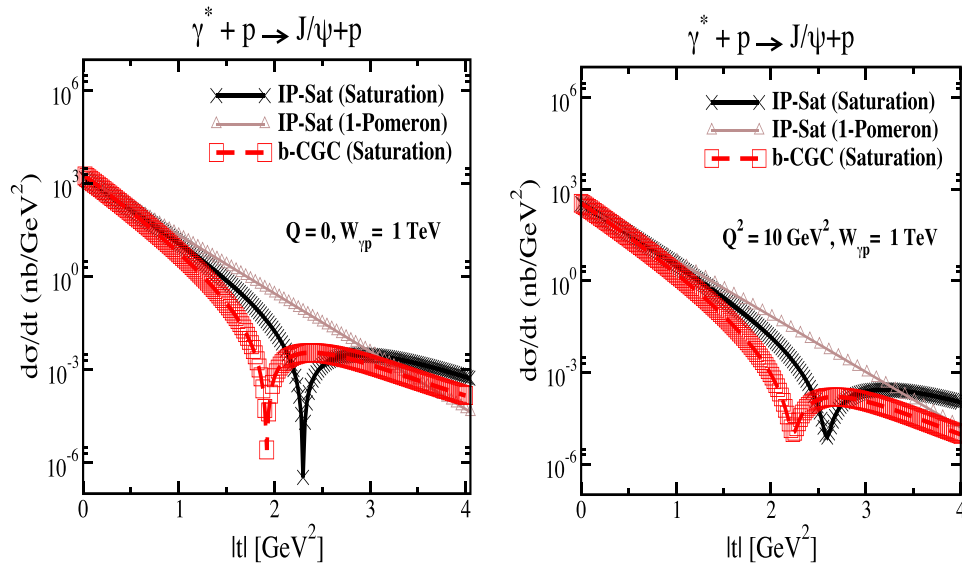


**Figure 26.** Differential cross-section for the elastic  $J/\psi$  production as a function of  $|t|$  within the IP-Sat (saturation), b-CGC, and 1-Pomeron models at a fixed  $W_{\gamma p} = 1$  TeV, which corresponds to the LHeC kinematics, and for two different values of photon virtuality  $Q^2 = 0$  and  $Q^2 = 10$  GeV<sup>2</sup>. The thickness of the points includes the uncertainties associated with the freedom to choose different values for the charm quark mass within the range  $m_c = 1.2\text{--}1.4$  GeV.

the eikonalised formula of the IP-Sat amplitude (3.26). First, let us observe that all three models coincide for very low values of  $t$ , where the dependence on  $t$  is exponential. This is because for low  $|t|$ , relatively large values of the impact parameter are probed in equation (3.24) where the amplitude is small, and therefore the tail in the impact parameter is Gaussian in all three cases. Since the Fourier transform of the Gaussian in  $b$  is an exponential in  $t$ , the result at low  $t$  follows. On the other hand, the three scenarios differ significantly for large values of  $|t|$ . In the case of the 1-Pomeron approximation the dependence is still exponential, without any dips, which is easily understood since the impact parameter profile is perfectly Gaussian in this case. For the two other scenarios, dips in  $d\sigma/dt$  emerge as a function in  $t$ . They signal a departure from the Gaussian profile in  $b$  for small values of  $b$ , where the system is dense. A similar pattern can be observed when performing the Fourier transform of the Wood–Saxon distribution, which is the typical distribution used for the description of the matter density in nuclei. When  $Q^2$  is increased the pattern of dips also changes. This is illustrated in figure 26. It can be seen that the dips move to higher values of  $|t|$  for DIS than for photoproduction. This can be understood from the dipole formula equation (3.24), which contains the integral over the dipole size. Larger values of  $Q^2$  select smaller values of the dipole size  $r$  where the amplitude is smaller and thus in the dilute regime where the profile in  $b$  is Gaussian again. On the other hand, small scales select large dipole sizes, for which the dipole amplitude is larger and thus the saturation effects are more prominent, leading to the distortion of the impact parameter profile and therefore to the emergence of dips in the differential cross-section  $d\sigma/dt$  when studied as a function of  $t$ .

In figure 27 we show the same calculation but for an even higher energy of  $W = 2.5$  TeV, which could be explored in the FCC-eh. In this case we see that the dips move to lower

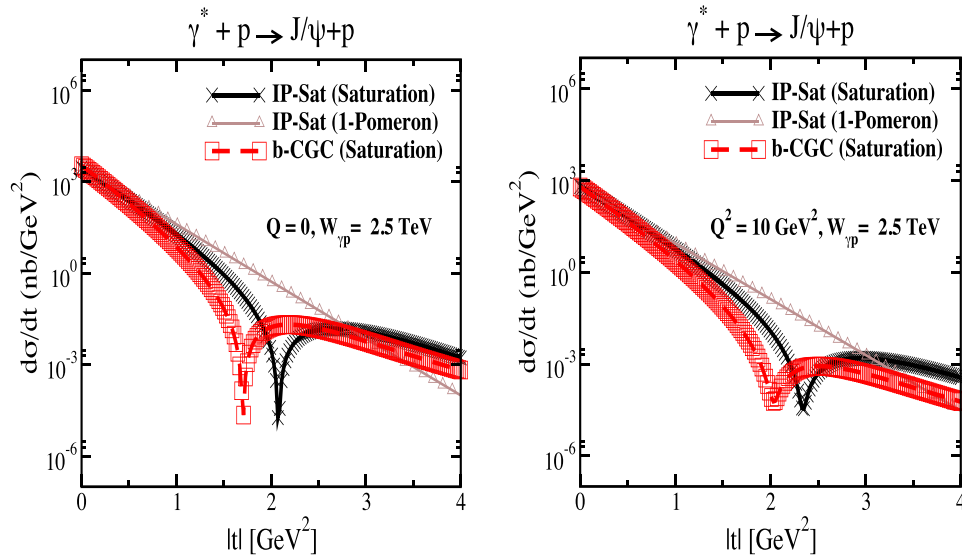


**Figure 27.** Differential cross-section for elastic  $J/\psi$  production as a function of  $|t|$  within the IP-Sat (saturation), b-CGC, and 1-Pomeron models at a fixed  $W_{\gamma p} = 2.5$  TeV, which corresponds to the region that can be explored by FCC-eh, and for two different values of photon virtuality  $Q = 0$  (left plot) and  $Q^2 = 10$  GeV<sup>2</sup> (right plot). The thickness of the points includes the uncertainties associated with the freedom to choose different values for the charm quark mass within the range  $m_c = 1.2\text{--}1.4$  GeV.

values of  $|t|$ . This can be easily understood, because with increasing energy, the dipole scattering amplitude increases, and thus the dilute–dense boundary shifts to larger values of  $b$ , meaning that the deviation from the exponential falloff occurs for smaller values of  $|t|$ . Similar studies [113] also show the change of the position of the dips with the mass of the vector meson: for lighter vector mesons such as  $\rho$ ,  $\omega$ , and  $\phi$ , the dips occur at smaller  $t$  than for the heavier vector mesons  $J/\psi$  and  $\Upsilon$ . We note that, naturally, the positions of the dips crucially depend on the details of the models, which are currently not constrained by the existing HERA data. We also note the sizeable uncertainties due to the charm quark mass (the fits to inclusive HERA data from which parameters of the models have been extracted are performed at each fixed value of the charm mass that is then used to compute the exclusive  $J/\psi$  production).

We thus see that the precise measurement of the  $t$ -slope in the elastic production of vector mesons at the LHeC, and its variation with  $x$  and scales, provide a unique opportunity to explore the transition between the dilute and dense partonic regimes. As mentioned earlier, elastic diffractive production is one of several different measurements that can be performed to explore the 3D structure of the hadron. Another is DVCS, which is a process that is sensitive to the spatial distribution of quarks inside the hadron. Previous preliminary analyses [1] indicated the huge potential of the LHeC for the measurement of DVCS. Another example of a process that could be studied at the LHeC is diffractive exclusive dijet production. It has been suggested [118] that this process is sensitive to the Wigner function, and that the transverse momentum and spatial distribution of partons can be extracted by measuring this process. The transverse momentum of jets would be sensitive to the transverse momentum of the participating partons, whereas the momentum transfer of the elastically scattered proton would indicate the impact

parameter distribution of the partons in the target [119–121], thus offering the possibility of extracting information about the Wigner distribution.

So far, we have referred to coherent diffraction, i.e. to a scenario in which the proton remains intact after the collision. Incoherent diffraction also exists, where the proton gets excited into some state with the quantum numbers of the proton and separated from the rest of the event by a large rapidity gap. In order to apply the dipole formalism to the incoherent case, the reader is referred to section 6.3.1, where the formulae applicable to both protons and nuclei are shown. Here, one must consider a more involved structure of the proton (e.g. as composed by a fixed number of hot spots [122–125], or a number of hot spots that increases with  $1/x$ ) [126–128]). As discussed in section 6.3.1, coherent diffraction is sensitive to the gluon distribution in transverse space, while incoherent diffraction is particularly sensitive to fluctuations of the gluon distribution. One prediction of the model with a growing number of hot spots, both in models where this increasing number is implemented by hand [126–128] and in those where it is dynamically generated [125] from a fixed number at larger  $x$ , is that the ratio of incoherent to coherent diffraction will decrease with  $W$ , and that this decrease is sensitive to the details of the distribution of hot spots, and thus, to the fluctuations of the gluon distribution in transverse space. In order to check these ideas, both the experimental capability to separate coherent from incoherent diffraction and a large lever arm in  $W$ , as available at the LHeC, are required.

In conclusion, measurements at the LHeC (in particular, exclusive diffractive production of vector mesons, photons, and other final states such as dijets) will offer unprecedented opportunities to unravel the three-dimensional structure of hadrons in a kinematic region complementary to that at the EIC. Note that such structure varies with  $x$  or energy, so its measurement at small enough values of  $x$  is key as an input for both analytic calculations and MC simulators at high-energy hadron colliders. In addition, large lever arms in both  $x$  and  $Q^2$ , such as those offered by the LHeC, are required to understand the perturbative evolution of such quantities, as much as they are required for collinear PDFs. Ultraperipheral collisions (UPCs) at the LHC (see references [129, 130] and references therein) offer an alternative, albeit less precise and only for photoproduction.

#### 4. Exploration of quantum chromodynamics

The gauge theory formalism of QCD provides a very successful description of strong interactions between confined partons. Despite the undoubted success of QCD, the strong force still remains one of the least-known fundamental sectors of (particle) physics, which needs to be explored much more deeply.

For an improved understanding of strong interactions and to answer a variety of open questions, additional measurements will have to be performed at the highest precision. At the LHeC, deep inelastic electron–proton and lepton–nucleus reactions will extend tests of QCD phenomena to a new and as yet unexplored domain up to the TeV scale and to  $x$  values as low as  $10^{-6}$ , allowing QCD measurements to be performed with very high experimental precision. This is because the proton is a *strongly* bound system, and in DIS, the *colourless* photon (or  $Z$ ) exchanged between the electron and the parton inside the proton acts as a neutral observer with respect to the phenomena of the strong force. In addition, the over-constrained kinematic system in DIS allows for the precise (*in situ*) calibrations of the detector required to measure the kinematics of the scattered lepton, and, more importantly here, the hadronic final state as well. In DIS, in many cases, the virtuality of the exchanged  $\gamma/Z$  boson often provides a reasonable scale to stabilise theoretical predictions.

In this chapter, selected topics of QCD studies at the LHeC are discussed.

#### 4.1. Determination of the strong coupling constant

QCD [131, 132] has been established as the theory of strong interactions within the SM of particle physics. While this theory has manifold aspects from both the theoretical and experimental points of view, by far the most important parameter of QCD is the coupling strength, which is most commonly expressed at the mass of the Z boson,  $M_Z$ , as  $\alpha_s(M_Z)$ . Its (renormalisation) scale dependence is given by the QCD gauge group  $SU(3)$  [133, 134]. Predictions for numerous processes in  $e^+e^-$ ,  $pp$ , or  $ep$  collisions are then commonly performed using the framework of perturbative QCD, and the (lack of) higher-order QCD corrections often represents a limiting aspect for precision physics. Therefore, the determination of the strong coupling constant  $\alpha_s(M_Z)$  constitutes one of the most crucial tasks for future precision physics, while, at the same time, the study of the scale dependence of  $\alpha_s$  provides an inevitable test of the validity of QCD as the theory of strong interactions and the portal for GUT theories.

Different processes and methodologies can be considered for the determination of  $\alpha_s(M_Z)$  (see e.g. reviews [135–137]). Since QCD is an asymptotically free theory, with free behaviour at high scales but confinement at low scales, a high sensitivity to the value of  $\alpha_s(M_Z)$  is naturally obtained from small-scale measurements. However, the large-scale behaviour must then be calculated by solving the renormalisation group equation, which implies the strict validity of the theory and an excellent understanding of all subleading effects, such as the behaviour around quark-mass thresholds.

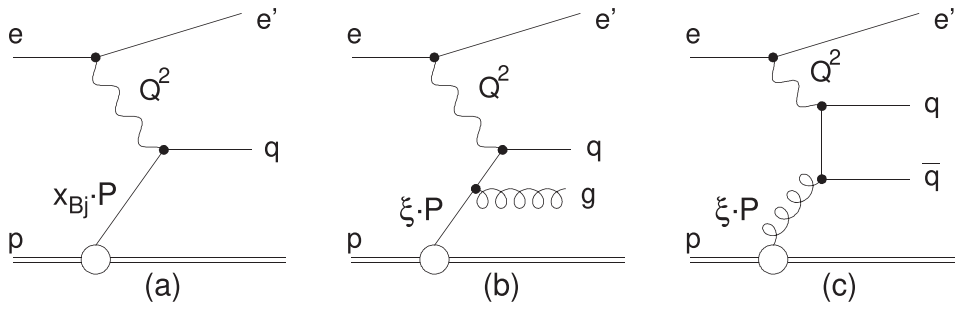
Precision measurements at the LHeC offer the unique opportunity to exploit many of these aspects. Measurements of jet production cross-sections or inclusive NC and CC DIS cross-sections offer high sensitivity to the value of  $\alpha_s(M_Z)$ , since these measurements can be performed at comparably small scales and at high experimental precision. At the same time, the LHeC provides the opportunity to test the running of the strong coupling constant over a large kinematic range. In this section, the prospects for a determination of the strong coupling constant using inclusive jet cross-sections and inclusive NC/CC DIS cross-sections are studied.

**4.1.1. Strong coupling due to inclusive jet cross-sections.** The measurement of inclusive jet or dijet production cross-sections in NC DIS exhibits high sensitivity to the strong coupling constant and the gluon PDF of the proton. This is because jet cross-sections in NC DIS are measured in the Breit reference frame [138], where the virtual boson,  $\gamma^*$  or Z, collides head-on with the struck parton from the proton, and the outgoing jets are required to have a non-zero transverse momentum in that reference frame. The leading-order QCD diagrams show QCD Compton and boson–gluon fusion and are both  $\mathcal{O}(\alpha_s)$ , see figure 28.

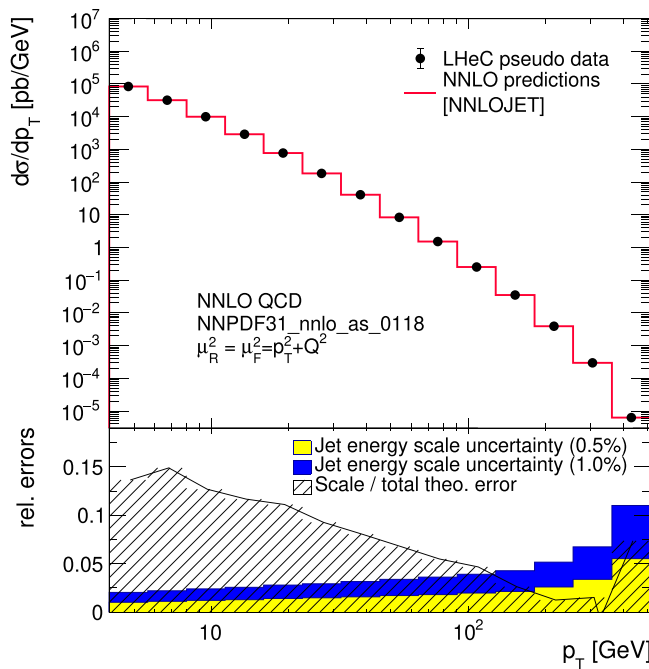
At HERA, jets are most commonly defined by the longitudinally invariant  $k_t$  jet algorithm [140], using a distance parameter  $R = 1.0$  [139, 141–157]. This provides an infrared-safe jet definition and the chosen distance parameter guarantees a small dependence on non-perturbative effects, such as hadronisation. In contrast to  $pp$  at the LHC [158–161], jet algorithms at the LHeC do not require any pile-up subtraction or any reduction of the dependence on the minimum bias or the underlying event, due to the absence of such effects. Therefore, for this study, we adopt the choices made at HERA.

Figure 29 displays NNLO QCD predictions [162, 163] for cross-sections of inclusive jet production in NC DIS as a function of the transverse momentum of the jets in the Breit frame. The calculations are performed for an electron-beam energy of  $E_e = 60$  GeV and they include the  $\gamma/Z$  and Z exchange terms and account for the electron polarisation  $P_e = -0.8$ . The NC DIS kinematic range is set to  $Q^2 > 4$  GeV<sup>2</sup>. The calculations are performed using the NNLO-JET program [164] interfaced to the APPLfast library [165–167] which provides a generic interface to the APPLgrid [168, 169] and fastNLO [170, 171] interpolation grid code.





**Figure 28.** Leading-order diagrams for inclusive DIS (a) and jet production (b) and (c) in the Breit frame. Reproduced from [139]. [CC BY 4.0](https://creativecommons.org/licenses/by/4.0/).



**Figure 29.** Inclusive jet cross-sections calculated in NNLO QCD as a function of the jet transverse momentum in the Breit frame,  $p_T$ . The shaded area indicates NNLO scale uncertainties and the yellow band shows the estimated experimental jet energy scale (JES) uncertainty of 0.5%. The blue band shows a very conservative assumption for the JES of 1%.

The kinematically accessible range of jet  $p_T$  values covers more than two orders of magnitude,  $4 < p_T \lesssim 400$  GeV. The size of the cross-section extends over many orders of magnitude, thus imposing challenging demands on the LHeC experimental conditions, triggers, data acquisition (DAQ) bandwidth, calibration, and data-processing capabilities. The scale uncertainty of the NNLO predictions is about 10% at low values of  $p_T$  and it decreases significantly with increasing values of  $p_T$ . In the future, improved predictions will further reduce these theoretical uncertainties.

**Table 9.** Anticipated uncertainties of inclusive jet cross-section measurements at the LHeC.

Exp. uncertainty	Shift	Size in $\sigma$ (%)
Statistics for $1 \text{ ab}^{-1}$	Min. 0.15%	0.15–5
Electron energy	0.1%	0.02–0.62
Polar angle	2 mrad	0.02–0.48
Calorimeter noise	$\pm 20 \text{ MeV}$	0.01–0.74
JES	0.5%	0.2–4.4
Uncorrelated uncert.	0.6%	0.6
Normalisation uncert.	1.0%	1.0

To estimate the uncertainty of  $\alpha_s(M_Z)$  based on inclusive jet cross-sections at the LHeC, double-differential cross-sections are generated as functions of  $Q^2$  and  $p_T$  with a full set of experimental uncertainties. Altogether, 509 cross-section values are calculated in the kinematic range  $8 < Q^2 < 500\,000 \text{ GeV}^2$  and  $4 < p_T < 512 \text{ GeV}$ , and the bin grid is similar to those used by CMS, H1, and ZEUS [45, 158, 167, 172]. The various error sources considered are summarised in table 9. The uncertainties related to the reconstruction of the NC DIS kinematic variables,  $Q^2$ ,  $y$ , and  $x_{Bj}$  are similar to the estimates for the inclusive NC DIS cross-sections (see section 3.2). To reconstruct the hadronic final-state particles that are the inputs to the jet algorithm, the JES uncertainty, calorimetric noise, and the polar angle uncertainty are considered. The size of the uncertainties is gauged using the values achieved by H1, ZEUS, ATLAS, and CMS [148, 156, 173, 174]. The size of the dominant JES uncertainty is assumed to be 0.5% for reconstructed particles in the laboratory rest frame, yielding an uncertainty of 0.2%–4.4% for the cross-section after the boost to the Breit frame. A JES uncertainty of 0.5% is certainly justified by improved calorimeters, since H1 and ZEUS already reported uncertainties of 1% [148, 156, 175], and ATLAS and CMS achieved 1% over a wide range of  $p_T$  [173, 174], despite the presence of pile-up and the considerably more complicated definition of a reference object for the *in situ* calibration. The size of the JES uncertainty is also displayed in figure 29. The calorimetric noise of  $\pm 20 \text{ MeV}$  in every calorimeter cluster, as reported by H1, yields an uncertainty of up to 0.7% in the jet cross-sections. A minimum statistical uncertainty size of 0.15% is imposed for each cross-section bin. An overall normalisation uncertainty of 1.0% is assumed, which will mainly be dominated by the luminosity uncertainty. In addition, an uncorrelated uncertainty component of 0.6% includes various smaller error sources, such as radiative corrections, unfolding, or model uncertainties. Studies of the size and the correlation model of these uncertainties are performed below.

The value and uncertainty of  $\alpha_s(M_Z)$  is obtained from a  $\chi^2$  fit of NNLO predictions [162, 163] to the simulated data, where  $\alpha_s(M_Z)$  is a free fit parameter. The methodology closely follows analyses of HERA jet data [167, 172], and the  $\chi^2$  quantity is calculated from the relative uncertainties, i.e. those of the right column of table 9. The predictions for the cross-section  $\sigma$  account for both  $\alpha_s$ -dependent terms in the NNLO calculations, i.e. in the DGLAP operator and the hard matrix elements, using

$$\sigma = f_{\mu_0} \otimes P_{\mu_0 \rightarrow \mu_F}(\alpha_s(M_Z)) \otimes \hat{\sigma}(\alpha_s(M_Z), \mu), \quad (4.1)$$

where  $f_{\mu_0}$  are the PDFs at a scale of  $\mu_0 = 30 \text{ GeV}$ , and  $P_{\mu_0 \rightarrow \mu_F}$  denotes the DGLAP operator, which is dependent on the value of  $\alpha_s(M_Z)$ . The  $\alpha_s$  uncertainty is obtained by linear error propagation and is validated by a separate study of the  $\Delta\chi^2 = 1$  criterion.

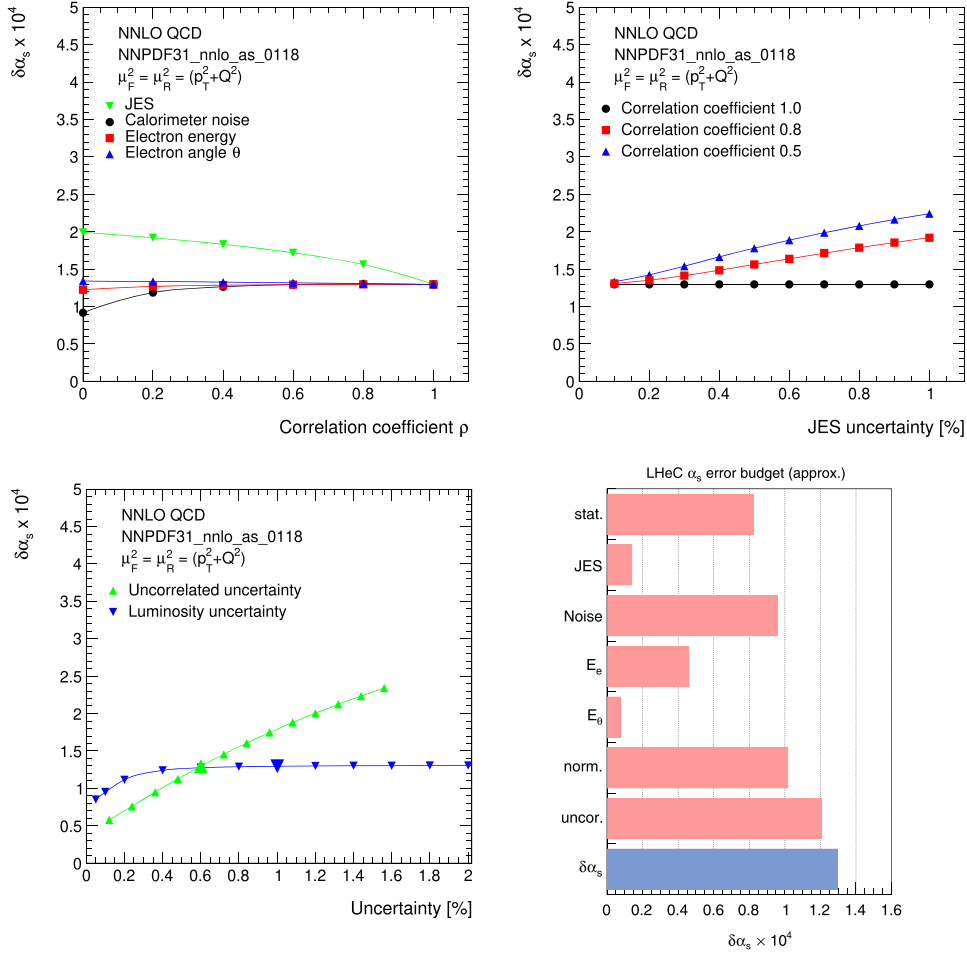


**Figure 30.** Studies of the sizes and correlations of experimental uncertainties that impact the uncertainty of  $\alpha_s(M_Z)$ . Top left: study of the value of the correlation coefficient  $\rho$  for different systematic uncertainties. Common systematic uncertainties are considered to be fully correlated,  $\rho = 1$ . Top right: size of the JES uncertainty for three different values of  $\rho_{\text{JES}}$ . Bottom left: impact of the uncorrelated and normalisation uncertainties on  $\Delta\alpha_s(M_Z)$ . Bottom right: contributions of individual sources of experimental uncertainty to the total experimental uncertainty of  $\alpha_s(M_Z)$ .

In the fit of NNLO QCD predictions to the simulated double-differential LHeC inclusive jet cross-sections, an uncertainty of

$$\Delta\alpha_s(M_Z)(\text{jets}) = \pm 0.00013_{(\text{exp})} \pm 0.00010_{(\text{PDF})} \quad (4.2)$$

is found. The PDF uncertainty is estimated from a PDF set obtained from LHeC inclusive DIS data (see section 3.3). These uncertainties promise a determination of  $\alpha_s(M_Z)$  with the highest precision and would represent a considerable reduction of the current world average value, which has an uncertainty of  $\pm 0.00110$  [136].

The uncertainty of  $\alpha_s$  is studied for different values of the experimental uncertainties in the inclusive jet cross-section measurement and for different assumptions for bin-to-bin correlations expressed by the correlation coefficient  $\rho$  of individual uncertainty sources, as shown in figure 30. It can be observed that even for quite conservative scenarios,  $\alpha_s(M_Z)$  is determined with an uncertainty of less than 2%. To achieve this, it is important to keep the size of the uncorrelated uncertainty or the uncorrelated components of the other systematic uncertainties under good control. This is also visible in figure 30 (bottom right), where the contributions of the individual uncertainty sources to the total uncertainty of  $\alpha_s(M_Z)$  are displayed, and it can be seen that the uncorrelated and normalisation uncertainties are the largest individual uncertainty components. It can further be observed that the size of the statistical uncertainty (stat.) is non-negligible, which is, however, strongly dependent on the *ad hoc* assumption of a minimum size of 0.15%. The noise uncertainty mainly contributes to jets at low- $p_T$ , and occurs because these have a high sensitivity to  $\alpha_s(M_Z)$  due to their low scale  $\mu_R$ . It is of great importance to keep this experimental uncertainty under control or make better use of track-based information for the measurement of jets.

In the present formalism theoretical uncertainties arising from scale variations of the NNLO predictions amount to about  $\Delta\alpha_s(M_Z) = 0.0035(\text{NNLO})$ . These can be reduced to about  $\Delta\alpha_s(M_Z) \approx 0.0010$  with suitable cuts in  $p_T$  or  $Q^2$ . However, it is expected that improved predictions, e.g. with resummed contributions, or next-to-next-to-next-to-leading order (N3LO) predictions, will significantly reduce these uncertainties in the future. Uncertainties in non-perturbative hadronisation effects will have to be considered as well, but these will be well controlled due to the measurements of charged particle spectra at the LHeC and improved phenomenological models.

**4.1.2. Pinning down  $\alpha_s$  using inclusive and jet LHeC data.** The dependence of the coupling strength as a function of the renormalisation scale  $\mu_R$  is predicted by QCD, which is often called the *running* of the strong coupling. Its study using experimental data represents an important consistency and validity test of QCD. Using inclusive jet cross-sections the running of the strong coupling can be tested by determining the value of  $\alpha_s$  at different values of  $\mu_R$  by grouping data points with similar values of  $\mu_R$ , and determining the value of  $\alpha_s(\mu_R)$  from these subsets of data points. The assumptions about the running of  $\alpha_s(\mu_R)$  are then only imposed for the limited range of the chosen interval, and not to the full measured interval as in the previous study. Here, we set  $\mu_R^2 = Q^2 + p_T^2$ .<sup>171</sup>

The experimental uncertainties from the fits to subsets of the inclusive jet pseudodata are displayed in figure 31. These results demonstrate a high sensitivity to  $\alpha_s$  over two orders of magnitude in the renormalisation scale for values up to about  $\mu_R \approx 500$  GeV. In the range  $6 < \mu_R \lesssim 200$  GeV the experimental uncertainty is found to be smaller than the expectation from the world average value [183]. This region is of particular interest since it connects the precision determinations from lattice calculations [184] or  $\tau$  decay measurements [185], which are at small scales  $\mathcal{O}(\text{GeV})$ , to measurements at the Z pole [186] and to applications at scales that are relevant to the LHC, e.g. for Higgs, top-quark physics, or high-mass searches. This

<sup>171</sup> The choice of scale follows a *conventional* scale-setting procedure; uncertainties for the scale choice and unknown higher-order terms are estimated by varying the scales. Such variations are only sensitive to the terms that govern the behaviour of the running coupling, and may become unreliable due to renormalons [176]. An alternative way to fix the scales is provided by the PMC [177–181]. The PMC method was recently applied to predictions of event shape observables in  $e^+e^- \rightarrow \text{hadrons}$  [182]. When applying the PMC method to observables in DIS, the alternative scale setting provides a profound alternative to verifying the running of  $\alpha_s(\mu_R)$ . Such a procedure could be particularly relevant for DIS event shape observables, where the leading-order terms are insensitive to  $\alpha_s$  and conventional scale choices may not be adequately related to the  $\alpha_s$ -sensitive higher-order QCD corrections.

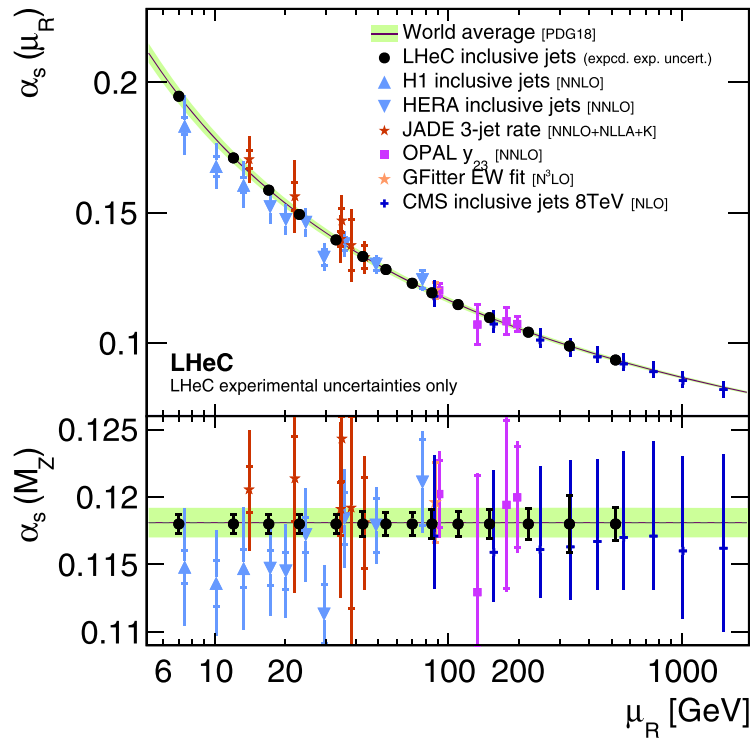


**Figure 31.** Uncertainties of  $\alpha_s(M_Z)$  and corresponding  $\alpha_s(\mu_R)$  in a determination of  $\alpha_s$  using LHeC inclusive jet cross-sections at different values of  $\mu_R^2 = Q^2 + p_T^2$ . Only experimental uncertainties are shown for the LHeC, and they are compared with a number of available measurements and the world average value.

kinematic region of scales  $\mathcal{O}(10 \text{ GeV})$  cannot be accessed by (HL-)LHC experiments because of the limitations imposed by pile-up and underlying events [187].

Inclusive DIS cross-sections are sensitive to  $\alpha_s(M_Z)$  through higher-order QCD corrections, contributions from the  $F_L$  structure function, and the scale dependence of the cross-section at high  $x$  (*scaling violations*). The value of  $\alpha_s(M_Z)$  can then be determined from a combined fit of the PDFs and  $\alpha_s(M_Z)$  [172]. While a simultaneous determination of  $\alpha_s(M_Z)$  and PDFs is not possible with HERA inclusive DIS data alone, due to its limited precision and kinematic coverage [45, 172], the large kinematic coverage, high precision, and integrated luminosity of the LHeC data will allow such an  $\alpha_s$  analysis for the first time.

To determine  $\alpha_s(M_Z)$  from inclusive NC/CC DIS data, a combined PDF and  $\alpha_s$  fit to the simulated data is performed in a similar manner to the studies presented above in section 3. Other technical details are outlined in reference [172]. In this fit, however, the number of free parameters in the gluon parameterisation is increased, since the gluon PDF and  $\alpha_s(M_Z)$  are highly correlated and LHeC data are sensitive to values down to  $x < 10^{-5}$ , which requires additional freedom for the gluon parameterisation. The inclusive data are restricted to  $Q^2 \geq 5 \text{ GeV}^2$  in order to avoid a region where effects beyond fixed-order perturbation theory may become sizeable [45, 188].

By exploiting the full LHeC inclusive NC/CC DIS data with  $E_e = 50 \text{ GeV}$ , the value of  $\alpha_s(M_Z)$  can be determined with an uncertainty  $\Delta\alpha_s(M_Z) = \pm 0.00038$ . With a more optimistic

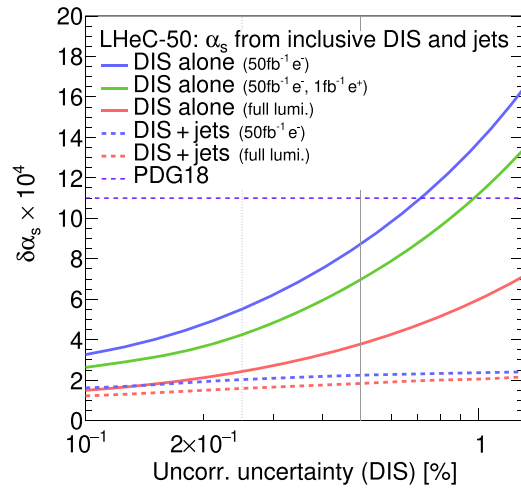


**Figure 32.** Uncertainties of  $\alpha_s(M_Z)$  from simultaneous fits of  $\alpha_s(M_Z)$  and PDFs to inclusive NC/CC DIS data as a function of the size of the uncorrelated uncertainty of the NC/CC DIS data. The full lines indicate the uncertainties obtained using different assumptions for the data collection scenario and integrated luminosity. The dashed lines indicate results where, in addition to the inclusive NC/CC DIS data, inclusive jet cross-section data are considered.

assumption for the dominant uncorrelated uncertainty of  $\delta\sigma_{(\text{uncor.})} = 0.25\%$ , an uncertainty as small as

$$\Delta\alpha_s(M_Z)(\text{incl. DIS}) = \pm 0.00022_{(\text{exp+PDF})} \quad (4.3)$$

can be achieved. This would represent a considerable improvement over the present world average value. Given these small uncertainties, theoretical uncertainties due to missing higher orders or heavy quark effects also have to be considered. In a dedicated study, this fit is repeated with a reduced data set which can be accumulated during a single year of operation<sup>172</sup>, corresponding to about  $\mathcal{L} \sim 50 \text{ fb}^{-1}$ . These data will already be able to improve the world average value. These studies are displayed in figure 32.

High sensitivity to  $\alpha_s(M_Z)$  and an optimal treatment of the PDFs are obtained by using inclusive jet data together with inclusive NC/CC DIS data in a combined determination of  $\alpha_s(M_Z)$  and the PDFs. The jet data provide an enhanced sensitivity to  $\alpha_s(M_Z)$ , while the inclusive DIS data have the highest sensitivity for the determination of the PDFs. In such combined QCD analyses, heavy-quark data may be further analysed to determine  $m_c$  and  $m_b$ . However, since jet cross-sections have sufficiently large scales ( $p_T \gg m_b$ ), these are fairly insensitive to the actual value of the heavy quark masses. On the contrary, heavy quark data are predominantly sensitive to the quark mass parameters rather than to  $\alpha_s(M_Z)$ , and their correlation is commonly found to be small in such combined analyses, see e.g. reference [52]. In fact, at the LHeC, the masses of the charm and bottom quarks will be determined with high precision, and uncertainties of 3 MeV and 10 MeV are expected, respectively [1]. Therefore, for our sole purpose of estimating the uncertainty of  $\alpha_s(M_Z)$  from the LHeC data, we do not consider the heavy quark

<sup>172</sup>Two different assumptions are made. One fit is performed with only electron data corresponding to  $\mathcal{L} \sim 50 \text{ fb}^{-1}$ , and an alternative scenario further considers positron data corresponding to  $\mathcal{L} \sim 1 \text{ fb}^{-1}$ .



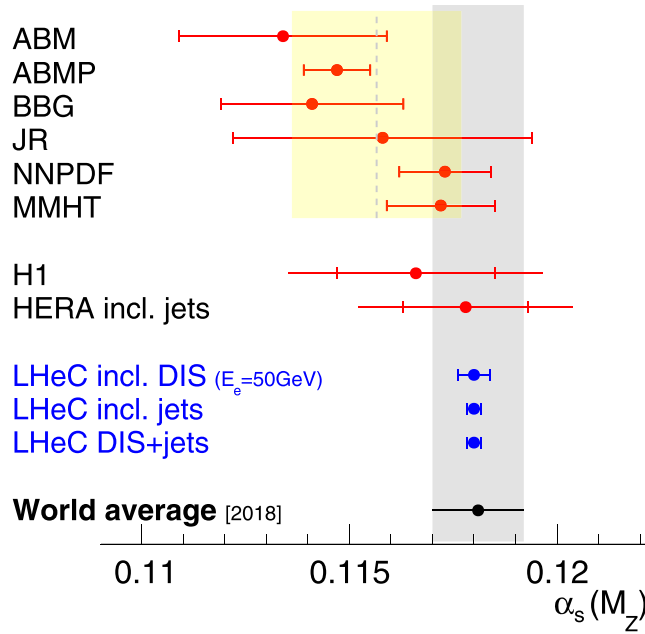


**Figure 33.** Summary of  $\alpha_s(M_Z)$  values in comparison with current values.

data, nor free values of  $m_c$  or  $m_b$  in the analysis, and we leave the outcome of such a complete QCD analysis to a time when real data are available and the actual values of the parameters are of interest. At such a time, better theoretical predictions will also be used, including higher-order corrections, heavy-quark mass effects, and higher-twist terms, which can be expected as a result of steady progress [189–194].

For this study, we employed the double-differential inclusive jet data as described above and additionally the inclusive NC/CC DIS data with  $E_e = 50$  GeV as introduced in section 3.2. Apart from the normalisation uncertainty, all the sources of systematic uncertainties are considered to be uncorrelated between the two processes. A fit of the NNLO QCD predictions to these data sets is then performed, and  $\alpha_s(M_Z)$  and the parameters of the PDFs are determined. This methodology closely follows the methodology outlined in section 3. Using inclusive jet and inclusive DIS data in a single analysis, the value of  $\alpha_s(M_Z)$  can be determined with an uncertainty of

$$\Delta\alpha_s(M_Z)(\text{incl. DIS \& jets}) = \pm 0.00018_{(\text{exp} + \text{PDF})}. \quad (4.4)$$

This result will improve the world average value considerably. However, theoretical uncertainties are not included, and new mathematical tools and an improved understanding of QCD will be needed in order to achieve small values that are similar to the experimental ones. The dominant sensitivity in this study arises from the jet data. This can be seen from figure 32, where  $\Delta\alpha_s(M_Z)$  only changes moderately when different assumptions are imposed on the inclusive NC/CC DIS data. The assumptions made for the uncertainties of the inclusive jet data were studied above, and these results can easily be translated to this PDF and  $\alpha_s$  fit.

The expected values for  $\alpha_s(M_Z)$  obtained from inclusive jets or from inclusive NC/CC DIS data are compared in figure 33 with current determinations from global fits based on DIS data (called *PDF fits*) and the world average value [136]. It can be observed that the LHeC will

have the potential to considerably improve the world average value. Already, after one year of data collection, the experimental uncertainties of the NC/CC DIS data are competitive with the world average value. The measurement of jet cross-sections will further improve that value (not shown).

Furthermore, the LHeC will be able to address a long-standing puzzle. All the  $\alpha_s$  determinations from global fits based on NC/CC DIS data result in a lower value of  $\alpha_s(M_Z)$  than determinations made using the lattice QCD framework, from  $\tau$  decays, or in a global electroweak fit. With the expected precision of the LHeC, this discrepancy will be resolved.

**4.1.3. Strong coupling from other processes.** A detailed study of the determination of  $\alpha_s(M_Z)$  from NC/CC DIS and from inclusive jet data was presented in the previous paragraphs. However, a large number of additional processes and observables that are measured at the LHeC can also be considered for a determination of  $\alpha_s(M_Z)$ . Suitable observables or processes are dijet and multijet production, HF production, jets in photoproduction, and event-shape observables. These processes all exploit the  $\alpha_s$  dependence of the hard interaction. Using suitable predictions, *softer* processes can also be exploited for an  $\alpha_s$  determination. Examples could include jet shapes or other substructure observables, or charged particle multiplicities.

Since  $\alpha_s(M_Z)$  is a parameter of a phenomenological model, the total uncertainty of  $\alpha_s(M_Z)$  is always the sum of the experimental and theoretical uncertainties which are related to the definition of the observable and to the applied model, e.g. hadronisation uncertainties, diagram removal/subtraction uncertainties, or uncertainties from missing higher orders. Therefore, credible prospects for the total uncertainty of  $\alpha_s(M_Z)$  from other observables or processes altogether are difficult to predict, which is even more the case because the LHeC will explore a new kinematic regime that was previously unmeasured.

To a first approximation, for any process, the sensitivity to  $\alpha_s(M_Z)$  scales with the order  $n$  of  $\alpha_s$  in the leading-order diagram,  $\alpha_s^n$ . The higher the power  $n$ , the higher the sensitivity to  $\alpha_s(M_Z)$ . Consequently, the experimental uncertainty of an  $\alpha_s$  fit may reduce with increasing values of  $n$ . At HERA, trijet cross-sections have already been proven to have a high sensitivity to  $\alpha_s(M_Z)$ , despite their sizeable statistical uncertainties [139, 149]. At the LHeC, due to the higher  $\sqrt{s}$  and huge integrated luminosity, as well as the larger acceptance of the detector, three-, four- or five-jet cross-sections represent highly sensitive observables for a precise determination of  $\alpha_s(M_Z)$ , and high experimental precision can be achieved. In these cases, fixed-order pQCD predictions may become the limiting factors, since they are more complicated for large  $n$ .

Di-jet observables are expected to yield a fairly similar experimental uncertainty to those of inclusive jet cross-sections, as studied in the previous paragraphs, since both have  $n = 1$  at LO. However, their theoretical uncertainties may be smaller, since dijet observables are less sensitive to additional higher-order radiation, in particular, at smaller scales, where  $\alpha_s(\mu_R)$  is larger.

Event-shape observables in DIS exploit additional radiation in DIS events (see e.g. review [195] or the HERA measurements [196, 197]). Consequently, once measured at the LHeC, the experimental uncertainties of  $\alpha_s(M_Z)$  from these observables are expected to become very similar to that in equation (4.4), since both the event sample and the process are similar to the inclusive jet cross-sections<sup>173</sup>. However, different reconstruction techniques for the observables may yield reduced experimental uncertainties, the calculation of event-shape observables

<sup>173</sup> It should be noted that event shape observables in NC DIS can be defined in the laboratory rest frame or the Breit frame.

allows for the resummation of large logarithms, and steady theoretical advances promise small theoretical uncertainties [198–204].

Jet production cross-sections in photoproduction represent a unique opportunity for another precision determination of  $\alpha_s(M_Z)$ . Such measurements have been performed at HERA [205–208]. The sizeable photoproduction cross-section provides a huge event sample which is statistically independent of NC DIS events, and the leading-order predictions are already sensitive to  $\alpha_s(M_Z)$  [209]. Its running can also be largely measured, since the scale of the process is accurately estimated by the transverse momentum of the jets  $\mu_R \sim p_T^{\text{jet}}$ . The limiting theoretical aspects are due to the presence of a quasi-real photon and the poorly known photon PDF [210, 211].

A different class of observables represents HF cross-sections, which are discussed in section 3.3.5. Due to flavour conservation, these are commonly proportional to  $\mathcal{O}(\alpha_s^1)$  at the leading order. However, when considering inclusive HF cross-sections above the heavy-quark mass threshold, heavy quarks can be factorised into the PDFs, and the leading structure functions  $F_2^{c,b}$  are only sensitive to  $\alpha_s$  beyond the LO approximation (see reviews [81, 82], recent HERA measurements [65, 212], and references therein). The presence of the heavy-quark mass as an additional scale stabilises perturbative calculations, and reduced theoretical uncertainties can be expected.

At the LHeC the structure of jets and the formation of hadrons can be studied with unprecedented precision. This is because of the presence of a single hadron in the initial state. Therefore, limiting effects such as an underlying event or pile-up are absent or greatly diminished. Precise measurements of jet shape observables, or the study of jet substructure observables [213], are highly sensitive to the value of  $\alpha_s(M_Z)$ , because parton showers and hadronisation take place at smaller scales, at which the strong coupling becomes large and an increased sensitivity to  $\alpha_s(M_Z)$  is attained [165, 214].

Finally, the determination of  $\alpha_s(M_Z)$  from inclusive NC DIS cross-sections can also be improved. For NC DIS the dominant sensitivity to  $\alpha_s$  arises from the  $F_L$  structure function and from scaling violations of  $F_2$  at lower values of  $Q^2$  but at very high values of  $x$ . Dedicated measurements of these kinematic regions will further improve the experimental uncertainties from the estimated values in equation (4.3).

#### 4.2. Discovery of new strong interaction dynamics at small $x$

The LHeC machine will offer access to a completely novel kinematic regime of DIS characterised by very small values of  $x$ . From the kinematical plane in  $(x, Q^2)$  depicted in figure 1, it is clear that the LHeC will be able to probe Bjorken- $x$  values as low as  $10^{-6}$  for perturbative values of  $Q^2$ . At low values of  $x$  various phenomena may occur that go beyond the standard collinear perturbative description based on DGLAP evolution. Since the seminal works of Balitsky, Fadin, Kuraev, and Lipatov [117, 215, 216] it has been known that, at large values of centre-of-mass energy  $\sqrt{s}$  or, to be more precise, in the Regge limit, there are large logarithms of energy that need to be resummed. Thus, even at low values of the strong coupling  $\alpha_s$ , logarithms of energy  $\ln s$  may be sufficiently large, so that terms such as  $(\alpha_s \ln s)^n$  start to dominate the cross-section.

In addition, other novel effects may appear in the low- $x$  regime, which are related to high gluon densities. At large parton densities the recombination of the gluons may become important in addition to gluon splitting. This is known as the parton saturation phenomenon in QCD, and is deeply related to the restoration of unitarity in QCD. As a result, the linear evolution equations will need to be modified by the additional nonlinear terms for the gluon density. In the next two subsections we shall explore the potential and sensitivity of the LHeC to these

small- $x$  phenomena in  $ep$  collisions. Note also that because parton saturation is a density effect, the nonlinear phenomena leading to it are enhanced by an increase in the mass number of the nucleus in  $eA$ . Section 6, devoted to the physics opportunities provided by  $eA$  collisions at the LHeC, discusses this aspect, see also reference [1].

**4.2.1. Resummation at small  $x$ .** The calculation of scattering amplitudes in the high-energy limit and the resummation of the  $(\alpha_s \ln s)^n$  series in the leading logarithmic order were performed in references [117, 215, 216], resulting in the famous BFKL evolution equation. This small- $x$  evolution equation, written for the so-called gluon Green's function or the unintegrated gluon density, is a differential equation in  $\ln 1/x$ . An important property of this equation is that it keeps the transverse momenta unordered along the gluon cascade. This is in contrast with DGLAP evolution which is differential in the hard scale  $Q^2$  and relies on strong ordering in the transverse momenta of the partons exchanged in the parton cascade. The solution to the BFKL equation is a gluon density that grows sharply with decreasing  $x$ , as a power, i.e.  $\sim x^{-\omega_{IP}}$ , where  $\omega_{IP}$  is the hard Pomeron intercept, and in the leading logarithmic approximation equals  $\frac{N_c \alpha_s}{\pi} 4 \ln 2$ , which gives a value of about 0.5 for typical values of the strong coupling. The leading logarithmic (LLx) result yielded a growth of the gluon density which was too steep for the experimental data at HERA. The next-to-leading logarithmic (NLLx) calculation performed in the late 1990s [217, 218] resulted in large negative corrections to the LLx value of the hard Pomeron intercept and yielded some instabilities in the cross-section [219–222]; it is important to account for subleading effects, since these are large [223, 224].

The appearance of the large negative corrections at NLLx motivated the search for an appropriate resummation that would stabilize the result. It was understood from an early stage that the large corrections that appear in the BFKL equation at NLLx are mostly due to the kinematics [225–227] as well as the DGLAP terms and the running of the strong coupling. The first attempts at combining the BFKL and DGLAP dynamics together with the proper kinematics [228–230] yielded encouraging results, and allowed a description of the HERA data for structure functions with good accuracy. The complete resummation programme was developed in a series of works [231–247] which developed the resummation for the gluon Green's function and the splitting functions.

The low- $x$  resummation was recently applied to the description of structure function data at HERA using the NNPDF methodology [248]. It was demonstrated that the resummed fits provide a better description of the structure function data than the pure DGLAP-based fits at a fixed NNLO order. In particular, it was shown that the  $\chi^2$  of the fits does not vary appreciably when more small- $x$  data are included, in the case of the fits that include the effects of the small- $x$  resummation. On the other hand, fits based on the NNLO DGLAP evolution exhibit a reduction of their quality in the region of low  $x$  and at low to moderate values of  $Q^2$ . This indicates that there is some tension in the fixed-order fits based on DGLAP, and that resummation alleviates it. In addition, it was shown that the description of the longitudinal structure function  $F_L$  from the HERA data is improved in fits with the small- $x$  resummation. This analysis suggests that the small- $x$  resummation effects are indeed visible in the HERA kinematic region. Such effects will be strongly magnified at the LHeC, which probes values of  $x$  more than one order of magnitude smaller than those of HERA. The NNPDF group also performed simulations of the structure functions  $F_2$  and  $F_L$  with and without resummation in the LHeC range, as well as for the next-generation electron–hadron collider, the FCC-eh [248]. The predictions for the structure functions as a function of  $x$  for fixed values of  $Q^2$  are shown in figure 34.

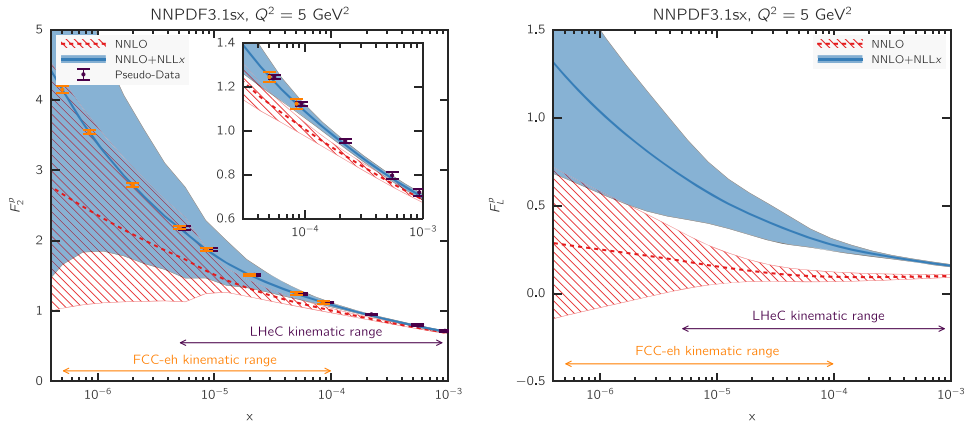


**Figure 34.** Predictions for the  $F_2$  and  $F_L$  structure functions using the NNPDF3.1sx NNLO and combined NNLO and NLLx (NNLO+NLLx) fits at  $Q^2 = 5 \text{ GeV}^2$  for the kinematics of the LHeC and FCC-eh. In the case of  $F_2$ , we also show the expected total experimental uncertainties based on the simulated pseudodata, assuming the combined NNLO and NLLx values as the central prediction. A small offset has been applied to the LHeC pseudodata, as some of the  $x$  values overlap with the FCC-eh pseudodata points. The inset in the left plot shows a magnified view in the kinematic region  $x > 3 \times 10^{-5}$ , corresponding to the reach of the HERA data. Reproduced from [248]. CC BY 4.0.

The simulations were done using APFEL [249] together with the HELL package [250] which implements the small- $x$  resummation. From figure 34 it is clear that LHeC will have a much higher sensitivity with which to discriminate between the fixed-order and resummed scenarios than the HERA collider, and that the FCC-eh will have even better discrimination. The differences between the central values for the two predictions are of the order of 15% for the case of  $F_2$ , and this is much larger than the projected error bar on the reduced cross-section or structure function  $F_2$  which could be measured at the LHeC. For comparison, the simulated pseudodata for  $F_2$  are shown together with the expected experimental uncertainties. The total uncertainties of the simulated pseudodata are at the few percent level at most, and are therefore much smaller than the uncertainties of the PDFs over most of the kinematic range.

It is evident that fits to the LHeC data will have the power to discriminate between the different frameworks. The predictions for the longitudinal structure function are shown in the right-hand plot of figure 34. We can see that in the case of the  $F_L$  structure function, the differences between the fixed-order and resummed predictions are consistently larger over the entire range of  $x$ . This indicates the importance of the measurement of the longitudinal structure function  $F_L$  which can provide further vital constraints on the QCD dynamics in the low- $x$  region due to its sensitivity to the gluon density in the proton.

To further illustrate the power of a high-energy DIS collider such as the LHeC in exploring the dynamics at low  $x$ , fits which include the simulated data were performed. The NNLO and NLLx resummed calculation was used to obtain the simulated pseudodata, for both the LHeC, using the scenario of a 60 GeV electron beam on a 7 TeV proton beam, and an FCC-eh scenario with a 50 TeV proton beam. All the experimental uncertainties for the pseudodata were added in quadrature. Theoretical fits were then performed to the DIS HERA as well as the LHeC and FCC-eh pseudodata, with and without resummation at low  $x$ . Hadronic data such as jet, DY, or top data were not included in this analysis but, as demonstrated in [248],

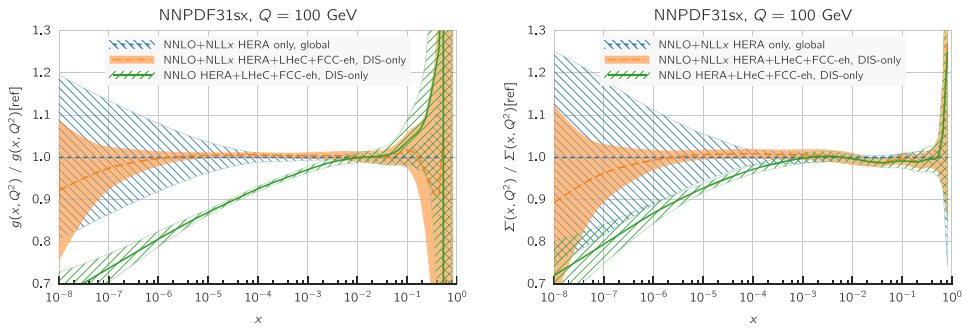


**Figure 35.** Comparison between the gluon (left plot) and the quark singlet (right plot) PDFs in the NNPDF3.1sx NNLO and NLLx fits without (blue hatched band) and with the LHeC and FCC-eh pseudodata (orange band) for inclusive structure functions. For completeness, we also show the results of the corresponding NNPDF3.1sx NNLO fit with LHeC and FCC-eh pseudodata (green hatched band). Reproduced from [248]. [CC BY 4.0](#).

these data do not have much constraining power at low  $x$ , and therefore the results of the analysis at low  $x$  are independent of the additional non-DIS data sets. The quality of the fits characterised by the  $\chi^2$  was markedly worse when the NNLO DGLAP framework was used to fit the HERA data and the pseudodata from LHeC and/or FCC-eh than was the case with resummation. To be precise, the  $\chi^2$  per degree of freedom for the HERA data set was equal to 1.22 for the NNLO fit, and 1.07 for the resummed fit. For the case of the LHeC (FCC-eh) the  $\chi^2$  values per degree of freedom were equal to 1.71 (2.72) and 1.22 (1.34) for the NNLO and NNLO-and-resummation fits, respectively. These results demonstrate the huge power of the new DIS machines to discriminate between the DGLAP and resummed frameworks, and the large sensitivity to the low- $x$  region while simultaneously probing low-to-moderate  $Q^2$  values.

In figure 35 a comparison of the gluon and quark distributions from the combined NNLO and NLLx fits is shown at  $Q = 100$  GeV as a function of  $x$ , with and without the inclusion of the simulated pseudodata from the LHeC as well as from the FCC-eh. The differences at large  $x$  are due to the fact that only DIS data were included in the fits, and not the hadronic data. The central values of the PDFs extracted using only HERA or using HERA and the simulated pseudodata coincide with each other, but a large reduction in uncertainty is visible when the new data are included. The uncertainties from the fits based on the HERA data only increase sharply at  $x \sim 10^{-4}$ . On the other hand, including the pseudodata from the LHeC and/or the FCC-eh can extend this regime downwards by order(s) of magnitude of  $x$ . Furthermore, fits without resummation, based only on NNLO DGLAP, were performed using the HERA data and the pseudodata. We can see that in this case the extracted gluon and singlet quark densities differ significantly from the fits using the combined NNLO and NLLx framework. Already at  $x = 10^{-4}$  the central values of the gluon density differ by 10%, and at  $x = 10^{-5}$ , which is the LHeC regime, the central values for the gluon density differ by 15%. This difference is much larger than the precision with which the gluon density can be extracted from the DIS data, which is of the order of  $\sim 1\%$ .

The presented analysis demonstrates that the fixed-order prediction based on the DGLAP evolution would most likely fail to accurately describe the structure function data in the new DIS machines and that, in that regime, new dynamics, including resummation, are mandatory



for quantitative predictions. Therefore, the LHeC machine has an unprecedented potential to pin down the details of the QCD dynamics at low values of Bjorken  $x$ .

*4.2.2. Disentangling nonlinear QCD dynamics at the LHeC.* As mentioned previously the kinematic extension of the LHeC will allow unprecedented tests of the strong interaction in the extremely low- $x$  region, and allow for tests of the novel QCD dynamics at low  $x$ . The second effect, which may be expected in addition to resummation, is the parton saturation phenomenon (which may manifest itself as a deviation from the linear DGLAP evolution), and the emergence of the saturation scale.

In particular, it has been argued that the strong growth of the gluon PDF at small  $x$  should eventually lead to gluon recombination [251] to avoid violating the unitary bounds. The onset of such nonlinear dynamics, also known as saturation, has been extensively sought, but so far, there has been no conclusive evidence of its presence, at least within the HERA inclusive structure function measurements. In this context, the extended kinematic range of the LHeC provides unique avenues with which to explore the possible onset of nonlinear QCD dynamics at small  $x$ . The discovery of saturation, a radically new regime of QCD, would then represent an important milestone in our understanding of the strong interactions.

The main challenge in disentangling saturation lies in the fact that nonlinear corrections are expected to be moderate, even at the LHeC, since they are small (if present at all) in the region covered by HERA. Therefore, great care needs to be employed in order to separate such effects from those of standard DGLAP linear evolution. Indeed, it is well known that the HERA data at small  $x$  in the perturbative region can be equally well described, at least at the qualitative level, both by PDF fits based on the DGLAP framework as well as by saturation-inspired models. However, rapid progress both in theoretical calculations and methodological developments has pushed QCD fits to a new level of sophistication, and it has recently been shown that subtle but clear evidence of BFKL resummation at small  $x$  is present in the HERA data, for both inclusive and heavy-quark structure functions [252, 253]. Such studies highlight that it should be possible to distinguish nonlinear from linear dynamics using state-of-the-art fitting methods, even if these are moderate, provided that they are within the LHeC reach.

Here, we want to assess the sensitivity of the LHeC for detecting the possible onset of nonlinear saturation dynamics. This study will be carried out by generalising a recent analysis [59] that quantified the impact of LHeC inclusive and semi-inclusive measurements on the PDF4LHC15 PDFs [254, 255] by means of Hessian profiling [256]. In that analysis, the LHeC pseudodata were generated by assuming that linear DGLAP evolution was valid over the entire LHeC kinematic range and using the PDF4LHC15 set as the input. To ascertain the possibility of pinning down saturation at the LHeC, we revisit this study here, but now generate the LHeC pseudodata by means of a saturation-inspired calculation. By monitoring the statistical significance of the tension that will be introduced (by construction) between the saturation pseudodata and the DGLAP theory assumed in the PDF fit, we aim to determine the likelihood of disentangling nonlinear from linear evolution effects at the LHeC. See also [257] for previous related studies along the same lines.

*4.2.2.1. Analysis settings.* In this study we adopt the settings used in [59, 258], to which we refer the interested reader for further details. Reference [59] quantified the impact of inclusive and semi-inclusive NC and CC DIS structure functions from the LHeC on the proton PDFs. These results were then compared with the corresponding projections for the PDF sensitivity of the high-luminosity upgrade of the LHC (HL-LHC). Figure 7 displays the kinematic range in the  $(x, Q^2)$  plane of the LHeC pseudodata employed in that analysis, which illustrates that

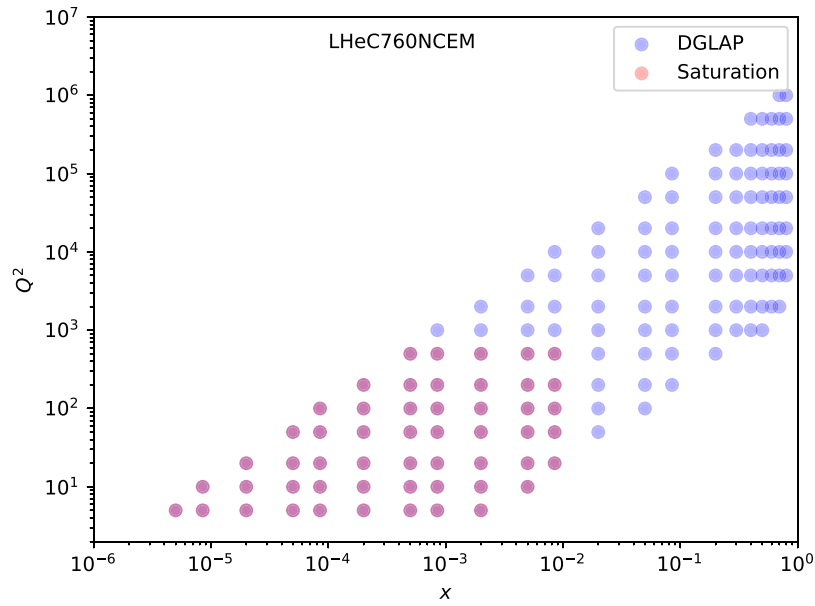


**Figure 36.** Kinematic coverage of the NC  $e^-p$  scattering pseudodata at the LHeC, in which the blue (red) points indicate those bins for which DGLAP (saturation) predictions are available.

the LHeC can provide unique constraints on the behaviour of the quark and gluon PDFs in the very-small- $x$  region.

Since nonlinear dynamics are known to become sizeable only at small  $x$ , for the current analysis, it is sufficient to consider the NC  $e^-p$  inclusive scattering cross-sections of proton-beam energies of  $E_p = 7$  TeV and  $E_p = 1$  TeV. In figure 36 we show the bins in  $(x, Q^2)$  for which LHeC pseudodata for inclusive structure functions have been generated according to a saturation-based calculation. Specifically, here, we have adopted the DGLAP-improved saturation model of reference [259], in which the scattering matrix is modelled through the eikonal iteration of two gluon exchanges. This model was further extended to include HF in reference [260]. The specific parameters that we use were taken from fit two in reference [261], where parameterisations are provided that can be used for  $x < 0.01$  and  $Q^2 < 700$  GeV<sup>2</sup>. These parameters were extracted from a fit to the HERA legacy inclusive structure function measurements [45], restricted to  $x < 0.01$  and  $0.045 < Q^2 < 650$  GeV<sup>2</sup>. In contrast to other saturation models, the one we assume here [261] provides a reasonable description for large  $Q^2$  in the small- $x$  region, where it ensures a smooth transition to standard fixed-order perturbative results.

Note that the above discussion only refers to the generated LHeC pseudodata: all other aspects of the QCD analysis of reference [59] are left unchanged. In particular, the PDF profiling will be carried out using theoretical calculations obtained by means of DGLAP evolution with the NNLO PDF4LHC15 set (see also reference [262]), with heavy quark structure functions evaluated by means of the FONLL-B general-mass VFNS [89]. In order to ensure consistency with the PDF4LHC15 prior, here we will only replace the DGLAP pseudodata by the saturation calculation in the kinematic region of  $x \lesssim 10^{-4}$ , rather than for all the bins indicated in red in figure 36. The reason for this choice is that PDF4LHC15 already includes HERA data down to  $x \simeq 10^{-4}$  which are successfully described via the DGLAP framework,

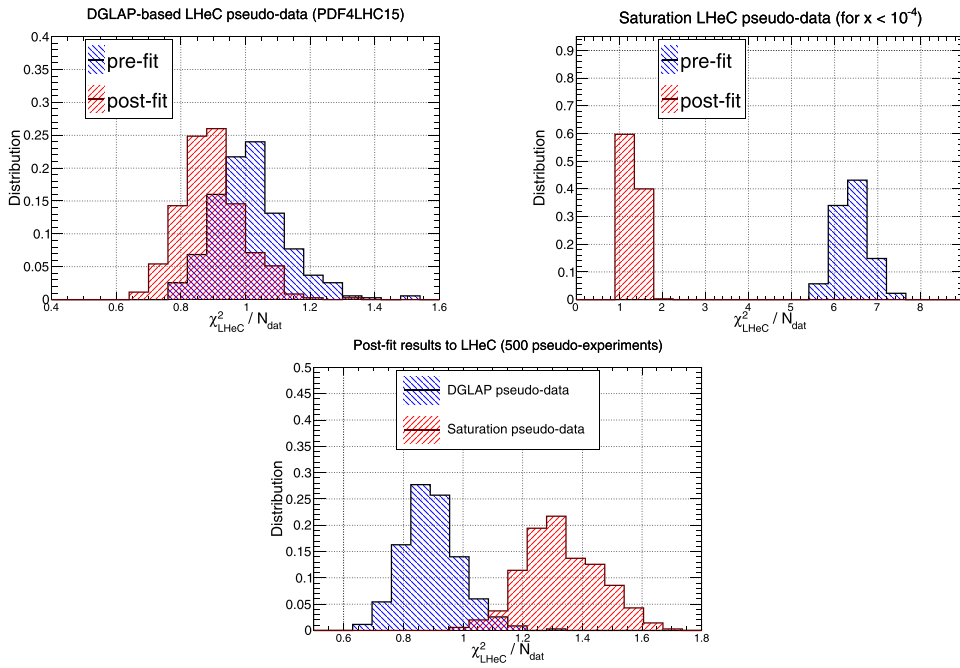


**Figure 37.** Upper plots: the distribution of pre-fit and post-fit values of  $\chi^2/n_{\text{dat}}$  for the  $N_{\text{exp}} = 500$  sets of generated LHeC pseudodata. We compare the results of the profiling of the LHeC pseudodata based on DGLAP calculations in the entire range of  $x$  (left) with those where the pseudodata are based on the saturation model in the region  $x < 10^{-4}$  (right plot). Bottom plot: comparison of the post-fit  $\chi^2/n_{\text{dat}}$  distributions between these two scenarios for the pseudodata generation.

and therefore, if we assume departures from DGLAP in the LHeC pseudodata, this should only be done for smaller values of  $x$ .

**4.2.2.2. Results and discussion.** Using the analysis settings described above, we have carried out the profiling of PDF4LHC15 with the LHeC inclusive structure function pseudodata, which were generated for  $x \leq 10^{-4}$  ( $x > 10^{-4}$ ) using the Golec-Biernat-Wuesthoff (GBW) saturation (DGLAP) calculations, and we compared them with the results of the profiling in which the pseudodata follow the DGLAP prediction. We have generated  $N_{\text{exp}} = 500$  independent sets of LHeC pseudodata, each one characterised by different random fluctuations (determined by the experimental uncertainties) around the underlying central value.

To begin with, it is instructive to compare the data versus theory agreement,  $\chi^2/n_{\text{dat}}$ , between the pre-fit and post-fit calculations, in order to assess the differences between the DGLAP and saturation cases. In the upper plots of figure 37 we show the distributions of the pre-fit and post-fit values of  $\chi^2/n_{\text{dat}}$  for the  $N_{\text{exp}} = 500$  sets of generated LHeC pseudodata. We compare the results of the profiling of the LHeC pseudodata based on DGLAP calculations over the entire range of  $x$  with those where the pseudodata are based on the saturation model in the region  $x < 10^{-4}$ . In the bottom plot we then compare the post-fit  $\chi^2$  distributions of the two scenarios. Note that in these three plots the ranges in the  $x$  axes are different.

From this comparison we can observe that for the case where the pseudodata are generated using a consistent DGLAP framework (PDF4LHC15) as the framework adopted for the theoretical calculations used in the fit, as expected, the agreement is already good at the pre-fit

level, and it is further improved at the post-fit level. However, the situation is rather different in the case where a subset of the LHeC pseudodata is generated using a saturation model: at the pre-fit level, the agreement between theory and pseudodata is poor, with  $\chi^2/n_{\text{dat}} \simeq 7$ . The situation markedly improves at the post-fit level, where the  $\chi^2/n_{\text{dat}}$  distributions now peak at around 1.3. This result implies that the DGLAP fit manages to absorb most of the differences in theory present in the saturation pseudodata. This said, the DGLAP fit cannot entirely *fit away* the nonlinear corrections: as shown in the lower plot of figure 37, even at the post-fit level, one can still tell the difference between the  $\chi^2/n_{\text{dat}}$  distributions of the two cases, as the DGLAP (saturation) pseudodata peak at around 0.9 (1.3). This comparison highlights that it is not possible for the DGLAP fit to completely absorb the saturation effects into a PDF redefinition.

In order to identify the origin of the worse agreement between the theoretical predictions and the LHeC pseudodata in the saturation case, it is illustrative to take a closer look at the pulls defined as

$$P(x, Q^2) = \frac{\mathcal{F}_{\text{dat}}(x, Q^2) - \mathcal{F}_{\text{fit}}(x, Q^2)}{\delta_{\text{exp}}\mathcal{F}(x, Q^2)}, \quad (4.5)$$

where  $\mathcal{F}_{\text{fit}}$  is the central value of the profiled results for the observable  $\mathcal{F}$  (in this case the reduced neutral-current DIS cross-section),  $\mathcal{F}_{\text{dat}}$  is the corresponding central value of the pseudodata, and  $\delta_{\text{exp}}\mathcal{F}$  represents the associated total experimental uncertainty. In figure 38 we display the pulls between the post-fit prediction and the central value of the LHeC pseudodata for different bins in  $Q^2$ . We compare the cases where the pseudodata have been generated using a consistent theoretical calculation (DGLAP) with that based on the GBW saturation model.

The comparisons in figure 38 show first of all that in the DGLAP case, the pulls are  $\mathcal{O}(1)$  over the entire kinematical range. This is, of course, expected, given that the LHeC pseudodata are generated using the same theory as the one subsequently used for the fit. In the case where the pseudodata have been partially generated using the saturation calculation, on the other hand, one finds a systematic tension between the theory used for the fit (DGLAP) and the one used to generate the pseudodata (saturation). Indeed, we find that at the smallest values of  $x$ , the theoretical prediction overshoots the data by a significant amount, while at higher  $x$  the opposite behaviour takes place. One can also see that in the region  $10^{-4} \lesssim x \lesssim 10^{-3}$ , the fit undershoots the pseudodata by a large amount.

These comparisons highlight that a QCD fit to the saturation pseudodata is obtained as a compromise between opposite trends: the theory wants to overshoot the data at very small  $x$  and undershoot it at larger values of  $x$ . These tensions result in a distorted fit, explaining the larger  $\chi^2/n_{\text{dat}}$  values as compared to the DGLAP case. This behaviour can be partially traced back to the different scalings in  $Q^2$  used by DGLAP and GBW: while a different  $x$  dependence could eventually be absorbed into a change of the PDFs at the parameterisation scale  $Q_0$ , this is not possible with a  $Q^2$  dependence.

The pull analysis of figure 38 highlights how, in order to distinguish linear from nonlinear QCD evolution effects at small  $x$ , it is crucial to ensure that the lever arm in  $Q^2$  is as large as possible in the perturbative region. In this way, it becomes possible to disentangle the different scalings in  $Q^2$  for the two cases. The lack of a sufficiently large lever arm in  $Q^2$  at HERA at small  $x$  could explain, in part, why both frameworks are able to describe the same structure function measurements at the qualitative level. Furthermore, we find that an amplification of the significance of these subtle effects can be achieved by monitoring the  $\chi^2$  behaviour in the  $Q^2$  bins that are more affected by the saturation corrections. The reason for this is that the total  $\chi^2$ , for example, that reported in figure 37, is somewhat less informative, since the deviations

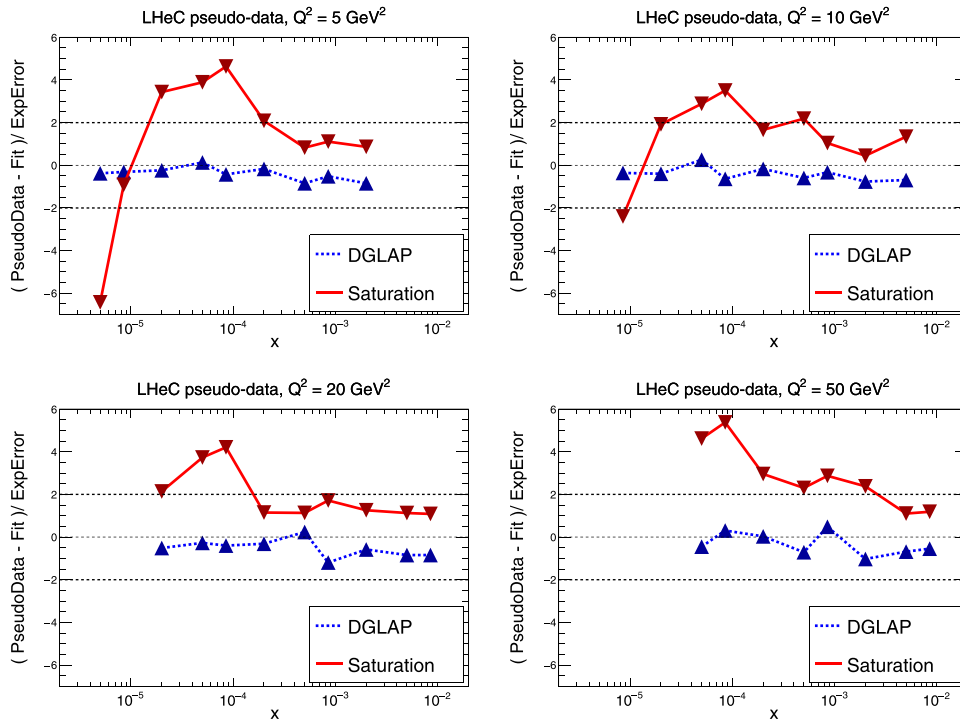


**Figure 38.** The pulls between the central value of the LHeC pseudodata and post-fit prediction, equation (4.5), for four different bins in  $Q^2$ . We compare the results of the profiling where the LHeC pseudodata have been generated using a consistent DGLAP theory with the result that is partially based on the saturation calculations.

at small  $Q$  are masked by the good agreement between the theory and the pseudodata over the rest of the kinematical range of the LHeC summarised in figures 7 and 36.

To conclude this analysis, in figure 39 we display a comparison between the PDF4LHC15 baseline and the results of the PDF profiling of the LHeC pseudodata for the gluon (left) and quark singlet (right) for  $Q = 10$  GeV. We show the cases where the pseudodata is generated using DGLAP calculations and where they are partially based on the GBW saturation model (for  $x \lesssim 10^{-4}$ ). We find that the distortion induced by the mismatch between theory and pseudodata in the saturation case is typically larger than the PDF uncertainties expected once the LHeC constraints are taken into account. While, of course, in a realistic situation, such a comparison would not be possible, the results of figure 39 show that saturation-induced effects are expected to be larger than the typical PDF errors in the LHeC era, and thus that it should be possible to tell them apart using tools such as the pull analysis of figure 38 or other statistical methods.

**4.2.2.3. Summary.** Here, we have assessed the feasibility of disentangling DGLAP evolution from nonlinear effects at the LHeC. By means of a QCD analysis where LHeC pseudodata are generated using a saturation model, we have demonstrated that the LHeC should be able to identify nonlinear effects with large statistical significance, provided their size is the one predicted by current calculations such as those of [261], which were tuned to the HERA data. A more refined analysis would require to study whether or not small- $x$  BFKL resummation effects can partially mask the impact of nonlinear dynamics, though this is unlikely, since the

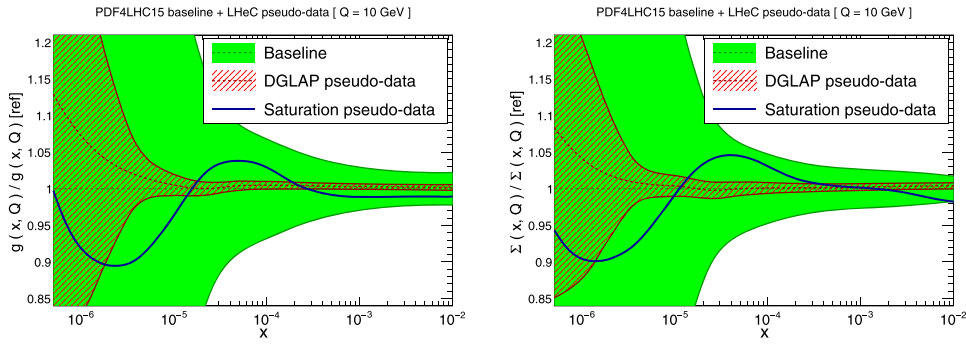


**Figure 39.** Comparison between the PDF4LHC15 baseline (green band) and the results of the profiling of the LHeC pseudodata for the gluon (left) and quark singlet (right) for  $Q = 10$  GeV. We show the cases where the pseudodata are generated using DGLAP calculations (red hatched band) and where they are partially based on the GBW saturation model (blue curve).

main difference arises in their  $Q^2$  scaling. The discovery of nonlinear dynamics would represent an important milestone for the physics programme of the LHeC, demonstrating the onset of a new gluon-dominated regime of strong interactions and paving the way for detailed studies of the properties of this new state of matter. Such a discovery would also have implications outside nuclear and particle physics; for instance, it would affect the theoretical predictions for the scattering of ultra-high-energy neutrinos with matter [263].

#### 4.2.3. Small $x$ and the longitudinal structure function $F_L$ .

4.2.3.1. DIS cross-section and the challenge of accessing  $F_L$  The inclusive, deep inelastic electron–proton scattering cross-section at low  $Q^2 \ll M_Z^2$ ,

$$\frac{Q^4 x}{2\pi\alpha^2 Y_+} \cdot \frac{d^2\sigma}{dx dQ^2} = \sigma_T \simeq F_2(x, Q^2) - f(y) \cdot F_L(x, Q^2) = F_2 \cdot \left(1 - f(y) \frac{R}{1+R}\right) \quad (4.6)$$

is defined by two proton structure functions,  $F_2$  and  $F_L$ , where  $y = Q^2/sx$ ,  $Y_+ = 1 + (1 - y)^2$ , and  $f(y) = y^2/Y_+$ . The cross-section may also be expressed [264] as the sum of two contributions,  $\sigma_T \propto (\sigma_T + \epsilon\sigma_L)$ , referring to the transverse and longitudinal polarisation states of the exchanged boson, where  $\epsilon$  characterises the ratio of the longitudinal to the transverse polarisation. The ratio of the longitudinal to transverse cross-sections is given by

$$R(x, Q^2) = \frac{\sigma_L}{\sigma_T} = \frac{F_L}{F_2 - F_L}, \quad (4.7)$$

which is related to  $F_2$  and  $F_L$  as given above. Due to the positivity of the cross-sections  $\sigma_{L,T}$ , one may observe that  $F_L \leq F_2$ . The reduced cross-section  $\sigma_T$ , equation (4.6), is therefore a direct measure of  $F_2$ , apart from a limited region of high  $y$  where the contribution of  $F_L$  may be sizeable. To the leading order, for spin 1/2 particles, one expected  $R = 0$ . The initial measurements of  $R$  at SLAC [265, 266] showed that  $R$  was indeed small,  $R \simeq 0.18$ , which was taken as evidence that quarks carry a spin of 1/2.

The task of measuring  $F_L$  thus requires the precise measurement of the inclusive DIS cross-section near  $y = 1$  and then the disentanglement of the two structure functions by exploiting the  $f(y) = y^2/Y_+$  variation, which depends on  $x$ ,  $Q^2$ , and  $s$ . By varying the cms beam energy,  $s$ , one can disentangle  $F_2$  and  $F_L$  and obtain independent measurements at each common, fixed point



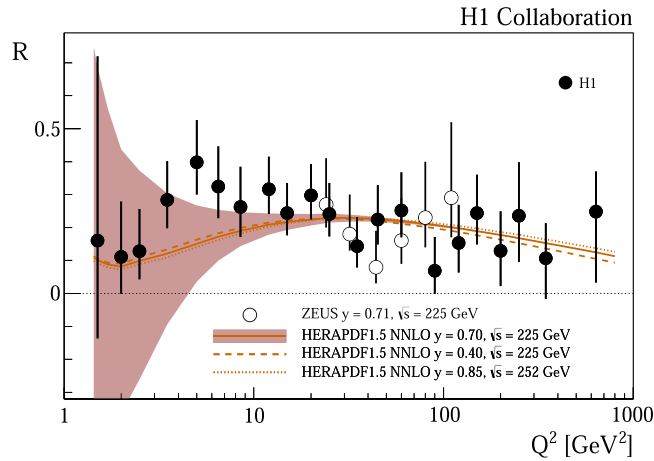


**Figure 40.** Measurement of the structure function ratio  $R = F_L / (F_2 - F_L)$  by H1 (solid points) and ZEUS (open circles), from a variation of the proton-beam energy over the final half-year of HERA operation. The curve represents an NNLO QCD fit analysis of the other HERA data. This becomes uncertain for  $Q^2$  below 10 GeV<sup>2</sup>, where the  $Q^2$  dependence of  $F_2$  at HERA does not permit an accurate determination of the gluon density, which dominates in the prediction of  $F_L$ . Reproduced from [274]. CC BY 4.0.

of  $x, Q^2$ . This is particularly challenging not only because the  $F_L$  part is small, calling for the utmost precision, but also because it requires a measurement at high  $y$ . The inelasticity  $y = 1 - E'/E_e$ , however, is large only for scattered electron energies  $E'_e$  much smaller than the electron beam energy  $E_e$ , for example  $E'_e = 2.7$  GeV for  $y = 0.9$  at HERA<sup>174</sup>. In the region where  $E'$  is only a few GeV, electron identification becomes a major problem and the electromagnetic ( $\pi^0 \rightarrow \gamma\gamma$ ) and hadronic backgrounds, mainly from unrecognised photoproduction, increase strongly.

The history and achievements with  $F_L$ , the role of HERA, and the prospects as sketched in the CDR of the LHeC, were summarised in detail in [53]. The measurement of  $F_L$  at HERA [267] was given very limited time and it collected about 5.9 and 12.2 pb<sup>-1</sup> of data at reduced beam energies which were analysed together with about 100 pb<sup>-1</sup> at nominal HERA energies. The results may be illustrated well by the data obtained for the ratio  $R(x, Q^2)$ , as shown in figure 40. To a good approximation,  $R(x, Q^2)$  is a constant which was determined to be  $R = 0.23 \pm 0.04$ , in good agreement with the SLAC value of  $R \simeq 0.18$ , despite the hugely extended kinematic range. The rather small variation of  $R$  towards small  $x$  at fixed  $y = Q^2/sx$  may appear to be astonishing, since one observes that  $F_2$  increases strongly towards low  $x$ . A constant  $R$  of e.g. 0.25 means that  $F_2 = (1 + R)F_L/R$  is five times larger than  $F_L$ , and that they increase together, since they have a common origin, namely, the increase in the gluon density. This can be understood in approximations to the DGLAP expression of the  $Q^2$  derivative of  $F_2$  and the so-called Altarelli–Martinelli relation of  $F_L$  to the parton densities [268, 269] (see the discussion in reference [53]). The resulting H1 value also obeys the condition  $R \leq 0.37$ , which was obtained in a rigorous attempt to derive the dipole model for DIS [270].

<sup>174</sup>The nominal electron-beam energy  $E_e$  at the LHeC is double that of HERA. Ideally, one would like to vary the proton beam energy in an  $F_L$  measurement at the LHeC, which would, however, affect the hadron collider operation. In this study, it was therefore considered preferable to lower  $E_e$ , which may be done independently of the HL-LHC.

**4.2.3.2. Parton evolution at low  $x$**  Parton distributions have to be extracted from experiments, as their  $x$  dependence and flavour sharing are not predicted by QCD. They acquire a particular meaning through the theoretical prescription of their kinematic evolution. PDFs, as frequently used for LHC analyses, are predominantly defined through the now-classic DGLAP formalism, in which the  $Q^2$  dependence of parton distributions is regulated by splitting functions, while the DIS cross-section, determined by the structure functions, is calculable by folding the PDFs with coefficient functions. DIS is known to be the most suitable process for extracting PDFs from experiments, for which the HERA collider has, so far, delivered the most useful data. Through factorisation theorems, PDFs are considered to be universal, such that PDFs extracted in  $ep$  DIS are suitable for describing, for example, DY scattering cross-sections in  $pp$  at the LHC. This view has already been formulated for third-order pQCD, and has been quite successful in the interpretation of LHC measurements, which by themselves also constrain PDFs in parton–parton scattering sub-processes.

As mentioned in section 4.2.1, a question has long been posed about the universal validity of the DGLAP formalism, especially for the region of small Bjorken  $x$  where logarithms  $\propto \ln(1/x)$  become very sizeable. This feature of the perturbation expansion is expected to significantly modify the splitting functions. This, in turn, changes the theory underlying the physics of parton distributions, and predictions for the LHC and its successor will correspondingly have to be altered. This mechanism is illustrated in figure 41 (taken from reference [253]) for an equivalent  $Q^2$  of a few  $\text{GeV}^2$ , which shows the  $x$  dependence of the gluon–gluon and the quark–gluon splitting functions,  $P_{gg}$  and  $P_{qg}$ , calculated by DGLAP QCD. It can be observed that at the NNLO  $P_{gg}$  decreases strongly towards small  $x$ , becoming smaller than  $P_{qg}$  for values of  $x$  less than  $10^{-4}$ . Resummation of the large  $\ln(1/x)$  terms (see reference [253]), performed here to the next-to-leading  $\log x$ , restores the dominance of  $gg$  splitting over  $qg$  splitting. Consequently, the gluon distribution in the resummed theory exceeds that derived by pure DGLAP. While this observation has been supported by the HERA data, it still relies on limited kinematic coverage and precision. The LHeC will examine this in detail, at a hugely extended range, and is thus expected to resolve the long-standing question about the validity of the BFKL evolution and the transition from DGLAP to BFKL as  $x$  decreases while  $Q^2$  remains large enough for pQCD to apply.

**4.2.3.3. Kinematics of Higgs production at the HL-LHC** The clarification of the evolution and the accurate and complete determination of the parton distributions is of direct importance for the LHC. This can be illustrated by the kinematics of Higgs production at HL-LHC, which is dominated by gluon–gluon fusion. With the luminosity upgrade, the detector acceptance is being extended into the forward region to pseudorapidity values of  $|\eta| = 4$ , where  $\eta = \ln \tan \theta/2$  is a very good approximation of the rapidity. The DY scattering of two partons with Bjorken  $x$  values of  $x_{1,2}$  is related to rapidity via the relation  $x_{1,2} = \exp(\pm\eta) \cdot M/\sqrt{s}$  where  $\sqrt{s} = 2E_p$  is the cms energy and  $M$  is the mass of the produced particle. It is interesting to see that  $\eta = \pm 4$  corresponds to  $x_1 = 0.5$  and  $x_2 = 0.00016$  for the SM Higgs boson with a mass of  $M = 125 \text{ GeV}$ . Consequently, Higgs physics at the HL-LHC will depend on understanding PDFs at high  $x$  (a challenge that will also be resolved by the LHeC) and on clarifying the evolution at small  $x$ . At the FCC-hh, in its 100 TeV energy version, the small- $x$  value for  $\eta = 4$  will be as low as  $2 \times 10^{-5}$ . Both laws of QCD and the resulting phenomenology of particle production at the HL-LHC and its successor demand a clarification of the evolution of the parton contents at small  $x$  as a function of the resolution scale  $Q^2$  [271–273]. In particular, this relates to the unambiguous, accurate determination of the gluon distribution, which dominates the small- $x$  parton densities as well as the production of the Higgs boson in  $pp$  scattering.

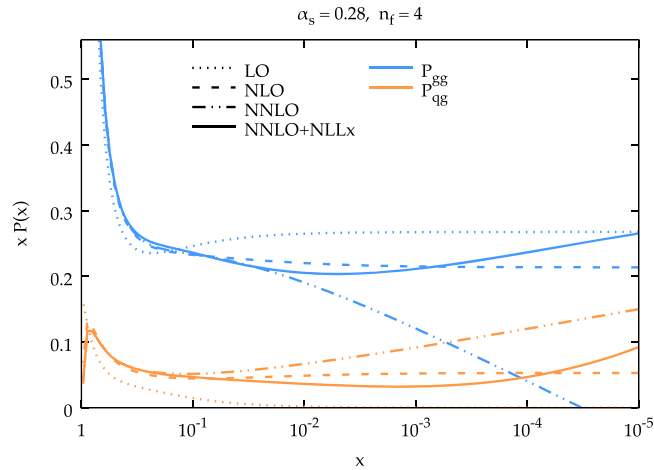


**Figure 41.** Calculation of splitting functions  $P_{gg}$  (top, blue) and  $P_{qg}$  (bottom, brown) in the resummed NNLO (solid) as compared to non-resummed calculations at the LO (dotted), the NLO (dashed), and the NNLO (dashed and dotted) as functions of  $x$  for  $n_f = 4$  at a large value of  $\alpha_s$  corresponding to a  $Q^2$  of a few  $\text{GeV}^2$ . Reproduced from [253]. CC BY 4.0. The resummed calculation is seen to restore the dominance of  $P_{gg}$  over  $P_{qg}$  as  $x$  becomes small (towards the right side), which is violated at the NNLO.

**4.2.3.4. Indications for resummation in H1  $F_L$  data** The simultaneous measurement of the two structure functions  $F_2$  and  $F_L$  is the cleanest way to establish new parton dynamics at low  $x$ . This is so because their independent constraints on the dominating gluon density at low  $x$  ought to lead to consistent results. In other words, one may constrain all partons with a complete PDF analysis of the inclusive cross-section in the kinematic region where the cross-section's  $F_L$  part is negligible and compare the  $F_L$  measurement with this result. A significant deviation from the  $F_L$  data signals the necessity of introducing new, non-DGLAP physics into the theory of parton evolution, especially at small  $x$ . The salient value of the  $F_L$  structure function is a result of its inclusive character, which enables a clean theoretical treatment, as recognised at an early stage [268, 269]. This procedure has recently been illustrated [253] using the H1 data for  $F_L$  [274], which are the only accurate data from HERA at the smallest  $x$ . The results are shown in figure 42. One can observe the trend described above: the resummed prediction is larger than the pure NNLO curve, and the description at the smallest value of  $x$  (i.e. at less than  $5 \times 10^{-4}$ ) appears to be improved. The difference between the two curves increases as  $x$  decreases. However, due to the peculiarity of the DIS kinematics, which relates  $x$  to  $Q^2/sy$ , one faces the difficulty that  $Q^2$  decreases with  $x$  at fixed  $s$  for large  $y \geq 0.6$ , which is the region of sensitivity to  $F_L$ . Thus, one not only wishes to substantially improve the precision of the  $F_L$  data, but also to substantially increase  $s$  in order to avoid the region of non-perturbative behaviour while performing theoretical testing at small  $x$ . This is the double and principal advantage that the LHeC offers—a much-increased precision and more than a decade's worth of kinematic range extension.

**4.2.3.5. The longitudinal structure function at the LHeC** Following the method described above, inclusive cross-section data have been simulated for  $E_p = 7$  TeV and three electron-beam energies  $E_e$  of 60, 30, and 20 GeV. The assumed integrated luminosity values are 10, 1, and again  $1 \text{ fb}^{-1}$ , respectively. These are about a factor of a hundred larger than the corresponding H1 luminosities. At large  $y$ , the kinematics is best reconstructed using the scattered

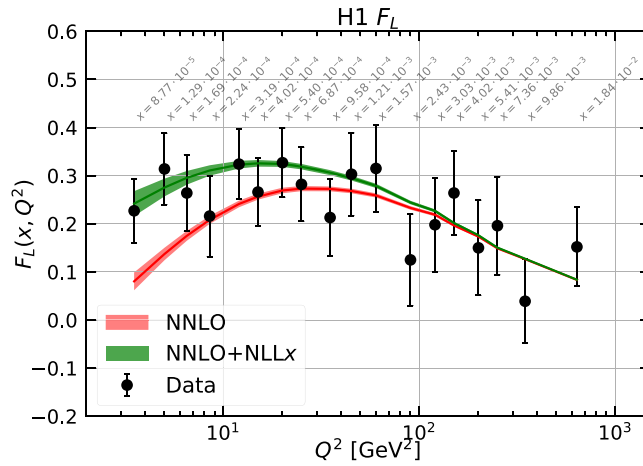


**Figure 42.** Measurement of the longitudinal structure function  $F_L$ , obtained as average results over a number of  $x$ -dependent points at fixed  $Q^2$ , plotted vs  $Q^2$  with the corresponding  $x$  values indicated in grey. Red curve: the NNLO fit to the H1 cross-section data; green curve: the NNLO fit including the NLLx resummation. Reproduced from [253]. CC BY 4.0.

electron energy,  $E'_e$ , and the polar angle,  $\theta_e$ . The experimental methods used to calibrate the angular and energy measurements are described in [267]. For this study similar results are assumed: for  $E'_e$ , a scale uncertainty of 0.5% at small  $y$  (compared to 0.2% for H1) rising linearly to 1.2%, in the range from  $y = 0.4$  to 0.9. For the polar angle, given the superior quality of the anticipated LHeC silicon tracker as compared to the H1 tracker, it is assumed that  $\theta_e$  may be calibrated to 0.2 mrad, as compared to 0.5 mrad at H1. The residual photo-production background contamination is assumed to be 0.5% at the largest value of  $y$ , which is twice as good as that of H1. A further assumption is made for the radiative corrections which are assumed to be uncertain to 1% and treated as a correlated error. The main challenge is to reduce the uncorrelated uncertainty, which was varied here between 0.2 and 0.5%. This is about ten to three times more accurate than the H1 result, which may be a reasonable assumption: the hundredfold increase in statistics defines a totally different scale for the treatment of uncorrelated uncertainties, for example, those originating from imperfect simulations, trigger efficiency, or MC statistics. It is very difficult to transplant previous results into modern and future conditions. There could, however, be an important fixed point if one knew that the most precise measurement of  $Z$  boson production by ATLAS at the LHC had a total systematic error of just 0.5% [275].

The method used here is that of a simple straight-line fit of  $\sigma_r = F_2 - f(y)F_L$  (equation (4.6)), in which  $F_L$  is obtained as the slope of the  $f(y)$  dependence<sup>175</sup>. The predictions for  $F_2$  and  $F_L$  were obtained using LO formulae for the PDF set of MSTW 2008. In this method, any common factor does not alter the absolute uncertainty of  $F_L$ . This also implies that the estimated absolute error of  $F_L$  is independent of whether  $F_L$  is larger or smaller than assumed here. For illustration,  $F_L$  was scaled by a factor of two. Since  $f(y) \propto y^2$ , the accuracy is optimised using a nonlinear choice of reduced beam energies. The fit takes the cross-section

<sup>175</sup> Better results were achieved by H1 using a  $\chi^2$  minimisation technique (see reference [276]), which has not been considered for the rough estimate of the projected  $F_L$  uncertainty at the LHeC.

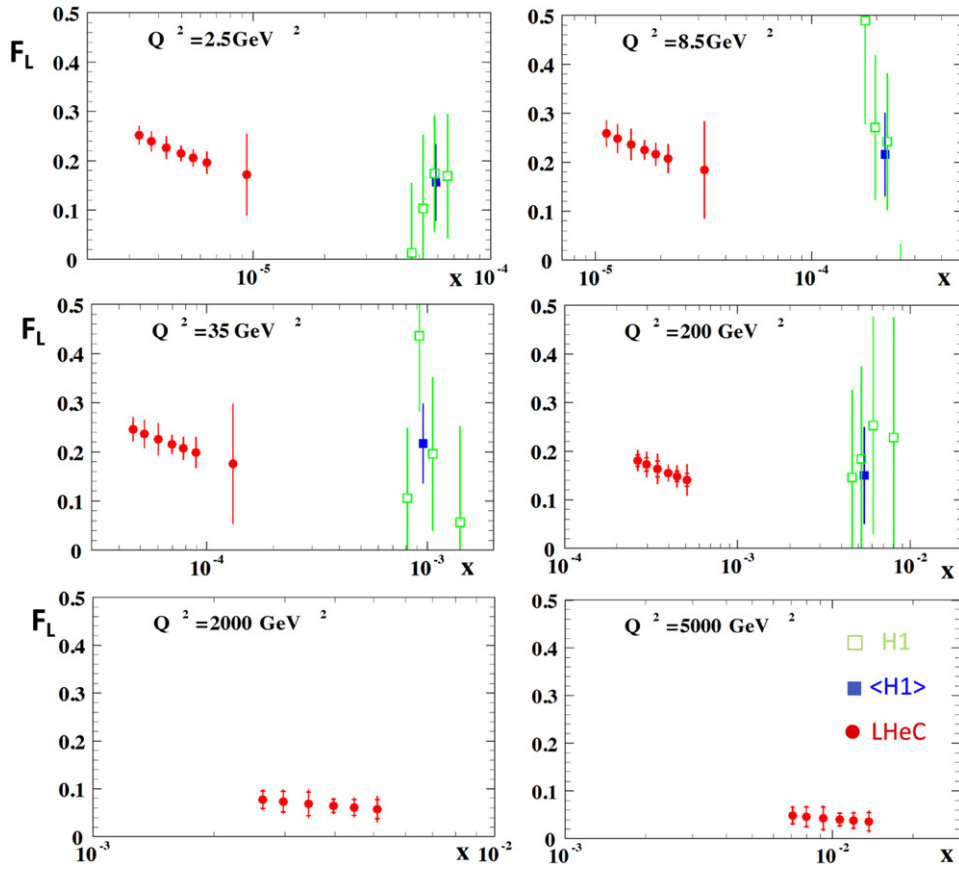


**Figure 43.** H1 measurement and LHeC simulation of data for the longitudinal structure function  $F_L(x, Q^2)$ . Green: data from H1, for selected  $Q^2$  intervals from reference [274]; blue: weighted average of the (green) data points at fixed  $Q^2$ ; red: simulated data from an  $F_L$  measurement at the LHeC with varying beam energy, see text. The H1 error bars denote the total measurement uncertainty. The LHeC inner error bars represent the data statistics, which are only visible for  $Q^2 \geq 200 \text{ GeV}^2$ , while the outer error bars represent the total uncertainty. Since the  $F_L$  measurement is sensitive only at high values of inelasticity,  $y = Q^2/sx$ , each  $Q^2$  value is sensitive only to a certain limited interval of  $x$  values which increase with  $Q^2$ . Thus, each panel has a different  $x$  axis. The  $x$  range covered varies similarly with  $s$ , i.e. the H1  $x$  values are roughly 20 times larger at a given  $Q^2$ . There are no H1 data for high  $Q^2$  beyond 1000  $\text{GeV}^2$ . Reproduced from [274]. CC BY 4.0.

uncertainties and their correlations into account and is calculated numerically following [58, 277] by considering each source separately and adding the results of the various correlated sources to one correlated systematic error, which is, in turn, quadratically added to the statistical and uncorrelated uncertainties to obtain one total error.

The results are illustrated in figure 43 which shows the  $x$ -dependent results, for some selected  $Q^2$  values, of both H1, with their average over  $x$ , and the prospective LHeC results. These results reflect the huge extension of kinematic range towards low  $x$  and high  $Q^2$  available at the LHeC, as compared to HERA. They also illustrate the striking improvement in precision that the LHeC promises to provide. The  $F_L$  measurements will cover an  $x$  range from  $2 \times 10^{-6}$

to more than  $x = 0.01$ . Surely, when compared with figure 42, one can safely expect that any non-DGLAP parton evolution should be discovered by using such data in combination with a very precise  $F_2$  measurement.

A few comments are in order on the variation of the different error components with the kinematics, essentially  $Q^2$ , since the whole  $F_L$  sensitivity is restricted to high  $y$ , which, in turn, for each  $Q^2$ , defines a narrow interval of  $x$  values covered. One may observe in figure 43 that the precision is spoilt towards large  $x \propto 1/y$ ; see e.g. the result for  $Q^2 = 8.5 \text{ GeV}^2$ . The assumptions for the integrated luminosity basically define a  $Q^2$  range for the measurement. For example, the statistical uncertainty for  $Q^2 = 4.5 \text{ GeV}^2$  and  $x = 10^{-5}$ , a medium  $x$  value at this  $Q^2$  interval, is only 0.6% (or 0.001 in absolute terms for  $F_L = 0.22$ ). At  $Q^2 = 2000 \text{ GeV}^2$  it rises to 21% (or 0.012 for  $F_L = 0.064$ ). One can thus perform the  $F_L$  measurement at the LHeC, with a focus on only small  $x$ , using much less luminosity than the  $1 \text{ fb}^{-1}$  used here. The relative sizes of the various systematic error sources also vary considerably, which is due to the kinematic relations between angles and energies and their dependence on  $x$  and  $Q^2$ . This is detailed in [58]. This implies, for example, that the 0.2 mrad polar angle scale uncertainty becomes the dominant error at small  $Q^2$ , which is the backward region where the electron is scattered near the beam axis relative to the direction of the electron beam. For large  $Q^2$ , however, the electron is more centrally scattered and the  $\theta_e$  calibration requirement may be more relaxed. The  $E'_e$  scale uncertainty has a effect that is twice as small as that due to the  $\theta_e$  calibration at lowest  $Q^2$ , but it becomes the dominant correlated systematic error source at high  $Q^2$ . The overall assumptions for the scale uncertainties used here are therefore only rough first approximations and will be replaced by kinematics and detector-dependent requirements when this measurement is pursued. These could also exploit the cross-calibration opportunities that result from the redundant determination of the inclusive DIS scattering kinematics through both the electron and the hadronic final states. This was noted very early in the lifespan of HERA (see references [55, 57, 277]) and was worked out in considerable detail by both H1 and ZEUS using independent and different methods. A feature used by H1 in their  $F_L$  measurement included a number of decays, such as  $\pi^0 \rightarrow \gamma\gamma$  and  $J/\psi \rightarrow e^+e^-$ , used to calibrate the low-energy measurements and  $K_s^0 \rightarrow \pi^+\pi^-$  and  $\Lambda \rightarrow p\pi$ , used for the determination of tracker scales, see reference [267].

It is obvious that the prospect of measuring  $F_L$ , as presented here, is striking. For nearly a decade, Guido Altarelli was a chief theory advisor for the development of the LHeC. In 2011, he published an article [276] in honour of Mario Greco, about *the early days of QCD (as seen from Rome)* in which he described one of his main achievements [268] and persistent irritation regarding the longitudinal structure function,  $F_L$ , and its measurement: *The present data, recently obtained by the H1 experiment at DESY, are in agreement with our [!this] LO QCD prediction but the accuracy of the test is still far from being satisfactory for such a basic quantity.* The LHeC developments have not been rapid enough to let Guido see the much higher-quality results for  $F_L$ , using which, the existence of departures from DGLAP evolution to high orders of pQCD may be expected to be most safely discovered.

**4.2.4. Associated jet final states at low  $x$ .** The dynamic effects of the resummation or nonlinear corrections which we have discussed above can arise at the LHeC, not only in the inclusive structure functions, as we have illustrated so far, but also in more exclusive observables describing the structure of the jet final states associated with low- $x$  DIS.

Baseline predictions for jet final states in DIS are obtained from perturbative finite-order calculations (see e.g. [203, 278] for third-order calculations), supplemented by parton-shower MC generators for realistic event simulation (as, for example, in [202]). However, owing to the large phase space that opens up at LHeC energies and the complex kinematics possibly



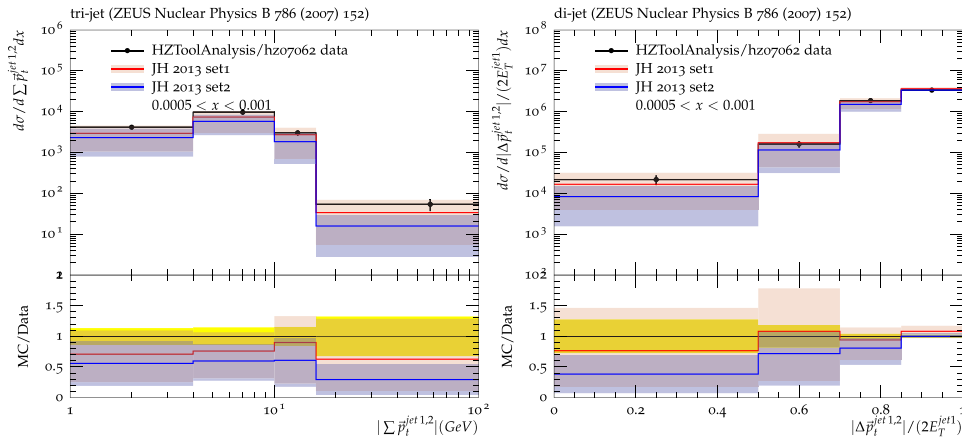


**Figure 44.** Momentum correlations in DIS multijet final states at low  $x$  computed by the CCFM MC simulation [288] with TMD parton densities from JH2013 [296], compared with measurements [295]: (left) trijets; (right) dijets.

involving multiple hard scales, jet events are potentially sensitive to the soft-gluon coherence effects of initial-state radiation [225, 279–281], which go beyond finite-order perturbative evaluations and collinear parton showers, and show up as logarithmic  $x \rightarrow 0$  corrections to all orders of perturbation theory. These corrections can be resummed and combined with large- $x$  contributions via Catani-Ciafaloni-Fiorani-Marchesini (CCFM) exclusive evolution equations [225, 279], and affect the structures of jet multiplicities and angular jet correlations [281] as well as heavy-quark distributions [280]. Observables based on forward jets, transverse energy flow, and angular and momentum correlations constitute probes of low- $x$  dynamics in DIS final states [282–284]. Phenomenological studies started with HERA [285–287] and will continue with the LHeC.

Computational tools are being developed to address the structure of multijet final states by including low- $x$  dynamic effects. These include CCFM MC tools [288, 289], off-shell matrix-element parton-level generators [290, 291], and BFKL MC generators [292–294]. Figure 44 gives an example of transverse momentum correlations in DIS at small  $Q^2$ , where the electron is scattered in the backward region near the beam axis [288], compared with the measurements [295].

Furthermore, exclusive parton-branching (PB) formalisms are being proposed in which not only gluon distributions but also quark distributions are treated at an unintegrated level in transverse momentum [297–299]. This is instrumental in connecting low- $x$  approaches with DGLAP approaches to parton showers beyond the leading order [300, 301]. Applications of these new developments have, so far, been mostly carried out for final states in hadron–hadron collisions, while extensions to lepton–hadron collisions are underway. Figure 45 gives examples of transverse momentum spectra in low-mass DY lepton-pair production computed in [302] by the PB method [298], compared with measurements [303, 304].

**4.2.5. Relation to ultra-high-energy neutrino and astroparticle physics.** The small- $x$  region probed by the LHeC is also very important in the context of ultra-high-energy neutrino physics and astroparticle physics. Highly energetic neutrinos provide a unique window into the Universe, due to their weak interaction with matter; for a review, see, for example, [305]. They can travel long distances from their sources, undeflected by the magnetic fields inside and

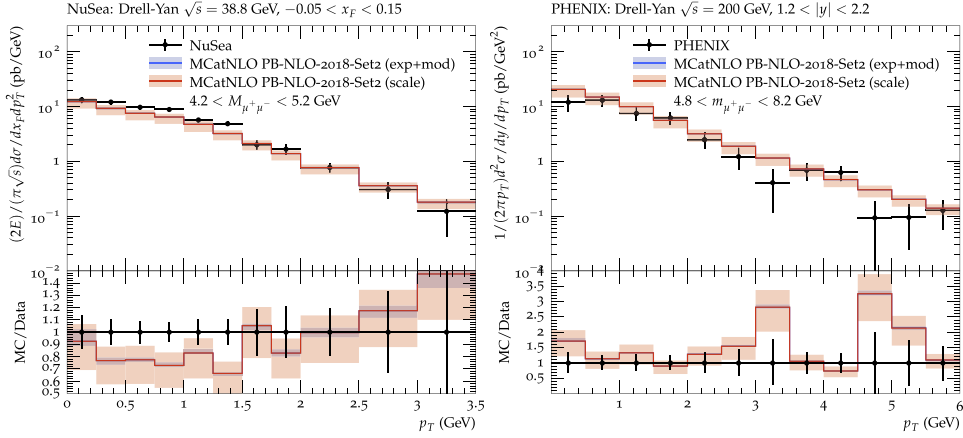


**Figure 45.** Transverse momentum spectra in low-mass DY lepton-pair production [302] using the PB method, compared with measurements by the NuSea Collaboration [303] (right) and the PHENIX Collaboration [304] (left). Reproduced from [302]. CC BY 4.0

in between galaxies, and thus provide complementary information to that provided by cosmic rays, gamma rays, and gravitational-wave signals. The IceCube observatory in Antarctica [306] is sensitive to neutrinos with energies of 100 GeV and above (or as low as 10 GeV with the use of their Deep Core detector). Knowledge about low- $x$  physics becomes indispensable in two contexts: neutrino interactions and neutrino production. At energies beyond the TeV scale the dominant part of the cross-section is due to neutrino DIS CC and NC interactions with hadronic targets [305].

In figure 46 we show the CC neutrino cross-section as a function of the neutrino energy for an isoscalar target (in the laboratory frame, where the target is at rest), using a calculation [307] based on the resummed model in [230]. We see that at energies below  $\sim 50$  TeV the cross-section grows roughly linearly with energy, and in this region, it is dominated by contributions from the large- $x$  valence region. Beyond that energy the neutrino cross-section grows more slowly, roughly as a power of  $\sim E_\nu^\lambda$  with  $\lambda \simeq 0.3$ . This high-energy behaviour is totally controlled by the small- $x$  behaviour of the parton distributions. The dominance of the sea contributions to the cross-section is clearly seen in figure 46. To more precisely illustrate the contributing values of  $x$  and  $Q^2$ , in figure 47 we show the differential cross-section for the CC interaction  $xQ^2 d\sigma^{CC}/dx dQ^2$  for a neutrino energy of  $E_\nu = 10^{11}$  GeV (in the frame where the hadronic target is at rest). We can see a clear peak of the cross-section at a rough value of  $Q^2 = M_W^2$  and an  $x$  value of

$$x \simeq \frac{M_W^2}{2ME_\nu}, \quad (4.8)$$

which, in this case, is about  $3 \times 10^{-8}$ . We note that IceCube extracted the DIS cross-section from neutrino observations [308] in the region of neutrino energies of 10–1000 TeV. The extraction is consistent, within the large error bands, with the predictions based on QCD, such as those illustrated in figure 46. It is important to note that the IceCube extraction is limited to these energies by the statistics caused by the steeply falling neutrino flux at high energies. We thus see that the neutrino interaction cross-section at high energies is sensitive to a region that is currently completely unconstrained by existing precision DIS data.

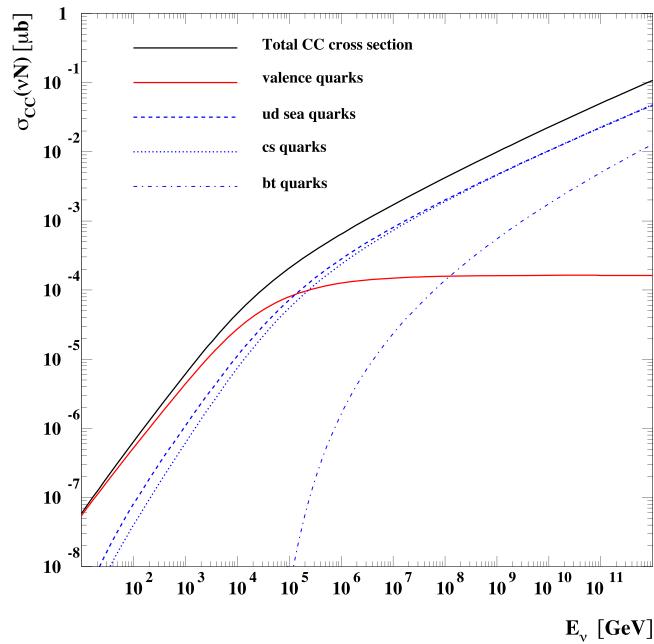


**Figure 46.** CC cross-section for the neutrino–nucleon interaction on an isoscalar target as a function of neutrino energy. The total CC cross-section is broken down into the contributions of the valence, up–down, strange–charm, and bottom–top quarks. The calculation was based on reference [307].

Another instance where the dynamics at low  $x$  is crucial for neutrino physics is in understanding the mechanisms of ultra-high-energy neutrino production. Such neutrinos are produced in interactions that involve hadrons, either in  $\gamma p$  or in  $pp$  interactions. They emerge as decay products of pions, kaons, and charmed mesons, and possibly beauty mesons if the energy is high enough [309]. For example, in the atmosphere, neutrinos are produced by interactions between highly energetic cosmic rays and nitrogen and oxygen nuclei. The lower-energy part of the atmospheric neutrino spectrum, up to about 100 TeV or so, is dominated by the decay of pions and kaons. This is called the conventional atmospheric neutrino flux. Above that energy the neutrino flux is dominated by the decay of shorter-lived charmed mesons. Thus, this part of the neutrino flux is called the prompt neutrino flux. The reason that the prompt neutrino flux dominates at high energies is specifically related to the lifetime of the intermediate mesons (and also baryons such as  $\Lambda_c$ ). The longer-lived pions and kaons have a high probability of interacting before they decay, thus degrading their energy and leading to a steeply falling neutrino flux. The cross-section for the production of charmed mesons is smaller than that for pions and kaons, but the charmed mesons  $D^\pm$ ,  $D^0$ , and  $D_s$  and the baryon  $\Lambda_c$  have shorter lives than pions and kaons, and thus decay prior to any interaction. Thus, at energies of about 100 TeV the prompt neutrino flux will dominate over the conventional atmospheric neutrino flux. Therefore, the knowledge of this part of the spectrum is essential as it provides a background for the sought-after astrophysical neutrinos [310]. Charmed mesons in high-energy hadron–hadron interactions are produced through gluon–gluon fusion into  $c\bar{c}$  pairs, where one gluon carries rather large  $x$  and the other carries very small  $x$ . Since the scales are small, of the order of the charm masses, the values of the longitudinal momentum fractions involved are also very

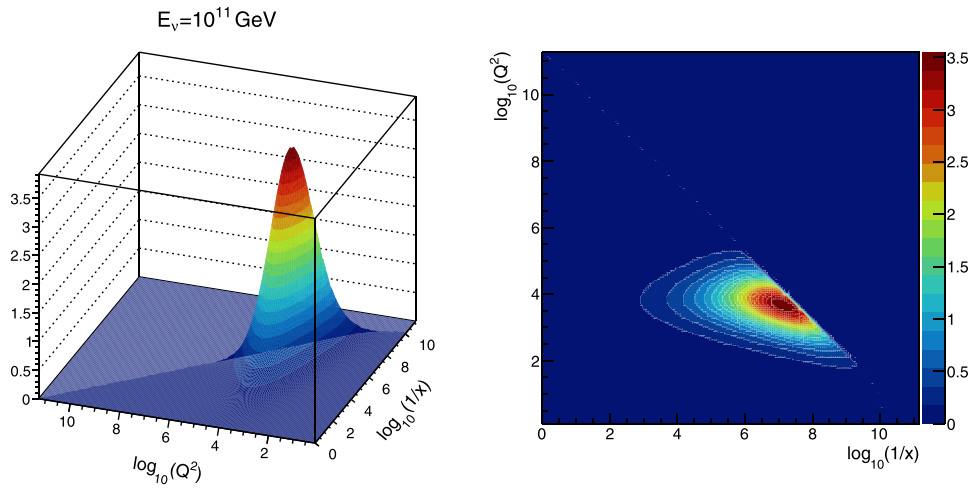


**Figure 47.** Differential CC neutrino cross-section  $10^5 \times xQ^2 d\sigma^{\text{CC}}/dx dQ^2$  (nb) as a function of  $Q^2$  and  $x$  for a fixed neutrino energy of  $E_\nu = 10^{11}$  GeV. Left: surface plot; right: contour plot.

small and thus the knowledge of the parton distributions in this region is essential [311]. The predictions for the prompt neutrino flux become extremely sensitive to the behaviour of the gluon distribution at low  $x$  (and low  $Q^2$ ), where novel QCD phenomena such as resummation as well as gluon saturation are likely to occur [312].

In addition, the LHeC measurements could help to pin down one enduring mystery—what is the composition of the most energetic cosmic rays? The best measurements of their composition at energies of more than  $10^{18}$  eV are based on studies of how showers develop in the atmosphere. The main observable is the depth (in the atmosphere) of the shower maximum—the so-called  $X_{\text{max}}$ . The absolute value of  $X_{\text{max}}$  and the elongation rate  $dX_{\text{max}}/dE$  of cosmic rays depend on the assumed details of the hadronic physics. A change in the elongation rate observed by the Auger observatory has often been interpreted as a signature of composition change (i.e. from mostly protons to mostly iron) with increasing energy [313, 314]. However, new hadronic phenomena, such as a colour glass condensate, might also lead to a change in the elongation rate. The observation of saturation in a Large Hadron–electron Collider would help in the selection of one of these two options [315, 316].

Finally, low- $x$  dynamics will become even more important at the HL-LHC and FCC hadron colliders, see section 9.6. With increasing centre-of-mass energy, hadron colliders will probe values of  $x$  previously unconstrained by HERA data. It is evident that all the predictions for  $pp$  interactions at high energy will heavily rely on PDF extrapolations to the small- $x$  region, which carry large uncertainties. As discussed in detail in this section, resummation will play an increasingly important role in the low- $x$  region of PDFs. A precision DIS machine is thus an indispensable tool for constraining QCD dynamics at low  $x$  with great precision as well as for providing complementary information and independent measurements to those of hadronic colliders.

#### 4.3. Diffractive deep inelastic scattering at the LHeC

**4.3.1. Introduction and formalism.** The diffractive events in DIS are characterized by the presence of large, non-exponentially suppressed rapidity gaps. By ‘large rapidity gap’, one means

that there is a large region of the detector which is free of any particle activity between the proton (or a state with proton quantum numbers) and the rest of the produced particles. During the 1990s, both the H1 and ZEUS experiments at HERA observed diffraction in DIS [317–320], which constituted a large fraction (about 10%) of all DIS events.

Diffraction events in DIS can typically be characterized by the presence of two scales: soft and hard. The soft scale is related to the size of the proton, which, in diffractive events, typically remains intact<sup>176</sup>, and the second scale,  $Q^2$ , which is perturbative. It was the presence of the latter, hard scale which enabled us to describe the diffraction in DIS in terms of the collinear factorization theorems [321–323]. In a series of groundbreaking papers [319, 320, 324–330] (see reference [331] for a review), the HERA experiments performed an analysis and determined that the diffractive events could be described in terms of the diffractive parton densities.

The precise measurement of diffractive DIS over a wide kinematic range can provide unique insights into many facets of the strong interaction dynamics. Because of the presence of the large rapidity gap, it has been understood that the diffractive process proceeds through the exchange of a composite object that preserves colour neutrality, and which has the quantum numbers of the vacuum. Thus, the mechanism through which a composite object interacts perturbatively [332–338] can offer information about confinement and in general about emergent phenomena in strong interactions. It was established some time ago [339–342] that the diffractive phenomena are closely related to low- $x$  dynamics, and in particular to the partonic structure of the proton in this regime. Therefore, an investigation of diffraction can offer unique insights into the role and importance of higher twists and nonlinear parton evolution. It is also known [343] that there is a relation between the diffraction in  $ep$  and nuclear shadowing. This relation has been used, for example, to successfully predict the amount of shadowing in some processes in LHC ultraperipheral collisions [344, 345]. Finally, precise measurements of the diffractive structure functions in the extended kinematic range of LHeC with respect to HERA will allow for the accurate extraction of diffractive PDFs and provide more stringent constraints on the uncertainties. This, in turn, will facilitate tests of the range of validity of perturbative factorisation [321–323] and of the potential importance of the higher twist effects.

In the following we will present studies of the inclusive diffraction that will be possible at the LHeC. The detailed analysis was performed in reference [346], and we shall summarize these results in this and the following two subsections. The LHeC will substantially extend the kinematic coverage of the HERA analyses, leading to much more detailed tests of theoretical ideas than have been possible hitherto. Although the analysis done in [346] and summarized here was done at the NLO of QCD, it is worth noting that similar analyses in the HERA context have recently been extended to the NNLO [347].

A diffractive deep inelastic event is schematically depicted in the diagram shown in figure 48. It is assumed that this process proceeds through a neutral-current exchange. CCs could also be considered, and were measured at HERA [326] but with large statistical uncertainties and in a very restricted region of phase space. The LHeC and the FCC-eh will allow the measurement of charge currents in diffractive DIS with larger statistics and more extended kinematics than at HERA. However, in the study [346] summarized here, only neutral currents were considered, hence we shall also limit ourselves to that case.

The incoming electron or positron, with a four-momentum  $k$ , scatters off the proton, with a four-momentum  $p$ . Here, we only consider protons, though in principle, one could also have

<sup>176</sup>Or dissociates into a low-mass excitation with quantum numbers of the proton.

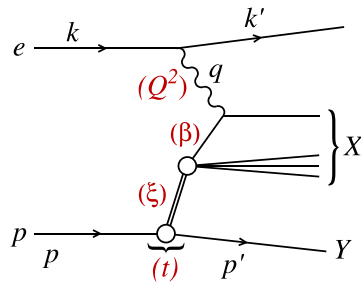


**Figure 48.** Diagram of a diffractive NC event in DIS together with the corresponding variables, in the one-photon exchange approximation. The incoming proton scatters elastically or is dissociated into a low-mass excitation  $Y$ . The system of particles denoted by  $X$  is then separated from the proton (or its excitation  $Y$ ) by a large rapidity gap. The double line indicates a diffractive exchange in the  $t$  channel.

nuclei. The inclusive diffraction in the nuclear case will be considered in section 6. The interaction proceeds through the exchange of a virtual photon with a four-momentum  $q$  and the diffractive exchange in the  $t$  channel (indicated by the double line in figure 48). The kinematic variables for such an event include the standard deep inelastic variables

$$Q^2 = -q^2, \quad x = \frac{-q^2}{2p \cdot q}, \quad y = \frac{p \cdot q}{p \cdot k}, \quad (4.9)$$

where  $Q^2$  is the (minus) photon virtuality,  $x$  is the Bjorken variable, and  $y$  the inelasticity of the process. In addition, the variables

$$s = (k + p)^2, \quad W^2 = (q + p)^2, \quad (4.10)$$

are the electron–proton centre-of-mass energy squared and the photon–proton centre-of-mass energy squared, respectively. A diffractive event  $ep \rightarrow eXY$  is uniquely characterized by the presence of a large rapidity gap between the diffractive system (with an invariant mass  $M_X$ ) and the final proton (or its low-mass excitation)  $Y$  with a four-momentum  $p'$ . Therefore, in order to fully describe the diffractive event in DIS, an additional set of variables is necessary. They are defined as follows:

$$t = (p - p')^2, \quad \xi = \frac{Q^2 + M_X^2 - t}{Q^2 + W^2}, \quad \beta = \frac{Q^2}{Q^2 + M_X^2 - t}. \quad (4.11)$$

In the above,  $t$  is the squared four-momentum transfer at the proton vertex,  $\xi$  (alternatively denoted by  $x_{tP}$ ) can be interpreted as the momentum fraction of the *diffractive exchange* with respect to the incoming hadron, and  $\beta$  is the momentum fraction of the struck parton with respect to the diffractive exchange. The two diffractive momentum fractions are constrained to give Bjorken- $x$ ,  $x = \beta\xi$ .

The kinematic range in  $(\beta, Q^2, \xi)$  that we consider at the LHeC is restricted by the following cuts:

- $Q^2 \geq 1.8 \text{ GeV}^2$ : due to the fact that the initial distribution for the DGLAP evolution is parameterised at  $\mu_0^2 = 1.8 \text{ GeV}^2$ . The renormalisation and factorisation scales are taken to be equal to  $Q^2$ .



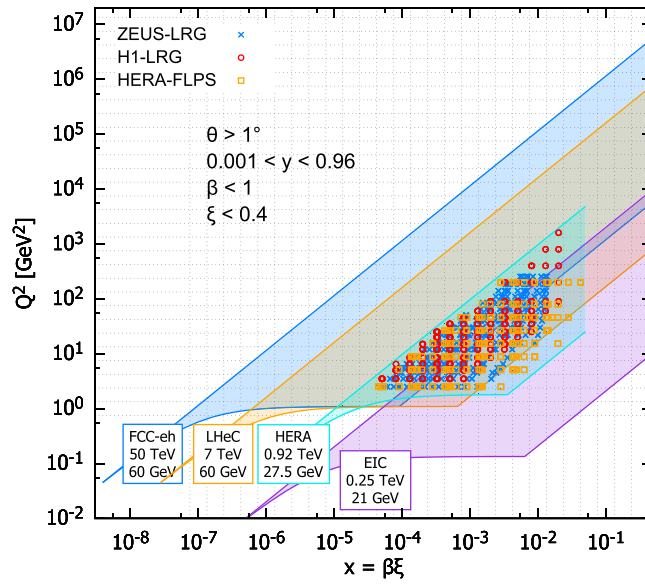


**Figure 49.** Kinematic phase space for inclusive diffraction in  $(x, Q^2)$  for the EIC (magenta region), the LHeC (orange region), and the FCC-eh (dark blue region) as compared with the HERA data (light blue region, ZEUS-LRG [327], H1-LRG [330], HERA-FLPS [348]). The acceptance limit for the electron in the detector design has been assumed to be  $1^\circ$ , and we take  $\xi < 0.4$  (see text for details). Reproduced from [346]. CC BY 4.0.

- $\xi < 0.4$ : constrained by physical and experimental limitations. This rather high  $\xi$  value is an experimental challenge and physically enters the phase-space region where the Pomeron contribution should become negligible compared with sub-leading exchanges. Within the two-component model, see equation (4.16) below, at high  $\xi$ , the cross-section is dominated by the secondary Reggeon contribution, which is poorly fixed by the HERA data. Nevertheless, we present this high  $\xi$  ( $> 0.1$ ) region for illustrative purposes and for the sake of discussion of the fit results below. It is also worth mentioning that with an appropriate detector design, it might be possible to reach this region of high  $\xi$ , which would be very interesting and provide new constraints on the Pomeron and Reggeon contributions with respect to HERA.

In figure 49 the accessible kinematic range in  $(x, Q^2)$  is shown for four machines: HERA, the EIC, the LHeC, and the FCC-eh [346]. For the LHeC design, the range in  $x$  is increased by a factor of  $\sim 20$  compared to that of HERA, and the maximum available  $Q^2$  is increased by a factor of  $\sim 100$ . The FCC-eh machine would further increase this range with respect to LHeC by roughly one order of magnitude in both  $x$  and  $Q^2$ . We also show the EIC kinematic region for comparison, which could cover high values of  $x$  as well as the low  $Q^2$  range. The three different machines are clearly complementary in their kinematic coverage, since the LHeC and the EIC add sensitivity at lower and higher values of  $x$  than HERA, respectively.

In figure 50 the phase space specific to diffractive processes in  $(\beta, Q^2)$  is shown for fixed  $\xi$  for the LHeC [346]. Thanks to its high centre-of-mass energy the LHeC machine probes very small values of  $\xi$ , reaching  $10^{-4}$  with a wide range of  $\beta$ , and for the perturbative values of  $Q^2$ .

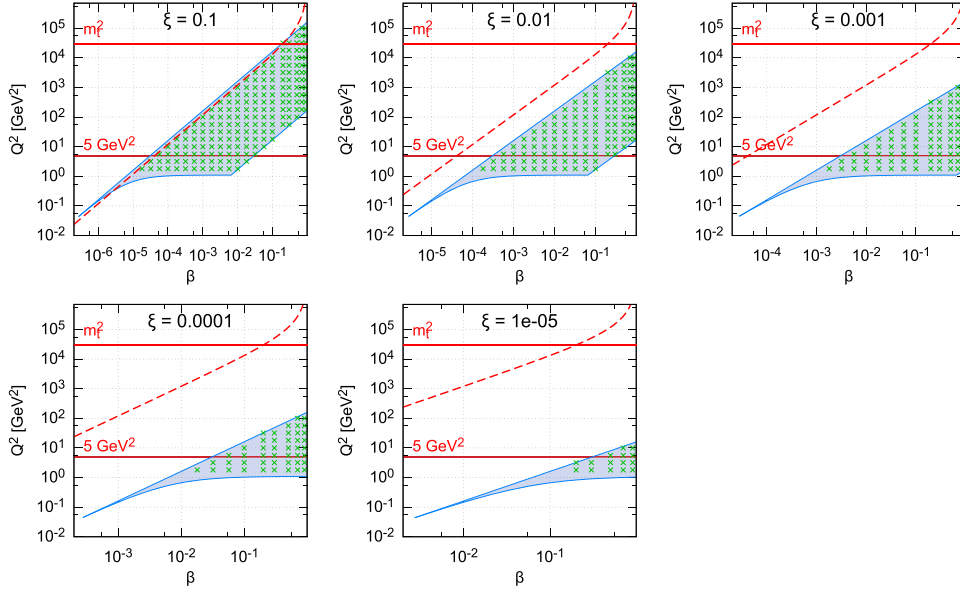


**Figure 50.** Kinematic phase space for inclusive diffraction in  $(\beta, Q^2)$  for fixed values of  $\xi$  for the LHeC design. The horizontal lines correspondingly indicate  $Q^2 = 5 \text{ GeV}^2$ , the smallest data value for the DGLAP fit performed in this study, and  $m_t^2$  the six-flavour threshold. The dashed line marks the kinematic limit for  $t\bar{t}$  production. Reproduced from [346]. CC BY 4.0.

Of course, the ranges in  $\beta$  and  $\xi$  are correlated, since  $x = \beta\xi$ . Therefore, for small values of  $\xi$  only large values of  $\beta$  are accessible, while for large  $\xi$ , the range of  $\beta$  extends to very small values. The two horizontal lines denote  $Q^2 = 5 \text{ GeV}^2$  and the  $m_t^2$  threshold. The first value is the scale corresponding to the smallest data in the DGLAP fit and diffractive parton distribution function (DPDF) extraction discussed later. The dashed line corresponds to the kinematic limit of  $t\bar{t}$  production.

In analogy to the inclusive case, the diffractive cross-sections in the neutral current case can be represented in the form of the reduced cross-sections [326]:

$$\frac{d^3\sigma^D(3)}{d\xi d\beta dQ^2} = \frac{2\pi\alpha_{\text{em}}^2}{\beta Q^4} Y_+ \sigma_{\text{red}}^{D(3)}, \quad (4.12)$$

where  $Y_+ = 1 + (1-y)^2$  and the reduced cross-sections can be expressed in terms of two diffractive structure functions  $F_2^D$  and  $F_L^D$ . In the one-photon approximation, the relations are

$$\sigma_{\text{red}}^{D(3)} = F_2^{D(3)}(\beta, \xi, Q^2) - \frac{y^2}{Y_+} F_L^{D(3)}(\beta, \xi, Q^2). \quad (4.13)$$

In the above, both the cross-sections and the structure functions are integrated over the momentum transfer,  $t$ . This is indicated by the  $\sigma^{D(3)}, F_2^{D(3)}, F_L^{D(3)}$  notation, where ‘3’ means that the cross-section or structure function depends on three variables,  $(\beta, \xi, \text{and } Q^2)$ . Depending on the detector setup and luminosity it could also be possible to measure  $\sigma^{D(4)}, F_2^{D(4)}, F_L^{D(4)}$  which depends on four variables  $(\beta, \xi, Q^2, t)$ . Also, in principle, for the neutral-current case, one needs to consider  $Z^0$  exchange in addition to photon exchange, but in the analysis [346] presented here, it was neglected.

Both  $\sigma_{\text{red}}^{D(3)}$  and  $\sigma_{\text{red}}^{D(4)}$  have been measured at the HERA collider [319, 320, 324–330] and were used to obtain QCD-inspired parameterisations.

The standard perturbative QCD approach to diffractive cross-sections is based on the collinear factorisation [321–323]. In those works, it was demonstrated that, similarly to the inclusive DIS cross-section, the diffractive cross-section can be written, up to terms of order  $\mathcal{O}(\Lambda^2/Q^2)$ , where  $\Lambda$  is the hadronic scale, in a factorised form

$$d\sigma^{ep \rightarrow eXY}(\beta, \xi, Q^2, t) = \sum_i \int_{\beta}^1 dz d\hat{\sigma}^{ei} \left( \frac{\beta}{z}, Q^2 \right) f_i^D(z, \xi, Q^2, t), \quad (4.14)$$

where the sum is performed over all parton flavours (gluon,  $d$ -quark,  $u$ -quark, etc). The hard-scattering partonic cross-section  $d\hat{\sigma}^{ei}$ , corresponding to short-distance physics, can be computed order by order in perturbative QCD and is the same as in the inclusive DIS case. The long-distance part,  $f_i^D$  is the DPDF. These functions can be interpreted as the conditional probabilities of finding partons in the proton, provided the latter is scattered into a final-state system  $Y$  with specified four-momentum  $p'$ . They are evolved using the DGLAP evolution equations [349–352], similarly to the inclusive case. The analogous formula to (4.14) for the  $t$ -integrated structure functions reads

$$F_{2/L}^{D(3)}(\beta, \xi, Q^2) = \sum_i \int_{\beta}^1 \frac{dz}{z} C_{2/L,i} \left( \frac{\beta}{z} \right) f_i^{D(3)}(z, \xi, Q^2), \quad (4.15)$$

where the coefficient functions  $C_{2/L,i}$  are the same as in inclusive DIS, and can be computed perturbatively in QCD.

Fits to the diffractive structure functions [326, 328] usually parameterise the diffractive PDFs in a two-component model, which is the sum of two diffractive exchange contributions,  $IP$  and  $IR$ :

$$f_i^{D(3)}(z, \xi, Q^2, t) = f_{IP}^p(\xi, t) f_i^{IP}(z, Q^2) + f_{IR}^p(\xi, t) f_i^{IR}(z, Q^2). \quad (4.16)$$

For both of these terms proton vertex factorisation is separately assumed, meaning that the diffractive exchange can be interpreted as colourless objects called *Pomerons* or *Reggeons* with parton distributions  $f_i^{IP,IR}(\beta, Q^2)$ . Note that this factorization is completely different from the collinear factorization for the structure functions mentioned above. It is an additional assumption motivated by the Regge theory and is supported by the fits to the diffractive data. The flux factors  $f_{IP,IR}^p(\xi, t)$  represent the probability that a Pomeron/Reggeon with given values of  $\xi, t$  couples to the proton. They are parameterised using the form motivated by Regge theory,

$$f_{IP,IR}^p(\xi, t) = A_{IP,IR} \frac{e^{B_{IP,IR}t}}{\xi^{2\alpha_{IP,IR}(t)-1}}, \quad (4.17)$$

with a linear trajectory  $\alpha_{IP,IR}(t) = \alpha_{IP,IR}(0) + \alpha'_{IP,IR}t$ , where  $B_{IP,IR}$  is the  $t$  slope and  $A_{IP,IR}$  are normalization factors. One can also introduce the diffractive PDFs which correspond to the  $t$ -integrated cross-sections

$$f_i^{D(3)}(z, \xi, Q^2) = \phi_{IP}^p(\xi) f_i^{IP}(z, Q^2) + \phi_{IR}^p(\xi) f_i^{IR}(z, Q^2), \quad (4.18)$$

with

$$\phi_{IP,IR}^p(\xi) = \int dt f_{IP,IR}^p(\xi, t). \quad (4.19)$$

Note that the notions of *Pomeron* and *Reggeon* used here to model hard diffraction in DIS are, in principle, different from those describing the soft hadron–hadron interactions; in particular, the parameters of the fluxes may be different.

As is usual for the DGLAP evolution one needs to specify suitable initial conditions (see [346] for details). The diffractive parton distributions of the Pomeron at the initial scale  $\mu_0^2 = 1.8 \text{ GeV}^2$  are parameterised as

$$z f_i^{IP}(z, \mu_0^2) = A_i z^{B_i} (1-z)^{C_i}, \quad (4.20)$$

as in the ZEUS-SJ parametrisation, and where  $i$  is a gluon or a light quark and the momentum fraction  $z = \beta$  in the case of quarks. In the diffractive parameterisations the contributions of all the light quarks (antiquarks) are assumed to be equal. For the treatment of HFs, a VFNS is adopted, in which the charm and bottom quark DPDFs are radiatively generated via DGLAP evolution, and no intrinsic heavy quark distributions are assumed. The structure functions are calculated using a general-mass variable flavour number scheme (GM-VFNS) [353, 354] which ensures a smooth transition of  $F_{2,L}$  across the flavour thresholds by including  $\mathcal{O}(m_h^2/Q^2)$  corrections. The parton distributions for the Reggeon component are taken from a parameterisation which was obtained from fits to the pion structure function [355, 356].

In equation (4.16) the normalisation factors of fluxes  $A_{IP,IR}$  and of DPDFs  $A_i$  appear in the product. In order to resolve the ambiguity<sup>177</sup> the normalization  $A_{IP}$  was fixed and  $f_i^{IR}(z, Q^2)$  was normalised to the pion structure function. This resulted in  $A_i$  and  $A_{IR}$  being well-defined free-fit parameters. For full details of the parametrisations, see reference [346].

**4.3.2. Pseudodata for the reduced cross-section.** In order to generate the pseudodata for the LHeC, one needs to use a certain model which extrapolates the data from HERA. In the study [346] described here, the reduced cross-sections are extrapolated using the ZEUS-SJ DPDFs. Following the scenario of the ZEUS fit [328] we work within the VFNS scheme at the NLO accuracy. As mentioned before, calculations at the NNLO accuracy exist; however, for the purposes of this analysis, it is sufficient to work at the NLO accuracy. The transition scales for DGLAP evolution are fixed by the heavy-quark masses,  $\mu^2 = m_h^2$  and the structure functions are calculated in the Thorne–Roberts GM-VFNS [357]. The Reggeon PDFs are taken from the GRV pion set [356], the numerical parameters are taken from tables one and three of reference [328], and the heavy-quark masses are  $m_c = 1.35 \text{ GeV}$ ,  $m_b = 4.3 \text{ GeV}$ , and  $\alpha_s(M_Z^2) = 0.118$ .

The pseudodata were generated [346] using an extrapolation of the fit to the HERA data, which provided the central values, amended with a random Gaussian smearing with a standard deviation corresponding to the relative error  $\delta$ . An uncorrelated 5% systematic error was assumed giving a total uncertainty of

$$\delta = \sqrt{\delta_{\text{sys}}^2 + \delta_{\text{stat}}^2}. \quad (4.21)$$

The statistical error was computed by assuming a very modest integrated luminosity of  $2 \text{ fb}^{-1}$ , see reference [36, 37]. For the binning adopted in the study [346], the statistical uncertainties have a very small effect on the uncertainties in the extracted DPDFs. Obviously, a much larger luminosity would allow a denser binning that would result in smaller DPDF uncertainties. An extended analysis could, in principle, be performed for  $\sigma^{D(4)}$ , which would include  $t$  dependence, provided the latter could be extracted by suitable forward instrumentation.

<sup>177</sup> Here, as in the HERA fits,  $A_{IP}$  is fixed by normalizing  $\phi_{IP}^p(0.003) = 1$ .

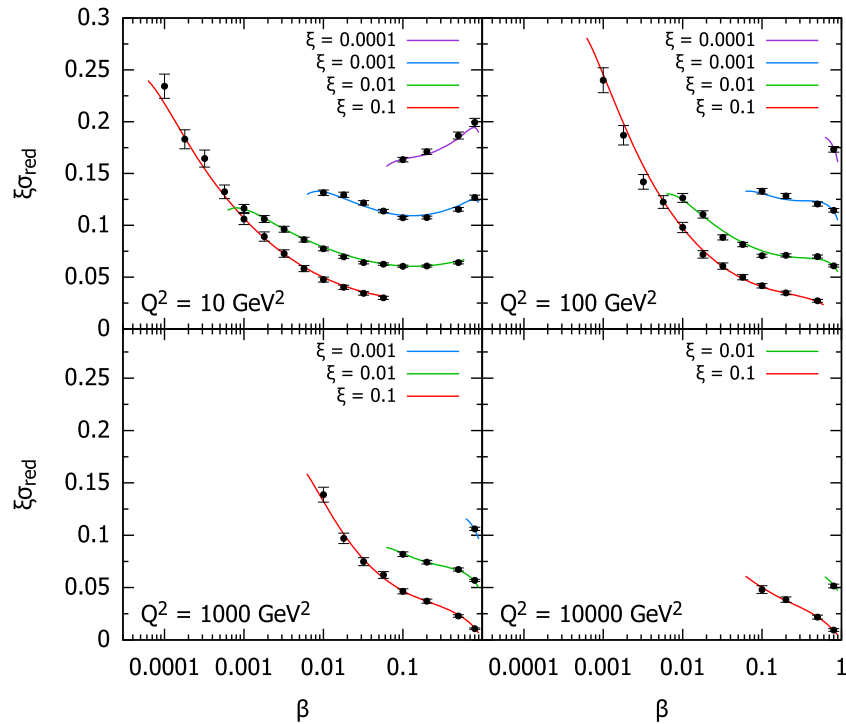


**Figure 51.** Selected subset of the simulated data for the diffractive reduced cross-section as a function of  $\beta$  in bins of  $\xi$  and  $Q^2$  for  $ep$  collisions at the LHeC, based on the extrapolation of the ZEUS-SJ fit to the HERA data. The curves for  $\xi = 0.01, 0.001$ , and  $0.0001$  are shifted upwards by  $0.04, 0.08$ , and  $0.12$ , respectively. The integrated luminosity is taken to be  $2 \text{ fb}^{-1}$ . Reproduced from [346]. [CC BY 4.0](#).

In figure 51 we show a subset of the simulated data for the diffractive reduced cross-section  $\xi\sigma_{\text{red}}$  as a function of  $\beta$  in selected bins of  $\xi$  and  $Q^2$  for the LHeC [346]. For the most part the errors are very small, and are dominated by the systematics. The breaking of Regge factorisation, evident at large  $\xi$ , is caused by the large Reggeon contribution in that region, whose validity could be further investigated at the LHeC.

We see that for the LHeC parameters, the integrated luminosity is sufficient for the precise measurement of the diffractive reduced cross-section. The study could be further refined by implementing more information about the potential sources of the systematic errors, including correlations. In addition, by varying the centre-of-mass energy one could also extract the longitudinal structure function  $F_L^{D(3)}$ . A pioneering measurement of this quantity was performed at HERA [358], albeit with very limited precision. The longitudinal diffractive structure function could be extremely valuable information, as it is an independent diffractive structure function and provides an additional constraint on the diffractive PDFs. It may also be a quantity that is more sensitive to the higher twist contribution. However, a more detailed analysis needs to be performed to determine the feasibility and precision of such measurements at the LHeC.

**4.3.3. Potential to constrain diffractive PDFs at the LHeC.** We next discuss the prospects for the extraction and constraint of the diffractive PDFs from the future experimental data to be

obtained at the LHeC. The strategy for assessing the constraining potential was developed in [346], which we summarise below. First, the central values of the pseudodata are generated using the central set of the ZEUS-SJ fit and distributed according to a Gaussian with an experimental width given by equation (4.21), which also provides the uncertainty in the pseudodata. After that, the pseudodata in a fit are included alongside the existing HERA data using the same functional form of the initial parametrisation. The quality of the resulting fit is very good, as expected, and  $\chi^2/\text{ndf} \sim 1$  is obtained, which demonstrates the consistency of the approach.

To evaluate the experimental precision with which the DPDFs can be determined, several pseudodata sets, corresponding to independent random error samples, were generated [346]. Each pseudodata set was fitted separately. The minimal value of  $Q^2$  for the data considered in the fits was set to  $Q_{\min}^2 = 5 \text{ GeV}^2$ . The reason for this cutoff was to demonstrate the feasibility of the fits that only included the range in which the standard twist-2 DGLAP evolution was expected to be trustworthy. At HERA, the  $Q_{\min}^2$  values that gave acceptable DGLAP (twist-2) fits were  $8 \text{ GeV}^2$  [326] and  $5 \text{ GeV}^2$  [327] for H1 and ZEUS, respectively. At smaller values, the fits deteriorated. The maximum value of  $\xi$  was set by default to  $\xi_{\max} = 0.1$ , above which, the cross-section started to be dominated by the Reggeon exchange. The binning adopted in the study [346] roughly corresponded to four bins per order of magnitude for each of  $\xi$ ,  $\beta$ , and  $Q^2$ .

For  $Q_{\min}^2 = 5 \text{ GeV}^2$ ,  $\xi_{\max} = 0.1$  and below the top threshold, this results in 1229 pseudodata points for the LHeC. The top-quark region adds 17 points for the LHeC. The LHeC offers a window with which to study the top-quark contribution to diffraction over a limited range of kinematics; going further, to FCC-eh, would expand that possibility greatly. By reducing  $Q_{\min}^2$  to  $1.8 \text{ GeV}^2$  we get 1589 pseudodata points, while increasing  $\xi$  to 0.32 adds around 180 points for the LHeC machine. Of course, in the case of the lower value of  $Q^2$ , the collinear formalism with a leading twist contribution may become questionable. The fact that the ZEUS and H1 fits based on DGLAP did not describe the data well in the low- $Q^2$  region may indicate that other effects may start to play important roles. In reference [359] it was argued that this deviation from the leading twist DGLAP evolution might be an indication of higher twist effects. The larger lever arm in  $x$ , and the high precision of the data produced by the LHeC will be extremely helpful in mapping out the region of validity of the leading twist description and should help to constrain the higher twist effects in diffraction. Dedicated studies of the LHeC potential in this area will need to be performed.

The potential for the determination of the gluon DPDF was investigated by fitting the inclusive diffractive DIS pseudodata using two models with different numbers of parameters, named  $S$  and  $C$  (see reference [346] for details), with a fixed value of  $\alpha_{IP,IR}(0)$ , in order to focus on the shape of the Pomeron PDFs. At HERA, both  $S$  and  $C$  fits provided equally good descriptions of the data with  $\chi^2/\text{ndf} = 1.19$  and  $1.18$ , respectively, despite different gluon DPDF shapes. The LHeC pseudodata are much more sensitive to gluons, resulting in  $\chi^2/\text{ndf}$  values of  $1.05$  and  $1.4$  for the  $S$  and  $C$  fits, respectively. This also clearly shows the potential of the LHeC to better constrain the low- $x$  gluons and therefore unravel eventual departures from standard linear evolution.

In figure 52 the diffractive gluon and quark distributions are shown for the LHeC as a function of the longitudinal momentum fraction  $z$  for fixed scales of  $\mu^2 = 6, 20, 60, \text{ and } 200 \text{ GeV}^2$ , see [346]. The bands labelled  $A, B, \text{ and } C$  denote fits to three statistically independent pseudodata replicas, obtained from the same central values and statistical and systematic uncertainties. Hereafter, the uncertainty bands shown correspond to  $\Delta\chi^2 = 2.7$  (at a 90% confidence level (CL)). Also, the extrapolated ZEUS-SJ DPDFs are shown with error bands marked by the



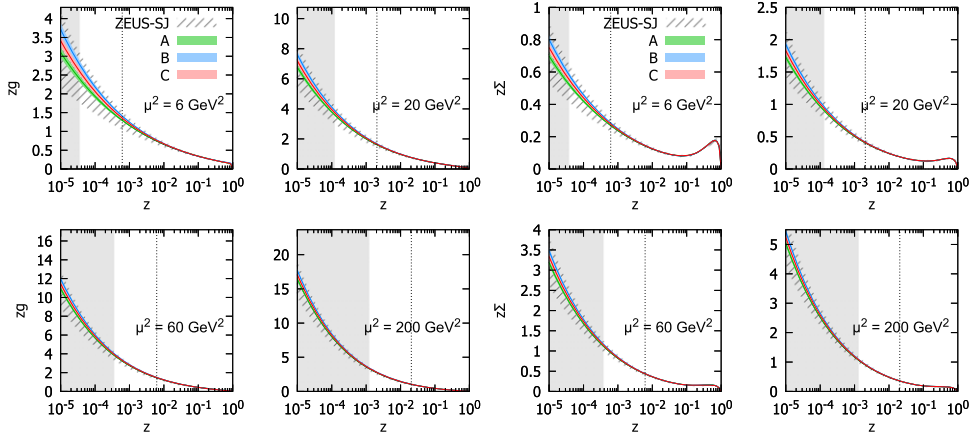


**Figure 52.** Diffractive PDFs for gluons and quarks in the LHeC kinematics as a function of the momentum fraction  $z$  for fixed values of scale  $\mu^2$ . Results of fits to three (A, B, and C) pseudodata replicas are shown together with the experimental error bands. For comparison, the extrapolated ZEUS-SJ fit is also shown (black) by hatched error bands. The vertical dotted lines indicate the HERA kinematic limit. The bands indicate only the experimental uncertainties. The shaded band indicates the region that is inaccessible to the LHeC. Reproduced from [346]. CC BY 4.0.

diagonally hatched area. Note that the depicted uncertainty bands are solely due to experimental errors and neglect theoretical sources such as fixed input parameters and parameterisation biases. The area of extrapolation beyond the reach of the LHeC is marked in grey and the HERA kinematic limit is marked with a vertical dotted line. The low- $x$  DPDF determination accuracy is improved with respect to HERA by a factor of five to seven for the LHeC, and completely new kinematic regimes are accessed.

For a better illustration of the precision, in figure 53 the relative uncertainties are shown for parton distributions at different scales, see [346]. The different bands show the variation with upper cutoffs on the available  $\xi$  range from 0.01 to 0.32. In the best-constrained region of  $z \simeq 0.1$ , the precision reaches the 1% level. We observe only a modest improvement in the achievable accuracy of the extracted DPDFs with a change of  $\xi$  by an order of magnitude from 0.01 to 0.1. An almost negligible effect is observed when the  $\xi$  range is further extended up to 0.32. This is very encouraging, since measurements for very large values of  $\xi$  are challenging. This reflects the dominance of the secondary Reggeon in this region.

We stress again that only experimental errors are included in our uncertainty bands. Neither theoretical uncertainties nor parameterisation biases are considered. Of course, such studies could be expanded to obtain more precise estimates of the potential of the LHeC measurements, in order to constrain and detect deviations from the factorization of the importance of the higher twists, for example. For a detailed discussion of this and other aspects of the fits, see reference [346].

**4.3.4. Hadronic final states in diffraction and hard rapidity gap processes.** Various diffractive processes offer a unique opportunity to investigate factorisation properties and can help to disentangle DGLAP vs BFKL dynamics.

The factorisation properties of diffractive DIS were a major topic of study at HERA [331] and are highly relevant to the interpretation of diffractive processes at the LHC [360]. A general

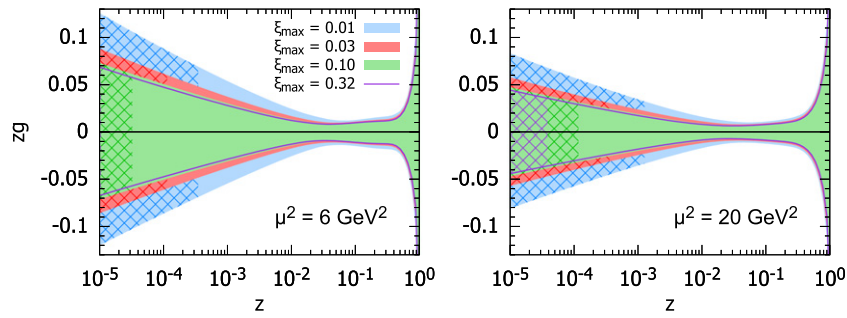


**Figure 53.** Relative uncertainties in the diffractive gluon PDFs for the LHeC kinematics. Two different choices of scale are considered,  $\mu^2 = 6$  and  $\mu^2 = 20 \text{ GeV}^2$ . The blue, red, and green bands and the magenta line correspond to different maximal values of  $\xi = 0.01, 0.03, 0.1$ , and  $0.32$ , respectively. The cross-hatched areas show kinematically excluded regions. The bands only indicate the experimental uncertainties, see the text. Reproduced from [346]. CC BY 4.0.

theoretical framework was provided by the proof [321] of a hard-scattering collinear QCD factorisation theorem for semi-inclusive DIS scattering processes such as  $ep \rightarrow epX$ . This implies that the DPDFs extracted in fits to inclusive diffractive DIS may be used to predict perturbative cross-sections for hadronic final-state observables such as HF or jet production. Testing this factorisation pushes at the boundaries of applicability of perturbative QCD and will be a major topic of study at the LHeC.

The tests of diffractive factorisation at HERA were strongly limited by its kinematics. The mass of the dissociation system  $X$  was limited to approximately  $M_X < 30 \text{ GeV}$ , which implied, for example, that jet transverse momenta could not be larger than about  $15 \text{ GeV}$  and more generally left very little phase space for any studies at perturbative scales. As well as restricting the kinematic range of studies, this restriction also implied large hadronisation and scale uncertainties in theoretical predictions, which in turn limited the precision with which tests could be made.

The higher centre-of-mass energy of the LHeC will open up a completely new regime for diffractive hadronic final-state observables, in which masses and transverse momenta are larger and theoretical uncertainties will be correspondingly reduced. For example,  $M_X$  values in excess of  $250 \text{ GeV}$  will be accessible, while remaining in the region  $\xi < 0.05$ , where the leading diffractive (Pomeron) exchange dominates. The precision of tests is also improved by the development of techniques for NNLO calculations for diffractive jets [361].

Figure 54 shows a simulation of the expected diffractive jet cross-section at the LHeC, assuming DPDFs extrapolated from H1 at HERA [326], using the nlojet++ framework [362]. An integrated luminosity of  $100 \text{ fb}^{-1}$  is assumed, the kinematic range considered is  $Q^2 > 2 \text{ GeV}^2$ ,  $0.1 < y < 0.7$ , and the scattered electron angles are larger than  $1^\circ$ . Jets are reconstructed using the  $k_T$  algorithm with  $R = 1$ . The statistical precision remains excellent up to jet transverse momenta of almost  $50 \text{ GeV}$ , and the theoretical scale uncertainties (shaded bands) are substantially reduced compared with the HERA measurements. A comparison between a measurement of this sort of quality and predictions refined using DPDFs from inclusive LHeC data would clearly provide an exacting test of diffractive factorisation.

Further interesting hadronic final-state observables that were studied at HERA and could be extended at the LHeC include open charm production, thrust and other event shapes, charged

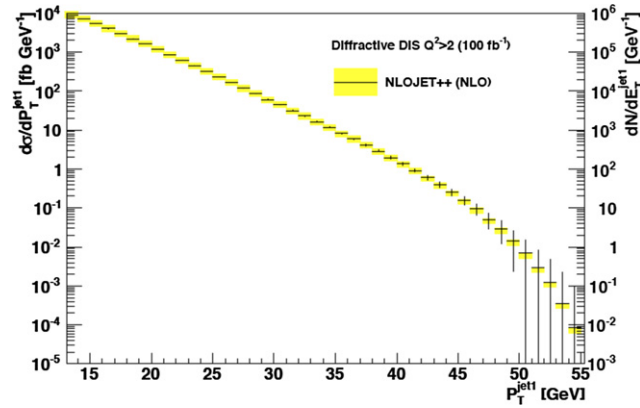


**Figure 54.** Simulated diffractive dijet cross-section as a function of leading jet transverse momentum in the kinematic range  $Q^2 > 2 \text{ GeV}^2$  and  $0.1 < y < 0.7$ , with scattered electron angles in excess of  $1^\circ$ . The error bars indicate predicted statistical uncertainties for a luminosity of  $100 \text{ fb}^{-1}$ . The coloured bands correspond to the theoretical uncertainties when the renormalisation and factorisation scales are varied by factors of two.

particle multiplicities, and energy flows. In addition, the LHeC opens up completely new channels, notably diffractive beauty and  $W$  and  $Z$  production; the latter gives a sensitivity to the quark densities that is complementary to that offered by inclusive diffraction.

Of separate interest are hard rapidity gap processes, for example  $\gamma^* p \rightarrow J/\psi + \text{rapidity gap}(\Delta y) + Y$  at large  $-t \gg 1 \text{ GeV}^2$ . In such processes DGLAP evolution is strongly suppressed, and therefore, this is an ideal laboratory with which to investigate BFKL dynamics. The dependence of the process on  $\Delta y$  is expected to be given by  $\sigma \sim \Delta y^{2\omega(t)}$ . Here, the effective Pomeron trajectory is parameterized as  $\alpha_P(t) = 1 + \omega(t)$ . The current models give  $\omega$  values between 0.5 (LO BFKL) and  $\omega = 0.2\text{--}0.3$  for the resummed BFKL. With an appropriate large-acceptance detector one would be able to study the dependence on  $\Delta y$  in a wide rapidity interval as well as the dependence on the momentum transfer  $t$ . Hence, this process offers a powerful test for the theoretical predictions of the properties of the BFKL Pomeron.

#### 4.4. Theoretical developments

**4.4.1. Prospects for higher-order pQCD in DIS.** With its large anticipated luminosity, the LHeC will be able to perform highly precise measurements for a wide variety of final states in DIS, often exploring novel kinematical ranges, challenging the theory of QCD at an unprecedented level of accuracy, and enabling precision determinations of QCD parameters and of the proton's parton structure. For this programme to succeed, it will be necessary to be able to confront the LHeC precision data with equally precise theoretical predictions.

In the SM, these predictions can be obtained through a perturbative expansion to sufficiently high order. These calculations are performed in the larger framework of QCD factorisation [39] and exploit the process-independence of parton distributions, whose evolution is controlled by the DGLAP equations. The DGLAP splitting functions have already been known to the NNLO level for quite some time [363, 364], and important progress has recently been made towards their N3LO terms [93, 94]. Moreover, mixed QCD/QED corrections have been derived for the

DGLAP splitting functions [365], enabling a consistent combination of QCD and electroweak effects.

The physics opportunities that are already offered by the HERA legacy data set have motivated substantial recent activity in the study of precision QCD calculations for deeply inelastic processes. At the inclusive level, although the QCD coefficients for the inclusive DIS structure functions have been known to three loops (N3LO) for some time [366], they were recently improved upon by the computation of heavy-quark mass effects [367, 368]. Fully differential predictions for final states with jets, photons, heavy quarks, or hadrons are generally available to the NLO in QCD, often dating back to the HERA epoch. Technical developments that were made in the context of fully differential higher-order QCD calculations for LHC processes have enabled substantial advances in the theoretical precision of DIS jet cross-sections. Fully differential predictions for single-jet production are now available to the NNLO [201] and the N3LO [203, 278] for neutral-current and CC DIS, and dijet production [162, 163, 369] has been computed to the NNLO. The latter calculations were performed with fully differential parton-level final-state information, thereby allowing their extension to jet production in diffractive DIS [361] and to DIS two-parton event shapes [204]. The newly derived NNLO jet cross-sections were partly used in the projections for LHeC precision jet studies in sections 4.1.2 and 4.3.4 above.

The NLO calculations in QCD [370–372] and the electroweak theory [373, 374] have been largely automated, and are now available in multipurpose event-generator programs [375–377] for processes of arbitrary multiplicity. These can be combined with parton-shower approximations to provide NLO-accurate predictions for fully exclusive final states. Although these tools have mostly been applied to hadron collider observables, they are also ready to be used for DIS processes [202], thereby offering novel opportunities for precision studies using the LHeC. In this context, electroweak corrections may become particularly crucial for high-mass final states at the LHeC, and have been largely unexplored up to now. A similar level of automation has not yet been reached at the NNLO, where calculations are performed on a process-by-process basis. For DIS processes, fully differential NNLO calculations for trijet final states or for heavy-quark production could become feasible in the near-term future. Moreover, a whole set of calculations at this order for specific final states (involving jets, vector bosons, or heavy quarks) in photoproduction could readily be taken over by adapting the respective hadron collider results.

The all-order resummation of large logarithmic corrections to hadron collider processes has made very substantial advances in the recent past, owing to the emergence of novel systematic frameworks from soft-collinear effective theory, or in momentum space resummation. As a result, threshold logarithms and transverse-momentum logarithms in benchmark hadron collider processes can now be resummed up to the third subleading logarithmic order, N3LL. A similar accuracy has been reached for selected event shapes in electron–positron annihilation. For DIS event shapes, the currently available predictions only include up to NLL resummation [378]. With the newly available frameworks, they could be improved by two more logarithmic orders, as demonstrated in exploratory work on the DIS one-jettiness event shape [199, 200]. Applications of this framework to final states in DIS at the small- $x$  limit (see section 4.2) are largely unexplored, and may provide important novel insights into the all-order dynamics in the high-energy limit.

The full exploitation of future LHeC data will require novel precision calculations for a variety of benchmark processes, often combining fixed-order, resummation, and parton-shower event generation to obtain theoretical predictions of matching accuracy. Recent advances in calculational techniques and an increasing degree of automation will help to enable this progress. A close interplay between experiment and theory will then be crucial in order to combine data

and predictions into precision measurements of physics parameters and probes of fundamental particle dynamics.

#### 4.4.2. Theoretical concepts for the light cone.

**4.4.2.1. Intrinsic heavy-quark phenomena.** Among the most interesting nonperturbative quantum-field theoretic aspects of hadron light-front wavefunctions in QCD are the intrinsic heavy-quark Fock states [379–381]. Consider a heavy-quark loop insertion into the proton’s self-energy. The heavy-quark loop can be attached by gluons to just one valence quark. The cut of such diagrams yields the standard DGLAP gluon splitting contribution to the proton’s heavy-quark structure function. In this case, the heavy quarks are produced at very small  $x$ . However, the heavy-quark loop can also be attached to two or more valence quarks in the proton self-energy. In the case of QED this corresponds to light-by-light lepton loop insertion in an atomic wavefunction. In the case of QCD, the heavy quark loop can be attached by three gluons to two or three valence quarks in the proton’s self-energy. This is a non-Abelian insertion into the hadron’s self-energy. The cut of such diagrams gives the *intrinsic* heavy-quark contribution to the proton’s light-front (LF) wavefunction. In the case of QCD, the probability for an intrinsic heavy  $Q\bar{Q}$  pair scales according to  $\frac{1}{M_Q^2}$ ; this is in contrast to heavy  $\ell\bar{\ell}$  lepton pairs in QED, where the probability for heavy lepton pairs in an atomic wavefunction scales according to  $\frac{1}{M_\ell^4}$ . This difference in heavy-particle scaling in mass distinguishes Abelian from non-Abelian theories.

A basic property of hadronic LF wavefunctions is that they have strong falloff with the invariant mass of the Fock state; for example, this is the case for the light-front wave functions (LFWFs) of the colour-confining AdS/QCD models [382] where  $\mathcal{M}^2 = [ik^{\mu i}]^2$  of the Fock state constituents. This means that the probability is maximised when the constituents have equal true rapidity, i.e.  $x_i \propto (\vec{k}_{\perp i}^2 + m_i^2)^{1/2}$ . Thus, the heavy quarks carry most of the momentum in an intrinsic heavy-quark Fock state. For example, the charm quark in the intrinsic charm Fock state  $|uudc\bar{c}\rangle$  of a proton carries about 40% of the proton’s momentum:  $x_c \sim 0.4$ . After a high-energy collision, the comoving constituents can then recombine to form the final-state hadrons along with the proton. Thus, in an  $ep$  collision the comoving  $udc$  quarks from the  $|uudc\bar{c}\rangle$  intrinsic five-quark Fock state can recombine to a  $\Lambda_c$ , where  $x_{\Lambda_c} = x_c + x_u + x_d \sim 0.5$ . Similarly, the comoving  $dcc$  in the  $|uudc\bar{c}\bar{c}\bar{c}\rangle$  intrinsic seven-quark Fock state can recombine to a  $\Xi(ccd)^+$ , with  $x_{\Xi(ccd)} = x_c + x_c + x_d \sim 0.9$ .

Therefore, in the intrinsic heavy-quark model, the wavefunction of a hadron in QCD can be represented as a superposition of Fock state fluctuations, e.g.  $|n_V\rangle$ ,  $|n_V g\rangle$ ,  $|n_V Q\bar{Q}\rangle$ , ... components, where  $n_V \equiv dds$  for the  $\Sigma^-$ ,  $uud$  for the proton,  $\bar{u}d$  for the  $\pi^-$  and  $u\bar{d}$  for the  $\pi^+$ . Charm hadrons can be produced by coalescence in the wavefunctions of the moving hadron. Doubly-charmed hadrons require fluctuations such as  $|n_V c\bar{c}\bar{c}\bar{c}\rangle$ . The probability that these Fock-state fluctuations will come on mass-shell is inversely proportional to the square of the quark mass,  $\mathcal{O}(m_Q^{-2n})$  where  $n$  is the number of  $Q\bar{Q}$  pairs in the hadron. Thus, the natural domain for heavy hadrons produced from heavy-quark Fock states consists of  $\vec{k}_{\perp Q}^2 \sim m_Q^2$  and a high LF momentum fraction  $x_Q$  [379, 380, 380, 381]. For example, the rapidity regime for double-charm hadron production  $y_{ccd} \sim 3$  at low energies is well within the kinematic experimental domain of a fixed-target experiment such as the Segmented Large-X Spectrometer (SELEX) at the Tevatron [383]. Note that the intrinsic heavy-quark mechanism can account for many previous observations of forward heavy-hadron and single and double  $J/\psi$  production by pions at high  $x_F > 0.4$  in the low-energy fixed-target NA3 experiment, the high- $x_F$  production of  $pp \rightarrow \Lambda_c + X$  and  $pp \rightarrow \Lambda_b + X$  observed at the ISR, single and double  $\Upsilon(b\bar{b})$  production,

and the *quadra-bottom* tetraquark  $[bb\bar{b}\bar{b}]$  production recently observed by the AnDY experiment at the RHIC [384]. In addition, the EMC Collaboration observed that the charm quark distribution in the proton at  $x = 0.42$  and  $Q^2 = 75 \text{ GeV}^2$  was 30 times larger than expected from DGLAP evolution. All of these experimental observations are naturally explained by the intrinsic heavy-quark mechanism. The SELEX observation [383] of double charm baryons at high  $x_F$  reflects production by double intrinsic heavy-quark Fock states of the baryon projectile. Similarly, the high- $x_F$  domain—which would be accessible at forward high  $x_F$ —is the natural production domain for heavy hadron production at the LHeC.

The production of heavy hadrons based on intrinsic heavy-quark Fock states is thus remarkably efficient and greatly extends the kinematic domain of the LHeC, e.g. for processes such as  $\gamma^* b \rightarrow Z^0 b$ . This is in contrast with the standard production cross-sections based on gluon splitting, in which only a small fraction of the incident momentum is effective in creating heavy hadrons.

**4.4.2.2. Light-front holography and superconformal algebra.** The LHeC has the potential to probe the high-mass spectrum of QCD, such as the spectroscopy and structure of hadrons consisting of heavy quarks. Insights into this new domain of hadron physics can now be derived by new non-perturbative colour-confining methods based on LF holography. Among the remarkable features of this domain are universal Regge trajectories with universal slopes in both the principal quantum number  $n$  and the internal orbital angular momentum  $L$ . Other key features are di-quark clustering and supersymmetric relations between the masses of mesons, baryons, and tetraquarks. In addition, the running coupling is determined at all scales, including the soft domain relevant to rescattering corrections to LHeC processes. The combination of lightfront holography with superconformal algebra leads to the novel prediction that hadron physics has supersymmetric properties in both spectroscopy and dynamics.

**4.4.2.3. Light-front holography and recent theoretical advances.** Five-dimensional  $\text{AdS}_5$  space provides a geometrical representation of the conformal group. Remarkably,  $\text{AdS}_5$  is holographically dual to  $3 + 1$  spacetime at fixed LF time  $\tau$  [385]. A colour-confining LF equation for mesons of arbitrary spin  $J$  can be derived from the holographic mapping of the *soft-wall model* modification of  $\text{AdS}_5$  space for the specific dilaton profile  $e^{+\kappa^2 z^2}$ , where  $z$  is the fifth-dimension variable of the five-dimensional  $\text{AdS}_5$  space. A holographic dictionary maps the fifth-dimension  $z$  to the LF radial variable  $\zeta$ , with  $\zeta^2 = b_\perp^2 (1 - x)$ . The same physics transformation maps the  $\text{AdS}_5$  and  $(3 + 1)$  LF expressions for electromagnetic and gravitational form factors to each other [386].

A key tool is the remarkable de Alfaro-Fubini-Furlan (dAFF) principle [387] which shows that a mass scale can appear in a Hamiltonian and its equations of motion while retaining the conformal symmetry of the action. When applying it to LF holography, a mass scale  $\kappa$  appears, which determines universal Regge slopes and the hadron masses. The resulting *LF Schrödinger equation* incorporates colour confinement and other essential spectroscopic and dynamical features of hadron physics, including Regge theory, the Veneziano formula [388], a massless pion for zero quark mass and linear Regge trajectories with the universal slope in the radial quantum number  $n$  and the internal orbital angular momentum  $L$ . The combination of LF dynamics, its holographic mapping to  $\text{AdS}_5$  space, and the dAFF procedure provides new insight into the physics underlying colour confinement, the non-perturbative QCD coupling, and the QCD mass scale. The  $q\bar{q}$  mesons and their valence LFWFs are the eigensolutions of the frame-independent relativistic bound-state LF Schrödinger equation.

The mesonic  $q\bar{q}$  bound-state eigenvalues for massless quarks are  $M^2(n, L, S) = 4\kappa^2(n + L + S/2)$ . This equation predicts that the pion eigenstate  $n = L = S = 0$  is massless for zero



quark mass. When quark masses are included in the LF kinetic energy  $\sum_i \frac{k_{\perp i}^2 + m^2}{x_i}$ , the spectroscopy of mesons is correctly predicted, with equal slopes of the principal quantum number  $n$  and the internal orbital angular momentum  $L$ . A comprehensive review is given in reference [385].

**4.4.2.4. The QCD running coupling at all scales based on light-front holography.** The QCD running coupling  $\alpha_s(Q^2)$  sets the interaction strengths of quarks and gluons as functions of the momentum transfer  $Q$  (see section 4.1). The dependence of the coupling  $Q^2$  is needed to describe hadronic interactions at both long and short distances [389]. It can be defined [390] at all momentum scales from a perturbatively calculable observable, such as the coupling  $\alpha_s^{g1}(Q^2)$ , which is defined using the Bjorken sum rule [391], and determined from the sum rule prediction at high  $Q^2$ , and below such values, from its measurements [392–394]. At high  $Q^2$ , such *effective charges* satisfy asymptotic freedom, obey the usual pQCD renormalisation group equations, and can be related to each other without scale ambiguity by commensurate scale relations [395].

The high  $Q^2$  dependence of  $\alpha_s^{g1}(Q^2)$  is predicted by pQCD. In the small- $Q^2$  domain its functional behaviour can be predicted by the dilaton  $e^{+\kappa^2 z^2}$  soft-wall modification of the AdS<sub>5</sub> metric, together with LF holography [396], to be  $\alpha_s^{g1}(Q^2) = \pi e^{-Q^2/4\kappa^2}$ . The parameter  $\kappa$  determines the mass scale of hadrons and Regge slopes in the zero-quark mass limit, and it has been shown that it can be connected to the mass scale  $\Lambda_s$ , which controls the evolution of the pQCD coupling [396–398]. Measurements of  $\alpha_s^{g1}(Q^2)$  [399, 400] are remarkably consistent with this predicted Gaussian form, and a fit gives  $\kappa = 0.513 \pm 0.007$  GeV, see figure 55.

The matching of the high and low  $Q^2$  regimes of  $\alpha_s^{g1}(Q^2)$  determines a scale  $Q_0$ , which forms the interface between perturbative and non-perturbative hadron dynamics. This connection can be made for any choice of renormalisation scheme and one obtains an effective QCD coupling at all momenta. In the  $\overline{\text{MS}}$  scheme one gets  $Q_0 = 0.87 \pm 0.08$  GeV [401]. The corresponding value of  $\Lambda_{\overline{\text{MS}}}$  agrees well with the measured world average value and its value allows the computation of hadron masses using the AdS/QCD superconformal predictions for hadron spectroscopy. The value of  $Q_0$  can further be used to set the factorisation scale for DGLAP evolution [350–352] or the Efremov–Radyushkin–Brodsky–Lepage (ERBL) evolution of distribution amplitudes [402, 403]. The use of the scale  $Q_0$  to resolve the factorisation scale uncertainty in structure functions and fragmentation functions, in combination with the scheme-independent *principle of maximum conformality* (PMC) [180] for setting renormalisation scales, can greatly improve the precision of pQCD predictions for collider phenomenology at the LHeC and the HL-LHC.

**4.4.2.5. Superconformal algebra and hadron physics with LHeC data.** If one generalises LF holography using *superconformal algebra* the resulting LF eigensolutions yield a unified Regge spectroscopy of mesons, baryons, and tetraquarks, including remarkable supersymmetric relations between the masses of mesons and baryons of the same parity<sup>178</sup> [404, 405]. This generalisation further predicts hadron dynamics, including vector meson electroproduction, hadronic LFWFs, distribution amplitudes, form factors, and valence structure functions [406, 407]. Applications to the deuteron elastic form factors and structure functions are given in references [408, 409]

<sup>178</sup> QCD is not supersymmetrical in the usual sense, since the QCD Lagrangian is based on quark and gluonic fields, not squarks or gluinos. However, its hadronic eigensolutions conform to a representation of superconformal algebra, reflecting the underlying conformal symmetry of chiral QCD and its Pauli matrix representation.

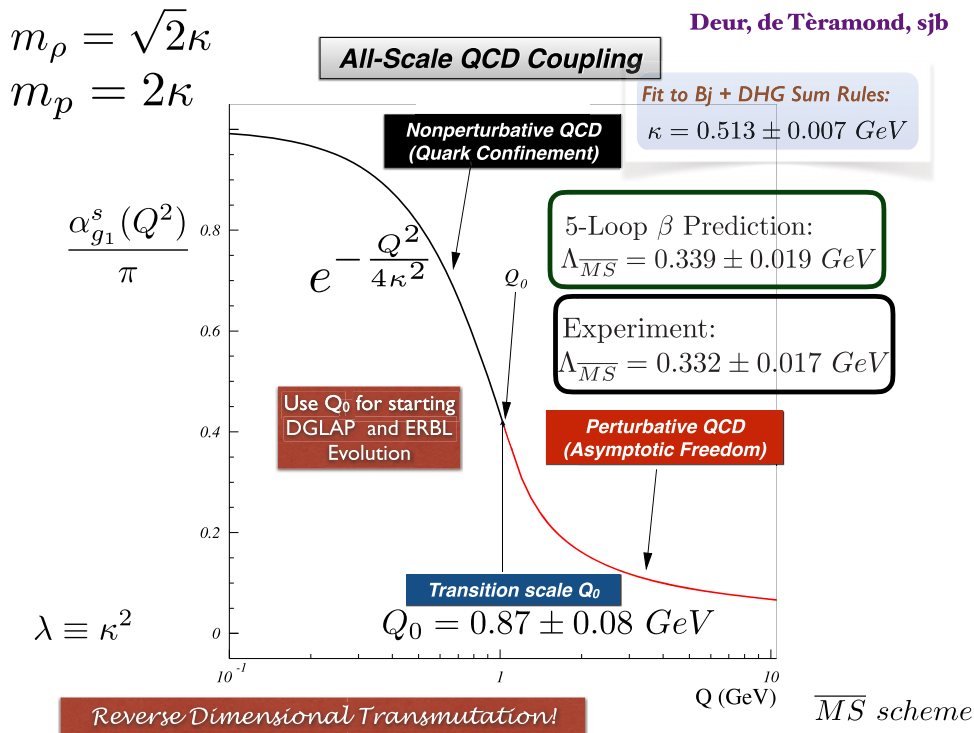


**Figure 55.** Prediction for the running coupling  $\alpha_s^{g1}(Q^2)$  at all scales. At lower  $Q^2$  predictions are obtained from LF holography, and at higher  $Q^2$ , they are obtained from perturbative QCD. The magnitude and derivative of the perturbative and non-perturbative couplings are matched at the scale  $Q_0$ . This matching connects the perturbative scale  $\Lambda_{\overline{MS}}$  to the non-perturbative scale  $\kappa$  which underlies the hadron mass scale.

The eigensolutions of superconformal algebra predict the Regge spectroscopy of mesons, baryons, and tetraquarks of the same parity and twist as equal-mass members of the same four-plet representation with a universal Regge slope [410–412]. A comparison with experimental results is shown in figure 56. The  $q\bar{q}$  mesons with an orbital angular momentum of  $L_M = L_B + 1$  have the same mass as their baryonic partners with an orbital angular momentum of  $L_B$  [410, 413].

The predictions of LF holography and superconformal algebra can also be extended to mesons, baryons, and tetraquarks with strange, charm, and bottom quarks. Although conformal symmetry is strongly broken by the heavy quark masses, the basic underlying supersymmetric mechanism, which transforms mesons to baryons (and baryons to tetraquarks) still holds and gives remarkable mass degeneracy across the entire spectrum of light, heavy-light, and double-heavy hadrons.

The four-plet symmetries of quark–antiquark mesons, quark–diquark baryons, and diquark–antidiquark tetraquarks are important predictions of superconformal algebra [401, 404]. Recently, the AnDY experiment at RHIC reported the observation of a state at 18 GeV which can be identified with the  $[bb][\bar{b}\bar{b}]$  tetraquark [384]. It will be possible to produce states with heavy quarks such as the  $[bb][\bar{b}\bar{b}]$  tetraquark at the LHeC, especially at high  $x_F$  in the proton-beam direction. New measurements at the LHeC are therefore inevitable in order to manifest the superconformal nature of hadronic bound states.

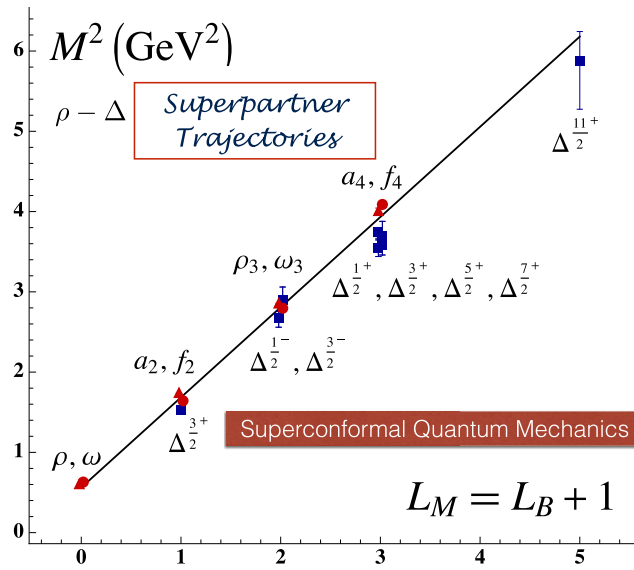


**Figure 56.** Comparison between the  $\rho/\omega$  meson Regge trajectory and the  $J = 3/2\Delta$  baryon trajectory. Superconformal algebra predicts the mass degeneracy of the meson and baryon trajectories if one identifies a meson with internal orbital angular momentum  $L_M$  with its superpartner baryon with  $L_M = L_B + 1$ . See references [410, 413].

## 5. Electroweak and top quark physics

### 5.1. Electroweak physics with inclusive DIS data

With the discovery of the SM Higgs boson by the CERN LHC experiments and the subsequent measurements of its properties, all the fundamental parameters of the SM have now been measured directly and with remarkable precision. To further validate the theory of electroweak interactions [25, 414–417], the mechanism of electroweak symmetry breaking, and the nature of the Higgs sector [418–420], new electroweak measurements have to be performed to the highest precision. Such high-precision measurements can be considered as a portal to NP, since non-SM contributions, for instance, loop insertions, may cause significant deviations in some precisely measurable and calculable observables. At the LHeC, the greatly enlarged kinematic reach to higher mass scales, compared to those of HERA [421–423], and the large targeted luminosity will enable electroweak measurements in  $ep$  scattering with higher precision than ever before.

In this section, the sensitivity of inclusive DIS cross-sections to electroweak parameters is discussed. An extended analysis and a more comprehensive discussion can be found in reference [424], and some aspects are described in the following. The direct production of  $W$  and  $Z$  bosons is discussed in the subsequent section.

**5.1.1. Electroweak effects in inclusive NC and CC DIS cross sections.** Electroweak NC interactions in inclusive  $e^\pm p$  DIS are mediated by the exchange of a virtual photon ( $\gamma$ ) or a  $Z$  boson in the  $t$ -channel, while CC DIS is exclusively mediated by  $W$ -boson exchange as a purely weak process. Inclusive NC DIS cross-sections are expressed in terms of generalised structure

functions  $\tilde{F}_2^\pm$ ,  $x\tilde{F}_3^\pm$  and  $\tilde{F}_L^\pm$  at the electroweak (EW) leading order (LO) by

$$\frac{d^2\sigma^{\text{NC}}(e^\pm p)}{dx dQ^2} = \frac{2\pi\alpha^2}{xQ^4} [Y_+\tilde{F}_2^\pm(x, Q^2) \mp Y_-\tilde{F}_3^\pm(x, Q^2) - y^2\tilde{F}_L^\pm(x, Q^2)] , \quad (5.1)$$

where  $\alpha$  denotes the fine structure constant. The terms  $Y_\pm = 1 \pm (1-y)^2$ , where  $y = Q^2/sx$ , describe the helicity dependence of the process. The generalised structure functions are separated into the contributions made by pure  $\gamma$ - and  $Z$ -exchanges and their interference [97, 136]:

$$\tilde{F}_2^\pm = F_2 - (g_V^e \pm P_e g_A^e) \kappa_Z F_2^{\gamma Z} + [(g_V^e g_V^e + g_A^e g_A^e) \pm 2P_e g_V^e g_A^e] \kappa_Z^2 F_2^Z , \quad (5.2)$$

$$\tilde{F}_3^\pm = -(g_A^e \pm P_e g_V^e) \kappa_Z F_3^{\gamma Z} + [2g_V^e g_A^e \pm P_e (g_V^e g_V^e + g_A^e g_A^e)] \kappa_Z^2 F_3^Z . \quad (5.3)$$

Similar expressions hold for  $\tilde{F}_L$ . In the naive quark-parton model, which corresponds to the LO QCD approximation, the structure functions are calculated by

$$[F_2, F_2^{\gamma Z}, F_2^Z] = x \sum_q [Q_q^2, 2Q_q g_V^q, g_V^q g_V^q + g_A^q g_A^q] \{q + \bar{q}\} , \quad (5.4)$$

$$x [F_3^{\gamma Z}, F_3^Z] = x \sum_q [2Q_q g_A^q, 2g_V^q g_A^q] \{q - \bar{q}\} , \quad (5.5)$$

which represent two independent combinations of the quark and antiquark momentum distributions,  $xq$  and  $x\bar{q}$ . In equation (5.3), the quantities  $g_V^f$  and  $g_A^f$  stand for the vector and axial-vector couplings of a fermion ( $f = e$  or  $f = q$  for electrons or quarks, respectively) to the  $Z$  boson, and the coefficient  $\kappa_Z$  accounts for the  $Z$ -boson propagator, including the normalisation of the weak couplings. Both parameters are fully calculable from the electroweak theory. The (effective) coupling parameters depend on the electric charge  $Q_f$  and the third component of the weak isospin,  $I_{L,f}^3$ . Using  $\sin^2 \theta_W = 1 - \frac{M_W^2}{M_Z^2}$ , one can write

$$g_V^f = \sqrt{\rho_{\text{NC},f}} (I_{L,f}^3 - 2Q_f \kappa_{\text{NC},f} \sin^2 \theta_W) , \quad (5.6)$$

and

$$g_A^f = \sqrt{\rho_{\text{NC},f}} I_{L,f}^3 \quad \text{with } f = (e, u, d). \quad (5.7)$$

The parameters  $\rho_{\text{NC},f}$  and  $\kappa_{\text{NC},f}$  are calculated as real parts of complex form factors which include the higher-order loop corrections [425–427]. They contain non-leading flavour-specific components.

The predictions for CC DIS are written in terms of the CC structure functions  $W_2$ ,  $xW_3$ , and  $W_L$  and higher-order electroweak effects are collected in two form factors,  $\rho_{\text{CC},eq}$  and  $\rho_{\text{CC},e\bar{q}}$  [428, 429].

In this study, the on-shell scheme is adopted for the calculation of higher-order corrections. This means that the independent parameters chosen are the fine structure constant  $\alpha$  and the masses of the weak bosons, the Higgs boson, and the fermions. The weak mixing angle is then fixed, and  $G_F$  is a prediction whose higher-order corrections are included in the well-known correction factor  $\Delta r$  [430–432] (see the discussion of further contributions in reference [136]).

The predicted single-differential inclusive NC and CC DIS cross-sections for polarised  $e^-p$  scattering as a function of  $Q^2$  are displayed in figure 57. For NC DIS and at higher  $Q^2$ ,

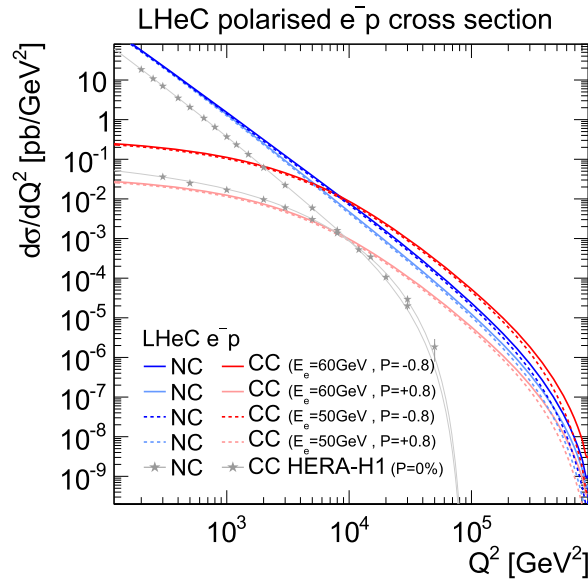


**Figure 57.** Single differential cross-sections for polarised  $e^-p$  NC and CC DIS at the LHeC for two different electron-beam energies ( $E_e$ ). Cross-sections for longitudinal electron-beam polarisations of  $P_e = -0.8$  and  $+0.8$  are displayed. For comparison, measurements at centre-of-mass energies of  $\sqrt{s} = 920$  GeV by H1 at HERA for unpolarised ( $P_e = 0\%$ ) electron beams are also displayed [433].

electroweak effects are important through  $\gamma Z$  interference and pure  $Z$ -exchange terms, and the polarisation of the LHeC electron beam of  $P_e = \pm 0.8$  will considerably alter the cross-sections. For CC DIS, the cross-section scales linearly with  $P_e$ . Two different electron-beam energies are displayed in figure 57, and even though the impact of a reduction from  $E_e = 60$  to 50 GeV appears to be small, a larger electron-beam energy would yield higher precision for the measurement of the electroweak parameters, since these are predominantly sensitive to the cross-sections at the highest scales, as shown in the following.

**5.1.2. Methodology of a combined EW and QCD fit.** A complete electroweak analysis of the DIS data has to consider PDFs together with electroweak parameters [434]. In this study, the uncertainties of electroweak parameters are obtained from a combined fit of the electroweak parameters and the PDFs, and the inclusive NC and CC DIS pseudodata (see section 4.3.2) are explored as input data. The PDFs are parameterised with 13 parameters at a starting scale of  $Q_0^2$  and NNLO DGLAP evolution is applied [48, 49]. In this way, the uncertainties in the PDFs are taken into account, which is very reasonable, since the PDFs will predominantly be determined from those LHeC data in the future. The details of the PDF fit are altogether fairly similar to the PDF fits outlined in section 3. Noteworthy differences are that additional EW effects are included in the calculation by considering the full set of one-loop electroweak corrections [435], and that the  $\chi^2$  quantity [148], which is an input to the minimisation and error propagation, is based on normal-distribution relative uncertainties. In this way, a dependence on the actual size of the simulated cross-sections is avoided. The size of the pseudodata is therefore set to be equivalent to the predictions [436].

5.1.3. *Weak boson masses  $M_W$  and  $M_Z$ .* The expected uncertainties for a determination of the weak boson masses,  $M_W$  and  $M_Z$ , are determined in the PDF and EW-fit, where one of the masses is determined together with the PDFs, while the other mass parameter is taken as an external input. The expected uncertainties for  $M_W$  are

$$\begin{aligned}\Delta M_W(\text{LHeC} - 60) &= \pm 8_{(\text{exp})} \pm 5_{(\text{PDF})} \text{ MeV} = 10_{(\text{tot})} \text{ MeV} \text{ and} \\ \Delta M_W(\text{LHeC} - 50) &= \pm 9_{(\text{exp})} \pm 8_{(\text{PDF})} \text{ MeV} = 12_{(\text{tot})} \text{ MeV}\end{aligned}\quad (5.8)$$

for the LHeC with  $E_e = 60$  GeV and 50 GeV, respectively. The breakdown into experimental and PDF uncertainties is obtained by repeating the fit with fixed PDF parameters. These uncertainties are displayed in figure 58 and compared to the values obtained by the LEP2 collider [438], Tevatron [437], ATLAS [439] and the particle data group (PDG) value [183]. The LHeC measurement will become the most precise measurement performed by a single experiment and will be a great improvement over the best measurement achieved by H1, which was  $M_W(\text{H1}) = 80.520 \pm 0.115$  GeV [423]. If the dominant uncorrelated uncertainties can be reduced from the projected range of 0.5% to 0.25%<sup>179</sup>, precisions for  $M_W$  of up to

$$\begin{aligned}\Delta M_W(\text{LHeC} - 60) &= \pm 5_{(\text{exp})} \pm 3_{(\text{PDF})} \text{ MeV} = 6_{(\text{tot})} \text{ MeV} \text{ and} \\ \Delta M_W(\text{LHeC} - 50) &= \pm 6_{(\text{exp})} \pm 6_{(\text{PDF})} \text{ MeV} = 8_{(\text{tot})} \text{ MeV}\end{aligned}\quad (5.9)$$

for LHeC-60 and LHeC-50 may be achieved, respectively. The complete dependence of the expected total experimental uncertainty  $\Delta M_W$  on the size of the uncorrelated uncertainty component is displayed in figure 58; with a more optimistic scenario, an uncertainty of up to  $\Delta M_W \approx 5$  MeV can be achieved. In view of such a high accuracy, it will be important to study the theoretical uncertainties carefully. For instance, the parametric uncertainty due to the dependence on the top-quark mass of 0.5 GeV will yield an additional error of  $\Delta M_W = 2.5$  MeV. In addition, higher-order corrections, at least the dominant two-loop corrections in DIS, will have to be studied and kept under control. Then, the expected determination of the  $W$ -boson mass from the LHeC data will be among the most precise determinations and will significantly improve the world average value of  $M_W$ . It will also become competitive with its prediction according to global EW fits, which has current uncertainties of about  $\Delta M_W = 7$  MeV [183, 440, 441].

While the determination of  $M_W$  from the LHeC data will be competitive with other measurements, the experimental uncertainties of the determination of  $M_Z$  are estimated to be about 11 MeV and 13 MeV for LHeC-60 and LHeC-50, respectively. Therefore, the precision of the determination of  $M_Z$  at the LHeC cannot compete with the precise measurements at the  $Z$ -pole made by the LEP collider and the SLAC Large Detector (SLD), and future  $e^+e^-$  colliders may even improve on that.

A simultaneous determination of  $M_W$  and  $M_Z$  is displayed in figure 59 (left). Although the precision of these two mass parameters is only moderate, a meaningful test of the high-energy behaviour of electroweak theory is obtained by using  $G_F$  as an additional input; the high precision of the  $G_F$  measurement [442] yields a very shallow error ellipse, and a precise test of the SM can be performed with NC and CC DIS cross-sections alone. Such a fit determines and simultaneously tests the high-energy behaviour of electroweak theory, while using only

<sup>179</sup> For performance reasons, the pseudodata are generated for a rather coarse grid. With the use of a binning that is closely related to the resolution of the LHeC detector, much finer grids are feasible for  $x$  and  $Q^2$ . Already such a change would alter the uncertainties of the fit parameters. However, such an effect can be reflected by a changed uncorrelated uncertainty, and a value of 0.25% appears to be an optimistic but achievable alternative scenario.



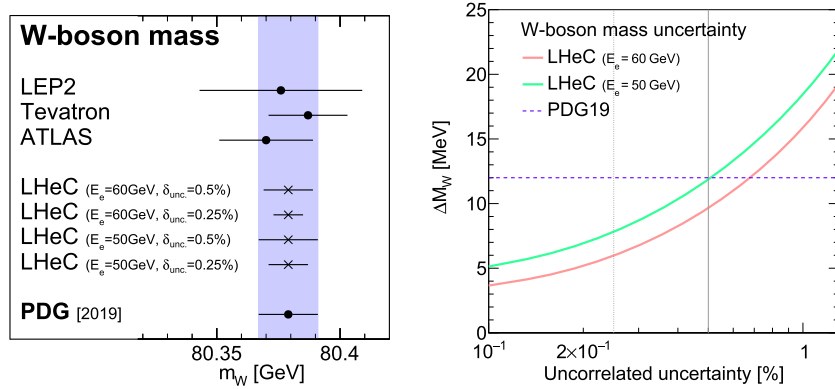


**Figure 58.** Left: measurements of the  $W$ -boson mass assuming fixed values for the top-quark and  $Z$ -boson masses at the LHeC for different scenarios in comparison with today’s measurements [437–439] and the world average value (PDG19) [183]. Prospects for  $E_e = 60\text{ GeV}$  and  $50\text{ GeV}$  are displayed for the LHeC, as well as results for two scenarios with  $0.5\%$  and  $0.25\%$  of uncorrelated uncertainty (see text). Right: comparison of the precision of  $M_W$  for different assumptions of the uncorrelated uncertainty of the pseudodata. The uncertainty of the world average value is displayed as a horizontal line. The nominal (and alternative) size of the uncorrelated uncertainty of the inclusive NC/CC DIS pseudodata is indicated by the vertical line (see text).

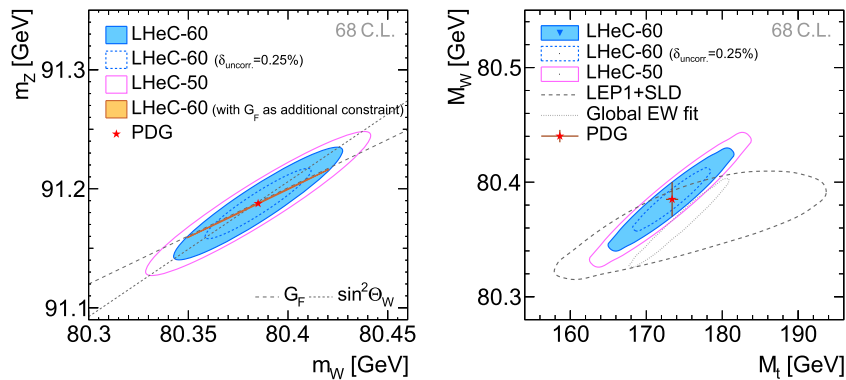


**Figure 59.** Simultaneous determination of the top-quark mass  $M_t$  and the  $W$ -boson mass  $M_W$  from LHeC-60 or LHeC-50 data (left). Simultaneous determination of the  $W$ -boson and  $Z$ -boson masses from LHeC-60 or LHeC-50 data (right).

the low-energy parameters  $\alpha$  and  $G_F$  as inputs (plus values for masses such as  $M_t$  and  $M_H$ , which are needed for loop corrections).

**5.1.4. Further mass determinations.** Inclusive DIS data are indirectly sensitive to the top-quark mass  $M_t$  through radiative corrections. The  $M_t$ -dependent terms are mainly due to corrections from the gauge boson self-energy corrections. They are contained in the  $\rho$  and  $\kappa$  parameters and in the correction factor  $\Delta r$ . The leading contributions are proportional to  $M_t^2$ . This allows for an indirect determination of the top-quark mass using LHeC inclusive DIS data, and a determination of  $M_t$  will yield an uncertainty of  $\Delta M_t = 1.8\text{ GeV}$  to  $2.2\text{ GeV}$ .

**Table 10.** Light-quark weak NC couplings ( $g_A^u, g_A^d, g_V^u,$  and  $g_V^d$ ) and their current most precise values from the PDG [183], compared with the prospective uncertainties for different LHeC scenarios. The LHeC prospects are obtained from a simultaneous fit of the PDF parameters and all four coupling parameters determined at a time.

Coupling parameter	PDG value	Expected uncertainties		
		LHeC-60	LHeC-60 ( $\delta_{\text{uncor.}} = 0.25\%$ )	LHeC-50
$g_A^u$	$0.50^{+0.04}_{-0.05}$	0.0022	0.0015	0.0035
$g_A^d$	$-0.514^{+0.050}_{-0.029}$	0.0055	0.0034	0.0083
$g_V^u$	$0.18 \pm 0.05$	0.0015	0.0010	0.0028
$g_V^d$	$-0.35^{+0.05}_{-0.06}$	0.0046	0.0027	0.0067

Assuming an uncorrelated uncertainty of the DIS data of 0.25% the uncertainty of  $M_t$  becomes as small as

$$\Delta M_t = 1.1\text{--}1.4 \text{ GeV} \quad (5.10)$$

for 60 and 50 GeV electron beams, respectively. This would represent a very precise indirect determination of the top-quark mass solely from electroweak corrections and would thus be fully complementary to measurements based on real  $t$ -quark production, which often suffer from sizeable QCD corrections. The precision achievable in this way will be competitive with those of indirect determinations from global EW fits after the HL-LHC era [443].

More generally, and to some extent depending on the choice of the renormalisation scheme, the leading self-energy corrections are proportional to  $\frac{M_t^2}{M_W^2}$  and thus a simultaneous determination of  $M_t$  and  $M_W$  is desirable. The prospects for a simultaneous determination of  $M_t$  and  $M_W$  are displayed in figure 59 (right). It is remarkable that the precision of the LHeC is superior to that of the LEP and SLD combination [444]. In an optimistic scenario an uncertainty similar to the global electroweak fit [441] can be achieved. In a fit without PDF parameters similar uncertainties are found (not shown), which illustrates that the determination of EW parameters is, to a large extent, independent of the QCD phenomenology and the PDFs.

The subleading contributions to self-energy corrections have a Higgs-boson mass dependence and are proportional to  $\log \frac{M_H^2}{M_W^2}$ . When all the other EW parameters are fixed, the Higgs boson mass could be indirectly constrained through these loop corrections with an experimental uncertainty of  $\Delta m_H = {}^{+29}_{-23}$  to  ${}^{+24}_{-20}$  GeV for different LHeC scenarios, which is again similar to the indirect constraints from a global electroweak fit [441], but not competitive with direct measurements.

**5.1.5. Weak neutral-current couplings.** The vector and axial-vector couplings of up-type and down-type quarks to the  $Z$ ,  $g_V^q$  and  $g_A^q$ , see equation (5.7), are determined by a fit of the four coupling parameters together with the PDFs.

The resulting uncertainties are collected in table 10. The two-dimensional uncertainty contours at a 68% CL obtained from LHeC data at  $E_e = 50$  GeV are displayed in figure 60 for the two quark families and compared with available measurements. While all the current determinations from  $e^+e^-$ ,  $ep$ , and  $p\bar{p}$  data have a similar precision, the future LHeC data will greatly improve the precision of the weak neutral-current couplings, and the expected uncertainties are an order of magnitude smaller than today's most precise ones [183]. An increased electron-beam energy of  $E_e = 60$  GeV or a reduction in the experimental uncertainties would further improve this measurement.

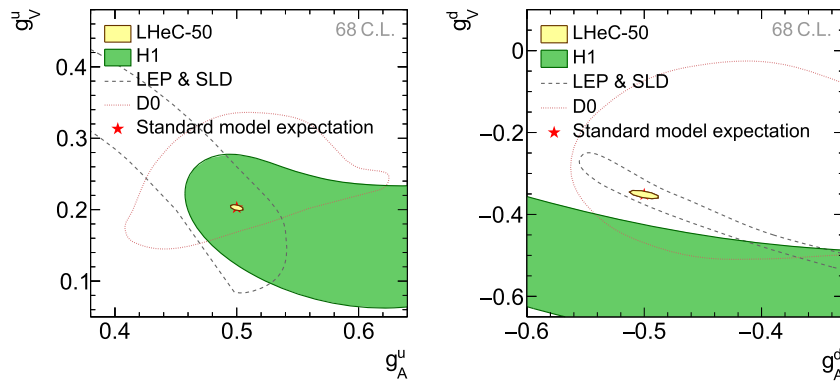


**Figure 60.** Weak NC vector and axial-vector couplings of  $u$ -type (left) and  $d$ -type quarks (right) at a 68% CL for simulated LHeC data at  $E_e = 50$  GeV. The LHeC expectation is compared with results from the combined LEP and SLD experiments [444], a single measurement from D0 [445], and one from H1 [423]. The SM expectations are denoted by a red star, partially hidden by the LHeC prospects.

The couplings of the electron to the  $Z$  boson,  $g_V^e$  and  $g_A^e$ , can be determined at the LHeC with uncertainties of up to  $\Delta g_V^e = 0.0013$  and  $\Delta g_A^e = \pm 0.0009$ , which are similar to the results of a single LEP experiment and about a factor of three larger than the results from a combination of the LEP collider and the SLD [444].

**5.1.6. The neutral-current  $\rho_{\text{NC}}$  and  $\kappa_{\text{NC}}$  parameters.** Beyond the Born approximation, the weak couplings are subject to higher-order loop corrections. These corrections are commonly parameterised by the quantities  $\rho_{\text{NC}}$ ,  $\kappa_{\text{NC}}$ , and  $\rho_{\text{CC}}$ . They are sensitive to contributions beyond the SM and the structure of the Higgs sector. It is important to keep in mind that these effective coupling parameters depend on the momentum transfer and are, indeed, form factors rather than constants. It is particularly interesting to investigate the so-called effective weak mixing angle, defined as  $\sin^2 \theta_W^{\text{eff}} = \kappa_{\text{NC}} \sin^2 \theta_W$ . At the  $Z$ -pole it is very accessible through asymmetry measurements in  $e^+e^-$  collisions. In DIS at the LHeC, the scale dependence of the effective weak mixing angle is not negligible. It can only be determined together with the  $\rho$  parameter, due to the  $Q^2$  dependence and the presence of the photon-exchange terms. Therefore, we introduce (multiplicative) anomalous contributions to these factors, denoted by  $\rho'_{\text{NC,CC}}$  and  $\kappa'_{\text{NC}}$ , and test their agreement with unity (for more details, see reference [423]). The uncertainties of these parameters are obtained from a fit together with the PDFs. The two-dimensional uncertainty contours of the anomalous form factors  $\rho'_{\text{NC},f}$  and  $\kappa'_{\text{NC},f}$  are displayed for three different LHeC scenarios in figure 61 (left), and compared with uncertainties obtained from the combination of the LEP collider and the SLD<sup>180</sup> [444]. It can be seen that these parameters can be determined with very high experimental precision.

Assuming that the couplings of the electron are given by the SM, the anomalous form factors for the two quark families can be determined; the results are displayed in figure 61 (right).

<sup>180</sup> Since the values of  $\rho_{\text{NC}}$  and  $\kappa_{\text{NC}} \sin^2 \theta_W$  are determined in the LEP + SLD analysis, we only compare the sizes of the uncertainties in these figures. Furthermore, it should be noted that the LEP is mainly sensitive to the parameters of leptons or heavy quarks, while LHeC data is more sensitive to light quarks ( $u, d, s$ ), and thus, the LHeC measurements are highly complementary to those of the LEP.

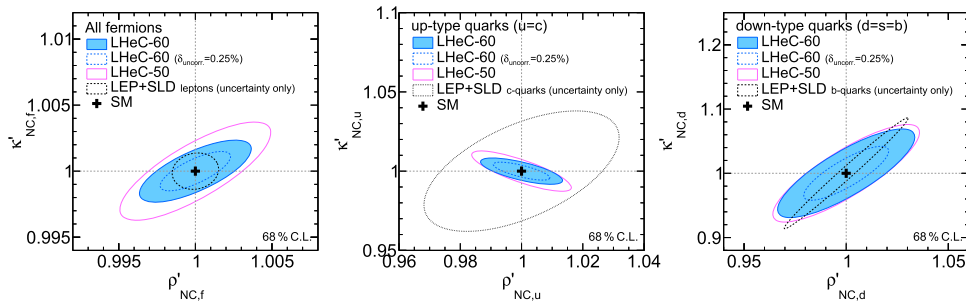


**Figure 61.** Expectations at a 68% CL for the determination of the  $\rho'_{NC}$  and  $\kappa'_{NC}$  parameters, assuming a single anomalous factor that is equal for all fermions (left). The results for three different LHeC scenarios are compared with the uncertainties obtained from the combination of the LEP collider and the SLD combination [444] for the determination of the respective leptonic quantities. Right: uncertainties for the simultaneous determination of the anomalous form factors for the  $u$ - and  $d$ -type quarks, assuming known values for the electron parameters. The values are compared with the uncertainties reported by the combination of the LEP collider and the SLD for the determination of the values  $\rho_{NC,(c,b)}$  and  $\sin \theta_W^{\text{eff}(c,b)}$  for charm and bottom quarks, respectively.

Since these measurements represent unique determinations of parameters sensitive to the light-quark couplings, we can only compare them with today’s measurements of the parameters for heavy quarks of the same charge, and it is found that the LHeC will provide high-precision determinations of the  $\rho'_{NC}$  and  $\kappa'_{NC}$  parameters.

A meaningful test of the SM can be performed by determining the effective coupling parameters as a function of the momentum transfer. In the case of  $\kappa'_{NC}$ , this is equivalent to measuring the running of the effective weak mixing angle,  $\sin \theta_W^{\text{eff}}(\mu)$  (see also section 5.1.7). However, DIS is quite complementary to other measurements, since the process is mediated by a space-like momentum transfer, i.e.  $q^2 = -Q^2 < 0$ , where  $q$  is the boson four-momentum. The prospects for a determination of  $\rho'_{NC}$  and  $\kappa'_{NC}$  at different  $Q^2$  values are displayed in figure 62 and compared to the results obtained by H1. The value of  $\kappa'_{NC}(\mu)$  can easily be translated to a measurement of  $\sin \theta_W^{\text{eff}}(\mu)$ . From figure 62 one can conclude that this quantity can be determined with a precision of up to 0.1% and better than 1% over a wide kinematic range of about  $25 < \sqrt{Q^2} < 700$  GeV.

**5.1.7. The effective weak mixing angle  $\sin^2 \theta_W^{\text{eff},\ell}$ .** The leptonic effective weak mixing angle is defined as  $\sin^2 \theta_W^{\text{eff},\ell}(\mu^2) = \kappa_{NC,\ell}(\mu^2) \sin^2 \theta_W$ . Due to its high sensitivity to loop corrections it represents an ideal quantity for precision tests of the SM. Its value is scheme dependent and it exhibits a scale dependence. Near the  $Z$  pole,  $\mu^2 = M_Z^2$ , its value was precisely measured at the LEP collider and the SLD. Those analyses were based on the measurement of asymmetries, and their interpretation in terms of the leptonic weak mixing angle was simplified by the fact that many non-leptonic corrections and contributions from box graphs cancelled or could be taken into account by subtracting their SM predictions. The highest sensitivity to  $\sin^2 \theta_W^{\text{eff},\ell}(M_Z)$  to date arises from a measurement of  $A_{fb}^{0,b}$  [444], in which the non-universal flavour-specific corrections to the quark couplings are taken from the SM, and consequently, these measurements are interpreted to be sensitive only to the universal, i.e. flavour-independent<sup>181</sup>, non-SM

<sup>181</sup> Flavour-specific tests were discussed to some extent in the previous section.

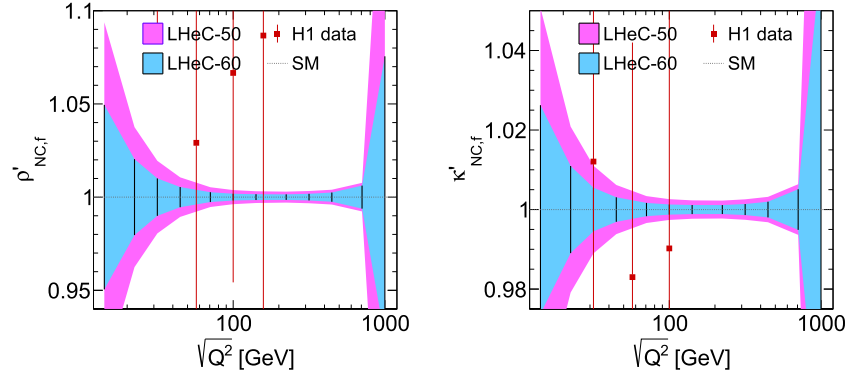


**Figure 62.** Test of the scale dependence of the anomalous  $\rho$  and  $\kappa$  parameters for two different LHeC scenarios. For the case of LHeC-60, i.e.  $E_e = 60$  GeV, we assume an uncorrelated uncertainty of 0.25%. The uncertainties of the parameter  $\kappa'_{NC,f}$  can be interpreted as sensitivity to the scale dependence of the weak mixing angle,  $\sin^2 \theta_W^{\text{eff}}(\mu)$ .

contributions to  $\kappa_{NC}$ . By applying this assumption to the DIS cross-sections as well, the determination of  $\kappa'_{NC,f}$  can be directly interpreted as a sensitivity study of the leptonic effective weak mixing angle  $\sin^2 \theta_W^{\text{eff},\ell}$ .

The prospects for a determination of  $\sin^2 \theta_W^{\text{eff},\ell}$  are listed in table 11. Two fits were studied: one with a fixed parameter  $\rho'_{NC}$  and one where  $\sin^2 \theta_W^{\text{eff},\ell}$  is determined together with  $\rho'_{NC}$  (see figure 61 (left)). At the LHeC, it will be possible to determine the value of  $\sin^2 \theta_W^{\text{eff},\ell}(M_Z^2)$  with an experimental uncertainty of up to

$$\Delta \sin^2 \theta_W^{\text{eff},\ell} = \pm 0.00015, \quad (5.11)$$

where the PDF uncertainties are already included. If the PDF parameters are kept artificially fixed, the uncertainties are of very similar size, which demonstrates that these measurements are fairly insensitive to the QCD effects and the PDFs. The uncertainties are compared<sup>182</sup> to recent average values in figure 63. One can see that in the future the LHeC measurement has the potential to become the most precise single measurement, with a significant impact on the world average value. It is obvious that a conclusive interpretation of experimental results with such a high precision will require correspondingly precise theoretical predictions, and the investigation of two-loop corrections for DIS will become important.

This LHeC measurement will become competitive with measurements at the HL-LHC [187]. Since in  $pp$  collisions, one of the dominant uncertainties is from the PDFs [448, 449, 452–454], future improvements can (only) be achieved by a common analysis of the LHeC and HL-LHC data. Such a study will yield the highest experimental precision, and the challenging theoretical and experimental aspects for a complete understanding of such an analysis will deepen our understanding of the electroweak sector.

<sup>182</sup> It should be noted that in order to compare the LHeC measurements with the  $Z$ -pole measurements at  $\mu^2 = M_Z^2$  in a conclusive way, one has to assume the validity of the SM framework. In particular, the scale-dependence of  $\kappa_{NC,\ell}$  must be known, in addition to the flavour-specific corrections. On the other hand, the scale dependence can, itself, be tested with the LHeC data, which cover a large range of space-like  $Q^2$ . In this respect, DIS provides a unique opportunity for precision measurements in the space-like regime ( $\mu^2 < 0$ ), as discussed in the previous section, see figure 62 (right).

**Table 11.** Determination of  $\sin^2 \theta_W^{\text{eff},\ell}(M_Z^2)$  with inclusive DIS data at the LHeC for different scenarios. Since the value of the effective weak mixing angle at the Z pole cannot be determined directly in DIS, a fit of the  $\kappa'_{\text{NC},f}$  parameter is performed instead, and its uncertainty is translated into  $\sin^2 \theta_W^{\text{eff},\ell}(M_Z^2)$ . Different assumptions for the fit parameters are studied, and the results include uncertainties from the PDFs. Only the last line shows results for fixed PDF parameters. See the text for further details.

Fit parameter	Parameter of interest	SM value	Expected uncertainty			
			LHeC-50 ( $\delta_{\text{uncor.}} = 0.50\%$ )	LHeC-60	LHeC-50 ( $\delta_{\text{uncor.}} = 0.25\%$ )	LHeC-60
$\kappa'_{\text{NC},f}$ PDFs	$\sin^2 \theta_W^{\text{eff},\ell}(M_Z^2)$	0.231 54	0.000 33	0.000 25	0.000 22	0.000 15
$\kappa'_{\text{NC},f} \rho'_{\text{NC},f}$ PDFs	$\sin^2 \theta_W^{\text{eff},\ell}(M_Z^2)$	0.231 54	0.000 71	0.000 36	0.000 56	0.000 23
$\kappa'_{\text{NC},e}$ PDFs	$\sin^2 \theta_W^{\text{eff},e}(M_Z^2)$	0.231 54	0.000 59	0.000 47	0.000 38	0.000 28
$\kappa'_{\text{NC},e}, \kappa'_{\text{NC},u}, \kappa'_{\text{NC},d}$ PDFs	$\sin^2 \theta_W^{\text{eff},e}(M_Z^2)$	0.231 54	0.001 11	0.000 95	0.000 69	0.000 56
$\kappa'_{\text{NC},f}$	$\sin^2 \theta_W^{\text{eff},\ell}(M_Z^2)$	0.231 54	0.000 28	0.000 23	0.000 17	0.000 14

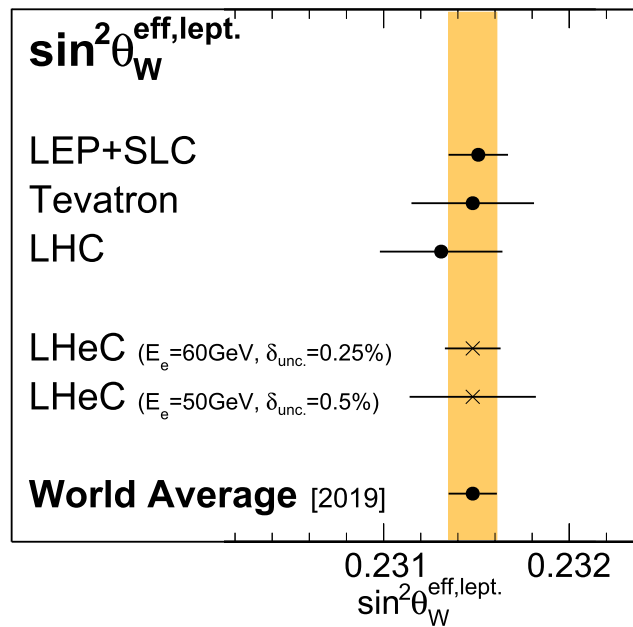


**Figure 63.** Comparison of the determination of  $\sin^2 \theta_W^{\text{eff},\ell}(M_Z^2)$  from LHeC inclusive DIS data using recent averaged values. The results from the LEP collider and the SLC [444], the Tevatron [446], the LHC [447–450] and the world average value [450] are all obtained from a combination of various separate measurements (not shown individually) (see also reference [451] for additional discussions). For the LHeC, the experimental and PDF uncertainties are displayed.

It may further be of interest to separately determine the value of the effective weak mixing angle of the electron for a comparison with measurements in  $pp$  and furthermore to test lepton-specific contributions to  $\kappa_{\text{NC},\text{lept.}}$ . Such fits are summarised in table 11 and a reasonable precision is achieved with the LHeC.



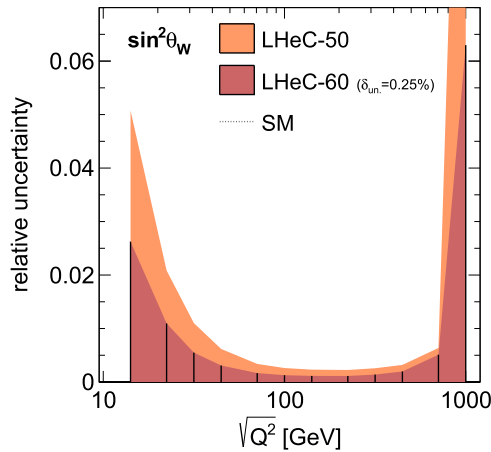


**Figure 64.** Expected uncertainties of the weak mixing angle determined in subregions of  $Q^2$ . Two scenarios for the simulation of LHeC inclusive NC/CC DIS data are considered.

The measurement of the weak mixing angle can be performed in subregions of  $Q^2$  due to the wide kinematic range accessible at the LHeC. The relative uncertainties for the determination of the weak mixing angle for different  $Q^2$  intervals are displayed in figure 64. We find that the weak mixing angle can be determined in the range of about  $25 < \sqrt{Q^2} < 700$  GeV with a precision of better than 0.1%. If a calculation of DIS cross-sections including higher-order EW corrections in the  $\overline{\text{MS}}$  scheme is available, these relative uncertainties can be mapped into a test of the running of the weak mixing angle. Note that in DIS, the scattering process is mediated by boson exchange with spacelike momenta and is therefore complementary to other measurements, since the scale is  $\mu^2 = -Q^2$ .

**5.1.8. Electroweak effects in charged-current scattering.** The charged-current sector of the SM can be uniquely measured at high scales over many orders of magnitude in  $Q^2$  at the LHeC, due to the excellent tracking detectors, calorimetry, and high-bandwidth triggers. The form factors of the effective couplings of the fermions to the  $W$  boson can be measured in a similar way to those of the NC case. In the SM formalism, only two of these form factors are present,  $\rho_{CC,eq}$  and  $\rho_{CC,e\bar{q}}$ . We thus introduce two anomalous modifications to them,  $\rho_{CC,(eq/e\bar{q})} \rightarrow \rho'_{CC,(eq/e\bar{q})}\rho_{CC,(eq/e\bar{q})}$  (see reference [423]). The prospects for the determination of these parameters are displayed in figure 65, and it is found that with the LHeC, these parameters can be determined with a precision of up to 0.2%–0.3%. Their  $Q^2$  dependence can also be uniquely studied with high precision at  $\sqrt{Q^2}$  values of up to about 400 GeV.

**5.1.9. Conclusions.** With LHeC inclusive NC and CC DIS data, unique measurements of electroweak parameters can be performed to the highest precision. Since inclusive DIS is mediated through a space-like momentum transfer ( $t$ -channel exchange), the results are often complementary to those of other experiments, such as  $pp$  or  $e^+e^-$  collider experiments, where measurements are performed in the time-like regime and most often at the  $Z$  peak. Among many other quantities, measurements of the weak couplings of the light quarks,  $u$  and  $d$ , or their anomalous form factors  $\rho'_{NC,u/d}$  and  $\kappa'_{NC,u/d}$ , can be uniquely performed due to the important contributions of valence quarks in the initial state. Scale-dependent measurements of weak interactions can also be performed over a large range in  $\sqrt{Q^2}$ , which provides an interesting portal to BSM physics. The  $W$  boson mass can be determined with very small experimental

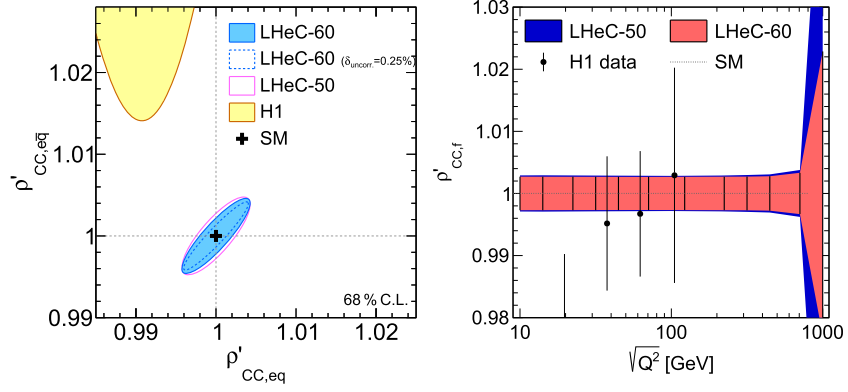


**Figure 65.** Left: anomalous modifications of the CC form factors  $\rho'_{CC,eq}$  and  $\rho'_{CC,eq}$  for different LHeC scenarios in comparison with the H1 measurements [423]. Right: scale-dependent measurement of the anomalous modification of the CC form factor  $\rho'_{CC}(Q^2)$ , assuming  $\rho'_{CC,eq} = \rho'_{CC,eq} = \rho'_{CC}$ .

uncertainties, such that the theoretical uncertainties are expected to become more important than the experimental uncertainties. While the parameters of the PDFs are determined together with the EW parameters in this study, it is found that the PDFs do not create a limitation in the uncertainties. Considering the dominant top-quark mass dependence of the higher-order electroweak effects, one realises that the LHeC results will be competitive with the global electroweak fit after the HL-LHC era [187, 443].

Besides proving its own remarkable prospects for high-precision electroweak physics, the LHeC will further significantly improve the electroweak measurements in  $pp$  collisions at the LHC by reducing the currently sizeable influence of PDF and  $\alpha_s$  uncertainties. This is discussed in section 9.

## 5.2. Direct $W$ and $Z$ production and anomalous triple gauge couplings

**5.2.1. Direct  $W$  and  $Z$  production.** The direct production of single  $W$  and  $Z$  bosons is a crucial signal that represents an important channel for EW precision measurements. The production of  $W$  bosons was measured at  $\sqrt{s} \simeq 320$  GeV at HERA [455–457]. With the full  $e^\pm p$  data set collected by the H1 and ZEUS experiments together, corresponding to an integrated luminosity of about  $\mathcal{L} \sim 1 \text{ fb}^{-1}$ , a few dozens of  $W$  boson event candidates were identified in the  $e$ ,  $\mu$ , and  $\tau$  decay channels.

Detailed studies of direct  $W/Z$  production in  $ep$  collisions at higher centre-of-mass energies have been presented in the past, see references [458–460]. These theoretical studies were performed with a proton-beam energy of  $E_p = 8$  TeV and electron-beam energies of  $E_e = 55$  GeV or 100 GeV, which correspond to a very similar centre-of-mass energy to that of the LHeC. Measurements at the LHeC will benefit considerably from its large integrated luminosity, in comparison to earlier projections.

In  $e^- p$  collisions,  $W$  and  $Z$  direct production can be classified into five processes:

$$\begin{aligned}
 e^- p &\rightarrow e^- W^+ j, e^- p \rightarrow e^- W^- j, \\
 e^- p &\rightarrow \nu_e^- W^- j, e^- p \rightarrow \nu_e^- Z j
 \end{aligned} \tag{5.12}$$

**Table 12.** SM predictions of direct  $W$  and  $Z$  production cross-sections in  $e^-p$  collisions for different collider-beam energy options,  $E_e$ , and final-state forward electron transverse momentum cuts,  $p_T^e$ . Two different electron-beam energy options are considered,  $E_e = 50$  GeV and 60 GeV.

Process	$E_e = 50$ GeV, $E_p = 7$ TeV $p_T^e > 10$ GeV	$E_e = 60$ GeV, $E_p = 7$ TeV $p_T^e > 10$ GeV	$E_e = 60$ GeV, $E_p = 7$ TeV $p_T^e > 5$ GeV
$e^-W^+j$	1.00 pb	1.18 pb	1.60 pb
$e^-W^-j$	0.930 pb	1.11 pb	1.41 pb
$\nu_e^-W^-j$	0.796 pb	0.956 pb	0.956 pb
$\nu_e^-Zj$	0.412 pb	0.502 pb	0.502 pb
$e^-Zj$	0.177 pb	0.204 pb	0.242 pb

and

$$e^-p \rightarrow e^-Zj, \quad (5.13)$$

where  $j$  denotes the hadronic final state (i.e. the *forward jet*). According to the above classification, the four processes in equation (5.12) can be used to study triple gauge couplings (TGCs), e.g.  $WW\gamma$  and  $WWZ$  couplings, since some of the contributing diagrams represent the vector boson fusion (VBF) processes. The process shown in equation (5.13) does not contain any TGC vertex. The processes for positron–proton collisions can easily be derived from equations (5.12) and (5.13), but are not discussed further here, due to the small integrated luminosity of the LHeC  $e^+p$  data.

The MadGraph5\_v2.4.2 program [375] is employed for matrix element calculation and event generation and the PDF NNPDF23\_nlo\_as\_0119\_qed [461] is used. Technical cuts are imposed on the transverse momentum of the outgoing scattered lepton,  $p_T^e$ , of 10 GeV or alternatively 5 GeV, and the other basic cuts are  $p_T^j > 20$  GeV,  $|\eta_{e,j}| < 5$ , and  $\Delta R_{ej} < 0.4$ . The resulting SM total cross-sections of the above processes are listed in table 12.

The process with the largest production cross-section in  $e^-p$  scattering is single  $W^+$  boson production. This will be the optimal channel for both SM measurements and new physics probes in the EW sector. Also, this channel is experimentally preferred; because the  $W^+$  is produced by NC scattering, the beam electron is measured by the detector and the  $W$ -boson has an opposite charge to that of the beam lepton, and thus, in a leptonic decay, an oppositely charged lepton and missing transverse momentum are observed. Altogether, it is expected that a few million direct  $W$ -boson events will be measured at the LHeC.

Several  $10^5$  direct  $Z$  events are expected to be measured, corresponding approximately to the size of the event sample of the SLD experiment [444], but at the LHeC, these  $Z$  bosons will predominantly be produced in VBF events.

All these total cross-sections increase significantly with smaller transverse momentum of the outgoing scattered lepton. Therefore, it will become important to decrease that threshold by the use of dedicated electron taggers, see section 12.

**5.2.2. Anomalous triple gauge couplings.** The measurement of gauge boson production processes provides a precise measurement of the triple gauge boson vertex. This measurement is sensitive to the new physics contributions of *anomalous* triple gauge couplings (aTGCs). In the measurement of aTGCs, the LHeC has the advantages of a higher centre-of-mass energy and easier kinematic analysis.

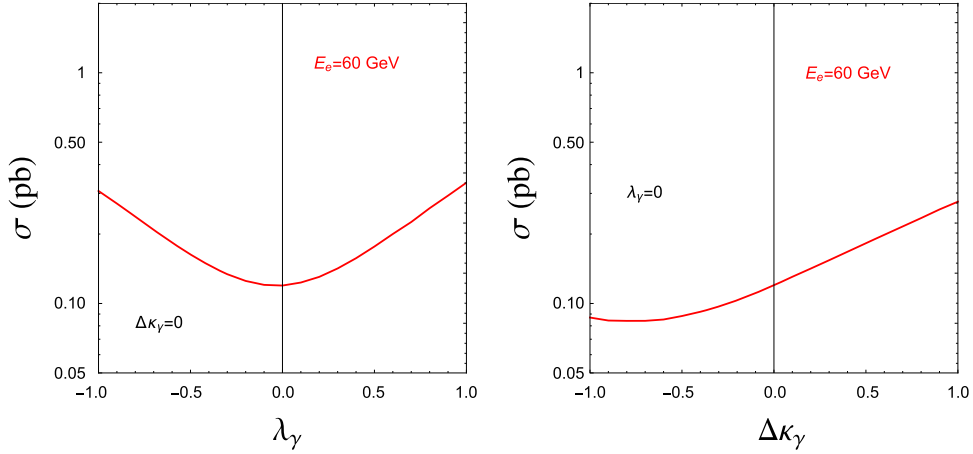


**Figure 66.** Total cross-sections of the  $e^- p \rightarrow e^- \mu^+ \nu_\mu j$  process with varying  $\lambda_\gamma$  (left plot) and  $\Delta\kappa_\gamma$  (right plot). Reproduced from [467]. CC BY 4.0.

In the language of effective field theory, aTGCs in the Lagrangian are generally parameterised as

$$\begin{aligned}
\mathcal{L}_{\text{TGC}}/g_{WWV} = & ig_{1,V} (W_{\mu\nu}^+ W_\mu^- V_\nu - W_{\mu\nu}^- W_\mu^+ V_\nu) + i\kappa_V W_\mu^+ W_\nu^- V_{\mu\nu} + \frac{i\lambda_V}{M_W^2} W_{\mu\nu}^+ W_{\nu\rho}^- V_{\rho\mu} \\
& + g_5^V \epsilon_{\mu\nu\rho\sigma} (W_\mu^+ \overleftrightarrow{\partial}_\rho W_\nu^-) V_\sigma - g_4^V W_\mu^+ W_\nu^- (\partial_\mu V_\nu + \partial_\nu V_\mu) \\
& + i\tilde{\kappa}_V W_\mu^+ W_\nu^- \tilde{V}_{\mu\nu} + \frac{i\tilde{\lambda}_V}{M_W^2} W_{\lambda\mu}^+ W_{\mu\nu}^- \tilde{V}_{\nu\lambda}, \tag{5.14}
\end{aligned}$$

where  $V = \gamma, Z$ . The gauge couplings  $g_{WW\gamma} = -e$  and  $g_{WWZ} = -e \cot \theta_W$  and the weak mixing angle  $\theta_W$  are taken from the SM.  $\tilde{V}_{\mu\nu}$  and  $A \overleftrightarrow{\partial}_\mu B$  are defined as  $\tilde{V}_{\mu\nu} = \frac{1}{2} \epsilon_{\mu\nu\rho\sigma} V_{\rho\sigma}$  and  $A \overleftrightarrow{\partial}_\mu B = A(\partial_\mu B) - (\partial_\mu A)B$ , respectively. There are five aTGCs ( $g_{1,Z}$ ,  $\kappa_\gamma$ ,  $\kappa_Z$ ,  $\lambda_\gamma$  and  $\lambda_Z$ ). Conserving the charge conjugation (C) and charge-parity (CP) symmetry with electromagnetic gauge symmetry requires  $g_{1,\gamma} = 1$ . Only three of them are independent because  $\lambda_Z = \lambda_\gamma$  and  $\Delta\kappa_Z = \Delta g_{1,Z} - \tan^2 \theta_W \Delta\kappa_\gamma$  [462–464]. The LHeC can set future constraints on  $\Delta\kappa_\gamma$  and  $\lambda_\gamma$ .

In the direct  $Z/\gamma$  production process, the anomalous  $WWZ$  and  $WW\gamma$  couplings can be separately measured without being influenced by their interference [465, 466]. In the direct  $W$  production process, both the deviation in the signal cross-section and the kinematic distributions can effectively constrain the  $WW\gamma$  aTGC, while anomalous  $WWZ$  contribution in this channel is insensitive as a result of the suppression due to the  $Z$  boson mass [467–469].

$W$  decay into the muon channel is expected to be the optimal measurement approach for the anomalous  $WW\gamma$  coupling, because of the discrimination of final states and mistagging efficiencies [467]. Figure 66 shows the cross-section of a single  $W^+$  production process followed by  $W^+ \rightarrow \mu^+ \nu_\mu$  decay, with different  $\lambda_\gamma$  and  $\Delta\kappa_\gamma$  values. A large anomalous coupling leads to a measurable deviation from the SM prediction. The cross-section increases monotonically with  $\Delta\kappa_\gamma$  and the absolute value of  $\lambda_\gamma$  within the region of  $-1.0 \leq \lambda_\gamma/\Delta\kappa_\gamma \leq 1.0$ .

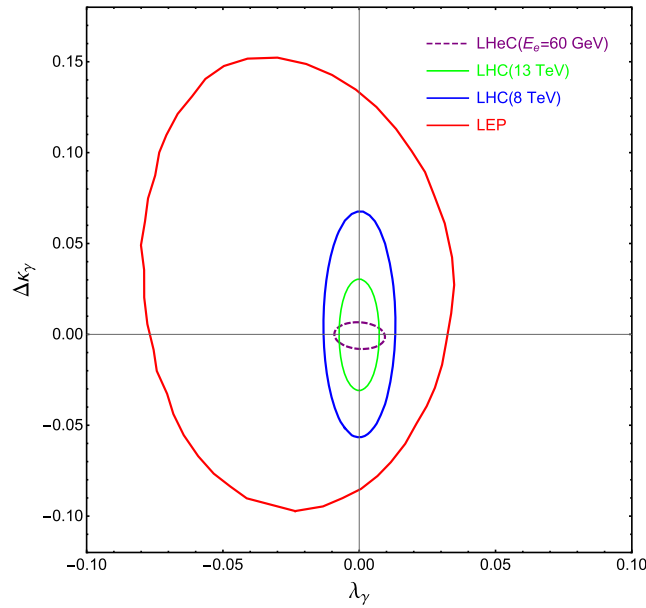


**Figure 67.** The 95% CL exclusion limit on the  $\Delta\kappa_\gamma$ - $\lambda_\gamma$  plane. The purple dashed contour is the projected LHeC exclusion limit with an integrated luminosity of  $1 \text{ ab}^{-1}$ . Reproduced from [467]. CC BY 4.0. The blue, green, and red contours are the current bounds of the LHC [470, 471] and the LEP collider [472].

Kinematic analysis is necessary for the precise aTGC measurement. At the LHeC, the  $e^-p \rightarrow e^-W^\pm j$  process with leptonic  $W$  boson decay can be fully reconstructed because the undetected neutrino information is reconstructed using either energy-momentum conservation or the recoil mass method. This allows the use of angular correlation observables, which are sensitive to  $W$  boson polarisation. A helicity amplitude calculation indicates that a non-SM value of  $\lambda_\gamma$  leads to a significant enhancement in the transverse polarisation fraction of the  $W$  boson in the  $e^-p \rightarrow e^-W^\pm j$  process, while a non-SM value of  $\Delta\kappa_\gamma$  leads to an enhancement of the longitudinal component fraction [458]. The angle  $\theta_{\ell W}$  is defined as the angle between the decay-product lepton  $\ell$  in the  $W$  rest frame and the direction of  $W$  movement in the collision rest frame. Making use of the energetic final states in the forward direction, a second useful angle  $\Delta\phi_{ej}$  is defined as the separation of the final-state jet and the electron on the azimuthal plane. In an optimised analysis, assuming an integrated luminosity of  $1 \text{ ab}^{-1}$ , the observable  $\Delta\phi_{ej}$  can impose stringent constraints on both  $\lambda_\gamma$  and  $\Delta\kappa_\gamma$ , and uncertainties within  $[-0.007, 0.0056]$  and  $[-0.0043, 0.0054]$  can be achieved, respectively. The  $\cos\theta_{\mu W}$  observable is also sensitive to  $\Delta\kappa_\gamma$  at the same order, but fails to constrain  $\lambda_\gamma$ . This analysis is described in detail in reference [467].

Figure 67 shows the two-parameter aTGC constraint on the  $\lambda_\gamma$ - $\Delta\kappa_\gamma$  plane, based on a  $\chi^2$  analysis of  $\Delta\phi_{ej}$  at the parton level and assuming an electron-beam energy of  $E_e = 60 \text{ GeV}$ . When compared with the current LHC (blue and green) and LEP collider (red) bounds, the LHeC has the potential to significantly improve the constraints, in particular, those imposed on the  $\Delta\kappa_\gamma$  parameter. The polarised electron beam is found to improve the aTGC measurement

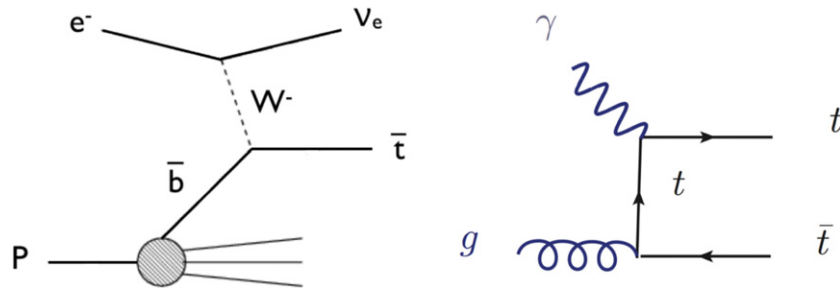


**Figure 68.** Example graphs for top quark production in CC DIS (left) and for  $t\bar{t}$  photoproduction (right). Reproduced from [14]. CC BY 4.0.

[466, 469]. In consideration of the *realistic* analysis at detector level, one can expect  $2\text{--}3\text{ ab}^{-1}$  of integrated luminosity to achieve the same results [467].

One uncertainty in the aTGC measurement at the (HL-)LHC originates from the PDF uncertainty. Future LHeC PDF measurements will improve the precision of aTGC measurement in the  $x \simeq \mathcal{O}(10^{-2})$  region.

### 5.3. Top quark physics

SM top quark production at a future  $ep$  collider is dominated by single top quark production, mainly via CC DIS production. A leading-order Feynman diagram is displayed in figure 68 (left). The total cross-section for single top quark production is  $1.89\text{ pb}$  at the LHeC [473] at a centre-of-mass energy of  $1.3\text{ TeV}$ , i.e. with an electron-beam energy of  $60\text{ GeV}$  and an LHC proton beam of  $7\text{ TeV}$ . The second important production mode for top quarks at the LHeC is photoproduction of top–antitop quark pairs ( $t\bar{t}$ ), for which a total cross-section of  $0.05\text{ pb}$  is expected at the LHeC [474]. Figure 68 (right) shows an example Feynman diagram. This makes the future LHeC a top quark factory and an ideal tool for studying top quarks with high precision, and, in particular, analysing their electroweak interactions. Selected highlights in top quark physics are summarised here.

**5.3.1.  $Wtq$  couplings.** The top quark couplings to gauge bosons can be modified significantly in models with new top (or third-generation) partners, such as in some extensions of the minimal supersymmetric SM, in little Higgs models, top-color models, top seesaw, top compositeness, and others. Testing such extensions is therefore of the utmost importance to find out whether there are other sources of electroweak symmetry breaking that are different from the standard Higgs mechanism.

One highlight at the LHeC is the direct measurement of the CKM matrix element  $|V_{tb}|$ . Such a measurement can be done without making any model assumptions, for instance, about the unitarity of the CKM matrix or the number of quark generations. An elaborate analysis of the single top quark CC DIS process at the LHeC, which makes use of a detailed detector simulation using the DELPHES package [475], shows that at  $100\text{ fb}^{-1}$  of integrated luminosity, an uncertainty of  $1\%$  can already be expected. This can be compared to the total uncertainty of  $4.1\%$  for the most accurate current result of LHC run-I performed by the CMS experiment [476].



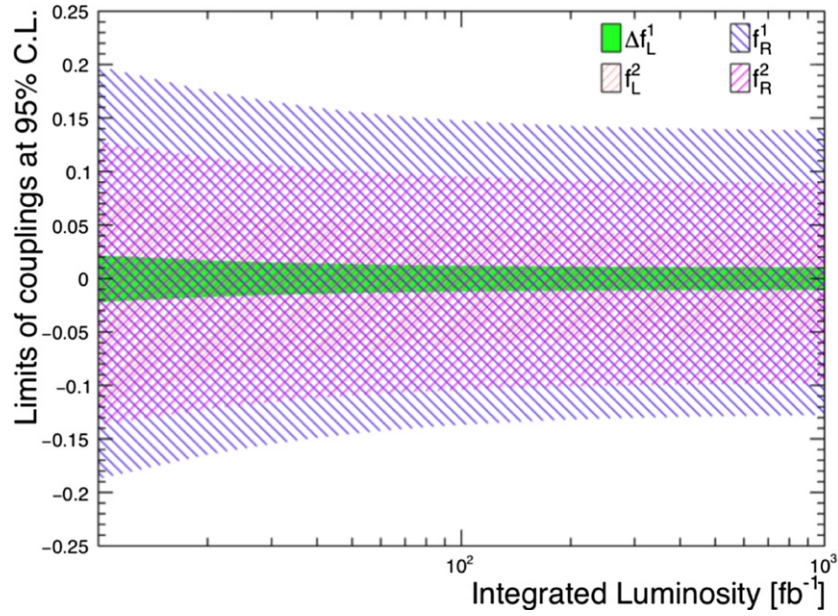


**Figure 69.** Expected sensitivities to the SM and anomalous  $Wtb$  couplings, as a function of the integrated luminosity. Reproduced from [473]. CC BY 4.0.

The same process is also highly sensitive to the search for anomalous left- and right-handed  $Wtb$  vector ( $f_1^L$ ,  $f_1^R$ ) and tensor ( $f_2^L$ ,  $f_2^R$ ) couplings [473]. These are given by an effective Lagrangian,

$$\mathcal{L}_{Wtb} = -\frac{g}{\sqrt{2}}\bar{b}\gamma^\mu V_{tb} (f_1^L P_L - f_1^R P_R) t W_\mu^- - \frac{g}{\sqrt{2}}\bar{b}\frac{i\sigma^{\mu\nu}q_\nu}{M_W} (f_2^L P_L - f_2^R P_R) t W_\mu^- + \text{h.c.} \quad (5.15)$$

In the SM formalism,  $f_1^L = 1$  and  $f_1^R = f_2^L = f_2^R = 0$ . The effect of anomalous  $Wtb$  couplings is consistently evaluated in the production and the decay of the antitop quark, see figure 68 (left)<sup>183</sup>.

The expected limits for the anomalous couplings at the 95% CL from a measurement of single top quark production in CC DIS at the LHeC are displayed in figure 69. This analysis only exploits hadronic top quark decays [473]. The coupling parameters are expected to be measured with accuracies of 1% for the SM  $f_1^L$  coupling that determines  $|V_{tb}|$  (as discussed above), 4% for  $f_2^L$ , 9% for  $f_2^R$ , and 14% for  $f_1^R$  at  $1 \text{ ab}^{-1}$ .

In a similar way, through  $W$  boson and bottom (light) quark-associated production, the CKM matrix elements  $|V_{tx}|$  ( $x = d, s$ ) can be extracted with very high precision utilising a parameterisation of the deviations from the respective SM values. Here, the  $W$  boson and the  $b$  jet (light jet  $j = d, s$ ) are produced via  $t$ -channel top quark exchange, or via  $s$ -channel single top quark decay, as outlined in [478]. As an example, the processes

<sup>183</sup> Further studies of the top-quark CC coupling can be found in [477], where a more general framework is employed using the full basis of  $SU(2)_L \times U(1)$  operators, including the relevant four-fermion ones.

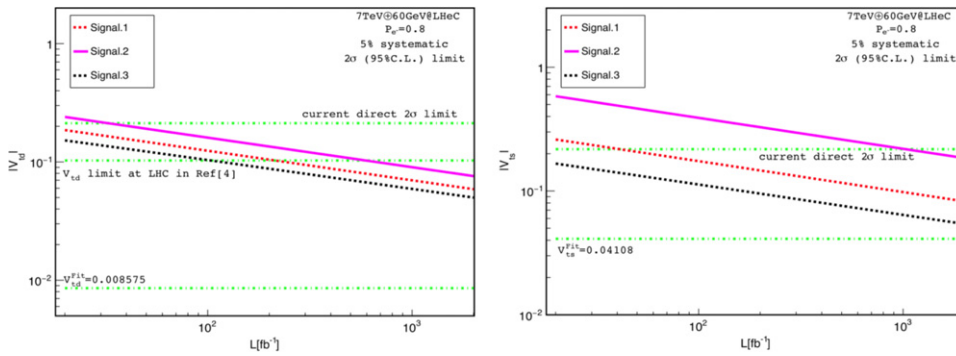


**Figure 70.** Expected sensitivities to  $|V_{td}|$  (left) and  $|V_{ts}|$  (right), as a function of the integrated luminosity. Reproduced from [478]. CC BY 4.0.

Signal 1:  $pe^- \rightarrow \nu_e \bar{t} \rightarrow \nu_e W^- \bar{b} \rightarrow \nu_e \ell^- \nu_\ell \bar{b}$

Signal 2:  $pe^- \rightarrow \nu_e W^- b \rightarrow \nu_e \ell^- \nu_\ell b$

Signal 3:  $pe^- \rightarrow \nu_e \bar{t} \rightarrow \nu_e W^- j \rightarrow \nu_e \ell^- \nu_\ell j$

have been analysed in an elaborate study, in which a detailed detector simulation was performed using the DELPHES package [475]. Figure 70 shows the resulting accuracies at the  $2\sigma$  CL for an expected measurement of  $|V_{td}|$  and  $|V_{ts}|$ , respectively, as a function of the integrated luminosity. At  $1 \text{ ab}^{-1}$  of integrated luminosity and an electron polarisation of 80%, the  $2\sigma$  limits improve on the existing limits of the LHC [479] (interpreted by [480]) by a factor of  $\approx 3.5$ . Analyzing Signal 3 alone, and, to a greater extent, combining Signals 1, 2 and 3, will, for the first time, allow us to achieve an accuracy of the order of the actual SM value of  $|V_{ts}^{\text{SM}}| = 0.04108^{+0.0030}_{-0.0057}$  as derived from an indirect global CKM matrix fit [481], and will therefore represent a direct high-precision measurement of this important top quark property. In these studies, upper limits at the  $2\sigma$  level down to  $|V_{ts}| < 0.06$  and  $|V_{td}| < 0.06$  can be achieved.

**5.3.2. Top quark polarisation.** Single top quarks produced via the  $e^+p \rightarrow t\bar{\nu}$  processes possess a high degree of spin polarisation in terms of a basis which decomposes the top quark spin in its rest frame in the direction of the incoming e beam [482]. It has been shown for  $\sqrt{s} = 1.6 \text{ TeV}$  in  $e^+p$  scattering that the spin fraction, defined as the ratio of the polarised cross-section to the unpolarised one, reaches 96%, allowing a detailed study of the polarisation and the spin of the top quark. By exploring the angle between the momentum direction of the charged lepton produced by top quark decay and the spin quantisation axis in the top quark rest frame, anomalous  $Wtb$  couplings can be tested. Assuming a total systematic uncertainty of 10% the expected sensitivity for  $\sqrt{s} = 1.6 \text{ TeV}$  reaches  $\pm 3\%$  for  $f_2^L$ , and  $\pm 7\%$  for  $f_2^R$  as defined in equation (5.15).

**5.3.3. Top- $\gamma$  and top-Z couplings.** The LHeC is particularly well suited to the measurement of the  $t\bar{t}\gamma$  vertex, since in the photoproduction of top quark pairs (see figure 68, right), the highly energetic incoming photon only couples to the top quark, and therefore the cross-section directly depends on the  $t\bar{t}\gamma$  vertex. This provides a direct measurement of the coupling between the top quark and the photon and therefore of another important top quark property, the top quark charge. In contrast, at the LHC, the  $t\bar{t}\gamma$  vertex is probed in  $t\bar{t}\gamma$  production, where the final-state photon can also be produced from other vertices than the  $t\bar{t}\gamma$  vertex, such as from initial-state radiation or radiation from charged top quark decay products.

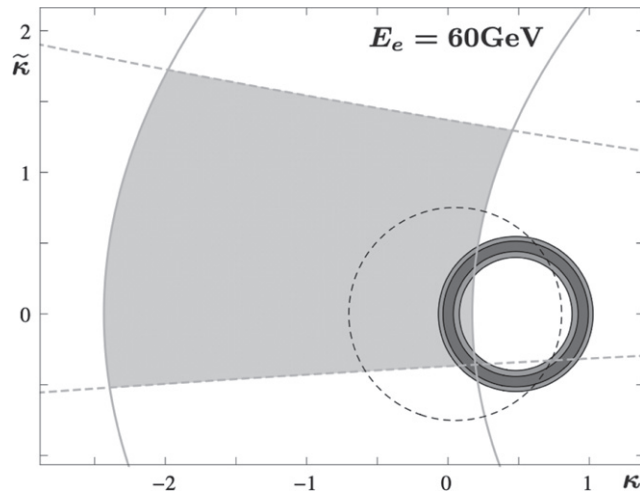


**Figure 71.** Allowed region of the MDM  $\kappa$  and the EDM  $\tilde{\kappa}$  of the top quark as expected in a measurement of the photoproduction cross-section  $\sigma(e(\gamma)p(g) \rightarrow t\bar{t})$  in semileptonic final states, assuming experimental uncertainties of 8% (dark grey) and 16% (dark and medium grey). Reprinted figure with permission from [474], Copyright 2013 by the American Physical Society. Light grey area: region allowed by the measurements of the branching ratio (solid grey lines) and the CP asymmetry (dashed grey lines) of  $B \rightarrow X_s \gamma$  [483]. Black dashed line: region allowed by a hypothetical experimental result for  $\sigma(pp \rightarrow t\bar{t}\gamma)$  utilizing semileptonic final states at the LHC at  $\sqrt{s} = 14$  TeV with phase-space cuts as defined in equations (5), (6) of reference [483] (including  $E_T^\gamma > 10$  GeV), and assuming an experimental uncertainty of 5%.

The LHeC also provides a high potential for measuring the  $t\bar{t}\gamma$  magnetic and electric dipole moments (MDM and EDM, respectively) in  $t\bar{t}$  production [474]. In an effective Lagrangian framework, effective  $t\bar{t}\gamma$  couplings can be written in terms of the form factors:

$$\mathcal{L}_{Wtb} = e\bar{t} \left( Q_t \gamma^\mu A_\mu + \frac{1}{4m_t} \sigma^{\mu\nu} F_{\mu\nu} (\kappa + i\tilde{\kappa}\gamma_5) \right) t + \text{h.c.} \quad (5.16)$$

using the anomalous MDM of the top quark,  $\kappa$ , and the EDM of the top quark,  $\tilde{\kappa}$ . The top quark charge is given by  $eQ_t$ .

By solely measuring the  $t\bar{t}$  production cross section, remarkably tight bounds can be derived for the MDM and the EDM of the top quark, as presented in figure 71. In this parton-level study, for the computation of the cross-section, a set of appropriate phase-space cuts are imposed on the final-state momenta. The application of further cuts to remove the background would result in a substantial reduction of the signal. It is therefore assumed that this would lead to a statistical uncertainty of about 8%, represented by the dark inner ring in figure 71. When uncertainties due to mistagging are included and to allow for other unspecified sources of systematic uncertainty, it is assumed that the total uncertainty will be about 16%, corresponding to the full ring in figure 71. This would yield bounds of  $-0.13 < \kappa < 0.18$  and  $|\tilde{\kappa}| < 0.38$ , respectively, at the  $2\sigma$  CL. Figure 71 shows that the LHeC could greatly improve both on the limits imposed by the indirect constraints from  $b \rightarrow s\gamma$ , and on the limits derived by a future measurement of  $t\bar{t}\gamma$  production at the LHC at  $\sqrt{s} = 14$  TeV.

Furthermore, the DIS regime of  $t\bar{t}$  production will allow us to probe the  $t\bar{t}Z$  coupling, albeit with reduced sensitivity [474].

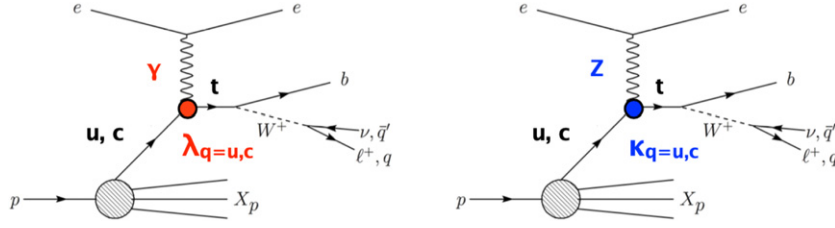


**Figure 72.** Example graphs for single top quark production via FCNC  $tq\gamma$  (left) and  $tuZ$  (right) couplings.

**5.3.4. Top–Higgs coupling.** The CP nature of the top–Higgs coupling can be analysed at the LHeC in  $ep \rightarrow \bar{t}H$  production, which explores top quark polarisation and other angular variables, such as the difference in rapidity between the antitop quark and the Higgs boson. Measurement of just the fiducial inclusive production cross-section already provides a powerful probe of the CP properties of the  $\bar{t}tH$  coupling [484]. Further details are given in section 7.5.

**5.3.5. Top quark PDF and the running of  $\alpha_s$ .** Parton distributions are usually released in a variable-flavour number scheme, where the number of active flavours changes as the scale is increased [254]. However,  $n_f = 5$  is normally taken by default as the maximum number of flavours, even though, in some PDF releases,  $n_f = 6$  PDF sets are also made available [485]. The top PDF is unlikely to be required for precision phenomenology, even at very high scales, because the top threshold is high enough that collinear resummation is not necessary up to extremely large scales; indeed,  $\frac{\alpha_s(M_t^2)}{\pi} \ln \frac{Q^2}{m_t^2} \sim \frac{1}{2}$  only for  $Q \gtrsim 10^6 m_t$ . On the other hand, the use of  $n_f = 6$  active flavours in the running of  $\alpha_s$  is important for precision phenomenology, since the values of  $\alpha_s$  with five and six active flavours already differ by about 2% at the TeV scale [486]. Investigations of the top quark structure inside the proton are also discussed in references [1, 41].

**5.3.6. FCNC top quark couplings.** Like all FCNCs, the top quark FCNC interactions are also extremely suppressed in the SM, which renders them a good test of new physics. The contributions from FCNC to top interactions can be parameterised via an effective theory and studied by analysing specific processes.

The NC DIS production of single top quarks can be explored to search for FCNC  $tu\gamma$ ,  $tc\gamma$ ,  $tuZ$ , and  $tcZ$  couplings [487, 488], as represented by the Lagrangian

$$\mathcal{L}_{\text{FCNC}} = \sum_{q=u,c} \left( \frac{g_e}{2m_t} \bar{t} \sigma^{\mu\nu} (\lambda_q^L P_L + \lambda_q^R P_R) q A_{\mu\nu} + \frac{g_W}{4c_W m_Z} \bar{t} \sigma^{\mu\nu} (\kappa_q^L P_L + \kappa_q^R P_R) q Z_{\mu\nu} \right) + \text{h.c.} \quad (5.17)$$

Here, the electromagnetic (weak) coupling constant is denoted by  $g_e$  ( $g_W$ ), while  $c_W$  is the cosine of the weak mixing angle,  $\lambda_q^{L,R}$  and  $\kappa_q^{L,R}$  are the anomalous top FCNC coupling strengths. The values of these couplings vanish at the lowest order in the SM. This study assumes that  $\lambda_q^L = \lambda_q^R = \lambda_q$  and  $\kappa_q^L = \kappa_q^R = \kappa_q$ . Top FCNC couplings as introduced in equation (5.17) would lead to the Feynman graphs shown in figure 72.

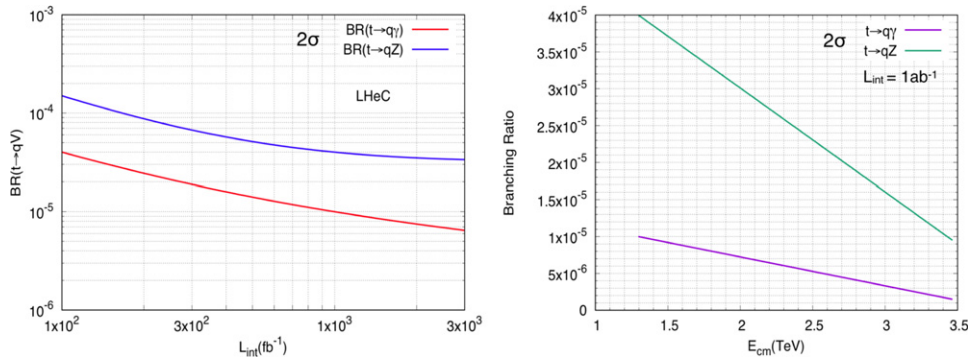


**Figure 73.** Expected sensitivities to FCNC  $t \rightarrow qV$  branching ratios (left) as a function of the integrated luminosity. Reproduced from [488]. CC BY 4.0. Right: the expected upper limits on FCNC  $t \rightarrow qV$  branching ratios are shown with their dependence on the centre-of-mass energy.

In an elaborate analysis, events are selected that include at least one electron and three jets from hadronic top quark decay, with high transverse momentum, and within the detector's pseudorapidity acceptance range. The invariant masses of two jets, reconstructing the  $W$  boson mass, and an additional jet tagged as the  $b$ -jet, are used to reconstruct the top quark mass. The respective distribution is used to further enhance the signal over background events, and is mainly given by  $W$ +jets production. Interference effects between the signal and the background are included. The DELPHES package [475] is used to simulate the detector.

Figure 73 (left) presents the expected limits on the branching ratios  $\text{BR}(t \rightarrow q\gamma)$  and  $\text{BR}(t \rightarrow qZ)$  at the  $2\sigma$  CL, as a function of the integrated luminosity. Assuming an integrated luminosity of  $1 \text{ ab}^{-1}$ , limits of  $\text{BR}(t \rightarrow q\gamma) < 1 \times 10^{-5}$  and  $\text{BR}(t \rightarrow qZ) < 4 \times 10^{-5}$  are expected. This level of precision is close to the concrete predictions of new phenomena models which have the potential to produce FCNC top quark couplings, such as SUSY, little Higgs, and technicolour. These limits are expected to improve on existing limits from the LHC by one order of magnitude [14], and will be similar to the limits expected from the HL-LHC with  $3000 \text{ fb}^{-1}$  [187]. They will also improve on the limits obtained from the International Linear Collider (ILC) with an integrated luminosity of  $500 \text{ fb}^{-1}$  at a centre-of-mass energy of  $\sqrt{s} = 250 \text{ GeV}$  [489, 490] by an order of magnitude (see also figure 75). The expected sensitivities to  $\text{BR}(t \rightarrow q\gamma)$  and  $\text{BR}(t \rightarrow qZ)$  are presented in figure 73 (right), as a function of the centre-of-mass energy. At a future FCC-ep [14] with a 60 GeV electron-beam energy, and a 50 TeV proton-beam energy, leading to a centre-of-mass energy of 3.5 TeV, the sensitivity to FCNC  $tq\gamma$  couplings is expected to exceed the sensitivity of the HL-LHC with  $3000 \text{ fb}^{-1}$  at  $\sqrt{s} = 14 \text{ TeV}$  [187].

A further search for top quark FCNC  $tuZ$  and  $tcZ$  couplings has been performed [491] in a detailed analysis including a DELPHES [475] detector simulation. The effective couplings investigated are of vector and tensor natures, the latter corresponding to those in equation (5.17). The effects of these couplings are probed in single top quark production (see figure 72 right). It can be observed that the polar angle  $\theta$  of the scattered initial-state electron, in association with top quark polarisation asymmetries constructed from angular distributions of the lepton from top quark decay, allow us to distinguish the Lorentz structure of the couplings. From a multiparameter analysis, reaches of the order of  $\mathcal{O}(10^{-2})$  in the case of vector couplings and  $0.1\text{--}0.5 \text{ TeV}^{-1}$  in the case of tensor couplings are obtained at the 95% CL for



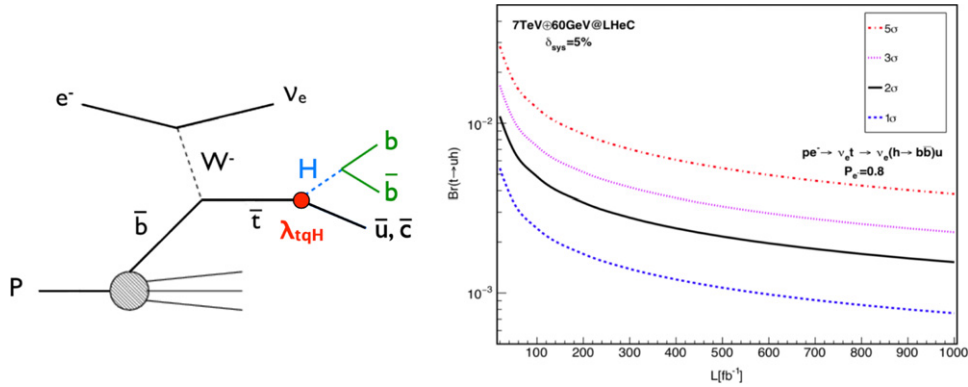


**Figure 74.** Example Feynman graph for associated single top quark and Higgs boson production via FCNC  $tqH$  couplings (left). Expected sensitivities to FCNC  $t \rightarrow uH$  branching ratios are given as a function of the integrated luminosity. Reproduced from [492]. CC BY 4.0. (right).

an integrated luminosity of  $2 \text{ ab}^{-1}$ . This corresponds to respective limits on the branching ratio  $\text{BR}(t \rightarrow uZ)$  of  $9 \times 10^{-5}$  ( $15 \times 10^{-5}$ ) for the left- (right-) handed vector coupling, and of  $4 \times 10^{-5}$  ( $6 \times 10^{-5}$ ) for the left- (right-) handed tensor coupling.

Another sensitive search for FCNC  $tqH$  couplings as defined in

$$\mathcal{L}_{\text{FCNC}} = \kappa_{uH} \bar{t}uH + \kappa_{cH} \bar{t}cH + \text{h.c.} \quad (5.18)$$

can be performed in CC DIS production, as shown in figure 74 (left). Here, singly produced top antiquarks can decay via such couplings into a light up-type antiquark and a Higgs boson which further decays into a bottom quark–antiquark pair,  $e^- p \rightarrow \nu_e \bar{t} \rightarrow \nu_e H \bar{q} \rightarrow \nu_e b \bar{b} \bar{q}$  [492]. Another signal process is given by the appearance of the FCNC  $tqH$  coupling in the production vertex, involving a light quark from the proton interacting via  $t$ -channel top quark exchange with a  $W$  boson which is radiated from the initial electron, producing a  $b$  quark and a Higgs boson decaying into a bottom quark–antiquark pair,  $e^- p \rightarrow \nu_e H b \rightarrow \nu_e b \bar{b}$  [492]. This channel has a similar sensitivity to that of the previous one because of the clean experimental environment that can be achieved by requiring three jets to be identified as  $b$ -jets. The most important backgrounds are expected to be  $Z \rightarrow b \bar{b}$ ,  $\text{SM } H \rightarrow b \bar{b}$ , and single top quark production, where the top quark decays hadronically. In order to account for the limited accuracy of the background yield calculations, 5% of systematic uncertainty is added. In this analysis, parameterisations for the resolutions of electrons, photons, muons, jets, and unclustered energy are applied utilizing typical parameter values as measured at the ATLAS experiment. Furthermore, it is assumed that the  $b$ -tag rate is 60%, the  $c$ -jet fake rate is 10%, and the light-jet fake rate is 1%. For the different signal contributions, separate selections are established and optimised. As a result, the expected upper limits on the branching ratio  $\text{Br}(t \rightarrow Hu)$  with  $1\sigma$ ,  $2\sigma$ ,  $3\sigma$ , and  $5\sigma$  CLs are presented in figure 74 (right), as functions of the integrated luminosity. The signal process  $e^- p \rightarrow \nu_e \bar{t} \rightarrow \nu_e H \bar{q} \rightarrow \nu_e b \bar{b}$  is presented. Upper limits of  $\text{Br}(t \rightarrow Hu) < 1.5 \times 10^{-3}$  are expected at the  $2\sigma$  CL for an integrated luminosity of  $1 \text{ ab}^{-1}$ .

In figure 75 the different expected limits on various FCNC top quark couplings from the LHeC are summarised and compared to results from the LHC and the HL-LHC. This documents the competitiveness of the LHeC results, and clearly shows the complementarity of the results gained at different colliders.



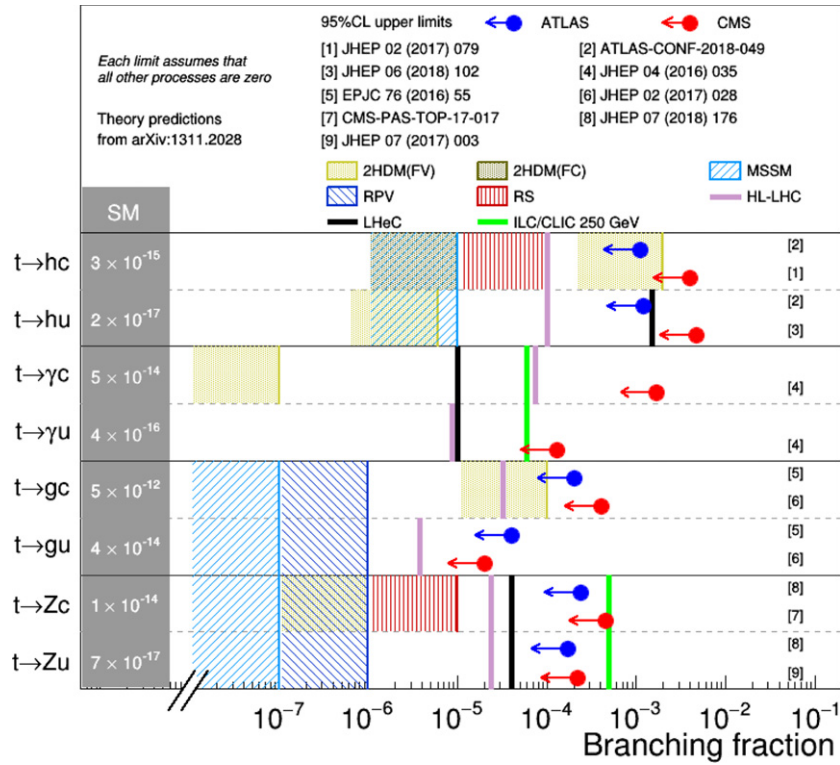


**Figure 75.** Summary of 95% CL limits on top quark branching fractions in searches for FCNC in top quark production or decays. The LHeC results (black lines) are compared to current LHC limits (blue and red dots), to HL-LHC predictions with  $3000 \text{ fb}^{-1}$  at  $\sqrt{s} = 14 \text{ TeV}$  [187] (magenta lines), and to predictions for a future ILC with  $500 \text{ fb}^{-1}$  at  $\sqrt{s} = 250 \text{ GeV}$  [489, 490] (green lines). The results are also compared to various theoretical predictions (hatched areas).

**5.3.7. Summary of top quark physics.** Top quark physics at the LHeC represents a very rich and diverse field of research involving high-precision measurements of top quark properties and sensitive searches for new physics. In particular, the top couplings to the photon, the  $W$  boson and possible FCNC interactions can be studied in a uniquely clean environment. One signature analysis is the expected direct measurement of the CKM matrix element  $|V_{tb}|$  with a precision of less than 1% in CC DIS. In top quark pair photoproduction the MDMs and EDMs of the top quark can be directly probed with a higher sensitivity than the indirect limits from  $b \rightarrow s\gamma$  and the potential limits from the LHC through  $t\bar{t}\gamma$  production. Furthermore, FCNC top quark couplings can be studied with a precision high enough to explore those couplings in a regime that might be affected by actual new phenomena models, such as SUSY, little Higgs, and technicolour.

It has been shown [14] that results from future  $e^+e^-$ -colliders,  $eh$ -colliders, and  $hh$ -colliders will deliver complementary information and will therefore give us a more complete understanding of the properties of the heaviest elementary particle known to date, and of the top quark sector in general.

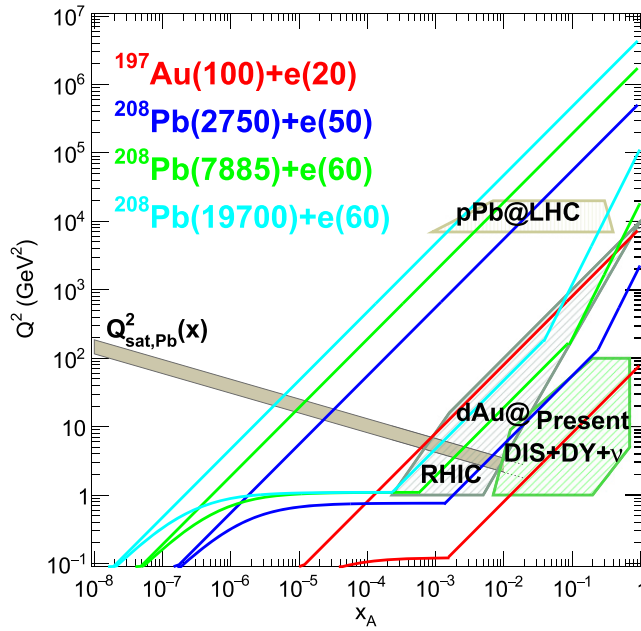


**Figure 76.** Kinematic regions in the  $x$ - $Q^2$  plane explored by different data sets (charged lepton and neutrino DIS, DY,  $d$ Au at RHIC and  $p$ Pb at the LHC) used in recent nPDF analyses [503], compared to the regions accessible at the EIC (red), the LHeC (ERL against the HL-LHC beams, dark blue) and two FCC-eh versions (with Pb beams corresponding to proton energies of  $E_p = 20$  TeV—green and  $E_p = 50$  TeV—light blue). The acceptance of the electron detector is taken to be  $1^\circ < \theta < 179^\circ$ , and  $0.01(0.001) < y < 1$  for the EIC (all other colliders). The saturation scale  $Q_{\text{sat}}$  shown here for indicative purposes only (see also [504]) has been drawn for a Pb nucleus, considering an uncertainty of  $\sim 2$  and a behaviour with energy that follows the model in [505]. Note that it only indicates a region where saturation effects are expected to be important, but there is no sharp transition between the linear and nonlinear regimes.

## 6. Nuclear particle physics with electron–ion scattering at the LHeC

### 6.1. Introduction

The LHeC accelerator, in addition to being a powerful machine for exploring proton structure, will, for the first time, allow studies of DIS off nuclei in a collider mode at the energy frontier. The nuclear structure has previously been studied in fixed-target experiments with charged lepton and neutrino beams, see [69–71, 493–502] and references therein. Due to the energy limitations of the machines operating in this mode, the kinematic range covered by these experiments is rather narrow, and is mostly limited to relatively large values of  $x \geq 0.01$  and low to moderate  $Q^2$  in the range  $Q^2 < 100$  GeV<sup>2</sup>. The precise kinematic range covered by experiments is shown in figure 76, where it can be seen that the DIS experiments overlap to a large degree with the data from hadronic collisions using the DY process. These fixed-target DIS and DY data dominate the data sets used in the fits for the nuclear PDFs. In addition, some analyses of nuclear PDFs include data for inclusive single-hadron production in  $d$ Au collisions at RHIC and for EW bosons and dijets in  $p$ Pb collisions at the LHC.

As is clear from figure 76, the LHeC will be able to cover a very large range of  $(x, Q^2)$  in  $eA$  that has previously been unexplored in experiments. It will extend the range of  $x$  down to  $\sim 10^{-6}$  and have a huge lever arm in  $Q^2$  from very low values up to  $\sim 10^6$  GeV<sup>2</sup>. It will also be complementary to the EIC [101] machine, compared to which, it will extend the range of  $x$  and  $Q^2$  by about two orders of magnitude. The extension of these ranges will be even larger at the FCC-eh.

Due to its large statistics and modern, specialised detectors, it will be possible to study nuclear structure at the LHeC with unprecedented precision, over a far wider kinematical range than was previously possible, and with the controlled systematics of a single experiment. There are a large number of important physics topics that can be addressed in  $eA$  collisions at the LHeC:

- A precise determination of nuclear parton densities for a single nucleus (lead, and eventually lighter ions) will be possible. In particular, the current huge uncertainties in nuclear gluon and sea quark densities at low  $x$  will be dramatically improved using the data from the LHeC. In analogy to the proton PDF extraction described in previous sections, full flavour decomposition in the nuclear case could be achieved using both NC and CC data with HF identification.
- Precision measurements of semi-inclusive and exclusive processes will enable an exploration of new details of the nuclear structure. Similarly to the proton case, DVCS and exclusive vector-meson production will provide unique insight into 3D nuclear structure.
- The LHeC will offer unprecedented opportunities to extract diffractive parton densities in nuclei for the first time. A first detailed analysis [346] indicates that the achievable precision for diffractive PDFs in nuclei will be comparable to that possible in the proton case. The measurements of diffraction of protons and nuclei as well as the inclusive structure functions in the nuclear case will allow us to explore the very important relation between nuclear shadowing and diffraction [344].
- The LHeC will be able to test and establish or exclude the phenomenon of parton saturation at low  $x$  in protons and nuclei. According to the Color Glass Condensate (CGC) framework [506, 507], parton saturation is a density effect that can be achieved in two ways, either by decreasing the value of  $x$  or by increasing the size of the target by increasing  $A$ . The LHeC will be a unique machine with which to address both of their variations, such that the saturation concepts can be precisely tested. It will be possible to search for parton saturation in a variety of ways, which include, among others, the search for tensions in DGLAP fits, the study of diffraction—in particular, the ratios of diffractive to inclusive cross-sections, and the study of particle azimuthal de-correlations.
- Finally, the LHeC machine in  $eA$  mode will have a huge impact on physics explored in  $pA$  and  $AA$  collisions, see section 9.7, where it will provide vital input and constraints on the ‘baseline’ initial state in nuclear collisions and measurements of the impact of a cold nuclear medium on hard probes and the effects of hadronisation. It will also explore the effect of the initial-state correlations on the final-state observables, which are relevant in order to understand collectivity in small systems explored in  $pp$  or  $pA$  collisions.

As discussed below, these aims will require an experimental apparatus with large rapidity coverage and associated forward and backward electron, photon, hadron, and nuclear detectors. In addition, the detector design should allow the precise measurement of diffractive events in  $eA$  and the clean separation of radiative events, which are most important for the cases of DVCS and exclusive diffraction.

Photonuclear interactions at high energies can also be studied through UPCs at the RHIC and the LHC [129, 130, 316, 508], which offer an alternative, albeit with less precision. This is briefly discussed in section 9, where the relation between the LHeC and the HL-LHC is presented.

In this chapter we do not address the issues of the nuclear modification of jet yields and fragmentation, which are expected to show dramatic effects and to be of great importance for heavy-ion collisions. These aspects were previously discussed in reference [1]. Besides, electron–deuteron collisions that offer additional possibilities for determining proton and neutron parton densities and for studying weak interactions with neutron targets at high energies are not considered here; see reference [1], where an analysis of parton densities in  $eD$  collisions can be found.

## 6.2. Nuclear parton densities

PDFs are essential ingredients in our understanding of the dynamics of the strong interaction. First, they encode important information about the structure of hadrons [509, 510]. Second, they are indispensable for the description of hadronic collisions within standard collinear factorisation [39]. Concerning nuclei, it has been known for more than 40 years that structure functions are strongly affected by the nuclear environment [501, 502], so that they cannot be interpreted as a simple superposition of the structure functions of free nucleons. In the standard approach, within collinear factorization, the nuclear modification is included in the parametrisation of the parton densities. This means that the parton densities in a bound nucleon are different from those in a free nucleon, and the difference is encoded in the non-perturbative initial conditions of the parton densities at some low, initial scale  $Q_0^2$ . The present status of nuclear parton densities (nPDFs), see, for example [511, 512], can be summarised as follows:

- Modern analyses [503, 513–515] are performed at the next-to-leading order (NLO) and the next-to-next-to-leading order (NNLO) [516, 517]. Differences between the different groups mainly arise from the different sets of data included in the analyses<sup>184</sup> and from the different functional forms employed for the initial conditions.
- Many sets of data are presented as cross-section ratios for a given nucleus to that of deuterium, which is loosely bound and isoscalar. Therefore, it has become customary to work in terms of ratios of nPDFs:

$$R_i(x, Q^2) = \frac{f_i^A(x, Q^2)}{A f_i^p(x, Q^2)}, \quad i = u, d, s, c, b, g, \dots, \quad (6.1)$$

where  $f_i^{p(A)}(x, Q^2)$  is the corresponding parton density in a free proton  $p$  or a nucleus  $A$ . These nuclear modification factors are parametrised at the initial scale  $Q_0^2$  (assuming that isospin symmetry holds). The nPDFs are then obtained by multiplying the nuclear modification factors by some given set of free-proton PDFs.

- The available data come from a large variety of nuclei, and the number of data points for any of them is individually very small compared to the numbers for the proton analyses. In particular, for the Pb nucleus, there are less than 50 points that originate from the fixed-target DIS and DY experiments and from particle production data in  $pPb$  collisions at

<sup>184</sup>The main difference lies in the use or non-use of neutrino-Pb cross-sections (whose usage has been controversial [518–520]), particularly the data from the NuTeV experiment [170]) from the CHORUS experiment and the  $\pi^{0,\pm}$  transverse-momentum spectra from  $dAu$  collisions at the relativistic heavy-ion collider (RHIC).

the LHC. A fit for a single nucleus is therefore impossible, and the modelling of the  $A$ -dependence of the parameters in the initial conditions becomes necessary [503, 515]. The most up-to-date analyses include between 1000 and 2000 data points for 14 nuclei.

- The kinematic coverage in  $Q^2$  and  $x$  with existing data is very small compared to that of future hadronic colliders. The ultimate precision and large coverage of the kinematic plane for nPDFs can only be provided by a high-energy electron–ion collider. Meanwhile, the only experimental collision systems in which nPDFs can currently be constrained are hadronic and UPCs. It is important to stress that extracting PDFs from these collisions presents many theoretical challenges. These are related to the question of the applicability of collinear factorization to nuclear collisions, higher twist effects, scale choices, and other theoretical uncertainties.

All parton species are very weakly constrained at small  $x < 10^{-2}$  [521], gluons are poorly known at large  $x > 0.2$ , and the flavour decomposition is largely unknown—a natural situation for  $u$  and  $d$ , due to the approximate isospin symmetry in nuclei<sup>185</sup>. The impact of the currently available LHC data, studied using reweighting [256, 522] in [523, 524] and included in the fit in [503], is quite modest, and imposes some constraints on the gluon and the strange quark in the region  $0.01 < x < 0.3$ . On the other hand, theoretical predictions for the nuclear shadowing of quark and gluon PDFs based on  $s$ -channel unitarity and diffractive nucleon PDFs are available down to  $x \sim 10^{-4}$  to  $10^{-5}$  [344, 525–527]. Predictions of the flavour dependence of nuclear effects in the antishadowing region [528] cannot be confirmed with present data.

Future runs at the LHC will offer some further possibilities for improving our knowledge of nPDFs [508]. However, the ideal place to determine parton densities is DIS, either at the EIC [101] in the USA or, in a much larger kinematic domain (see figure 76), at the LHeC. DIS measurements in such configurations offer unprecedented possibilities to enlarge our knowledge of parton densities through a complete unfolding of all flavours.

In the following, we show the possibilities for constraining the PDFs for a Pb nucleus at the LHeC. In the next subsection, subsection 6.2.1, we discuss the corresponding pseudodata for the inclusive cross-section in electron–nucleus scattering. Then, in subsection 6.2.2 we discuss how the pseudodata will be introduced into a global nPDF fit. Finally, in subsection 6.2.3 it is demonstrated how the PDFs of Pb can be extracted with very good precision from the LHeC data only, without requiring any other set of data.

**6.2.1. Pseudodata.**  $eA$  scattering at the LHeC provides measurements of inclusive neutral and CC cross-sections in the DIS region of  $1 < Q^2 < 5 \times 10^5 \text{ GeV}^2$  and at  $x$  values from a few times  $10^{-6}$  to near  $x = 1$ ; see reference [63], which contains the material that is summarised in this subsection. Achieving  $Q^2$  much larger than the  $W$ -boson mass squared CC measurements, together with the NC contributions from photon and  $Z$ -boson exchanges, will be most important for flavour separation. In CC, charm tagging will determine the anti-strange quark contribution to an accuracy of 10%–20%. In NC, charm and beauty tagging will precisely constrain nuclear  $xc$  and  $xb$ . The use of data from a single experiment will allow nPDF uncertainties to follow from a straightforward  $\Delta\chi^2 = 1$  criterion. As often emphasised, knowledge of heavy quark densities is of key importance for our understanding of nuclear structure and for the development of QCD.

The following QCD analyses of LHeC cross-section pseudodata employ sets of simulated NC and CC measurements. The corresponding assumptions about precision are summarised in table 13, see reference [63]. The cross-section simulations were performed using derivative

<sup>185</sup> The  $u$ – $d$  difference is suppressed by a factor of  $2Z/A - 1$ .

**Table 13.** Summary of assumed systematic uncertainties for future inclusive cross-section measurements at the LHeC. Reproduced from [63]. CC BY 4.0.

Source of uncertainty	Error in the source or cross-section
Scattered electron energy scale	0.1%
Scattered electron polar angle	0.1 mrad
Hadronic energy scale	0.5%
Calorimeter noise ( $y < 0.01$ )	1%–3%
Radiative corrections	1%–2%
Photoproduction background	1%
Global efficiency error	0.7%

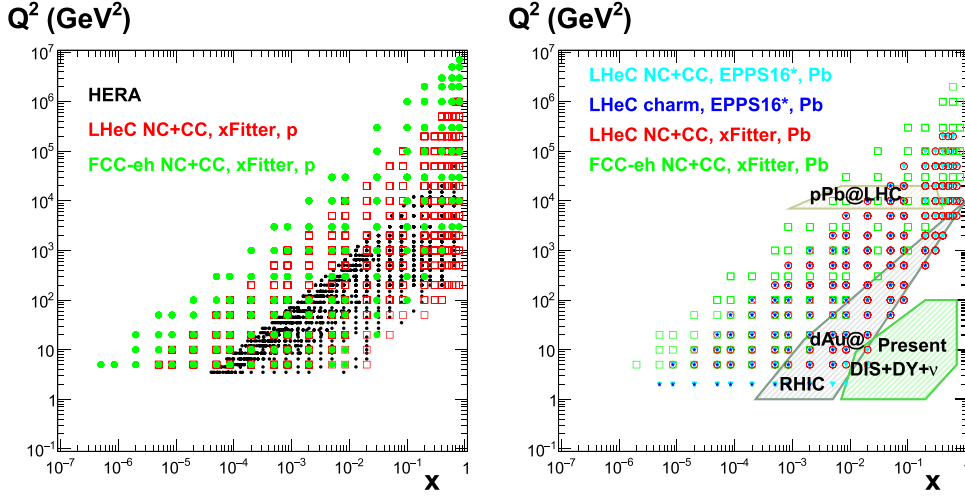
formulae from [58]. They compare well to detailed MC simulations performed using the conditions of the H1 experiment. The assumptions made, which are reasonable when compared to the H1 achievements, leave room for further improvement if new detector techniques and higher statistics are to be considered. A particular challenge is the control of radiative corrections, which grow according to  $\propto Z^2$  in  $eA$  scattering. Therefore, the LHeC detector should be equipped with photon detectors. The exploitation of energy–momentum conservation via  $E-p_z$  cuts should further reduce the effect of photon radiation to the few per cent level. Note that semi-inclusive measurements of the  $s$ ,  $c$ , and  $b$  quark distributions contain further uncertainties corresponding to tagging, acceptance, and background influences.

Figure 77 illustrates the kinematic reach of the NC and CC pseudodata at the LHeC and the FCC-eh in  $ep$  and  $ePb$  collisions (for per-nucleon integrated luminosities of  $\leq 1$  and  $10 \text{ fb}^{-1}$ , respectively). In addition to the inclusive data, semi-inclusive measurements with flavour sensitivity are also included. A determination of the strange, charm, beauty, and even top PDFs will thus become possible. The main techniques required for flavour studies are charm (in CC for  $xs$ , in NC for  $xc$ ) and beauty tagging (in NC for  $xb$ ), for which the following considerations are in order, see reference [63]. The transverse extension of the LHeC beam spot is about  $(7 \mu\text{m})^2$ . The typical decay lengths of charm and beauty particles are hundreds of  $\mu\text{m}$ , compared with resolutions of a few microns for modern Si detectors. The experimental challenges are therefore the forward tagging acceptance, which is similar to the situation at the HL-LHC, and the beam pipe radius, which, at the LHeC, will have to cope with strong synchrotron radiation effects.

A study was made [63] of the possibilities of measuring the nuclear anti-strange density (see figure 78) through impact parameter tagging in  $eA$  CC scattering and of measuring the charm and beauty cross-sections in NC (see figure 79). The charm and beauty tagging efficiencies were assumed to be 10% and 60%, respectively, following experience of HF tagging at HERA and ATLAS. The degrees of control of the light quark background in the charm analysis and of the charm background in the beauty tagging sample were assumed to be 1 and 10%, respectively. Tagging efficiencies and background contaminations affect the statistical error. Besides, additional systematic errors of 3(5)% were assumed in the simulated NC (CC) measurements. These assumptions resulted in very promising measurements of the heavier quark distributions, to about 10%–20% (3%–5%) of total uncertainty for the strange (charm and beauty) measurements, for  $10^{-4} < x < 0.1$  and  $Q^2$  extending from below the threshold  $m_Q^2$  up to a few times  $10^4 \text{ GeV}^2$ .

**6.2.2. Nuclear gluon PDFs in a global-fit context.** To illustrate the impact of the LHeC  $ePb$  pseudodata in the global context, they were added [529] into the EPPS16 global analysis of nuclear PDFs [503]. The EPPS16 strategy is to parametrise the nuclear modification ratios





**Figure 77.** Left: kinematic  $x-Q^2$  plot of the NC and CC pseudodata for a proton at the LHeC (red symbols) and the FCC-eh (green symbols) used in the  $xFitter$  analysis in section 6.2.3; data used in analysis at HERA (black symbols) are shown for comparison. Right: kinematic  $x-Q^2$  plot of the pseudodata for Pb used in the EPPS16 analysis at the LHeC (NC and CC (light blue symbols); charm (dark blue symbols)) in section 6.2.2, and in the  $xFitter$  analysis in subsection 6.2.3 (at the LHeC (red symbols); at the FCC-eh (green symbols)); the regions explored by currently available data sets (charged lepton and neutrino DIS, DY,  $dAu$  at RHIC, and  $pPb$  at the LHC) used in recent nPDF analyses [503] are shown for comparison.

$R_i(x, Q^2)$  between the bound-proton PDFs  $f_i^{p/Pb}$  and the proton PDFs  $f_i^p$ ,

$$R_i(x, Q^2) \equiv \frac{f_i^{p/Pb}(x, Q^2)}{f_i^p(x, Q^2)}, \quad (6.2)$$

at the charm mass threshold  $Q^2 = m_{\text{charm}}^2 = (1.3 \text{ GeV})^2$ . At higher values of  $Q^2$  the nuclear PDFs are obtained by solving the standard DGLAP evolution equations at the next-to-leading order in QCD. As the LHeC pseudodata reach significantly lower  $x$  values than the data that were used in the EPPS16 analysis, an extended small- $x$  parametrisation was used for gluons, see figure 80. The framework used is almost identical to that of reference [530]. The functional form introduced allows for rather wild—arguably unphysical—behaviour at small  $x$ , where e.g. significant enhancement is allowed. This is contrary to the theoretical expectations of the saturation conjecture and also appears to be an improbable scenario, given the recent D and B meson measurements by the LHCb Collaboration [531, 532] which impressively indicate [533] gluon shadowing down to  $x \sim 10^{-5}$  at interaction scales as low as  $Q^2 \sim m_{\text{charm}}^2$ . On the other hand, given that there are no prior DIS measurements in this kinematic range for nuclei other than the proton, and that the D and B meson production in  $pPb$  collisions could be affected by strong final-state effects (which could eventually be resolved by e.g. measurements of forward prompt photons [534] in  $pPb$ ), we hypothesise that any kind of behaviour is possible at this stage. Anyway, with the extended parametrisation—called EPPS16\* here—the uncertainties in the small- $x$  regime become significantly larger than in the standard EPPS16 set. This is reflected by significantly larger PDF error bands, in comparison to the projected LHeC pseudodata. These are shown in figure 81 where the EPPS16\* predictions are compared

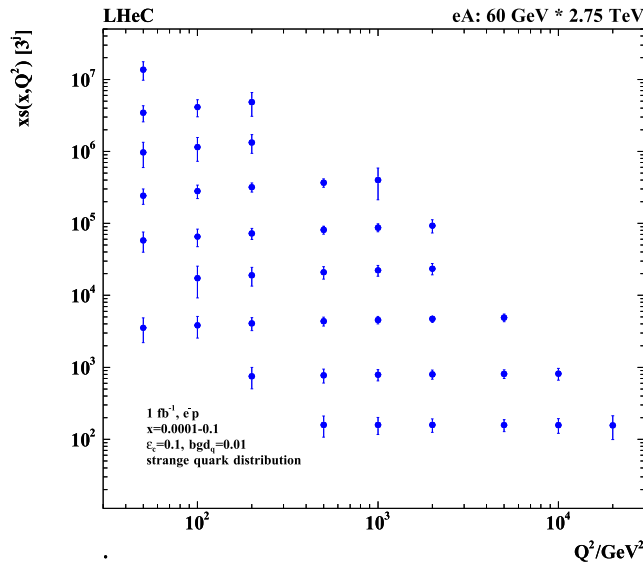


**Figure 78.** Simulation of the measurement of the (anti)-strange quark distribution  $x\bar{s}(x, Q^2)$  in CC  $eA$  scattering through the  $t$ -channel reaction  $W^- \bar{s} \rightarrow c$ . The data are plotted with full systematic and statistical errors added in quadrature. Reproduced from [63]. CC BY 4.0.

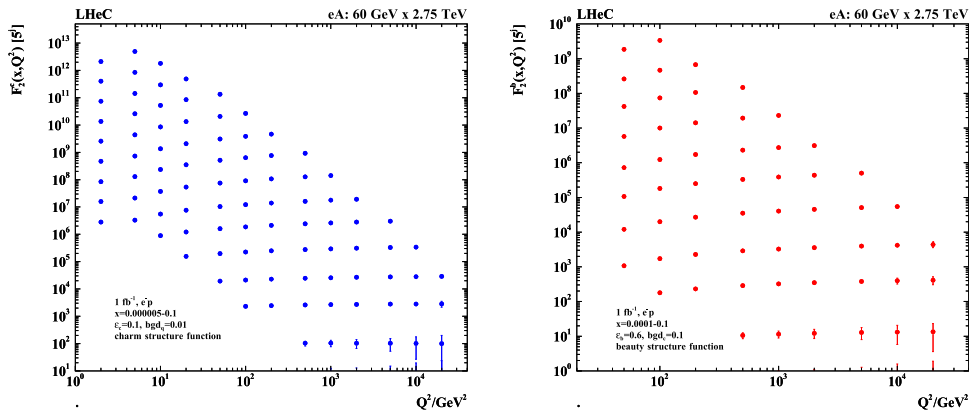


**Figure 79.** Left: simulation of the measurement of the charm quark distribution expressed by  $F_2^c = e_c^2 x(c + \bar{c})$  in neutral current  $eA$  scattering; right: simulation of the measurement of the bottom quark distribution expressed by  $F_2^b = e_b^2 x(b + \bar{b})$  in neutral current  $eA$  scattering. The data are plotted with full systematic and statistical errors added in quadrature. Reproduced from [63]. CC BY 4.0.

with the LHeC pseudodata for inclusive NC and CC reactions, as well as charm production in neutral-current scattering. The uncertainties are estimated using the Hessian method [535], and the same overall tolerance  $\Delta\chi^2 = 52$  as in the EPPS16 analysis is used when defining the error bands. Because there are no small- $x$  data constraints for gluons, the gluon uncertainty is enormous, and since the Hessian method used to estimate the uncertainties is not particularly

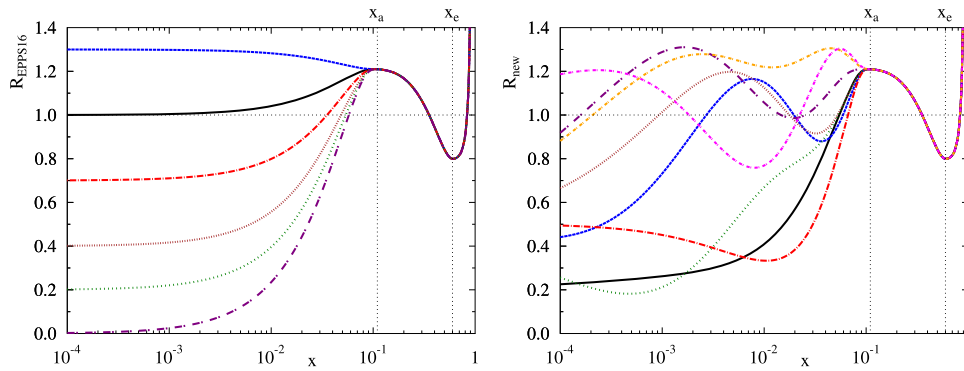


**Figure 80.** Left: illustration of the functional behaviours allowed at small  $x$  in the EPPS16 analysis. Right: illustration of the possible functional variations at small  $x$  in the extended parametrisation that we employ here.

accurate, the true  $\Delta\chi^2 = 52$  error bands are likely to be even larger. At some point, the downward uncertainty will be limited by positivity constraints e.g. for  $F_L$ , but will depend strongly on which  $Q^2$  is used to set the positivity constraints (e.g. in the EPPS16 analysis,  $F_L$  is required to remain positive at  $Q^2 = m_{\text{charm}}^2$ ).

After the LHeC  $e\text{Pb}$  pseudodata are included in the fit, the new nPDFs adapt by reproducing the pseudodata, and their uncertainties are greatly reduced, as shown in figure 82. The overall tolerance has been kept fixed at the default value  $\Delta\chi^2 = 52$ . The impact on the nuclear modification of the gluon PDF is illustrated in figure 83 at two values of  $Q^2$ :  $Q^2 = 1.69 \text{ GeV}^2$  (the parametrisation scale) and  $Q^2 = 10 \text{ GeV}^2$ . The inclusive pseudodata are already able to reduce the small- $x$  gluon uncertainty quite significantly, and the addition of the charm data promises an even more dramatic reduction in the errors. The analysis indicates that the LHeC will pin down the nuclear gluon PDF to a high precision, down to an  $x$  value of at least  $10^{-5}$ .

**6.2.3. nPDFs from DIS on a single nucleus.** Another approach that becomes possible with the large kinematic coverage and volume of data for a single nucleus, Pb, at the LHeC and FCC-eh, is to perform a fit to Pb data only, in order to extract the Pb PDFs, thus removing the need to interpolate between different nuclei. The corresponding ratios or nuclear modification factors for each parton species can then be obtained using either a proton PDF set from a global fit or, as we do here (see [14, 536, 537]), from a fit to proton LHeC and FCC-eh pseudodata. In this way, there will be no need to introduce a nuclear size dependence in the parameters for the initial condition for DGLAP evolution. Such nPDFs can then be used in a comparison to those obtained from global fits and for precision tests of collinear factorisation in nuclear collisions.

The fits are performed using *xFitter* [538], in which 484 (150) NC and CC Pb data points at the LHeC (FCC-eh) were used in the fitted region  $Q^2 > 3.5 \text{ GeV}^2$ , see figure 77. A HERAPDF2.0-type parametrisation [45] was employed to provide both the central values for the reduced cross-sections (therefore, the extracted nuclear modification factors are centred at 1) and the fit functional form; in this way, neither theoretical uncertainties (the treatment of

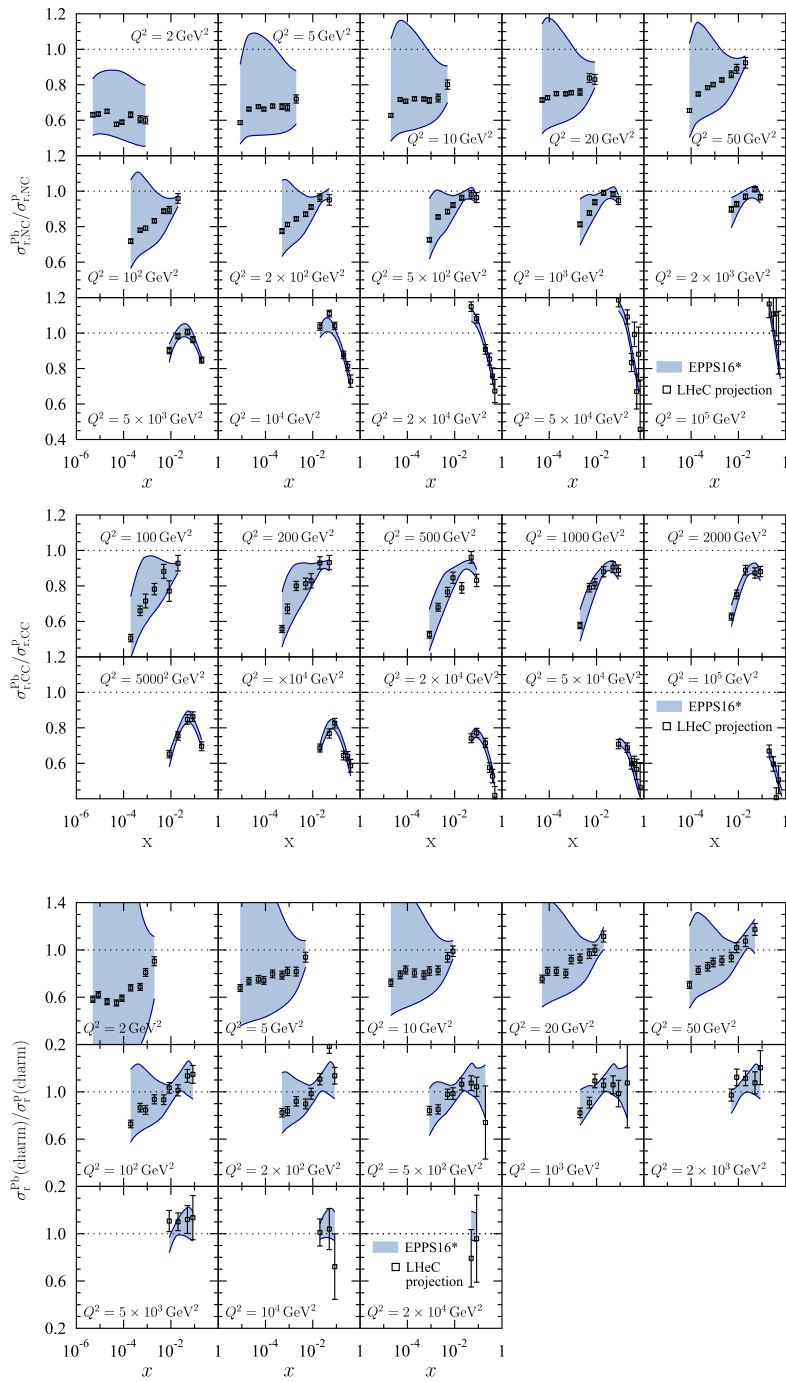


**Figure 81.** Top: simulated ratios of neutral-current reduced cross-sections between  $e\text{Pb}$  and  $ep$  collisions compared with the predictions from a EPPS16-type global fit of nuclear PDFs using an extended parametrisation for gluons. Middle: charged-current cross-section ratios. Bottom: neutral-current charm-production cross-section ratios.

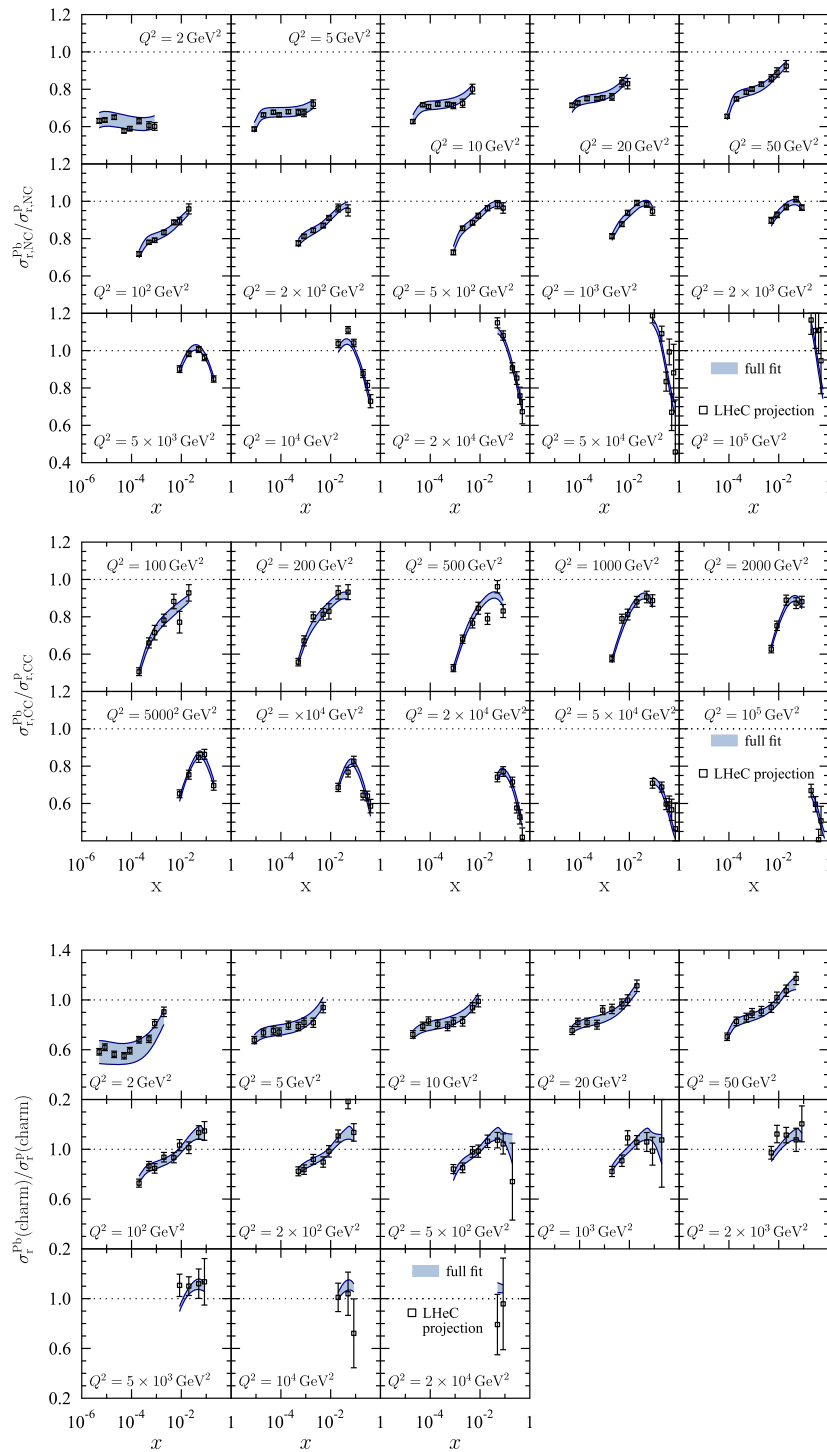


**Figure 82.** The same as figure 81 but with fit results obtained after the LHeC pseudodata are included in the global analysis.

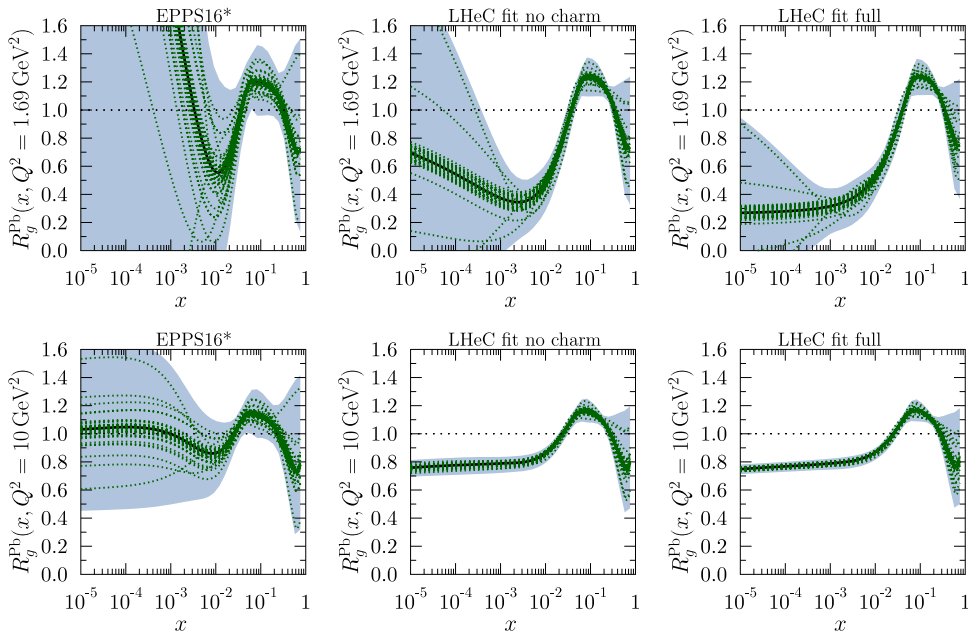


**Figure 83.** Upper panels: the gluon nuclear modification for the Pb nucleus at  $Q^2 = 1.69 \text{ GeV}^2$  in EPPS16\* (left), LHeC analysis without charm pseudodata (middle), and full LHeC analysis (right). The blue bands mark the total uncertainty and the green dotted curves correspond to individual Hessian error sets. Lower panels: the same as the upper panels but for  $Q^2 = 10 \text{ GeV}^2$ . Reproduced with permission from [529].

HFs, the value of  $\alpha_s$ , order in the perturbative expansion) nor the uncertainty related to the functional form of the initial condition—parametrisation bias—are considered in our study, in agreement with our goal of estimating the *ultimate achievable experimental* precision in the extraction of nPDFs. We worked at the NNLO using the Roberts-Thorne improved heavy quark scheme and  $\alpha_s(m_Z^2) = 0.118$ . The treatment of systematics and the tolerance  $\Delta\chi^2 = 1$  are identical to the approach used in the HERAPDF2.0 fits, and are achievable in a single experiment.

The results for the relative uncertainties in the nuclear modification factors are shown in figures 84–86 for valence quarks, sea quarks, and gluons, respectively. The uncertainties in these plots reflect the assumed uncertainties in the pseudodata, both statistical (mainly at large  $x$ ) and systematics from detector efficiencies, radiative corrections, etc., see section 6.2.1. As expected, the uncertainty in the extraction of the valence quark at small  $x$  is sizeably larger than those for the sea quark and the gluon.

While a very high precision appears achievable at the LHeC and the FCC-eh, in a comparison with EPPS16 (or any other global fit) shown in the plots and with previous results including LHeC pseudodata in that setup, see section 6.2.2 and [529, 530], some caution is required. First, the effective EPPS16 tolerance criterion  $\Delta\chi^2 \simeq 52$  implies that, naively, the uncertainty bands should be compared after rescaling them by a factor of  $\sqrt{52}$ . Second, the treatment of systematics is rather different, considering correlations in the *xFitter* exercise and taking them as fully uncorrelated (and added quadratically to the statistical ones) in the EPPS16 approach. Finally, EPPS16 uses parametrisations for the nuclear modification factors for different parton species, while in *xFitter*, just the (n)PDF combinations that enter the reduced cross-sections



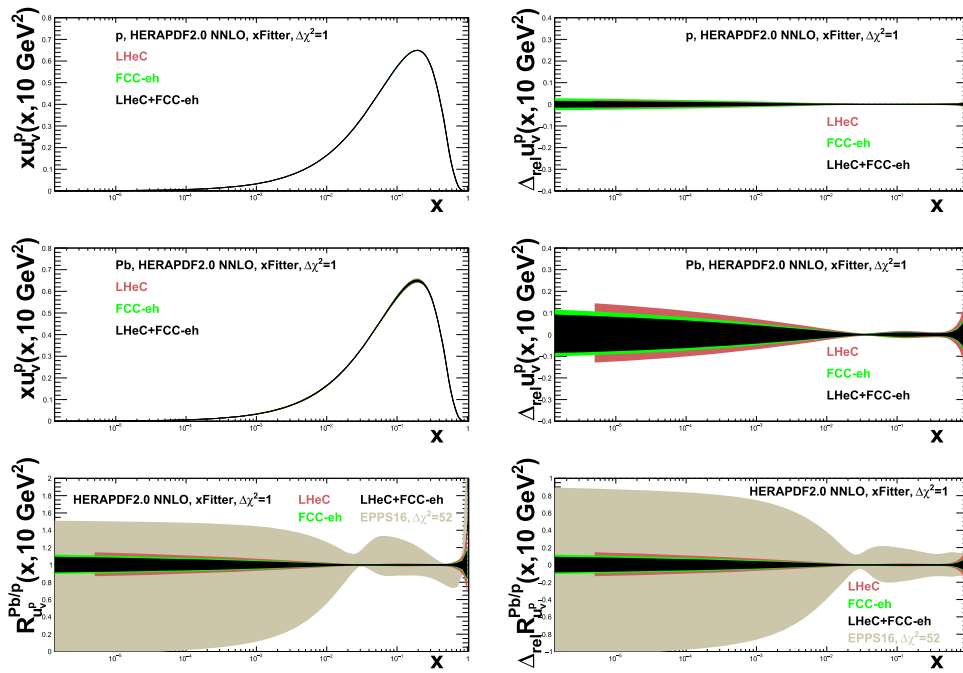


**Figure 84.** Distributions (left) and their relative uncertainties (right) of the valence  $u$ -quark density in the proton (top), Pb (middle), and the corresponding nuclear modification factor (bottom) in an analysis of  $ep$  and  $ePb$  LHeC and FCC-eh NC plus CC pseudodata using  $xFitter$  (for both a single set of data and all data combined), compared to the results of EPPS16 [503]; see the text for details.

are parametrised and employed for the fit<sup>186</sup>. With all these considerations in mind, the results shown in this section are fully compatible with those in the previous one.

### 6.3. Nuclear diffraction

In section 3.4 we discussed specific processes which will probe the details of the 3D structure of the proton. The same processes can be studied in the context of electron–ion scattering and used to learn about the partonic structure of nuclei. Inclusive diffraction on nuclei can provide important information about the nuclear diffractive parton distribution, similarly to the diffraction on the proton, see section 4.3. Diffractive vector meson production can be studied in the nuclear case as well, e.g. within the framework of the dipole model, which is suitable for high energies and includes nonlinear effects in density. In the nuclear case, though, one needs to make a distinction between coherent and incoherent diffraction. In the coherent process, the nucleus scatters elastically and stays intact after the collision. In incoherent diffraction, the nucleus breaks up, and individual nucleons can be set free. Still, there is a large rapidity gap between the diffractive system produced and the dissociated nucleus. It is expected that this

<sup>186</sup> In this respect, let us note that, by analogy to proton PDFs, a full flavour decomposition can be achieved using both NC and CC with HF identification, which will verify existing ideas about the flavour dependence of nuclear effects on parton densities [528].

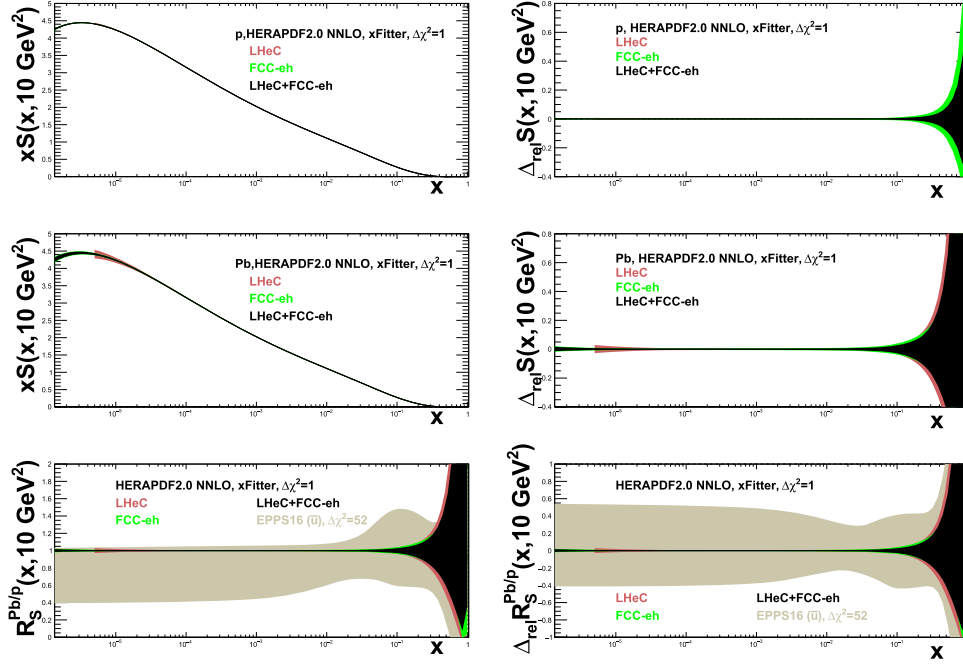


**Figure 85.** Distributions (left) and their relative uncertainties (right) of the sea quark density in the proton (top), Pb (middle), and the corresponding nuclear modification factor (bottom) in an analysis of  $ep$  and  $ePb$  LHeC and FCC-eh NC plus CC pseudodata using  $xFitter$  (for both a single set of data and all data combined), compared to the results of EPPS16 [503] for  $\bar{u}$ , see the text for details.

process will dominate the diffractive cross-section for medium and large values of momentum transfer. Only in the region of small values of momentum transfer is elastic diffraction the dominant contribution. Dedicated instrumentation must be constructed in the forward region in order to clearly distinguish between the two scenarios, see section 10.

**6.3.1. Exclusive vector meson diffraction.** Calculations for the case of Pb for coherent diffractive  $J/\psi$  production were performed using the dipole model [124], see section 3.4. In order to apply the dipole model calculation to the nuclear case, one takes the independent scattering approximation described by Glauber theory [539]. The dipole amplitude can then be represented in the form

$$N_A(x, \mathbf{r}, \mathbf{b}) = 1 - \prod_{i=1}^A [1 - N(x, \mathbf{r}, \mathbf{b} - \mathbf{b}_i)]. \quad (6.3)$$

Here,  $N(x, \mathbf{r}, \mathbf{b} - \mathbf{b}_i)$  is the dipole amplitude for the nucleon (see section 3.4) and  $\mathbf{b}_i$  denotes the transverse positions of the nucleons in the nucleus. The interpretation of equation (6.3) is that  $1 - N$  is the probability that scattering from an individual nucleon does not occur, and thus  $\prod_{i=1}^A [1 - N(\mathbf{r}, \mathbf{b} - \mathbf{b}_i, x)]$  is the probability that scattering does not occur from the entire nucleus.

In addition, the following simulation includes the fluctuations of the density profile in the proton, following the prescription given in [122–124]. To include these proton structure fluctuations, one assumes that the gluonic density of the proton in the transverse plane is distributed

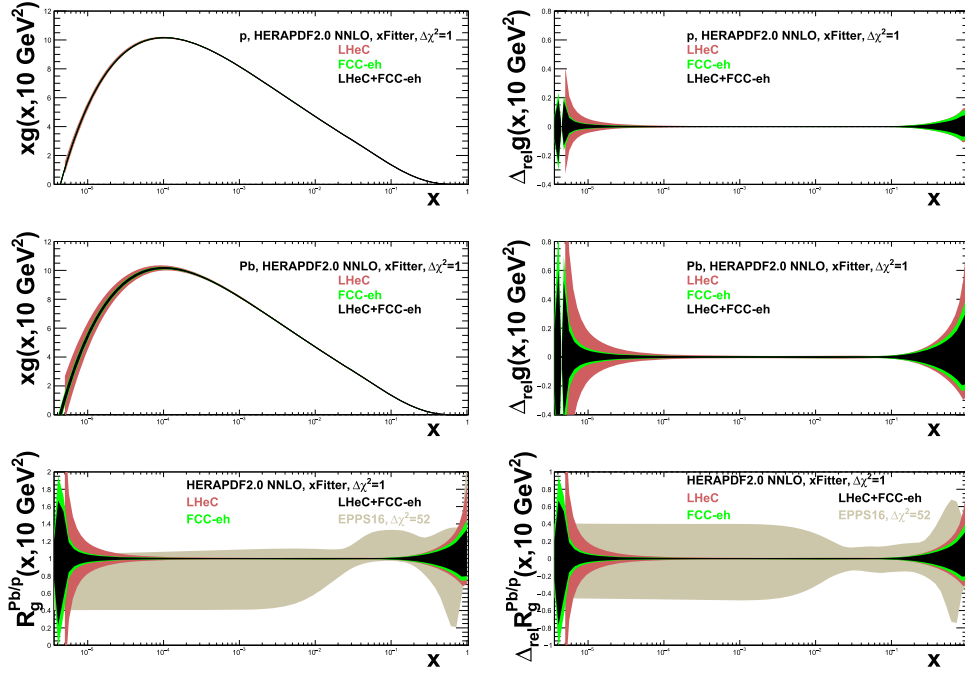


**Figure 86.** Distributions (left) and their relative uncertainties (right) of the gluon density in the proton (top), Pb (middle), and the corresponding nuclear modification factor (bottom) in an analysis of  $ep$  and  $ePb$  LHeC and FCC-eh NC plus CC pseudodata using  $xFitter$  (both a single set of data and all combined), compared to the results of EPPS16 [503], see the text for details.

around three constituent quarks (hot spots). These hot spots are assumed to be Gaussian. In practical terms one replaces the proton profile  $T_p(\mathbf{b})$

$$T_p(\mathbf{b}) = \frac{1}{2\pi B_p} e^{-b^2/(2B_p)}, \quad (6.4)$$

that appears in each individual nucleon scattering probability  $N(x, \mathbf{r}, \mathbf{b} - \mathbf{b}_i)$  with the function

$$T_p(\mathbf{b}) = \sum_{i=1}^3 T_q(\mathbf{b} - \mathbf{b}_{q,i}), \quad (6.5)$$

where the ‘quark’ density profile is given by

$$T_q(\mathbf{b}) = \frac{1}{2\pi B_q} e^{-b^2/(2B_q)}. \quad (6.6)$$

Here,  $\mathbf{b}_{q,i}$  are the locations of the hotspots that are sampled from a two-dimensional Gaussian distribution whose width is given by the parameter  $B_{qc}$ . The free parameters  $B_q$  and  $B_{qc}$  were obtained in [123] by a comparison with the HERA data for coherent and incoherent  $J/\psi$  production at a photon–proton centre-of-mass energy of  $W = 75$  GeV, corresponding to a fractional hadronic target energy loss of  $x_{IP} = 10^{-3}$ . The proton fluctuation parameters obtained are  $B_{qc} = 3.3$  GeV $^{-2}$  and  $B_q = 0.7$  GeV $^{-2}$ .

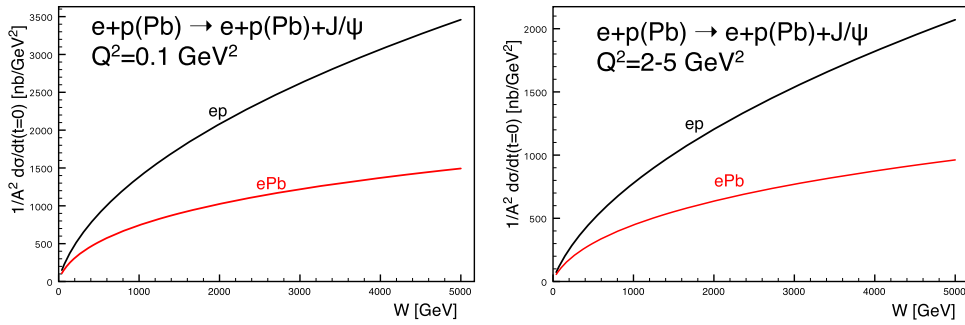


**Figure 87.** Cross-section for the coherent diffractive production of the vector meson  $J/\psi$  in  $ePb$  (red solid curves) and  $ep$  (black solid curves) collisions, as a function of the energy  $W$ . Left: photoproduction case  $Q^2 \simeq 0$ , right:  $Q^2 = 2\text{--}5 \text{ GeV}^2$ .

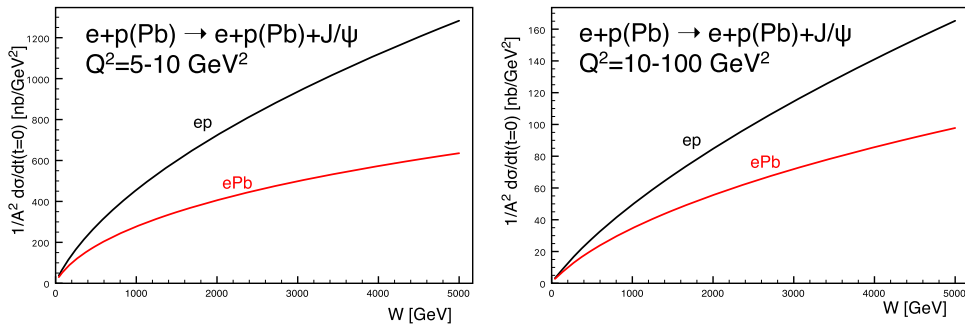


**Figure 88.** Cross-section for the coherent diffractive production of the vector meson  $J/\psi$  in  $ePb$  (red solid curves) and  $ep$  (black solid curves) collisions, as a function of the energy  $W$ . Left:  $Q^2 = 5\text{--}10 \text{ GeV}^2$ , right:  $Q^2 = 10\text{--}100 \text{ GeV}^2$ .

The results for the differential cross-section at  $t = 0$  for coherent production of  $J/\psi$  as a function of (virtual) photon-proton energy  $W$  for fixed values of  $Q^2$  are shown in figures 87 and 88. The calculations for Pb are compared to those for the proton target. We see that the cross-sections for the nuclear case increase with energy more slowly than for the proton case and are always smaller. Note that we have already rescaled the diffractive cross-sections by a factor of  $A^2$ , as appropriate for a comparison of the diffractive cross-sections on the proton and nucleus. In the absence of nuclear corrections, their ratio should be equal to one. The differences between the scattering from a nucleus and that from a proton are also a function of  $Q^2$ . They are larger for smaller values of  $Q^2$  and for photoproduction. This is understood from the dipole formulae, see equations (3.23)–(3.25). As explained previously, larger values of scale  $Q^2$  select smaller dipoles, for which the density effects are smaller. Similarly, the differences between the lead and proton cases are larger for higher energies. This is because the dipole amplitude grows with decreasing values of  $x$  which are probed when the energy is increased, and thus the nonlinear density effects are more prominent at low values of  $x$  and  $Q^2$ .

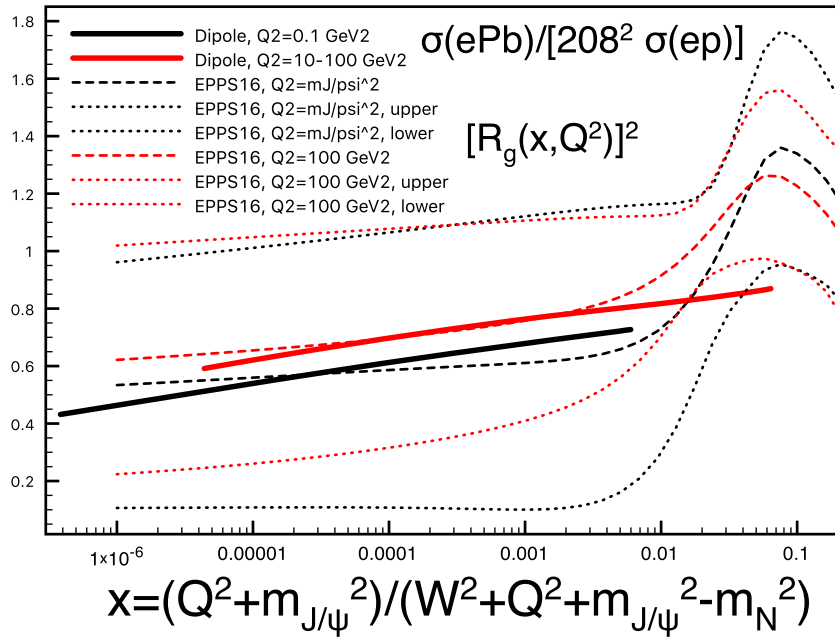


**Figure 89.** Ratio of coherent  $J/\psi$  production diffractive cross-sections for Pb and the proton as a function of the variable  $x$  (defined in equation (6.7) for the dipole model results). Solid lines: dipole model calculation for  $Q^2 = 0.1 \text{ GeV}^2$  (black) and  $Q^2 = 10\text{--}100 \text{ GeV}^2$  (red). Dotted and dashed lines correspond to the nuclear ratio for the gluon density squared using the EPPS16 parametrisation [503] of the nuclear PDFs. Black and red dashed lines are the central sets for  $Q^2 = M_{J/\psi}^2$  and  $Q^2 = 100 \text{ GeV}^2$ . The dotted lines correspond to the low and high edges of the Hessian uncertainty in the EPPS16 parametrisation. The difference between the two dotted lines is thus indicative of the parametrisation uncertainty for the nuclear ratio. These ratios, which can also be measured in UPCs [129], are larger than the values 0.2–0.4 at  $x \simeq 10^{-5}$  predicted by the relation between diffraction and nuclear shadowing [344].

These findings can be summarised by inspecting the ratio of the cross-sections, presented as a function of  $x$  defined as<sup>187</sup>

$$x = \frac{Q^2 + m_{J/\psi}^2}{Q^2 + W^2 + m_{J/\psi}^2 - m_N^2} \quad (6.7)$$

which is shown in figure 89. We observe that the ratio is smaller for smaller values of  $Q^2$ , and it decreases for decreasing values of  $x$ . The results of the dipole-model calculations are compared with the ratio of the gluon density squared (evaluated at  $x$  and  $Q^2$ ) obtained from the nuclear PDFs using the EPPS16 set [503]. The reason that one can compare the diffractive cross-section ratios with the ratios for the gluon density squared can be understood from equations (3.23) and (3.24). The diffractive amplitude is proportional to the gluon density  $xg(x, Q^2)$ . On the other hand, the diffractive cross-section is proportional to the amplitude squared, thus having an enhanced sensitivity to the gluon density. The nuclear PDFs have large uncertainties, as

<sup>187</sup>This choice to translate  $W$  and  $Q^2$  into  $x$  in the dipole-model calculations differs from the choices made in other published reports, but the difference is only significant at large  $x$ , where the dipole model is not applicable.

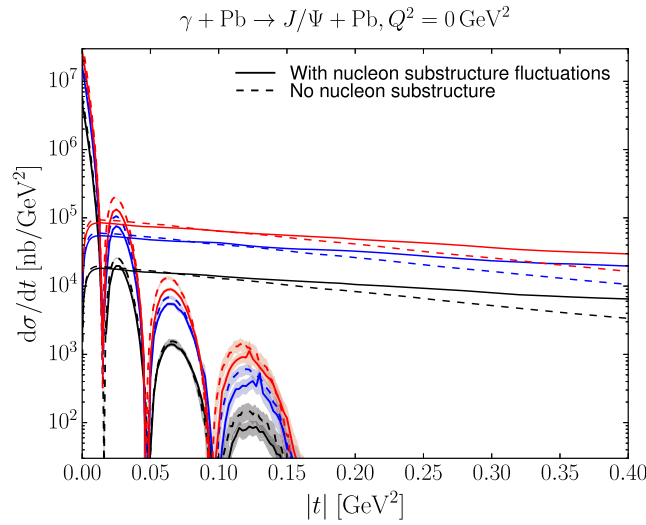


**Figure 90.** Differential cross-sections for coherent and incoherent production of  $J/\psi$  in  $e\text{Pb}$  as a function of the negative four-momentum transfer squared  $-t$ , for photo-production,  $Q^2 = 0$ . The lines showing dips are for coherent production, and those extending to large  $|t|$  are for incoherent production. The solid (dashed) lines are the results with (without) nucleon substructure fluctuations. Black, blue, and red represent  $W = 0.1, 0.813,$  and  $2.5$  TeV, respectively.

indicated by the region between the two sets of dotted lines. The EPPS16 parametrisation is practically unconstrained in the region of  $x$  less than 0.01. Nevertheless, the estimate based on the dipole-model calculation and the central value of the EPPS16 parametrisation are consistent with each other. This strongly suggests that it will be hard to disentangle nuclear effects from saturation effects and that only through a detailed combined analysis of data for the proton and the nucleus can firm conclusions be established for the existence of a new nonlinear regime of QCD.

The differential cross-sections  $d\sigma/dt$  as a function of the negative four-momentum transfer squared  $-t$  for the cases of coherent and incoherent production are shown in figure 90. Coherent and incoherent diffractive cross-sections are computed from the dipole model in the following way. The coherent diffractive cross-section is obtained by averaging the diffractive scattering amplitude over the target configurations and taking the square

$$\frac{d\sigma}{dt} = \frac{1}{16\pi} |\langle \mathcal{A}(x, Q, \Delta) \rangle|^2. \quad (6.8)$$

Here, the brackets  $\langle \dots \rangle$  refer to averages over different configurations of the target. The incoherent cross-section is obtained by subtracting the coherent cross-section from the total diffractive cross-section. It is standardly assumed that it takes the form of a variance of the diffractive scattering amplitude

$$\frac{d\sigma}{dt} = \frac{1}{16\pi} (\langle |\mathcal{A}(x, Q, \Delta)|^2 \rangle - |\langle \mathcal{A}(x, Q, \Delta) \rangle|^2), \quad (6.9)$$

which should be valid for small  $|t|$ . The  $t$  dependence, and the relation between the impact parameter and  $t$  through the Fourier transform, makes diffractive scattering a sensitive probe



of the internal geometric structure of hadrons and nuclei; see reference [540] for an extraction of the transverse profile of the nucleus in UPCs at the RHIC and also reference [541] for a study at the EIC. In particular, because the incoherent cross-section has the form of a variance of the amplitude, it is sensitive to the amount of fluctuation in impact parameter space.

The results in figure 90 (results for higher  $Q^2$  are very similar) indicate that incoherent production is dominant for most values of  $-t$ , except for very small momentum transfers, about  $|t| < 0.02 \text{ GeV}^2$ . Thus, dedicated instrumentation which will allow us to distinguish between the two cases is essential if one wants to measure the coherent process over a reasonably wide range of  $|t|$ . As in the proton case, the coherent  $t$  distribution exhibits characteristic dips. However, in the case of the nuclear targets, the dips occur for much smaller values of  $t$ . This is related to the much larger value of the dipole amplitude for a wide range of impact parameters in the case of nuclear targets, compared to the proton case.

Another interesting aspect, see section 3.4, is the effect of the transverse structure of the target in nuclear coherent and incoherent diffraction [542]. For example, in the formulation shown above [124], a fixed number of hot spots was considered, while in [128] (see also [125] for a realisation using small- $x$  evolution) a growing number with  $1/x$  was implemented. In both cases, the ratio of incoherent to coherent diffraction decreased with  $W$ , and was smaller for larger nuclei. This decrease is sensitive to the details of the distribution of hot spots—thus, to the fluctuations of the gluon distribution in transverse space. It also shows interesting dependencies on the mass of the produced vector meson and on  $Q^2$ , with the result that the ratio is smaller for lighter vector mesons and for lower  $Q^2$ . Besides, the hot-spot treatment also has some effects on the distributions of momentum transfer, see figure 90. In order to check these ideas, both the experimental capability to separate coherent from incoherent diffraction, and a large lever arm in  $W$  and  $Q^2$ , as available at the LHeC, are required.

We thus conclude that by investigating coherent and incoherent diffractive scattering on nuclei, one can obtain a unique insight into the spatial structure of matter in nuclei. On the one hand, the coherent cross-section, which is obtained by averaging the amplitude before squaring it, is sensitive to the average spatial density distribution of gluons in transverse space. On the other hand, the incoherent cross-section, which is governed by the variance of the amplitude with respect to the initial nucleon configurations of the nucleus, measures fluctuations of the gluon density inside the nucleus. In the case of a nucleus, the diffractive production rate is controlled by two different scales related to the proton and nucleus sizes. At momentum scales corresponding to the nucleon size  $|t| \sim 1/R_p^2$  the diffractive cross-section is almost purely incoherent. The  $t$ -distribution in coherent diffractive production from the nucleus gives rise to a dip-type structure for both saturation and non-saturation models, while in the case of incoherent production at small  $|t|$ , both saturation and non-saturation models do not lead to dips [124]. This is in drastic contrast to diffractive production by the proton, where only saturation models lead to a dip-type structure in the  $t$ -distribution at values of  $|t|$  that are experimentally accessible. Therefore, diffractive production offers a unique opportunity to measure the spatial distribution of partons in protons and nuclei. It is also an excellent tool with which to investigate the approach to unitarity in the high-energy limit of QCD.

While we have focussed here on  $J/\psi$  production, lighter vector mesons such as  $\rho$ ,  $\omega$ , and  $\phi$  could also be studied. They should show a different  $Q^2$  dependence, and their larger sizes would make them lie closer to the black-disk regime. The dominance of dijet events in photoproduction would also provide sensitivity to the approach to the unitarity limit [344].

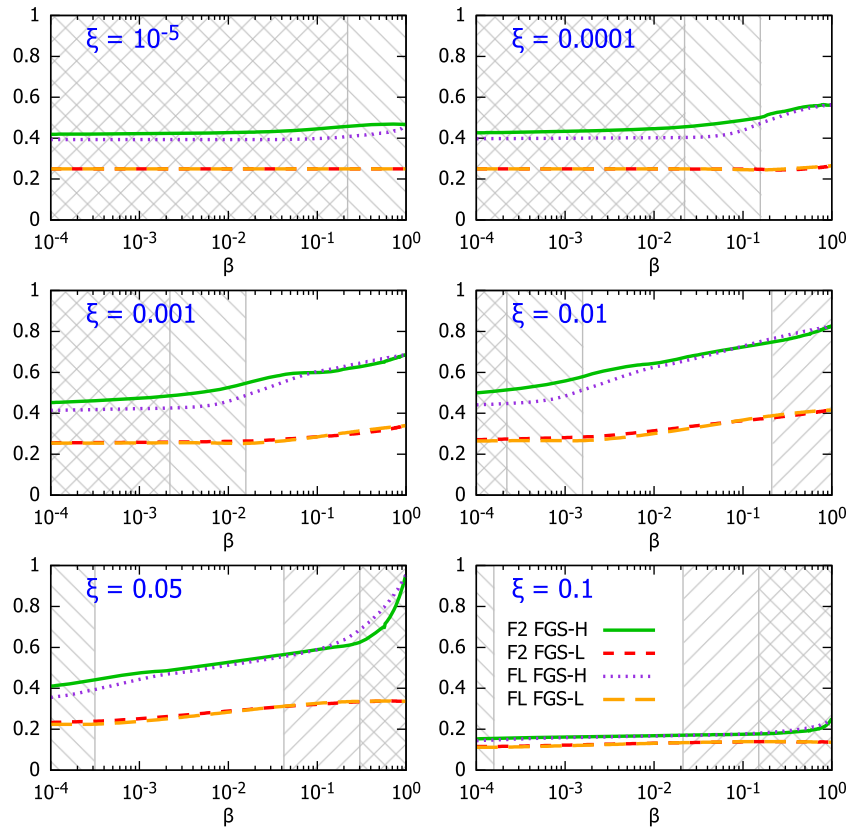


**Figure 91.** Nuclear modification factor, equation (6.10), for  $F_2^{D(3)}$  and  $F_L^{D(3)}$  in  $^{208}\text{Pb}$  versus  $\beta$ , at  $Q^2 = 10 \text{ GeV}^2$  and for different  $\xi$ , for the models H and L in [344]. The ‘\’ and ‘/’ hatched areas show the kinematically excluded regions for  $E = 2.76$  and  $19.7 \text{ TeV/nucleon}$ , respectively. Reproduced from [346]. CC BY 4.0.

**6.3.2. Inclusive diffraction on nuclei.** In section 4.3, a study of the prospects for extracting diffractive parton densities in the proton was presented, following [346]. Diffraction in  $eA$  is similar to that in  $ep$ , the main difference being a smaller contribution from incoherent  $e + A \rightarrow e + X + A^*$  than from coherent  $e + A \rightarrow e + X + A$  diffraction, where  $A^*$  denotes a final state in which the nucleus dissociates into at least two hadrons, but the event still shows a rapidity gap. Incoherent diffraction dominates for  $|t|$  larger than a few hundredths of a  $\text{GeV}^2$ . Forward detectors [1] will allow the separation of coherent diffraction, on which we focus in the following, summarising the study in reference [346].

Assuming that the same framework (collinear factorization for hard diffraction, equation (4.14), and Regge factorization, equation (4.16)) introduced in section 4.3 for  $ep$  also holds for  $eA$ , nuclear diffractive PDFs (nDPDFs) can be extracted from the diffractive reduced cross-sections. Note that such nDPDFs have never been measured. For an electron energy of  $E_e = 60 \text{ GeV}$  and nuclear beams with  $E_N = 2.76 \text{ TeV/nucleon}$ , the kinematic coverage at the LHeC is very similar to that shown in figure 49. For details, see reference [346].

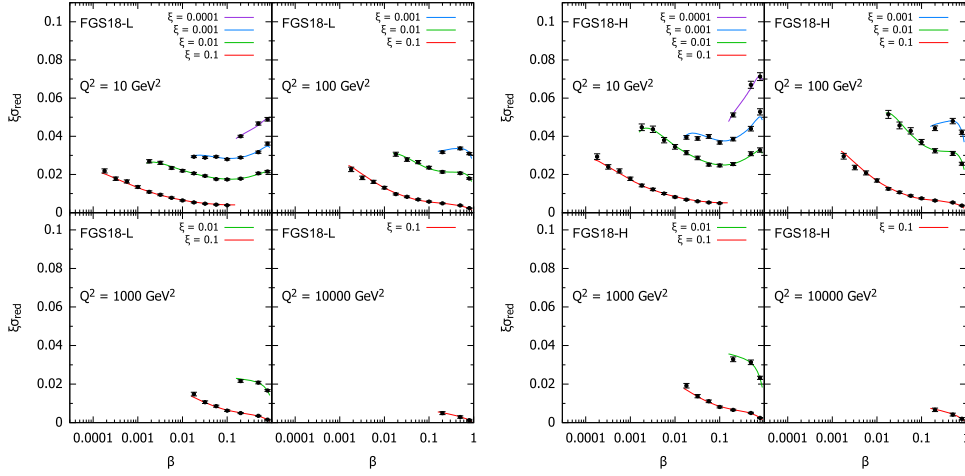


**Figure 92.** An indicative subset of the simulated data for the diffractive reduced cross-section as a function of  $\beta$  in bins of  $\xi$  and  $Q^2$  for  $e^{208}\text{Pb}$  collisions at the LHeC, using the models in [344]. The curves for  $\xi = 0.01, 0.001$ , and  $0.0001$  are shifted upwards by  $0.01, 0.02$ , and  $0.03$ , respectively. Reproduced from [346]. CC BY 4.0.

Defining the diffractive nuclear modification factor analogously to equation (6.1),

$$R_k^A(\beta, \xi, Q^2) = \frac{f_{k/A}^{D(3)}(\beta, \xi, Q^2)}{A f_{k/p}^{D(3)}(\beta, \xi, Q^2)}, \quad (6.10)$$

in figure 91 we show the results for  $F_2^{D(3)}$  and  $F_L^{D(3)}$  from the Frankfurt-Guzey-Strikman (FGS) models [344]. These models are based on Gribov inelastic shadowing [343] which relates diffraction in  $ep$  to nuclear shadowing for total and diffractive  $eA$  cross-sections. The nuclear wave function squared is approximated by the product of one-nucleon densities, the  $t$ -dependence of the diffractive  $\gamma^*$ -nucleon amplitude is neglected compared to the nuclear form factor, and a real part is introduced into the amplitudes [543] and colour fluctuations for the inelastic intermediate nucleon states [544]. There are two models, named H and L, that correspond to different strengths of the colour fluctuations and result in larger and smaller probabilities of diffraction in nuclei with respect to that in the proton, respectively. In figures 91 and 92 we show results [346] for both models.

A subset of the simulated pseudodata for the reduced cross-sections is shown in figure 92 [346]. It is generated assuming 5% of systematic error and statistical errors calculated for an integrated luminosity of  $2 \text{ fb}^{-1}$ . Compared to figure 51, the comparably large kinematic coverage and small (systematics-dominated) uncertainty illustrated in figure 92 clearly show that an extraction of nDPDFs in  $^{208}\text{Pb}$ , analogous to that shown in figures 52 and 53 for the DPDFs, will be possible with similar accuracy in an extended kinematic region.

#### 6.4. New dynamics at small $x$ with nuclear targets

As discussed in section 4.2.1, theoretical expectations [507] indicate that the fixed-order perturbation theory leading to the DGLAP evolution equations should eventually fail. When  $x$  decreases,  $\alpha_s \ln 1/x$  becomes large and these large logarithms must be resummed, leading to

the BFKL equation. Furthermore, when the parton density becomes large, the linear approximation that underlies both DGLAP and BFKL breaks, and nonlinear processes must be taken into account to compute parton evolution. The CGC [506] offers a non-perturbative but weak coupling effective theory with which to treat dense parton systems in a systematic and controlled way. One of the important predictions of the CGC is that in a dense parton system, saturation occurs, leading to the emergence of a new dynamical scale—the saturation scale  $Q_{\text{sat}}$ , which increases with the energy.

The parton density in a hadron becomes high both through evolution—when energy or  $1/x$  becomes large, and/or when partons are accumulated by overlapping nucleons—when the mass number  $A$  becomes large in a nucleus. In the nucleus rest frame, the virtual photon fluctuations at small  $x < (2m_N R_A)^{-1}$ , where  $m_N$  is the nucleon mass and  $R_A$  is the nuclear radius, acquire a lifetime larger than the time taken to traverse the nucleus and, thus, all partons within a transverse area  $\sim 1/Q^2$  are simultaneously probed. In fact, the parameter that determines the transition between linear and nonlinear dynamics is the parton density and, therefore, the onset of this new regime of QCD and its explanation must be tested, as discussed in [1], by exploring both decreasing values of  $x$  and increasing values of  $A$  in a kinematic  $x-Q^2$  region, where, in order to be sensitive to differences in evolution, a sufficient lever arm is available in  $Q^2 \gg \Lambda_{\text{QCD}}^2$  at small  $x$ . The saturation scale  $Q_{\text{sat}}$  that characterises the typical gluon momentum in a saturated hadron wave function increases with nuclear size,  $Q_{\text{sat}}^2 \propto A^{1/3}$ . Therefore, in  $eA$  collisions the perturbatively saturated regime is achieved at a parametrically larger value of  $x$  than in a proton—a prediction not only of the CGC but of all multiple-scattering models that anticipate an approach to the black-disk, unitarity limit.

The opportunities to establish the existence of saturation in lepton–nucleus collisions are numerous. They include inclusive observables, both total and diffractive cross-sections, and less inclusive observables, such as correlations:

- Tension in DGLAP fits for inclusive observables: as discussed in [1, 257] and in section 4.2.2, deviations from fixed-order perturbation theory can be tested by the tension that would appear in the description within a DGLAP fit of observables with different sensitivities to the sea and the glue, for example  $F_2$  and  $F_L$  (or reduced cross-sections at different energies) or  $F_2^{\text{inclusive}}$  and  $F_2^{\text{heavy quarks}}$ . In [545], such an exercise was performed, which considered  $F_2$  and  $F_L$  pseudodata for  $e\text{Au}$  collisions at the EIC [101] using reweighting techniques. While the results for EIC energies are shown to be inconclusive due to the reduced lever arm in  $Q^2 > Q_{\text{sat}}^2 \gg \Lambda_{\text{QCD}}^2$ , the much larger centre-of-mass energies at the LHeC (and FCC-eh) should make it possible to search for tensions between different observables.
- Saturation effects in diffraction: a longstanding prediction of saturation [107, 546, 547] is a modification of the diffractive cross-section in nuclei with respect to protons, with a suppression (enhancement) at small (large)  $\beta$  due to the approach of the nucleus to the black-disk limit (where elastic and diffractive scattering become maximal) and the behaviour of the different Fock components of the virtual photon wave function. Such effects can also be discussed in terms of a competition between nuclear shadowing and the probability that the event remains diffractive in the multiple scattering process [344]. This leads to the generic expectation of an enhancement of the ratio of the coherent diffractive cross-section in the nucleus over that in the proton, in nonlinear approaches with respect to linear ones [101].
- Correlations: For a long time, correlations have been considered to be sensitive probes of the underlying production dynamics. For example, the cross-section for the production

of two jets with the same hardness and widely separated in rapidity, called Mueller-Navelet jets [548], was proposed as a test of BFKL versus DGLAP dynamics, but the effect of saturation has not been widely studied, although it has a large potential to differentiate linear resummation from nonlinear saturation (where non-trivial nuclear effects could appear). Correlations between jets were analysed in [1] for the LHeC kinematics, in both inclusive and diffractive events; see the formalism in [549]. On the other hand, the azimuthal decorrelation of particles and jets when saturation effects are at work—at small  $x$ , studied by the difference between collisions involving proton and nuclei, was proposed long ago in  $d$ Au collisions at the RHIC [550, 551]. It was studied in [1] for the LHeC kinematics; see recent developments in [552] and the extension to forward dijet production in [553]. It could also be analysed in UPCs at the LHC, see section 9.7.

### 6.5. Collective effects in dense environments—the ‘ridge’

One of the most striking discoveries [554] at the LHC is that in all collision systems, from small ( $pp$  and  $pA$ ) to large (AA), many of the features that are considered to be indicative of the production of a dense hot partonic medium are observed (see e.g. reviews [555–557] and references therein). The most celebrated of such features are the long-rapidity-range particle correlations collimated in azimuth, named the ‘ridge’, shown in figure 93. The dynamics underlying these phenomena, either the formation of a QGP and the existence of strong final-state interactions, or some initial state dynamics that leaves an imprint on the final observables, is under discussion [558]. While they have been observed in photoproduction on Pb in UPCs at the LHC [559], their existence in smaller systems such as  $e^+e^-$  [560] at the LEP collider and  $ep$  at HERA [561] has been scrutinised, but the results are inconclusive.

In this respect, measurements in  $ep$  and  $eA$  collisions at the LHeC at considerable centre-of-mass energies will offer crucial additional information. For example, the collision of the virtual photon with the proton at the LHeC can be considered to be a high-energy collision of two jets or ‘flux tubes’, as discussed in references [564, 565] and illustrated in figure 93. This can lead to the production of ‘ridges’ and other novel configurations of gluons and quarks and will be uniquely measured at the LHeC.

### 6.6. Novel QCD nuclear phenomena at the LHeC

Beyond the topics discussed above there are many novel phenomena which can be explored in  $eA$  collisions at LHeC or FCC-eh, in a high-energy regime and using dedicated instrumentation. We shall briefly review some of these phenomena, which can be understood utilizing the LF framework of QCD; for a review, see [566].

One of the most important theoretical tools in high-energy physics is Dirac’s LF time:  $\tau = x^+ = t + z/c$ , the time along the LF [567], a concept which allows all of the tools and insights of Schrödinger’s quantum mechanics and the Hamiltonian formalism to be applied to relativistic physics [566]. When one takes a photograph, the object is observed at a fixed LF time. Similarly, Compton  $\gamma p \rightarrow \gamma' p''$  and deep-inelastic lepton–proton scattering are measurements of proton structure at a fixed LF time. Unlike ordinary *instant time*  $t$ , physics at fixed  $\tau$  is Poincaré invariant; i.e. independent of the observer’s Lorentz frame. Observations at fixed  $\tau$  are made within the causal horizon. LF time  $\tau$  reduces to ordinary time  $t$  in the nonrelativistic limit  $c \rightarrow \infty$ .

The LF wavefunctions (LFWF) of hadrons are superpositions of  $\Psi_n^H(x_i, \vec{k}_{\perp i}, \lambda_i) = \langle \Psi_H | n \rangle$ , the Fock-state projections of the eigensolution of the QCD LF Hamiltonian  $H_{\text{QCD}} | \Psi_H \rangle = M_H^2 | \Psi_H \rangle$ . They encode the underlying structure of bound states in quantum field theory and

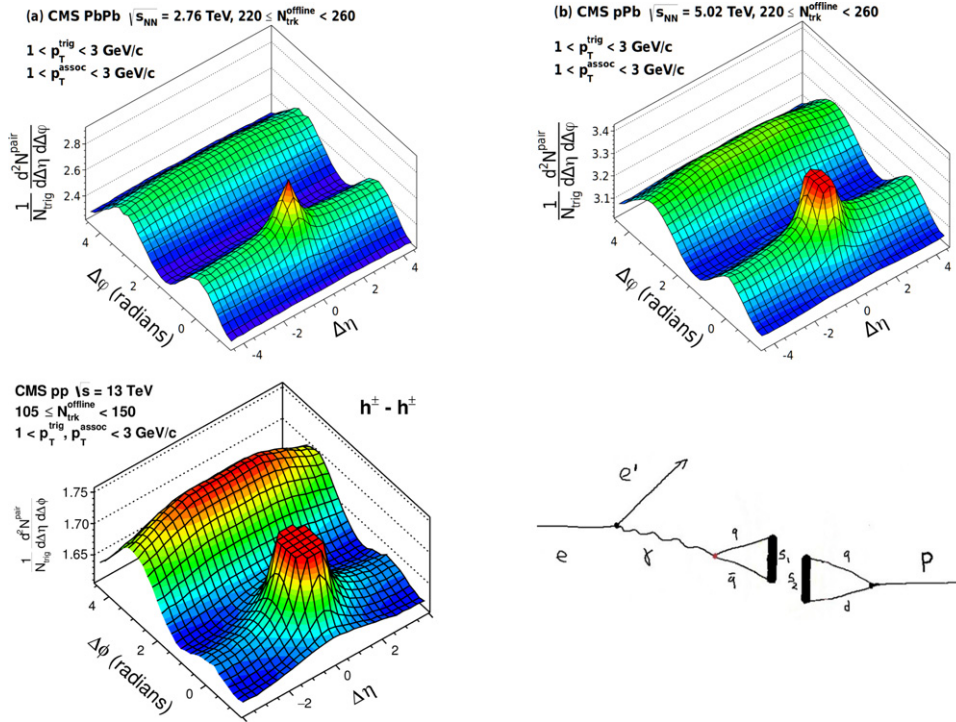


**Figure 93.** Left and top right: collective effects seen in high-multiplicity two-particle azimuthal correlation, as observed by CMS in PbPb, pPb (reproduced from [562]. CC BY 4.0), and pp (reproduced from [563]. CC BY 4.0) collisions. Bottom right: schematic illustration of the production of ridge-like effects in ep or eA scattering at the LHeC. Reproduced from [564]. CC BY 4.0.

underlie virtually every observable in hadron physics. Hadronic LFWFs can also be directly measured by the Ashery method [568], the coherent diffractive dissociation of high-energy hadrons into jets [569, 570]. In the diffractive dissociation of a high-energy hadron into quark and gluon jets by two-gluon exchange, the cross-section measures the square of the second transverse derivative of the projectile’s LFWF. Similarly, the dissociation of a high-energy atom such as positronium or true muonium ( $[\mu^+ \mu^-]$ ) can be used to measure the transverse derivative of its LFWFs.

Hadronic LFWFs are defined at fixed  $\tau = x^+ = t + z/c$ ; they are thus off-shell in the total  $P^- = P^0 - P^z$ , not energy  $P^0$  [566]. Thus, LFWFs are also off-shell in  $\mathcal{M}^2 = P^+ P^- - P_\perp^2 = [\sum_i k_i^\mu]^2 = \sum_i \frac{k_i^2 + m^2}{x_i}$ , the invariant mass squared of the constituents in the  $n$ -particle Fock state. LFWFs are thus functions of the invariant mass squared of the constituents in the Fock state. For a two-particle Fock state,  $\mathcal{M}^2 = \frac{k_\perp^2 + m^2}{x(1-x)}$ . Thus, the constituent transverse momenta  $k_{\perp i}^2$  appear alone as a separate factor in the LFWF; the transverse momenta are always coupled to the longitudinal LF momentum fractions  $x_i$ . This is the LF version of rotational invariance. Only positive  $k_i^+ = k_i^0 + k_i^z \geq 0$  and  $0 \leq x_i = \frac{k_i^+}{P^+} \leq 1$  appear, where  $\sum_i x_i = 1$ . In addition,  $J^z = \sum_i L_i^z + S_i^z$ , as well as  $P^+ = \sum_i k_i^+$  and  $\vec{P}_\perp = \sum_i \vec{k}_{\perp i}$  are conserved at every vertex—essential covariant kinematical constraints. It is notable that the anomalous gravitomagnetic moment of every LF Fock state vanishes at  $Q^2 = 0$ . The LFWFs of bound states



are off-shell in  $P^- = \sum_i k_i^-$ , but they tend to be maximal when they are least off-shell, i.e. they have minimal invariant mass. In fact, in the holographic LFWFs where colour is confined, the LFWFs of hadrons have fast Gaussian fall-off in invariant mass. This feature also underlies intrinsic heavy-quark Fock states: the LFWFs have maximal support when all of the constituents have the same rapidity  $y_i$ ; i.e.  $x_i \propto \sqrt{m_i^2 + k_{\perp i}^2}$ . Thus, the heavy quarks have the highest momentum fractions  $x_i$ .

Conversely, LF wavefunctions provide the boost-invariant transition amplitude which converts free quarks and gluons into the hadronic eigenstates of QCD. Thus, knowing the LFWFs allows one to compute *hadronization at the amplitude level*—how the coloured quarks and gluons produced in a DIS event  $ep \rightarrow e'X$  at the LHeC are confined and emerge as final-state hadrons.

The LF formalism leads to many novel nuclear phenomena, such as *hidden colour* [571], *colour transparency* [572], *nuclear-bound quarkonium* [573], *nuclear shadowing and antishadowing* of nuclear structure functions, etc. For example, there are five distinct colour-singlet QCD Fock-state representations of the six colour-triplet quarks of the deuteron. These hidden-colour Fock states become manifest when the deuteron fluctuates to a small transverse size, as in measurements of the deuteron form factor at large momentum transfer. One can also probe the hidden-colour Fock states of the deuteron by studying the final state of the dissociation of the deuteron in deep inelastic lepton scattering at the LHeC, i.e.  $eD \rightarrow e'X$ , where  $X$  can be  $\Delta^{++} + \Delta^-$ , six quark jets, or other novel colour-singlet final states.

The LF wave functions provide the input for scattering experiments at the amplitude level, encoding the structure of a projectile at a single LF time  $\tau$  [566]. For example, consider photon–ion collisions. The incoming photon probes the finite size structure of the incoming nucleus at fixed LF time, like a photograph—not at a fixed instant time, which is acausal. Since the nuclear state is an eigenstate of the LF Hamiltonian, its structure is independent of its momentum, as required by Poincaré invariance. One gets the same answer in the ion rest frame, the CM frame, or even if the incident particles move in the same direction but collide transversely. There are no colliding *pancakes* using the LF formalism.

The resulting photon–ion cross-section is not point-like; it is shadowed:  $\sigma(\gamma A \rightarrow X) = A^\alpha \sigma(\gamma N \rightarrow X)$ , where  $A$  is the mass number of the ion,  $N$  stands for a nucleon, and the power  $\alpha \approx 0.8$  reflects Glauber shadowing [574]. The shadowing stems from the destructive interference of two-step and one-step amplitudes, where the two-step processes involve diffractive reactions on a front-surface nucleon which shadows the interior nucleons. Thus, the photon primarily interacts on the front surface. Similarly, a high-energy ion–ion collision  $A_1 + A_2 \rightarrow X$  involves the overlap of the incident frame-independent LFWFs. The initial interaction on the front surface of the colliding ions can resemble a shock wave.

In the case of a deep inelastic lepton–nucleus collision  $\gamma^* A \rightarrow X$ , the two-step amplitude involves a leading-twist diffractive deep inelastic scattering (DDIS)  $\gamma^* N_1 \rightarrow V^* N_1$  on a front-surface nucleon  $N_1$  and then the on-shell propagation of the vector system  $V^*$  to a downstream nucleon  $N_2$  where it interacts inelastically:  $V^* N_2 \rightarrow X$ . If the DDIS involves Pomeron exchange, the two-step amplitude interferes destructively with the one-step amplitude  $\gamma^* N_1 \rightarrow X$ , thus producing shadowing of the nuclear PDF at low  $x < 0.1$ . On the other hand, if the DDIS process involves an  $I = 1$  Reggeon exchange, the interference is constructive, producing *flavour-dependent* leading-twist antishadowing [574] in the domain  $0.1 < x < 0.2$ .

One can also show that the Gribov–Glauber processes, which arise from leading-twist diffractive deep inelastic scattering on nucleons and which underlie the shadowing and antishadowing of nuclear structure functions [574], prevent the application of the opera-



tor product expansion to the virtual Compton scattering amplitude  $\gamma^*A \rightarrow \gamma^*A$  on nuclei and thus negate the validity of the momentum sum rule for deep inelastic nuclear structure functions [575].

## 7. Higgs physics with the LHeC

### 7.1. Introduction

The Higgs boson was discovered in 2012 by ATLAS [576] and CMS [577] at the LHC. It is the most recently discovered and least explored part of the SM. The Higgs boson (H) is of fundamental importance. It is related to the mechanism predicted by [419, 420, 578] and independently by [579], in which the intermediate vector bosons of the spontaneously broken electroweak symmetry acquire masses<sup>188</sup>, while the photon remains massless. Fermions obtain a mass via the Yukawa couplings with the Higgs field. Following the discovery of the Higgs boson, its physics and thorough exploration have become central themes of the physics programme at the LHC. Any high-energy future collider project, beginning with the high-luminosity upgrade of the Large Hadron Collider, the HL-LHC, which is underway and will collect data a decade hence, has the potential to precisely study the properties of the Higgs boson as its centre of attention, to understand its characteristics and in the hope of opening a new window into physics extending beyond the SM; see, for example, [580, 581]. In this section we present the potential for exploring SM Higgs physics at the LHeC and, to a certain extent, at the FCC-eh as well.

A first challenge for the physics of the Higgs boson is to establish whether it indeed satisfies the properties inherent to the SM regarding its production and decay mechanisms. The SM neutral  $H$  boson decays into pairs of fermions,  $f\bar{f}$ . The dominant decay is  $H \rightarrow b\bar{b}$  with a branching fraction of about 58%. The branching scales with the square of the fermion mass,  $m_f^2$ . The next prominent fermionic decay is therefore  $H \rightarrow \tau^+\tau^-$  at 6.3%, followed by charm decay with a predicted branching fraction of 2.9%. The Higgs boson also decays into pairs of  $W$  and  $Z$  bosons at rates of 21.5% and 2.6%, respectively. Loop diagrams enable the decay into gluon and photon pairs with a branching of 8.2 and 0.2%, respectively. The seven most frequent decay channels, ordered according to descending branching fractions, are thus those resulting in  $b\bar{b}$ ,  $W^+W^-$ ,  $gg$ ,  $\tau^+\tau^-$ ,  $c\bar{c}$ ,  $ZZ$  and  $\gamma\gamma$ . Together these are predicted to represent a total SM branching fraction of 99.9%. At the LHC these and rarer decays can be reconstructed, with the exception of the charm decay, for reasons of prohibitive combinatorial background. The main purpose of this paper is to evaluate the prospects for precisely measuring these channels in electron–proton scattering.

### 7.2. Higgs production in deep inelastic scattering

In deep inelastic electron–proton scattering, the Higgs boson is predominantly produced through  $WW$  fusion in CC DIS scattering; see figure 94. The next large Higgs production mode in  $ep$  is  $ZZ \rightarrow H$  fusion in neutral current (NC) DIS scattering, figure 94, which has a smaller but still sizeable cross-section. These  $ep$  Higgs production processes are very clean for a number of reasons:

<sup>188</sup> The mass of the  $W$  boson,  $M_W$ , is generated through the vacuum expectation value,  $\eta$ , of the Higgs field ( $\Phi$ ) and given by the simple relation  $M_W = g\eta/\sqrt{2}$  where  $g$  is the weak interaction coupling. Here  $\eta = \sqrt{-\mu^2/2\lambda}$  with the two parameters of the Higgs potential that is predicted to be  $V = -\mu^2\Phi^\dagger\Phi - \lambda(\Phi^\dagger\Phi)^2$ . The Higgs mass is given by  $M_H = 2\eta\sqrt{\lambda}$  while the mass of the  $Z$  boson is related to  $M_W$  by the electroweak mixing angle,  $M_Z = M_W/\cos\Theta_W$ .

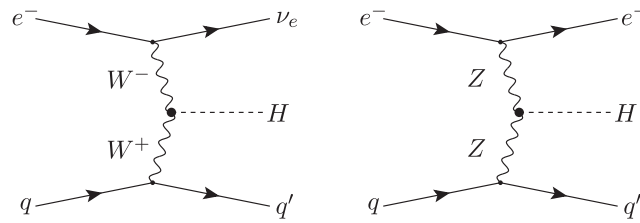


**Figure 94.** Higgs boson production in charged (left) and neutral (right) current deep inelastic electron–proton scattering to the leading order.

- Even at the high luminosity of  $10^{34} \text{ cm}^{-2} \text{ s}^{-1}$  the inclusive pileup is only 0.1 (1) for the LHeC (FCC-eh), and the final-state signature is therefore free from event overlap, in contrast to the case of the HL-LHC, where it will typically be 150;
- In  $ep$ , contrary to  $pp$ , there is no initial nor final-state colour (re)connection;
- The higher-order corrections are small. For the total CC process, they were estimated [582] to be of the order of only 1% for the QCD part, subject to cut dependencies yielding shape changes up to 20%, and  $-5\%$  for the QED part (with a weak dependence on the PDF choice).

The smallness of the QCD corrections was mainly attributed to the absorption of gluon and quark radiation effects in the evolution of the parton distributions (PDFs) [582]. The PDFs will be measured with very high precision at any of the  $ep$  colliders considered here (see section 3), thus allowing a unique self-consistency of Higgs cross-section measurements.

The NC reaction is even cleaner than the CC process, since the scattered electron fixes the kinematics more accurately than the missing energy. While in  $pp$  both  $WW$  and  $ZZ$  processes are hardly distinguishable, in  $ep$  they are uniquely distinguishable, which provides an important, precise constraint on the  $WWH$  and  $ZZH$  couplings.

**7.2.1. Kinematics of Higgs production.** At HERA the kinematics was conveniently reconstructed through event-wise measurements of  $Q^2$  and  $y$ . The reconstruction of the kinematics in CCs uses the inclusive hadronic final-state measurements. Based on the energies  $E'_e$  and  $E_h$  and the polar angles  $\Theta_e$  and  $\Theta_h$  of the scattered electron and the hadronic final state, respectively, one obtains a redundant determination of the kinematics in NC scattering. This permits a cross-calibration of calorimetric measurements, of the electromagnetic and hadronic parts, and of different regions of the detector, which is a major means of achieving superb, sub-percent precision in  $ep$  collider measurements. Methods have been developed to optimise the kinematics reconstruction and maximise the acceptance by exploiting the redundant determination of the scattering kinematics; see, for example, [56]. The basic DIS kinematic distributions of  $Q^2$ ,  $x$ , and  $y$  for Higgs production at  $\sqrt{s} = 3.5 \text{ TeV}$  are illustrated in figure 95. The average  $Q^2$  and  $x$  values probed are  $Q^2 \approx 2000 \text{ GeV}^2$ ,  $x \approx 0.02$  at the LHeC and  $Q^2 \approx 6500 \text{ GeV}^2$ ,  $x \approx 0.0016$  at the FCC-eh.

As described elsewhere in this paper, constraints arise for a large pseudorapidity or polar angle ( $\eta = \ln \tan \theta/2$ ) acceptance of the apparatus (i) for the backward region (the polar angle is defined w.r.t. the proton-beam direction), due to the need to reconstruct electrons at low  $Q^2$ , thereby enabling low- $x$  physics and (ii) for the forward region, to cover a maximum region towards large  $x$  at medium  $Q^2$  with the reconstruction of the hadronic final state. For the LHeC, the acceptance therefore extends to pseudorapidities of  $\eta = \pm 5$ , which, for the FCC-eh case, is extended to  $\eta = \pm 6$ . The large acceptance is, in particular, suitable for the reconstruction of

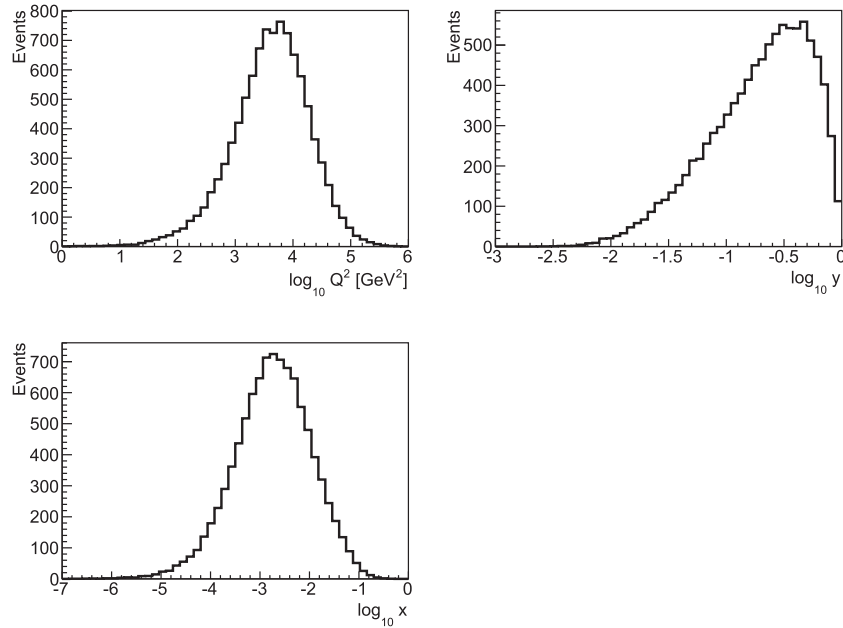


**Figure 95.** Distributions of  $ep \rightarrow \nu H X$  events at the parton level for the negative four-momentum transfer squared,  $Q^2$  (top left), Bjorken  $x$  (bottom left) and the inelasticity  $y = Q^2/sx$  (top right) at  $\sqrt{s} = 3.5$  TeV (FCC-eh). Events were generated with MadGraph [375], see table 14.

event signatures of collisions in which a Higgs boson is produced by vector-boson fusion; see figure 96 for the typical pseudorapidity distributions of Higgs-boson event signatures in DIS obtained using the most asymmetric FCC-eh collider configuration.

Geometric acceptances due to kinematic constraints on the pseudorapidity of the Higgs decay products for both the LHeC and the FCC-eh are further illustrated in figure 97. The acceptances are calculated for a basic selection of all final states with  $p_T > 15$  GeV and coverages of the forward jet of up to  $\eta = 5$  and  $\eta = 6$ , respectively, for both colliders. As can be seen from figure 97, the acceptances are higher for the less asymmetric LHeC beam configuration and about the same for hadronic calorimetry up to  $\eta = 5$  and  $\eta = 6$ . Hence, the LHeC calorimeter is designed for  $\eta = 5$ . The optimal hadronic calorimetry coverage for FCC-eh is clearly  $\eta = 6$ , which yields significantly higher acceptances, compared to  $\eta = 5$  calorimetry. From figure 97, it is apparent that for both collider configurations, the Higgs decay products would require tagging capabilities up  $\eta = 3.5$ , e.g. for HF and tau decays. Suitably designed muon detectors covering  $\eta = 4$  appear feasible for both collider configurations; these would result in high  $H \rightarrow \mu\mu$  acceptances of about 72% (63%) for LHeC (FCC-eh) when selecting all final states with  $p_T > 15$  GeV and a coverage of the forward jet of up to  $\eta = 5$  ( $\eta = 6$ ). A further extension to a  $1^\circ$  muon acceptance would change the acceptances marginally to 72.9% (67.5%) for the LHeC (FCC-eh).

**7.2.2. Cross-sections and rates.** The cross-sections for Higgs production in CC and NC DIS  $e^-$  scattering of a 60 GeV electron beam with protons at three different energies for the LHeC, the High Energy Large Hadron electron Collider (HL-LHeC), and the FCC-eh are summarised in table 14. The cross-sections are calculated to the leading order with MadGraph (MG5 v2.5.1)

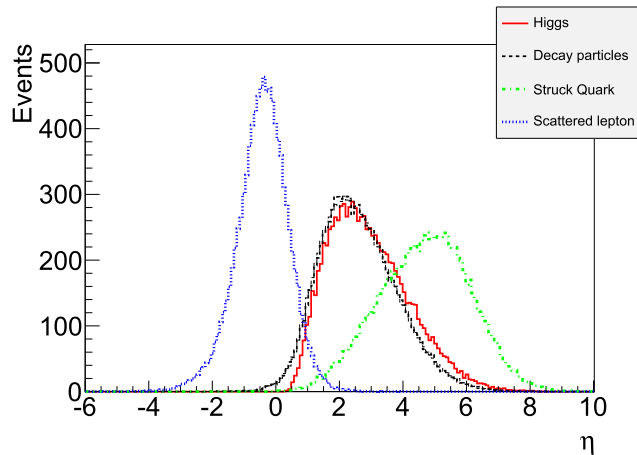


**Figure 96.** Pseudorapidity ( $\eta$ ) distributions at parton level that characterise the vector-boson-fusion production and decay of the Higgs boson to  $WW$  in DIS scattering at the FCC-eh. The scattered lepton (blue) in the NC case (or missing energy for CC) has an average  $\eta$  of about  $-0.5$ , i.e. it is scattered somewhat backwards (relative to the electron-beam direction). The pseudorapidity distributions of the generated Higgs boson (red) and its decay particles (black) are very similar and peak at  $\eta \simeq 2$ . The struck quark, especially at the FCC-eh as compared to LHeC, generates a very forward-pointing jet, requiring forward calorimetry up to  $\eta \simeq 6$ , as foreseen in the FCC-eh detector design. Events are generated with MadGraph; see the setup in table 14.

using the CTEQ6L1 proton PDF and  $M_H = 125$  GeV. The CC  $e^-p$  cross-section is directly proportional to the beam polarisation,  $P$ , as  $\sigma_{CC} \propto (1 - P)$ , while the NC cross-section only weakly depends on the polarisation [97].

It can be observed that the CC Higgs production cross-section at the LHeC is comparable to that of a 250 GeV  $e^+e^-$  collider. One thus expects results of roughly comparable sensitivity, the difference being that  $e^+e^-$  favours the  $H$  to  $ZZ$  couplings, while  $ep$  is dominantly sensitive to  $WW \rightarrow H$  production. This provides a fundamental complementarity between  $e^+e^-$  and  $ep$  collider Higgs physics.

The CC  $e^-p$  cross-section is enlarged with the (negative) electron beam polarisation,  $P_e$ , while the NC cross-section is less sensitive to  $P_e$ . The cross-section at the FCC-eh reaches values in the pb region. Combined with long operation times, one can reach a sub-per-mille precision of the Higgs couplings. Similarly, the  $HH$  cross-section approaches 0.5 fb values only at the highest energies, as expected for  $\sqrt{s} > 3$  TeV at the FCC-eh or CLIC-ee colliders. A first-cut-based study aiming to access the Higgs self-coupling at the FCC-eh to within 20% is detailed in reference [584]. Further prospects are not discussed here since measuring the  $HH$  coupling is one of the foremost tasks of the HL-LHC and the FCC-hh [586].

The polarised  $e^+p$  cross-section is calculated to be significantly smaller than the  $e^-p$  value, by a factor of  $197/58 \simeq 6$  at the LHeC, mainly because the  $W^-u \rightarrow \bar{d}$  reaction is more frequent than  $W^+d \rightarrow u$ . Furthermore, positron sources are currently considered to be much less intense (by a factor of about ten or even a hundred) than electron sources. It is desirable to collect  $e^+p$  data at future  $ep$  colliders for electroweak physics, but in the linac-ring version, their volume will be limited, and they will most likely be unsuitable for precision Higgs physics.

Table 15 provides an illustration of the statistics which is expected to be available in charged- and neutral-current scattering for nine decay channels ordered by their branching ratios for the

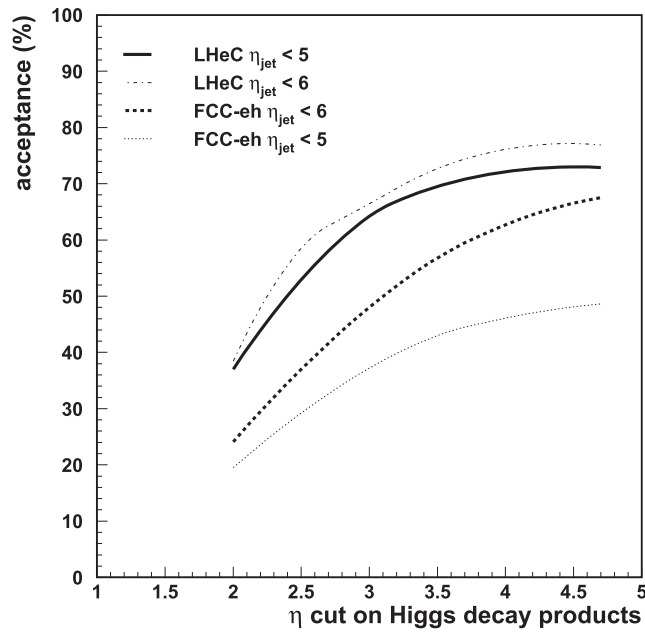


**Figure 97.** Dependence of the acceptance of DIS Higgs candidates (y axis) on the pseudorapidity ( $\eta$ ) cut requirement of the Higgs decay products (x axis) for two scenarios of the hadronic final-state coverage. All final states are selected with  $p_T > 15$  GeV. The forward jet is accepted up to  $\eta = 5$  and  $\eta = 6$  for the LHeC (full lines and dashed-and-dotted lines), and FCC-eh (dotted lines and dashed lines), respectively. Calculations are at the parton level and performed using MadGraph.

**Table 14.** Total cross-sections, in fb, for inclusive Higgs production at  $M_H = 125$  GeV, in charged- and neutral-current deep inelastic  $e^-p$  scattering for unpolarised ( $P = 0$ ) and polarised ( $P = -0.8$ )  $E_e = 60$  GeV electron beams and four different proton-beam energies,  $E_p$ , for the LHeC, the HE-LHeC, and two FCC-eh versions. The cms. energy squared in  $ep$  is  $s = 4E_e E_p$ . The last row shows the double-Higgs CC production cross-sections in fb. The calculations are at the LO of QCD using the CTEQ6L1 PDF [583] and the default scale of MadGraph [375] with dependencies due to scale choices of 5%–10%.

Parameter	Unit	LHeC	HE-LHeC	FCC-eh	FCC-eh
$E_p$	TeV	7	13.5	20	50
$\sqrt{s}$	TeV	1.30	1.77	2.2	3.46
$\sigma_{CC} (P = -0.8)$	fb	197	372	516	1038
$\sigma_{NC} (P = -0.8)$	fb	24	48	70	149
$\sigma_{CC} (P = 0)$	fb	110	206	289	577
$\sigma_{NC} (P = 0)$	fb	20	41	64	127
HH in CC	fb	0.02	0.07	0.13	0.46

nominal LHeC and FCC-eh configurations. The statistics at the LHeC will be about ten times lower than that at FCC-eh, since the cross-section is diminished by  $\simeq 1/5$  and due to a shorter expected running time, i.e. the integrated luminosity is assumed to be half of that at the FCC-eh. Accessing rarer SM Higgs decay channels is the particular strength of luminous  $pp$  scattering at the highest energies, rather than that of anticipated  $ep$  or  $e^+e^-$  colliders.

**Table 15.** Total event rates and cross-sections for SM Higgs decays in the charged- ( $ep \rightarrow \nu HX$ ) and neutral- ( $ep \rightarrow eHX$ ) current production in polarised ( $P = -0.8$ ) electron–proton DIS at the LHeC ( $\sqrt{s} = 1.3$  TeV) and the FCC-eh ( $\sqrt{s} = 3.5$  TeV), for integrated luminosities of 1 and 2  $\text{ab}^{-1}$ , respectively. The branching fractions are taken from [585]. The estimates are at the LO of QCD using the CTEQ6L1 PDF and the default scale of MadGraph, see the setup in table 14.

Channel	Fraction	Number of events			
		CC		Neutral current	
		LHeC	FCC-eh	LHeC	FCC-eh
$b\bar{b}$	0.581	114 500	1 208 000	14 000	175 000
$W^+W^-$	0.215	42 300	447 000	5160	64 000
$gg$	0.082	16 150	171 000	2000	25 000
$\tau^+\tau^-$	0.063	12 400	131 000	1500	20 000
$c\bar{c}$	0.029	5700	60 000	700	9000
$ZZ$	0.026	5100	54 000	620	7900
$\gamma\gamma$	0.0023	450	5000	55	700
$Z\gamma$	0.0015	300	3100	35	450
$\mu^+\mu^-$	0.0002	40	410	5	70
$\sigma$ (pb)		0.197	1.04	0.024	0.15

The signal strength and coupling analyses subsequently presented address the seven most frequent decays, representing 99.9% of the SM Higgs decays. In addition, there is a significant potential for a measurement of the  $H \rightarrow \mu\mu$  decay at the FCC-eh, which, as seen in table 15, may provide about 500 (45) events from CC and NC DIS at the FCC-eh (LHeC). Thus, one may be able to measure this process to a precision of about 6% at the FCC-eh and 18% at LHeC.

### 7.3. Higgs signal-strength measurements

SM Higgs production in deep inelastic  $ep$  scattering proceeds via vector-boson fusion in either charged- or neutral-current scattering, as illustrated in figure 94. The scattering cross-sections, including the decay of the Higgs boson into a pair of particles  $A_i\bar{A}_i$  can be written as

$$\sigma_{\text{CC}}^i = \sigma_{\text{CC}} \cdot \frac{\Gamma^i}{\Gamma_H} \quad \text{and} \quad \sigma_{\text{NC}}^i = \sigma_{\text{NC}} \cdot \frac{\Gamma^i}{\Gamma_H}. \quad (7.1)$$

Here, the ratio of the partial to the total Higgs decay width defines the branching ratio,  $\text{br}_i$ , for each decay into  $A_i\bar{A}_i$ . The  $ep$  Higgs production cross-section and the  $O(1)$   $\text{ab}^{-1}$  luminosity prospects will allow us to investigate the seven most frequent SM Higgs decays, i.e. those into fermions ( $b\bar{b}$ ,  $c\bar{c}$ ,  $\tau^+\tau^-$ ) and into gauge particles ( $WW$ ,  $ZZ$ ,  $gg$ ,  $\gamma\gamma$ ) with high precision at the LHeC and its higher-energy versions.

In  $ep$  one obtains constraints on the Higgs production characteristics from CC and NC scattering, which uniquely probe HWW and the HZZ production, respectively. Via the per-event selection of the final-state lepton, which is either an electron (NC DIS) or missing energy (CC DIS), those production vertices can be uniquely distinguished, in contrast to the case of  $pp$ . In  $e^+e^-$ , at the ILC, operations at 250 GeV and separately at 500 GeV have been considered in order to optimise the HZZ- versus HWW-sensitive production cross-section measurements [586]. For CLIC the cms energy may be set to 380 GeV as a compromise working point for



joint NC and CC measurements, including access to top production [587]. The salient advantage of the  $e^+e^-$  reaction, similarly considered for the more recent circular collider proposals, the Circular Electron Positron Collider (CEPC) [18] and the FCC-ee [15], stems from the kinematic constraint of the Higgs-strahlung,  $e^+e^- \rightarrow Z^* \rightarrow ZH$ , which determines the total Higgs production cross-section independently of its decay.

The sum of the branching ratios for the seven Higgs decay channels studied here for  $ep$  adds up to 99.87% of the total SM width [588]. As is discussed in section 7.6, significant constraints on the  $H \rightarrow$  invisible decay can also be set with  $ep$ , although they are not able to exclude exotic, unnoticed Higgs decays. The accurate reconstruction of all decays considered here will impose a severe constraint on the total cross-section and also of the total decay width of the Higgs boson in the SM. To evaluate the measurement accuracy, the cross-section measurement prospects for a decay channel  $i$  are presented here as relative signal strengths  $\mu^i(\text{NC, CC})$  obtained from division by the SM cross-section.

Initially, detailed simulations and Higgs extraction studies for the LHeC were performed for the dominant  $H \rightarrow b\bar{b}$  [589–593] and the challenging  $H \rightarrow c\bar{c}$  [593–595] channels. The focus on the  $H \rightarrow b\bar{b}$  decay has been driven not only by its dominance but also by the difficulty of its accurate reconstruction at the LHC. It has been natural to extend this to the  $H \rightarrow c\bar{c}$  which is currently considered to be unobservable at the HL-LHC, for permutation and large background reasons. The results of the updated  $b$  and  $c$  decay studies, produced using cuts and boosted decision tree (BDT) techniques, are presented below.

A further detailed analysis has been performed for the  $H \rightarrow W^+W^-$  decay. The total of the  $WW$  decays represents 21.5% of the Higgs branching into SM particles. There is a special interest in its reconstruction in the DIS CC reaction, because this channel uniquely determines the  $HWW$  coupling to its fourth power. A complete signal and background simulation and eventual BDT analysis of the  $H \rightarrow W^+W^-$  decay in CCs has been performed, as described below. Unlike the LHC, this uses purely hadronic decays, which are very difficult to exploit in  $pp$ .

Finally, as summarised below, an analysis using acceptance, efficiency, and signal-to-background scale factors has been established for the residual four of the seven dominant decay channels; see table 15. This estimate could be successfully benchmarked with the detailed simulations for heavy-quark and  $W$  decays. This study therefore covers more than 99% of the SM Higgs decays, which are redundantly measured in  $ep$ , in both neutral and CC reactions. This opens interesting prospects for precision Higgs physics in  $ep$ , but also in combination with  $pp$ , i.e. using the LHeC combined with the HL-LHC, and later using the FCC-eh combined with the FCC-hh.

**7.3.1. Higgs decay into bottom and charm quarks.** The Higgs boson predominantly decays into  $b\bar{b}$  with a 58% branching ratio in the SM. Its reconstruction at the LHC has been complicated by the large combinatorial background. Recently, this decay was established with signal strengths, relative to the SM, of  $\mu_{bb} = 1.01 \pm 0.12(\text{stat}) \pm_{0.15}^{0.16}(\text{exp})$  by ATLAS [596] with a luminosity of  $79.8 \text{ fb}^{-1}$  and of  $\mu_{bb} = 1.01 \pm 0.22$  by CMS [597] with a luminosity of  $41.3 \text{ fb}^{-1}$ . This is a remarkable experimental LHC achievement, because for a long time, one expected to be unable to measure this decay to better than about 10% at the future HL-LHC. Meanwhile, this expectation has become more optimistic with the updated HL-LHC prospects [598]; however, the most hopeful assumption for the  $H \rightarrow c\bar{c}$  decay is a limit of two times the SM expectation.

Because of the special importance of determining the frequent  $b\bar{b}$  decay most accurately, and with it, the full set of SM branchings, the prime attention of the studies of the LHeC Higgs prospects has been given to these two channels. The first PGS detector-level study was

published with the CDR [1] before the announcement of the discovery of the Higgs boson and assuming  $M_H = 120$  GeV. This and subsequent analyses use samples generated by MadGraph5 [375] for both signal and background events, with fragmentation and hadronization via PYTHIA 6.4 [599] in an  $ep$  customised program version<sup>189</sup>. Subsequent analyses have been updated to  $M_H = 125$  GeV and to state-of-the-art fast detector simulation with DELPHES 3 [601] as a testbed for  $ep$  detector configurations. Both cut-based and BDT analyses were performed in independent evaluations.

As shown in the CDR, the  $H \rightarrow b\bar{b}$  decay could be measured by applying classical kinematic selection requirements, as follows:

- CC DIS kinematic cuts of  $Q_h^2 > 500$  GeV<sup>2</sup>,  $y_h < 0.9$ , missing energy of  $E_T^{\text{miss}} > 30$  GeV, and no electrons in the final state to reject NC DIS;
- At least three anti-kt  $R = 0.7$  jets with  $p_T > 20$  GeV which are subject to further b-tagging requirements;
- A Higgs candidate from two b-tagged jets with b-tagging efficiencies of 60 to 75%, charm (light quark) misidentification efficiencies of 10 to 5% (1%);
- Rejection of single-top events, which is achieved by requiring a dijet W candidate mass of greater than 130 GeV and a trijet top candidate mass of more than 250 GeV using a combination with one of the b-jets of the Higgs mass candidate;
- A forward scattered jet with  $\eta > 2$  and a large  $\Delta\phi_{b,\text{MET}} > 0.2$  between the b-tagged jet and the missing energy.

The dominant backgrounds are CC DIS multijet and single top production, while the CC Z, W, and NC Z contributions are small. The background due to multijets from photoproduction (where  $Q^2 \sim 0$ ) can be reduced considerably by tagging the small-angle scattered electron with an electron tagger. The result of a cut-based analysis is shown in figure 98 where clear Z and  $H \rightarrow b\bar{b}$  peaks are seen. Assuming that the photoproduction background is rejected with a 90% efficiency, the resulting signal is shown in figure 98, corresponding to an SM  $H \rightarrow b\bar{b}$  signal strength  $\delta\mu/\mu$  of 2% for an integrated luminosity of 1000 fb<sup>-1</sup> and  $P_e = -0.8$ . This result is consistent with earlier analysis and robust w.r.t. the update of the Higgs mass from 120 to 125 GeV, which confirmed the high  $S/B > 1$  (see also reference [592], where an alternative approach used to estimate the multijet photoproduction background gave a similar signal strength uncertainty). The result illustrates that even with harsh kinematic requirements and a small luminosity of 100 fb<sup>-1</sup>, this important decay channel could be measured to an uncertainty of about 6%.

The stability of the cut-based results has been further shown for different hadronic calorimeter resolution setups

$$\frac{\sigma}{E} = \frac{a}{\sqrt{E}} \oplus b \quad \text{for } |\eta| < |\eta_{\text{min}}|, \quad (7.2)$$

$$\frac{\sigma}{E} = \frac{c}{\sqrt{E}} \oplus d \quad \text{for } |\eta_{\text{min}}| < |\eta| < 5, \quad (7.3)$$

where for  $\eta_{\text{min}} = 3$ , the parameter  $b$  ( $d$ ) is varied between 1 (3) and 7 (9)% for two resolution parameters  $a$  ( $c$ ) of either 30 (60) or 35 (45)%. Alternatively, the central range was restricted to

<sup>189</sup> Hadronic showering is not expected to change the kinematics of the DIS-scattered leptons. This has been shown (see page 11 of reference [600]), with a very good level of agreement of the NC DIS electron kinematics, with and without  $ep$ -customized Pythia showering. Specifically, for 99.8% of events, the kinematics in the momentum vector components remain unchanged, and for 98% of the events, the energy of the scattered electrons remains unchanged.

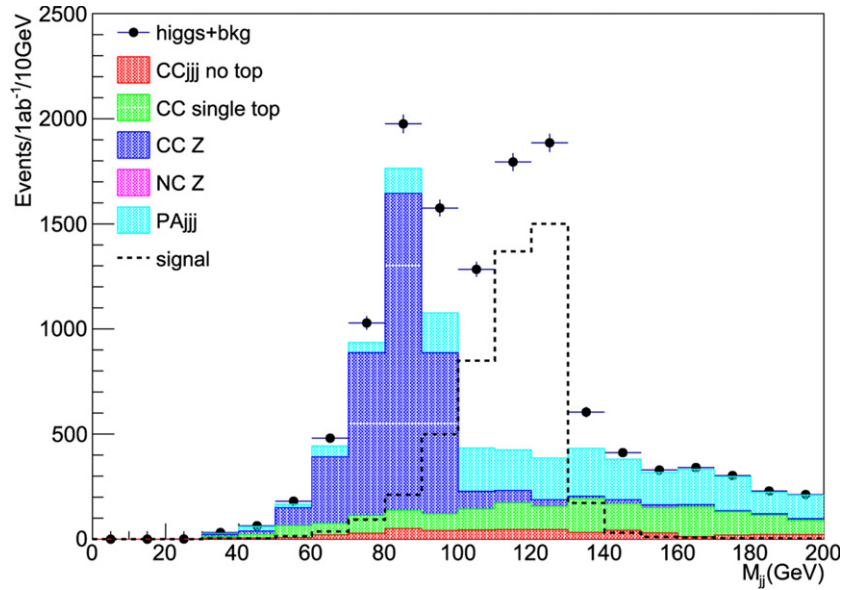


**Figure 98.** Expected invariant dijet mass distribution at DELPHES detector level for  $1 \text{ ab}^{-1}$  and  $-80\%$  electron polarisation at the LHeC. The  $S/B$  is about 2.9 for events in the Higgs mass range of 100–130 GeV. Events are generated with MadGraph using  $M_H = 125 \text{ GeV}$ , showered with PYTHIA 6.4, and subject to cut-based event selection criteria; see the text for further details. Note that samples are generated with a minimum dijet mass cut of 60 GeV.

$\eta_{\min} = 2$  with a parameter  $b$  ( $d$ ) of 3 (5)% for resolution parameters  $a$  ( $c$ ) of 35 (45)%. Although the signal yields varied within 34% when the same analysis cuts were used, it was shown that with an adjusted set of cuts (notably, the choices of cuts for the Higgs mass range,  $\Delta\phi_{b,\text{MET}}$ , and forward  $\eta$ ), the SM  $H \rightarrow b\bar{b}$  signal strength  $\delta\mu/\mu$  varied with a fractional uncertainty of up to 7%.

The cut-based  $H \rightarrow b\bar{b}$  signal strength analyses suffer from rather low total selection efficiencies in the range of only 3 to 4%. Modern state-of-the-art analysis techniques, e.g. those used to find  $H \rightarrow b\bar{b}$  at the LHC regardless of the overwhelming QCD jet background, are based on the use of neural networks for the HF tagging as well as in the analysis.

BDT  $H \rightarrow b\bar{b}$  and  $H \rightarrow c\bar{c}$  analyses using the TMVA package with ROOT [602] are performed using independently produced signal and background samples based on the same setup as for the cut-based analyses, see figure 98. Those analyses start with loose preselections of at least three anti-kt jets with  $p_{\text{T}} > 15 \text{ GeV}$  without any further HF tagging, in addition to CC DIS kinematic cuts of  $Q_h^2 > 400 \text{ GeV}^2$  and  $y_h < 0.9$  and a missing energy  $E_{\text{T}}^{\text{miss}} > 20 \text{ GeV}$ . The invariant mass distributions using anti-kt  $R = 0.5$  jets are illustrated in figure 99, where the mass distributions in the upper plots illustrate, in particular, the single top contributions and the subsequent significant Higgs signal loss if simple anti-top cuts were to be applied. In the lower plot of figure 99 the invariant dijet mass distribution of untagged Higgs signal candidates is seen clearly above the background contributions in the expected mass range of 100–130 GeV. It can be observed that the remaining background is dominated by CC multi jets. The quantities represented in the three distributions of figure 99 are important inputs for the BDT neural network, in addition to further variables describing e.g. the pseudorapidities

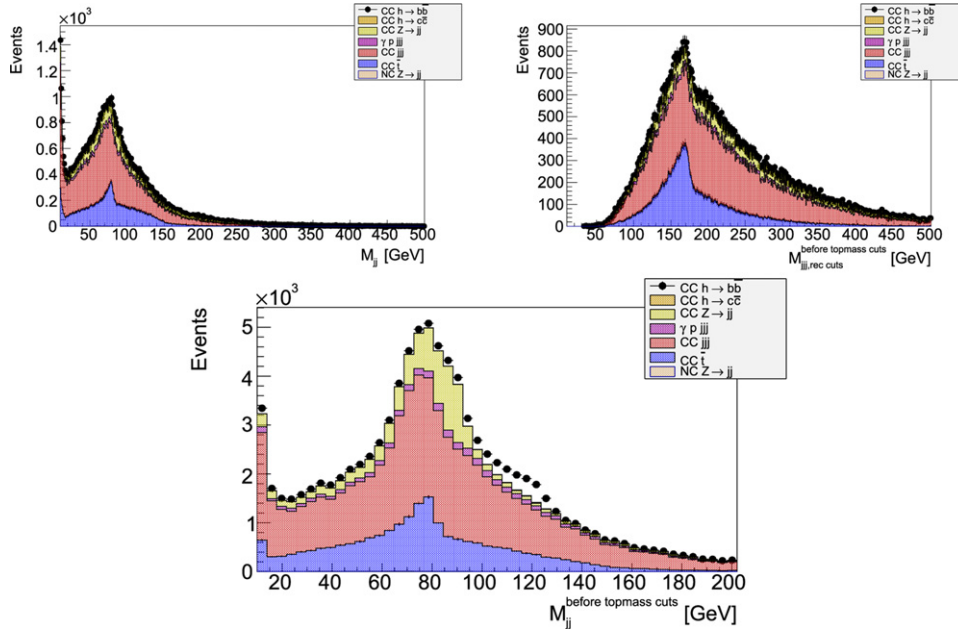


**Figure 99.** Invariant mass distributions at DELPHES detector level for an integrated luminosity of  $100 \text{ fb}^{-1}$  and  $-80\%$  electron polarisation. Events passed preselection cuts of  $Q_h^2 > 400 \text{ GeV}^2$ ,  $y_h < 0.9$ ,  $E_T^{\text{miss}} > 20 \text{ GeV}$  and at least three flavour-untagged anti-kt  $R = 0.5$  jets with  $p_T > 15 \text{ GeV}$ . The different colours show the contributions per process; the photoproduction background ( $\gamma p \text{ jjj}$ ) is assumed to be rejected with an efficiency of 90%. Note that samples are generated with a minimum dijet mass cut of 60 GeV. Upper left: invariant dijet mass, showing  $W$  candidates from single top production (blue), based on combining jets with the second- and third-lowest  $|\eta|$  values per event. Upper right: invariant mass distribution combining the three highest  $p_T$  jets per event, showing single top-mass candidates (blue). Lower middle: invariant dijet mass, showing Higgs candidates (black dots, including background), combining jets with the two lowest  $|\eta|$  values per event.

of the Higgs and forward jet candidates, including jet and track HF probabilities; see details below and also in reference [595].

As a novel element in these analyses, HF tagging based on track and jet probabilities has been implemented in the DELPHES detector analysis following the Tevatron D0 experimental ansatz described e.g. in reference [603]. The resulting  $b$  and  $c$ -jet efficiencies versus the light-jet misidentification efficiencies are illustrated in figure 100 for an assumed nominal impact parameter resolution of 10 ( $5$ )  $\mu\text{m}$  for tracks with  $0.5 < p_T < 5$  ( $> 5$ ) GeV and three choices of the distance parameter  $R = 0.5, 0.7, 0.9$  for the anti-kt jets. In particular, for the charm tagging, impact parameters are studied with resolutions of 5 ( $2.5$ )  $\mu\text{m}$  (half-vertex resolution) and 20 ( $10$ )  $\mu\text{m}$  (double-vertex resolution) for tracks with  $0.5 < p_T < 5$  ( $> 5$ ) GeV within  $|\eta| < 3.5$ . For a conservative light-jet efficiency of 5%, the  $b$ -jet tagging efficiency is rather robust, around 60% for the considered nominal impact parameter performance and the three considered anti-kt distance parameters and in slight favour of the anti-kt  $R = 0.5$  choice. For the expected charm tagging, however, an excellent impact parameter resolution and  $R = 0.5$  jets give the best tagging efficiency of around 30%. This means a significant improvement e.g. w.r.t. a 23% charm tagging efficiency for  $R = 0.9$  jets at a nominal impact parameter resolution. These

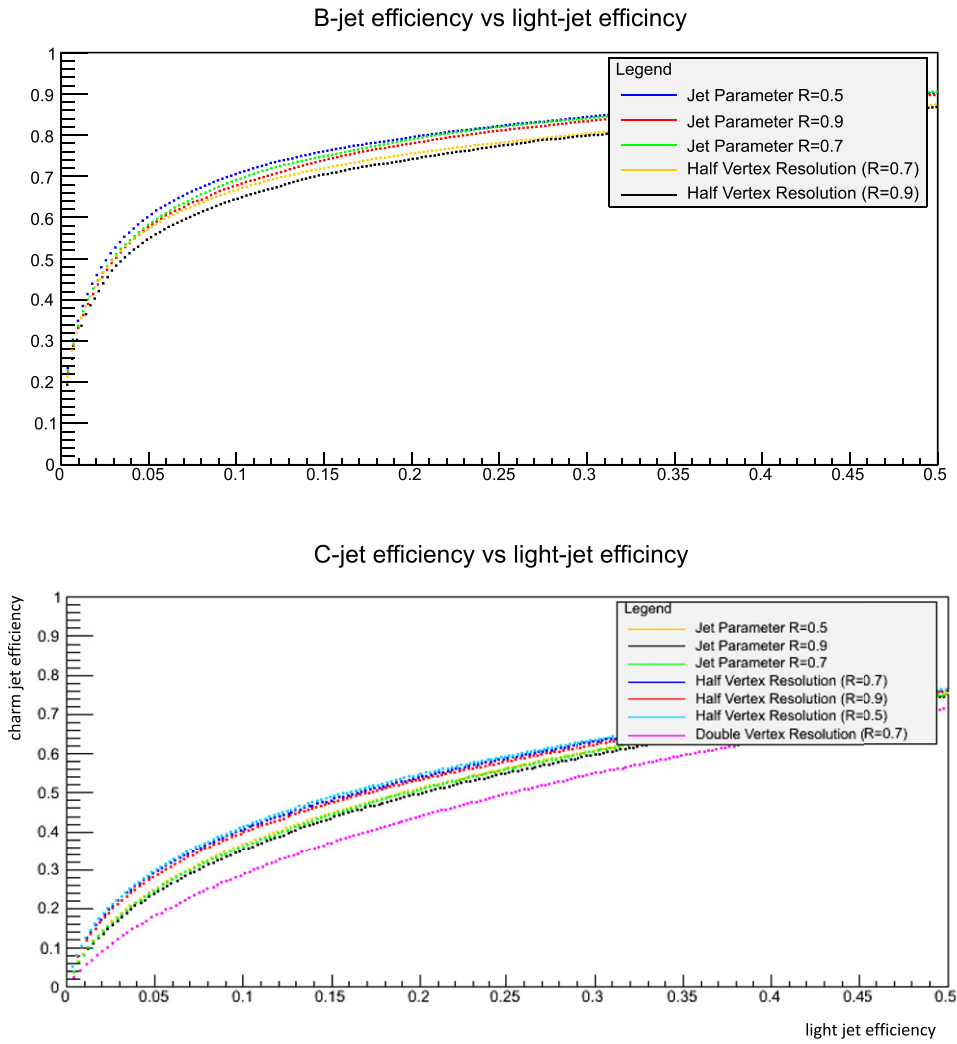


**Figure 100.** Expected average efficiencies of tagging a  $b$  jet (upper plot) and a charm jet (lower plot) versus the light-jet efficiency ( $x$ -axis) based on Tevatron-style jet tagging [603]. Events are selected at the DELPHES detector level using a CC multijet sample and for an integrated luminosity of  $100 \text{ fb}^{-1}$ . The coloured lines correspond to the choice of the anti- $k_t$  distance parameter  $R$  and various assumed impact parameter resolutions of  $10$  ( $5$ )  $\mu\text{m}$  (nominal, no text added in legend),  $5$  ( $2.5$ )  $\mu\text{m}$  (half-vertex resolution), and  $20$  ( $10$ )  $\mu\text{m}$  (double-vertex resolution) for tracks with  $0.5 < p_T < 5(> 5)$  GeV within  $|\eta| < 3.5$ .

tagging efficiencies can be considered as realistic but rather conservative, in particular, for the remaining light-jet efficiency, which is expected to be about 0.1% at a  $b$ -jet efficiency of 60% using LHC-style neural-network-based taggers.

A series of BDT score tests was performed using the preselected signal samples and a CC multijet as the main background sample to determine the optimal combination of impact resolution parameters while resolving the two jets from the Higgs decay in dependence of  $R$ . The



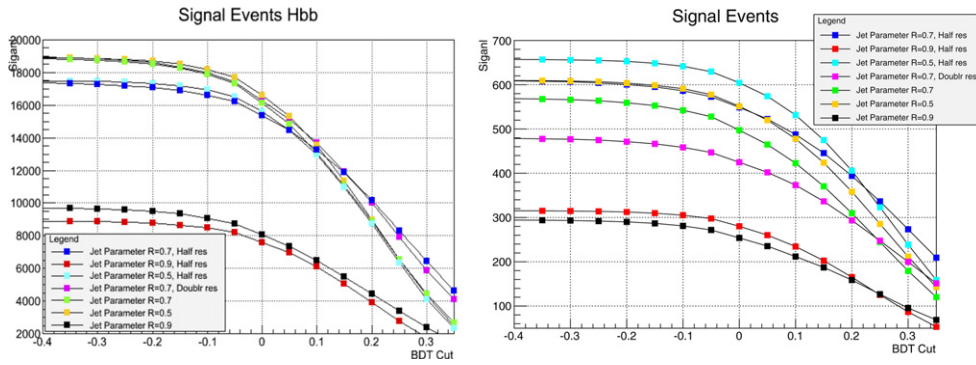


**Figure 101.** Expected  $H \rightarrow b\bar{b}$  (left) and  $H \rightarrow c\bar{c}$  (right) signal events as a function of the BDT score. Events are selected at the DELPHES detector level for an integrated luminosity of  $1 \text{ ab}^{-1}$  and  $-80\%$  electron polarisation. The symbols correspond to the choice of the anti-kt distance parameter  $R$  and various assumed impact parameter resolutions of  $10$  ( $5$ )  $\mu\text{m}$  (nominal, no further text added in the legend),  $20$  ( $10$ )  $\mu\text{m}$  (double resolution), and  $5$  ( $2.5$ )  $\mu\text{m}$  (half resolution) for tracks with  $0.5 < p_T < 5$  ( $>5$ ) GeV within  $|\eta| < 3.5$ .

resulting number of  $H \rightarrow b\bar{b}$  ( $c\bar{c}$ ) signal events versus the BDT score is illustrated in figure 101, which shows the evident interplay between detector performance and the choice of jet parameters  $R$ , where the  $R = 0.9$  anti-kt jets show the worst performance. At a score of BDT = 0, the highest number of signal events are achieved for  $R = 0.5$  anti-kt jets for both charm and beauty decays, where the effect of the impact resolution is much more constricted for the charm than for the beauty tagging. Following figure 101, complete BDT-based  $H \rightarrow b\bar{b}$  ( $c\bar{c}$ ) analyses are performed for anti-kt  $R = 0.5$  jets and an impact parameter resolution of  $5$  ( $2.5$ )  $\mu\text{m}$  (half-vertex resolution) for tracks with  $0.5 < p_T < 5$  ( $>5$ ) GeV within  $|\eta| < 3.5$ . The acceptance times efficiency values are about  $28\%$  for the  $H \rightarrow b\bar{b}$  channel and about  $11\%$  for the  $H \rightarrow c\bar{c}$  channel at BDT = 0.

The results of the BDT  $H \rightarrow b\bar{b}$  and  $H \rightarrow c\bar{c}$  analyses, assuming that each background contribution is understood to be at the  $2\%$  level via the control regions and that there are negligible statistical MC uncertainties for the background predictions for the signal region, as shown in figure 102. Using these assumptions, the resulting signal strengths are  $0.8\%$  for the  $H \rightarrow b\bar{b}$  channel and  $7.4\%$  for the  $H \rightarrow c\bar{c}$  channel. For the latter, the SM Higgs decays, in particular,  $H \rightarrow b\bar{b}$ , also represent also a part of the  $cc$  background contribution, but can be controlled by the high precision of the genuine  $bb$  result. Advanced analysis strategies for distinguishing  $bb$  and  $cc$  SM Higgs decays via several layers of neural networks are discussed e.g. in reference [604] for a  $250 \text{ GeV}$  ILC and  $M_H = 120 \text{ GeV}$ , where the expected  $H \rightarrow c\bar{c}$  cross-section of  $6.9 \text{ fb}$  for  $M_H = 120 \text{ GeV}$  yields a signal-strength uncertainty of  $8.8\%$  in the  $ZH$  all-hadronic channel ( $Z \rightarrow q\bar{q}$ ) at an integrated luminosity of  $250 \text{ fb}^{-1}$ . The ILC charm cross-section is quite similar to the  $5.7 \text{ fb}$  cross-section for  $M_H = 125 \text{ GeV}$  at the LHeC. The number of preselected charm events and SM Higgs contributions used in the ILC analysis are at a similar level as for this analysis, while the non-Higgs background at the ILC is larger by a factor of  $6.8$  than that of the LHeC preselected events. Comparing the two results gives confidence in the expected  $H \rightarrow c\bar{c}$  signal-strength results at LHeC using the aforementioned assumptions.

In conclusion, Higgs to HF signal-strength measurements require excellent state-of-the-art calorimetry with high acceptance and excellent resolution as well as an impact parameter



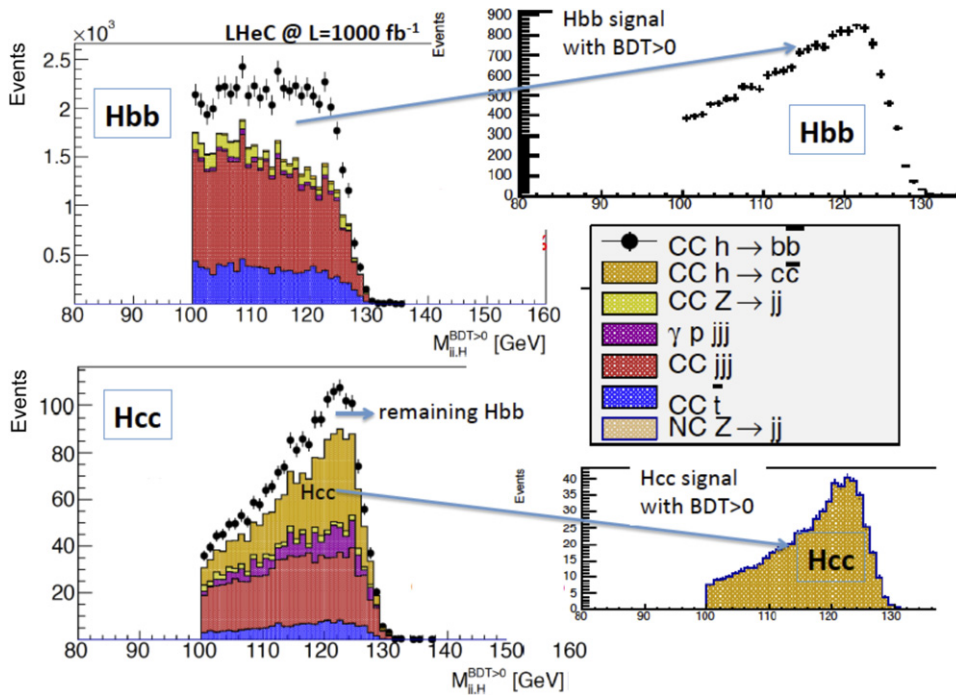


**Figure 102.** Result of the joint  $H \rightarrow b\bar{b}$  and  $H \rightarrow c\bar{c}$  analysis for an integrated luminosity of  $1 \text{ ab}^{-1}$  and  $-80\%$  electron polarisation at the LHeC. Left: invariant mass distributions for the two channels with signal and background; see the text. Right: expected Higgs signal distributions after background subtraction. The background is assumed to be at the 2% level via control-region measurements.

resolution such as that achieved, for example, with the ATLAS inner-b layer. In addition, the details of the analysis strategy, which uses a neural network and advanced statistical methods (e.g. via RooStats/RooFit, see e.g. complex analysis methods using constraints via well-measured control regions in signal fits [605]) will be important to control high signal at low background yields, where the background is expected to be constrained via control regions to better than the 2% level.

**7.3.2. Higgs decay into  $WW$ .** Inclusive CC scattering, the CC production of the Higgs boson with a  $WW$  decay, and the main backgrounds are illustrated in figure 103. The  $ep \rightarrow \nu H X \rightarrow \nu W^* W X$  process with hadronic  $W$  decays (see figure 103(a)) causes a final state, which to the lowest order comprises  $4 + 1$  jets and the escaping neutrino identified via missing energy (MET). The pure hadronic  $WW$  Higgs decay has a branching ratio of about 45%. Using MadGraph (MG5) and a version of PYTHIA customised for  $ep$  DIS, events have been generated and analysed after passing a DELPHES description of the FCC-eh detector. This study has been performed for the most asymmetric beam configuration of  $E_e = 60 \text{ GeV}$  and  $E_p = 50 \text{ TeV}$ , yielding  $\sqrt{s} = 3.5 \text{ TeV}$ .

This analysis has been focussed on the requirement for four fully resolved jets from the Higgs decay and at least one forward jet, where the jets are reconstructed using the anti- $k_T$  algorithm with  $R = 0.7$ . Further event categories in which the jets from the Higgs decay products may merge and yield either three or only two large- $R$  jets in the final state have not yet

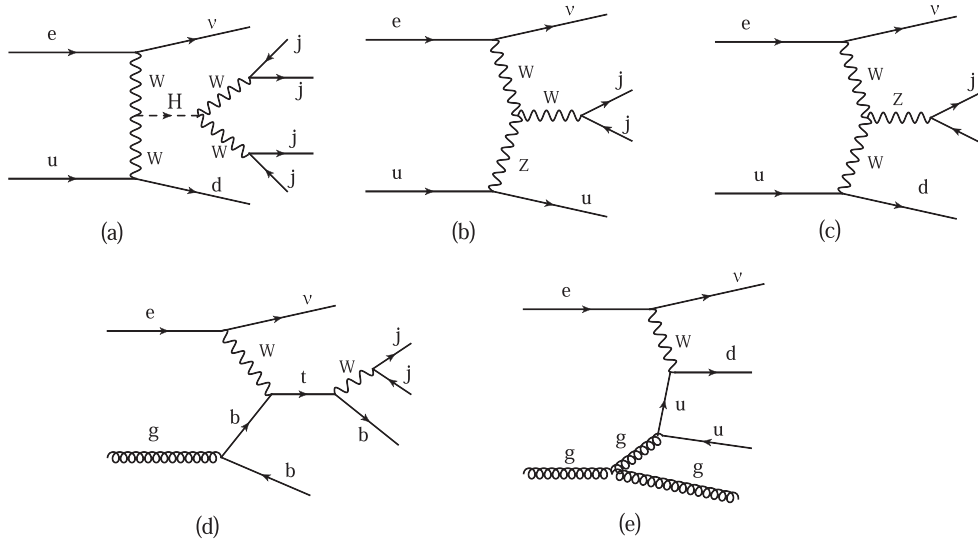


**Figure 103.** Typical lepton–parton diagrams relevant to the  $H \rightarrow W^*W$  analysis: (a) signal: CC DIS with a Higgs produced in the  $t$ -channel and its decay into a pair of  $W$  bosons, which generates a four-jet final state, as well as the forward jet. The other diagrams are examples to illustrate background channels which, at higher orders with extra emissions, may mimic the signal configuration: (b) single  $W$ -boson production; (c) single  $Z$ -boson production; (d) single top-quark production; (e) QCD multijet production.

been considered. However, as shown by state-of-the-art LHC-style studies, those event categories and the use of e.g. dedicated top- and  $W$ -tagging based on large- $R$  jet substructures may give additional access to Higgs signal-strength measurements.

The analysis, which requires fully resolved jets from the  $H \rightarrow W^*W \rightarrow 4j$  decay, and at least one forward jet, proceeds according to the following steps:

- Study of the reconstructed event configuration and recognition of its characteristics for defining a set of loose cuts. These are: the  $p_T$  of any jet has to be larger than 6 GeV, the rapidity difference between the forward jet and the reconstructed four-jet Higgs candidate must be larger than 1.5, the azimuthal difference between that Higgs candidate and either the forward jet or the scattered lepton (MET) must be larger than 1, and the dijet masses of the virtual and the real  $W$  boson candidate must be larger than 12 GeV and less than 90 GeV ( $Z$  mass).
- Verification of truth matching to check that the combinatorial association of jets reproduces the Higgs candidate (four jets) and its  $W$  (dijet) decays (see figure 104 and the text).
- Application of this algorithm to the simulated background samples. The MadGraph single  $W$ , top, and  $Z$  production samples are turned into a multijet background by PYTHIA. The cross-sections are reliably calculated, as there is a hard scale available. The initial cuts reduce this background to about 3% for single vector boson production and to 9% for top quark production.
- Due to the size of the  $Hb\bar{b}$  decay and jet radiation, a residual background occurs due to the Higgs itself, which is also reduced to 3% through the cuts.

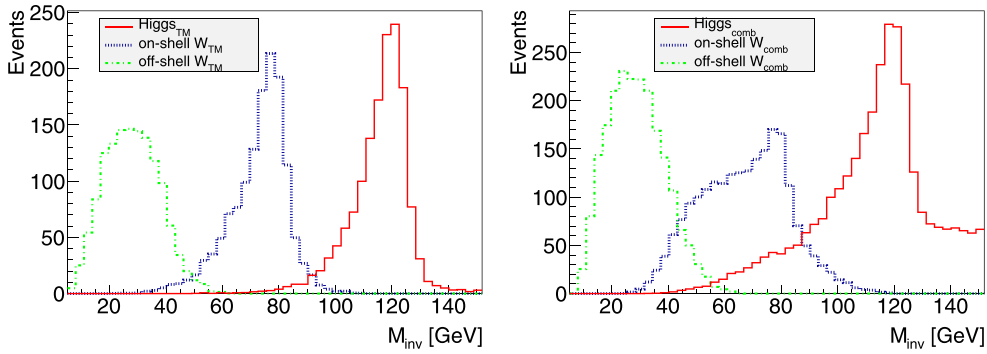


**Figure 104.** Reconstructed signal mass distributions (at the DELPHES detector level) of truth-matched events (left) and after the just combinatorial association of jets to the two  $W$  bosons forming Higgs candidates (right). Green: virtual  $W^*$  boson; blue:  $W$  boson; red: Higgs signal from  $W^*W$  reconstruction. It can be observed that the combination causes some background, while the respective signal peaks are clearly preserved with a purity of 68%, so that the correct forward jet is identified.

- The final background is due to multijets. The MadGraph cross-section for a  $4 + 1$  jet CC configuration is considered much too large in view of the cross-section measurement results as a function of the jet number, both at HERA and the LHC; see, for example, [606]. The sample was thus scaled using a conservative  $\alpha_s$  renormalisation to the inclusive cross-section. The initial cuts reduce the multijet background to about 13%.
- Following a detailed training study, a BDT analysis was used. This determined a final event number of about 12k for to a signal-to-background ratio of 0.23.

The result of this analysis translates to an estimated uncertainty of 1.9% in  $\mu_{WW}$  at the FCC-eh. The four-jet mass distribution after the BDT requirement exhibits a clear  $WW$  Higgs peak (see figure 104), which illustrates the suitability of using the electron–proton environment for Higgs measurements in clearly challenging final-state configurations.

**7.3.3. Accessing further decay channels.** Following the detailed studies of the  $b\bar{b}$  and  $c\bar{c}$  decay channels presented above, a coarser analysis was established for other frequent decay channels, both in NC and CC. Here, acceptances and backgrounds were estimated with MadGraph, and efficiencies that distinguish the leptonic and hadronic decay channels for  $W$ ,  $Z$ , and  $\tau$ , were taken from prospective studies on Higgs coupling measurements at the LHC [607]. This provided a systematic scale factor  $f$  for the pure statistical error  $\delta_s$ , which comprised the signal-to-background ratio  $S/B$ , the product of acceptance  $A$ , and extra reconstruction efficiency  $\epsilon$ , according to

$$f = \sqrt{\frac{1 + \frac{B}{S}}{A \cdot \epsilon}}. \quad (7.4)$$

The error in the signal strength  $\mu_i$  for each of the Higgs decay channels  $i$  is determined by  $\delta\mu_i/\mu_i = f_i \cdot \delta_s$ .

To a good approximation these factors apply to the LHeC, the HE-LHeC, and the FCC-eh, because the detector dimensions and acceptances scale with the proton energy; conceptually, they use the same technology and very similar resolution assumptions. Therefore, one main matrix is used for the subsequent experimental deterioration of the pure statistics precision,

**Table 16.** Statistical uncertainties for the seven most abundant Higgs decay channels for the CC Higgs measurement prospects with the FCC-eh, together with their systematic scale factors  $f$ , equation (7.4), resulting from acceptance, background, and efficiency effects as given. Note that the results for  $b\bar{b}$  and  $c\bar{c}$  are taken from the BDT analysis (section 7.3.1) with an efficiency of one. The  $WW$  result is replaced by the BDT analysis (section 7.3.2) in order to quote the expected signal strength uncertainty.

Parameter	$b\bar{b}$	$WW$	$gg$	$\tau\tau$	$cc$	$ZZ$	$\gamma\gamma$
Branching fraction	0.581	0.215	0.082	0.063	0.029	0.026	0.0023
Statistical error ( $\delta_s$ ) (%)	0.09	0.15	0.24	0.28	0.41	0.43	1.41
Acceptance ( $A$ )	0.14	0.10	0.40	0.40	0.11	0.10	0.40
Signal/background ( $S/B$ )	9	0.2	0.1	0.2	0.43	0.33	0.5
Extra efficiency ( $\epsilon$ )	1	0.3	0.5	0.43	1	0.5	0.7
Scale factor $f$	2.8	16	7.4	5.9	5.5	9.0	3.3

**Table 17.** Summary of estimates for the experimental uncertainty of the signal strength  $\mu$ , in per cent, for the seven most abundant Higgs decay channels, in charged and neutral currents, for the LHeC, the HE-LHeC, and the FCC-eh. The  $b\bar{b}$  channel is the one which is most sensitive to theoretical uncertainties and for illustration is given two corresponding columns, see section 7.3.4.

Setup	$b\bar{b}$	$b\bar{b} \oplus \text{Thy}$	$WW$	$gg$	$\tau\tau$	$cc$	$ZZ$	$\gamma\gamma$
LHeC NC	2.3	2.4	17	16	15	20	35	42
LHeC CC	0.80	0.94	6.2	5.8	5.2	7.1	12	15
HE-LHeC NC	1.15	1.25	8.9	8.3	7.5	10	17	21
HE-LHeC CC	0.41	0.65	3.2	3.0	2.7	3.6	6.2	7.7
FCC-eh NC	0.65	0.82	5.0	4.7	4.2	5.8	10	12
FCC-eh CC	0.25	0.56	1.9	1.8	1.6	2.2	3.8	4.6

both for CC and NC. Future detailed analyses will lead to a refinement of this expectation, which, for the current purpose, was beyond the scope of the study. The results of the analysis of uncertainties are summarised in table 16 for the CC channel at the FCC-eh.

The resulting signal-strength uncertainty values are provided in table 17. Note that for the beauty, charm, and  $WW$  channels, the table contains the BDT analysis<sup>190</sup> results of sections 7.3.1 and 7.3.2, respectively. The beauty and charm CC results stem from the BDT analysis for the LHeC and are applied to the FCC-eh using a factor of about 1/3. The CC  $WW$  results are due to the FCC-eh BDT analysis and are used for the LHeC, enlarged by a factor of 3.2 determined by the different cross-sections and luminosities. For the HE-LHC, the values are about twice as precise as the LHeC values, because the cross-section is enlarged by about a factor of two (see table 14), and the integrated luminosity, at  $2 \text{ ab}^{-1}$ , is twice that of the LHeC. All signal-strength uncertainties, in both CC and NC, for the three collider configurations are shown in figure 105.

**7.3.4. Systematic and theoretical errors.** The signal strength is expressed relative to a theoretical calculation of the CC Higgs cross-section, including its decay into a chosen channel,

<sup>190</sup>This is in very good agreement with the scale-factor method: for example, the  $WW$  result in table 16 leads to a value that is slightly (2.1%) worse than the BDT analysis.

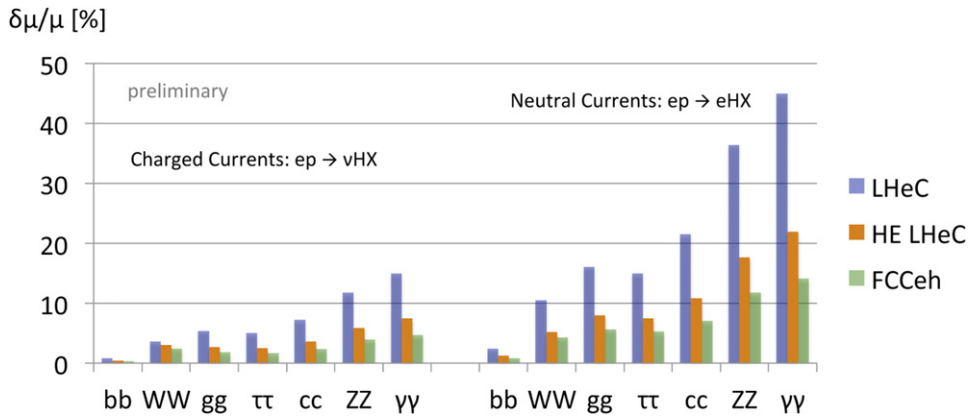


**Figure 105.** Uncertainties of signal-strength determinations in the seven most abundant SM Higgs decay channels for the FCC-eh (green, 2 ab<sup>-1</sup>), the HE LHeC (brown, 2 ab<sup>-1</sup>) and the LHeC (blue, 1 ab<sup>-1</sup>), in charged- and neutral-current DIS production.

according to

$$\mu = \frac{\sigma_{\text{exp}}}{\sigma_{\text{thy}}} = \frac{\sigma_{\text{exp}}}{\sigma_{\text{Hty}} \cdot \text{br}}. \tag{7.5}$$

Consequently, one can decompose the (relative) error of  $\mu$  into the genuine measurement error, denoted by  $\delta\sigma_{\text{exp}}$ , which includes a possible systematic error contribution,  $E$ , and two further components, as follows:

$$\frac{\delta\mu}{\mu} = \left\{ \left( \frac{\delta\sigma_{\text{exp}}}{\sigma_{\text{exp}}} \right)^2 \cdot (1 \oplus E) + \left( \frac{\delta\sigma_{\text{Hty}}}{\sigma_{\text{Hty}}} \right)^2 + \left( \frac{\delta\text{br}}{\text{br}} \right)^2 \right\}^{1/2}, \tag{7.6}$$

which are due to imperfections in the theoretical model of the Higgs production cross-section,  $\sigma_{\text{Hty}}$ , and uncertainties in the branching ratio, br, in the channel under study, respectively. Note that the experimental uncertainty takes into account possible variations of the backgrounds, which are conservatively estimated and thus represent more than genuine statistics.

The channel-dependent signal-strength uncertainties quoted in table 17 are estimates of the first, experimental term in equation (7.6), neglecting additional systematic error effects. They are derived, as stated above, from the purely statistical error ( $\delta_s = 1/\sqrt{N}$ ), its increase due to acceptance ( $A$ ) and efficiency ( $\epsilon$ ) effects and, furthermore, the modulation caused by the background-to-signal ratio ( $B/S$ ). These factors are all involved in the BDT analysis, but the scale-factor equation, equation (7.4), may be used to estimate further systematic effects for any channel. From the relation

$$\frac{\delta\sigma_{\text{exp}}}{\sigma_{\text{exp}}} = \delta_s \cdot \sqrt{\frac{1 + B/S}{A \cdot \epsilon}} \tag{7.7}$$

the combined systematic error contribution,  $E$ , caused by variations  $\Delta$  of  $A$ ,  $\epsilon$ , and the background  $B$  can be estimated as follows:

$$E = \frac{1}{2} \left\{ \left( \frac{\Delta A}{A} \right)^2 + \left( \frac{\Delta \epsilon}{\epsilon} \right)^2 + \left( \frac{\Delta B}{B} \cdot \frac{B/S}{1 + B/S} \right)^2 \right\}^{1/2}. \tag{7.8}$$

This formula shows that if the background-to-signal ratio is very small, then the background effect is suppressed,  $\propto B/S$ . If it is larger than one, the relative uncertainty of the background appears as an additional component of the signal-strength error.

Given the fact that the experimental  $H \rightarrow b\bar{b}$  result in the CC reaction is especially precise (compare table 17), an estimate was performed of the systematic error in this channel. The following effects were included: a variation of the light-quark misidentification by a factor of three, a variation of the reduction of the photoproduction via tagging of between 2% and 10%, a variation of the combined acceptance-time efficiency effect by 10%, and a variation of the hadronic energy resolution, studied in reference [590], leading to a 7% signal variation. The overall effect of these contributions determines a systematic error of about 10% in  $\mu_{bb}$ , i.e.  $\delta\mu/\mu = 0.80 \pm 0.09$  for  $H \rightarrow b\bar{b}$  at the LHeC in the CC channel. Similar levels of uncertainty are expected to occur for other channels, but have not been estimated to such detail, as those channels are measured less precisely.

A separate effect arises from the measurement of the luminosity. While that will be measured to an accuracy of 0.5%, based on Bethe–Heitler scattering and its accurate description to higher-order QEDC [1], it will additionally be negligible to a good approximation; the LHeC and its successors will provide a very precise determination of all parton distributions from the  $ep$  data alone. Any systematic mistake in the normalisation will therefore affect both the measured and the calculated cross-sections and drop out in their ratio  $\mu$ .

A further uncertainty in the signal strength arises from the theoretical description of  $\sigma_{CCH}$ , to which the measured cross-section is normalised. From a simulation of the systematic uncertainties due to imperfect calibrations and extra efficiencies, one may expect the cross-section to be known to better than 1%. The prediction will be available to the N3LO,  $\alpha_s$  will be determined to a precision of 0.1%–0.2%, and the cross-section can be gauged using the inclusive cross-section measurement. This uncertainty, following equation (7.8), appears directly as a contribution to the  $\mu$  measurement result. A 0.5% uncertainty, as can be seen in table 17, becomes noticeable in most of the  $b\bar{b}$  results, but is negligible for all other channels. In this analysis, uncertainty values of 0.5% and 1% have been considered, and their effect on the  $\kappa$  result been evaluated, see section 7.4.

A final uncertainty is caused by the branching fractions and their uncertainty. For the branching ratio that is most relevant here, the  $H \rightarrow b\bar{b}$  branching ratio, a recent uncertainty estimate [585] quotes a theoretical contribution due to missing higher orders of 0.65%, a parameterisation uncertainty depending on the quark masses of 0.73%, and an  $\alpha_s$ -induced part of 0.78%. The LHeC, or similarly, the higher-energy  $ep$  colliders, will determine the  $b$  mass (in DIS) to about 10 MeV and  $\alpha_s$  to per-mille precision [1] which would render corresponding uncertainty contributions to  $\text{br}_{bb}$  negligible. The genuine theoretical uncertainty would also be largely reduced with an extra-order pQCD. In the following study the contribution from the branching fraction uncertainty has been neglected. This may also be justified by the programme sketched here, and similarly for other future colliders: the  $ep$  colliders will measure the couplings, especially those of the  $WW$ ,  $bb$ , and  $ZZ$ , very precisely, which will enable an iterative treatment of the branching-ratio uncertainties.

It may be noted [585] that the  $\alpha_s$  contribution to the  $H \rightarrow gg$  branching fraction uncertainty is about 3.7%, i.e. twice as large as the estimated signal-strength measurement uncertainty of this channel at the FCC-eh. This highlights another important benefit of the future  $ep$  colliders and their high-precision DIS programme for precision Higgs physics at the combined  $ep$  &  $pp$  facilities.



**Table 18.** Summary of  $\kappa$  uncertainty values obtained from separate fits of the signal strength uncertainty estimates for the seven most abundant Higgs decay channels, in charged and neutral currents, for the LHeC, the HE-LHeC, and the FCC-eh; see the text.

Setup	$b\bar{b}$	$WW$	$gg$	$\tau\tau$	$cc$	$ZZ$	$\gamma\gamma$
LHeC	1.9	0.70	3.5	3.1	3.8	1.2	6.8
HE-LHeC	1.0	0.38	1.8	1.6	1.9	0.6	3.5
FCC-eh	0.60	0.22	1.1	0.93	1.2	0.35	2.1

#### 7.4. Higgs coupling analyses

In order to quantify possible deviations from the SM expectation one may use the  $\kappa$  parameterisation framework, introduced in reference [608], which enables easy comparisons between different collider configurations independently of their ability to access the total Higgs decay width. It should be noted that there are differences between the results of the effective field theory (EFT) and those of the  $\kappa$  formalism [609]. Therefore, it would also be very interesting to go beyond the  $\kappa$  framework for the  $ep$  colliders presented here, because out of the 2499 dimension-6 Wilson coefficients, a total of  $13 \cdot n_g^4 = 1053$  involve leptons and quarks [610], for  $n_g = 3$  generations. This has, however, been beyond the scope of this study. In the following, results are presented for the various  $ep$  collider configurations (section 7.2.2).

The  $\kappa$  parameters are factors in the various Higgs couplings, equal to one in the SM, which scale  $\sigma_{\text{NC/CC}}$  with  $\kappa_{Z/W}^2$ . The Higgs decay width  $\Gamma^i$  for a decay channel scales with  $\kappa_i^2$  and lead to the replacement of  $\Gamma_H$  by the sum  $\sum_j \kappa_j \Gamma^j$ , where we have assumed no non-SM H decays. This defines the following modifications of the cross-sections (equation (7.1))

$$\sigma_{\text{CC}}^i = \sigma_{\text{CC}} \text{br}_i \cdot \kappa_W^2 \kappa_i^2 \frac{1}{\sum_j \kappa_j^2 \text{br}_j} \quad \text{and} \quad \sigma_{\text{NC}}^i = \sigma_{\text{NC}} \text{br}_i \cdot \kappa_Z^2 \kappa_i^2 \frac{1}{\sum_j \kappa_j^2 \text{br}_j}. \quad (7.9)$$

By dividing these expressions by the SM cross-section predictions one can obtain the variations of the relative signal strengths,  $\mu^i$ , for charged and neutral currents and their  $\kappa$  dependence

$$\mu_{\text{CC}}^i = \kappa_W^2 \kappa_i^2 \frac{1}{\sum_j \kappa_j^2 \text{br}_j} \quad \text{and} \quad \mu_{\text{NC}}^i = \kappa_Z^2 \kappa_i^2 \frac{1}{\sum_j \kappa_j^2 \text{br}_j}. \quad (7.10)$$

With seven decay channels considered in CC and NC, one finds that for each of the  $ep$  collider configurations, there are eight constraints on  $\kappa_W$  and  $\kappa_Z$  and two constraints on the other five  $\kappa$  parameters. Using the signal-strength uncertainties listed in table 17, fits to all seven channels, in NC and CC, are performed using a minimisation procedure to determine the resulting uncertainties for the  $\kappa$  parameters. This is done separately for each of the  $ep$  collider configurations; the results are listed in table 18. A naive expectation would have been that  $\delta\kappa \simeq \delta\mu/2$ . Comparing the results, for example, for the LHeC (top rows), of the signal strengths (table 17) with the  $\kappa$  fit results (table 18), one can observe that this relation approximately holds for the  $gg$ ,  $\tau\tau$ ,  $c\bar{c}$ ,  $\gamma\gamma$  channels. However, due to the dominance of  $H \rightarrow b\bar{b}$  in the total H width and owing to the presence of the  $WWH$  and  $ZZH$  couplings in the initial state, a reshuffling of the precisions occurs in the joint fit:  $\kappa_b$  is relatively less precise than  $\mu_{b\bar{b}}$ , while both  $\kappa_W$  and  $\kappa_Z$  become more precise than the naive estimates, even when one takes into account that the  $H \rightarrow WW$  decay in CC measures  $\kappa_W^4$ . The seven channel results are displayed in figure 106.

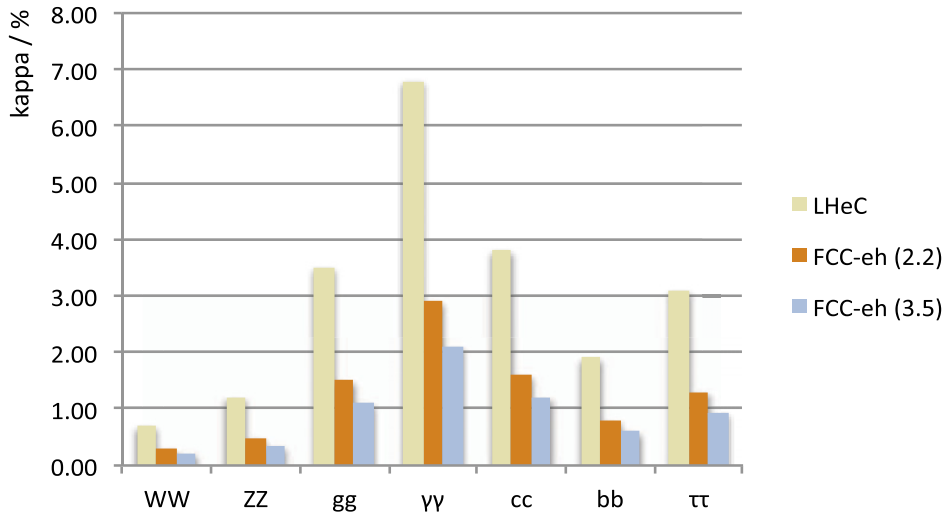


**Figure 106.** Summary of uncertainties of Higgs couplings from  $ep$  for the seven most abundant decay channels, for the LHeC (gold), the FCC-eh at 20 TeV of proton energy (brown) and for  $E_p = 50$  TeV (blue).

In the electroweak theory there is an interesting relation between the ratio of the  $W$  and  $Z$  couplings and the mixing angle,

$$\frac{\sigma(WW \rightarrow H \rightarrow AA)}{\sigma(ZZ \rightarrow H \rightarrow AA)} = \frac{\kappa_W^2}{\kappa_Z^2} = (1 - \sin^2 \theta_W)^2 \quad (7.11)$$

This relation can be particularly well tested with the  $ep$  colliders as they measure both  $WWH$  and  $ZZH$  in one experiment and using a common theoretical environment. If one assumes the  $WW$  and  $ZZ$  measurements to be independent, the resulting error in  $\sin^2 \theta_W \simeq 0.23$  is 0.003 for the LHeC and 0.001 for the FCC-eh. However, these figures should probably be smaller, because there are correlations in the measurements that a genuine data-based analysis would have to evaluate and take into account.

The effect of the theoretical uncertainties has been studied for the FCC-eh, where the experimental precision is highest. Table 19 presents the results of a  $\kappa$  analysis using the CC and NC FCC-eh signal-strength inputs (table 17), neglecting the theoretical uncertainty and adding 0.5% or 1% in quadrature to  $\mu_{bb}$  only where it matters. This results in a roughly linear increase of the uncertainty for  $bb$  (by a factor of 1.5),  $WW$  (by 1.7), and  $ZZ$  (by 1.5), while all other  $\kappa$  uncertainties are only slightly deteriorated. The effect of such uncertainties is much smaller for the LHeC as the  $\mu$  uncertainties are three times those of the FCC-eh, see table 17. Therefore, in the LHeC case, the theoretical uncertainties are neglected.

The role of electron-beam polarisation raises an interesting question. Assuming a maximum polarisation of  $P = -0.8$ , the CC (NC) Higgs cross-section is calculated to be 1.8(1.09) times larger than in unpolarised scattering. Therefore, the signal CC and NC strength uncertainties scale by 1.34 and 1.09, respectively. This has been studied for the LHeC. If the default fit is made, then the  $\kappa$  uncertainties quoted in table 18 for  $bb$ ,  $WW$ ,  $gg$ ,  $\tau\tau$  and  $cc$  are enhanced by a factor of 1.28. This is due to the combined effect of CC and NC which reduces the deterioration a bit, from 1.34 to 1.28. Thus, for example, the  $\kappa_W$  uncertainty moves from 0.7 to 0.9% in the unpolarised case. The uncertainty in  $\kappa_Z$  is enhanced by just a factor of 1.14, becoming 1.38

**Table 19.** Summary of  $\kappa$  uncertainty values obtained from separate fits to the signal-strength uncertainty estimates for the seven most abundant Higgs decay channels, in charged and neutral currents for the FCC-eh, with no theoretical uncertainty, half a per cent, and one per cent of added uncertainty.

Setup	$b\bar{b}$	$WW$	$gg$	$\tau\tau$	$cc$	$ZZ$	$\gamma\gamma$
FCC-eh (no thy)	0.60	0.22	1.1	0.93	1.2	0.35	2.1
FCC-eh (0.5% thy)	0.72	0.28	1.1	1.0	1.2	0.41	2.2
FCC-eh (1.0% thy)	0.91	0.37	1.1	1.0	1.3	0.53	2.3

instead of 1.21, because the NC channel has a particularly strong effect on the  $ZZH$  coupling. Since the prospect of detecting the  $\gamma\gamma$  channel in NC is very poor, the  $\kappa_\gamma$  uncertainty is enlarged by the full CC factor of 1.34. For maximum precision, it is very desirable to polarise the beam. This, together with electroweak physics, represents an important reason to continue to develop high-current polarised electron sources.

### 7.5. Measuring the top-quark–Higgs Yukawa coupling

Electron–proton collisions at high energy are known to provide a unique window of opportunity with which to perform precision measurements in the top sector [473]. This is due to the large cross-sections of the production of single top quarks, which amount to about 2 pb for  $E_e = 60$  GeV and  $E_p = 7$  TeV, where clean signatures are provided without the challenges posed by pile-up. As a result, the cross-section of the SM in association with a single top quark in  $e^-p$  collisions is large enough to perform competitive measurements. This includes the measurement of the absolute value of the top–Yukawa coupling and, most prominently, its CP phase [484].

To investigate top–Yukawa coupling, the SM interaction can be modified in terms of mixtures of CP-even and CP-odd states. In terms of a CP phase ( $\zeta_t$ ), the generalised Lagrangian can be written as [611]:

$$\mathcal{L} = -\frac{m_t}{v}\bar{t}[\kappa \cos \zeta_t + i\gamma_5 \sin \zeta_t]th. \quad (7.12)$$

Here,  $\zeta_t = 0$  and  $\zeta_t = \pi$  correspond to a pure scalar state, while  $\zeta_t = \frac{\pi}{2}$  corresponds to a pure pseudo-scalar state. Therefore, the  $\zeta_t$  ranges  $0 < \zeta_t < \pi/2$  and  $\pi/2 < \zeta_t < \pi$  represent a mixture of the different CP states, and the case  $\zeta_t = 0$  with  $\kappa = 1$  corresponds to the SM.

In  $e^-p$  collisions, the top-quark–Higgs couplings are accessed via the associated production of the Higgs boson with an anti-top quark through the process  $e^-p \rightarrow \bar{t}h\nu_e$ , where five-flavour protons include the  $b$ -quark parton distribution. Figure 107 shows the Feynman diagrams for the process of interest. Interestingly, this process involves three important couplings, namely  $hWW$ ,  $Wtb$ , and the top–Higgs ( $tth$ ). Detailed studies of  $hWW$  and  $Wtb$  couplings at the  $e^-p$  collider have been described in references [473, 612], respectively.

At the LHC [611], an interesting feature can be quantitatively observed: in the pure SM case, there is constructive interference between the diagrams shown in figure 107, left and middle, for  $\zeta_t > \pi/2$ , resulting in a significant enhancement in the total production total cross-section of associated top–Higgs couplings. This is also true for  $\zeta_t < \pi/2$ —however, the degree of enhancement is much smaller, owing to the flipped sign of the CP-even part of the coupling.

A study of the sensitivity to top-quark–Higgs couplings in terms of a  $\zeta_t$  model was presented in reference [484]. In the following, the methodology and results are briefly described. In order to assess the sensitivity to top-quark–Higgs couplings, a model file was built in `FeynRules` [613] which incorporates the Lagrangian; see equation (7.12). The associated top–Higgs

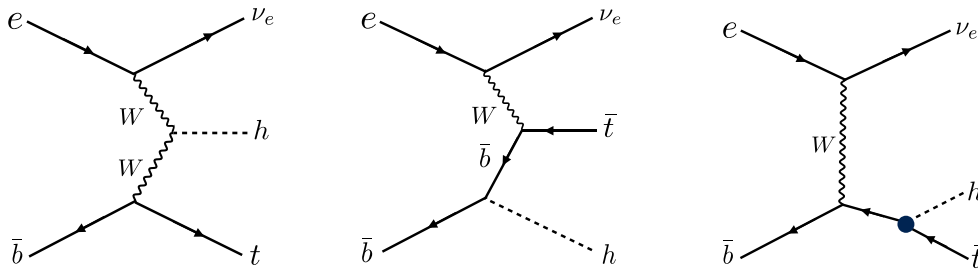


**Figure 107.** Leading-order Feynman diagrams contributing to the process  $pe^- \rightarrow \bar{t}h\nu_e$  in high-energy  $e^-p$  collisions. The full circle in the right diagram shows the top-quark–Higgs coupling of interest in this section. Reproduced from [484]. CC BY 4.0.

production in the charged-current channel  $pe^- \rightarrow \bar{t}h\nu_e$  is then simulated (cf figure 107), where it is assumed that  $h$  decays into a  $b\bar{b}$  pair, and that the anti-top quark decays leptonically. An electron–proton centre-of-mass energy of  $\sqrt{s} \approx 1.3$  TeV is assumed. In this study [484], the analysis is performed at the parton level. For signal and background event generation, the MC event-generator package MadGraph5 [375] is employed, together with NNPDF23\_10\_as\_0130\_qed [614] PDFs. The renormalisation and factorisation scales for the signal sample are chosen to be  $\mu_F = \mu_R = (m_t + m_h)/4$ . The background samples are generated using the default MadGraph5 [375] dynamic scales. The longitudinal polarisation of the electron beam is assumed to be  $-0.8$ .

In figure 108 we present the variation of the total cross-section versus the electron-beam energy for the signal process  $pe^- \rightarrow \bar{t}h\nu_e$  by considering un-polarised and polarised  $e^-$  beams. Also, the effects of branchings of  $h \rightarrow b\bar{b}$  and the  $\bar{t}$  decay for both leptonic and hadronic modes are shown. Possible background events typically arise from  $W+$  multijet events,  $Wb\bar{b}$  with missing energy. The missing energy can be accounted for by considering the top-quark line only, the Higgs line only, and neither the top nor the Higgs line in charged- and neutral-current deep inelastic scattering and in photoproduction by further decays of  $W$  into the leptonic mode. To estimate the cross-sections of the signal and all possible backgrounds using only basic cuts on rapidity  $|\eta| \leq 10$  for light-jets, leptons, and  $b$ -jets, the transverse momentum cut  $p_T \geq 10$  GeV and  $\Delta R_{\min} = 0.4$  for all particles considered.

An estimation of the sensitivity of the associated top–Higgs production cross-section,  $\sigma(\zeta_t)$ , as a function of the CP phase of the  $tth$ -coupling is shown in figure 109. In this study, the electron and proton beams are assumed to have energies of 60 GeV and 7 TeV, respectively. The scale uncertainties are obtained by varying the nominal scale,  $\mu_F = \mu_R \leq (m_t + m_h)/4$ , by factors of 0.5 and 2. It can be observed that the size of the cross-section is strongly dependent on the value of  $\zeta_t$ , in particular, in the region  $\zeta_t > \frac{\pi}{2}$  where the interference between the diagrams becomes constructive. At lower values of  $\zeta_t$  the interference is still constructive, but it decreases with decreasing  $\zeta_t$ . Note that  $\zeta_t = 0$  represents the cross-section in the strict SM formalism.

At  $\zeta_t = \frac{\pi}{2}$ , which corresponds to the pure CP-odd case, the cross-section is increased by about a factor of five in comparison to the SM expectation. At  $\zeta_t = \pi$ , which corresponds to the pure CP-even case with the opposite sign of  $tth$ -coupling, the cross-section can be enhanced by a factor of up to 24 times. Over the whole range of  $\zeta_t$ , the scale uncertainty is found to be about 7%.

To evaluate the sensitivity to the measurement of the top–Yukawa coupling and its CP phase, the following criteria for fiducial selection are used [484]:

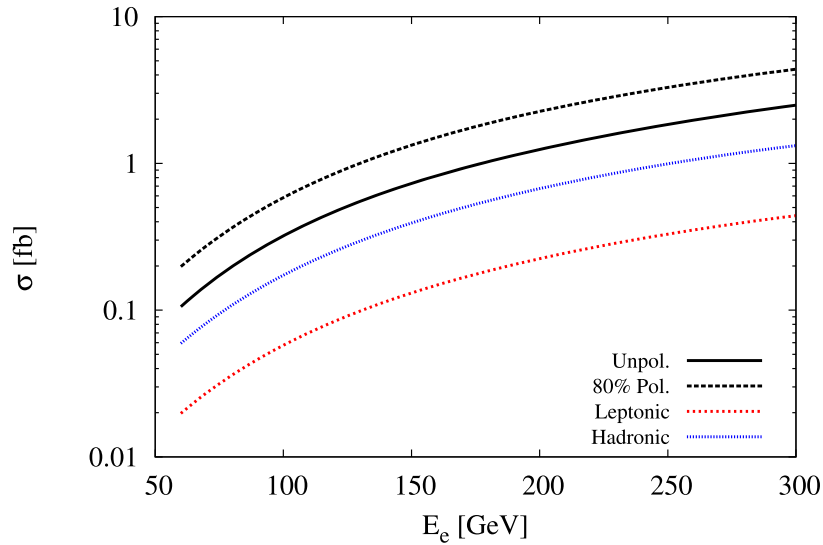


**Figure 108.** Cross-sections of the Higgs boson produced in association with a top quark in  $e^-p$  collisions at  $E_p = 7$  TeV for different electron-beam energies. Reproduced from [484]. CC BY 4.0. The dotted and solid black lines correspond to  $pe^- \rightarrow \bar{t}h\nu_e$  with and without longitudinal polarisation of the electron beam, respectively. The dotted red and blue lines correspond to  $\sigma \times \text{BR}$  for the leptonic and hadronic decay modes of  $\bar{t}$  in which, for this estimation, we use basic cuts (see the text and reference [484]).

- $p_T \geq 20$  GeV for  $b$ -tagged jets and light-jets, and  $p_T \geq 10$  GeV for leptons.
- $b$ -jets must be within  $-2 \leq \eta \leq 5$
- Light jets and the scattered lepton must be identified within  $2 \leq \eta \leq 5$
- All final-state particles must be separated by a distance  $\Delta R$  greater than 0.4.
- The missing transverse energy must exceed 10 GeV
- The invariant mass windows for the Higgs through  $b$ -tagged jets and the top are required to be  $115 < m_{bb} < 130$  GeV and  $160 < m_t < 177$  GeV.

In these selections the  $b$ -tagging efficiency is assumed to be 70%, with false rates from  $c$ -initiated jets and light jets to the  $b$  jets of 10% and 1%, respectively. The last requirement is important to reduce background processes.

Using the Poisson formula  $S = \sqrt{2[(S+B)\log(1+S/B) - S]}$ , where  $S$  and  $B$  are the number of expected signal and background events at a particular luminosity ( $L$  in  $\text{fb}^{-1}$ ), the exclusion regions of  $\zeta_t$  are estimated as a function of  $L$ . Here, a 10% systematic uncertainty is expected for the background yields. Figure 110 displays the exclusion contours at different CLs. It can be observed that the shape of the exclusion limit changes at around  $\zeta_t = \pi/2$ . Therefore, in order to obtain significant exclusion limits in the region  $0 < \zeta_t < \pi/2$ , a larger integrated luminosity is required. This is in keeping with the feature exhibited in figure 109: for  $\zeta_t$  values for which constructive interference between the signal diagrams enhances the cross-section to more than the SM value, i.e. for  $\zeta_t > \pi/2$ , less integrated luminosity is required in order to obtain precise exclusion limits. For example, for  $L = 100 \text{ fb}^{-1}$ , the regions above  $\pi/5 < \zeta_t \leq \pi$  and  $3\pi/10 < \zeta_t \leq \pi$  are excluded at confidence levels of  $2\sigma$  and  $3\sigma$ , respectively. With  $L = 400 \text{ fb}^{-1}$ , the regions above  $\pi/6 < \zeta_t \leq \pi$  and  $\pi/4 < \zeta_t \leq \pi$  are excluded at  $4\sigma$  and  $5\sigma$  CLs, respectively. The asymmetry studies at the HL-LHC [611] have helped up to

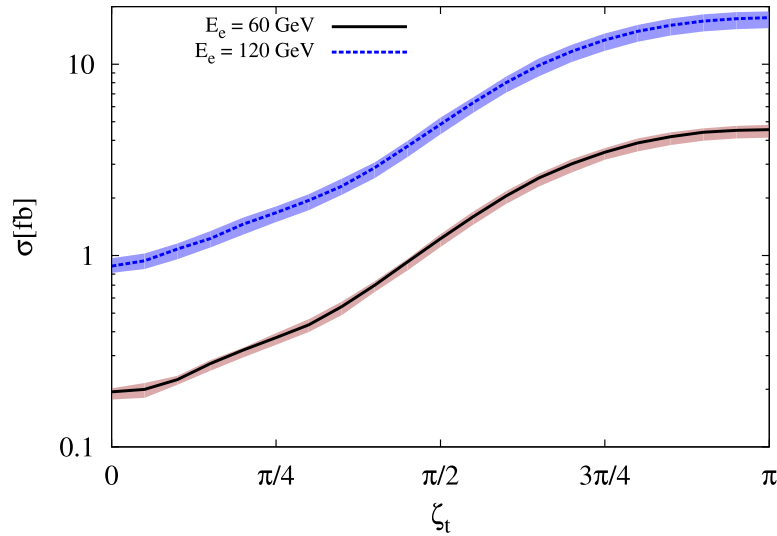


**Figure 109.** Total cross-section of the Higgs boson produced in association with a single top quark as a function of  $\zeta_t$ , including scale uncertainties. Reproduced from [484]. CC BY 4.0. The *black solid* and *blue dotted* lines correspond to  $E_e = 60$  and  $120$  GeV, respectively. These are obtained for fixed  $E_p = 7$  TeV and scales  $\mu_F = \mu_R = (m_t + m_h)/4$ .

$\zeta_t = \pi/6$  to be probed, for a total integrated luminosity of  $3 \text{ ab}^{-1}$ . However, the LHeC provides a better environment with which to test the CP nature of Higgs-boson couplings. For a targeted integrated luminosity of  $L = 1 \text{ ab}^{-1}$ , almost all values of  $\zeta_t$  can be excluded with at a CL of at least  $4\sigma$ .

While investigating the overall sensitivity of  $\zeta_t$  by applying these two observables, it is also important to measure the accuracy of SM  $tth$  coupling  $\kappa$  at LHeC energies. Using the formula  $\sqrt{(S+B)/(2S)}$  at a selected luminosity of  $L = 1 \text{ ab}^{-1}$ , the value of  $\kappa$  can be determined with an uncertainty of about pm0.17. In this estimate, a 10% systematic uncertainty has been taken for the background yields.

These results are obtained based on the evaluation of the fiducial cross-sections alone. As pointed out in reference [484], a number of other observables provide sensitivity to the structure of the top–Higgs Yukawa coupling, such as the rapidity difference between the top quark and the Higgs boson and a number of angular variables. While the fiducial rate studied here is the single most sensitive observable, it is evident that a multivariate approach would significantly enhance the sensitivity reported here.

### 7.6. Higgs decay into invisible particles

Higgs decay into invisible particles could be a key to BSM physics. The SM branching ratio of  $H \rightarrow ZZ \rightarrow 4\nu$  is only 0.1%. Any sizeable decay rate into invisible particles would thus indicate an exotic decay, for example, to dark-matter particles. Its non-observation would give the SM cross-section measurement, and reconstructing more than 99% of the ordinary decays would provide a better constraint on the total Higgs decay width.

For the LHeC at a luminosity of  $1 \text{ ab}^{-1}$ , initial parton-level studies of this decay were presented in reference [615], with the estimate of a two  $\sigma$  sensitivity to a branching fraction of



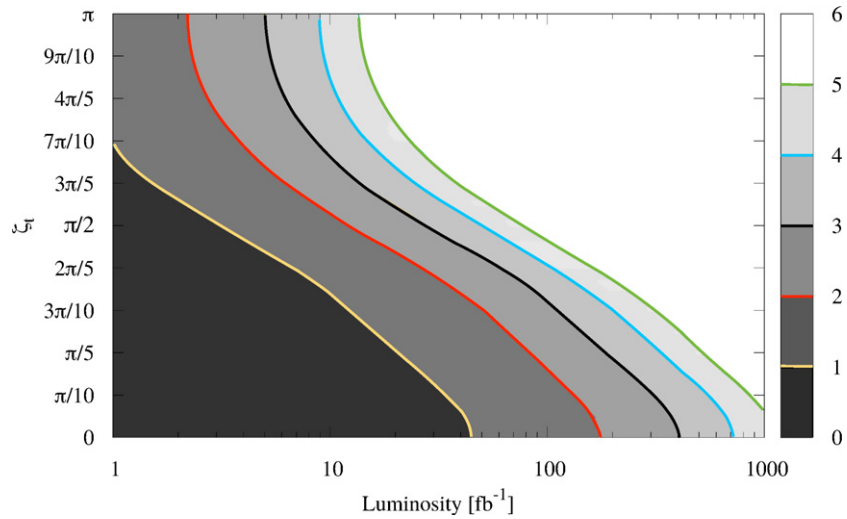


**Figure 110.** Exclusion contours for  $\zeta_l$  as a function of integrated luminosity for  $\sqrt{s} = 1.3$  TeV. Reproduced from [484]. CC BY 4.0. The shaded areas under a contour line are excluded. The blue and black lines represent the  $4\sigma$  and  $3\sigma$  regions. The results obtained are based on fiducial cross-sections (see the text).

6%. For this study, NC production via  $ZZ$  fusion  $eq \rightarrow eqZZ \rightarrow eqH$  was used, which has a cross-section of about 25 fb at the LHeC. The CC production via  $WW$  fusion has a larger cross-section, but entails a missing-energy signal, which itself requires a further study of a potentially significant gain in precision. This channel, when employed for the invisible decay study, results in a mono-jet signature which is hard to separate from the SM DIS CC background.

The neutral-current study has been repeated using the LHeC Higgs WG analysis tools introduced above: MadGraph, Pythia, and DELPHES. Similarly to [615], a 60 GeV electron beam with a polarization of  $-80\%$  is assumed. The basic event topology contains the scattered electron, the jet, and the missing transverse energy. Its main background results from SM  $W$  and  $Z$  productions (followed by  $W \rightarrow \ell\nu$  and  $Z \rightarrow \nu\bar{\nu}$ ). In this study, NC and CC  $W$  production and NC  $Z$  production were considered, while single top, NC multijets, and  $W$  photoproduction were all found to be negligible. By requiring a missing transverse energy of 60 GeV, exactly one electron, one jet, and no other leptons (including  $\tau$ ), as well as imposing several selection criteria on the kinematics of the electron, the jet, and the missing transverse momentum, we get a two  $\sigma$  sensitivity to a branching ratio of 7.2%, which is similar to the earlier result [615]. Figure 111 shows the electron-jet invariant mass distribution after the selection of the signal (normalized to a 100% branching ratio) and the background.

The analysis was further refined by the use of multivariate analysis (BDT in the TMVA package). Basically, the set of selection variables used in the cut-based analysis above was used as an input to the multivariate analysis and tuned to yield the best output score to discriminate the signal from the backgrounds. Figure 112 shows the distribution of the discriminant variable for the signal and background (both areas are normalised). An optimization of the statistical significance is found at the BDT score  $> 0.25$ , and the resulting mass distribution is shown in figure 113. With  $1 \text{ ab}^{-1}$  of integrated luminosity, a two  $\sigma$  sensitivity of 5.5% is obtained, which is consistent with the previous results. For a comparison, an estimate of 3.5% was given by an HL-LHC sensitivity study of this channel [616]. The result for the LHeC may be further

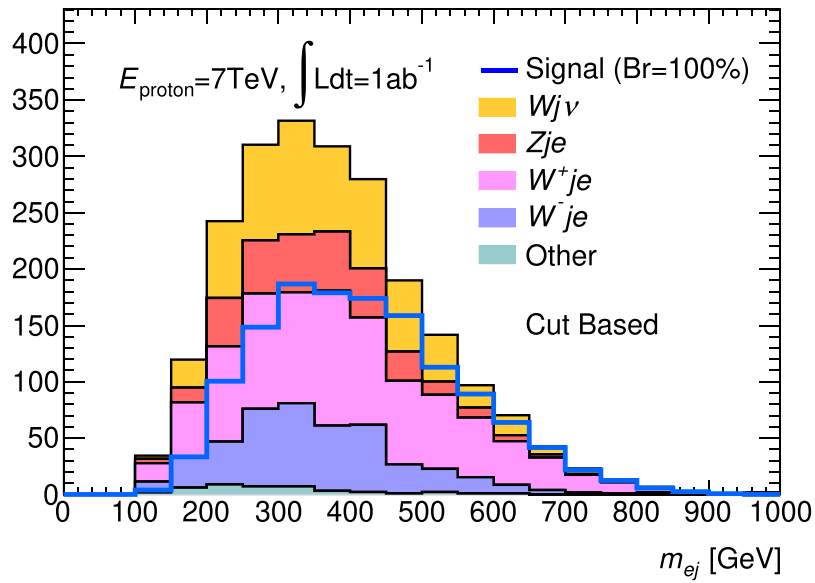


**Figure 111.** Electron-jet invariant mass distribution for the Higgs-to-invisible-decay signal (normalized to a 100% branching ratio) and the stacked backgrounds for an integrated luminosity of  $1 \text{ ab}^{-1}$  at the LHeC after all selection cuts.

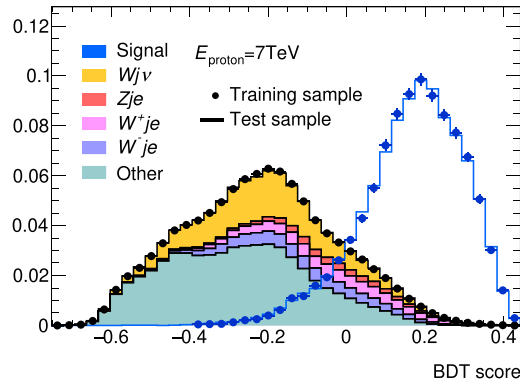


**Figure 112.** BDT output-score distribution for the Higgs-to-invisible-decay signal and the stacked backgrounds (both areas are normalized) at the LHeC.

improved in the future by a refined BDT analysis when extra parameters are introduced, beyond those initially introduced for the cut-based analysis.

In these initial studies, no systematic uncertainties were considered. This may be justified by the very clean environment of electron–hadron colliders, in which precise measurements of  $W$  and  $Z$  production will be made, for example, of their decays to muons, which accurately limits the systematics in the background prediction to a negligible level.

The BDT analysis was repeated for higher proton energies. At the HE-LHeC ( $E_p = 13.5 \text{ TeV}$ ) the NC production cross-section increases to  $45 \text{ fb}$  and the branching ratio

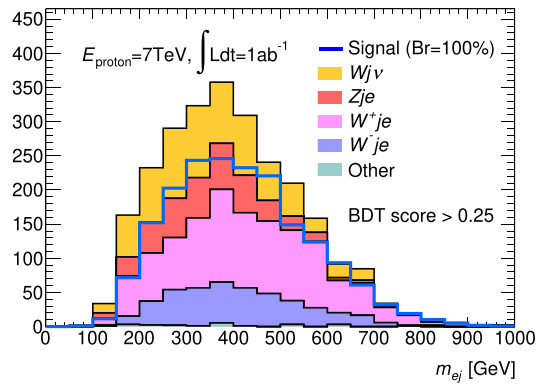


**Figure 113.** Electron-jet invariant mass distribution for the Higgs-to-invisible-decay signal (normalized to 100% of the branching ratio) and the stacked backgrounds for an integrated luminosity of  $1 \text{ ab}^{-1}$  at the LHeC after a BDT score cut of 0.25.

sensitivity improves to 3.4%, because the luminosity is doubled in the configurations assumed here. At the FCC-eh, the cross-section increases to 120 fb and the sensitivity of the branching ratio reaches about 1.7%.

## 8. Searches for physics beyond the Standard Model

### 8.1. Introduction

The LHC was originally envisioned as the ultimate machine to search for physics beyond the SM at the TeV scale. Since electrons and quarks only share electroweak interactions, an electron–proton collider could allow the measurement of the same phenomena in a different environment with generally higher precision. It could add complementary search channels or lead to the discovery of a weak signal. The possibility of undiscovered new physics (NP) below the TeV scale could thus also be addressed by the LHeC, which is projected to be in operation when the LHC is in its high-luminosity phase, in spite of the lower centre-of-mass energy. Exotic phenomena that can be studied at  $ep$  colliders have been reviewed, for example, in [617]. More recently, when the LHC was only beginning to yield data in run I, an overview of the potential of the LHeC for probing physics beyond the SM was provided in the CDR [1]. Since then, stringent constraints on NP phenomena have been obtained from the LHC, and the absence of hints from NP to date is presently changing this paradigm to two alternative scenarios: NP may actually reside at an even larger energy scale; NP may be at or below the TeV scale, but more weakly coupled, and thus hidden in the SM backgrounds [618].

A similar  $pp$ – $ep$  synergy could be envisaged using higher proton-beam energies at the FCC 100 km tunnel. With an electron beam of 60 GeV, the expected centre-of-mass energies for  $ep$  could be 2.9 TeV for  $E_p = 19 \text{ TeV}$  (low-energy FCC) and 3.5 TeV for  $E_p = 50 \text{ TeV}$  (FCC). Below, we list recent developments in regard to NP opportunities at the LHeC and its potential future high-energy upgrades.

### 8.2. Extensions of the SM Higgs sector

Today, given the precision of measurements in the Higgs sector, it appears that the discovered 125 GeV scalar is indeed the SM Higgs boson. The question remains, however, of whether

the scalar potential is truly that of the SM or if it should be extended, possibly with additional degrees of freedom. Several extensions of the Higgs sector have been proposed and can be studied at the  $ep$  colliders, with results that are often complementary to those of  $pp$  colliders and other future facilities.

**8.2.1. Modifications of the top–Higgs interaction.** In electron–proton collisions, heavy top quarks can be produced in association with a Higgs boson, which allows us to study the sensitivity of the LHeC or the FCC-eh to top–Higgs ( $tH$ ) interactions. In reference [484] the sensitivity of the process  $pe^- \rightarrow \bar{t}H\nu_e$  to the CP nature of the  $tH$  coupling is investigated by considering a CP phase  $\zeta_t$  at the  $tH$  and  $bbH$  vertices. The authors conclude, based on several observables and using an appropriate error-fitting methodology, that better limits on  $\zeta_t$  could be obtained at the LHeC than at the HL-LHC. At a design luminosity of  $1 \text{ ab}^{-1}$ , almost all values of  $\zeta_t$  are excluded up to a  $4\sigma$  CL, and the SM top–Higgs coupling could be measured relative to its SM value with a precision of  $\kappa = 1.00 \pm 0.17$ .

FCNCs are completely absent at the tree level in the SM and are strongly constrained, especially by low-energy experiments. Anomalous FCNC Yukawa interactions between the top quark, the Higgs boson, and either an up or charm quark are documented in section 3 and section 5.3.6. Among other studies, the authors of reference [619] consider the Higgs decay modes  $H \rightarrow \gamma\gamma, bb$  and  $\tau\tau$  at  $E_e = 150 \text{ GeV}$ . The results are published in reference [492] for  $E_e = 60 \text{ GeV}$ , including estimates for lower electron-beam energies, and the  $2\sigma$  sensitivity for the branching ratio  $\text{br}(t \rightarrow uh)$  is found to be  $0.15 \times 10^{-2}$ . By making use of the polarisation of the electron beam and multivariate techniques, reference [620] shows that limits on the branching ratio  $\text{br}(t \rightarrow uh)$  of  $\mathcal{O}(0.1)\%$  can be obtained, representing an improvement over the current LHC limit of  $0.19\%$  [621, 622]. These results vary with  $E_e$  and  $E_p$ .

**8.2.2. Charged scalars.** The prospects of observing a light charged Higgs boson through the decay  $H^+ \rightarrow c\bar{b}$  are investigated within the framework of the two-Higgs doublet model (2HDM) type III, assuming a four-zero texture in the Yukawa matrices and a general Higgs potential [623]. The CC production process  $e^-p \rightarrow \nu H^+ q$  is considered. The analysed signature stems from the subsequent decay  $H^+ \rightarrow c\bar{b}$ . The parton-level analysis accounts for irreducible SM backgrounds and considers scenarios up to a mass of  $200 \text{ GeV}$ , which is consistent with current limits obtained from Higgs and flavour physics. The authors show that for  $L = 100 \text{ fb}^{-1}$  a charged Higgs boson could be observed with about  $3\text{--}4\sigma$  significance. This should be compared with the results of current LHC searches, in which strong limits are set on the branching fraction  $\text{br}(t \rightarrow H^+ b)$  by assuming  $\text{br}(H^+ \rightarrow c\bar{b}) = 1.0$  or  $\text{br}(H^+ \rightarrow c\bar{s}) = 1.0$  for the charged Higgs boson mass range  $\sim 90\text{--}160 \text{ GeV}$  [624, 625].

A similar study of  $H^\pm \rightarrow sc + su$  for the FCC-eh (with  $\sqrt{s} \approx 3.5 \text{ TeV}$ ) is presented in reference [626], in the context of a next-to-minimal supersymmetric model (NMSSM). Using dedicated optimisation techniques, the authors show that a light charged boson,  $H^\pm$ , can be observed with a maximal significance of  $4.4 (2.2)\sigma$ , provided its mass is at most  $m_{H^\pm} = 114 (121) \text{ GeV}$ , for a total luminosity of  $1 \text{ ab}^{-1}$ .

The Georgi–Machacek (GM) model extends the Higgs sector by including higher multiplet states while preserving custodial symmetry. The physical states include, besides the SM Higgs, a heavier singlet  $H$ , a triplet  $(H_3^+, H_3^0, H_3^-)$  and a quintuplet  $(H_5^{++}, H_5^+, H_5^0, H_5^-, H_5^{--})$ . The  $H_5$  scalars do not couple to fermions and can therefore only be produced by VBF. An analysis of the prospects of discovering doubly charged Higgs bosons in the GM model at the LHeC and the FCC-eh is presented in reference [627], which studies the production of a doubly-charged member of the five-plet Higgs bosons ( $H_5^{\pm\pm}$ ) by  $W^\pm W^\pm$  fusion. The authors find that  $2\text{--}3\sigma$  limits can be obtained for mixings  $\sin(\theta_H)$  as low as  $0.2$ , for  $M(H_5) < 300 \text{ GeV}$ . The prospects

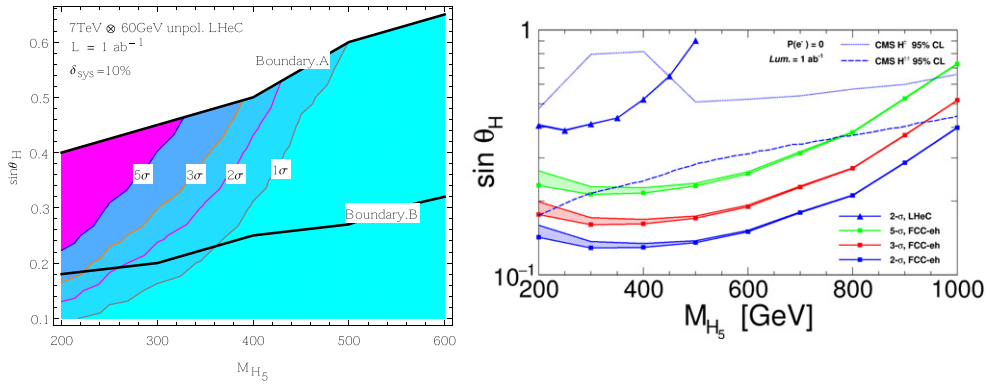


**Figure 114.** Left: discovery contour with respect to  $\sin \theta_H$  and  $M(H_5^{++/--})$  at the LHeC using an unpolarized beam. Reprinted figure with permission from [627], Copyright 2017 by the American Physical Society. Right: limit contours for the case of singly charged Higgs for the FCC-eh and the LHeC. The blue dotted curve and the blue dashed curves give the 95% CL limit from CMS for  $H_5^{+/-}$  and for  $H^{++/--}$ , respectively. Reproduced from [628]. CC BY 4.0. An unpolarized beam with an integrated luminosity of  $1 \text{ ab}^{-1}$  and a 10% systematic uncertainty for background yields are assumed in both plots.

can be improved at the FCC-eh collider, where doubly charged Higgs bosons can be tested for masses  $M_{H_5} < 400 \text{ GeV}$  and also for small scalar mixing angles (figure 114 (left)).

The discovery prospects for the singly charged Higgs,  $H_5^\pm$  of the GM model, produced in  $W^\pm Z$  fusion, are evaluated in reference [628]. The authors perform a multivariate analysis, including a fast detector simulation, and consider the LHeC and the FCC-eh for a mass range from 200–1000 GeV. They find that the LHeC can improve over current LHC limits on  $H_5^\pm$  for masses of up to about 400 GeV and scalar mixing angles  $\sin \theta_H \sim 0.5$  (figure 114 (right)).

**8.2.3. Neutral scalars.** Neutral scalar bosons generally appear in many extensions of the scalar sector. They can be added directly, as  $SU(1)$  singlets, or be part of higher-representation  $SU(2)$  multiplets. They generally mix with the SM Higgs boson, from which they inherit a Higgs-like phenomenology.

The potential for testing the heavier CP-even scalar that is contained in the 2HDM type-I is presented in reference [631]. Therein, the lighter scalar particle is considered to be an SM-like Higgs boson, and the properties of a heavy scalar, assumed to have a specific mass 270 GeV, are discussed. The authors state that the final-state  $H \rightarrow Sh$ , where  $S$  is a scalar singlet with a mass of around 100 GeV, is of particular interest, as it is connected to the findings of reference [618].

The prospects of searching for a generic heavy neutral scalar particle are presented in detail in reference [632], which uses a model that is a minimal extension of the SM with one additional complex scalar singlet that mixes with the SM Higgs doublet, which governs its production and decay mode. The heavy scalar is produced via vector-boson fusion and decays into two vector bosons. A multivariate analysis is performed and detector simulation is taken into account. Masses between 200 and 800 GeV and scalar mixings as small as  $\sin^2 \alpha \sim 10^{-3}$  are considered. The resulting sensitivity for a total luminosity of  $1 \text{ ab}^{-1}$  is shown in figure 115, including existing bounds from the LHC and also from future HL-LHC projections. A significant improvement is found, compared to existing LHC limits, as the LHeC will be able to probe scalar boson masses below  $\sim 500 \text{ GeV}$ , a region which remains difficult at the HL-LHC.

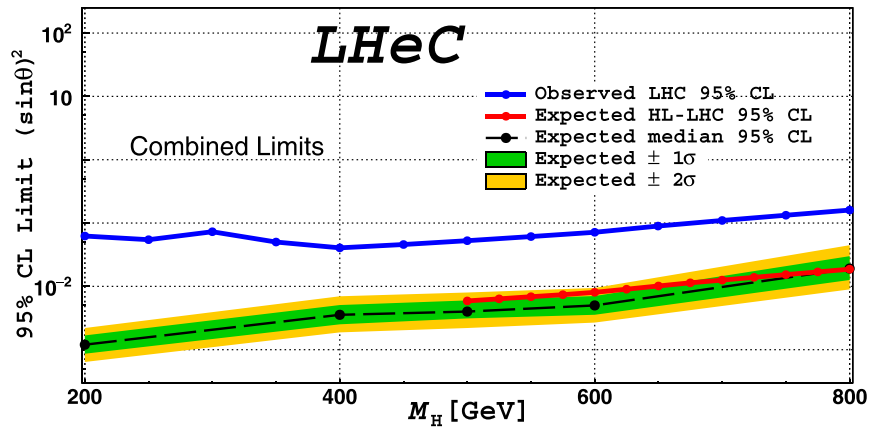


**Figure 115.** Expected exclusion limits (green and yellow bands) for a heavy scalar search at the LHeC, assuming a systematic uncertainty for the SM background of 2%. Reproduced from [632]. CC BY 4.0. The blue line represents the current LHC limit at a 95% CL, as extracted from [633], and the red line represents the forecast of the HL-LHC sensitivity via  $h_2 \rightarrow ZZ$  searches from reference [634]. The LHeC results correspond to an integrated luminosity of  $1 \text{ ab}^{-1}$ .

The scalar bosons from the 2HDM type-III framework may give rise to flavour-violating signatures, as discussed in reference [635]. The prospects of observing the light and heavy CP-even neutral Higgs bosons via their decays into flavour-violating  $b\bar{s}$  channels were studied with specific Yukawa textures and a general Higgs potential. The signature of these decays consists of one jet originating from b-hadron fragmentation (b-tagged jets) and one light-flavour jet in the central rapidity region, with a remaining jet in the forward region. Relevant SM backgrounds are considered and the results show that flavour-violating decays of the SM-like Higgs boson will be accessible with  $L = 100 \text{ fb}^{-1}$  at  $ep$  colliders.

The prospects of observing the light CP-even neutral Higgs bosons of the NMSSM framework (the minimal supersymmetric model (MSSM) with an additional singlet superfield), via their decays into b-quarks and in the neutral and CC production processes, are studied in reference [636]. In this work the following constraints are incorporated into the spectrum: neutralino relic density corresponding to the observed dark-matter relic density and direct and indirect mass bounds from searches for specific sparticles; the SM-like Higgs boson has a mass of around 126 GeV and an invisible branching ratio of less than 0.25. The signal is given by three jets plus an electron or missing transverse momentum ( $E_T^{\text{miss}}$ ) arising from the neutral- or charged-current interaction, where two jets are required to originate from a b-quark, and the remaining jet is required to be in the forward region. For the cut-based analysis a number of reducible and irreducible SM backgrounds are considered, which are generated using a fast detector simulation with an adaptation of the LHeC detector. It is found that the boson  $h_1$  could be observable for some of the NMSSM benchmark points: at a level of up to  $2.5\sigma$  in the  $e + 3j$  channel, for masses of up to 75 GeV; in the  $3j + E_T^{\text{miss}}$  channel,  $h_1$  could be discovered at a level of  $2.4\sigma$  for masses of up to 88 GeV with  $L = 100 \text{ fb}^{-1}$ ; a  $5\sigma$  observation is also possible with  $\mathcal{L} = 1 \text{ ab}^{-1}$  for masses of up to 90 GeV.

**8.2.4. Modifications of Higgs self-couplings.** As in the chapter on Higgs physics above, the  $e^-p$  collisions are a very convenient environment with which to study the properties of the SM Higgs boson itself. The latter is produced through vector-boson fusion processes and the



precise measurement of its properties provides a unique opportunity to probe the interaction  $HVV$ , ( $V = W^\pm, Z$ ). These interactions are, in general, sensitive to certain classes of beyond-the-SM physics, which can be parameterized, for instance, via higher-dimensional operators and their coefficients; see references [584, 612, 637–639].

The prospects of inferring the strengths of the two couplings  $HWW$  and  $HZZ$  are described in references [612, 638] in the context of electron–proton collisions. The authors find that the higher-dimensional operator coefficients can be tested for values of around  $\mathcal{O}(10^{-1})$  at the LHeC. This sensitivity is improved at the FCC-eh due to larger centre-of-mass energies, which, in general, enhance the vector-boson fusion cross-sections.

The Higgs self-coupling itself  $HHH$  can be tested through the measurement of the di-Higgs production cross-section, as shown in reference [584]. Using an appropriate error-fitting methodology this study illustrates that Higgs boson self-coupling could be measured with an accuracy of  $g_{HHH}^{(1)} = 1.00^{+0.24(0.14)}_{-0.17(0.12)}$  of its expected SM value at  $\sqrt{s} = 3.5$  (5.0) TeV, given an ultimate  $10 \text{ ab}^{-1}$  of integrated luminosity.

An analysis presented in reference [639] evaluates the LHeC sensitivity to sixth-dimensional operators. The authors employ jet substructure techniques to reconstruct the boosted Higgs boson in the final state. In some cases, a shape analysis of the differential cross-sections shows improvements with respect to the high-luminosity LHC forecasts.

**8.2.5. Exotic Higgs boson decays.** The LHeC sensitivity to an invisibly decaying Higgs boson was investigated in reference [615]. Therein the focus is on the neutral-current production channel due to its enhanced number of observables, compared to that of its CC counterpart. The signal contains one electron, one jet, and a large missing energy. A cut-based parton-level analysis yields an estimated sensitivity of  $\text{br}(h \rightarrow \text{invisible}) = 6\%$  at a  $2\sigma$  level. Exotic decays of the Higgs boson into a pair of light spin-0 particles, referred to as  $\Phi$ , were discussed in reference [640]. The signature studied is a final state with 4 b quarks, motivated by models in which the scalars can mix with the Higgs doublet, which suffers from multiple backgrounds at the LHC. The analysis is carried out at the parton level, for which simple selection requirements render the signature nearly free of SM background and which makes  $\Phi$  particles with masses in the range 20–60 GeV testable for a  $hVV$  ( $V = W, Z$ ) coupling strength relative to the SM at a level of a few per mille and at a 95% CL.

The prospects for testing exotic Higgs decays into pairs of light long-lived particles at the LHeC were studied in reference [641], where it was shown that proper lifetimes as small as  $\mu\text{m}$  could be tested, which is significantly better than the corresponding lifetimes at the LHC. This is shown in figure 116 (left). This information can be interpreted using a model in which the long-lived particles are light scalars that mix with the Higgs doublet, where both production and decay are governed by the scalar mixing angle. The area in the mass-mixing parameter space that gives rise to at least three observable events with a displaced vertex is shown in figure 116. It is apparent that mixings as small as  $\sin^2 \alpha \sim 10^{-7}$  can be tested at the LHeC for scalar masses of between 5 and 15 GeV [641].

### 8.3. Searches for supersymmetry

Several SUSY scenarios might still remain elusive in searches performed at  $pp$  colliders. While the null results of current searches by the LHC experiments have produced impressive constraints on the SUSY coloured sector (squarks and gluinos) because of their large production cross-sections in strong interactions, less stringent constraints have been placed on weakly-produced SUSY particles, namely neutralinos  $\tilde{\chi}^0$ , charginos  $\tilde{\chi}^\pm$ , and sleptons  $\tilde{\ell}^\pm$ . Some of the scenarios in which  $ep$  colliders might have a discovery potential that is complementary to that of the HL-LHC are discussed below. These include R-parity-conserving SUSY models, e.g.

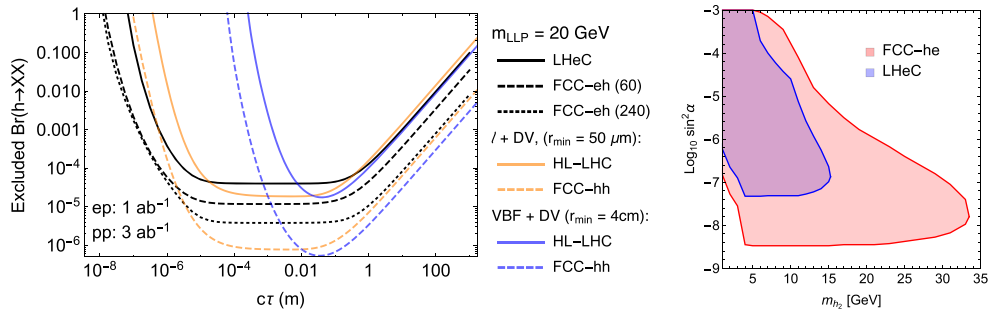


**Figure 116.** Sensitivity contours for displaced vertex searches for Higgs decays into long-lived scalar particles (LLPs), which are pair produced by decays of the Higgs boson, and which themselves decay via scalar mixing into fully visible final states. Left: as a function of the LLP lifetime for a fixed mass. Reproduced from [641]. CC BY 4.0. Right: for a specific model, in which the lifetime and production rate of the LLP are governed by the scalar mixing angle. The contours are for three events and correspond to displacements larger than 50  $\mu\text{m}$ , in order to be free of background.

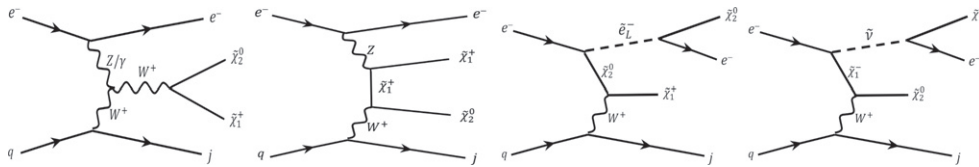


**Figure 117.** Representative production diagrams for the signal processes. Reproduced from [642]. CC BY 4.0. The *decoupled-slepton* scenario only applies to the first two diagrams, while the *compressed-slepton* scenario applies to all four diagrams.

those motivated by the search for dark matter, or R-parity-violating SUSY models, e.g. those that include the single production of bottom and top squarks and low-mass gluinos.

**8.3.1. Search for the SUSY electroweak sector: prompt signatures.** Electroweakino scenarios in which charginos, neutralinos, and sleptons have similar masses can be characterised using the neutralino mass  $m$  and the mass splitting between charginos and neutralinos  $\Delta m$ . We refer here to scenarios with  $\Delta m < 50$  GeV as *compressed*. A subtlety arises for  $\Delta m \leq 1$  GeV, at which the  $\tilde{\chi}_1^\pm/\tilde{\chi}_2^0$  becomes long-lived and its decays are displaced. For  $\Delta m > 1$  GeV the decays are prompt, the visible decay products from  $\tilde{\ell}$  and  $\tilde{\chi}_1^\pm/\tilde{\chi}_2^0$  have very soft transverse momenta ( $p_T$ ), and the SM backgrounds are kinematically similar to the signal. The analyses therefore become challenging and sensitivities decrease substantially. Two SUSY scenarios are considered in reference [642] and depicted in figure 117, in which the lightest supersymmetric particle (LSP)  $\tilde{\chi}_1^0$  is bino-like,  $\tilde{\chi}_1^\pm$  and  $\tilde{\chi}_2^0$  are wino-like with almost degenerate masses, and the mass difference between  $\tilde{\chi}_1^0$  and  $\tilde{\chi}_1^\pm$  is small. The signal is produced via the process  $pe^- \rightarrow je^- \tilde{\chi}\tilde{\chi}$ , in which  $\tilde{\chi} = \tilde{\chi}_1^0$  and  $\tilde{\chi}_1^\pm$  or  $\tilde{\chi}_2^0$ . Conservative leading-order cross-sections are considered for the SUSY signal models. The kinematic observables are input into the TMVA package to perform a multivariate analysis at the detector level.

In the compressed-slepton scenario, the case is considered in which the left-handed slepton  $\tilde{\ell}_L$  and sneutrino  $\tilde{\nu}$  are slightly heavier than  $\tilde{\chi}_1^\pm$  or  $\tilde{\chi}_2^0$ . When the mass difference is fixed at  $\Delta m = m_{\tilde{\ell}} - m_{\tilde{\chi}_1^\pm, \tilde{\chi}_2^0} = 35$  GeV, and ignoring the systematic uncertainty for the background, the

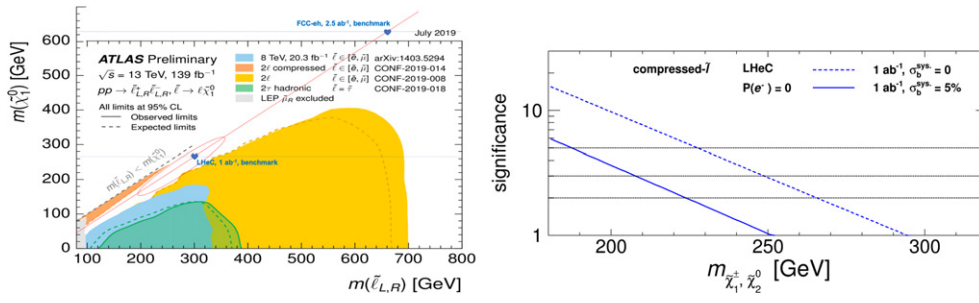


**Figure 118.** Left: benchmark assumption for slepton masses and the 2019 reach of ATLAS searches for sleptons. Reproduced from [643]. [CC BY 4.0](#). Right: significances with varying masses of  $\tilde{\chi}_1^\pm$  and  $\tilde{\chi}_2^0$  for the compressed-slepton scenario at the LHeC with unpolarised beams and  $1 \text{ ab}^{-1}$  of luminosity. For the dashed (solid) curves, systematic uncertainties of 0% (5%) are used for the background. Reproduced from [642]. [CC BY 4.0](#).

analysis indicates that the 2 (5) $\sigma$  limits on the  $\tilde{\chi}_1^\pm$ ,  $\tilde{\chi}_2^0$  masses are 616 (517) GeV for a  $2.5 \text{ ab}^{-1}$  luminosity at the FCC-eh, and 266 (227) GeV for a  $1 \text{ ab}^{-1}$  luminosity at the LHeC, respectively. An illustration of the model assumptions in terms of sleptons and neutralino masses and the current constraints at the LHC is presented in figure 118 (left). The results are illustrated in figure 118 (right). The effects of varying  $\Delta m$  are investigated: by fixing  $m_{\tilde{\chi}_1^\pm, \tilde{\chi}_2^0}$  at 400 GeV, it is found that at the FCC-eh, the significance is maximal when  $\Delta m$  is around 20 GeV.

In the decoupled-slepton scenarios where only  $\tilde{\chi}_1^0$ ,  $\tilde{\chi}_1^\pm$  and  $\tilde{\chi}_2^0$  are light and the other SUSY particles are heavy and decoupled, the  $2\sigma$  limits are obtained for the  $\tilde{\chi}_1^\pm$ ,  $\tilde{\chi}_2^0$  masses are 230 GeV for  $2.5 \text{ ab}^{-1}$  luminosity at the FCC-eh when the systematic uncertainty for the background is neglected. Large systematic uncertainties for the SM background processes can substantially affect the sensitivity; hence, good control of the experimental and theoretical sources of uncertainty is very important.

Finally, it is also found that the possibility of using a negatively polarised electron beam ( $P_e = 80\%$ ) could potentially extend the sensitivity to electroweakinos by up to 40%.

Overall, since the sensitivity to the electroweak SUSY sector depends on the mass hierarchy of  $\tilde{\chi}_1^\pm$ ,  $\tilde{\chi}_1^0$ ,  $\tilde{\chi}_2^0$  and sleptons, and given the difficulty of efficiently probing small  $\Delta m$  regions at the LHC today and possibly at the HL-LHC, measurements at  $ep$  colliders may turn out to offer complementary or additional reaches, in particular, for the compressed scenarios.

**8.3.2. Search for the SUSY electroweak sector: long-lived particles.** Studies of Higgsinos ( $\chi$ ) with masses of  $\mathcal{O}(100)$  GeV are motivated by natural SUSY theories and help to avoid large amounts of fine-tuning of the Higgs boson mass. In these scenarios, the low-energy charginos ( $\chi^+$ )/neutralinos ( $\chi^0$ ) are all Higgsino-like and their masses are nearly degenerate, being only slightly more than the mass of the neutralino.

As mentioned above, a compressed spectrum with nearly degenerate masses results in a kinematic suppression of the heavier  $\chi^+$  decays into  $W^\pm \chi^0$ , which has twofold consequences: it yields final states without hard leptons and it enhances the  $\chi^+$  lifetime up to  $\mathcal{O}(1)$  mm. At the LHC, the absence of hard leptons with sizeable transverse momenta makes this signature difficult to investigate. One possible solution is to search for the tracks from  $\chi^+$ , which effectively disappear once it decays and are thus called *disappearing tracks*.

The discovery prospects for prompt signatures of electroweakino decays in electron–proton collisions are presented in reference [644]. The light  $\chi^+$  (and  $\chi^0$ ) can be produced in pairs via

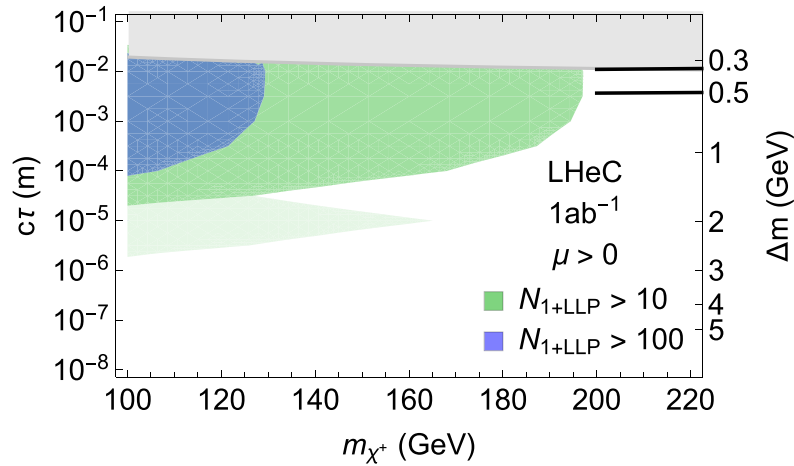


**Figure 119.** Exclusion limits on Higgsino masses as a function of their lifetime. Reproduced from [641]. CC BY 4.0. Coloured regions denote areas where 10 or 100 events with at least one LLP decay are observed. Light shading indicates the uncertainty in the predicted number of events due to different hadronisation and LLP reconstruction assumptions. The black curves are the optimistic and pessimistic projected bounds from HL-LHC disappearing-track searches.

VBF of the charged or neutral currents. A cut-based analysis of these processes at the LHeC, assuming prompt  $\chi^+$  decays, yields  $2\sigma$  discovery prospects for masses of up to 120 GeV.

Taking into account the finite lifetime of the charginos, two comments are in order: first, the lifetimes and boosts of the  $\chi^+$  are, in general, too small to resolve a disappearing track; second, the soft final state is not a problem *per se* and can, in principle, be observed.

Instead of searching for a disappearing track, the long lifetimes of the  $\chi^+$  can be exploited via the measurement of the impact parameter of the soft hadronic final state, as discussed in reference [641]. The crucial machine performance parameters are the tracking resolution, which should be as good as  $\mathcal{O}(10)$   $\mu\text{m}$ , and the absence of pile-up, which allows us to identify and measure a single soft pion's impact parameter. In this way, the LHeC can test  $\chi$  with masses of up to 200 GeV. The corresponding sensitivity is shown in figure 119, and the bounds on disappearing track searches at the HL-LHC are shown as black lines in the figure. By considering nonprompt Higgsino decays, the discovery prospects, compared to the prompt analysis, are thus significantly improved. A further means of improving the prospects is an increased centre-of-mass energy, which enhances the production rate of the Higgsinos.

**8.3.3. Signatures that violate R-parity.** Supersymmetry typically evokes the so-called R-parity, which implies that each fundamental vertex contains an even number of sparticles and helps to prevent rapid proton decays. In general, R-parity need not be an exact symmetry of the theory, meaning that interactions can be present that allow for sparticles to decay into SM particles and also that there is a possibility of violating lepton and/or baryon numbers.

Interactions that violate R-parity are particularly interesting in electron–proton collisions, where single superpartners might be resonantly produced and detected via the corresponding  $2 \rightarrow 2$  process. This is discussed in references [645, 646] for the case of the *sbottom*, showing that a good level of precision could be achieved at LHeC, compared with all the knowledge derived from indirect measurements.

Single (anti-)top quark production associated with R-parity-breaking coupling of the lightest neutralino in the MSSM is investigated in reference [647] for the LHeC. The study, which includes calculations of QCD contributions at the NLO, concludes that the available constraints would allow a notable production rate.

Certain SUSY scenarios might produce prompt signals of multiple soft jets, which generally resemble QCD backgrounds at the LHC and are thus notoriously difficult to test. The largely QCD-free environment of electron–proton collisions allows us to test this class of signatures. One example of this signal can originate from gluinos, which are tested at the LHC via signatures that involve large amounts of missing energy. If the gluino has an all-hadronic decay—such as in scenarios that violate R-parity or the stealth SUSY models—the current experimental searches have a gap in sensitivity for masses of between about 50 to 70 GeV [648]. Gluinos within this gap could be tested at the LHeC [649], for which a three-sigma exclusion sensitivity was demonstrated using simple signal-selection cuts.

#### 8.4. Feebly interacting particles

NP may interact with the SM via the so-called portal operators, including the vector, scalar, pseudoscalar, or neutrino portal. In these scenarios, the SM is often extended by an entire sector of NP, comprising new forces and several particle species, which may be connected to the big open questions of dark matter or the origin of neutrino mass.

These hypothetical new sectors derive their typical very feeble interaction strengths with the known particles from mass mixing with an SM particle that shares their quantum numbers. Some examples are discussed below.

**8.4.1. Searches for heavy neutrinos.** The observation of neutrino oscillations requires physics beyond the SM that gives rise to the light neutrino masses. One well-motivated class of models for this purpose is the so-called symmetry protected type-I seesaw scenario, which features heavy neutrinos with signatures that are, in principle, observable at colliders; see reference [650] and references therein. A comprehensive overview of collider searches for the heavy and mostly sterile neutrinos can be found in reference [651], in which the promising signatures for such searches at electron–proton colliders have been identified.

In electron–proton collisions, heavy neutrinos can be produced via the CC (see the left panel of figure 120). The heavy neutrino production cross-section is dependent on the active–sterile neutrino mixing with the electron flavour called  $|\theta_e|^2$ . The most promising searches at the LHeC are those using processes with lepton-flavour-violating (LFV) final states and displaced vertices, the prospects of which are evaluated in reference [652] and which are shown in the right panel of figure 120. It is remarkable that the prospects for detecting heavy neutrinos with masses of more than about 100 GeV are much better in electron–proton collisions, compared to proton–proton or electron–positron collisions, due to the much smaller reducible backgrounds.

The prospects for heavy neutrino detection can be further enhanced by jet substructure techniques when the  $W$  boson in the decay  $N \rightarrow eW$ ,  $W \rightarrow jj$  is highly boosted. Reference [653] shows that these techniques can help to distinguish the heavy neutrino signal from the few SM backgrounds. A considerable improvement in the bounds of  $|V_{eN}|^2$  compared to the current limits of the LHC,  $0\nu 2\beta$  experiments, and electroweak precision data is obtained with  $1 \text{ ab}^{-1}$  of integrated luminosity at the LHeC.

An alternative approach is employed in reference [658], in which the dominant sterile neutrino interactions with the SM are taken to be higher-dimension effective operators (parameterizing a wide variety of UV-complete NP models), while contributions from neutrino mixing are neglected. The study shows prospects that Majorana neutrinos can be detected using masses of less than 700 and 1300 GeV at the LHeC with  $E_e = 50$  and 150 GeV, respectively, for

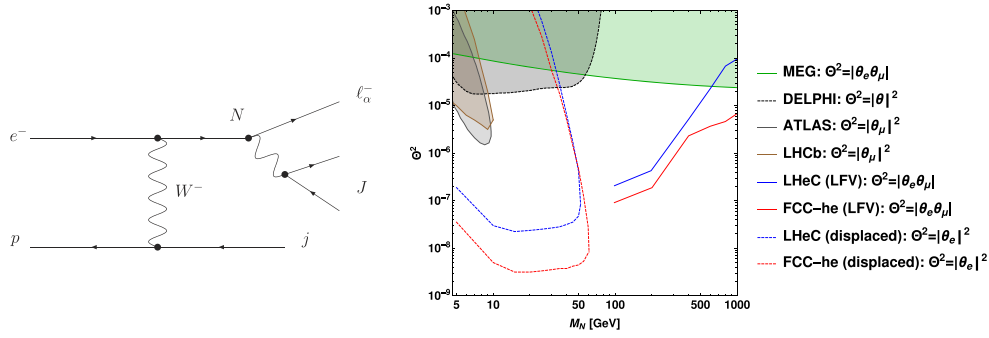


**Figure 120.** Left: dominant tree-level production mechanism for sterile neutrinos at the LHeC. Sterile neutrino decay via the CC gives rise to the so-called LFV lepton-trijet signature. Right: sensitivity of the LFV lepton-trijet searches (at a 95% CL) and the displaced vertex searches (at a 95% CL) (reproduced from [652], CC BY 4.0), compared to the current exclusion limits of ATLAS [654], the LHCb [655], the LEP collider [656], and the and the MEG Collaboration [657].

$E_p = 7$  TeV. Recently, the influences of vector and scalar operators on the angular distribution of the final anti-lepton were investigated. The forward–backward asymmetry is studied in reference [659], which, in particular, studied the feasibility of initial electron polarisation as a discriminator between different effective operators.

The prospects of testing left–right symmetric models featuring additional charged and neutral gauge bosons and heavy neutrinos were studied in the context of electron–proton collisions in references [660, 661]. The authors show that the production of heavy right-handed neutrinos with a mass of  $\mathcal{O}(10^2\text{--}10^3)$  GeV at the LHeC, with a lepton-number-violating final state, can yield information on the parity-breaking scale in left–right symmetric theories. Heavy neutrinos with sub-TeV masses were investigated in an inverse seesaw model with a Yukawa coupling of  $\mathcal{O}(0.1)$  for the LHeC in reference [662].

**8.4.2. Fermion triplets in a type-III seesaw.** Another technically natural way of generating the light neutrino masses is the so-called type-III seesaw mechanism, which extends the SM with a fermion  $SU(2)$  triplet. In minimal versions of these models the neutral- and charged-triplet fermions have almost degenerate masses that are around the TeV scale.

In the three-generation triplet extension of the type-III seesaw, the role of mixings between active neutrinos and neutral-triplet fermions was investigated in reference [663]. Depending upon the choice of Dirac Yukawa coupling, the mixing angles can take many possible values, from very small to large. With very small mixings, the decay length of the triplet fermion can be very large. It can show a displaced decay inside or outside the detectors of high-energy colliders. The proper decay length as a function of the lightest light neutrino mass  $m_1(m_3)$  for the normal (inverted) hierarchy case is shown in figure 121.

The prospects of probing this mechanism via searches for new fermions are evaluated in reference [665], wherein signatures from long-lived particles at various experiments are considered. The triplet fermions are primarily produced through their gauge interactions, as shown in the left panel of figure 122, and can be observed via displaced vertices and disappearing track searches for masses of a few hundred GeV. The authors find that the LHeC can observe vertices displaced by the decays of the charged fermion triplet components via the soft pion impact parameters for triplet masses of up to about 220 GeV. It also has a sensitivity to the light neutrino mass scale (which governs the lifetime of the neutral fermion), which is complementary



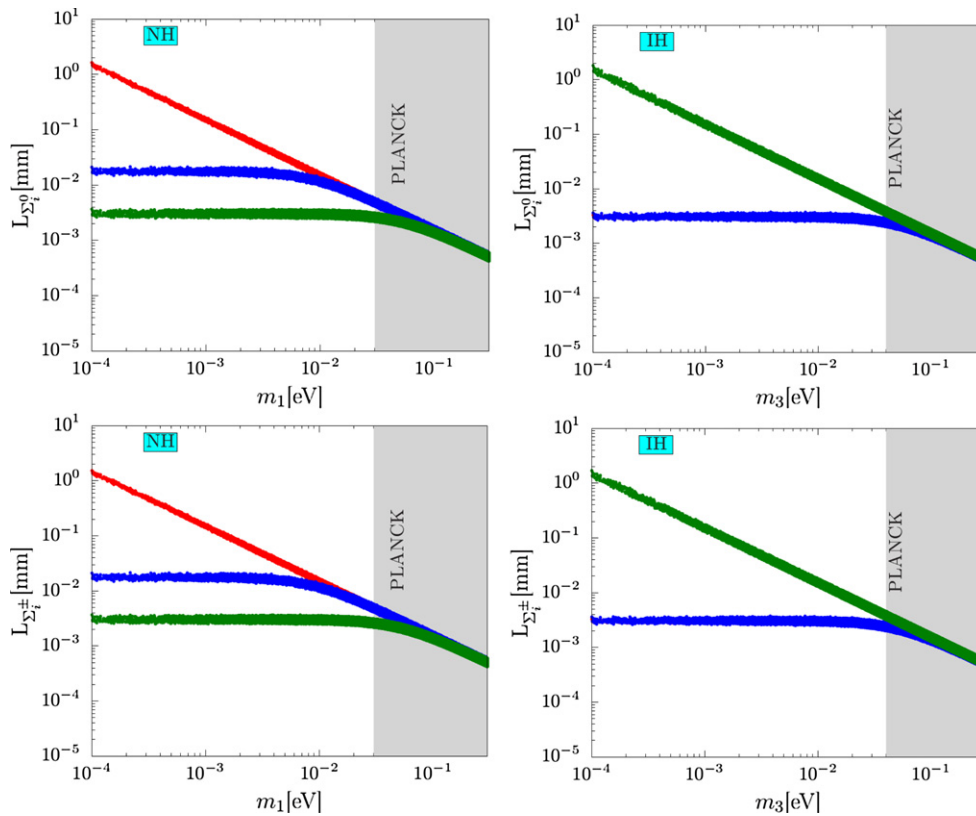


**Figure 121.** Proper decay length of  $\Sigma_i^0(\Sigma_i^\pm)$  with respect to the lightest light neutrino mass in the upper (lower) panel for a 1 TeV triplet. The normal (inverted) hierarchy case is shown in the left (right) panel. The first-generation triplet is represented by the red band, the second generation is represented by the blue band, and the third generation is represented by the green band. The shaded region is excluded by the PLANCK data. Reproduced with permission from [664].

to those of the LHC and the MAssive Timing Hodoscope for Ultra-Stable neutral pArticles (MATHUSLA). The final results from reference [665] for the LHeC are shown in the right panel of figure 122.

If the mixing becomes sufficiently large, and/or if the masses are  $\mathcal{O}(100)$  GeV, the triplet fermions decay promptly. In this case, the heavy triplets can also show a variety of interesting collider signatures, including fat jets. The latter have been studied for FCC-eh in reference [666].

**8.4.3. Dark photons.** Minimal extensions of the SM often involve additional gauge factors. In particular, the  $U(1)_X$  extensions are interesting, because they are often connected to a dark charge that can be associated with dark matter.

An SM-extending  $U(1)_X$  predicts an additional gauge boson that naturally kinetically mixes with the  $U(1)_Y$  factor of the SM [667]. This kinetic mixing allows the SM photon to couple to fermions that carry the dark charge  $X$ , and it allows the other gauge boson to couple to the electric charge. Both interactions are suppressed by the mixing parameter  $\epsilon$ . In most models, the additional gauge boson also receives a mass, possibly from spontaneous breaking of the

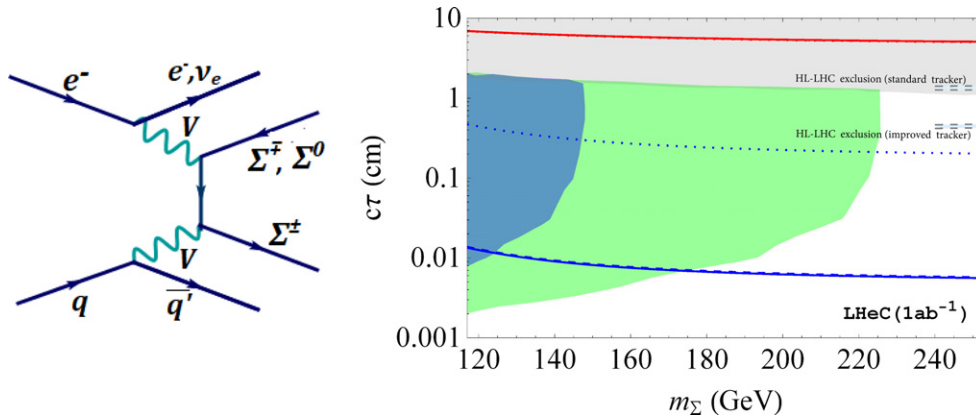


**Figure 122.** Left: diagram of the dominant production of triplet fermion pairs via their gauge interactions. Right: prospects of searches for vertices displaced by charged fermion triplets  $\Sigma^\pm$ . The blue (green) shaded regions denote the expected observabilities of 10 (100) events, dashed lines denote the HL-LHC exclusion sensitivity, and the red line is connected to the light neutrino properties. Reproduced with permission from [665]. For details, see the text and reference [665].

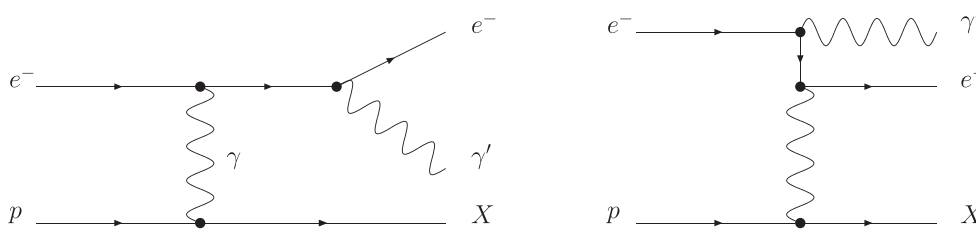


**Figure 123.** Feynman diagrams for the dark photon production processes in electron–proton collisions. Here,  $X$  denotes the final-state hadrons after the scattering process. Reproduced from [668]. CC BY 4.0.

$U(1)_X$ , and the corresponding mass eigenstate is called a dark photon. Dark photons typically have masses that are around the GeV scale and their interactions are QED-like, scaled with the small mixing parameter  $\epsilon$ . They can decay to pairs of leptons, hadrons, or quarks, which can give rise to a displaced vertex signal, due to their long lifetime.

The prospects for dark photon searches via their displaced decays in  $ep$  collisions are presented in reference [668]. The dark photon production process targeted in this search is depicted in figure 123. The signal is given by the process  $e^-p \rightarrow e^-X\gamma'$ , where  $X$  denotes the final-state hadrons, and the dark photon  $\gamma'$  decays into two charged fermions or mesons.

The most relevant performance characteristics of the LHeC are the very good tracking resolution and the very low level of background, which allow the detection of a secondary vertex with a displacement of  $\mathcal{O}(0.1)$  mm.

The resulting sensitivity contours in the mass-mixing parameter space are shown in figure 124, in which the different colours correspond to different assumptions for the irreducible background, and the solid and dashed lines represent different signal reconstruction efficiencies. Also shown, for comparison, are the existing exclusion limits from different experiments and the region that is currently being investigated by the LHCb collaboration [669].

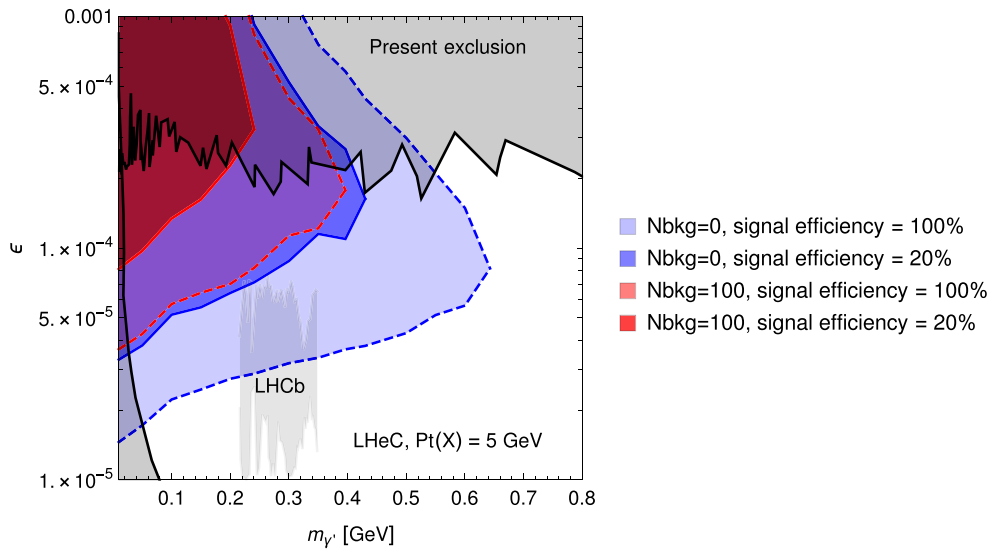


**Figure 124.** Projected sensitivity of dark-photon searches at the LHeC via displaced dark-photon decays. Reproduced from [668]. CC BY 4.0. The sensitivity contour lines are at the 90% CL after a transverse momentum cut of 5 GeV on the final-state hadrons. The blue and red areas denote assumptions of zero and 100 background events, respectively; the solid and dashed lines correspond to reconstruction efficiencies of 100% and 20%, respectively. See reference [668] for details.

The domain in parameter space tested in electron–proton collisions is complementary to other current and planned experiments. In particular, searches for masses below the di-muon threshold are practically impossible at the LHC. It is remarkable that dark photons in this mass range can be part of a dark sector that explains the observed dark matter in the Universe via a freeze-in mechanism; see, for example, reference [670].

**8.4.4. Axion-like particles.** The axion is the Goldstone boson related to a global  $U(1)$  symmetry, which is spontaneously broken at the so-called Peccei–Quinn scale, assumed to be around the GUT scale. Its mass, which is inversely proportional to the Peccei–Quinn scale, is therefore usually in the sub-eV regime, and it provides a dynamical solution to the strong CP problem of the SM. Axions are a very attractive candidate for *cold* dark matter, despite their tiny mass.

The concept of axion-like particles (ALPs) is motivated by the original idea of the QCD axion, and, like the QCD axion, they are good dark-matter candidates. ALPs are pseudoscalar particles that are usually assumed to be relatively light (i.e. with masses around and below one GeV) and that couple to the QCD field strength. In addition, they may have a number of further interactions; for instance, they can interact with the other fields of the SM and also mix with the pion. Particularly interesting is the possibility of producing ALPs via VBF processes.

A recent study [671] has evaluated the prospects of detecting ALPs at the LHeC via the process  $e^- \gamma \rightarrow e^- a$ , as shown in the left panel of figure 125, in a model-independent fashion. The signature investigated was the decay  $a \rightarrow \gamma \gamma$ , which allowed the testing of effective ALP–photon coupling for ALPs with masses in the range of  $10 \text{ GeV} < m_a < 3 \text{ TeV}$ . It was found that sensitivities can improve current LHC bounds considerably, especially for ALP masses of less than 100 GeV, as shown in the right panel of figure 125. The authors stated that

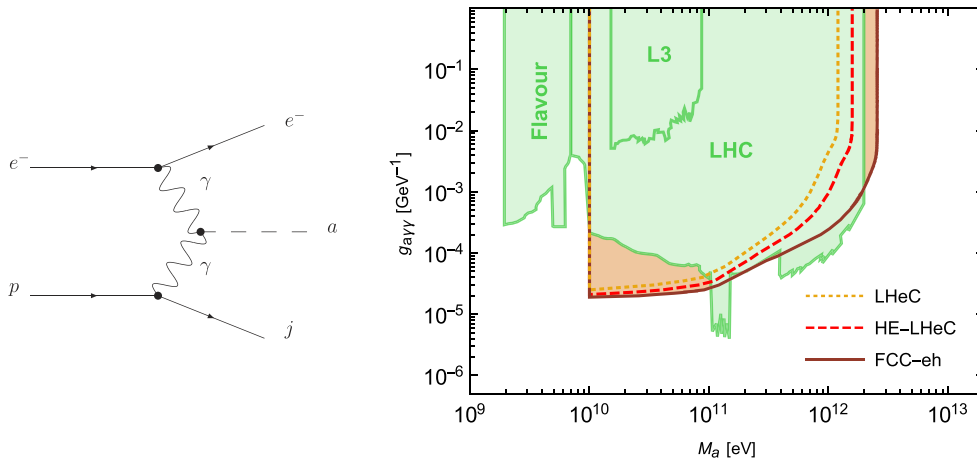


**Figure 125.** Left: production of ALPs via photon fusion. Right: projected sensitivity of the LHeC to ALPs coupled with photons at a 95% CL. The existing exclusion limits are shown by the green regions. Reproduced from [671]. CC BY 4.0.

ALP searches at  $ep$  colliders might offer an important way of approaching this class of NP scenario [671].

### 8.5. Anomalous gauge couplings

NP beyond the SM can modify SM interactions, for instance, at the loop level. Such contributions could either modify the interaction strength of SM particles or introduce additional interactions that are not present in the SM, such as flavour-changing neutral couplings (FCNC).

Searches for anomalous couplings of top quarks are summarised in section 5.3. They are parametrised via an effective Lagrangian and are studied by analysing specific processes. For example, anomalous  $Wtb$  couplings are studied using  $e^- p \rightarrow \nu_e \bar{t}$ , and anomalous  $t\bar{t}\gamma$  and  $t\bar{t}Z$  couplings are studied using top quark pair production. In addition, FCNC  $tu\gamma$  and  $tuZ$  couplings are analysed in NC DIS single top quark production, and FCNC  $tHu$  couplings are investigated in CC DIS single top quark production. Limits on the corresponding FCNC branching ratios are discussed in section 5.3.6 and summarised and compared to different colliders in figure 75.

Triple gauge boson couplings (TGC)  $W^+W^-V$ ,  $V = \gamma, Z$  are precisely defined in the SM, and any significant deviation from the predicted values could indicate NP. Present constraints on anomalous triple vector boson couplings are dominated by the LEP collider (but they are not free of assumptions) and the  $WWZ$  and  $WW\gamma$  vertices can be tested at the LHeC in great detail.

The search for anomalous  $WW\gamma$  and  $WWZ$  couplings using a polarised electron beam was studied via the processes  $ep \rightarrow \nu q \gamma X$  and  $ep \rightarrow \nu q ZX$ , as described in reference [466]. It was found that the LHeC sensitivity with  $E_e = 60$  GeV and  $L = 100 \text{ fb}^{-1}$  is comparable to the existing experimental limits of lepton and hadron colliders and that the sensitivity to anomalous  $Z$  couplings might be better, reaching  $(\Delta\kappa_{\gamma,Z}, \lambda_{\gamma,Z})$  values as small as  $\mathcal{O}(10^{-1}, 10^{-2})$ . In general, beam polarisation and larger electron-beam energies improve the sensitivity, and the LHeC was found to provide information on anomalous couplings that was complementary to that of the LHC.

The prospects of testing anomalous triple gauge couplings are also investigated in reference [465]. Therein, the authors study the kinematics of an isolated hard photon and a single jet

## Radiation-Amplitude Zero at the LHeC

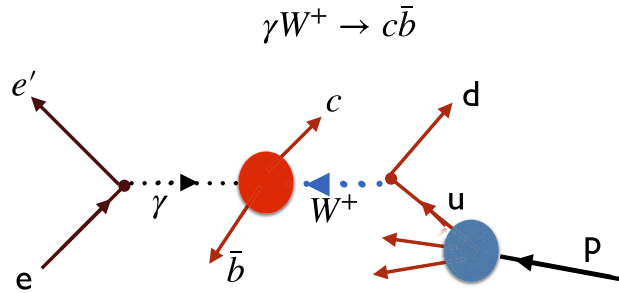


**Figure 126.** The radiation amplitude zero of the SM in  $\gamma W^+ \rightarrow c\bar{b}$  and  $\gamma u \rightarrow W^+ d$ . A prediction for the angular distribution  $\frac{d\sigma}{d\cos(\theta_{\text{CM}})}(\gamma u \rightarrow W^+ d)$  is provided in reference [675].

with a substantial amount of missing transverse momentum. The authors show that the LHeC is sensitive to anomalous triple gauge couplings via the azimuthal angle differences in the final state considered. It is pointed out that in such an analysis, it is possible to separately probe the  $WW\gamma$  vertex, with no contamination from possible BSM contributions to the  $WWZ$  coupling. The estimates cover the cases of  $E_e = 100, 140,$  and  $200$  GeV, and it is claimed that while higher energies yield better sensitivities, the differences are not very large. For an integrated luminosity of  $200 \text{ fb}^{-1}$  and  $E_e = 140$  GeV, the exclusion power of the LHeC is superior to all existing bounds, including those of the LEP collider.

The process  $e^- p \rightarrow e^- \mu^+ \nu j$  is investigated in reference [467]. The analysis is carried out at the parton level and includes the cross-section measurement and a shape analysis of angular variables, in particular, of the distribution of the azimuthal angle between the final-state forward electron and the jet. It is shown that the full reconstruction of leptonic  $W$  decay can be used for  $W$  polarization, which is another probe of anomalous triple gauge couplings. The results show that the LHeC could reach a sensitivity to  $\lambda_\gamma$  and  $\Delta k_\gamma$  as small as  $\mathcal{O}(10^{-3})$  for  $L = 2\text{--}3 \text{ ab}^{-1}$ .

**8.5.1. Radiation amplitude zero.** The LHeC is ideal for testing a novel feature of the SM: the *radiation amplitude zero* [672–675] of the amplitude  $\gamma W^- \rightarrow c\bar{b}$  and related amplitudes, see figure 126. The Born amplitude is predicted to vanish and change sign at  $\cos \theta_{\text{CM}} = \frac{e_b}{e_w} = -1/3$ . This LHeC measurement will test the compositeness of the  $W$  boson and its zero anomalous magnetic moment at the leading order, where one has  $g_W = 2, \kappa_W = 1$ , as well as  $g_q = 2$  for the quarks. More generally, one can also test the radiation amplitude zero for the top quark from measurements of the process  $\gamma b \rightarrow W^- t$ .

### 8.6. Theories with heavy resonance and contact interaction

In many other BSM scenarios, NP will manifest itself by the presence of new resonances. Although the high centre-of-mass energy of  $pp$  colliders allows for a better reach in most of these scenarios, the LHeC and the FCC-eh, thanks to their clean collision environments and virtual absence of pile-up, can complement the LHC in the search for these new phenomena. Deviations from SM predictions could signal NP, even if they are at an energy scale beyond the centre-of-mass energy of the collider. In this case, the effective four-fermion contact interaction (CI) could be explained by the exchange of a virtual heavy particle, such as an LQ, a heavy boson, or elementary constituents of quarks and leptons in composite models. The effective CI

scale then represents the typical mass scale of the new particles. Relevant studies of various topics, including scalar and vector LQs and excited leptons, are collected in this section.

**8.6.1. Leptoquarks.** In recent years, experiments that have studied heavy flavoured mesons have revealed intriguing hints of NP in the semileptonic decays of  $B$  mesons. A violation of lepton flavour universality at a level of  $3$  to  $5\sigma$  is apparent in both the CC- and neutral-current-mediated processes [676]. In this context, BSM theories involving LQs have gained renewed interest, as they can give rise to lepton-universality-violating decays of heavy mesons at tree level, provided that they couple to the second and third generation of quarks. LQs first appeared in reference [677] in Pati and Salam's  $SU(4)$  model, in which the lepton number was considered to be the fourth colour. They also appear in grand unified theories, extended technicolor models, and compositeness models. The nomenclature and classification are based on their transformation properties under the SM gauge groups [678, 679].

In  $ep$  collisions LQs can be produced in an  $s$ -channel resonance via their coupling to the first generation of quarks; their signature is a peak in the invariant mass of the outgoing  $\ell q$  system. Contrary to what is achievable in the LHC environment, it has been shown that, at the LHeC, many properties of LQs can be measured with high precision [1].

The search for LQs at the LHC is essentially insensitive to the coupling  $LQ-e-q$ , characterized by the parameter  $\lambda$ , since the dominant process is pair production via the strong interaction. Recent searches have therefore been able to exclude LQs of the first generation of mass up to 1.4 TeV, assuming a branching ratio to charged leptons = 1.0. For other generations, the bounds are  $\sim 1$  TeV (for the latest results, see, for example, references [680, 681]). Under the assumption that the LQ has  $O(0.1)$  branching ratios to a number of tested final states, some parameter space remains in which the LHeC can make a significant contribution to the search for LQs.

For LQs with masses less than the centre-of-mass energy of the collider, suitable searches promise a sensitivity to  $\lambda$  as small as  $O(10^{-3})$ . As shown in [682], production of the first-generation scalar LQs at the LHeC can have a much higher cross-section than at the LHC. The authors of that paper also show that, for the LQs known as  $R_2^{5/3} \sim (3, 2, 7/6)$  and  $\tilde{R}_2^{2/3} \sim (3, 2, 1/6)$ , a sensitivity to the Yukawa coupling better than an electromagnetic strength ( $\sim 0.3$ ) of  $5\sigma$  can be reached at masses of up to 1.2 TeV.

For the  $S_1$  scalar LQ  $(\bar{3}, 1, 1/3)$ , estimates of the sensitivities of the LHeC and the FCC-eh as a function of the LQ mass and the Yukawa coupling in the leading-logarithmic (LL) approximation are shown in figure 127, assuming  $1 \text{ ab}^{-1}$  of integrated luminosity. Here, the signal was generated at the leading order using MadGraph with the model files from reference [683], hadronisation performed by Herwig7 [376, 684], and detector simulation by DELPHES [475]. The SM background  $e^- p \rightarrow e^- j$  was also generated at the leading order. A simple set of cuts was applied to the  $p_T$  of the leading electron and jet, and a window was applied to the invariant mass of the e-jet system.

The  $\tilde{R}_2^{2/3}$  scalar LQ allows for coupling to right-handed neutrinos, providing interesting search channels. Its signatures have recently been investigated at  $ep$  colliders [685, 686]. In the lepton and jet final state, it is found that the LHeC can probe up to 1.2 TeV at a  $3\sigma$  level of significance with an  $e^-$  beam, and it can probe at the  $5\sigma$  level with an  $e^+$  beam and  $1 \text{ ab}^{-1}$  of integrated luminosity. At the FCC-eh, a  $5\sigma$  discovery can be achieved with an  $e^-$  beam of up to  $\sim 2.3$  TeV and  $1 \text{ ab}^{-1}$  of integrated luminosity.

**8.6.2.  $Z'$ -mediated charged-lepton-flavour violation.** Charged lepton flavour-violating signatures have been thoroughly tested using electrons and muons, but less so when they involve tau leptons. Interestingly, in many extensions of the SM, lepton flavour is much more strongly



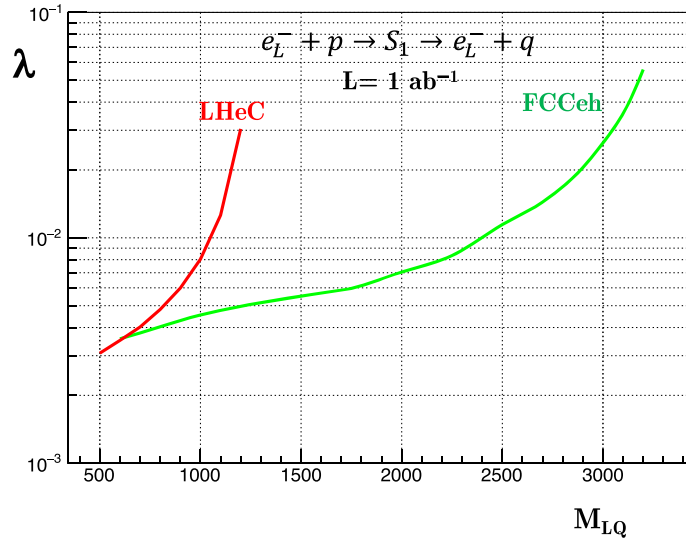


**Figure 127.** Estimated  $2\sigma$  significance of the coupling  $\lambda$  at the LHeC and the FCC-eh for the scalar leptoquark  $S_1$  as a function of its mass, assuming  $1 \text{ ab}^{-1}$  of luminosity and no systematic uncertainty.

violated in the tau sector, while weaker experimental constraints exist at low energies. In reference [687], the  $Z'$ -mediated  $e-\tau$  (and  $e-\mu$ ) conversion processes are studied in the context of the LHeC by considering the lepton flavour-violating processes  $pe^- \rightarrow \tau^- j$  (and  $pe^- \rightarrow \mu^- j$ ).

For this LHeC study, a 60 GeV electron beam with up to 80% polarization is considered in order to achieve a centre-of-mass energy close to 1.3 TeV with a total of  $1 \text{ ab}^{-1}$  of integrated luminosity. Several backgrounds featuring tau leptons are considered, and a parameterised reconstruction efficiency and misidentification of tau jets are included in the analysis. To distinguish between the signal events and all relevant backgrounds, 31 kinematic variables (at the reconstruction level, after the detector simulation) are used as the input to TMVA. A BDT algorithm is used to separate the signal events from the background events. Systematic uncertainties are evaluated and are found to be around 2%.

Assuming equal couplings  $|V_R^{ij}| = |V_L^{ij}| \equiv |V|$  of the  $Z'$  to quark–quark or lepton–lepton flavours  $i, j$ , the LHeC is found to be sensitive to  $Z'$  masses of up to  $\mathcal{O}(10)$  TeV, as depicted in figure 128 by the black line. Also included in the figure are the existing limits from ATLAS searches for  $Z'$  decays into  $e\tau$  [688] and the search for same-flavour final states [689]. The experimental limits based on the branching ratio  $\text{BR}(\tau \rightarrow e\gamma)$  [690] and  $\text{BR}(\tau \rightarrow eee)$  [691] are also reported.

Overall, lepton flavour violation in the tau sector can be tested extremely well at the LHeC, surpassing the sensitivity of the LHC and low-energy experiments over the whole of the considered mass range by more than two orders of magnitude. This is particularly interesting for very heavy  $Z'$ , which are not accessible for direct production, for which the LHeC provides an exciting new discovery channel for this kind of lepton flavour-violating process.

**8.6.3. Vector-like quarks.** In composite Higgs models, new vector-like quarks are introduced. The third generation is favoured, in particular, the top-partner ( $T$ ) with a charge of  $2/3$ . The prospects for detecting  $T$  at the LHeC are discussed in reference [692]. For this search, a

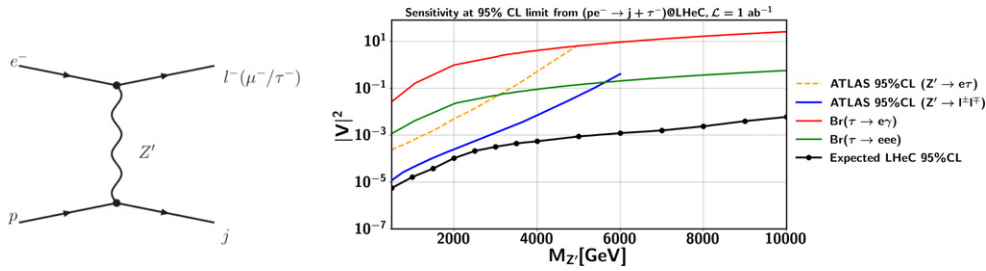


**Figure 128.** Left: Feynman diagram for the  $e\text{-}\tau$  (and  $e\text{-}\mu$ ) conversion processes  $pe^- \rightarrow \tau^- + j$  (and  $pe^- \rightarrow \mu^- + j$ ) mediated by a  $Z'$  with flavour-violating couplings to charged leptons at the LHeC. Reproduced from [687]. CC BY 4.0. Right: limits on the coupling parameter  $|V|^2$  for the signal hypothesis, compared with the existing limits from experimental constraints on the relevant flavour-conserving and flavour-violating processes. The black line represents the LHeC sensitivity for the process  $pe^- \rightarrow \tau j$ . For the other limits, see the text.

simplified model is considered in which  $T$  is produced by positron–proton scattering via inter-generational mixing and decays by  $T \rightarrow tZ$ , with a final state of  $\nu_e \ell^+ \ell^- bjj'$  at  $E_e = 140$  GeV. The authors find that for  $L = 1 \text{ ab}^{-1}$ , top partner  $T$  masses of around 800 GeV can be tested when the model-related coupling constants are  $\mathcal{O}(0.1)$  and that mixing between  $T$  and the first-generation quarks can significantly enhance the LHeC sensitivity.

Another search strategy for singly produced top partners is given by their decays  $T \rightarrow Wb$  and  $T \rightarrow th$ , which are presented in reference [693]. The analysis is based on a simplified model in which the top partner is an  $SU_L(2)$  singlet and only interacts with the third generation of quarks. This model considers the collisions of positrons and protons at  $E_e = 140$  GeV. The analysis, carried out at the parton level, investigates the kinematic distributions of the final states. Useful kinematic variables for the  $bW$  final state are found to be the transverse momentum of the lepton and the  $b$ -jet missing energy, while for the  $th$  final state, the most useful observable is the transverse hadronic energy. For masses of  $\mathcal{O}(1)$  TeV, the LHeC is found to be sensitive to the new interactions when they are  $\mathcal{O}(0.1)$  for  $L = 1 \text{ ab}^{-1}$ , in agreement with [692]. A very similar analysis was performed for the  $T \rightarrow Wb$  signal channel with comparable results [694].

**8.6.4. Excited fermions ( $\nu^*$ ,  $e^*$ , and  $u^*$ ).** The potentials of searches for excited spin-1/2 and spin-3/2 neutrinos are discussed in reference [695]. In their analysis, the authors consider effective currents that describe the interactions between excited fermions, gauge bosons, and SM leptons. For the signature, the production of the excited electron neutrino  $\nu^*$  and its subsequent decay  $\nu^* \rightarrow We$  with  $W \rightarrow jj$  was chosen. The analysis, carried out at the parton level, considers  $E_e = 60$  GeV, and consists of a study of the kinematic distributions of the final states. It concludes that the signature can clearly be distinguished from backgrounds, and that other lepton–hadron colliders would be required to test excited neutrinos of different flavours.

Analyses using similar models, which considered electron–proton collisions at the energies of the FCC-eh and beyond, were carried out for excited electron neutrinos and are presented in reference [696]. An analysis of the reach of the FCC-eh for testing excited electrons is discussed in reference [697], and for excited quarks in a composite model framework in reference [698].

**8.6.5. Colour octet leptons.** Unresolved issues of the SM, such as family replication and quark–lepton symmetry, can be addressed by composite models, in which quarks, leptons,

and gauge bosons are composite particles made up of more basic constituents. One general class of particles, predicted by most of the composite models, is colour octet leptons, which are the bound states of a heavy fermion and a heavy scalar particle that is assumed to be colour-charged. In this scenario, each SM lepton is accompanied by a colour octet lepton, which may have a spin of  $1/2$  or  $3/2$ . Since they are unobserved, the compositeness scale is expected to be at least  $\mathcal{O}(1)$  TeV.

At the LHeC, the colour octet partner of the electron  $e_8$  can be produced through the process  $e^- p \rightarrow e_8 g + X$  and studied via its decay products. An analysis that includes the study of kinematic distributions obtained at the parton level is presented in reference [699]. It is shown that discovery prospects exist for masses of  $\mathcal{O}(\text{TeV})$ . A similar analysis is performed for the FCC-eh at much higher energies in reference [700].

**8.6.6. Quark substructure and contact interactions.** Several long-standing questions arise in the SM, such as those enumerated in section 1.1. Perhaps most seriously, the SM does not appear to provide a clear, dynamical *raison d'être* for the existence of quarks. Leptons and quarks appear in the SM in a symmetric way, sharing electromagnetic interaction with the same charge quantization and with a cancellation of anomaly in the family structure. This strongly suggests that they may be composed of the same fundamental constituents, or that they form a representation of an extended gauge-symmetry group of a grand unified theory.

Assuming that the electron is a point-like particle, the quark substructure can be investigated by introducing a form factor  $f_q(Q^2)$  to describe deviations of the  $ep$  scattering cross-section:

$$\frac{d\sigma}{dQ^2} = \frac{d\sigma^{\text{SM}}}{dQ^2} f_q^2(Q^2) \quad (8.1)$$

$$f_q^2(Q^2) \simeq 1 - \frac{R^2}{6} Q^2. \quad (8.2)$$

Here,  $R$  is the root-mean-square (RMS) electric-charge quark radius. The current limit from HERA is  $4.3 \times 10^{-19}$  m [701], while it is estimated that the LHeC will be sensitive at up to  $\sim 10^{-19}$  m [702].

An electric precursor to QCD was formulated in 1969 that assumed that hadron constituents were highly electrically charged and that the strong attraction between positive and negative constituents bound them together [703]. Neither the electric model nor Schwinger's comparable model of monopoles [704] reproduce the observed particle spectrum of hadrons, or the observed pattern of weak interactions. The ATLAS collaboration has recently reported searches for free magnetic monopoles and free highly electrically charged particles produced in  $pp$  collisions at 13 TeV [705]. No candidates were detected with one or two Dirac magnetic charges or with electric charges  $20e < |z| < 100e$ . This extends the results of previous searches made at lower energies and in cosmic rays or bulk matter. A simple picture of what might emerge with highly electrically charged constituents is obtained by modelling the proton's substructure by a charge of (say)  $21|e|$  smeared uniformly over a region with a radius of  $10^{-19}$  m, and two charges of  $-10|e|$  smeared over a larger region with a radius of  $2 \times 10^{-19}$  m. Model II by Hofstadter [706] predicts the form-factor results shown in figure 129, which are consistent with the HERA upper limit.

More generally [707], CIs can be parameterized in the Lagrangian by coupling coefficients  $\eta_{ij}^q$  where the indices  $i, j$  indicate left-handed or right-handed fermion helicities and  $q$  denotes the quark flavour. The interaction can be of a scalar, vector, or tensor nature and the interference

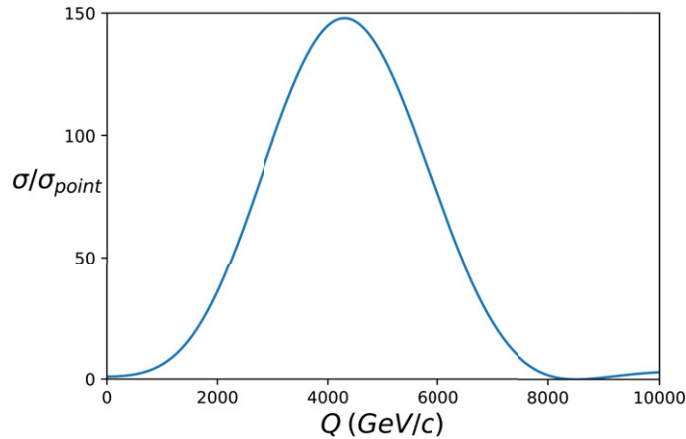


**Figure 129.** Form factor effect in the  $e-p$  interaction produced by substructure according to Hofstadter's model II of [706] using the model parameters given in the text.

with SM currents can be constructive or destructive. It has been estimated that the LHeC can be sensitive to a CI scale of  $\sim 40-60$  TeV with  $100 \text{ fb}^{-1}$  of integrated luminosity [702], while the current LHC limits are between 20 and 40 TeV, depending on the sign of the interference [708, 709].

### 8.7. Summary and conclusions

The lack of NP at the LHC to date has forced the community to develop new theoretical ideas and explore the complementarities between  $pp$  machines and other possible future facilities. In the context of  $ep$  colliders, several studies are being carried out to understand their potential to search for NP, considering that many interactions can be tested at high precision that are otherwise not easily accessible.

At  $ep$  colliders, most BSM physics is accessed via vector-boson fusion, which suppresses the production cross-section quickly with increasing mass. Nonetheless, scalar extensions of the SM as well as neutrino-mass-related BSM physics can be comprehensively tested using  $ep$  due to the smallness and reducibility of the SM backgrounds. The absence of pile-up and complicated triggering makes searches for soft-momenta final-state particles feasible, so that results for BSM theories, for example, those characterised by the presence of nonprompt, long-lived particles, are complementary to those at the LHC. Additionally, the excellent angular acceptance and resolution of its detector also renders the LHeC a very suitable environment for displaced vertex searches. An increase in the centre-of-mass energy as large as the one foreseen at the FCC would naturally considerably boost the reach in most scenarios.

Finally, it is worth noting that the LHeC can offer different or indirect ways to search for NP. It was recently shown that Lorentz invariance violation in the weak vector-boson sector can be studied in electron-proton scattering [710] via a Fourier analysis of the parity-violating asymmetry in DIS. Moreover, NP could be related to nucleon, nuclear, and top structure func-

tions, as discussed in references [41, 711, 712]. Investigations of the  $B_c^{(*)}$  meson and doubly heavy baryon have also been shown to have discovery potential for NP [713–715].

## 9. Influence of the LHeC on physics at the HL-LHC

After almost 10 years of scientific exploitation of the LHC and about  $175 \text{ fb}^{-1}$  of proton–proton collision data delivered to the ATLAS and CMS experiments, the sensitivity of a significant fraction of the leading measurements and searches has become limited by systematic uncertainties. Uncertainties induced by the strong interaction, in particular those related to the proton structure, play a prominent role and tend to saturate the physics reach of the experiments. This situation will only become more evident when the LHC enters its high-luminosity era.

With high-precision PDFs measured independently from the other LHC experiments, the LHeC project can resolve this situation. It allows a clean study of the pure QCD effects it aims to measure, resolving the ambiguity between new physics effects at high mass and PDF uncertainties that intrinsically affect the interpretation of proton–proton data alone. At the weak scale, improved PDFs will provide a significant boost to the achievable precision of measurements of the Higgs boson properties and of fundamental electroweak parameters. The LHeC is thus a perfect companion machine for the HL-LHC, allowing a full exploitation of the data and significantly extending its reach.

This chapter illustrates these points using a few selected examples in the domain of precision measurements of the  $W$ -,  $Z$ - and Higgs-boson properties. The impact of precise PDFs on searches for TeV-scale new physics is also illustrated. In addition, we also present the complementarity of PDF studies at the LHeC and the HL-LHC, the impact of new QCD dynamics at small  $x$  on measurements at hadron colliders, and the impact of electron–nucleus scattering data on heavy-ion physics at the LHC.

### 9.1. Precision electroweak measurements at the HL-LHC

**9.1.1. The effective weak mixing angle.** Prospective studies of the measurement of the effective weak mixing angle using the forward–backward asymmetry,  $A_{\text{FB}}$ , in DY di-lepton events at the HL-LHC were performed for ATLAS [716], CMS [717], and LHCb [718] and reported in the CERN report on SM physics at the HL-LHC [187]. A brief summary is given here, focussing on the impact of the LHeC on this measurement.

At the leading order, lepton pairs are produced through the annihilation of a quark and an antiquark via the exchange of a  $Z$  boson or a virtual photon. The definition of  $A_{\text{FB}}$  is based on the angle  $\theta^*$  between the initial- and final-state fermions:

$$A_{\text{FB}} = \frac{\sigma_{\text{F}} - \sigma_{\text{B}}}{\sigma_{\text{F}} + \sigma_{\text{B}}}, \quad (9.1)$$

where  $\sigma_{\text{F}}$  and  $\sigma_{\text{B}}$  are the cross-sections in the forward ( $\cos \theta^* > 0$ ) and backward ( $\cos \theta^* < 0$ ) hemispheres, respectively.

A non-zero  $A_{\text{FB}}$  in dilepton events arises from the vector and axial-vector couplings of electroweak bosons to fermions. At the tree level, the vector and axial-vector couplings of the  $Z$  boson to a fermion  $f$  are

$$g_{\text{V}}^f = T_3^f - 2Q_f \sin^2 \theta_W, \quad g_{\text{A}}^f = T_3^f. \quad (9.2)$$

**Table 20.** The breakdown of uncertainties in  $\sin^2 \theta^l \ell_{\text{eff}}$  from the ATLAS preliminary results at  $\sqrt{s} = 8$  TeV with  $20 \text{ fb}^{-1}$  [448] is compared to the projected measurements with  $3000 \text{ fb}^{-1}$  of data at  $\sqrt{s} = 14$  TeV for the two PDF sets considered in this note. All uncertainties are given in units of  $10^{-5}$ . Other sources of systematic uncertainty, such as the impact of the MC statistical uncertainty evaluated in reference [448], are not considered in the HL-LHC prospect analysis.

Parameter	Unit	ATLAS (reference [448])		HL-LHC projection	
		MMHT2014	CT14	HL-LHC PDF	LHeC PDF
Centre-of-mass energy, $\sqrt{s}$	TeV	8	14	14	14
Int. luminosity, $\mathcal{L}$	$\text{fb}^{-1}$	20	3000	3000	3000
Experimental uncert.	$10^{-5}$	$\pm 23$	$\pm 9$	$\pm 7$	$\pm 7$
PDF uncert.	$10^{-5}$	$\pm 24$	$\pm 16$	$\pm 13$	$\pm 3$
Other syst. uncert.	$10^{-5}$	$\pm 13$	—	—	—
Total uncert., $\Delta \sin^2 \theta^l \ell_{\text{eff}}$	$10^{-5}$	$\pm 36$	$\pm 18$	$\pm 15$	$\pm 8$

The coupling ratio,  $g_V^f/g_A^f = 1 - 4|Q_f|\sin^2 \theta_W$ , generates the asymmetry. Defining

$$A_f = 2 \frac{g_V^f/g_A^f}{1 + (g_V^f/g_A^f)^2} \tag{9.3}$$

one finds, for a given sub-process  $q\bar{q} \rightarrow Z \rightarrow \ell^+ \ell^-$ ,

$$A_{\text{FB}} = \frac{3}{4} A_q A_\ell. \tag{9.4}$$

As discussed in sections 5.1 and 9.1.3 below, equation (9.2) is subject to radiative corrections, which introduce the effective weak mixing angle  $\sin^2 \theta_{\text{eff}}^\ell$  replacing the leading-order observable  $\sin^2 \theta_W$ . The asymmetry definitions downstream are, however, unchanged.

The angle  $\theta^*$  is uniquely defined in  $e^+e^-$  collisions, for which the directions of the  $e^+$  and  $e^-$  beams are known. In proton–antiproton collisions at the Tevatron, the incoming quarks and antiquarks also have preferred directions, and a non-zero asymmetry exists for all lepton-pair rapidities. At the LHC the beams are symmetric, and a non-zero asymmetry only appears for high-rapidity events, since the direction of the longitudinal boost reflects, on average, the direction of the incoming valence quark. While the expected Z-boson statistics are very large, with  $\mathcal{O}(3 \times 10^9)$  events expected in ATLAS and CMS, the measurement is thus highly affected by PDF uncertainties, and in particular by the  $u$  and  $d$  valence and sea distributions.

Prospective studies were performed by ATLAS, CMS and LHCb, including a discussion of the expected PDF uncertainties. The impact of the LHeC PDFs was evaluated by ATLAS and is discussed further. Table 20 compares the published ATLAS results [448] with the prospects for  $3 \text{ ab}^{-1}$  for a variety of PDF sets. The statistical uncertainty for this sample is at the level of  $3 \times 10^{-5}$ , and the experimental systematic uncertainties are improved by 10%–25%, depending on the PDF scenario considered. While claims of comparable PDF uncertainties are made for MMHT2014 [719] and CT14 [720], the size of the PDF uncertainty is reduced by the increased sample size at the HL-LHC, which helps to constrain this component *in situ*. The HL-LHC PDF set [258], which incorporates the constraints expected from present and future LHC data,



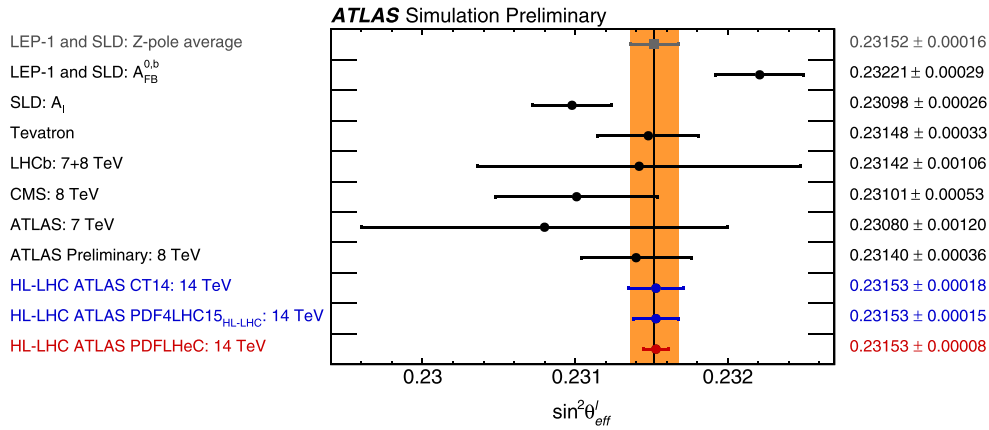


**Figure 130.** Comparison of measurements or combinations of  $\sin^2 \theta_{\text{eff}}^l$  with the world average value (orange band) and the projected uncertainties of measurements at the HL-LHC. Reproduced from [716]. CC BY 4.0. For the HL-LHC, the central values are set to the world average value, and uncertainties are displayed for different assumptions of the available PDF sets, similarly to table 20.

further decreases the associated uncertainty by about 20%. The LHeC projection [54] results from a QCD fit to  $1 \text{ ab}^{-1}$  of the  $ep$  scattering pseudodata, with  $E_e = 60 \text{ GeV}$  and  $E_p = 7 \text{ TeV}$ ; in this case, the PDF uncertainty is subleading compared to the experimental systematics.

Figure 130 compares the ATLAS sensitivity studies of  $\sin^2 \theta_{\text{eff}}^l$  to previous measurements made by the LHC experiments [447–449, 721], and to the legacy measurements made by the experiments at the LEP collider, the SLC [444], and the Tevatron [446]. The precision of the measurement of the weak mixing angle in  $Z$ -boson events, using  $3000 \text{ fb}^{-1}$  of  $pp$  collision data at  $\sqrt{s} = 14 \text{ TeV}$ , exceeds the precision achieved in all previous single experiments to date. The LHeC is thus essential to exploit the full potential of the HL-LHC data for this measurement.

**9.1.2. The  $W$ -boson mass.** This section summarises a study describing prospects for the measurement of  $m_W$  with the upgraded ATLAS detector, using low-pile-up data collected during the HL-LHC period [722]. Similar features and performance are expected for the CMS.

Proton–proton collision data at low pile-up are of great interest for  $W$  boson physics, as the low detector occupancy allows an optimal reconstruction of missing transverse momentum, and the  $W$  production cross-section is large enough to achieve small statistical uncertainties in a moderate running time. At  $\sqrt{s} = 14 \text{ TeV}$  and for an instantaneous luminosity of  $\mathcal{L} \sim 5 \times 10^{32} \text{ cm}^{-2} \text{ s}^{-1}$ , corresponding to two collisions per bunch crossing on average at the LHC, about  $\times 10^7$   $W$  boson events can be collected in one month. Such a sample provides a statistical sensitivity at the per-mille level for cross-section measurements, at the percent level for measurements of the  $W$  boson transverse momentum distribution, and of less than  $\pm 4 \text{ MeV}$  for a measurement of the mass of the  $W$ -boson,  $m_W$ .

Additional potential is provided by the upgraded tracking detector, the Inner Tracker (ITk), which extends the coverage in pseudorapidity from  $|\eta| < 2.5$  to  $|\eta| < 4$ . This increased acceptance allows  $W$ -boson measurements to probe a new region in Bjorken  $x$  at  $Q^2 \sim m_W^2$ .

This will, in turn, allow further constraints on the PDFs obtained from cross-section measurements, and reduce PDF uncertainties in the measurement of  $m_W$ . A possible increase in the LHC centre-of-mass energy, such as that offered by the HE-LHC programme with  $\sqrt{s} = 27$  TeV [723], could play a similar role on a longer timescale.

Leptonic  $W$  boson decays are characterised by an energetic, isolated electron or muon, and significant missing transverse momentum which reflects the neutrino. The hadronic recoil,  $u_T$ , is defined by the vector sum of the transverse momenta of all reconstructed particles in the event, excluding the charged lepton, and provides a measure of the  $W$  boson transverse momentum. The lepton transverse momentum  $p_T^\ell$ , the missing transverse momentum  $E_T^{\text{miss}}$ , and the hadronic recoil are related through  $\vec{E}_T^{\text{miss}} = -(\vec{p}_T^\ell + \vec{u}_T)$ . The  $p_T^\ell$  and  $E_T^{\text{miss}}$  distributions have sharp peaks at  $p_T^\ell \sim E_T^{\text{miss}} \sim m_W/2$ . The transverse mass  $m_T$ , defined as  $m_T = \sqrt{2p_T^\ell E_T^{\text{miss}} \cos(\phi_\ell - \phi_{\text{miss}})}$ , peaks at  $m_T \sim m_W$ .

Events are selected by applying the following cuts to the reconstructed final state observables:

- $p_T^\ell > 25$  GeV,  $E_T^{\text{miss}} > 25$  GeV,  $m_T > 50$  GeV, and  $u_T < 15$  GeV;
- $|\eta_\ell| < 2.4$  or  $2.4 < |\eta_\ell| < 4$ .

The first set of cuts selects the range of the kinematic peaks of the  $W$  boson decay products, restricting it to the region of small  $p_T^W$  to maximise the sensitivity of the distributions to  $m_W$ . Two pseudorapidity ranges are considered, corresponding to the central region accessible with the current ATLAS detector, and to the forward region accessible in the electron channel with the ITk.

The  $W$ -boson mass is determined by comparing the final-state kinematic peaks in the simulation to those observed in the data, and adjusting the value of  $m_W$  assumed in the former to optimise the agreement. The shift in the measured value of  $m_W$  resulting from a change in the assumed PDF set is estimated using a set of template distributions obtained for different values of  $m_W$  and a given reference PDF set, and the ‘pseudo-data’ distributions obtained for an alternate set representing, for example, uncertainty variations with respect to the reference set. The PDF uncertainty for a given set is calculated by summing the shifts obtained for all uncertainty variations in quadrature.

The PDF uncertainty is calculated for the CT14 [720], MMHT2014 [719], HL-LHC [258] and LHeC [54] PDF sets and their associated uncertainties. Compared to current sets, such as CT14 and MMHT2014, the HL-LHC set incorporates the constraints expected from present and future LHC data; it starts from the PDF4LHC convention [254] and is provided for three scenarios, corresponding to more or less optimistic projections of the experimental uncertainties.

The expected statistical and PDF uncertainties are illustrated in table 21 and figure 131. The CT10 and CT14 sets yield comparable uncertainties. The MMHT2014 uncertainties are about 30% lower. The three projected HL-LHC PDF sets give very similar uncertainties; scenario 2 is the most conservative and is shown here. Compared to CT10 and CT14, a reduction in PDF uncertainty of about a factor of two is obtained in this case.

The LHeC sample can be collected in about three years, synchronously with the HL-LHC operation. In this configuration, the neutral- and charged-current DIS samples are sufficient to disentangle the generation ( $u, d$ ) and second-generation ( $s, c$ ) parton densities without ambiguity, and reduce the PDF uncertainty to less than 2 MeV—an improvement by a factor of five to six, compared to present knowledge. In this case the  $m_W$  measurement will also benefit from

**Table 21.** Measurement uncertainty of the  $W$ -boson mass at the HL-LHC for different PDF sets (CT14, HL-LHC PDF, and LHeC PDF) and lepton acceptance regions in comparison with a measurement by ATLAS [439]. The HL-LHC projections are obtained from a combined fit to the simulated  $p_T^\ell$  and  $m_T$  distributions.

Parameter	Unit	ATLAS (reference [439])		HL-LHC projection		
		CT10	CT14	HL-LHC	LHeC	LHeC
Centre-of-mass energy, $\sqrt{s}$	TeV	7	14	14	14	14
Int. luminosity, $\mathcal{L}$	$\text{fb}^{-1}$	5	1	1	1	1
Acceptance		$ \eta  < 2.4$	$ \eta  < 2.4$	$ \eta  < 2.4$	$ \eta  < 2.4$	$ \eta  < 4$
Statistical uncert.	MeV	$\pm 7$	$\pm 5$	$\pm 4.5$	$\pm 4.5$	$\pm 3.7$
PDF uncert.	MeV	$\pm 9$	$\pm 12$	$\pm 5.8$	$\pm 2.2$	$\pm 1.6$
Other syst. uncert.	MeV	$\pm 13$	—	—	—	—
Total uncert. $\Delta m_W$	MeV	$\pm 19$	13	7.3	5.0	4.1

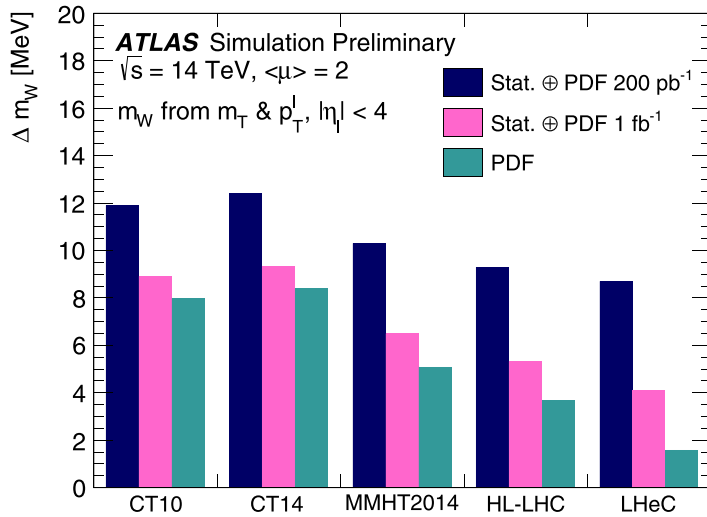


**Figure 131.** Measurement uncertainty of  $m_W$  at the HL-LHC with  $200 \text{ pb}^{-1}$  (dark blue) and  $1 \text{ fb}^{-1}$  (pink) of collected low-pile-up data for a selection of current and future PDF sets. Reproduced from [722]. CC BY 4.0. The green area indicates the PDF uncertainty from those sets alone. The projections are obtained from a combined fit to the simulated  $p_T^\ell$  and  $m_T$  distributions for the acceptance  $|\eta| < 4$ .

the large  $W$  boson samples collected at the LHC, and from the combination of the central and forward categories. In this context, PDF uncertainties become sub-leading, even with  $1 \text{ fb}^{-1}$  of low-pile-up LHC data.

**9.1.3. Impact on electroweak precision tests.** The theoretical expressions for the electroweak parameters discussed above are functions of the other fundamental constants of the theory. In

the SM, an approximate expression for  $m_W$ , valid at one loop for  $m_H > m_W$ , is [444]

$$m_W^2 = \frac{m_Z^2}{2} \left( 1 + \sqrt{1 - \frac{\sqrt{8\pi}\alpha_{em}}{G_F m_Z^2} \frac{1}{1 - \Delta r}} \right), \quad (9.5)$$

$$\Delta r = \Delta\alpha_{em} - \frac{\cos^2 \theta_W}{\sin^2 \theta_W} \Delta\rho, \quad (9.6)$$

$$\Delta\rho = \frac{3G_F m_W^2}{8\sqrt{2}\pi^2} \left[ \frac{m_{\text{top}}^2}{m_W^2} - \frac{\sin^2 \theta_W}{\cos^2 \theta_W} \left( \ln \frac{m_H^2}{m_W^2} - \frac{5}{6} \right) + \dots \right]. \quad (9.7)$$

Here,  $\Delta r$  includes all radiative corrections to  $m_W$ ,  $\Delta\alpha_{em}$  is the difference between the electromagnetic coupling constant evaluated at  $q^2 = 0$  and  $q^2 = m_Z^2$ , and  $\Delta\rho$  is the quantum correction to the tree-level relation  $\rho \equiv m_W^2/(m_Z^2 \cos^2 \theta_W) = 1$ , defined as  $\rho = 1 + \Delta\rho$ .

Similarly, approximate one-loop expressions for the vector and axial-vector couplings between the  $Z$  boson and the fermions,  $g_V$  and  $g_A$ , are

$$g_V = \sqrt{1 + \Delta\rho} (T_3 - 2Q(1 + \Delta\kappa)\sin^2 \theta_W), \quad (9.8)$$

$$g_A = \sqrt{1 + \Delta\rho} T_3, \quad (9.9)$$

where

$$\Delta\kappa = \frac{3G_F m_W^2}{8\sqrt{2}\pi^2} \left[ \frac{\cos^2 \theta_W}{\sin^2 \theta_W} \frac{m_{\text{top}}^2}{m_W^2} - \frac{10}{9} \left( \ln \frac{m_H^2}{m_W^2} - \frac{5}{6} \right) + \dots \right]. \quad (9.10)$$

At two loops, the strong coupling constant also appears.

A large class of theories beyond the SM predicts particles that contribute to the  $W$ - and  $Z$ -boson self-energies, modifying the above expressions. From the point of view of on-shell observables of the  $W$  and  $Z$ , these modifications are usually parameterized using the so-called oblique parameters,  $S$ ,  $T$ , and  $U$  [724]. Their values are, by definition, zero in the SM and, for example, a significant violation of the relation between  $m_W$ ,  $m_H$ , and  $m_{\text{top}}$  would translate into non-zero values of  $S$  and  $T$ .

A typical application of this formalism consists of using the measured properties of the  $W$  and  $Z$  bosons, the top quark mass, and the values of coupling constants to derive an indirect determination of the Higgs boson mass in the SM and compare the latter to the measured value. Beyond the SM, the measured values can be used to derive allowed contours in the  $(S, T)$  plane.

The current and future measurement uncertainties for the most relevant electroweak parameters are summarised in table 22, and are used to evaluate the impact of the improved measurements on electroweak precision tests. Specifically, we consider the effect of the improved measurements of  $m_W$  and  $\sin^2 \theta_{\text{eff}}^{\ell}$  discussed in this chapter, and of the improved precision of  $\alpha_s$  discussed in section 4. In addition, we examine an ultimate precision of 300 MeV for the top quark mass measured at the LHC.

The results are illustrated in figures 132 and 133. The former results from a fit performed using the GFitter framework [441], and compares the indirect determinations of the Higgs boson mass for the present and expected measurement precisions. The indirect uncertainty in  $m_H$  is reduced from about 20% to 10%.

Figure 133 was produced using HEPfit [725], and compares allowed contours for the  $S$  and  $T$  parameters. Here also, the allowed region is reduced by a factor of about two by the improved

**Table 22.** Current uncertainties for the relevant EW precision observables [136, 183, 444], and their expected precision in the LHeC and HL-LHC era.

Parameter	Unit	Value	Uncertainty	
			Present	Expected
$m_Z$	MeV	91 187.6	2.1	2.1
$m_W$	MeV	80 385	15	5
$\sin^2 \theta_{\text{eff}}^\ell$		0.231 52	0.000 16	0.000 08
$m_{\text{top}}$	GeV	173.1	0.7	0.3
$\alpha_s(M_Z)$		0.1179	0.0010	0.0001

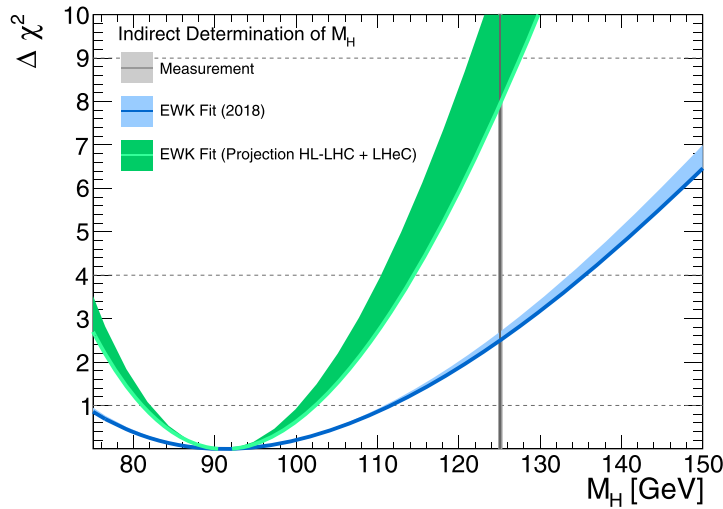


**Figure 132.** Comparisons of  $\chi^2$  distributions for different Higgs boson mass values, using current and future experimental uncertainties. The theoretical uncertainties are indicated by the filled areas. The Gfitter program [441] was used for this analysis.

measurements of  $m_W$ ,  $\sin^2 \theta_{\text{eff}}^\ell$ ,  $m_{\text{top}}$ , and  $\alpha_s$ . Improved theoretical calculations in the SM will provide an additional reduction of 10%–15%.

In summary, the LHeC data promise significant improvements in the measurement precision of fundamental electroweak parameters such as  $m_W$  and  $\sin^2 \theta_{\text{eff}}^\ell$ . The improved measurements enhance the sensitivity of electroweak tests by a factor of two or more.

## 9.2. Higgs physics

**9.2.1. Impact of LHeC data on Higgs cross-section predictions at the LHC.** A detailed analysis of Higgs boson production cross-sections was given in the report on Higgs physics at the HL-LHC and the HE-LHC [726]. Central values at  $\sqrt{s} = 14$  TeV and the corresponding uncertainties are reported in table 23. Perturbative uncertainties (labelled  $\Delta\sigma_{\text{scales}}$  in table 23) generally dominate, compared to the contributions of  $\alpha_s$  and the PDFs. This is especially true for gluon fusion, for which the residual theoretical uncertainties correspond to missing corrections beyond the N<sup>3</sup>LO in QCD, and for  $t\bar{t}H$  production, which is known to the NLO QCD and EW accuracies. The weak boson fusion,  $WH$  and  $ZH$  cross-sections are known to the NNLO

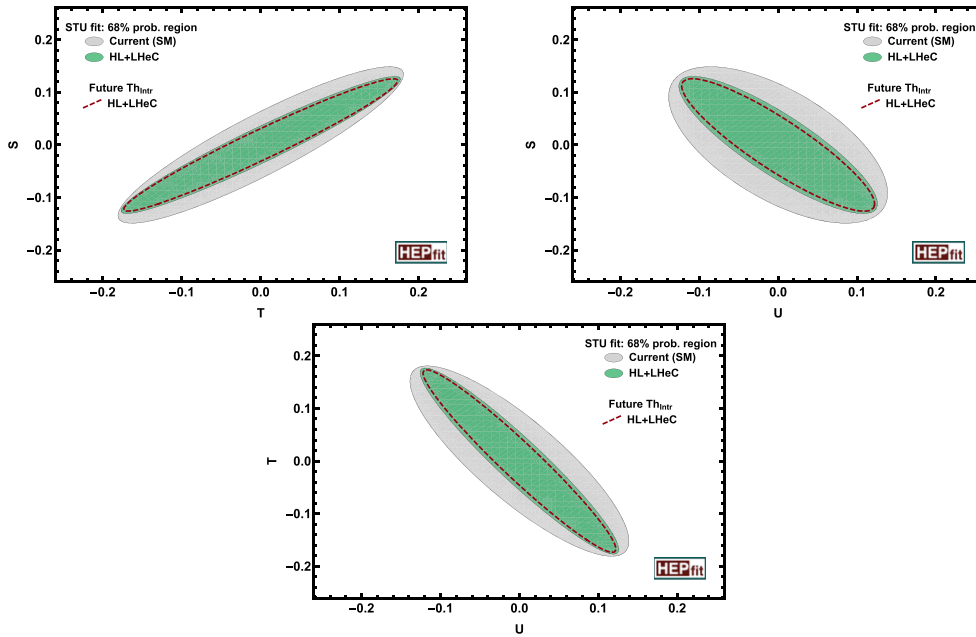


**Figure 133.** Allowed regions in the  $(S, T, U)$  plane showing all three combinations:  $S$  vs  $T$  (top left),  $S$  vs  $U$  (top right),  $T$  vs  $U$  (bottom). The grey and green areas indicate the current allowed region and the LHeC projection, respectively. The dashed line indicates the effect of expected theoretical improvements. The HEPfit programme [725] was used for this analysis.

**Table 23.** Predictions for Higgs boson production cross-sections at the HL-LHC at  $\sqrt{s} = 14$  TeV and their associated relative uncertainties from scale variations and two PDF projections, namely, the HL-LHC and LHeC PDFs,  $\Delta\sigma$ . The PDF uncertainties include uncertainties of  $\alpha_s$ .

Process	$\sigma_H$ (pb)	$\Delta\sigma_{\text{scales}}$	$\Delta\sigma_{\text{PDF}+\alpha_s}$	
			HL-LHC PDF	LHeC PDF
Gluon fusion	54.7	5.4%	3.1%	0.4%
Vector-boson fusion	4.3	2.1%	0.4%	0.3%
$pp \rightarrow WH$	1.5	0.5%	1.4%	0.2%
$pp \rightarrow ZH$	1.0	3.5%	1.9%	0.3%
$pp \rightarrow t\bar{t}H$	0.6	7.5%	3.5%	0.4%

QCD and NLO EW accuracies; the residual theoretical uncertainties are smaller for these weak interaction processes.

In reference [726],  $\alpha_s$ -related uncertainties are propagated assuming  $\alpha_s = 0.118 \pm 0.0015$ , and the assumed PDF uncertainties reflect the HL-LHC prospects [258]. They are in excess of 3% for gluon fusion and  $t\bar{t}H$ , less than 2% for  $WH$  and  $ZH$ , and 0.4% for weak boson fusion. The LHeC uncertainties in table 23 are calculated using the MCFM program [727] and interfaced to PDFs determined from LHeC pseudodata as described in section 3. Assuming the prospects



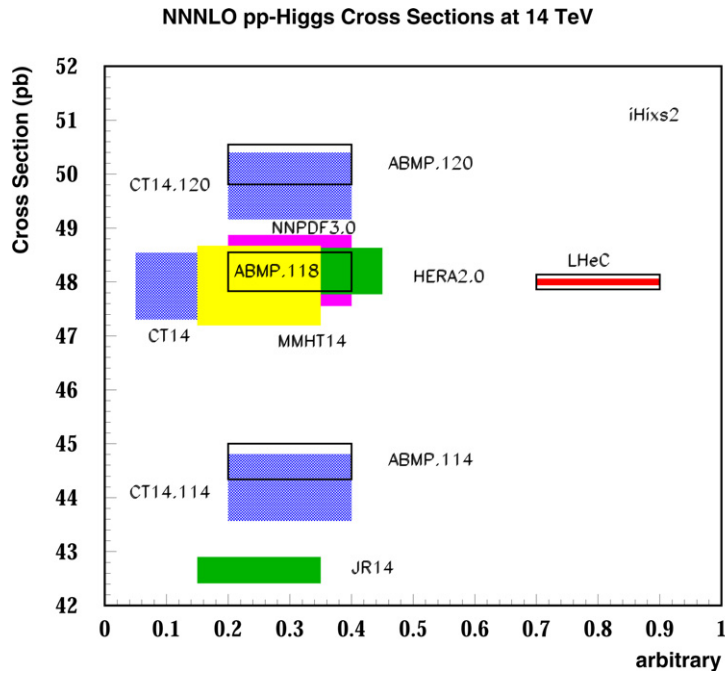


**Figure 134.** Cross-sections of Higgs production calculated to the  $N^3$ LO using the iHix program [729] for existing PDF parameterisation sets (left side) and for the LHeC PDFs (right side). The widths of the areas correspond to the uncertainties quoted by the various sets, having rescaled the CT14 uncertainties from a CL of 90 to a CL of 68%. Results (left) are also included for various values of the strong coupling constant  $\alpha_s(M_Z^2)$  in the range from 0.114 to 0.120. The inner LHeC uncertainty band (red) includes the expected systematic uncertainty due to the PDFs, while the outer box illustrates the expected uncertainty resulting from the determination of  $\alpha_s$  with the LHeC.

**Table 24.** Results of the combined HL-LHC and LHeC  $\kappa$  fit. The output of the fit is compared with the results of the HL-LHC and LHeC stand-alone fits. The uncertainties of the  $\kappa$  values are given in per cent.

Parameter	Uncertainty		
	HL-LHC	LHeC	HL-LHC and LHeC
$\kappa_W$	1.7	0.75	0.50
$\kappa_Z$	1.5	1.2	0.82
$\kappa_g$	2.3	3.6	1.6
$\kappa_\gamma$	1.9	7.6	1.4
$\kappa_{Z\gamma}$	10	—	10
$\kappa_c$	—	4.1	3.6
$\kappa_t$	3.3	—	3.1
$\kappa_b$	3.6	2.1	1.1
$\kappa_\mu$	4.6	—	4.4
$\kappa_\tau$	1.9	3.3	1.3

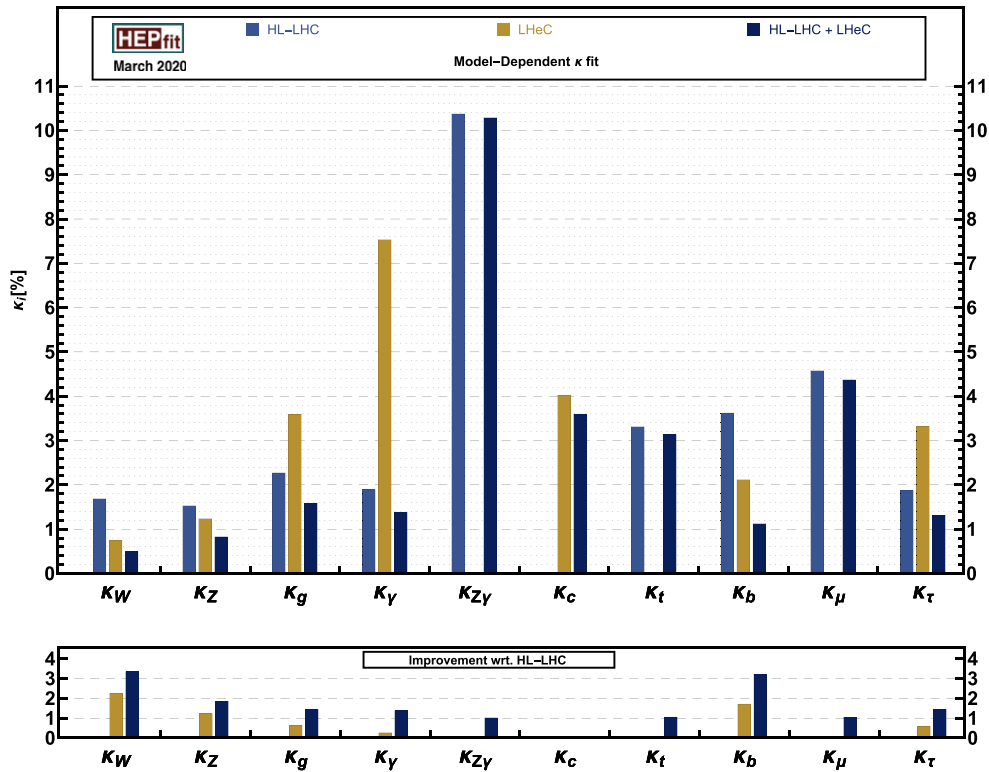


**Figure 135.** Top: uncertainty of the determination of the scale factor  $\kappa$  in the determination of the Higgs couplings, in per cent. Results are given for the combined HL-LHC and LHeC  $\kappa$  fit (dark blue) and for the HL-LHC (blue) and LHeC (gold) stand-alone fits. No accurate measurement of  $\kappa_c$  is expected at the LHC. Likewise, the precision of the rare channels  $Z\gamma$ ,  $t\bar{t}$  and  $\mu\mu$  will be very limited at the LHeC. Bottom: improvement of the  $\kappa$  determinations through the addition of the  $ep$  information (gold) and by the combined  $ep$  and  $pp$  analysis (dark blue), calculated with respect to the HL-LHC prospects. Strong improvements are seen for the  $W$ ,  $Z$ , and  $b$  couplings, while that for charm cannot be illustrated here, as  $\kappa_c$  is considered to be unmeasurable at the HL-LHC.

for  $\alpha_s$  and PDFs described in sections 3 and 4, and with the exception of weak-boson fusion production, the corresponding uncertainties decrease by a factor of between five and ten.

The important, beneficial role of  $ep$  PDF information for LHC Higgs physics can also be illustrated using the predictions for the total cross-section,  $pp \rightarrow HX$ , at the LHC. These have recently been calculated [728] to the  $N^3$ LO pQCD. Figure 134 shows calculations of this cross-section for several recent sets of parton distributions, including the LHeC set, calculated with the iHix code [729].

The effect of these improvements on Higgs boson coupling determination at the HL-LHC is, at present, modest, due to the combined effect of still-significant perturbative uncertainties and the expected experimental systematic uncertainties. The influence of the LHeC on these measurements is further discussed in the next section.

**9.2.2. Higgs couplings from a simultaneous analysis of  $pp$  and  $ep$  collision data.** The LHC data collected during Runs I and II have provided a first exploration of the properties of the Higgs boson. The so-called  $\kappa$  framework [730]—which allows modifications of the SM-like

couplings of the Higgs boson to each SM particle  $i$ , parameterised by coupling modifiers  $\kappa_i$ —has been widely used for the interpretation of these measurements. With current data, the  $\kappa$  parameters associated with the main couplings of the Higgs can be determined to a precision of roughly 10%–20%, see e.g. [731].<sup>191</sup> This knowledge will be further improved during the high-luminosity phase of the LHC, in many cases reaching a precision that is well below the 10% level [726]. Even at the HL-LHC it will, however, be difficult to obtain sensible measurements of certain Higgs interactions, especially the coupling to charm quarks. Such a gap will be covered by the precise measurements of that channel at the LHeC, as described in section 7. Channels measured to a few percent accuracy at both the HL-LHC and the LHeC will provide important cross-checks and additional physics information because of the different dominant Higgs production mechanisms,  $gg \rightarrow H$  in  $pp$  and  $WW \rightarrow H$  in  $ep$ . As a result, there is a remarkable complementarity between the measurements made by both machines and a joint precision comparable to that available at the ILC or the CLIC [732], which offers the important possibility of determining the total cross-section through the  $e^+e^- \rightarrow Z^* \rightarrow ZH$  reaction. Furthermore, as also explained in section 7, the LHeC environment will allow very precise determinations of certain interactions, well beyond those which will be possible at the high-luminosity  $pp$  collider. In this subsection, we briefly describe the complementarity between the Higgs measurements at the  $pp$  and  $ep$  colliders, illustrated via a combined fit to the HL-LHC and LHeC projections in the  $\kappa$  framework.

For a detailed description of the Higgs physics programme at the LHeC, we refer to section 7. The only information not included in the fit presented in this section is that of the determination of the top Yukawa coupling, since the projections made by that study are performed by assuming that any coupling other than  $\kappa_t$  is SM-like. Comments in this regard will be made, when necessary, below.

For the HL-LHC inputs of the combined fit we rely on the projections presented in reference [726], as used in the comparative study in reference [732]. These HL-LHC inputs include projections for the total rates in the main production ( $ggF$ ,  $VBF$ ,  $VH$ , and  $ttH$ ) and decay channels ( $H \rightarrow bb, \tau\tau, \mu\mu, ZZ^*, WW^*, \gamma\gamma$ , and  $Z\gamma$ ). They are available for both ATLAS and CMS. Regarding the theoretical systematics in these projections, we assume the scenario S2 described in [726], in which the SM theoretical uncertainties are reduced by roughly a factor of two with respect to their current values, a reduction to which LHeC would contribute by eliminating the PDF and  $\alpha_s$  parts of the uncertainty, see figure 134. Theoretical systematics are assumed to be fully correlated between ATLAS and CMS. These projections are combined with the LHeC projections, for which, as in reference [732], we use future projections for the SM theoretical uncertainties in the different production cross-sections and decay widths. In the  $\kappa$  fit performed here we assume: (1) no Higgs decays into particles other than the SM ones; (2) heavy particles are allowed to modify the SM loops, so we use effective  $\kappa$  parameters to describe the SM loop-induced processes, i.e. we use  $\kappa_g, \kappa_\gamma$ , and  $\kappa_{Z\gamma}$  as free parameters. The total list of free parameters considered for this combined HL-LHC and LHeC  $\kappa$  fit is, therefore,

$$\{\kappa_b, \kappa_t, \kappa_\tau, \kappa_c, \kappa_\mu, \kappa_Z, \kappa_W, \kappa_g, \kappa_\gamma, \text{ and } \kappa_{Z\gamma}\}, \quad (9.11)$$

for a total of ten degrees of freedom. The coupling modifiers associated with any other SM particles are assumed to be SM-like,  $\kappa_i = 1$ .

<sup>191</sup> Note that, at the LHC, one can only determine coupling ratios.

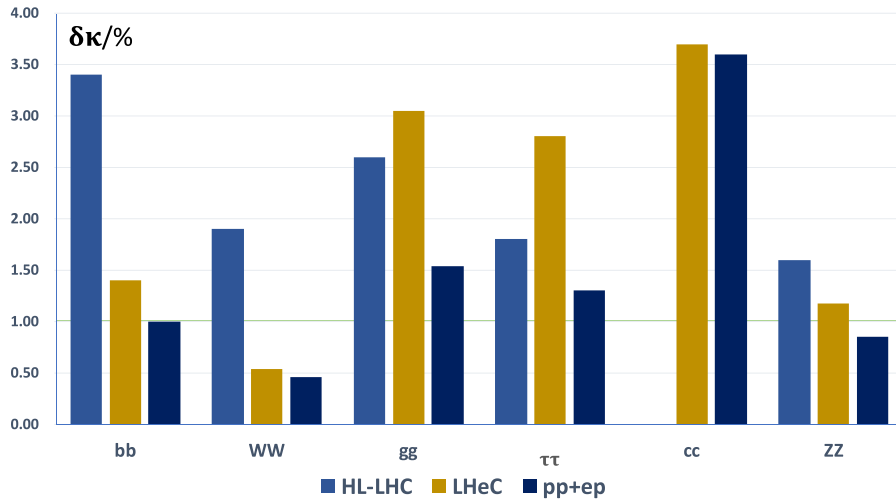


**Figure 136.** Uncertainty of the determination of the scale factor  $\kappa$  in the determination of the Higgs couplings, in per cent. Magnification of figure 135 to show the six most frequent H decay channels. Results are given for the combined HL-LHC and LHeC  $\kappa$  fit (dark blue) and for the HL-LHC (blue) and LHeC (gold) stand-alone fits. No accurate measurement of  $\kappa_c$  is expected at the LHC.

The results of the combined HL-LHC and LHeC fit, which was performed using the HEPfit code [725], are shown in table 24, figure 135, and its magnified version, figure 136.<sup>192</sup> The increment in constraining power after the LHeC measurements are added is especially apparent for the couplings to the  $W$  bosons and  $b$  quarks, making an improvement of a factor of  $\simeq 3$  with respect to the HL-LHC results. As explained at the beginning of this section, the LHeC measurements also create the possibility of setting sensible constraints on the Higgs interactions with charm quarks, with a precision of roughly 4%. The HL-LHC measurements, in turn, fill in some of the *gaps* in the fit at the LHeC, where there is little sensitivity to the couplings involved in rare Higgs decays, e.g.  $H \rightarrow \mu\mu$  and  $H \rightarrow Z\gamma$ . This manifests the complementarity between the measurements at  $ep$  and  $pp$  machines, in which the former lead in terms of precision in the largest Higgs couplings, while the high luminosity of the latter offers sensitivity to the smaller interactions.

Finally, as mentioned at the beginning, we did not include the projections for top Yukawa interactions at the LHeC from section 7.5 in this combined  $ep$  and  $pp$  fit, as these were not derived in a global setup, but instead assumed that all other interactions involved in  $\bar{t}H\nu_e$  production take their SM values. However, the main uncertainty introduced by the other  $\kappa$  parameters is expected to originate from the  $W$  and  $b$  couplings,  $\kappa_W$  and  $\kappa_b$ , which are determined with overall precisions of  $\sim 0.8\%$  and  $2\%$ . Therefore, one expects the LHeC result,  $\delta\kappa_t \sim 17\%$  for  $L = 1 \text{ ab}^{-1}$ , to be minimally affected. This number should be compared with the HL-LHC projection of  $\sim 4\%$ , which is expected to dominate in a combined result.

<sup>192</sup>The  $\kappa$  analysis of the LHeC has been performed independently using an MINUIT-based fit programme, leading to perfect agreement with the HEPfit result.

### 9.3. Further precision SM measurements at the HL-LHC

The LHeC measurements and the results of their phenomenological interpretations will have an important impact on many areas of the HL-LHC physics programme. This goes far beyond the precision electroweak and Higgs physics, as discussed in the dedicated analyses of the previous sections, and BSM or  $eA$  physics, as discussed in the subsequent sections. In this section, a few further selected topics of the SM physics programmes at the LHC and HL-LHC are discussed, in which substantial improvements can be expected due to the LHeC. For such improvements, two distinct aspects can be generally considered for any SM measurement:

- Improvements of the analysis of the recorded event data, and
- Improvements of the phenomenological interpretation of the measurements.

In order to assess the impact of the LHeC for the first point, one must recollect that an essential key ingredient of the analysis of any hadron collider data is the utilisation of phenomenological models; QCD-inspired MC event generators are commonly employed. These are used for calibration, corrections of limited acceptance and resolution effects (*unfolding*), training of machine-learning algorithms for event or object classification, extrapolations from the *fiducial* to the *full* phase space, estimates of different background sources, and also signal extraction. Although the implemented models are derived from more fundamental equations, such as the QCD Lagrangian, a number of model parameters remain poorly known and have to be *tuned* using data. Also, since most models involve approximations and may be numerically limited, any model naturally needs to be validated (or invalidated) using independent measurements prior to its use. As more and more data are recorded at the (HL-)LHC, statistical uncertainties become very small and systematic uncertainties are reduced due to improved calibration and analysis algorithms, so that uncertainties associated with the MC event models become important and limit the accuracy of the HL-LHC measurements. It should be noted that the MC parameters should be tuned using data from another experiment in order to avoid a potential bias of the actual measurement due to experimental correlations.

For the second point, the phenomenological interpretation of hadron collider measurements, such as tests of pQCD or the determination of SM parameters (e.g.  $\alpha_s(M_Z)$ ,  $\sin^2 \theta_{\text{eff}}^\ell$ ,  $m_W$ , the  $\kappa$  parameters, . . . ), the proton PDFs and SM parameters that constitute the inputs to the prediction must be known with high accuracy, most notably, the value of  $\alpha_s(M_Z)$ .

The most important inputs of the LHeC to the HL-LHC measurements are, of course, the precise determination of the PDFs and  $\alpha_s(M_Z)$ ; see section 3. These will improve both the data analysis and its interpretation. Beyond that, measurements of charged particle spectra, jet shape and jet substructure observables, jet cross-sections, and HF cross-sections will help to improve MC models further, for instance, by determining charm and bottom-quark masses, improving heavy quark ( $c$ ,  $b$ ) fragmentation functions finding optimal choices for all scales involved in the MC simulation, and deriving the optimal parameters for the generation of parton showers. Such measurements can be performed with high precision at the LHeC, since DIS represents a superior QCD laboratory. This is because there is always a lepton in the final state, which is used for triggering and vertexing, and simultaneously, there is a hadronic system, which is then the subject of interest. In addition, the overconstrained kinematic system allows for the precise calibration of hadronic final-state objects, limiting effects, such as minimum bias definition or pile-up, are absent.

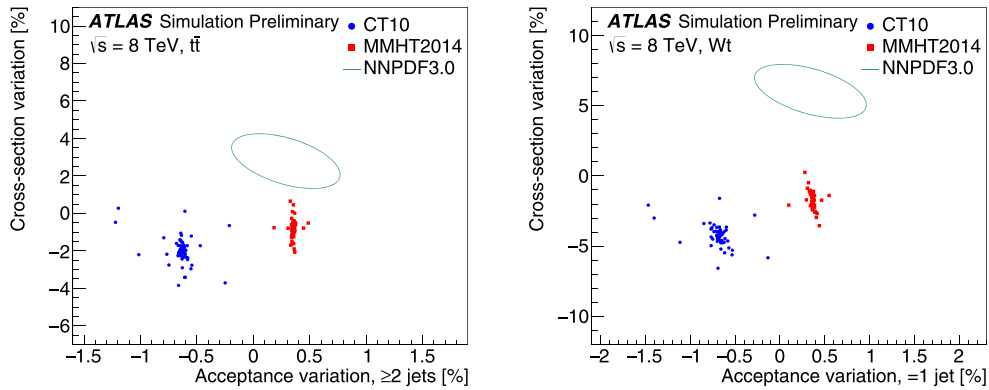


**Figure 137.** Impact of PDF uncertainty from CT10 and MMHT2014 eigenvectors or NNPDF3.0 replicas on the cross-section and the acceptance correction for top pair production  $t\bar{t}$  (left) and single top production  $Wt$  (right). Reproduced from [733]. CC BY 4.0. Events are selected with at least two jets or with exactly one jet, respectively. Depending on the PDF set and eigenvector employed, the cross-sections vary by up to 5%–7% for top-pair production and by more than 10% for single-top production. In addition, the acceptance correction varies by about 0.5%–1% for different PDF sets, and can become as large as 2.5% for different PDF sets and eigenvectors. Since the acceptance correction has to be imposed on the measurement, limited knowledge of the PDFs introduces a sizeable modelling uncertainty into the measurement.

In the following, a few selected subjects are discussed in terms of LHC analyses performed at centre-of-mass energies of  $\sqrt{s} = 8$  or 13 TeV, which thus give a tangible indication of the challenges for future HL-LHC measurements:

- The measurement of the integrated top-quark pair cross-section represents an outstanding benchmark quantity for the entire field of top-quark physics. Its measurement for top-transverse momenta  $p_T > 400$  GeV in the lepton+jets decay channel yields a high experimental precision with both small statistical and systematic uncertainties. However, its measurement precision is limited by theoretical uncertainties (also called *modelling* uncertainties), the largest individual source of which stems from the PDFs [183, 734]. A related study of PDF effects on the acceptance correction for the integrated top-pair production cross-section and single-top production  $Wt$  is displayed in figure 137. The acceptance correction changes by up to 0.5%–1% for different PDF sets, and can become as large as 2.5% for different PDF sets and eigenvectors. Another very important uncertainty in top-quark measurements originates from the modelling of the parton shower. Both the PDF and parton-shower modelling uncertainties are expected to be significantly reduced by the LHeC data.
- The determination of the top-quark mass  $m_t$  from the LHC data requires precise modelling of all top production signal and background processes with suitable MC models. This allows, at present, a determination of the value of  $m_t$  with uncertainties of 0.4–0.8 GeV [183, 735–739] for different analyses of top production and decay channels. Any of these individual precision determinations are limited by model uncertainties, and therefore improvements at the HL-LHC cannot be obtained with more data, but only with improved models. It is expected that some of the model uncertainties, e.g. PDF, parton-shower, and hadronization- or fragmentation-related uncertainties can be reduced using LHeC data.



- At the HL-LHC, rare decay channels can also be exploited for precision measurements. For example, the top-quark mass can be determined from top-quark pair production using a subsequent decay, in which a  $b$  quark hadronises into a  $B$  hadron, which then decays through a  $J/\psi$ -meson into a pair of muons,  $t\bar{t} \rightarrow W^+bW^-b \rightarrow \ell\nu_\ell J/\psi (\rightarrow \mu^+\mu^-) X_{qq'b}$  [740]. Such a measurement requires the precise knowledge of  $b$ -quark fragmentation, which can be measured well at the LHeC, and will thus improve the HL-LHC measurement.
- The value of the strong coupling constant  $\alpha_s(M_Z)$  is one of the least-known fundamental parameters in physics and an improved determination of this constant by new measurements constitutes a real challenge for LHC and HL-LHC experiments. A large number of observables at the LHC are *per-se* sensitive to  $\alpha_s(M_Z)$ , and its value was determined in the past from various definitions of jet cross-section observables (see e.g. [158, 159, 741, 742]) or transverse energy–energy correlations [743], combined  $Z$  and jet cross-sections [744], integrated [745] or differential top-quark cross-sections [746], inclusive  $W$  or  $Z$  production [747, 748], prompt photon data [749], and many other observables (see reference [183] for a review). Although the harsh environment in high-luminosity hadron–hadron collisions requires sophisticated analysis techniques and dedicated measurements, small experimental uncertainties could be achieved for  $\alpha_s(M_Z)$ . Hence,  $\alpha_s$  determinations are nowadays limited by theoretical uncertainties, and the dominant uncertainties are most commonly PDF related [744, 745, 747, 748] (with the exception that for observables where NNLO predictions are not yet applicable, the scale uncertainties may exceed the PDF uncertainties). Therefore, even today, knowledge of the PDFs already represents the limiting factor, and a significant reduction of the total uncertainty for  $\alpha_s(M_Z)$  can (only) be achieved using PDFs determined at the LHeC.
- The production of  $W^\pm Z$  pairs in  $pp$  collisions provides a crucial test of the electroweak sector of the SM, since di-boson production is sensitive to gauge-boson self-interactions. Small deviations in the observed distributions can already provide indications of new physics. This process can be accurately measured in a high-pile-up environment and can be clearly separated from its huge QCD background. However, due to the relatively small  $W^\pm Z$  cross-sections, high statistical precision can only be achieved with high luminosity. Recent measurements of  $W^\pm Z$  pairs at  $\sqrt{s} = 13$  TeV based on  $36 \text{ fb}^{-1}$  of integrated luminosity have been performed by ATLAS and CMS [752, 753]. Figure 138 displays the ratio of fiducial cross-sections  $\sigma_{W^+Z}/\sigma_{W^-Z}$ . The largest individual uncertainty is the statistical uncertainty and therefore future measurements at the LHC and HL-LHC are of great importance in order to reach higher precision. Nonetheless, even today, the overall phenomenological interpretation is limited by PDF uncertainties, as can be seen in figure 138, and these can best be improved by PDFs from the LHeC.

In the situation of the absence of indications for new physics, important goal of the future LHC and HL-LHC physics programme has to be devoted to precision measurements. From the examples discussed above ( $W$ -boson mass and Higgs measurements are discussed in previous sections), it is obvious that the limiting factors of such measurements arise from the signal and MC modelling, in which PDF uncertainties constitute a limiting factor, and an improved understanding of parton showers, hadronization, and fragmentation processes is also of importance. These aspects can all be ameliorated with independent precision measurements at the LHeC.

Similarly, the phenomenological interpretation of many processes is today already limited by PDF uncertainties, and as outlined,  $\alpha_s$  determinations, di-boson processes, top mass or top

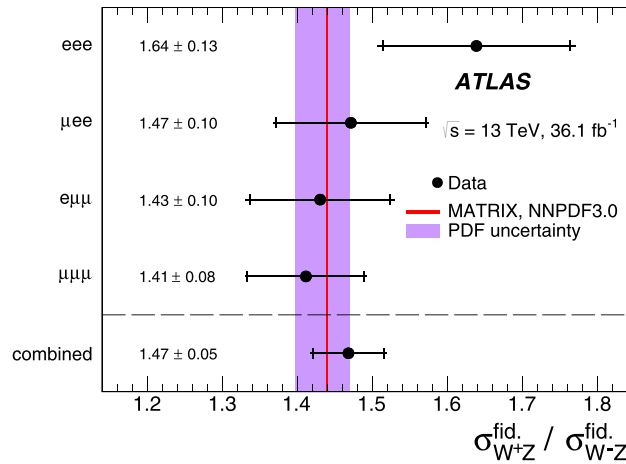


**Figure 138.** Measurement of the ratio of di-boson  $\sigma(W^+Z)/\sigma(W^-Z)$  integrated cross-sections in a fiducial phase space for four different decay channels and their combination at  $\sqrt{s} = 13$  TeV in comparison with the NNLO predictions [750, 751]. Reproduced from [752]. CC BY 4.0. The total uncertainties of the data points are dominated by statistical uncertainties that will be reduced in the future. The shaded violet band indicates the size of the PDF uncertainties that limit the overall interpretation of the measurement.

cross-section measurements, and many other topics, require higher-precision PDFs. In the HL-LHC era, for which data and predictions are more precise, detailed knowledge of the PDFs will become of even greater importance.

#### 9.4. High-mass searches at the LHC

**9.4.1. Supersymmetric particles produced by the strong interaction.** The potential of the HL- and HE-LHC to discover supersymmetry was extensively discussed in reference [754]. Here, we focus on searches for gluinos within MSSM scenarios. Gluino pairs are produced through the strong interaction, and their production cross-section is relatively large; naturalness considerations indicate that gluino masses should not exceed a few TeV and lie not too far above the EW scale. Hence, they are certainly among the first particles that could be discovered at the HL-LHC.

In the following, we assume that a simplified topology dominates the gluino decay chain, culminating in jets plus missing energy originating from a massless LSP,  $\tilde{\chi}_0$ . Reference [754] evaluated the sensitivity of the HL- and HE-LHC to gluino pair production, in which gluinos decay exclusively to  $q\bar{q}\tilde{\chi}_0$ , through off-shell first- and second-generation squarks, using a standard search for events with jets and missing transverse energy. Currently, the reach of this simplified model with  $36 \text{ fb}^{-1}$  of 13 TeV data is roughly 2 TeV gluinos, for a massless LSP [755, 756]. Through extrapolation to  $3 \text{ ab}^{-1}$  at 14 TeV, the limit can be increased to 3.2 TeV. For  $15 \text{ ab}^{-1}$  at 27 TeV, a limit of 5.7 TeV is found.

When deriving limits, an overall systematic uncertainty of 20% is assumed for the SM background contributions, and a generic 10% uncertainty is assumed for signal normalisation, without taking into account the PDF-related uncertainties, which are as large as 50% for gluinos of around 3 TeV. The effect of this additional source of uncertainty was found to induce a variation in the mass limit of  $\pm 200$  GeV at the HL-LHC, and as much as  $\pm 500$  GeV at the HE-LHC.

**Table 25.** CI limits from ATLAS based on  $36 \text{ fb}^{-1}$  of data [708], and extrapolated to the full HL-LHC dataset ( $3 \text{ ab}^{-1}$ ). The extrapolation is performed based on the assumption of the same PDF and  $\alpha_s$  uncertainties as in reference [708], and also assuming the improved uncertainties obtained from the LHeC.

Model	ATLAS (reference [708])	HL-LHC	
	$\mathcal{L} = 36 \text{ fb}^{-1}$ (CT14nnlo)	$\mathcal{L} = 3 \text{ ab}^{-1}$ (CT14nnlo)	$\mathcal{L} = 3 \text{ ab}^{-1}$ (LHeC)
LL (constr.)	28 TeV	58 TeV	96 TeV
LL (destr.)	21 TeV	49 TeV	77 TeV
RR (constr.)	26 TeV	58 TeV	84 TeV
RR (destr.)	22 TeV	61 TeV	75 TeV
LR (constr.)	26 TeV	49 TeV	81 TeV
LR (destr.)	22 TeV	45 TeV	62 TeV

We can invert this argument, and claim that with present PDF knowledge, mass limits could be as low as 3.0 TeV and 5.3 TeV at the HL- and HE-LHC, respectively. Data from the LHeC would make this contribution negligible compared to other sources of uncertainty. Compared to the most conservative scenario, the increase in sensitivity would correspond to an increase in the centre-of-mass energy of approximately 5%–10%.

**9.4.2. Contact interactions.** New, high-mass gauge bosons are most often sought in resonant final states. Peaks in the invariant-mass distributions of electron, muon, or jet pairs directly reflect the presence of such new particles; the accessible mass range is limited by the available centre-of-mass energy.

Particles with a mass beyond the kinematic limit generally interfere with the  $Z$  boson and the photon, generating non-resonant deviations in the invariant mass distributions. Such models can be parameterised as CI between two initial-state quarks and two final-state leptons of given chirality:

$$\mathcal{L}_{\text{CI}} = \frac{g^2}{\Lambda^2} \eta_{ij} (\bar{q}_i \gamma_\mu q_i) (\bar{\ell}_i \gamma^\mu \ell_i), \quad (9.12)$$

where  $i, j = \text{L or R}$  (for left- or right-handed chirality),  $g$  is a coupling constant set to  $4\pi$  by convention, and  $\Lambda$  is the CI scale. The sign of  $\eta_{ij}$  determines whether the interference between the SM DY process,  $q\bar{q} \rightarrow Z/\gamma^* \rightarrow \ell^+\ell^-$ , is constructive or destructive.

The size and sign of the observed deviation with respect to the SM probes the scale and interference pattern of the interaction. The sensitivity of the search is limited by experimental uncertainties (finite statistics and experimental systematic uncertainties) and by uncertainties in the theoretical modelling of the DY background.

The most recent results of the ATLAS and CMS collaborations [708, 709] are based on  $e^+e^-$  and  $\mu^+\mu^-$  final states in  $36 \text{ fb}^{-1}$  of data, and probe CIs up to a typical scale of 25 TeV, depending on the chirality and sign of the interaction's coupling parameter. The limits derived by ATLAS, summarised in table 25, accounted for theoretical uncertainties induced by the PDFs and by  $\alpha_s$ . The dominant PDF uncertainty was estimated from the 90% CL uncertainty in the CT14nnlo PDF set, with an added envelope from a comparison of the CT14nnlo, MMHT2014, and NNPDF3.0 [757] central sets. The strong coupling constant uncertainty was propagated using the assumption  $\alpha_s = 0.118 \pm 0.003$ , with a subleading effect.

This study evaluates the sensitivity of this search at the HL-LHC. The increase in sensitivity is estimated using samples of SM-like pseudo-data, corresponding to an integrated luminosity

of  $3 \text{ ab}^{-1}$ . In a first step, both the experimental and theoretical systematic uncertainties are kept in the publication. In this regime, the extrapolated statistical uncertainty is typically smaller than the theoretical uncertainty by a factor of five to ten. Improvements from the LHeC in  $\alpha_s$  and in the proton PDFs are incorporated in a second step. Assuming the prospects described in section 3, the  $\alpha_s$  and PDF uncertainties are smaller than the statistical fluctuations and can be neglected to a first approximation.

The results are summarised in table 25. Everything else being equal, increasing the sample size from  $36 \text{ fb}^{-1}$  to  $3 \text{ ab}^{-1}$  typically enhances the CI reach by a factor of two. Accounting for the improvement in the theoretical modelling of the DY process due to the LHeC adds another factor of 1.5–1.8 to the limits. In the latter case, the limits reach well into the range directly accessible with proton–proton collisions at  $\sqrt{s} = 100 \text{ TeV}$ , as envisioned at the FCC-hh.

### 9.5. PDFs, the HL-LHC, and the LHeC

As discussed in the previous sections, a precise determination of PDFs is an essential ingredient for the success of the HL-LHC. Conversely, the HL-LHC itself offers a significant opportunity to improve our understanding of proton structure. In this section we will discuss the possibilities that the combination of HL-LHC and LHeC measurements offers for the determination of PDFs in the proton.

**9.5.1. PDF prospects of the HL-LHC and the LHeC.** In reference [258] the potential of the HL-LHC to constrain PDFs was analysed in detail, focussing on SM processes that are expected to have the most impact at higher  $x$ . In particular, projections for the production of top quark pairs, inclusive jets, forward  $W$  and charm quark and direct photons, as well as forward and high-mass DY and the  $Z$  boson  $p_{\perp}$  distribution were included. It was found that PDF uncertainties for LHC processes can be reduced by a factor of between two and five, depending on the specific flavour combination and on optimistic assumptions about the reduction of the (experimental) systematic uncertainties.

It is of interest to compare these constraints with those expected to come from the LHeC itself, as well as potential improvements from a combined PDF fit to the HL-LHC and LHeC datasets; this was studied in [59]. The basic procedure consists of generating HL-LHC and LHeC pseudodata using the PDF4LHC15 set [254] and then applying Hessian PDF profiling [256, 758]; in other words, a simplified version of a full refit to this baseline, in order to assess the expected impact of the data. While the HL-LHC datasets are described above, the LHeC pseudodata correspond to the most recent publicly available official LHeC projections (see section 3.2) for electron and positron NC and CC scattering. As well as inclusive data at different beam energies ( $E_p = 1, 7 \text{ TeV}$ ), charm and bottom heavy-quark NC and charm production in  $e^-p$  CC scattering are included.

The expected impact of the HL-LHC, the LHeC, and their combination on the PDF uncertainties of the gluon, down quark, anti-up quark, and strangeness distributions are shown in figure 139. One can observe that at low  $x$ , the LHeC data generally impose by far the strongest constraint, in particular for the gluon, as expected from its greatly extended coverage at small  $x$ . At intermediate  $x$ , the impact of the HL-LHC and LHeC are more comparable in size, but nonetheless, the LHeC is generally expected to have the larger impact. At higher  $x$ , the constraints are again comparable in size; the HL-LHC offers a somewhat larger reduction in the gluon and strangeness uncertainty, while the LHeC has a somewhat larger impact on the down and anti-up quark distributions. Thus, the combination of both HL-LHC and LHeC pseudodata nicely illustrates a clear and significant reduction in PDF uncertainties over a very wide range of  $x$ , improving upon the constraints from the individual datasets in a non-negligible way.

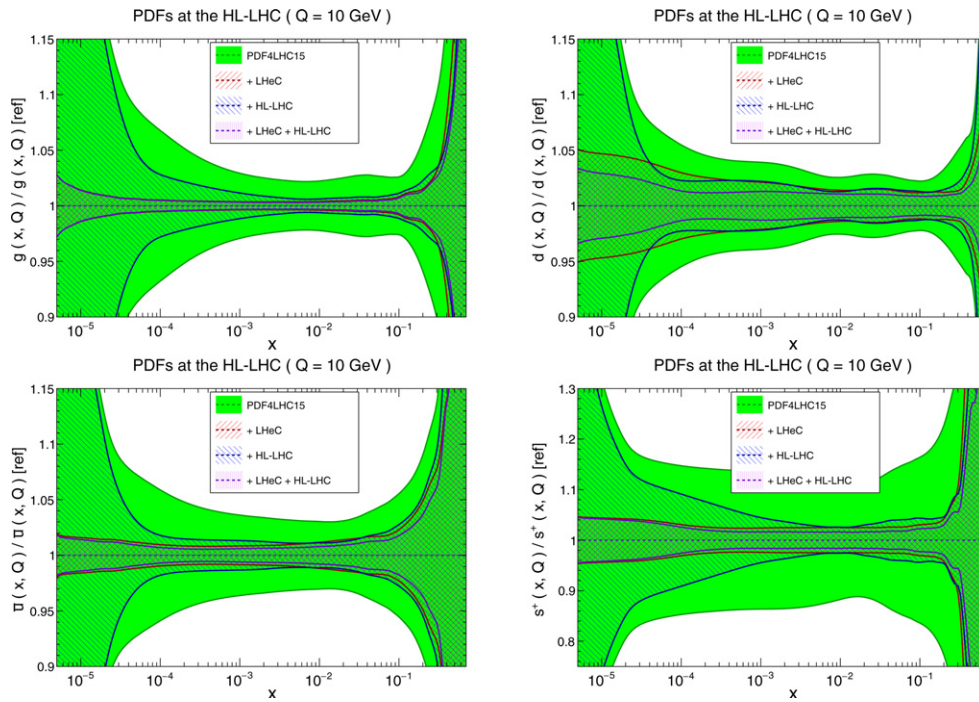


**Figure 139.** Impact of LHeC on the  $1\text{-}\sigma$  relative PDF uncertainties of the gluon, down quark, anti-up quark, and strangeness distributions with respect to the PDF4LHC15 baseline set (green band). Results are shown for the LHeC (red), the HL-LHC (blue), and their combination (violet). Reproduced from [59]. [CC BY 4.0](#).

**9.5.2. Parton luminosities at the HL-LHC.** In figure 140 we show the impact on the gluon–gluon, quark–gluon, quark–antiquark, and quark–quark partonic luminosities for a centre-of-mass energy of  $\sqrt{s} = 14$  TeV. Some clear trends are evident from this comparison, which are consistent with the results of the individual PDFs. We can, in particular, observe that at low masses, the LHeC imposes the dominant constraint, while at intermediate masses, the LHeC and HL-LHC constraints are comparable in size, and at high masses, the stronger constraint on the gluon–gluon and quark–gluon luminosities originates from the HL-LHC, while the LHeC dominates for the quark–quark and quark–antiquark luminosities. As in the case of the PDFs, for the partonic luminosities, the combination of the HL-LHC and LHeC constraints leads to a clear reduction in the PDF uncertainties in comparison to the individual cases, by up to an order of magnitude over a wide range of invariant masses,  $M_X$ , of the produced final state.

In summary, these results demonstrate that while the HL-LHC alone is expected to have a sizeable impact on PDF constraints, by comparison, the LHeC can significantly improve on our current PDF precision, particularly at low to intermediate  $x$ . Moreover, the combination of both the LHeC and the HL-LHC pseudodata leads to a significantly superior PDF error reduction in comparison to the two facilities individually. Further details, including LHeC-only studies, as well as an investigation of the impact of the PDF baseline on the uncertainty projections, can be found in reference [59].

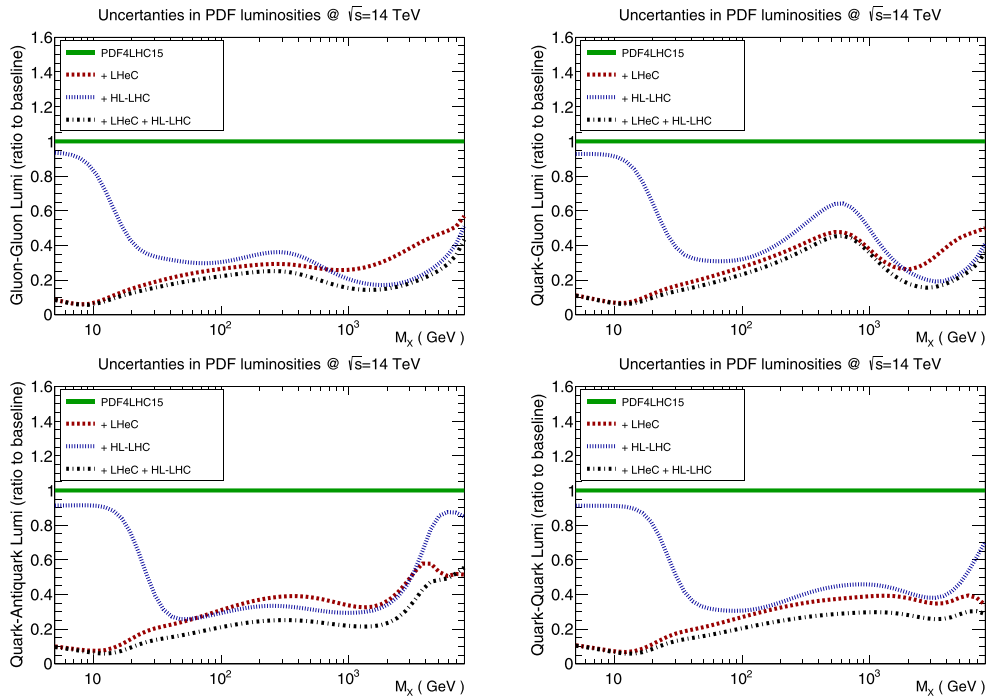


**Figure 140.** Impact of LHeC, HL-LHC and combined LHeC and HL-LHC pseudodata on the uncertainties of the gluon–gluon, quark–gluon, quark–antiquark, and quark–quark luminosities with respect to the PDF4LHC15 baseline set. In this comparison we display the relative reduction of the PDF uncertainty in the luminosities, compared to the baseline. Reproduced from [59]. [CC BY 4.0](#).

**9.5.3. PDF sensitivity: comparing the HL-LHC and the LHeC.** While the experimental reach of each facility in the  $\{x, Q^2\}$  kinematic plane provides a useful comparison, there are more factors to consider—especially when we are striving for ultra-high-precision measurements. One measure that provides a dimension beyond the  $\{x, Q^2\}$  plane is the *sensitivity*; this is a combination of the correlation coefficient multiplied by a scaled residual [759, 760]. This provides an extra dimension of information in comparison to a simple  $\{x, Q^2\}$  map and represents a measure of the impact of the data.

In figure 141 this PDF sensitivity for a sample PDF flavour is displayed for the LHeC and the HL-LHC pseudo-data. In particular, one may observe that the LHeC provides strong sensitivity in the high- $x$  region, which is of great importance for BSM searches, and also in the low- $x$  region, which is relevant for QCD phenomena such as saturation. The HL-LHC provides constraints that originate from  $W/Z$  production ( $Q \sim M_{W/Z}$ ) as well as from jets at high scales. The combination of these measurements will provide the strongest constraints on the various PDF flavours across the broad  $\{x, Q^2\}$  kinematic plane.

## 9.6. Impact of new small- $x$ dynamics on hadron collider physics

As discussed in subsections 4.2.1 and 4.2.3, the presence of new dynamics at small  $x$ , as claimed in references [248, 252, 253], will have an impact on hadronic observables. This impact is stronger for larger energies, and is therefore more important for the FCC-hh than for the LHC. However, it may compete with other uncertainties and thus become crucial for



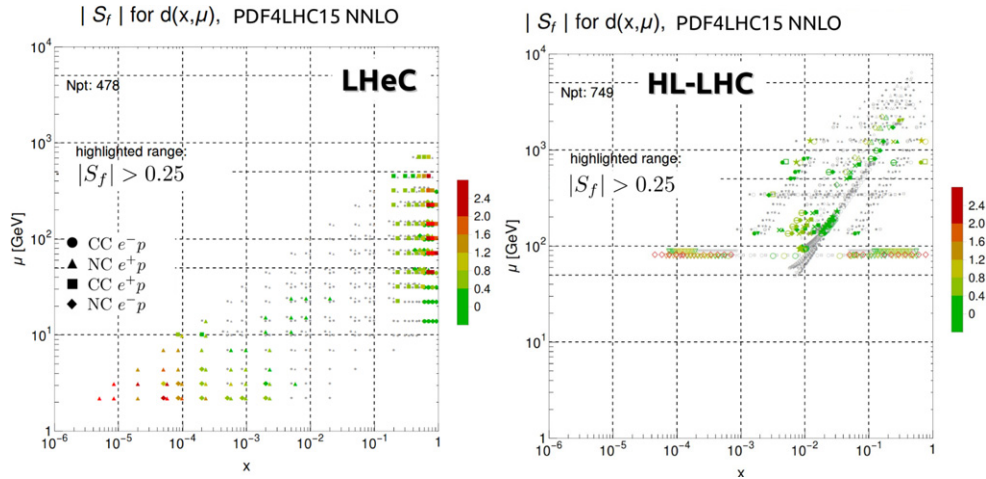


**Figure 141.** Sensitivity for a sample flavour  $\{d(x, Q)\}$  in the  $\{x, Q^2\}$  kinematic plane for the LHeC (left) and the HL-LHC (right) calculated using pseudodata. Reproduced from [760]. **CC BY 4.0.** As can be observed, the LHeC is particularly sensitive in both the high- and low- $x$  regions, and the HL-LHC covers the intermediate  $x$  region out to large  $Q$  scales.

precision studies, even at LHC energies. Studies of the impact of nonlinear dynamics at hadron colliders have mainly been devoted to photoproduction in UPCs; see e.g. [761–763] and references therein for the case of gauge boson production. In this section we focus on the effect of resummation at small  $x$ .

While hadronic data such as jet, DY, or top production at existing energies do not have much constraining power at low  $x$  [248] and thus need not be included in the extraction of PDFs using resummed theoretical predictions, this fact does not automatically mean that the impact of resummation is invisible at large scales for large energies. Indeed, the PDFs obtained using small- $x$  resummation may change at low energies in the region of  $x$  that is relevant for hadronic data, thereby also causing an effect at higher energies after evolving to those scales. A consistent inclusion of resummation effects on hadronic observables is thus crucial for achieving precision. The difficulty of implementing resummation for different observables lies in the fact that not only should evolution equations include it, but also the computation of the relevant matrix elements for the observable must be performed with matching accuracy.

Until present, the only observable that has been examined in detail is Higgs production cross section through gluon fusion [764]. Other observables, such as DY [765] or heavy quark [766] production, are being studied and will become available in the near future.

For  $gg \rightarrow H$ , the LL resummation of the matrix elements matched to fixed order at the N3LO was performed in references [273, 764] and the results are shown in figures 142 and 143. Figure 142 shows the increasing impact of resummation on the cross-section with increasing energy. It also illustrates the fact that the main effect of resummation originates from the modification of the extraction of parton densities and their extrapolation, not through the modification of the matrix elements or the details of the matching.

Figure 143 indicates the sizes of the different uncertainties for the absolute values of the cross-section with increasing accuracies of the perturbative expansion, at HL-LHC and FCC-hh energies. For the combined N3LO and LL it can be seen that, at the HL-LHC, the effect of resummation is of the same order as other uncertainties (such as those originated by scale



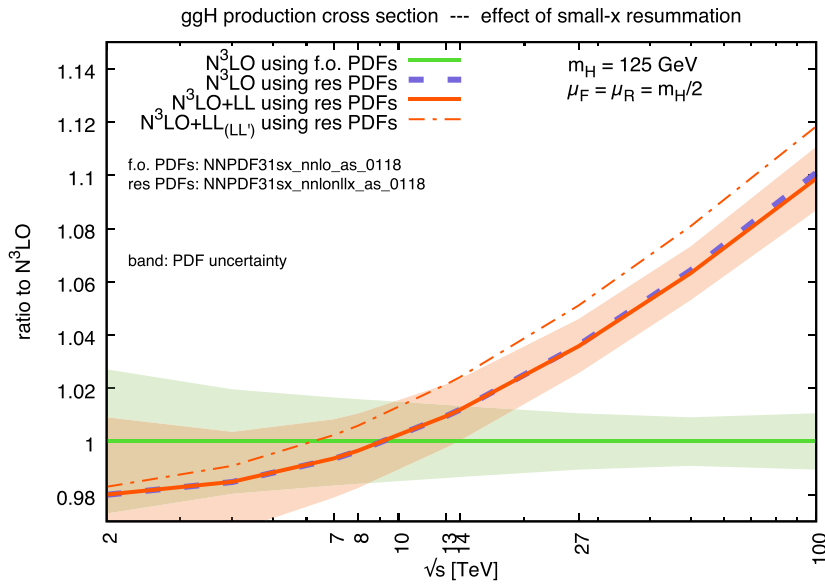


**Figure 142.** Ratio of the N3LO Higgs cross-section, with and without resummation, to the N3LO fixed-order cross-section, as a function of the collider’s centre-of-mass energy; ‘f.o.’ denotes fixed order, ‘res’ denotes resummed, and ‘LL’ denotes a different anomalous dimension match at the leading logarithmic accuracy; see the legend on the plot and reference [764] for details. The PDFs used are from the global dataset of reference [252]. Reproduced from [764]. [CC BY 4.0](#).

variations, PDFs, and subleading logarithms), but this is not the case for the FCC, where it can clearly be seen that the effect of resummation will dominate. Resummation should also strongly affect the rapidity distributions, a key requirement for extrapolating from the observed to the total cross-sections. In particular, the rapidity distributions are more directly sensitive to PDFs at given values of the momentum fraction  $x$ ; therefore, in regions where this momentum fraction is small (large rapidities), the effect of resummation may also be sizeable at lower collider energies. These facts underline the need to understand the dynamics at small  $x$  for any kind of precision physics measurements at future hadronic colliders, with increasing importance for increasing energies.

Finally, it should be mentioned that a different kind of factorisation, called transverse momentum (TMD) factorisation [39, 510, 767–770], may have an effect on large-scale observables in hadronic colliders. The extension of the TMD evolution equations towards small  $x$  [771] and the relation of such factorisation to new dynamics at small  $x$ , either through high-energy factorisation [772–775], or with the CGC [506, 507], is under development [776].

### 9.7. Heavy ion physics with eA input

The study of hadronic proton–proton, proton–nucleus, and nucleus–nucleus collisions at the RHIC and the LHC has produced several observations of crucial importance for our understanding of QCD in complex systems involving a large number of partons [777, 778]. The different stages of a heavy ion collision, as we presently picture it, are schematically drawn in figure 144.

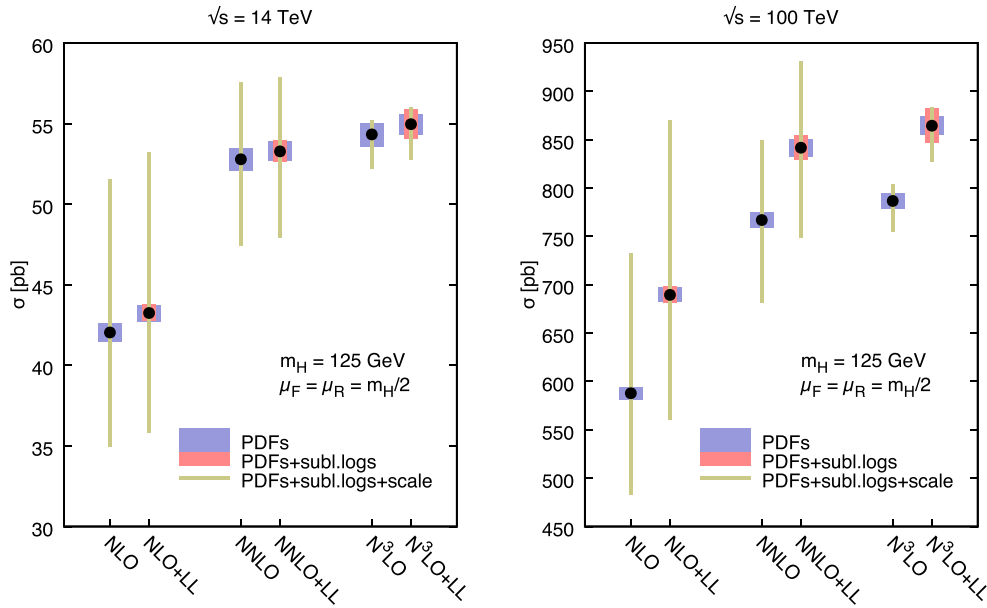


**Figure 143.** Perturbative progression of the Higgs cross-section for two collider energies  $\sqrt{s} = 14$  TeV (left) and 100 TeV (right). TeV. The NLO, combined NLO and LL, NNLO, combined NNLO and LL, N<sup>3</sup>LO, and combined N<sup>3</sup>LO and LL results are shown in each plot. The results are supplemented by uncertainty bands from PDFs, subleading logarithms, and scale uncertainties. Reproduced from [764]. CC BY 4.0.

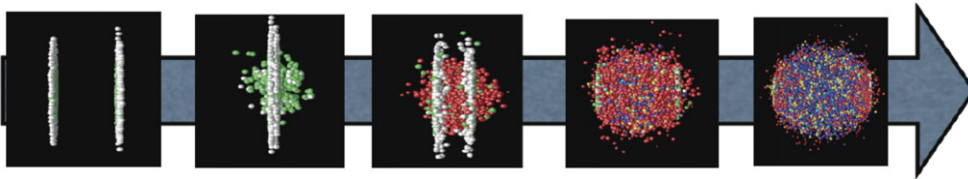


**Figure 144.** Sketch of a heavy ion collision with time running from left to right, starting with the approach of two ultrarelativistic Lorentz-contracted nuclei, the collision and parton creation in the central rapidity region, the beginning of expansion and formation of the QGP, the expansion of the QGP until hadronisation, and, finally, the expansion of the hadronic gas.

First, the hot and dense partonic medium created in heavy ion collisions, the quark–gluon plasma (QGP), exhibits a collective behaviour, in which azimuthal asymmetries and transverse spectra with a specific ordering of particle masses are the most prominent observables. This collectivity can be very well described by relativistic hydrodynamics [779]. For this description, the system has to undergo some dynamics leading to rough isotropisation in a short time,  $\lesssim 1$  fm/c, for which both strong and weak coupling explanations have been proposed [558].

Second, collisions between smaller systems,  $pp$  and  $pA$ , show many of the features [555–557] that are taken as indicative of the production of a dense hot partonic medium in heavy ion collisions. The most celebrated of such features, the long-rapidity-range particle

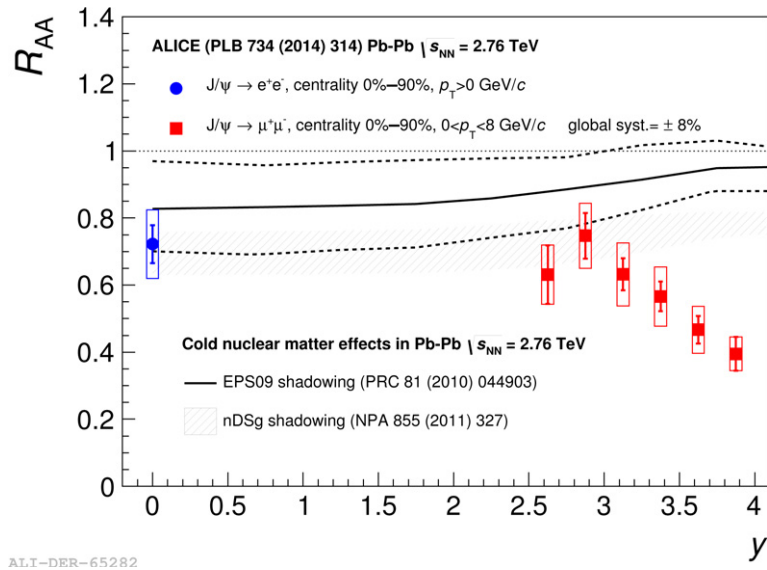


**Figure 145.** ALICE inclusive  $J/\psi$  nuclear modification factor versus rapidity [784], compared to nPDF calculations. Reproduced from [781]. CC BY 4.0.

correlations collimated in azimuth, named the ridge (see section 6.5), has been found in all collision systems. The dynamics underlying this phenomenon, either the formation of a QGP and the existence of strong final-state interactions, or some initial-state dynamics that leaves an imprint on the final observables, is under discussion [558].

Finally, the QGP is extremely opaque to both highly energetic partons [780] and quarkonia [781] traversing it. These observables, whose production in  $pp$  can be addressed through perturbative methods, are called hard probes [782]. The quantification of the properties of the QGP extracted through hard probes is performed by a comparison with predictions that assume that a nuclear collision is a superposition of collisions among free nucleons. Such predictions contain uncertainties that originate both from nuclear effects other than those in the QGP (known as cold nuclear matter effects), and from uncertainties in the dynamics that determine the interaction between the energetic parton or bound state and the medium. In the case of partons, this has motivated the development of sophisticated jet studies in heavy ion collisions [783].

$eA$  collisions studied in the energy range relevant to the corresponding hadronic accelerator—the LHeC for the LHC—would substantially improve our knowledge of all these aspects and, indeed, of all stages of the heavy ion collisions depicted in figure 144. Besides, they can significantly reduce the uncertainties in the extracted QGP parameters, which is the central goal of the heavy programme for understanding the different phases of QCD. Here, we provide three examples of such synergies:

- Nuclear parton densities: the current severe lack of precision in the determination of parton densities induces large uncertainties in the understanding of several QGP signatures. For example, the magnitude of  $J/\psi$  suppression at midrapidity at the LHC is compatible with the sole effect of nuclear shadowing on nPDFs [781], see figure 145. While data at lower energies and at forward and backward rapidities make it clear that this is not the only effect at work, only a reduction in the nPDF uncertainty, such as that feasible at the LHeC (see

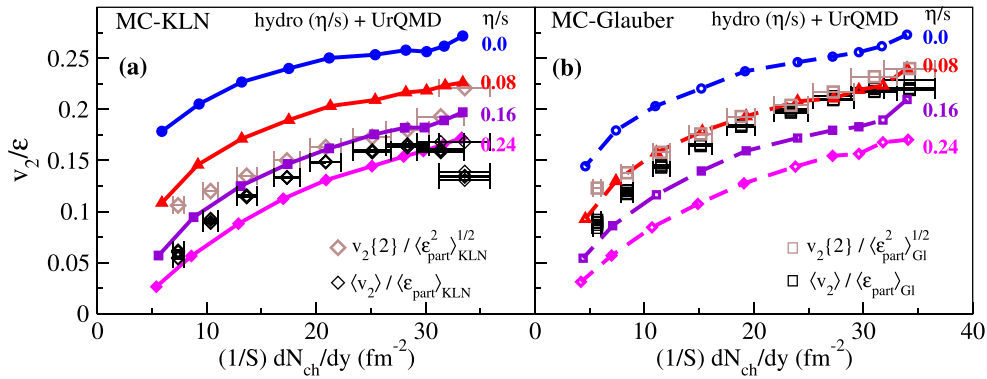


**Figure 146.** Comparison of the universal  $v_2(\eta/s)/\epsilon$  vs  $(1/S)(dN_{ch}/dy)$  curves with experimental data for  $\langle v_2 \rangle$  [789],  $v_2\{2\}$  [790], and  $dN_{ch}/dy$  [791] from the Solenoidal Tracker at RHIC by the STAR Collaboration. The experimental data used in (a) and (b) are identical, but the normalisation factors  $\langle \epsilon_{part} \rangle$  and  $S$  used on the vertical and horizontal axes, as well as the factor  $\langle \epsilon_{part}^2 \rangle^{1/2}$  used to normalize the  $v_2\{2\}$  data, are taken from the MC-Kharzeev-Levin-Nardi (MC-KLN) model in (a) and from the MC-Glauber model in (b). The theoretical curves are from simulations with MC-KLN initial conditions in (a) and with MC-Glauber initial conditions in (b). Reprinted figure with permission from [785], Copyright 2012 by the American Physical Society.

section 6.2), will enable a precise quantification of the different mechanisms causing either suppression (screening, gluon dissociation, energy loss) or enhancement (recombination or coalescence) that play a role for this observable.

- Initial conditions for the collective expansion and the small system problem: at present, the largest uncertainty in the determination of the transport coefficients of the partonic matter created in heavy ion collisions [785, 786] (see figure 146), required in hydrodynamic calculations, and in our understanding of the speed of the approach to isotropisation and of the dynamics prior to it [787], originates from our lack of knowledge of the nuclear wave function and of the mechanism of particle production at small to moderate scales—i.e. the soft and semihard regimes. Both aspects determine the initial conditions for the application of relativistic hydrodynamics. This is even more crucial in the discussion of small systems, for which the details of the transverse structure of protons are key [788] not only to provide such initial conditions, but also to establish the relative role of initial-versus final-state dynamics. For example, the description of azimuthal asymmetries in  $pp$  and  $pPb$  collisions at the LHC demands that the proton is modelled as a collection of constituent quarks or hot spots [779, 788]. At the LHeC,  $ep$  and  $eA$  collisions can constrain both aspects in the pertinent kinematic region; see sections 3.4 and 6.3. Besides, they can clarify the mechanisms of particle production and the possible relevance of initial-state correlations to the final-state observables, as suggested e.g. by CGC calculations (see sections 4.2.1 and 6.4), whose importance for LHC energies can be established at the LHeC.
- Impact on hard probes: besides the improvement in the determination of nPDFs that affects the quantification of hard probes, mentioned above,  $eA$  collisions can help us to understand the dynamics of the probes by analysing the effects of the nuclear medium on them. As two examples, the abundant yields of jets and large transverse momentum particles at the LHeC [1] will allow precise studies of the nuclear effects on jet

observables and of hadronisation inside the nuclear medium. These two aspects are of capital importance, not only in heavy ion collisions, but also in small systems, where the lack of jet modification is the only QGP-like characteristic not observed in  $p$ Pb. On the other hand, measurements of exclusive quarkonium production at the LHeC [1] will provide a better understanding of the cold nuclear matter effects on this probe, on top of which, the effects of the QGP will provide a quantitative characterisation of this new form of QCD matter.

As discussed in section 6.2,  $p$ Pb and PbPb collisions at the LHC offer possibilities for constraining nPDFs through the measurement of EW vector boson production [792], dijets [522],  $D$ -mesons at forward rapidities [533], and exclusive charmonium and dijet photoproduction in UPCs [345, 793, 794]. Specifically, dijets in UPCs could constrain nPDFs to the region  $10^{-3} \lesssim x \lesssim 0.7$  and  $200 \lesssim Q^2 \lesssim 10^4 \text{ GeV}^2$ .  $eA$  collisions would provide more precise nPDFs, whose compatibility with the aforementioned observables would clearly establish the validity of collinear factorisation and the mechanisms of particle production in collisions involving nuclei.

Furthermore,  $eA$  offers another system in which photon–photon collisions, recently measured in UPCs at the LHC [795], can be studied. For example, the observed acoplanarity of the produced muon pairs can be analysed in  $eA$  in order to clarify its possible origin and constrain the parton densities in the photon.

Finally, the possible existence of a new nonlinear regime of QCD—saturation—at small  $x$  is also under study at the LHC, for example, using dijets in the forward rapidity region in  $p$ Pb collisions [796]. As discussed in section 6.5, the ridge phenomenon (two particle correlations peaked at zero and  $\pi$  azimuthal angles and stretched along the full rapidity of the detector) observed in all collision systems,  $pp$ ,  $p$ Pb, and PbPb at the LHC, has been measured in photoproduction by Pb in UPCs at the LHC [559]. For the time being, its existence is scrutinised in smaller systems such as  $e^+e^-$  [560] at the LEP collider and  $ep$  at HERA [561], but the results are inconclusive. These studies are fully complementary to those in  $ep$  and  $eA$ . At the LHeC, a search for the ridge phenomenon at the smallest possible values of  $x$  at the LHeC would be most interesting. For example, the collision of the virtual photon with the proton at the LHeC can be considered as a high-energy collision of two jets or ‘flux tubes’.

In conclusion,  $ep$  and  $eA$  collisions, as studied at the LHeC, will have a large impact on the heavy ion programme, as the comparison of the kinematic reach of DIS and hadronic machines shown in figure 147 makes evident. It should be noted that there are proposals to extend such a programme into Runs 5 and 6 of the LHC [508], by running lighter ions and taking advantage of detector upgrades in ATLAS and CMS (starting already in Run 4), and the LHCb (upgrade II [797] starting in Run 5).

## 10. The electron-energy-recovery linac

We studied different options for the electron accelerator for the LHeC in reference [1], of which the ERL option is retained in this update of the CDR. This is due to the higher achievable luminosity of the linac–ring option, as compared to the ring–ring option, as well as the interference with the LHC’s operation caused by the installation of an electron ring in the LHC tunnel [798]. The clear advantage of the ERL, compared to its contenders in 2012, is the possibility of limiting the overall energy consumption, although, given its baseline configuration and the size of the return arcs, operation is still limited to lepton energies of less than 70 GeV to avoid excessive synchrotron radiation losses.

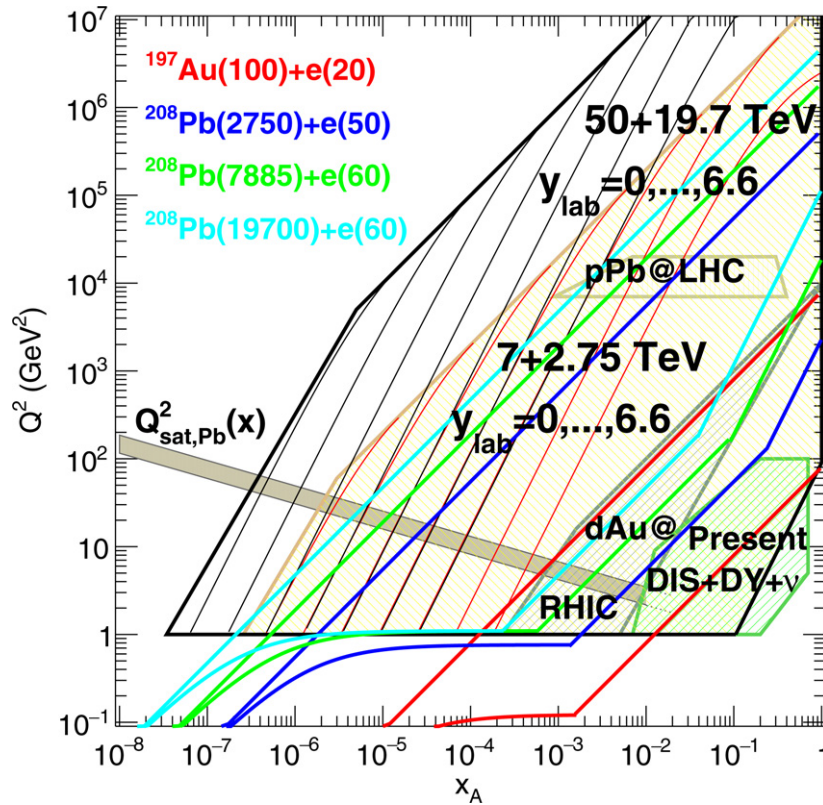


**Figure 147.** Kinematic regions in the  $x$ - $Q^2$  plane explored by data sets (charged lepton and neutrino DIS, DY,  $d$ Au at the RHIC, and  $p$ Pb at the LHC) used in current nPDF analyses [503], compared to those achievable at the EIC (red), the LHeC (ERL against the HL-LHC beams, dark blue), and two FCC-eh options with Pb beams corresponding to proton energies of 20 TeV (green) and 50 TeV (light blue). Acceptance is taken to be  $1^\circ < \theta < 179^\circ$  and  $0.01(0.001) < y < 1$  for the EIC (all other colliders). The areas delimited by thick brown and black lines show the regions accessible by  $p$ Pb collisions at the LHC and the FCC-hh (50 TeV) respectively, while the thin lines represent constant rapidities from 0 (right) to 6.6 (left) for each case. The saturation scale  $Q_{\text{sat}}$ , shown here for indicative purposes only (see also [504]), has been drawn for a Pb nucleus using an uncertainty of  $\sim 2$  and an energy behaviour that follows the model in [505]. Note that it only indicates a region where saturation effects are expected to be important, but there is no sharp transition between the linear and nonlinear regimes.

### 10.1. Introduction – design goals

The main guidelines for the design of the electron ERL and the IR with the LHC are:

- Electron–hadron operation in parallel with high luminosity hadron–hadron collisions in the LHC/HL-LHC;
- Centre-of-mass collision energy on the TeV scale;
- Power consumption of the electron accelerator smaller than 100 MW;
- Peak luminosity approaching  $10^{34} \text{ cm}^{-2} \text{ s}^{-1}$ ;



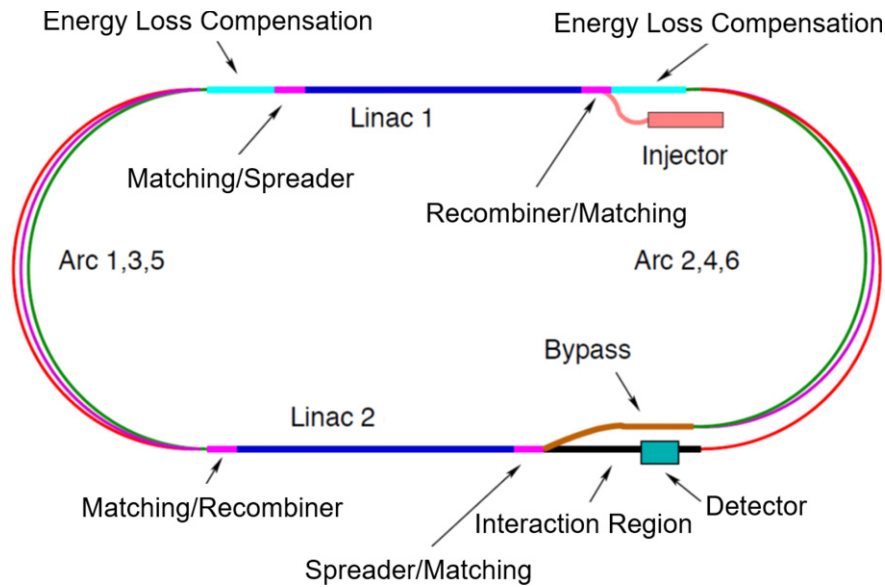


**Figure 148.** Schematic layout of the LHeC design based on an ERL. Reproduced from [1]. © IOP Publishing Ltd. CC BY 3.0.

- Integrated luminosity exceeding that achieved by HERA at DESY by at least two orders of magnitude.

The electron energy  $E_e$  chosen in the previous version of the CDR [1] was 60 GeV. This could be achieved with an ERL circumference of 1/3 of that of the LHC. Cost considerations and machine–detector performance aspects, in particular the amount of synchrotron radiation loss in the IR, have led us to define a new reference configuration with  $E_e = 49.2$  GeV and a circumference of  $\approx 5.4$  km, 1/5 of that of the LHC.

The ERL consists of two SC linacs operated in the continuous-wave (CW) mode, connected by at least three pairs of arcs to allow three accelerating and three decelerating passes (see figure 148). The length of the high-energy return arc following the interaction point should be such as to provide a half-RF-period wavelength shift to allow the deceleration of the beam in the linac structures down to the injection energy and its safe disposal in three passes. SC cavities with an unloaded quality factor  $Q_0$  that exceeds  $10^{10}$  are required in order to minimise the requirements on the cryogenic cooling power and to allow efficient ERL operation. The choice of three accelerating and three decelerating passes implies that the circulating current in the linacs is six times the current colliding with the hadron beam at the IP.

The choice of an ERL offers the advantage of a high-brightness beam and avoids performance limitations due to the beam–beam effect experienced by the electron beam [799], which has been a major performance limitation in many circular lepton colliders (e.g. the LEP collider) and would have been a limitation for the LHeC ring–ring option. The current of the ERL is limited by its source, and an operational goal of  $I_e = 20$  mA has been set, corresponding to a bunch charge of 500 pC at a bunch frequency of 40 MHz. This implies that the SRF cavities will be operated using a very high current of 120 mA for a virtual beam power (product of the beam current at the IP times the maximum beam energy) of 1 GW. The validation of this

**Table 26.** Parameters of LHeC ERL (spr/rec: spreader/recombiner).

Parameter	Unit	Value
Injector energy	GeV	0.5
Total number of linacs		2
Number of acceleration passes		3
Maximum electron energy	GeV	49.19
Bunch charge	pC	499
Bunch spacing	ns	24.95
Electron current	mA	20
Transverse normalized emittance	$\mu\text{m}$	30
Total energy gain per linac	GeV	8.114
Frequency	MHz	801.58
Acceleration gradient	$\text{MV m}^{-1}$	19.73
Cavity iris diameter	mm	130
Number of cells per cavity		5
Cavity length (active/real estate)	m	0.918/1.5
Cavities per cryomodule		4
Cryomodule length	m	7
Length of four-CM unit	m	29.6
Acceleration per cryomodule (four-CM unit)	MeV	289.8
Total number of cryomodules (four-CM units) per linac		112 (28)
Total linac length (with spr/rec matching)	m	828.8 (980.8)
Return arc radius (length)	m	536.4 (1685.1)
Total ERL length	km	5.332

performance, in terms of source brightness and ERL three-turn stable and efficient operation in the PERLE facility [11], is a key milestone for the LHeC design.

A small beam size is required at the IP to maximize luminosity and approach peak luminosities of  $10^{34} \text{ cm}^{-2} \text{ s}^{-1}$  and integrated luminosities of  $1 \text{ ab}^{-1}$  within the LHeC lifetime. In particular,  $\beta^* < 10 \text{ cm}$  needs to be achieved for the colliding proton beam in a manner that is compatible with the optical constraints imposed by the requirement to operate in parallel with proton–proton physics in the other IPs during the HL-LHC era [3]. The peak luminosity values quoted above exceed those at HERA by two to three orders of magnitude. The operation of HERA in its first, extended running period (1992–2000), provided an integrated luminosity of about  $0.1 \text{ fb}^{-1}$  for the H1 and ZEUS experiments, corresponding to the integrated luminosity expected to be collected over one day of LHeC operation.

## 10.2. The ERL configuration of the LHeC

The main parameters of the LHeC ERL are listed in table 26; their choices and optimisation criteria will be discussed in the following sections.

**10.2.1. Baseline design –lattice architecture.** The ERL, as sketched in figure 148, is arranged in a racetrack configuration, hosting two superconducting linacs in the parallel straights and three recirculating arcs on each side. The linacs are 828.8 m long and the arcs have a 536.4 m radius; an additional 76 m is taken up by utilities such as the spreader/recombiner (spr/rec) and matching and energy-loss-compensating sections adjacent to both ends of each linac (a total of 4 sections) [800]. The total length of the racetrack is 5.332 km:  $1/5$  of the LHC circumference  $2 \times (828.8 + 2 \times 76 + 536.4\pi) \text{ m}$ . Each of the two linacs provides an accelerating voltage of 8.114 GV, therefore, a 49.19 GeV energy is achieved in three turns. After the collision with

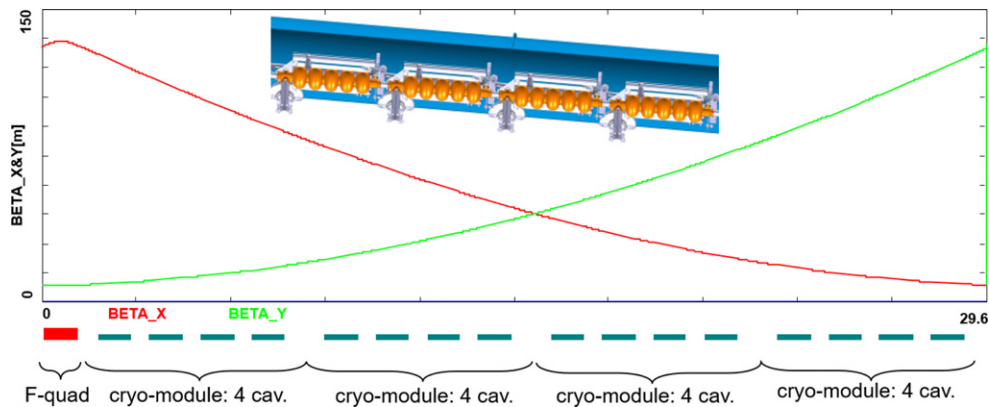


**Figure 149.** Layout of a half-cell composed of four cryomodules (each hosting four five-cell cavities: top insert) and a focussing quad. The beta functions reflect the properties of the Focusing and Defocusing quadrupole structure (a so-called FODO optics).

the protons in the LHC, the beam is decelerated in three subsequent turns. The injection and dump energies chosen are 0.5 GeV.

Injection into the first linac is performed by a fixed field-injection chicane, with its last magnet (closing the chicane) placed at the beginning of the linac. It closes the orbit *bump* at the lowest-energy, injection pass, but the magnet (physically located in the linac) deflects the beam on all subsequent linac passes. In order to close the resulting higher-pass *bumps*, the so-called re-injection chicane is instrumented by the placement of two additional opposing bends in front of the last chicane magnet. The chosen arrangement is such that the re-injection chicane magnets are only *visible* to the higher-pass beams. The second linac in the racetrack is configured as an exact mirror image of the first one, with a replica of the re-injection chicane at its end, which facilitates a fixed-field extraction of the energy-recovered beam to the dump.

**10.2.1.1. Linac configuration and multipass optics** . An appropriate choice of linac optics is of paramount importance for the transverse beam dynamics in a multipass ERL. The focussing profiles along the linac (quadrupole gradients) need to be set (and they stay constant), so that multiple-pass beams within a vast energy range may be transported efficiently. The chosen arrangement is such that adequate transverse focussing is provided for a given linac aperture. The linac optics is configured as a strongly focussing structure, based on  $130^\circ$  FODO cells. In a basic FODO cell a quadrupole is placed every four cryomodules, so that the full cell contains two groups of 16 RF cavities and a pair of quads (F, D) as illustrated in figure 149. The entire linac is built out of 14 such cells. Energy recovery in a racetrack topology explicitly requires that both the accelerating and decelerating beams share the individual return arcs [801]. This, in turn, imposes specific requirements for the Twiss function at the linac ends: the Twiss functions have to be identical for both the accelerating and decelerating linac passes which converge to the same energy and therefore enter the same arc. There is an alternative scheme, proposed by Peter Williams [802], who has argued that it would be beneficial to separate the accelerating and decelerating arcs. This would simplify energy compensation systems and linac-to-arc matching, but at a higher cost of the arc magnetic system. However, doubling the number of arcs is a very costly proposition. On the other hand, the CBETA experiment is pioneering multipass arcs to transport a vast energy range through the same beamline, and it still intends

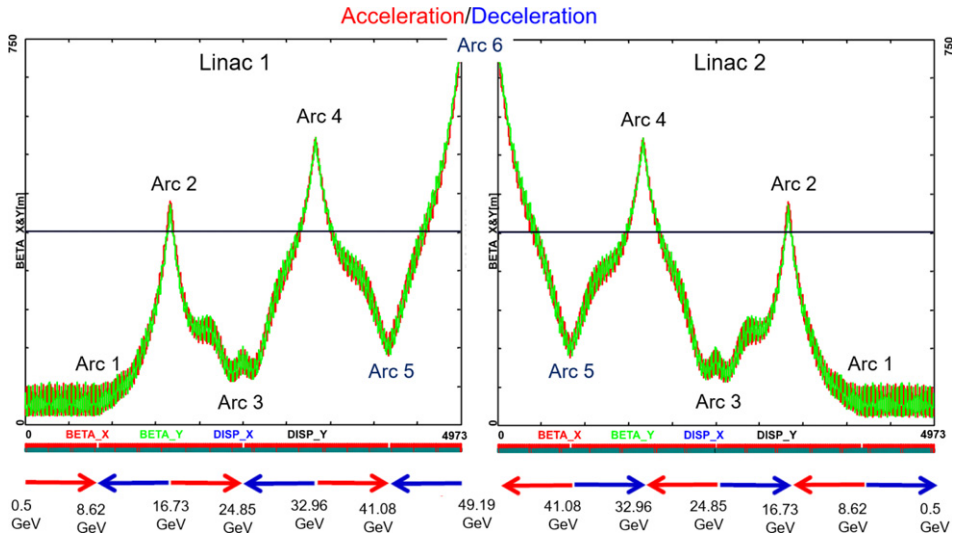


**Figure 150.** Beta function in the optimised multipass linacs (three accelerating passes and three decelerating passes in each of two linacs). The matching conditions are automatically built into the resulting multipass linac beamline.

to use them for energy recovery. Our approach, based on proven, Continuous Electron Beam Accelerator Facility (CEBAF)-like, Recirculating Linear Accelerator (RLA) technology [803] is ‘somewhere in the middle’.

To visualize beta functions for multiple accelerating and decelerating passes through a given linac, it is convenient to reverse the linac direction for all decelerating passes and string them together with the interleaved accelerating passes, as illustrated in figure 150. As a result, the corresponding accelerating and decelerating passes are joined together at the arc’s entrance/exit. Therefore, the matching conditions are automatically built into the resulting multipass linac beamline. One can see that both linacs uniquely define the Twiss functions for the arcs: Linac one fixes the inputs to all odd arcs and the outputs to all even arcs, while Linac two fixes the inputs to all even arcs and the outputs to all odd arcs. The optics of the two linacs are mirror symmetric; they are optimised so that Linac one is periodic for the first accelerating pass and Linac two has this feature for the last decelerating pass. In order to maximize the beam breakup (BBU) threshold current [804], the optics is tuned so that the integral of  $\beta/E$  along the linac is minimised. The resulting phase advance per cell is close to  $130^\circ$ . Nonlinear strength profiles and more refined merit functions were tested, but they only made negligible improvements.

**10.2.1.2. Recirculating arc-emittance-preserving optics** Synchrotron radiation effects on beam dynamics, such as the transverse emittance dilution induced by quantum excitations, have a paramount impact on the collider luminosity. All six horizontal arcs are accommodated in a tunnel with a radius of 536.4 m. The transverse emittance dilution accrued through a given arc is proportional to the emittance dispersion function,  $H$ , averaged over all the arc’s bends [805]:

$$\Delta\epsilon = \frac{2\pi}{3} C_q r_0 \langle H \rangle \frac{\gamma^5}{\rho^2}, \tag{10.1}$$

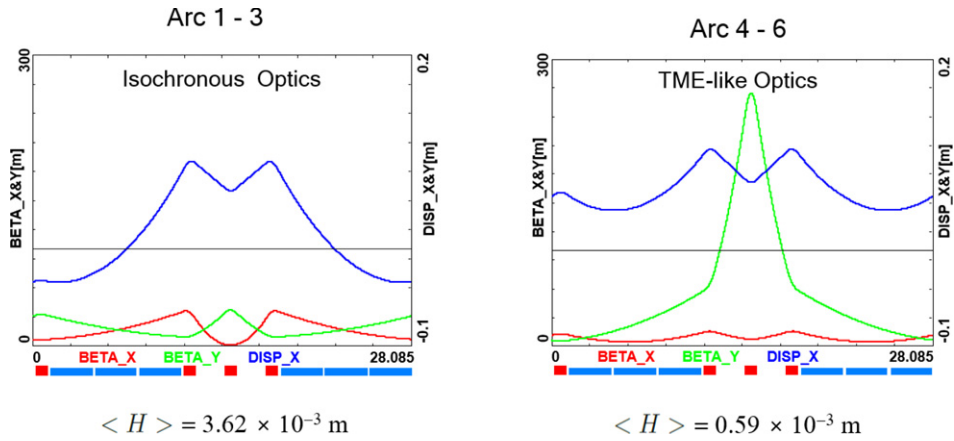


**Figure 151.** Two styles of FMC cell appropriate for different energy ranges. Left: lower-energy arcs (arcs one to three) configured with *isochronous* cells, right: higher-energy arcs configured with theoretical minimum emittance (TME)-like cells. Corresponding values of the emittance dispersion averages,  $\langle H \rangle$ , are listed for both types of cell.

where

$$C_q = \frac{55}{32\sqrt{3}} \frac{\hbar}{mc} \quad (10.2)$$

$r_0$  is the classical electron radius, and  $\gamma$  is the Lorentz boost. Here,  $H = (1 + \alpha^2)/\beta \cdot D^2 + 2\alpha DD' + \beta \cdot D'^2$  where  $D$ ,  $D'$  are the bending plane dispersion and its derivative, and  $\langle \dots \rangle = \frac{1}{\pi} \int_{\text{bends}} \dots d\theta$ .

Therefore, emittance dilution can be mitigated through an appropriate choice of arc optics (values of  $\alpha$ ,  $\beta$ ,  $D$ , and  $D'$  at the bends). In the presented design, the arcs are configured with FMC (flexible momentum compaction) optics to ease the individual adjustment of  $\langle H \rangle$  in various energy arcs.

The optical design of each arc takes into account the impacts of synchrotron radiation at different energies. At the highest energy, it is crucial to minimise the emittance dilution due to quantum excitation; therefore, the cells are tuned to minimise the emittance dispersion,  $H$ , in the bending sections, as in the TME lattice. On the other hand, at the lowest energy, it is beneficial to compensate for bunch elongation using isochronous optics. The higher-energy arcs (four, five and six) configured with TME cells are still quasi isochronous. To fully compensate for remnant bunch elongation, one could set higher-pass linacs slightly off-crest to compress the bunches, since one has full control of the gang phases for individual linac passes. All styles of FMC lattice cell, as illustrated in figure 151, share the same footprint for each arc. This allows us to stack magnets on top of each other or combine them in a single design. Here, we use substantially shorter cells than in the 60 GeV design, which uses a 28.1 m FMC cell configured with six 3 m bends, in groups of three flanked by a quadrupole singlet and a triplet, as illustrated in figure 151. The dipole filling factor of each cell is 63%; therefore, the effective bending radius  $\rho$  is 336.1 m. Each arc is followed by a matching section and a recombiner (a mirror symmetric to the spreader and matching section). Since the linacs are mirror symmetric, the matching conditions described in the previous section impose mirror-symmetric arc optics (identical betas and sign-reversed alphas at the arc ends).

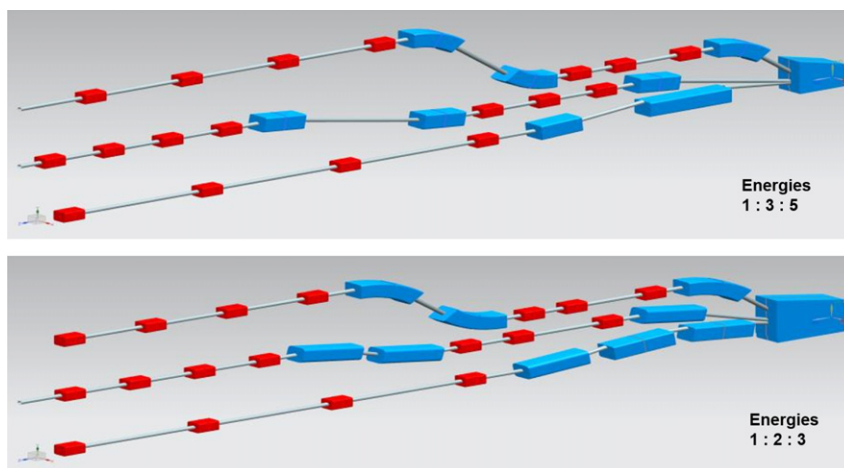


**Figure 152.** Layout of a three-beam switchyard for different energy ratios: 1:3:5 and 1:2:3 corresponding to specific switchyard geometries implemented on both sides of the racetrack.

It was predicted that path-length-adjusting chicanes would be required to tune the beam time of flight in order to hit the proper phase at each linac injection. Later investigations proved them to be effective only with lower-energy beams, as these chicanes trigger unsupported energy losses if applied to the highest-energy beams. A possible solution may consist of distributing the perturbation along the whole arc with small orbital excitations. This issue will be fully addressed in a subsequent section on ‘synchrotron radiation effects—emittance dilution’.

**10.2.1.3. Spreaders and recombiners** . The spreaders are placed directly after each linac to separate beams of different energies and to route them to the corresponding arcs. The recombiners facilitate just the opposite: merging beams of different energies into the same trajectory before they enter the next linac. As illustrated in figure 152, each spreader starts with a vertical deflective magnet, common to all three beams, that initiates the separation. The highest energy, at the bottom, is brought back to the horizontal plane using a chicane. The lower energies are captured by a two-step vertical deflection adapted from the CEBAF design [803].

The functional modularity of the lattice requires spreaders and recombiners to be achromats (in both the horizontal and vertical planes). To facilitate that, the vertical dispersion is suppressed by a pair of quadrupoles located in between vertical steps; they naturally induce strong vertical focussing, which needs to be compensated by the middle horizontally focussing quad. An overview of the spreader optics is illustrated in figure 153. The complete layouts of two styles of switchyard with different energy ratios are depicted in figure 152. Following the spreader, there are four matching quads to *bridge* the Twiss function between the spreader and the following  $180^\circ$  arc (two betas and two alphas). The combined spreader–arc–recombiner optics feature a high degree of modular functionality to facilitate momentum compaction management, as well as orthogonal tunability for both the beta functions and dispersion, as illustrated in figure 154.

**10.2.1.4. Alternative design of the spreader/recombiner** . The desire to reduce the number of elements included in the spreader led to a reduction in the number of steps required to vertically separate the different beams and route them into their specific arcs. In particular, this



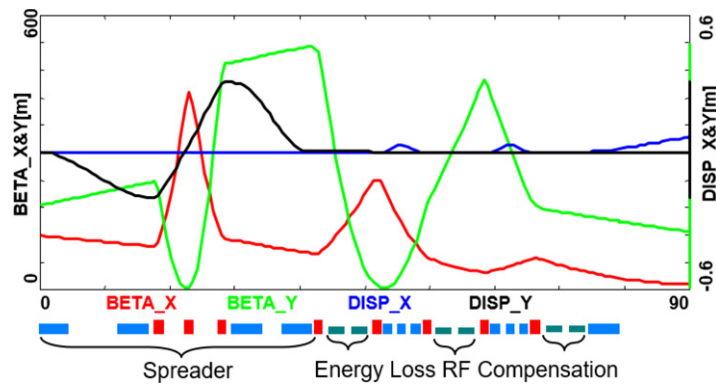


**Figure 153.** Spreader three (24.8 GeV) optics, featuring a vertical achromat with three dispersion-suppressing quads in between the two steps, a pair of path-length-adjusting dogleg chicanes and four betatron matching quads, interleaved with three energy-loss-compensating sections (second-harmonic RF cavities are marked in green).

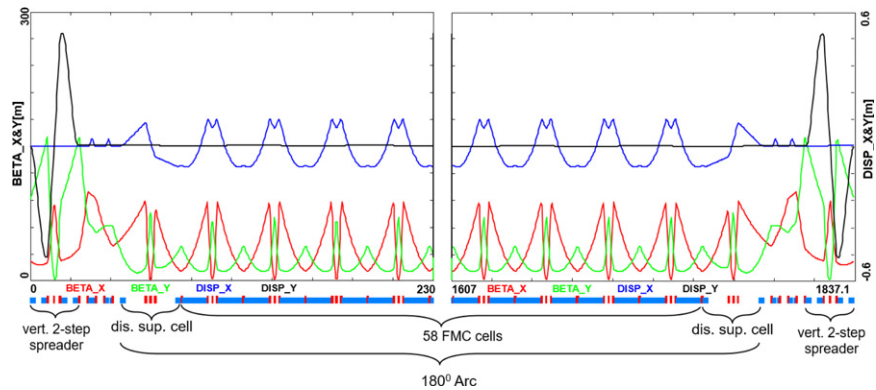


**Figure 154.** Complete optics for arc three (including the switchyard), featuring: a low-emittance  $180^\circ$  arc based on isochronous cells (30 cells flanked by a dispersion suppression cell with missing dipoles on each side), spreaders and recombiners with matching sections, and doglegs symmetrically placed on each side of the arc proper.

alternative spreader design uses a single vertical step instead of two. Although the concept was briefly discussed in [1] it was not retained due to the superconducting technology needed for the quadrupoles, which must be avoided in this highly radiative section. Nevertheless, recent studies have been pursuing a one-step spreader version based on normal conducting-magnet technology. It assumes a pole tip field of less than 1 T for an aperture radius of 30 mm, allowing the use of thin quadrupoles and thus minimises potential overlap with the other beamlines. With respect to the previous study, the use of normal conductors was made possible by increasing the overall spreader length and reducing the number of quadrupoles. In particular, the focussing magnets are limited to two outer quadrupoles for the achromatic function and one quadrupole

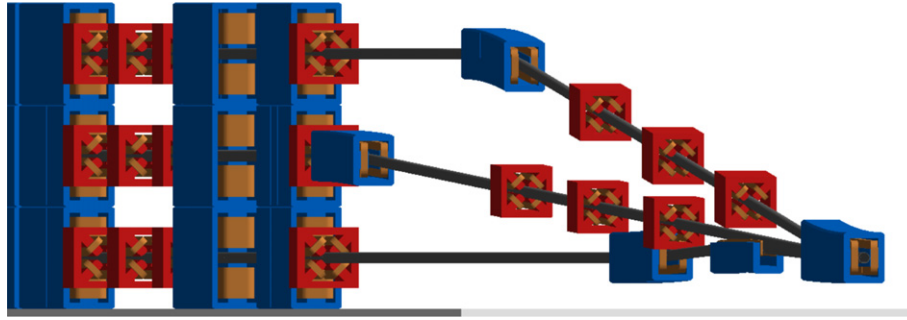


**Figure 155.** 3D visualisation of spreaders one, three, and five inserted at the end of the linac and routing the different beamlines into their respective dispersion suppressors.

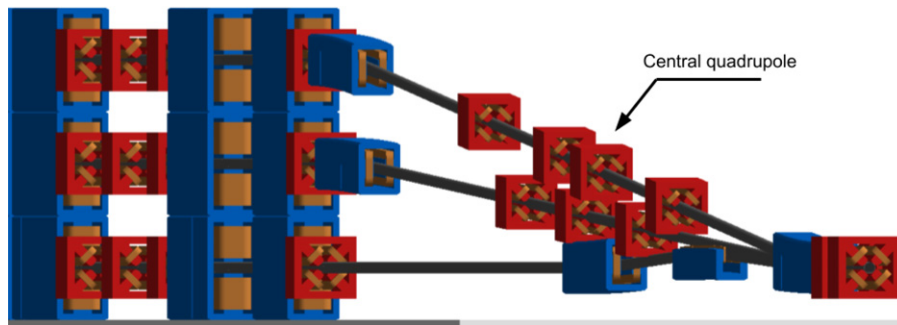


**Figure 156.** 3D visualisation of spreaders two, four, and six inserted at the end of the linac and routing the different beamlines into their respective dispersion suppressors.

in the middle, where the dispersion is zero, to control the beta function in the defocusing plane. Two visualisations are given in figures 155 and 156.

Both spreader types start with a first dipole that vertically separates the different beamlines in a 1:3:5 ratio for the odd-numbered spreaders and in a 1:2:3 ratio for the even-numbered spreaders. These ratios are defined by the beam energies of the corresponding turn. Therefore, by fixing the length of the longest beamline for each spreader (odd and even numbers), one obtains the angle required to get a 50 cm vertical offset between each beamline. The equations below represent the bending angle in the dipole and beamline lengths required to meet the requirements,

$$\theta_3 = \frac{0.5}{l_3 - L} \quad l_1 = \frac{2E_1}{E_3}(l_3 - L) + L \quad (10.3)$$

$$\theta_2 = \frac{1}{l_2 - L} \quad l_4 = \frac{1}{2} \frac{E_4}{E_2}(l_2 - L) + L \quad (10.4)$$

where the index  $i$  corresponds to the beamline number associated with an energy  $E_i$ ,  $L$  is the dipole length, and  $l$  is the whole spreader beamline length.

For beamlines two and four we obtain  $l_4 \approx l_2$  according to the energy ratio of 1.97. On the other hand,  $l_3$  will be longer than  $l_1$  because the energy ratio is 2.88. One can therefore tune the angle of the even-numbered spreaders by defining  $l_2$ , as it will be the longest. However,

the angle of the odd-numbered spreaders will be determined by the length of  $l_3$ . Regarding the chicane used for the highest energy, only a minimum separation between the highest energy and the intermediate energy allows the introduction of the opposite bending dipole. In return, this constrains the placement of the intermediate-energy quadrupoles. The location of the magnets is the main limitation on the minimization of the spreader length: the shorter the lattice gets, the stronger the quadrupoles need to be in order to preserve the achromatic function.

As a result, a one-step spreader halves the number of dipoles present in the lattice and relaxes the constraint on magnet interference and overlap, which is favorable for compactness. Dividing the number of dipoles by two has a noticeable effect on the synchrotron power radiated in the spreader which is, in addition, beneficial for the emittance growth. The dipole fields required for a maximal length of 50 m are 226 mT for the odd-numbered spreaders and 326 mT for the even-numbered spreaders. The schematic of the multipass linac optics in figure 150 shows that the even-numbered spreaders, i.e. two, four, and six, have the highest beta functions at their entrance, which is detrimental from the perspective of minimizing the emittance growth within the spreader lattice. A solution to this issue is to insert a doublet of quadrupoles at the exit of the linac. All three energies pass through the doublet and, therefore, a compromise has to be found for the gradients. Finally, the reduction of the  $\mathcal{H}$  function over the length of the spreader and specifically in the dipoles contributes to a further reduction of the emittance growth.

The energy loss for spreader one is low, due to the low beam energy; spreaders two and three have similar values that are acceptable, which is also true for spreader four. Spreaders five and six have the highest beam energies and therefore the largest energy loss. In addition, the dipoles used to produce the chicane need double the field strength, compared to the other dipoles, for the same length, i.e. half the bending radius, in order to save space for the elements in the other beamlines. The vertical emittance growth is well controlled, just as in the even-numbered spreaders. Only spreader six has a contribution that is an order of magnitude higher, but one has to keep in mind that the even-numbered spreaders will only act as recombiners, since a horizontal bypass will perform the separation from the detector and a vertical separation will only occur for arcs two and four. Consequently, the contribution of spreader six should not be included in the emittance growth up to the interaction point.

The optics for the spreaders/recombiners of arcs two and four are presented in figure 157, which shows the achromatic function supported by the outer quadrupoles, while the control of the horizontal beta function is provided by the ‘middle’ quadrupole. One can see that the lattice of arc two has to split the ‘middle’ quadrupole in two, in order to avoid overlap with the other beamline (arc four); see figure 156. These two optics are the most challenging, as they have high beta functions at the entrances to their lattices, due to the multipass linac optics as previously explained.

**10.2.1.5. IR bypasses** . After the last spreader the 49.19 GeV beam goes straight to the interaction region. However, the lower-energy beams at 16.7 and 33.0 GeV need to be further horizontally separated in order to avoid interference with the detector. Different design options were explored for the bypass section [806] and the one that minimised the extra deflection was chosen and implemented in the lattice.

Ten arc-like dipoles are placed very close to the spreader to provide an initial deflection,  $\theta$ , which results in an  $X = 10$  m separation from the detector located 120 m downstream. The straight section of the bypass is approximately 240 m long. After the bypass, in order to reconnect to the footprint of arc six, seven out of 30 standard cells in arcs two and four are replaced by seven higher-field junction cells. The number of junction cells is a compromise between the field strength increase and the length of the additional bypass tunnel, as can be inferred from

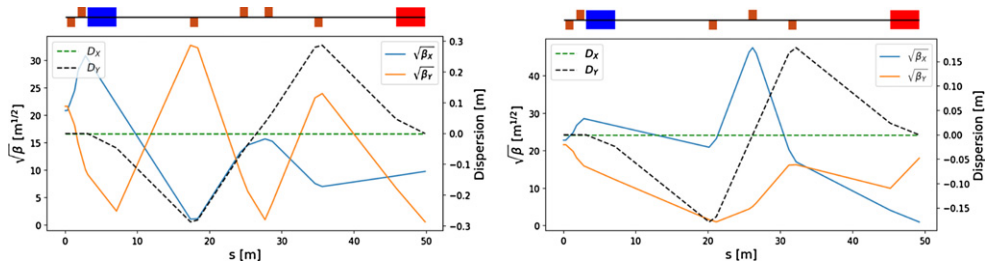


**Figure 157.** Left: spreader/recombiner optics of arc two for the 16.73 GeV electron beam. Right: spreader/recombiner optics of arc four for the 32.96 GeV electron beam.

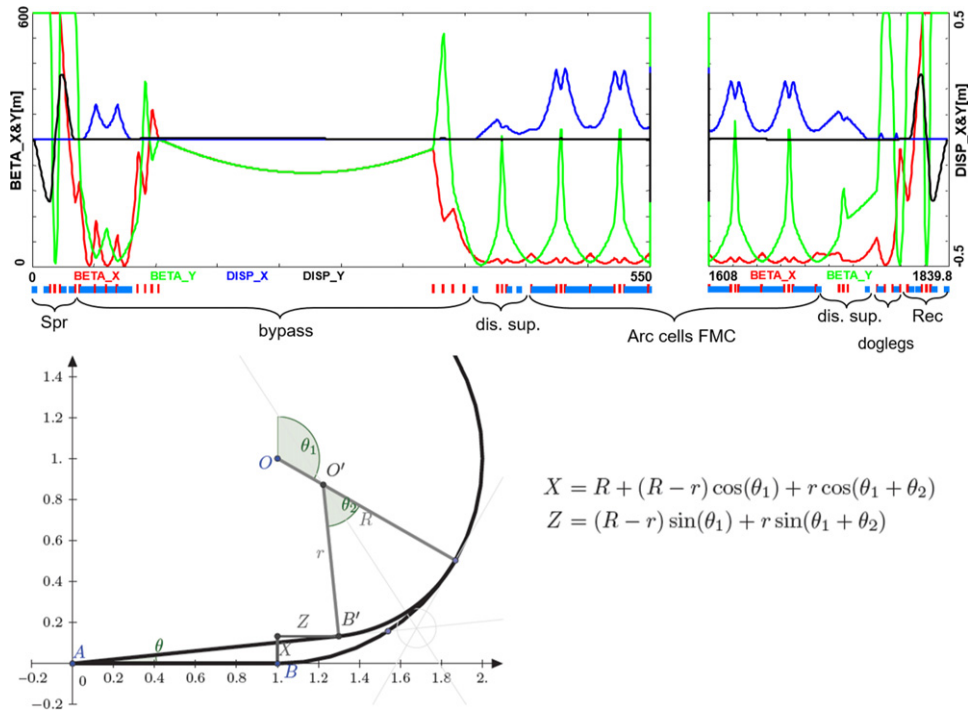


**Figure 158.** Optics and layout of arc four, including the detector bypass. The lattice (top insert) features a vertical spreader, an initial horizontal deflection, a straight section, a modified dispersion suppressor, seven junction cells, and four regular cells. The bypass geometry (bottom insert) features a long IP line  $AB$ , which for visual reasons has purposely been stretched, being in fact about 1/5 of the arc radius. All geometric dependencies of the bypass parameters are summarized in the inserted formulae.

the scheme summarised in figure 158. The stronger deflection in the junction cells creates a small mismatch, which is corrected by adjusting the strengths of the quadrupoles in the last junction cell and in the first regular cell.

10.2.1.6. *Synchrotron radiation effects—emittance dilution* ERL efficiency, as a source of multi-GeV electrons for a high-luminosity collider, is limited by the incoherent synchrotron

**Table 27.** Energy loss and emittance dilution (horizontal and longitudinal) due to synchrotron radiation generated by all six 180° arcs (not including spreaders, recombiners, and doglegs). Here,  $\Delta\sigma_{\frac{\Delta E}{E}} = \sqrt{\frac{\Delta\epsilon_E^2}{E^2}}$ .

Beamline	Beam energy (GeV)	$\Delta E$ (MeV)	$\Delta\epsilon_N^x$ (mm mrad)	$\Delta\sigma_{\frac{\Delta E}{E}}$ (%)
Arc one	8.62	0.7	0.0016	0.0005
Arc two	16.73	10	0.085	0.0027
Arc three	24.85	49	0.91	0.0072
Arc four	32.96	152	0.81	0.015
Arc five	41.08	368	3.03	0.026
Arc six	49.19	758	8.93	0.040

effects on beam dynamics, namely, the transverse emittance dilution and the longitudinal momentum spread (induced by quantum excitations). The first effect, the transverse emittance increase, will have a paramount impact on collider luminosity, due to stringent limits on the allowed emittance increase. The second, accrued momentum spread, governs the asymmetries of the accelerated and decelerated beam profiles. These asymmetries substantially complicate multipass energy recovery and matching, and ultimately, they limit the energy reach of the ERLs due to recirculating arc momentum acceptance.

The arc optics is designed to ease the individual adjustment of momentum compaction (needed for longitudinal phase-space control, essential for operation with energy recovery) and the horizontal emittance dispersion,  $H$ , in each arc. Table 27 lists the arc-by-arc dilution of the transverse,  $\Delta\epsilon$ , and longitudinal,  $\Delta\sigma_{\frac{\Delta E}{E}}$ , emittances due to quantum excitations calculated using analytic formulas, equations (10.5)–(10.7), introduced by M Sands [805]:

$$\Delta E = \frac{2\pi}{3} r_0 m c^2 \frac{\gamma^4}{\rho} \tag{10.5}$$

$$\Delta\epsilon_N = \frac{2\pi}{3} C_q r_0 \langle H \rangle \frac{\gamma^6}{\rho^2}, \tag{10.6}$$

$$\frac{\Delta\epsilon_E^2}{E^2} = \frac{2\pi}{3} C_q r_0 \frac{\gamma^5}{\rho^2}, \tag{10.7}$$

where  $C_q$  is given by equation (10.2). Here,  $\Delta\epsilon_E^2$  is an increment of the energy square variance,  $r_0$  is the classical electron radius,  $\gamma$  is the Lorentz boost, and  $C_q \approx 3.832 \times 10^{-13}$  m for electrons (or positrons).

Apart from the horizontal 180° arcs, there are other sources of emittance dilution due to synchrotron radiation, namely vertical spreaders and recombiners, as well as horizontal ‘doglegs’ used to compensate for seasonal variations of the path length. To minimise their contribution to the vertical emittance dilution, special optics with small vertical  $\langle H \rangle$  have been introduced in the spr/rec sections. The effects on vertical emittance dilution coming from these beamlines (spr/rec) are summarized in table 28 for the two-step spreaders and in table 29 for the alternative version of a one-step spreader.

Similarly, the horizontal emittance dilution induced by the doglegs (four dogleg chicanes per arc) in various arcs is summarized in table 30. Each dogleg chicane is configured with four 1 m bends (1 T each), so that they bend the lowest-energy beam at 8.6 GeV by 2 degrees. The corresponding path lengths gained in the doglegs of different arcs are also indicated.

**Table 28.** Energy loss and emittance dilution (vertical and longitudinal) due to synchrotron radiation generated by the two-step spreader or recombiner design of a given arc (spr/rec: spreader/recombiner). Here,  $\Delta\sigma_{\frac{\Delta E}{E}} = \sqrt{\frac{\Delta\epsilon_N^2}{E^2}}$ .

Beamline	Beam energy (GeV)	$\Delta E$ (MeV)	$\Delta\epsilon_N^y$ (mm mrad)	$\Delta\sigma_{\frac{\Delta E}{E}}$ (%)
Spr/rec one	8.62	0.2	0.035	0.0008
Spr/rec two	16.73	3.0	0.540	0.0044
Spr/rec three	24.85	6.0	0.871	0.0066
Spr/rec four	32.96	21.6	5.549	0.0143
Spr/rec five	41.08	7.1	0.402	0.0062
Spr/rec six	49.19	39.2	3.92	0.0205

**Table 29.** Energy loss and emittance dilution (vertical and longitudinal) due to synchrotron radiation generated by a one-step spreader, or recombiner design of a given arc. Here,  $\Delta\sigma_{\frac{\Delta E}{E}} = \sqrt{\frac{\Delta\epsilon_N^2}{E^2}}$ .

	Beam energy (GeV)	$\Delta E$ (MeV)	$\Delta\epsilon_N^y$ (mm mrad)	$\Delta\sigma_{\frac{\Delta E}{E}}$ (%)
Spreader 1	8.62	0.04	0.004	0.0002
Spreader 2	16.73	0.31	0.004	0.0007
Spreader 3	24.85	0.32	0.012	0.0006
Spreader 4	32.96	1.18	0.112	0.0013
Spreader 5	41.08	2.64	0.083	0.0019
Spreader 6	49.19	7.92	1.060	0.0040

**Table 30.** Energy loss and emittance dilution (horizontal and longitudinal) due to synchrotron radiation generated by the doglegs (four dogleg chicanes) of a given arc. Here,  $\Delta\sigma_{\frac{\Delta E}{E}} = \sqrt{\frac{\Delta\epsilon_N^2}{E^2}}$ .

Beamline	Beam energy (GeV)	$\Delta E$ (MeV)	$\Delta\epsilon_N^x$ (mm mrad)	$\Delta\sigma_{\frac{\Delta E}{E}}$ (%)	Path-length (mm)
Doglegs 1	8.62	2	0.201	0.007	7.32
Doglegs 2	16.73	9	0.667	0.009	1.96
Doglegs 3	24.85	19	5.476	0.014	0.84
Doglegs 4	32.96	33	5.067	0.014	0.52
Doglegs 5	41.08	52	12.067	0.028	0.36
Doglegs 6	49.19	74	2.836	0.011	0.28

As indicated in table 30, the doglegs in the highest-energy arcs, arcs five and six, provide only a submillimetre path-length gain with large synchrotron radiation effects. They are not very effective and generate strong, undesired emittance dilution. Therefore, it is reasonable to eliminate them from both arcs five and six. Instead, one could resort to an alternative path-length control via appropriate orbit steering with both horizontal and vertical correctors present at every girder and distributed evenly throughout the arc.

Combining all three contributions: (180° arc, spreader, recombiner, and doglegs (no doglegs in arcs five and six), the net cumulative emittance dilution is summarized in table 31 for the case of the two-step spreader.



**Table 31.** Energy loss and cumulative emittance dilution (transverse and longitudinal) due to synchrotron radiation at the end of a given beamline (complete arc including: 180° arc, spreader, recombiner, and doglegs in arcs one to four). The table covers the entire energy-recovery (ER) cycle: three passes ‘up’ and three passes ‘down’. The cumulative emittance dilution values just before the IP (past arc five and spr six), which are critical for the luminosity consideration, are highlighted in bold. That row accounts for contributions to energy loss from spr six (the last bending section before the IR), as well as the vertical and longitudinal emittance dilutions. Here,  $\Delta\sigma_{\frac{\Delta E}{E}} = \sqrt{\frac{\Delta\epsilon_x^2}{E^2}}$ .

Beamline	Beam energy (GeV)	$\Delta E$ (MeV)	$\Delta\epsilon_N^{\text{cum}x}$ (mm mrad)	$\Delta\epsilon_N^{\text{cum}y}$ (mm mrad)	$\Delta\sigma_{\frac{\Delta E}{E}}^{\text{cum}}$ (%)
Arc one	8.62	3	0.2	0.1	0.01
Arc two	16.73	25	1.0	1.2	0.03
Arc three	24.85	80	7.3	2.9	0.06
Arc four	32.96	229	13.2	14.0	0.12
Arc five	41.08	383	16.2	14.8	0.16
<b>IR</b>	49.19	39	<b>16.2</b>	<b>18.7</b>	<b>0.18</b>
Arc six	49.19	797	25.2	22.6	0.24
Arc five	41.08	383	28.2	23.4	0.28
Arc four	32.96	229	34.1	34.5	0.33
Arc three	24.85	80	40.5	36.3	0.37
Arc two	16.73	25	41.2	37.4	0.39
Arc one	8.62	3	41.4	37.4	0.40
Dump	0.5		41.4	37.4	0.40

Table 31 shows that the LHeC luminosity requirement for a total transverse emittance dilution in either plane (normalized) at the IP (at the end of arc five) not exceeding 20 mm mrad (hor: 16.2 mm mrad and ver: 18.7 mm mrad) is met by design, using the presented low-emittance lattices in both the arcs and the switchyards. In the case of the optimised one-step spreader design, another reduction—mainly of the vertical emittance budget—is obtained, providing the design with a comfortable safety margin.

Finally, one can see from equations (10.6) and (10.7) an underlying universal scaling of the transverse (unnormalized) and longitudinal emittance dilution with energy and arc radius; they are both proportional to  $\gamma^5/\rho^2$ . This, in turn, has a profound impact on arc size scalability with energy; namely, the arc radius should scale according to  $\gamma^{5/2}$  in order to preserve both the transverse and longitudinal emittance dilutions, which is a figure of merit for a synchrotron-radiation-dominated ERL.

**10.2.2. 30 GeV ERL options.** One may consider an upgrade path from a 30 GeV ERL to a 50 GeV ERL, using the same footprint, 1/5 of the LHC’s circumference (5.4 km). In this scenario, each linac’s straight section (front end) would initially be loaded with 18 cryomodules, forming two 5.21 GV linacs. One would also need to decrease the injector energy by a factor of 5.21/8.11. The maximum ERL energy, after three passes, would reach 31.3 GeV. For the upgrade to 50 GeV, one would then fill the remaining space in the linacs with ten additional cryomodules each, equalling 2.9 GV worth of RF in each linac. In this way, the energy ratios would be preserved for both the 30 and 50 GeV ERL options, so that the same switchyard geometry could be used. Finally, one would scale up the entire lattice, i.e. all magnets (dipoles and quads) by a ratio of 8.11/5.21.

If one wanted to stop at the 30 GeV option with no upgrade path, then a 1/14 of the LHC’s circumference (1.9 km) would be a viable footprint for the racetrack, featuring two linacs, each 503 m long, (17 cryomodules) with arcs of 94.5 m radius. Again, assuming 0.32 GeV of

**Table 32.** 50 GeV ERL—dipole magnet counts along with basic magnet parameters: magnetic field ( $B$ ), half-gap ( $g/2$ ), and magnetic length ( $L$ ).

Section	Arc dipoles (horiz.)				Spr/rec dipoles (vert.)				<i>Dogleg</i> dipoles (horiz.)			
	$N$	$B(T)$	$g/2(\text{cm})$	$L(\text{m})$	$N$	$B(T)$	$g/2(\text{cm})$	$L(\text{m})$	$N$	$B(T)$	$g/2(\text{cm})$	$L(\text{m})$
Arc one	352	0.087	1.5	3	8	0.678	2	3	16	1	1.5	1
Arc two	352	0.174	1.5	3	8	0.989	2	3	16	1	1.5	1
Arc three	352	0.261	1.5	3	6	1.222	2	3	16	1	1.5	1
Arc four	352	0.348	1.5	3	6	1.633	2	3	16	1	1.5	1
Arc five	352	0.435	1.5	3	4	1.022	2	3				
Arc six	352	0.522	1.5	3	4	1.389	2	3				
Total	2112				36				64			

**Table 33.** 50GeV ERL—quadrupole magnet and RF cavity counts along with basic magnet/RF parameters: magnetic-field gradient ( $G$ ), aperture radius ( $a$ ), magnetic length ( $L$ ), frequency ( $f$ ), number of cells per RF cavity (cell), and RF gradient ( $G_{RF}$ ).

Section	Quadrupoles				RF cavities			
	$N$	$G(\text{T m}^{-1})$	$a(\text{cm})$	$L(\text{m})$	$N$	$f(\text{MHz})$	Cell	$G_{RF}(\text{T m}^{-1})$
Linac one	29	7.7	3	0.25	448	802	5	20
Linac two	29	7.7	3	0.25	448	802	5	20
Arc one	255	9.25	2.5	1				
Arc two	255	17.67	2.5	1				
Arc three	255	24.25	2.5	1	6	1604	9	30
Arc four	255	27.17	2.5	1	12	1604	9	30
Arc five	249	33.92	2.5	1	18	1604	9	30
Arc six	249	40.75	2.5	1	36	1604	9	30
Total	1576				968			

injection energy, the maximum ERL energy would reach 30.2 GeV. Such a configuration may become relevant if time and funds permit a small version of the LHeC or none. This version of the LHeC would have a reduced potential for Higgs, top, and BSM physics. However, owing to the high proton-beam energy, this configuration would still have a TeV in the centre of mass such that the core QCD, PDF, and electroweak programme would still be striking.

*10.2.3. Component summary.* This closing section will summarise the active accelerator components: magnets (bends and quads) and RF cavities for the 50 GeV baseline ERL. The bends (both horizontal and vertical) are captured in table 32, while the quadrupole magnets and RF cavities are collected in table 33.

One would like to use a combined aperture (three-in-one) arc magnet design with a 50 cm vertical separation between the three apertures, proposed by Attilio Milanese [807]. That would reduce the net arc bend count from 2112 to 704. As far as the spr/rec vertical bends are concerned, the design was optimised to include an additional common bend separating the two highest passes. As a result, there are a total of eight trapezoid B-com magnets with a second

face tilted by  $3^\circ$  and a large 10 cm vertical aperture; the rest are simple rectangular bends with specs from the summary table 32.

### 10.3. Electron–ion collisions

As well as colliding proton beams, the LHC also provides collisions of nuclear (fully-stripped ion) beams with each other (AA collisions) or with protons ( $pA$ ). Either of these operating modes offers the possibility of electron–ion ( $eA$ ) collisions in the LHeC configuration<sup>193</sup>.

Here, we summarise the considerations leading to the luminosity estimates given in table 4 for collisions of electrons with  $^{208}\text{Pb}^{82+}$  nuclei, the nominal heavy ion species collided in the LHC. Other, lighter, nuclei are under consideration for future LHC operation [508] and could also be considered for electron–ion collisions.

The heavy ion beams that the CERN injector complex can provide to the LHC, the HE-LHC, and the FCC provide a unique basis for high-energy, high-luminosity deep inelastic electron–ion-scattering physics. Since HERA was restricted to protons only, the LHeC or the FCC-eh will extend the kinematic range in  $Q^2$  and  $1/x$  by four or five orders of magnitude. This is a huge increase in coverage and will be able to radically change the understanding of parton dynamics in nuclei and of the formation of the QGP.

An initial set of parameters in the maximum energy configurations was given in [36]. The Pb beam parameters are essentially those foreseen for the operation of the LHC (or the HL-LHC) in runs three and four (planned for the 2020s). These parameters have already largely been demonstrated [808], except for the major remaining step of implementing slip-stacking injection in the SPS, which would reduce the basic bunch spacing from 100 to 50 ns [809]. With respect to the proton spacing of 25 ns, this allows the electron bunch intensity to be doubled, while still respecting the limit on total electron current. In fact, without the slip-stacking in the SPS, the initial luminosity would be the same with a 100 ns Pb spacing (and quadrupled electron bunch intensity). However, one must remember that the evolution of the Pb beam intensity will be dominated by luminosity burn-off by the concurrent PbPb collisions at the other interaction points and that the integrated luminosity for both PbPb and  $e\text{Pb}$  collisions will be higher with the higher total Pb intensity. The details of this will depend on the operating scenarios, number of active experiments, etc, and are not considered further here. The time evolution of  $eA$  luminosity will be determined by that of PbPb and  $p\text{Pb}$  collisions, as discussed, for example, in reference [16, 508, 810].

Combining these assumptions with the default 50 GeV electron ERL for the LHeC and 60 GeV for the FCC-eh yields the updated parameter sets and initial luminosities given in table 4 (earlier in this report).

The radiation damping of Pb beams in the hadron rings is about twice as fast as for protons and can be fully exploited, since it takes longer to approach the beam–beam limit at the PbPb collision points. In the case of the FCC-hh [16], one can expect the emittance values in table 4 to be reduced during fills [16, 508, 810].

The Pb beam will be affected by UPC effects, mainly bound–free-pair production and Coulomb dissociation of the nuclei induced by the electromagnetic fields of the electrons, seen as pulses of virtual photons. The relevant cross-sections will be similar to those in  $p\text{Pb}$  collisions, which are smaller by a factor of  $Z^2$  compared to those in PbPb collisions and can be neglected in practice.

<sup>193</sup> In  $pA$  operation of the LHC, the beams may be reversed ( $Ap$ ) for some part of the operating time. Only one direction (ions in beam two) provides  $eA$  collisions, while the other provides  $ep$  collisions at significantly reduced luminosity compared to the  $pp$  mode, since there are fewer proton bunches, and those have lower intensity.

**Table 34.** Comparison of parameters for the LEP collider and the LHC. Taken from [1]

Parameter	Unit	LEP	LHC
Beam size $\sigma_x/\sigma_y$	$\mu\text{m}$	180/7	16.6/16.6
Intensity	$10^{11}$ particles/bunch	4.00	1.15
Energy	GeV	100	7000
$\beta_x^*/\beta_y^*$	cm	125/5	55/55
Crossing angle	$\mu\text{rad}$	0	0/285
Beam–beam tune shift $\Delta Q_x/\Delta Q_y$		0.0400/0.0400	0.0037/0.0034
Beam–beam parameter $\xi$		0.0700	0.0037

**Table 35.** Comparison of parameters for the LHeC at the HL-LHC. The parameters presented correspond to the default design.

Beam parameter	Unit	LHeC at the HL-LHC	
		Proton beam	Electron beam
Energy	GeV	7000	49.19
Normalized emittance	mm mrad	2.5	50
Beam size $\sigma_{x,y}$	$\mu\text{m}$	5.8	5.8
Intensity	$10^9$ particles/bunch	220.00	3.1
Bunch length $\sigma_s$	mm	75.5	0.6
$\beta_{x,y}^*$	cm	10.00	6.45
Disruption factor		$1.20 \times 10^{-5}$	14.5
Beam–beam parameter $\xi$		$1.52 \times 10^{-4}$	0.99

#### 10.4. Beam–beam interactions

In the framework of the LHeC, the concept of an ERL allows us to overcome the beam–beam limit that we would face in a storage ring. The electron beam can be heavily disturbed by the beam collision process, while the large acceptance of the ERL will still allow for successful energy recovery during the deceleration of the beam, so that power consumption is minimised. In order to compare the relevant beam–beam parameters and put them into the context of other colliders, two tables are shown that highlight, on the one hand, the parameters from LEP collider and LHC runs in table 34, and on the other hand, the parameters planned for the LHeC at the HL-LHC in table 35.

In the case of the LHeC, the  $\beta$ -functions at the interaction point are chosen such that the transverse beam sizes of the e- and p-beams are equal in both transverse planes. Although the proton and electron emittances are different, the beta functions at the interaction point are set accordingly, so that the two beams conserve  $\sigma_x^e = \sigma_x^p$  and  $\sigma_y^e = \sigma_y^p$ .

**10.4.1. Effect on the electron beam.** The disruption parameter for the electron beam is of the order of 14.5, which corresponds, in a linear approximation, to almost two oscillations of the beam envelope within the proton bunch. The nonlinearity of the interaction creates a distortion of the phase space and a mismatch with respect to the design optics (see figure 159). The mismatch and distortion can be minimized by tuning the Twiss parameters ( $\alpha^*, \beta^*$ ) at the interaction point.

In a series of studies, the optical parameters of the electron beam were tracked back to the interaction point in the presence of the beam–beam forces in order to show the impact of the beam–beam effect for different values of the electron Twiss parameters at the IP. In addition,

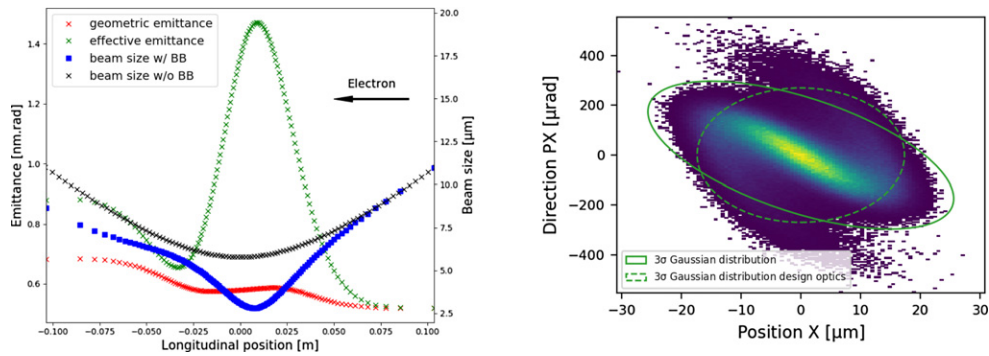


**Figure 159.** Left: electron beam sizes with (blue) and without (black) the beam–beam forces exerted on the electron beam. The geometric emittance is represented in red and the effective emittance that takes into account the difference from the original optics is illustrated in green. Right: the horizontal phase space of the spent electron distribution backtracked to the interaction point.  $3\sigma$  Gaussian distributions are highlighted for the post-collision distribution (solid line) and the design optics (dashed line).

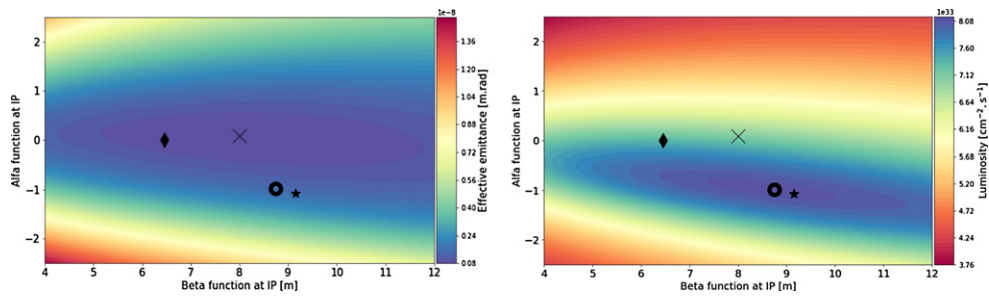


**Figure 160.** Left: contour plot describing the effective emittance post collision as a function of the alpha and beta functions at the IP. Right: contour plot describing the luminosity as a function of the alpha and beta functions at the IP. The diamond marker represents the initial Twiss parameters, the circle shows the luminosity optimum, the cross symbolizes the smallest difference from the original optics, and the star illustrates the minimal geometric emittance growth.

the influence of a waist shift from the IP (proportional to  $\alpha^*$ ), similar to changing the foci of the interacting beams, has been studied and allows us to keep the electron beam within the proton bunch for a longer time, thus optimizing the luminosity. The modification of the electron beam beta function ( $\beta^*$ ) leads to more freedom and gives access, from all the possibilities, to two different optima regarding the luminosity and the mismatch from the design optics. The results are summarized in the contour plots of figure 160.

As a consequence, the Twiss parameters at the interaction point can either be set to minimize the mismatch of the optics (i.e. the effective emittance) or to maximize the luminosity. If optimization of the luminosity is chosen (see the circle marker in figure 160), modified capture optics will be needed in the beam transfer to the arc structure in order to re-match the modified Twiss functions perturbed by the nonlinear beam–beam effects.

The effect of possible offsets between the two colliding beams has been characterized in previous beam–beam studies [811], and—if uncorrected—might lead to an electron-beam

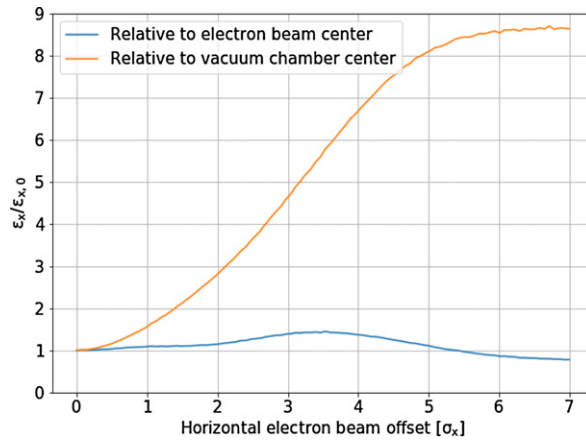


**Figure 161.** Electron beam emittance relative change with respect to its centroid (blue) and with respect to the vacuum chamber centre (orange).

emittance growth. The parameters for these studies have been updated and the results are presented in figure 161. As any offset between the two beams is amplified, it results in a larger increase of the beam envelope. As a solution, a fast feed-forward system is proposed across arc six, which aims to damp the transverse motion so that the beam emittance can be recovered. Using two sets of kickers placed at the centre and at the end of the arc, an offset of  $0.16\sigma$  can be damped. A single set cutting across the whole arc can correct a  $1\sigma$  offset with approximately 4.4 kV.

Additionally, the coupling of the beam–beam effect with long-range wakefields has been addressed [811]. Assuming a misaligned bunch injected among a train of nominal bunches, the coupling of the beam–beam effect with the wakefields leads to a reduction of the excitation damping created by the misaligned bunch. Nevertheless, it can be shown that beam stability is conserved and that the total amplification remains acceptable with respect to the study that did not consider the coupling.

**10.4.2. Effect on the proton beam.** The beam–beam interaction between the electron and proton beams is asymmetric in terms of beam rigidities. Although the less energetic 49.19 GeV electron beam is heavily distorted by the strong 7 TeV proton beam, the proton beam will suffer from an emittance growth that adds up turn by turn [811] due to the build up of the tiny disruption created by the offset between the beams. In fact, previous studies gave a growth rate of around  $0.01\% s^{-1}$  for a jitter of  $0.2\sigma_x$ . As long as adequate control of the bunches is preserved, this effect should be overshadowed by other effects leading to emittance blow-up in the LHC (e.g. due to intra beam scattering). Since the electron-beam energy has been decreased from 60 GeV to 49.19 GeV, this study needs to be updated; the results should remain in agreement with the previous statement.

### 10.5. Arc magnets

In this section, the conceptual design of the main magnets needed for the linac–ring (LR) accelerator at 50 GeV is described. The number and types of magnets are listed in tables 32 and 33.



**Table 36.** 50 GeV ERL—main parameters of the three-aperture bending magnets.

Parameter	Unit	Value
Beam energy	GeV	8.62–49.19
Magnetic field	T	0.087–0.522
Magnetic length	m	3
Vertical aperture	mm	30
Pole width	mm	90
Number of apertures		3
Distance between apertures	mm	500
Mass	kg	8000
Number of magnets		704
Current	A	4250
Number of turns per magnet		4
Current density	A mm <sup>-2</sup>	1
Conductor material		Aluminium
Magnet resistance	mΩ	0.17
Power	kW	3
Total power consumption for six arcs	MW	2.1
Cooling		Air

**10.5.1. Dipole magnets.** The bending magnets are used in the arcs of the recirculator. Each of the six arcs needs 352 horizontal bending dipoles. Additional dipoles are needed in the straight sections: 36 vertical bending dipoles in the spreader/recombiner and 64 horizontal bending dipoles for the ‘dogleg’. These magnets are not considered at the moment.

In the CDR issued in 2012 for a 60 GeV lepton ring (LR), a design based on three independent dipoles stacked on top of each other was proposed. A post-CDR design with three-aperture dipoles was introduced in 2014 [807]. This solution allows the reduction of the ampere-turns and the production cost of the dipoles. For a 50 GeV LR, the three-aperture dipole design is adapted to fulfil new magnetic-field requirements.

The 352 horizontal bending dipoles needed for each arc, combined in three-aperture dipoles, result in a total of 704 units. These magnets are 3 m long and provide a field in the 30 mm aperture ranging from 0.087 T to 0.522 T, depending on the arc energy, which ranges from 8.62 GeV to 49.19 GeV.

In the proposed design, the three apertures are stacked vertically but offset transversely. This allows the ampere-turns to be recycled from one aperture to the other. The coils are centrally located on the yoke and are made of simple aluminium bus-bars, all powered in series. A current density of 1 A mm<sup>-2</sup> in the coils is sufficiently low so as not to require water cooling, but it may be required to limit the temperature in the tunnel. Trim coils can be added on two of the apertures to provide some tuning. Alternatively, each stage could be separately powered. The dipole yokes are made of low-carbon steel plates. The relevant parameters are summarised in table 36 and the cross-section is illustrated in figure 162 for 500 mm between consecutive arcs.

### 10.5.2. Quadrupole magnets.

**10.5.2.1. Quadrupoles for recirculator arcs** . In total, 1518 quadrupoles are needed for the recirculator arcs: 255 each for arcs one to four and 249 each for arcs five and six. The required integrated gradients, comprising between 9.25 T and 40.75 T, can be achieved using one type of quadrupole 1 m long. However, instead of operating the magnets at low current for lower

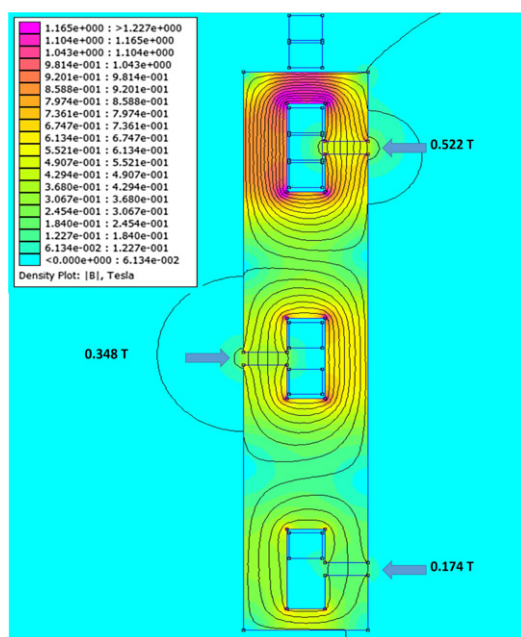


**Figure 162.** 50 GeV ERL—cross-section of the three-aperture bending magnets for arcs two, four, and six with 500 mm between consecutive arcs, based on the finite-element method (FEM).

arc energy, a shorter model, 0.6 m long, is under consideration for arcs one to three. These quadrupoles require water cooling for the coils. The relevant parameters are summarised in table 37 and the cross-section is illustrated in figure 163 (left).

In order to reduce the power consumption, a hybrid configuration could be envisaged for the quadrupoles, in which most of the excitation is created by permanent magnets. The gradient strength could be varied by trim coils or by mechanical methods.

**10.5.2.2. Quadrupoles for the two 8.1 GeV linacs** . In the two 8.1 GeV linacs, 29 + 29 quadrupoles, each providing an integrated strength of 1.93 T, are required. The present design solution specifies 30 mm aperture-radius magnets. The relevant parameters are summarised in table 38 and the cross-section is illustrated in figure 163 (right).

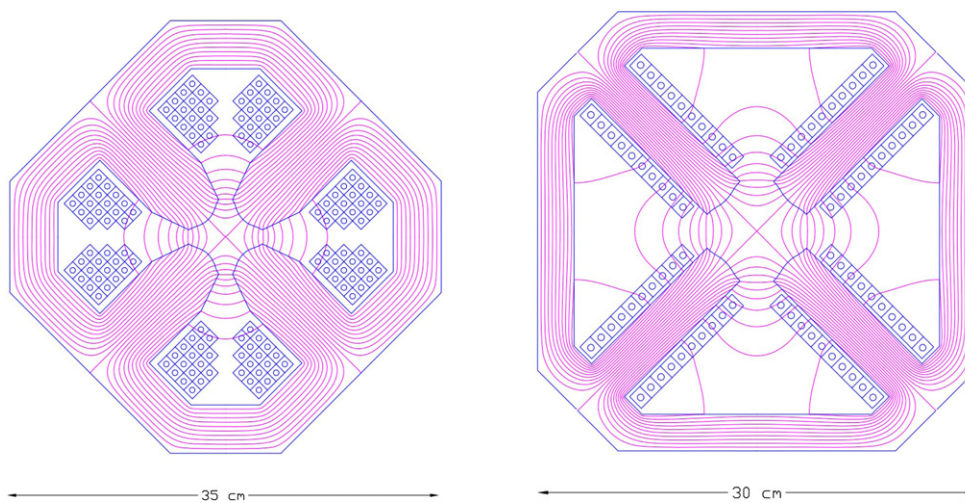
## 10.6. LINAC and superconducting RF system

Each of the two main linacs has an overall length of 828.8 m and provides an acceleration of 8.114 GV. Each linac consists of 112 cryomodules, arranged in 28 units of four cryomodules, with their focussing elements—each cryomodule contains four five-cell cavities, optimised to operate with a large beam current (up to 120 mA at the high-order mode (HOM) frequencies). The operating temperature is 2 K; the cavities are based on modern SRF technology and are fabricated from bulk Nb sheets; they are described in detail in section 10.6.2 below. The nominal acceleration gradient is  $19.73 \text{ MV m}^{-1}$ .

In addition to the main linacs, the synchrotron losses in the arcs will make additional linacs necessary, referred to here as *loss-compensation linacs*. These will have to provide different accelerations in the different arcs, depending on the energy of the beams, as shown in table 39.

**Table 37.** 50 GeV ERL—main parameters of the arc quadrupoles.

Parameter	Unit	Value
Beam energy	GeV	8.62–49.19
Field gradient	$\text{T m}^{-1}$	9.25–40.75
Magnetic length	m	1
Aperture radius	mm	25
Mass	kg	550
Number of magnets		1518
Current at 40.75 $\text{T m}^{-1}$	A	560
Number of turns per pole		17
Current density at 40.75 $\text{T m}^{-1}$	$\text{A mm}^{-2}$	6.7
Conductor material		Copper
Magnet resistance	$\text{m}\Omega$	33
Power at 8.62 GeV	kW	0.5
Power at 16.73 GeV	kW	1.9
Power at 24.85 GeV	kW	3.7
Power at 32.96 GeV	kW	4.6
Power at 41.08 GeV	kW	7.2
Power at 49.19 GeV	kW	10.3
Total power consumption for six arcs	MW	7.1
Cooling		Water

**Figure 163.** 50 GeV ERL. Left: cross-section of the arc quadrupole magnets. Right: cross-section of the linac quadrupole magnets.

The quoted beam energies are at entry into the arc. Their natural placement would be at the end of the arcs, just before the combiner, where the different energy beams are still separate. The largest of these linacs would have to compensate for the synchrotron radiation (SR) losses at the highest energy, requiring a total acceleration of about 700 MV. The loss-compensation linacs will be detailed in section 10.6.6 below.

**Table 38.** 50 GeV ERL—main parameters of the linac quadrupoles.

Parameter	Unit	Value
Beam energy	GeV	8.62–49.19
Field gradient	T m <sup>-1</sup>	7.7
Magnetic length	m	0.25
Aperture radius	mm	30
Mass	kg	110
Number of magnets		56
Current at 7.7 T m <sup>-1</sup>	A	285
Number of turns per pole		10
Current density at 7.7 T m <sup>-1</sup>	A mm <sup>-2</sup>	3
Conductor material		Copper
Magnet resistance	mΩ	6
Power at 8.1 GeV	kW	0.5
Total power consumption 2 linacs	MW	0.03
Cooling		Water

**Table 39.** Synchrotron radiation losses for the different arc energies.

Section	Beam energy (GeV)	$\Delta E$ (MeV)
Arc one	8.62	3
Arc two	16.73	25
Arc three	24.85	80
Arc four	32.96	229
Arc five	41.08	383
Arc six	49.19	836

The beam passes twice through all arcs except arc six, once during acceleration and once during deceleration. These additional *loss-compensation linacs* are planned to operate at 1603.2 MHz, which allows simultaneous energy compensation for both the accelerated and the decelerated beam. This subject will be discussed in detail in a subsequent section 10.6.6.

**10.6.1. Choice of frequency.** The RF frequency choice primarily takes into account the constraints of the LHC bunch repetition frequency,  $f_0$ , of 40.079 MHz, while allowing for a sufficiently high harmonic,  $h$ , for a flexible system. For an ERL with  $n_{\text{pass}} = 3$  recirculating passes and in order to enable equal bunch spacing for the three bunches—though not mandatory—it was originally considered desirable to suppress all harmonics that are not a multiple of  $n_{\text{pass}} \cdot f_0 = 120.237$  MHz. Initial choices were, for instance, 721.42 MHz ( $h = 18$ ) and 1322.61 MHz ( $h = 33$ ) in consideration of the proximity to the frequencies used for state-of-the-art SRF system developments worldwide [812]. However, in synergy with other RF system developments at CERN, the final choice was 801.58 MHz ( $h = 20$ ), for which the bunching between the three recirculating bunches can be made similar but not exactly equal. Note that this frequency is also very close to the 805 MHz SRF proton cavities operating at the Spallation Neutron Source (SNS) at Oak Ridge National Laboratory (ORNL), so that one could leverage that experience in regard to cryomodule and component design at this frequency.

Furthermore, in the frame of an independent study for a 1 GeV CW proton linac, a capital plus operational cost optimisation was conducted [813]. This optimisation took into account

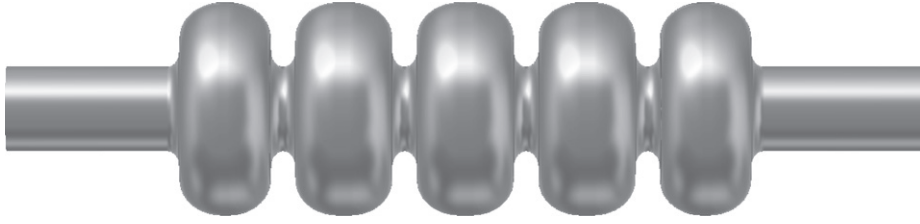


**Figure 164.** Bare 802 MHz five-cell cavity design (RF vacuum) with a 130 mm iris and beam tube aperture. Reproduced from [7]. © IOP Publishing Ltd. CC BY 3.0.

**Table 40.** Parameter table of the 802 MHz prototype five-cell cavity.

Parameter	Unit	Value
Frequency	MHz	801.58
Number of cells		5
Active length $l_{\text{act}}$	mm	917.9
Loss factor	VpC <sup>-1</sup>	2.742
$R/Q$ (linac convention)	$\Omega$	523.9
$R/Q \cdot G$ per cell	$\Omega^2$	28 788
Cavity equator diameter	mm	327.95
Cavity iris diameter	mm	130
Beam tube inner diameter	mm	130
Diameter ratio equator/iris		2.52
$E_{\text{peak}}/E_{\text{acc}}$		2.26
$B_{\text{peak}}/E_{\text{acc}}$	mT (MV <sup>-1</sup> m <sup>-1</sup> )	4.2
Cell-to-cell coupling factor $k_{\text{cc}}$	%	3.21
TE <sub>11</sub> cutoff frequency	GHz	1.35
TM <sub>01</sub> cutoff frequency	GHz	1.77

the expenditures for cavities, cryomodules, the linac tunnel as well as the helium refrigerator expenses as a function of frequency and thus component size. Labour costs were included based on the existing SNS linac facility work breakdown structure. It was shown that capital plus operating costs could be minimised with a cavity frequency between 800 MHz and 850 MHz, depending also on the choice of the operating He bath temperature (1.8–2.1 K). The clear benefits of operating in this frequency regime are the comparably small dynamic RF losses per installation length due to a relatively small BCS surface resistance, as well as the low residual resistance of the niobium at this operating temperature. This could be principally verified as part of the prototyping effort detailed in the next sub-section. Note that the cost optimum also favours cavities operating at rather moderate field levels ( $< 20\text{MV m}^{-1}$ ). This is seen as a benefit, given concerns about field emission and associated potential performance degradation.

**10.6.2. Cavity prototype.** Given the RF frequency of 801.58 MHz, the Jefferson Laboratory (JLab) has collaborated with CERN, and consequently proposed a five-cell cavity design that was accepted for prototyping, see figure 164. The cavity shape has also been adopted for PERLE. Table 40 summarises the relevant cavity parameters.

The cavity exhibits a rather large iris and beam tube aperture (130 mm) to support the examination of beam-dynamical aspects such as HOM-driven multibunch instabilities. Despite the

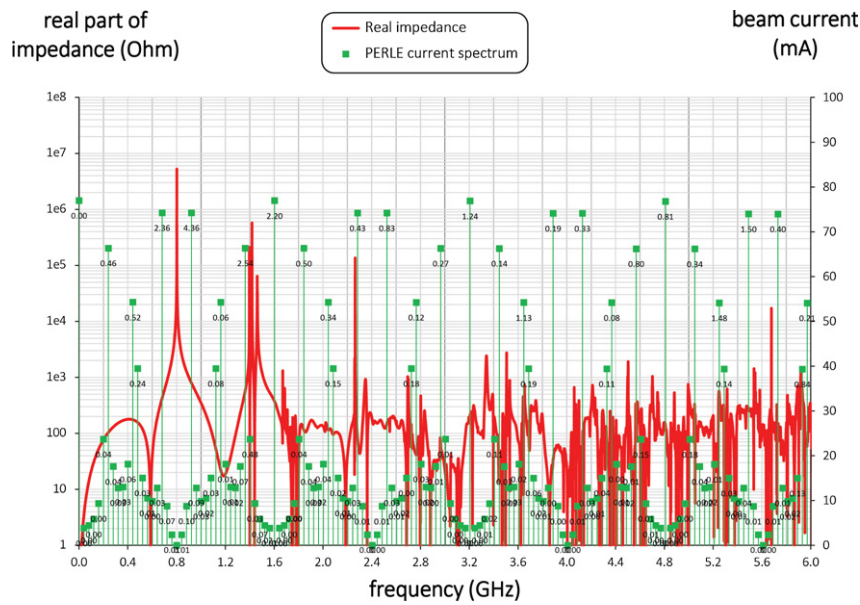


**Figure 165.** Real monopole impedance spectrum of the five-cell 802 MHz cavity prototype (red) together with the considered beam-current lines (green) for the three-pass PERLE machine (25 mA injected current). The numbers associated with the spectral lines denote the power dissipation (in W).

relatively large aperture, the ratios of the peak surface electric field,  $E_{pk}$ , with respect to the peak surface magnetic field,  $B_{pk}$ , and the accelerating field,  $E_{acc}$ , are reasonably low, while the factor  $R/Q \cdot G$  is concurrently kept reasonably high to limit cryogenic losses. This is considered to be a generically well-balanced cavity design [814]. The cavity cell shape also avoids the problem whereby crucial HOMs will coincide with the main spectral lines (multiples of 801.58 MHz), while the specific HOM coupler development is pending.

Furthermore, as shown in figure 165 for the case of the bunch recombination pattern originally considered for PERLE, the much denser intermediate beam-current lines (green) do not coincide with the cavity HOMs. Here, the figure plots the real part of the beam-excited cavity monopole impedance spectrum up to 6 GHz, and denotes the power deposited at each spectral line (in W) for an injected beam current of 25 mA. For instance, the summation of the power in this spectral range results in a moderate 30 W. This covers the monopole modes with the highest impedances residing below the beam tube cutoff frequency. The HOM-induced heat has to be extracted from the cavity and shared among the HOM couplers attached to the cavity beam tubes. The fraction of the power that escapes through the beam tubes above the cutoff frequency can be intercepted by beamline absorbers.

Note that for figure 165 a single HOM-coupler end-group consisting of three scaled TeV Superconducting Linear Accelerator (TESLA)-type coaxial couplers was assumed to provide damping. Instead of coaxial couplers, waveguide couplers could be utilized, which, for instance, have been developed at JLab in the past for high-current machines. These are naturally broadband and designed for high power capability, though a penalty is introduced, as this will increase the complexity of the cryomodule. Ultimately, the aim is to efficiently damp the most parasitic longitudinal and transverse modes (each polarization). An evaluation of the



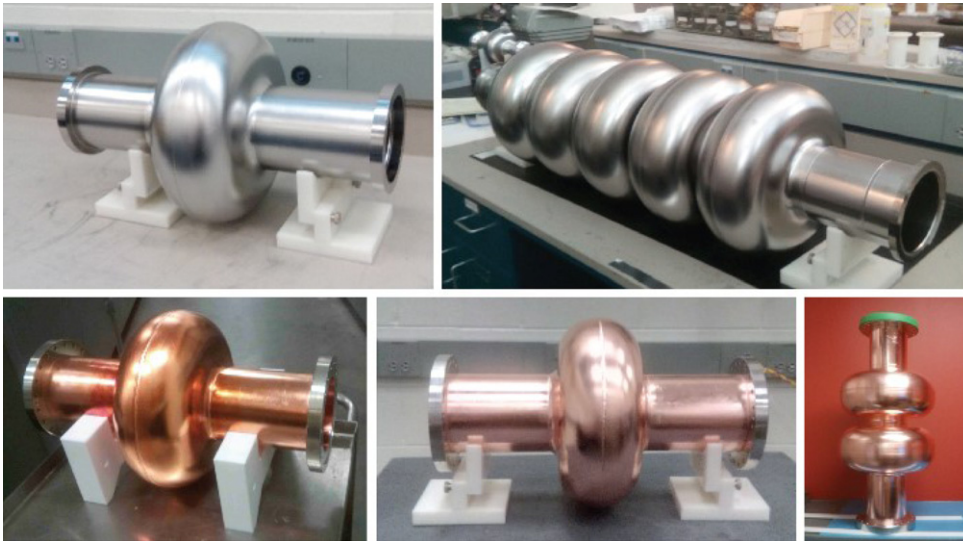


**Figure 166.** Ensemble of 802 MHz cavities designed and built at JLab for CERN. The Nb cavities have been tested vertically at 2 K in JLab’s vertical test area.

total power deposition is important for the LHeC, in order to decide which HOM coupler technology is most appropriate to cope with the dissipated heat and whether active cooling of the couplers is a requirement.

Though the prototype efforts focussed on the five-cell cavity development, JLab also produced single-cell cavities, i.e. one further Nb cavity and two OFE copper cavities. The former has been shipped to the Fermi National Accelerator Laboratory (FNAL) for N-doping/infusion studies, while the latter were delivered to CERN for Nb thin-film coating as a possible alternative to bulk Nb cavities. In addition, a copper cavity was built for low-power bench measurements, for which multiple half-cells can be mechanically clamped together. Currently, a mock-up can be created with up to two full cells. This cavity has been produced to support the pending HOM coupler development. The ensemble of manufactured cavities resonating at 802 MHz is shown in figure 166.

Results for the Nb cavities—made from fine-grained high-residual-resistivity-ratio (RRR) Nb—were encouraging, since both cavities achieved accelerating fields,  $E_{acc}$ , slightly greater than  $30 \text{ MV m}^{-1}$  and were ultimately limited by thermal breakdown (quench). Moreover, the RF losses were rather small, as a benefit of the relatively low RF frequency, as anticipated. The residual resistance extracted from the measurement data upon cooldown of the cavity was  $3.2 \Omega \pm 0.8 \Omega$ . This resulted in unloaded quality factors,  $Q_0$ , well above  $4 \times 10^{10}$  at 2 K at low field levels, while  $Q_0$ -values of more than  $3 \times 10^{10}$  could be maintained for the five-cell cavity at up to  $\sim 27 \text{ MV m}^{-1}$  (see figure 167). Only standard interior surface post-processing methods were applied, including bulk buffered chemical polishing, high-temperature vacuum annealing, light electropolishing, ultrapure high-pressure water rinsing, and a low temperature bakeout. While the vertical test results indicate generous headroom for a potential performance reduction once a cavity is equipped with all the ancillary components and installed in a cryomodule, clean cavity assembly procedure protocols must be established for the cryomodules to minimise the chance of introducing field-emitting particulates.

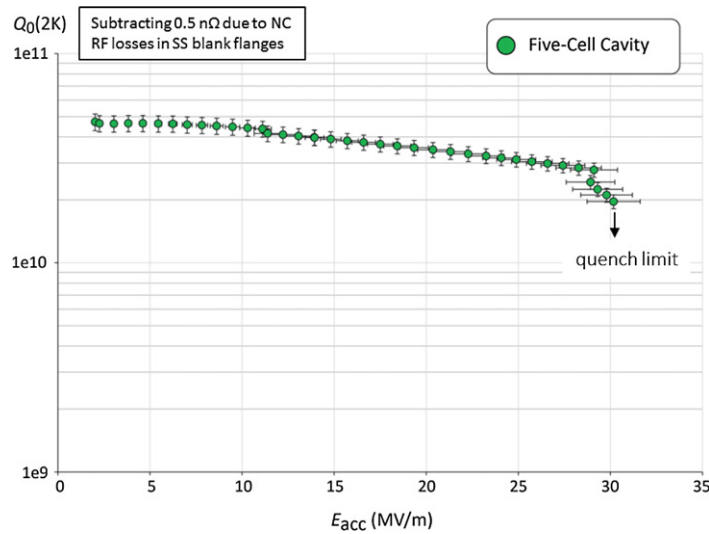


**Figure 167.** Vertical test results for the five-cell 802 MHz niobium cavity prototype.

**10.6.3. Cavity cryomodule.** The ERL cryomodules hosting the superconducting RF cavities are a key component of the accelerator. They should provide the proper mechanical, vacuum, and cryogenic environment for the SRF cavities equipped with their ancillary systems: helium tank, power coupler, and HOM couplers. Each cryomodule contains four superconducting 801.58 MHz five-cell elliptical cavities, as described in the previous chapters.

Recently, several projects worldwide have designed cryomodules for elliptical cavities with a cavity configuration (number, length and diameter) quite close to that required by the LHeC ERLs:

- SNS [815]: two different-sized cryomodules hosting either four elliptical six-cell 805 MHz cavities of  $\beta = 0.81$  or four elliptical 805 MHz six-cell cavities of  $\beta = 0.61$ ;
- SPL [816]: a cryomodule designed to integrate four elliptical five-cell 704 MHz cavities of  $\beta = 1$ ;
- European Spallation Source (ESS) [817]: two cryomodules of the same length that can host either four elliptical six-cell 704 MHz cavities of  $\beta = 0.67$  or four elliptical five-cell 704 MHz cavities of  $\beta = 0.85$ .

These three cryomodule designs are based on two completely different concepts for the cavity string support structure. The SNS and ESS cryomodules are based on an intermediate support system, called the spaceframe, which is horizontally translated inside the cryomodule vacuum vessel. The low-pressure cryogenic line is located above the cavity string and connected to the cryogenic transfer line by a double-angled connection, the jumper. RF waveguides are connected underneath the cryomodule, using a doorknob transition to the couplers. All the hanging and alignment operations of the cavity string and shielding are implemented outside the vacuum tank, using the spaceframe. In the ESS case, each cavity is hung by two sets of four cross-rods. The thermal shield is also hung from these rods by means of aluminium ‘elastic boxes’ that allow for thermal shrinkage while maintaining transverse stability. The thermal shield is made of 2.5 mm-thick aluminium and wrapped with multilayer insulation. It is directly fastened to the support rods of the cavity string.

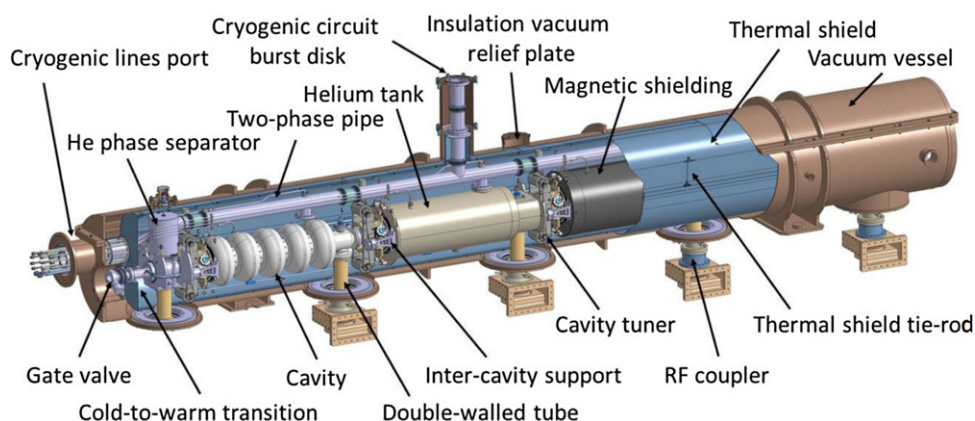


**Figure 168.** SPL cryomodule—general assembly view.

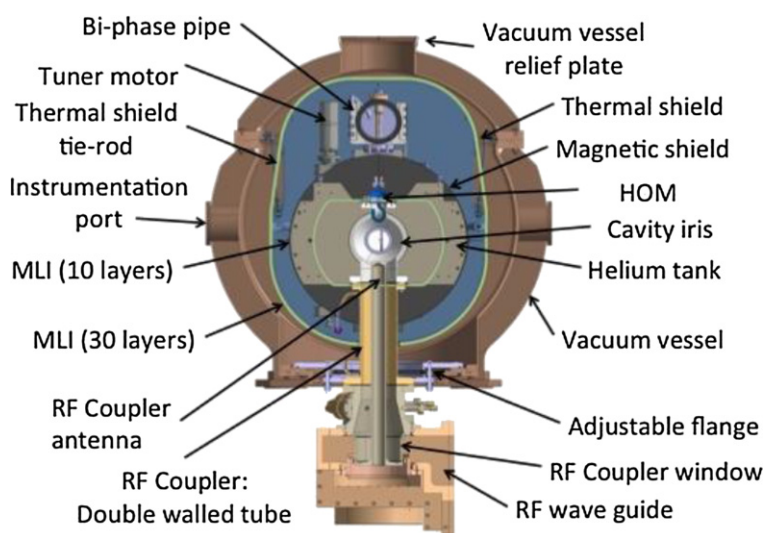


**Figure 169.** Cross-section of the SPL cryomodule.

In the SPL cryomodule, the cavity string is directly supported by the power coupler and by dedicated inter-cavity support features. Moreover, the SPL cryomodule integrates a full-length demountable top lid, enabling cavity string assembly to be performed from the cryomodule top (figure 168). The thermal shield is made of rolled aluminium sheets, and is composed of four main parts assembled before the vertical insertion of the string of cavities. The shield, wrapped in multilayer insulation, is suspended from the vacuum vessel via adjustable tie rods made of titanium alloy which also address its thermal contractions by angular movements. The cavity stainless-steel helium tanks are connected by a 100 mm-diameter two-phase pipe placed above the cavities. This pipe ensures that liquid feeds into the cavities by gravity, and is also used as a pumping line for gaseous helium.

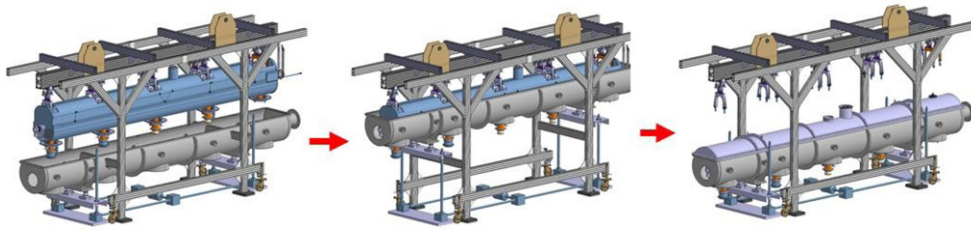


**Figure 170.** Cryomodule assembly procedure main steps.

With the aim of minimizing static heat loads from room temperature to 2 K by solid thermal conduction, the number of mechanical elements bridging the two extreme temperatures is reduced to the strict minimum: the cavities are directly supported via the external conductor of the RF coupler (figure 169), the double-walled tube. The latter is made out of a stainless-steel tube with an internal diameter of 100 mm, which is actively cooled by gaseous helium circulating inside a double-walled envelope in order to improve its thermal efficiency.

An additional supporting point that maintains cavity straightness and alignment stability within the required levels is obtained by supporting each cavity on the adjacent one via the inter-cavity support, which is composed of a stem sliding inside a spherical bearing. As a result, a pure vertical supporting force is exchanged by adjacent cavities, while all other degrees of freedom remain unrestrained, allowing thermal contraction movements to occur unhindered. The thermo-mechanical behaviour of this supporting system has been extensively studied on a dedicated test bench at CERN, proving its efficiency and reliability.

There are some specific additional constraints or requirements for a cryomodule to be used in an ERL, and some of them are quite challenging. The first set of constraints is linked to the CW operation of the cryomodules (in contrast to operation at SNS, SPL, and ESS, which are pulsed accelerators), where the dynamic heat loads are much larger than the static ones. Thus, reaching high  $Q_0$  (low cryogenic losses) is a main objective in these machines and besides specific optimization of cavity design and preparation (such as N-doping), magnetic shielding should be carefully studied in terms of the material, operating temperatures, number of layers, and active and/or passive shielding. Another important constraint is linked to the relatively high power to be extracted by the HOM couplers: a thermal analysis should be carefully performed to obtain an optimized evacuation of the HOM thermal load, so as not to degrade the cryogenic performance of the cryomodule.

At present the use of the existing SPL components is investigated to convert the original module to an rf frequency of 800 MHz and to employ it in the PERLE project at Orsay, which would serve as a validation of the cryomodule design and performance. One of the clear advantages of the SPL configuration is a much-simplified assembly procedure (figure 170), due to its top-lid configuration, which also allows easier maintenance.

The first study performed was to analyse the possibility of integrating the ERL cavities instead of the SPL ones. The 802 MHz cavities are a little bit shorter than the SPL ones and the cells are also smaller in diameter. The beam port internal diameter is about the same, as is the power coupler port. As a result, the SPL cryomodule is well suited for ERL 802 MHz superconducting cavities from the geometrical point of view, and they could be easily integrated, given minor mechanical feature adaptations.

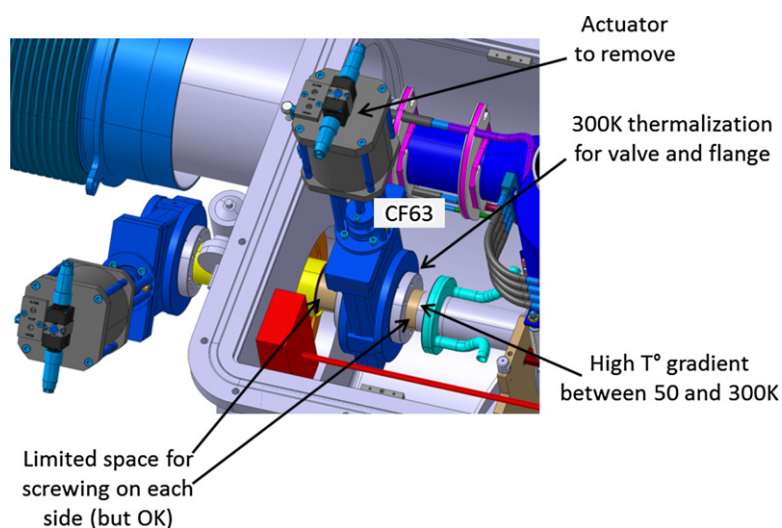


**Figure 171.** The two-stage vacuum valve solution for adapting the SPL cryomodule prototype to the 802 MHz cavities of the LHeC ERL.

The second analysed point is the beam vacuum. As the existing SPL cryomodule design was produced for a prototype, intended for RF and cryogenic testing only, without a beam, the vacuum valve is a VAT CF63 ‘vatterfly’ valve with viton seal and manual actuator, which is not adapted for a real operating cryomodule. Integration of an all-metal gate valve instead is not an issue and we also designed a specific solution based on two-stage valves (figure 171) to adapt the already fabricated SPL prototype cryomodule to the integration of 802 MHz cavities.

The third study performed examined the compatibility of the SPL cryogenic features with the ERL requirements. The SPL cryomodule was designed to operate 702 MHz cavities at  $25 \text{ MV m}^{-1}$  with a  $Q_0$  of  $5 \times 10^9$  and an 8.2% duty cycle. The LHeC ERL will operate SRF cavities in the CW regime, but at a lower field strength ( $20 \text{ MV m}^{-1}$ ) and with a higher expected  $Q_0$  at the nominal gradient (about  $1.5 \times 10^{10}$ ). As a result, and despite the different duty cycle, the dynamic cryogenic losses are estimated to be only about 30% more in the ERL case. The overall cryogenic dimensioning is then fully compatible, given some unavoidable adaptation of a few internal cryogenic pipes. The main issue that still has to be addressed is the need and consequences of the HOM coupler cooling. Even if the current engineering analysis showed that this point will not be a showstopper, it might have an impact on some cryogenic piping and cooling circuits.

Detailed engineering studies are being pursued to transform the SPL cryomodule prototype into an ERL LHeC cryomodule prototype. We are taking advantage of all the design and fabrication work previously performed on the SPL, and also of the fact that some parts, such as the thermal and magnetic shielding, are not yet fabricated and could be exactly adapted to the ERL requirements. This will offer the possibility of having an earlier full prototype cryomodule RF and cryogenic test than in a standard experimental plan, in which the complete study and fabrication is started from scratch.



**Table 41.** General specification of the LHeC ERL electron source.

Parameter	Unit	Value
Booster energy	MeV	7
Bunch repetition rate	MHz	40.1
Average beam current	mA	20
Bunch charge	pC	500
RMS bunch length	mm	3
Normalised transverse emittance	$\pi$ mm mrad	<6
Uncorrelated energy spread	keV	10
Beam polarisation		Unpolarised/polarised

#### 10.6.4. Electron sources and injectors.

**10.6.4.1. Specification of the electron source** The operation of the LHeC with an electron beam delivered by a full-energy ERL imposes specific requirements on the electron source. It should deliver a beam with the charge and temporal structure required at the interaction point. Additionally, because both the longitudinal and transverse emittances of the beam are increased during acceleration in a high-energy ERL due to SR, the 6D emittance of the beam delivered by the electron source should be small enough to mitigate this effect. The general specifications of the electron source are shown in table 41. Some parameters in this table, such as the RMS bunch length, uncorrelated energy spread, and normalised transverse emittance are given on the basis of the requirements for the acceleration in the ERL and to pre-compensate for the effects of SR. The most difficult of the parameters to specify is the injector energy. It should be as low as possible to reduce the unrecoverable power used to accelerate the beam before injection into the ERL, while still being high enough to deliver short electron bunches with high peak current. Another constraint on the injection energy is the average energy and energy spread of the returned beam. The average energy cannot be less than the energy of the electron source, but the maximum energy in the spectrum should not exceed 10 MeV (the neutron activation threshold). An injection energy of 7 MeV is a reasonable compromise to meet this constraint.

The required temporal structure of the beam and the stringent requirements for beam emittance do not allow the use of conventional thermionic electron sources for the LHeC ERL without using a bunching process that involves beam losses. While this option cannot completely be excluded as a source of unpolarised electrons, the additional requirement to deliver a polarised beam can only be met by photoemission-based electron sources.

There are now four possible electron source designs for delivering unpolarised beams and (potentially) three for delivering polarised beams:

- (a) A thermionic electron source with an RF-modulated grid or gate electrode followed by (multi)stage compression and acceleration. The electron source could either be a DC electron gun or an RF electron source in this case. Although these sources are widely used in the injectors of infra-red free-electron lasers (FELs) [818], their emittance is not good enough to meet the specifications of the LHeC injector. Moreover, thermionic sources cannot deliver polarised electrons.
- (b) A VHF photoemission source. This is a type of normal conducting RF source which operates in the frequency range 160–200 MHz. The relatively low frequency of these sources means that they are large enough that sufficient cooling could be provided to permit CW operation. This type of source has been developed for the new generation of CW FELs such as the Linac Coherent Light Source II (LCLS-II) [819], the Shanghai



High-Repetition-Rate XFEL and Extreme Light Facility (SHINE) [820] and a back-up option of the European XFEL upgrade [821], but they have not yet demonstrated the average current required for the LHeC injector. The possibility of generating polarised electrons with this type of source has not yet been investigated.

- (c) A superconducting RF photoemission source. This type of source is under development for different applications such as CW FELs (for example, the Electron Linear accelerator with high Brilliance and Low Emittance (ELBE) [822], the SRF option of the LCLS-II injector [823], and the European XFEL upgrade [824]), as the basis of injectors for ERLs (the Berlin Energy Recovery Linac Project (bERLinPro) [825]), and for electron cooling (BNL [826]). Though this type of source has already demonstrated the possibility of delivering the average current required for the LHeC with unpolarised beams (BNL), and has the potential for operation with GaAs-type photocathodes (Helmholtz-Zentrum Dresden-Rossendorf (HZDR)) which are required for the delivery of polarised beams, the current technology of SRF photoelectron sources cannot be considered mature enough for use in the LHeC.
- (d) A DC photoemission source. In this type of source, the electrons are accelerated immediately after emission by a potential difference between the source cathode and the anode. This type of source is the most commonly used source in ERL injectors. It has been used in projects which are already complete (JLab [827], Daresbury Laboratory [828]), is being used for ongoing projects (at KEK in Tsukuba, Japan [829] or CBETA at Cornell Laboratory, USA [830]) and is planned to be used in new projects such as the LHeC prototype, PERLE [831]. The technology of DC photoemission sources is well developed and has demonstrated the average current and beam emittance required for the LHeC ERL (Cornell). Another advantage of a photoelectron source with DC acceleration is the possibility of operation with GaAs-based photocathodes to deliver a polarised beam. Currently, this is the only source that can deliver highly polarised electron beams with a current of several mA, which is already in the range of the LHeC specifications (JLab [832]).

Based on this analysis at the CDR stage, we consider the use of a DC photoemission source as the basic option, keeping in mind that in the course of the injector development, other types of electron source may be considered, especially for the provision of an unpolarised beam.

*10.6.4.2. The LHeC unpolarised injector* . The injector layout follows the scheme depicted in figure 172. Its design will be similar to the unpolarised variant of the PERLE injector [831]. The electron source delivers a CW beam that has the required bunch charge and temporal structure using DC acceleration. Immediately after the source, there is a focussing and bunching section, consisting of two solenoids with a normal conducting buncher placed between them. The solenoids have two purposes. The first is to control the transverse size of the space-charge-dominated beam, which would otherwise rapidly expand transversely. This ensures that the beam will fit through all of the apertures in the injector beamline. Secondly, the solenoids are used for emittance compensation to counter the space-charge-induced growth in the projected emittance. This is then followed by a superconducting booster linac, which accelerates the beam up to its injection energy, provides further longitudinal bunch compression, and continues the emittance compensation process.

The DC electron source will have an accelerating voltage of 350 kV using a high-quantum-efficiency antimonide-based photocathode, such as Cs<sub>2</sub>K<sub>2</sub>Sb. The photoinjector laser required for this cathode type will be a 532 nm green laser. A load-locking system will be provided, to allow photocathodes to be replaced without breaking the source vacuum. This significantly reduces the downtime required for each replacement, which is a major advantage in a user facility such as the LHeC, where maximising uptime is very important. The cathode electrode

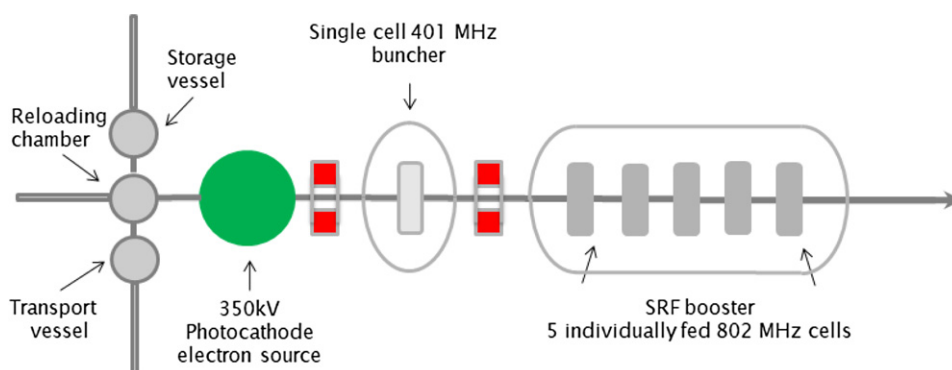


**Figure 172.** The layout of the unpolarised injector. Reproduced from [7]. © IOP Publishing Ltd. CC BY 3.0.

will be mounted from above, similarly to the Cornell [833] and KEK [834] sources. This electrode geometry makes the addition of a photocathode exchange mechanism much easier, as the photocathode can be exchanged through the back of the cathode electrode. In addition, the cathode electrode will be shaped to provide beam focussing. The source's operational voltage of 350 kV was chosen as practical estimate of what is achievable. A higher voltage would produce better performance, but would be challenging to achieve in practice. The highest operational voltage successfully achieved is 500 kV, which is produced by the DC electron source that is used for the compact Energy Recovery Linac (cERL) injector [835]. However, 350 kV is sufficient to achieve the required beam quality [831].

**10.6.4.3. Polarised electron source for ERL** . Providing polarised electrons has always been a challenging process, especially at relatively high average currents, as required for the LHeC. The only practically usable mechanism for producing polarised electrons is the illumination by circularly polarised laser light of GaAs-based photocathodes that are activated to the negative-electron-affinity state. The vacuum requirements for these cathodes mean that this must be done using a DC electron source only. In the course of the last 30 years significant progress has been achieved in improving the performance of polarised electron sources. The maximum achievable polarisation has reached 90% and the maximum quantum efficiency (QE) of the photocathode at the laser wavelength that produces the maximum polarisation has reached 6%. Meanwhile the implementation of a polarised electron source at the LHeC remains a challenge, as the practical operational charge lifetime of the GaAs-based photocathode does not exceed hundreds of Coulombs (JLab [836]) at an operational current in the mA range.

Figure 173 shows a preliminary design for the LHeC polarised-electron injector. In general, the design of the polarised-electron injector is close to that of the unpolarised-electron injector and is based on a DC electron source in which a photocathode is illuminated by a pulsed laser beam. The choice of a DC source is dictated by the necessity of achieving an extra high vacuum, with a pressure at a level of  $10^{-12}$  mbar, in the photocathode area. This level of vacuum is necessary to give the photocathode a long lifetime. In order to reduce photocathode degradation caused by electron stimulated gas desorption, the accelerating voltage in the source is reduced to 220 kV. The main differences, compared to an unpolarised-electron injector, are the presence of a photocathode preparation system (permanently attached to the source), and a Wien-filter-based spin manipulator between the source and the buncher. In order to reduce depolarisation of the beam in the spin manipulator, caused by the space-charge-induced energy spread of the

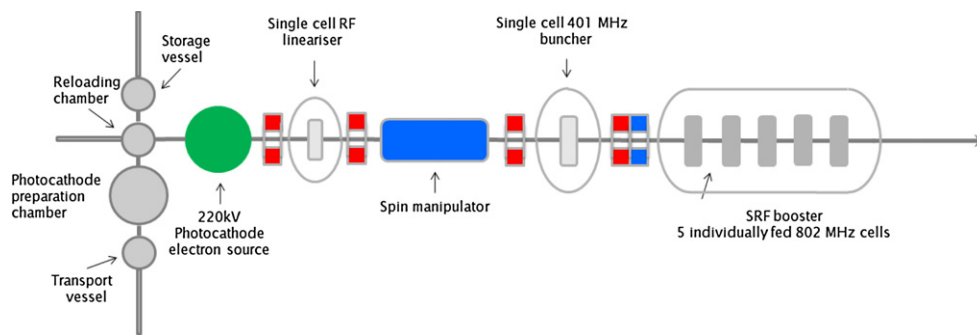


**Figure 173.** The layout of the polarised-electron injector.

beam, an RF dechirper is installed between the source and the spin manipulator. The injector is also equipped with a Mott polarimeter to characterise the polarisation of the beam delivered by the source.

An important consideration behind operating with interchangeable photocathodes is to minimise the downtime required for photocathode exchange. It typically takes a few hours to replace the photocathode and to characterise the polarisation of the beam. For a large facility such as the LHeC, this is unacceptable. A practical solution could be to deploy two or more electron sources which operate in rotation, in a similar manner to that proposed at BNL [837]. Another motivation for using a multisource injector is the nonlinear dependence of the photocathode charge lifetime on the average beam current (JLab [832]), which reduces with an increase in the average current. For example, in the case of three electron sources, two of them can be operated at half of the operational frequency (20.05 MHz) in opposite phases, delivering an average current of 10 mA each, while the third is in a standby regime and has a freshly activated photocathode. The only time when it is necessary to switch it on is the rise time of the high voltage. Another advantage of using a multisource scheme is the reduction of the average laser power deposited on the photocathode and, as a result, relaxed requirements for photocathode cooling. The implementation of a multisource polarised electron injector requires the development of a deflection system that is able to merge beams from different sources before they reach the the spin rotator.

**10.6.4.4. Lasers as electron sources** . In the proposed design of the LHeC injection system at least two lasers must be used. In the unpolarised-electron injector, which is going to operate with an antimionide-based photocathode, a laser with a wavelength of 532 nm is required. The typical initial QE of these photocathodes is 10%, and for practical application, a QE reduction of up to 1% may be expected. For a polarised electron source, the typical QE varies from 1% down to 0.1% and a laser with a wavelength of 780 nm is required. The optimised parameters of the required lasers are summarised in table 42. The laser's temporal profile and spot size on the photocathode are given on the basis of source optimisation for operation at 350 kV for the unpolarised regime and at 220 kV for the polarised regime.

#### 10.6.5. Positrons.

**10.6.5.1. Physics and intensity considerations** . Variations of the beam conditions (energies, lepton charge and polarisation, hadron types) provide a considerable extension of the physics programme of the LHeC. The LHC permits the proton-beam energy to be varied between about 1 and 7 TeV. It is a proton collider with options for heavy ions (primarily Pb),

**Table 42.** Parameters of the electron source drive laser.

Laser beam parameter	Unit	Unpolarised mode	Polarised mode
Laser wavelength	nm	532	780
Laser pulse repetition rate	MHz	40.1	40.1
Energy in a single pulse at the photocathode with QE = 1%	$\mu\text{J}$	0.12	
Average laser power at the photocathode with QE = 1%	W	4.7	
Energy in a single pulse at the photocathode with QE = 0.1%	$\mu\text{J}$		0.79
Average laser power at the photocathode with QE = 0.1%	W		32
Laser pulse duration	ps FWHM	118	80
Laser pulse rise time	ps	3.2	3.2
Laser pulse fall time	ps	3.2	3.2
Spot diameter on the photocathode's surface	mm	6.4	8
Laser spot shape on the photocathode's surface		Flat top	

and possibly lighter ones. The electron-beam energy may be varied between about 10 and the maximum of 50 (or eventually 60) GeV. Highly intense polarised electron-beam sources are under development, which will allow detailed investigations of weak interactions and searches for NP to be performed through variations of the electron-beam helicity,  $P$ . An advantage of the linac is that it can achieve very high values of  $P$ , compared to a ring electron accelerator in which the polarisation build-up due to the Sokolov–Ternov effect [838] runs into serious difficulties at higher energies. The electron-beam polarisation at HERA was limited to about 40%. Positrons are a genuine challenge for the LHeC and also for future  $e^+e^-$  linear colliders, because of the difficulty of generating intense beams, as already discussed for the LHeC in quite some detail in the 2012 CDR [1].

The physics reasons for wanting to use positrons at the LHeC are fairly obvious: positrons permit us to establish, exploit, and question the existence of charge symmetry, which may lead to discoveries. For example, the charm tagging process in electron-initiated CC scattering measures the anti-strange quark density  $x\bar{s}(x, Q^2)$  in the proton. There are expectations that the difference  $x(s - \bar{s})$  may be non-zero, i.e. that a strange-quark valence component exists. That would also require a precision measurement of  $x s(x, Q^2)$  for which one needs about  $1 \text{ fb}^{-1}$  of integrated  $e^+p$  luminosity, and preferably more. Further reasons presented in the CDR [1] include the nature of excited leptons, the origin of CIs, the spectroscopy of leptoquarks, the understanding of DIS, the measurement of  $F_L$  in the case in which the signal is charge sensitive but the background at high inelasticity is dominantly charge symmetric, the thorough resolution of the parton contents of hadrons, etc. Thus, one indeed has many reasons to also operate the LHeC as a positron–hadron collider.

However, from today's perspective, one has to be realistic in one's assumptions about the intensity that may realistically be achievable and required in the positron linac–proton ring configuration. The current luminosity goal of the LHeC had been set using the observation that the Higgs production cross-section in  $ep$  is about 200 fb, comparable to that of the  $e^+e^-$  colliders, and that the LHeC could become a Higgs factory [839]. Higgs production at the LHeC is dominantly due to  $e^-p \rightarrow \nu H X$  scattering, i.e. the LHeC has a competitive Higgs physics potential which is complementary to the  $e^+e^-$  and  $pp$  modes, as the dominant production mechanisms

**Table 43.** Characteristics of positron beams for the CLIC, the ILC, and the LHeC. Note that the muon collider target value in the Low EMittance Muon Accelerator (LEMMA) scheme is about  $4 \times 10^{16} e^+ s^{-1}$ .

Parameter	CLIC	ILC	LHeC
Energy (GeV)	1500	250	50
$e^+$ /bunch ( $10^9$ )	3.7	20	2
Norm. emittance (mm mrad)	0.66 (H)	10 (H)	50
	0.02 (V)	0.04 (V)	50
Norm. emittance (eV m)	5000	60 000	5000
Repetition rate (Hz)	50	10	CW
Bunches/s	15 600	26 250	$2 \times 10^7$
$e^+$ flux ( $10^{15} e^+ s^{-1}$ )	0.1	0.4	1–10

are  $WW-H$ ,  $Z^*-HZ$ , and  $gg-H$ , respectively. The electron–proton CC Higgs cross-section is much larger than that in positron–proton scattering, which is related to the dominance of up quarks as compared to down quarks in the proton. Much of the running optimisation used in this paper has targeted the maximisation of the number of Higgs events and the preference for electron operation over positron operation.

The target electron current required to achieve a  $10^{34} \text{ cm}^{-2} \text{ s}^{-1}$  luminosity has been set at 20 mA. This originates from a 500 pC gun which, for a 40 MHz LHC operational frequency, leads to a charge of  $3 \times 10^9$  electrons per bunch, corresponding to  $1.2 \times 10^{17} e^- s^{-1}$ . Given the current and near-future status of positron intensity requirements, one may set an LHeC target of the order of  $10^{15-16} e^+ s^{-1}$ . Note that the normalised transverse emittance of the electron beam is 50 mm mrad and the longitudinal emittance is 5 MeV mm.

The intensity above would potentially provide a luminosity of the order of  $1-10 \text{ fb}^{-1}$  within one year. With a drastic difference in the electron and positron intensities, later operation would favour  $e^- p$  over  $e^+ p$  running to maximise the statistics. We thus assume  $e^+ p$  would operate for about a year, which is fairly comparable to the heavy ion operation of the LHC. In the physics studies, for example, those of PDF and electroweak measurements, we have used values of integrated  $e^+ p$  luminosities corresponding to these assumptions. It was also assumed that the positrons were not polarised. The linac–ring  $ep$  configuration thus has a highly polarised, intense electron beam and a less intense, unpolarised positron beam. The ring–ring configuration, which is still a possible backup for the LHeC at the HE-LHC, has intense electron and positron beams but with rather lower polarisations.

**10.6.5.2. Positron sources** . One can compare the LHeC  $e^+$  intensity target with the goals for the CLIC and the ILC, as listed in table 43. One finds that the chosen LHeC value is more demanding than those of the CLIC and the ILC.

Recently, the interest in very intense  $e^+$  production has been renewed with the revival of the muon collider studies and the so-called LEMMA proposal [840] to generate muons from  $e^+e^-$  pairs (i.e. not from pion decays), to achieve small-emittance beams. This requires the generation of an intense 45 GeV-energy positron beam that annihilates electrons from a target for muon pair production near the threshold. In a study subsequent to the LEMMA proposal, a target positron intensity of  $3.9 \times 10^{16} e^+ s^{-1}$  was established [841], which requires considerable research and development effort.

A conventional positron source only uses a single amorphous target. An electron beam hits the target, where bremsstrahlung and pair production take place. Downstream from the target, particular devices (a quarter-wave transformer (QWT) or an adiabatic matching device (AMD))

allow the capture of as many positrons as possible, with a large emittance. The CLIC  $e^+$  source [842] takes advantage of a hybrid target design. A thin crystal target allows a reduction of the peak power deposition and enhances photon production via a channelling process. It is followed by an amorphous target that converts the photons into positrons. In between, a magnet sweeps out charged particles.

The ILC  $e^+$  source [843] takes advantage of a long helical undulator that uses the high-energy electron beam of the collider. The electron beam passing through the undulator produces polarised photons by impinging on a moving target, the design of which is still to be finalised. This target converts photons into positrons. The ILC-type positron source is not an option for the LHeC, since it requires an electron-beam energy of more than 100 GeV.

One option considered for the initial LHeC  $e^+$  source [1] was the use of ten hybrid targets in parallel. The bunch intensity and density would have been enhanced by a tri-ring transformer system that changed from the CW mode to the pulsed mode for accumulation, and back to the CW mode.

To evaluate the performance of  $e^+$  sources, one defines a *positron yield* parameter. This parameter is the number of positrons at a given place along the production channel, per electron, impinging on the target. It is crucial to improve the positron yield while keeping the peak energy density deposition (PEDD) and the shockwave inside the target within acceptable limits. The target lifetime suffers from cyclic thermal loads and stresses due to the beam pulses. The removal of the average power (in the kW to MW range) from the target is challenging and should be investigated for the reliability of the target. Heat dissipation in an amorphous target may be improved by replacing it with a granular target (see, for example, experiments at KEK). The capture and accelerating sections should also be optimised. The peak magnetic field and its shape, the aperture, and the accelerating gradient of the RF structures are important parameters. Given the large emittance of the  $e^+$  beam, a damping ring is mandatory. Due to the high requested  $e^+$  flux, an accumulation process should be considered. The  $e^+$  flux is

$$\frac{dN^+}{dt} = a \cdot y \cdot N^- \cdot f, \quad (10.8)$$

where  $a$  is the accumulation efficiency and is a function of the damping time,  $y$  is the yield, as defined above, which depends on the electron-beam energy  $E^-$ ,  $N^-$  is the number of electrons impinging on the target, and  $f$  is the linac repetition rate. This accumulation could be realised by means of a tri-ring system, as presented in the CDR.

**10.6.5.3. Approaches for LHeC positrons** It should be mentioned that positrons have not been in the focus of our recent LHeC design activity, such that basic discussions presented in the CDR [1] still hold.

The CLIC positron source was studied in great detail and many pertinent simulations were performed. Based on the expected flux of the CLIC  $e^+$  source, we have identified three possibilities for the LHeC:

- Option 1: keep the CW mode and the bunch spacing of 25 ns. This implies a bunch charge of  $2.5 \times 10^6 e^+$ /bunch and a current of 16  $\mu\text{A}$ ;
- Option 2: keep the CW mode with a bunch charge of  $2.5 \times 10^9 e^+$ /bunch. This implies a bunch spacing of 25  $\mu\text{s}$  and a current of 16  $\mu\text{A}$ ;
- Option 3: keep the bunch spacing of 25 ns with a bunch charge of  $1 \times 10^9 e^+$ /bunch. This implies a pulsed mode with a repetition rate of 50 Hz. The beam current is now 6.4 mA.

The CLIC source, however, just provides  $O(10^{14}) e^+ s^{-1}$ , which would provide a maximum of 100  $\text{pb}^{-1}$  of  $ep$  luminosity in an efficient year.



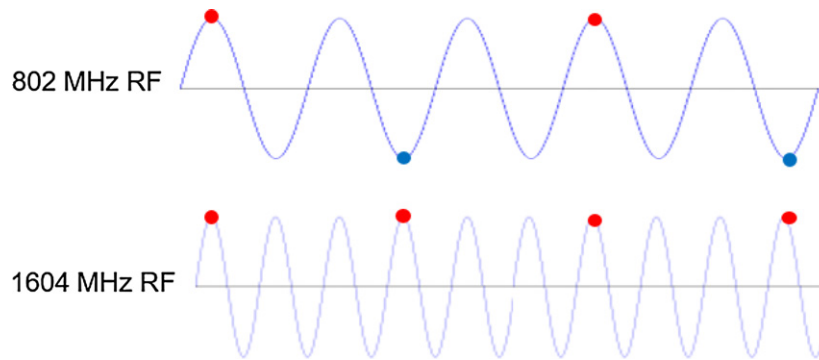


**Figure 174.** The second-harmonic RF restores the energy loss in both the accelerating and decelerating passes.

We note that the ILC luminosity upgrade foresees a positron rate that is up to eight times higher than the CLIC rate. A recent ILC status report cites novel concepts for very intense and polarised positron beams, obtained in an electron-beam-driven configuration [844].

Two alternative options, not yet studied in greater detail, promise to deliver a still much higher positron rate, indeed, close to that of the electrons, providing 1000 times more positrons per second than a CLIC-based source: one may possibly (i) convert high-energy photons from the LHC-based gamma factory [845] to produce a positron rate of up to  $10^{17} e^+ s^{-1}$  [846], or (ii) use the photons from an LHeC-based FEL [847] to generate a similarly high rate of positrons, which, in both cases, would already be at the correct bunch spacing. These two options rely on either the LHC hadron or the LHeC lepton–beam infrastructure, and thus do not need other, possibly additional investments.

Depending on how challenging the parameter requirements are, a more or less radical change of paradigm is necessary. There is no easy path, even to  $10^{14} e^+ s^{-1}$ . As for the LHeC, it may profit from recent and forthcoming developments for lepton colliders, for which more intense positron sources and beams are a matter of existence. When approved, however, serious research and development effort will also be inevitable for the LHeC, and later for the FCC-eh, for which positron beams may even be more important, if, for example, leptoquarks or SUSY particles in the few TeV range were found and had to be examined in  $e^\pm p$  scattering at the FCC.

**10.6.6. Compensation for synchrotron radiation losses.** Depending on the energy, each arc exhibits fractional energy loss due to synchrotron radiation, which scales according to  $\gamma^4/\rho$  (see equation (10.5)). Arc-by-arc energy loss was previously summarised in table 39. That energy loss has to be added back to the beam, so that at the entrance of each arc, the accelerated and decelerated beams have the same energy, unless separate arcs are used for the accelerated and decelerated beams. Before or after each arc, a matching section adjusts the optics from and to the linac. Additional cells are placed adjacent to these, hosting the RF compensating sections. The compensation makes use of a second-harmonic RF at 1603.2 MHz to replenish the energy loss for both the accelerated and the decelerated beams, therefore allowing them to have the same energy at the entrance to each arc, as shown in figure 174.

The parameters of the RF compensation cryomodules shown in table 44 have been extrapolated from the ILC cavity design, in the expectation that the higher frequency and lower gradient will support continuous operation.

**Table 44.** A tentative list of parameters for the compensating RF cryomodules, extrapolated from the ILC design.

Parameter	Unit	Value
Frequency	MHz	1603.2
Gradient	MV m <sup>-1</sup>	30
Design		Nine cells
Cell length	mm	841
Structure length	m	1
Cavity per cryomodule		6
Cryomodule length	m	6
Cryomodule voltage	MV	150

**Table 45.** Arc-by-arc synchrotron radiated power for both the accelerated and decelerated beams (only one beam in arc six) along with the number of second-harmonic RF cryomodules required to compensate for the energy loss.

Section	$\Delta E$ (MeV)	$P$ (MW)	Cryomodule
Arc one	3	0.12	0
Arc two	25	1.0	0
Arc three	80	3.2	1
Arc four	229	9.16	2
Arc five	383	15.32	3
Arc six	836	16.7	6

As schematically illustrated in figure 174, there are two beams in each arc (with the exception of arc six) that one needs to replenish energy loss for: the accelerated and the decelerated beams. Assuming a nominal beam current of 20 mA, the net current for two beams is doubled. Therefore, 40 mA of current in arcs one to five was used to evaluate the power required by a second-harmonic RF system to compensate for energy loss, as summarized in table 45.

The compensating cryomodules are placed on the linac one side of the racetrack, before the bending sections of arcs one, three, and five and after the bending sections of arcs two, four, and six. This saves space on the linac two side to better fit the IP line and the bypasses. Note that with the current vertical separation of 0.5 m, it will not be possible to stack the cryomodules on top of each other; therefore, they will occupy 36 m on the arc four and arc six side, and 18 m on the arc three and arc five side of the racetrack. Each of the compensating cavities in arc five needs to transfer up to 1 MW to the beam. Although a 1 MW continuous-wave klystron is available [848], the cryomodule integration and protection system will require a careful design. Table 45 shows the energy loss for each arc and the corresponding synchrotron radiated power, along with the number of cryomodules at an RF frequency of 1603.2 MHz RF required to replenish the energy loss.

**10.6.7. LINAC configuration and infrastructure.** Since the power supplied to the beam in the main linacs will be recovered, the average RF power requirements at 802 MHz are relatively small and are determined by the need to handle transients and microphonics.

The RF power required for the second-harmonic RF system is, however, substantial—it can be estimated from table 39 at a nominal current of 20 mA. Table 45 above summarizes the estimated power lost in each arc, depending on beam energy; these power values must be supplied by the six second-harmonic RF systems.

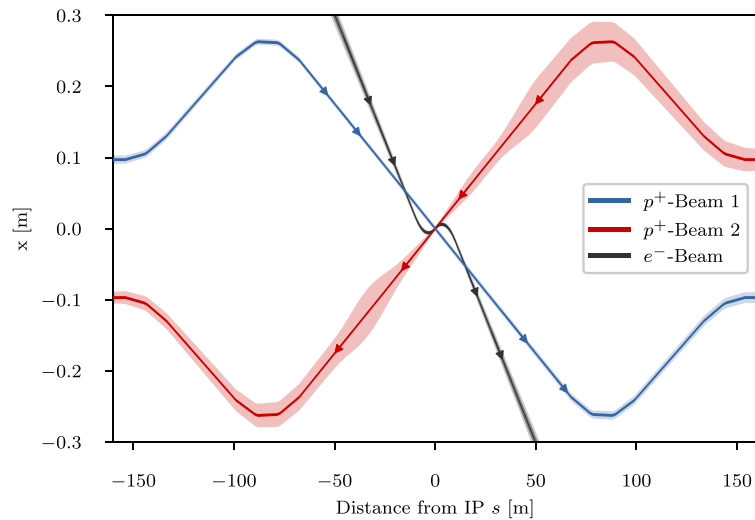


**Figure 175.** Geometry of the interaction region with  $10\sigma$  envelopes. The electron beam collides with the focussed anticlockwise-rotating LHC beam (beam two), while the clockwise-rotating LHC beam is unfocussed and passes the interaction region without interacting with the other two beams.

### 10.7. Interaction region

The design of the LHeC interaction region has been revised with respect to the LHeC CDR to take account of the reduction of the electron energy from 60 GeV to 50 GeV and the latest design of the HL-LHC optics, and it has been optimized to minimize the synchrotron radiation power and critical energy at the IP.

**10.7.1. Layout.** The basic principle of the linac–ring IR design remains unchanged; it is shown in figure 175: the two proton beams are brought into intersecting orbits by strong separation and recombination dipoles. A collision of the proton beams at the IP is avoided by appropriately selecting its location, i.e. by displacing it longitudinally with respect to the point where the two counter-rotating proton beams would collide. The large crossing angle keeps the long-range beam–beam effect small and separates the beams enough to allow septum quadrupoles to focus only the colliding beam (the anti-clockwise-rotating LHC beam—beam two). The non-colliding beam (the clockwise rotating LHC beam—beam one) is unfocused and passes the septum quadrupoles in a field-free aperture. The electron beam is brought in with an even larger angle, partly sharing the field-free aperture of the septum quadrupoles with the non-colliding beam. A weak dipole in the detector region bends the electron beam into a head-on collision with the colliding proton beam. The two proton beams are also exposed to the dipole field, but due to the large beam rigidity, they are barely affected. After the interaction point, a dipole of the opposite polarity separates the orbits of the electron and proton beams.

The high electron current (see table 26) required to approach the goal peak luminosity of  $10^{34} \text{ cm}^{-2} \text{ s}^{-1}$  poses a potential problem for the IR, as it increases the already high synchrotron radiation.

The ERL parameters are not the only major change the new IR design has to account for. The first design of the quadrupole septa featured a separation of 68 mm for the two proton beams.

**Table 46.** Parameters of the final focus quadrupole septa. The parameters Q1A/B and Q2 are compatible with the Nb<sub>3</sub>Sn-based designs described in [850], assuming that the inner protective layer of Q2 can be reduced to a thickness of 5 mm.

Magnet	Gradient (T m <sup>-1</sup> )	Length (m)	Free aperture radius (mm)
Q1A	252	3.5	20
Q1B	164	3.0	32
Q2 type	186	3.7	40
Q3 type	175	3.5	45

**Table 47.** Parameters of the separation and recombination dipoles. The respective interbeam distances are given for the magnet with the lowest value.

Magnet	Field strength (T)	Interbeam distance (mm)	Length (m)	Number
D1	5.6	≥ 496 mm	9.45	6
D2	4.0	≥ 194 mm	9.45	4
IP dipole	0.21	—	10	—

However, this design focussed strongly on providing a field-free region for the non-colliding beam. Unfortunately, this led to poor field quality for the strongly focussed colliding beam. The first quadrupole, Q1, was a half-quadrupole design, effectively acting as a combined-function magnet with a dipole component of 4.45 T [849]. The sextupole field component was also prohibitively high. Consequently, a new design approach focussing on the field quality in the quadrupole aperture was necessary. The parameters relevant to the interaction-region design are summarised in table 46.

It is noteworthy that the minimum separation of the two beams at the entrance of the first quadrupole Q1A is increased from 68 mm to 106 mm, requiring a stronger deflection of the electron beam. This would increase the already high synchrotron radiation in the detector region even more. In order to compensate for this increase, it was decided to increase  $L^*$  (i.e. the distance from the IP to the first superconducting septum quadrupole that focusses beam 2) to 15 m, an approach that was shown to have a strong impact on the emitted power [851].

The increased separation of the two proton beams, the longer  $L^*$  and the overall longer final focus triplet make longer and stronger separation and recombination dipoles necessary. The dipoles differ from the arc dipoles in that the magnetic field has the same direction in both apertures. Consequently, the crosstalk between both apertures is significant and the maximum achievable field is smaller. The new geometry keeps the required field to less than 5.6 T. The required lengths and strength of these dipoles are listed in table 47. It should be noted that the inter-beam distance is different for each of the five magnets per side, so each magnet will likely require an individual design. The design of the D1 dipoles is further complicated by the fact that an escape line will be necessary for neutral-collision debris travelling down the beam pipe [1], as well as a small-angle electron tagger. These issues have not been addressed so far; further studies will require detailed dipole designs.

The first design of the LHeC interaction region featured detector dipoles that occupied almost the entire drift space between the interaction point and the first quadrupole. The approach adopted was to have the softest synchrotron radiation possible, in order to minimise the power. However, since the purpose of the dipoles is to create spatial separation at the entrance of the first quadrupole, it is possible to make use of a short drift between the

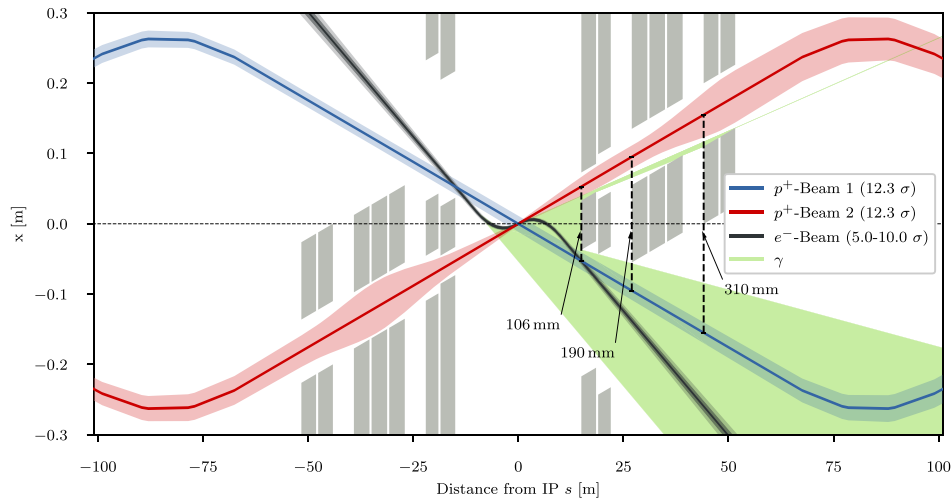


**Figure 176.** Schematic layout of the LHeC interaction region. The colliding proton beam and the electron beam are shown at the collision energy, while the non-colliding beam is shown at the injection energy, at which its emittance is maximised.

dipole and the quadrupole to increase the separation without increasing the synchrotron radiation power. A dipole length of  $\frac{2}{3}L^*$  is optimal in terms of synchrotron radiation power [852]. Compared to the full-length dipole, it reduces the power by 15.6% at the cost of a 12.5% increase in the critical energy. With an  $L^*$  of 15 m the optimum length of the detector dipoles is 10 m. A magnetic field of 0.21 T is sufficient to separate the electron and proton beams by 106 mm at the entrance of the first quadrupole. With these dipoles and an electron-beam current of 20 mA at 49.19 GeV, the total synchrotron radiation power is 38 kW with a critical energy of 283 keV, compared with a power of 83 kW and a critical energy of 513 keV for an electron-beam energy of 60 GeV. More detailed studies of the synchrotron radiation for different options and the inclusion of a beam envelope for the electron beam are summarised in table 50 below.

A schematic layout of the LHeC interaction region with the dipoles discussed above is shown in figure 176. The corresponding beam optics will be discussed in the following sections.

**10.7.2. Proton optics.** As discussed above, the  $L^*$  was increased to 15 m in order to compensate for the increased synchrotron radiation due to the larger separation. The final focus system is a triplet consisting of the quadrupoles Q1A and Q1B (see table 46), three elements of the Q2 type and two of the Q3 type. Between the elements a drift space of 0.5 m was left to account for the magnet interconnects in a single cryostat. Between Q1 and Q2 as well as Q2 and Q3, a longer drift of 5 m is left for cold-warm transitions, beam-position monitors, and vacuum equipment. Behind Q3, but before the first element of the recombination dipole D1, another 16 m of drift space is left to allow for the installation of nonlinear correctors in case the need arises, as well as local protection of the triplet magnets from asynchronous beam dumps caused by failures of the beam-dump kickers as discussed below.

As the recombination dipoles D1 and D2 for the LHeC interaction region require more space than the current ALICE interaction region, the quadrupoles Q4 and Q5 had to be moved further away from the IP. The position of Q6 is mostly unchanged, but due to a need for more focus, its

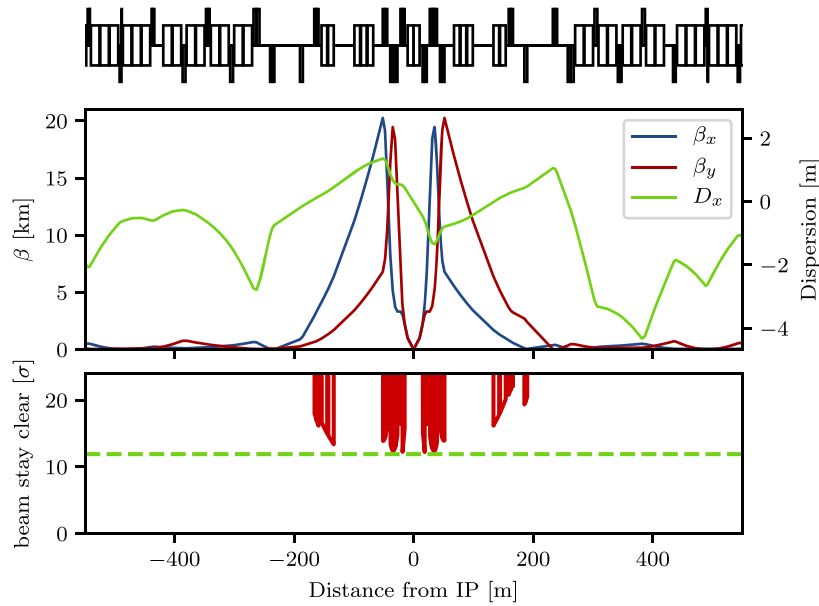


**Figure 177.** The optics (top) and beam clearance (bottom) of the colliding beam with  $\beta^* = 10$  cm.

length was increased by replacing the magnet by two main superconducting LHC quadrupoles (the so-called MQM type).

Using the triplet quadrupole parameters provided in table 46, we were able to match optics with a minimum  $\beta^*$  of 10 cm. The corresponding optics is shown in figure 177 and feature maximum  $\beta$  functions in the triplet in the order of 20 km. With these large  $\beta$  functions, the free apertures of the quadrupoles leave just enough space for a beam clearance of  $12.3\sigma$ , the specification of the LHC. This is illustrated in figure 177. However, since the LHeC is supposed to be incorporated into the HL-LHC lattice, this minimum beam clearance requires specific phase advances from the dump kicker to the protected aperture, as detailed later. The large  $\beta$  functions not only drive the aperture requirement of the final focus system, but also the required chromaticity correction in the adjacent arcs. To increase the leverage of the arc sextupoles, the achromatic telescopic squeezing (ATS) scheme developed for the HL-LHC [853] was extended to the arc upstream from IP2 for the colliding beam (beam two) (see figure 178). This limited the optical flexibility in the matching sections of IR2, specifically that of the phase advances between the arc and IP2. As a consequence, the optical solution that has been found (figure 177) still has a residual dispersion of 15 cm at the IP, and the polarities of quadrupoles Q4 and Q5 on the left side of the IP break up the usual sequence of focussing and defocussing magnets. A study is required of whether this is compatible with the injection optics. The latest optical designs can be found on the webpage [854].

The free apertures given in table 46 include a 10 mm-thick shielding layer for Q1 and 5 mm for Q2 and Q3. This is necessary to protect the superconducting coils from synchrotron radiation entering the magnets, as can be seen in figure 176. The absorber must also protect the magnets from collision debris. Simulations of both synchrotron radiation and collision debris are yet to be conducted in order to confirm the feasibility of this design.



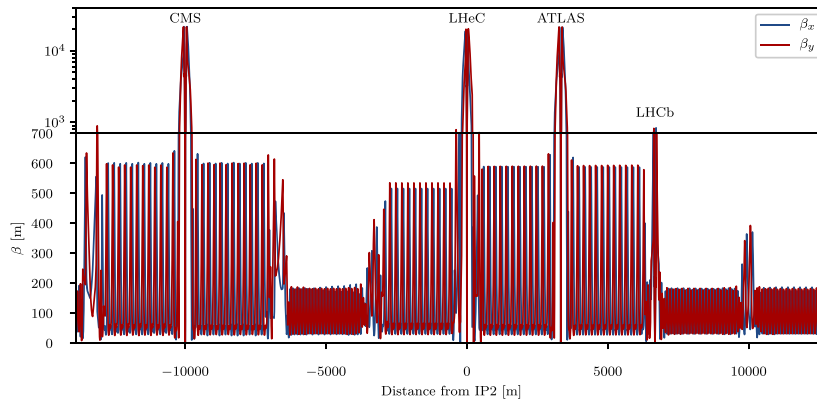


**Figure 178.** Optics of the full ring of the colliding LHC proton beam (beam two).

A temporal separation is currently foreseen between the two proton beams, i.e. while the orbits of the two proton beams cross, the bunches do not pass through the IP at the same time. This approach is complicated by the fact that the timing of the bunches in the other three interaction points should not be affected. The easiest way to accomplish this is by shifting the interaction point of LHeC by a quarter of a bunch separation, i.e.  $6.25 \text{ ns} \times c \approx 1.87 \text{ m}$  upstream or downstream from the current ALICE IP, in a similar way to what has been done for the LHCb detector in point eight of the LHC. This will, of course, impact the integration of the detector in the underground cavern [855]; however, it seems feasible [856].

The LHC protected aperture in the event of an asynchronous beam dump strongly depends on the phase advance between the dump kicker and the local aperture protection [857]. This is due to the oscillation trajectory of bunches deflected during the kicker rise time. With a phase advance of  $0^\circ$  or  $180^\circ$  from the kicker to the protected aperture, a direct hit should be unlikely, so aperture bottlenecks should be close to that. For a beam clearance of  $12.3\sigma$  a phase advance of less than  $30^\circ$  from either  $0^\circ$  or  $180^\circ$  was calculated to be acceptable [857]. The major complication comes from the fact that not only the final focus system of the LHeC, but also those of the two main experiments, ATLAS and CMS, need to have the correct phase advances, and since the phase advances between IP2 (LHeC) and IP1 (ATLAS) are locked into the ATS scheme, there are few degrees of freedom with which to make adaptations.

The ATS scheme [853] is a novel optical solution proposed for the HL-LHC to strongly reduce  $\beta^*$  while controlling the chromatic aberrations induced, among other benefits.

The principles of the ATS as implemented for the HL-LHC are as follows: first, in the presqueeze stage, a standard matching procedure is performed in the interaction regions to obtain a value of  $\beta^*$  that is achievable in terms of quadrupole strengths and chromaticity correction efficiency; in the case of the HL-LHC, this corresponds to IR1 and IR5. A further constraint at this point is to match the arc cell phase advance in the regions adjacent to the low- $\beta^*$  interaction regions to exactly  $\pi/2$ . Later, at the collision stage, the low- $\beta^*$  insertions remain unchanged, and instead, the adjacent interaction regions contribute to the reduction of  $\beta^*$ , that is, IR8 and IR2 for IR1, and IR4 and IR6 for IR5. The  $\pi/2$  phase advance allows the propagation of  $\beta$  waves in the arc. If phased correctly with the IP, these  $\beta$  waves will reach their maximum at every other sextupole, increasing the  $\beta$  function at their location at the same

rate as the decrease in  $\beta^*$ . The increase of the  $\beta$  function at the locations of the sextupoles will result in an increase in their efficiency, allowing the system to correct the high chromaticity produced by the high- $\beta$  function in the inner triplet. In this way, the ATS allows a further reduction of  $\beta^*$  while, at the same time, correcting the chromaticity aberrations produced in the low- $\beta$  insertions.

Following experience obtained with the HL-LHC, the ATS scheme was proposed for the LHeC project to overcome some of the challenges of this design in terms of limits in the quadrupole strengths of the interaction region and in the chromaticity correction.

A first integration of the LHeC IR into the HL-LHC lattice using the ATS scheme for the previous nominal case with  $\beta^* = 10$  cm and  $L^* = 10$  m was presented by extending the  $\beta$  wave into arc 23 [851]. The flexibility of this design was later explored to study the feasibility of minimising  $\beta^*$  to increase the luminosity and increasing  $L^*$  to minimise the synchrotron radiation. It was found that increasing  $L^*$  to 15 m provided a good compromise, but  $\beta^*$  was kept at 10 cm.

The changes made to the HLLHCv1.3 lattice [858] to obtain the LHeC lattice and the detailed matching procedure are described in reference [859]. At the end of this process a lattice was obtained for the required collision optics in all IRs ( $\beta^* = 15$  cm for IR1 and IR5 and  $\beta^* = 10$  cm for IR2), with the appropriate corrections (crossing, dispersion, tune, and chromaticity). The phases between the dump kicker in IR6 and the different low- $\beta^*$  triplets were also checked, resulting in  $15^\circ$  from the horizontal for IR1,  $22^\circ$  for IR2, and  $26^\circ$  for IR5, therefore fulfilling the  $< 30^\circ$  requirement for all three IRs.

Similarly, the chromaticity correction for the LHeC lattice is further developed from the HL-LHC chromaticity correction scheme [859], allowing us to correct the chromaticity for the case with  $\beta^* = 10$  cm in IP2 within the available main sextupole strength. Lattices with  $\beta^* = 7, 8,$  and  $9$  cm and  $L^* = 15$  m were also successfully matched in terms of both  $\beta^*$  and the chromaticity correction. It should be noted, however, that these cases require a larger aperture in the inner triplet.

Dynamic aperture (DA) studies were performed to analyse the stability of the lattice designs using SixTrack [860] on a thin-lens version of the LHeC lattice at collision ( $\beta^* = 0.15$  m in IP1 and IP5,  $\beta^* = 10$  cm in IP2) over  $10^5$  turns with crossing angles set to ‘on’, 30 particle pairs per amplitude step of  $2\sigma$ , five angles in the transverse plane, and a momentum offset of  $2.7 \times 10^{-4}$ . The energy was set to 7 TeV and the normalised emittance of the proton beam was set to  $\epsilon = 2.5 \mu\text{m}$ . No beam–beam effects were included in this study.

Previous DA studies had been performed for an earlier version of the LHeC lattice [851]. These studies did not include the triplet errors of either of the low- $\beta$  interaction regions, as these errors were not available at that stage. These studies were updated for the newer version of the LHeC lattice described in the previous sections and included errors for the triplets of IR1 and IR5. In the case of the IR2 errors, tables for the new triplet are not yet available, but it was estimated that the same field quality as that of the triplets for the HL-LHC IR can be achieved for these magnets, and therefore, the same field errors were applied, but adjusted to the LHeC triplet apertures.

The initial DA resulted in  $7\sigma$  but following the example of the HL-LHC and FCC studies [861], two further corrections were implemented: the use of nonlinear correctors to compensate for the nonlinear errors in the LHeC IR, and the optimisation of the phase advance between IP1 and IP5. With these corrections the DA was increased to  $10.2\sigma$ , more than the target of  $10\sigma$ . The case for lower  $\beta^*$ , particularly for the case of interest with  $\beta^* = 7$  cm proved to be more challenging, as expected, when adding errors to the LHeC IR; however, with the use of the latest corrections, a DA of  $9.6\sigma$  was achieved, which is not far from the target. The DA versus the angle for both these cases are shown in figure 179. It is important to point out that

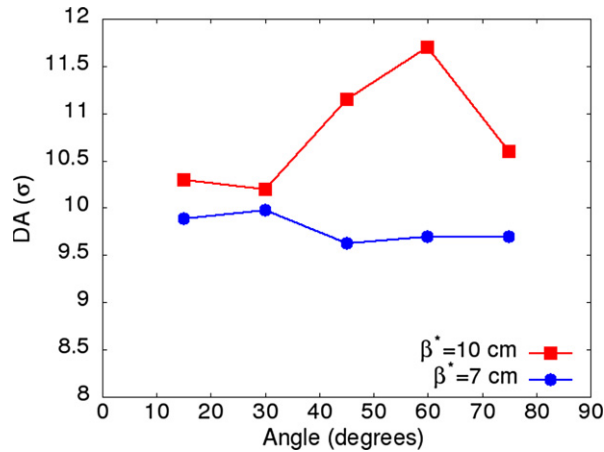


**Figure 179.** Dynamic aperture vs angle for 60 seeds for the LHeC lattice at collision for the cases  $\beta^* = 10$  cm (red) and  $\beta^* = 5$  cm in IP2.

the challenge for the  $\beta^* = 7$  cm case originates from the quadrupole aperture and gradient requirements, in particular, for the first magnet.

$\beta^*$  values less than 10 cm require a completely different final focus system, as the lower  $\beta^*$  means that the beam size in the triplet becomes larger. Larger apertures are required and consequently the gradients in the quadrupoles will decrease. However, similar integrated focussing strengths will be required, so the overall length of the triplet will increase. As this will, in turn, increase the  $\beta$  functions in the triplet further, it is imperative to optimise the use of the available space. An example of the available space is the drift between the detector region dipoles and the triplet magnets, as shown in figure 180. The optimum dipole length in terms of synchrotron radiation power was determined to be  $2/3 \cdot L^*$ , so a drift of 5 m is left. It is immediately clear that this region cannot be occupied by a superconducting quadrupole septum, as that would effectively decrease  $L^*$  and thus increase the synchrotron radiation power, as a stronger separation is necessary. Instead, it is thinkable that a normal conducting quadrupole septum can be built that either does not require a yoke or similar structure between the beams, or has a very thin yoke, or a septum can be built that has a very limited and controlled field in the region of the electron beam trajectory. In the latter case, it might even be used as part of the final focus system of the electron beam. Either way, it is clear that such a normal conducting septum must have a pole tip field far smaller than the saturation limit of iron. The section on electron optics shows that a normal quadrupole of this kind can also have benefits in terms of synchrotron radiation, but studies remain to be done to ensure that the parameters work for both cases. For our calculation, a pole tip field of 1 T was assumed. For  $\beta^* = 5$  cm an aperture radius of 20 mm is required at a distance of 14 m from the IP, resulting in a pole tip field of  $50 \text{ T m}^{-1}$  for the normal conducting septum called Q0. Possible ratios of apertures and gradients for the remaining triplet magnets were approximately based on the quadrupole parameters shown in table 46; however, these parameters would require a magnet design for confirmation. With the quadrupole parameters shown in table 48 we were able to obtain triplet optics that can accommodate a beam with a minimum  $\beta^*$  of 5 cm.

The corresponding optics is shown in figure 181. From a triplet point of view it appears possible to reach lower values of  $\beta^*$ ; however, many assumptions need verification: first the magnetic design for the normal conducting quadrupole septum must be shown to be possible.

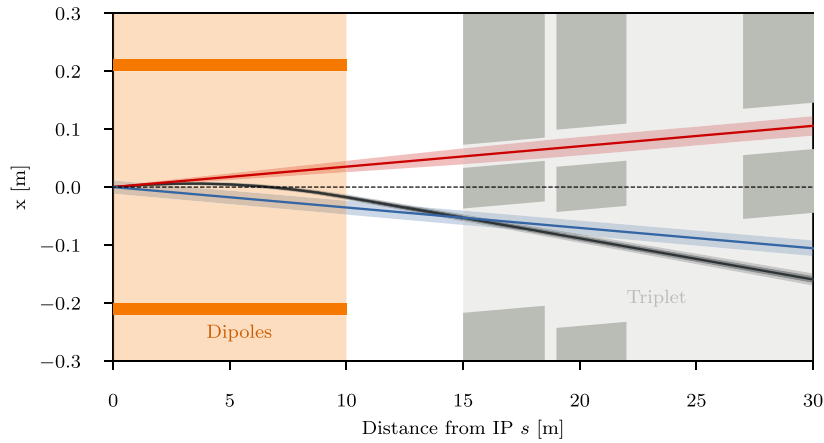


**Figure 180.** Empty space between the detector dipole and the superconducting quadrupoles of the final focus triplet.

**Table 48.** Parameters of the final focus quadrupole septa required to accommodate a  $\beta^*$  of 5 cm. The normal conducting quadrupole is called Q0, although it has the same polarity as Q1A/B.

Magnet	Gradient ( $T\ m^{-1}$ )	Length (m)	Aperture radius (mm)
Q0 (nc)	50	3.0	20
Q1A	110	3.5	27
Q1B	162	5.0	37
Q2	123	5.0	62
Q3	123	4.5	62

If there is a residual field in the space of the electron-beam trajectory, the impact on the electron beam and the synchrotron radiation power must be evaluated. The parameters of the modified superconducting triplet quadrupole septa, although scaled conservatively, must be confirmed. Furthermore, the larger aperture radius of Q1 might require a larger separation at the entrance of Q1, increasing the synchrotron power, which is already critical. Thus, a full design of such magnets is required. Lastly, the interaction region must be integrated into the full ring to verify that chromaticity correction is possible. Studies in reference [859] that were conducted on the normal triplet, without regard for aperture constraints, suggest that a chromaticity correction is only possible for a  $\beta^*$  down to around 7 cm.

So far, the optics of the final focus system have featured asymmetrically powered triplets on the two sides of the IP. This is inherited from the ALICE final focus system, in which the aperture is shared and the antisymmetry guarantees the same optics for both beams and similar chromaticities in both the horizontal and vertical planes. In the LHeC final focus system, however, the apertures of the quadrupoles are not shared between both beams, so the antisymmetry is not strictly necessary, although it eases the integration in the full ring. An alternative approach that is worth studying is a symmetric doublet. Doublets feature a large  $\beta$  function in one plane and a relatively low one in the other plane for equal  $\beta$  functions at the IP. Since the non-colliding proton beam is of no concern for the LHeC, it makes sense to create doublets on each side of the IP that have the peak  $\beta$  function in the horizontal plane, as the chromaticity

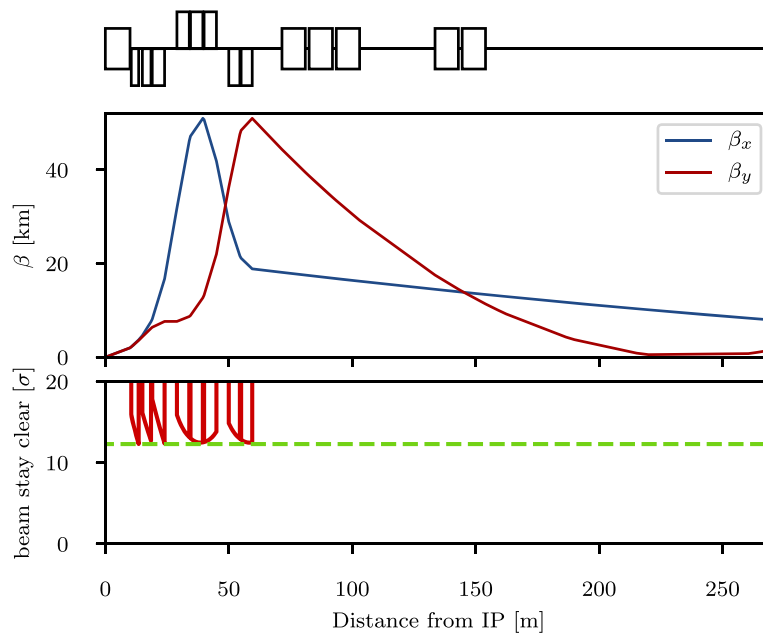


**Figure 181.** Optics (top) and beam clearance (bottom) in the triplet region of a colliding beam with  $\beta^* = 5$  cm.

correction is limited in the vertical plane. Furthermore, in a doublet, the integrated focussing strength required is lower, as fewer quadrupoles act against each other. This further reduces the chromaticity and should also reduce the overall length of the final focus system. With the space saved by the doublet it is possible to either shift the recombination dipoles D1 and D2 closer to the IP, reducing the integrated strengths needed, or even to increase  $L^*$  to further reduce the synchrotron radiation power and critical energy. In order to make best use of the available doublet quadrupole aperture, it is also possible to collide with flat beams. The main disadvantage of symmetric doublets is the breaking of the sequence of focussing and defocussing quadrupoles. As no changes should be made to the arcs, the left–right symmetry needs to be broken up again in one of the matching sections, either by introducing another quadrupole on one side of the IP, or by overfocusing the beam.

At the collision energy the non-colliding beam has no optics specification within the straight section. Consequently, the optics should transfer the beam from the left arc to the right arc without hitting the aperture and at a specific phase advance. The same is true at injection energy, but with a larger emittance, making the satisfaction of the aperture constraint more difficult. Thus, it is sufficient to find working injection optics, as no squeeze will be required for this beam. This approach will, of course, require some tuning, as at least one arc will apply the ATS scheme at collision, but as the aperture constraint is less tight at higher energy, there should be enough degrees of freedom available.

Finding injection optics appears trivial at first but is complicated by the fact that the distance between the IP and the first quadrupole magnet Q4 is larger than 159 m. A total distance of 318 m needs to be bridged without any available focussing. A solution has been found with  $\beta^* = 92$  m and  $\alpha^* = \pm 0.57$  that has the required beam size in the quadrupole septa and Q4 [859]. The corresponding optics is shown in figure 182. For the magnets Q4 and Q5, LHC

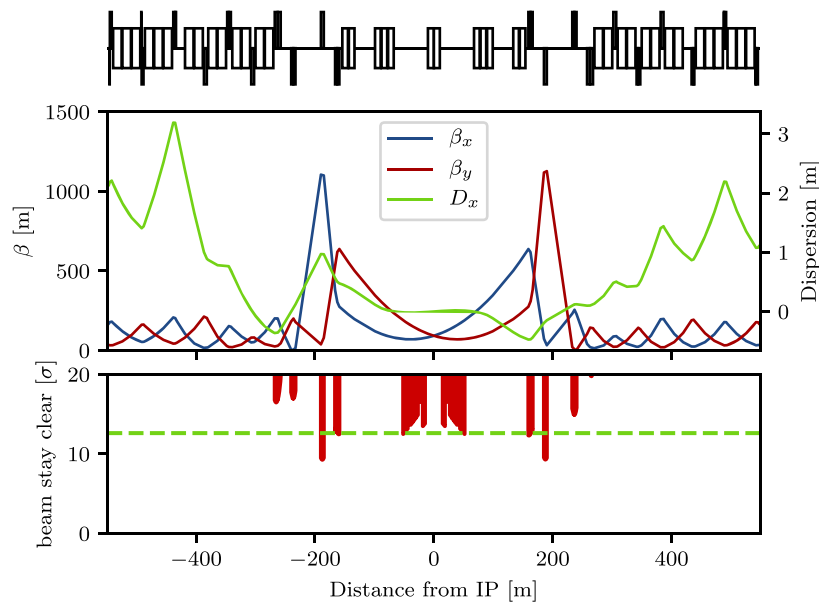


**Figure 182.** Optics (top) and beam clearance of the non-colliding beam at injection energy. The Q5 quadrupole magnets on either side of the IP are currently aperture bottlenecks. It should be possible to mitigate this problem by replacing the magnets with longer, larger-aperture magnets.

quadrupoles with large-aperture (so-called MQY type magnets) type with a 70 mm aperture diameter and a  $160 \text{ T m}^{-1}$  gradient were assumed. As can be seen in the aperture plot, the triplet quadrupoles Q1–Q3 as well as Q4 are just below the minimum beam clearance at an injection of  $12.6\sigma$ , but it is expected that a nominal aperture can be achieved with some minor optimisation. However, the Q5 magnets only have a beam clearance of about  $9.2\sigma$ , with little chance of decreasing the beam size without increasing it both in Q4 and in the mini beta quadrupoles. Consequently, it will be necessary to use quadrupoles with apertures larger than 106 mm and make up for the smaller gradient by increasing the length or by using  $\text{Nb}_3\text{Sn}$  technology. At injection energy the remaining magnets in the IR have strengths according to the HL-LHC specification and thus do not pose any problems. However, the injection optics shown in figure 182 will require some changes during the ramp, as Q4, Q5, and Q6 would become too strong at collision energy. This is not considered a problem, though, as the emittance reduction will ease the aperture requirements.

The non-colliding proton beam does not need to be focussed, and consequently passes the quadrupole septa of the colliding beam in the field-free region.

The large angle of  $7200 \mu\text{rad}$  between the two beams (compared to  $590 \mu\text{rad}$  in the high-luminosity IPs) should suffice to mitigate long-range beam–beam effects, considering that the shared aperture is only 30 m long, as opposed to the main experiments, in which the shared aperture exceeds a length of 70 m.

**10.7.3. Electron optics.** The first ideas for a possible layout and design of the LHeC IR have already been presented in reference [1]. Based on the principles explained there, a further optimisation of the beam separation scheme has been established, with the ultimate goal of the lowest synchrotron radiation power and critical energy in the direct environment of the particle



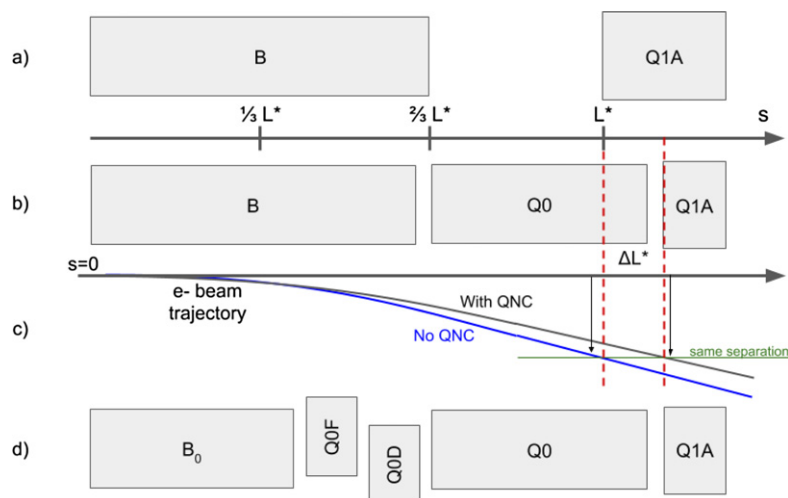


**Figure 183.** Separation scheme based on a long dipole magnet  $B$  (a) and an improved layout using  $Q0$ , a normal conducting half-quadrupole as the first focussing element of the proton beam (b). The last design features a doublet of off-center quadrupoles to minimise the electron beam size at the entrance of  $Q1A$  (d).

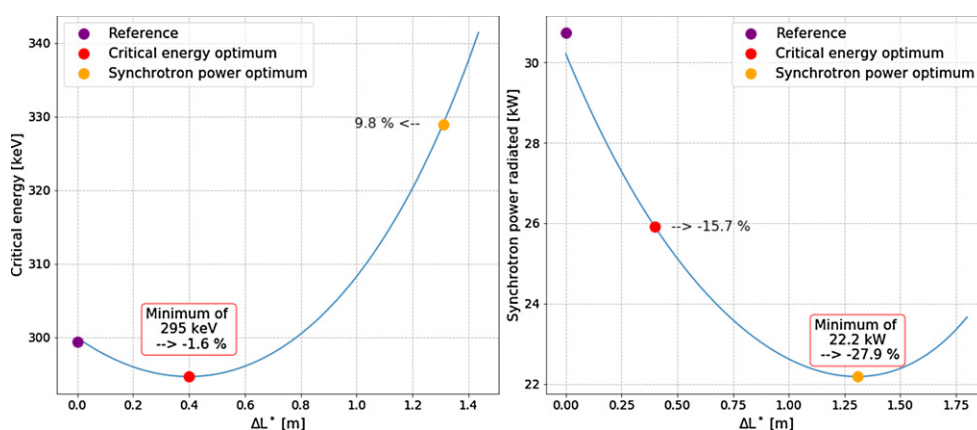


**Figure 184.** Improved critical energy and power of the synchrotron radiation for the half-quadrupole-based proton lattice. Left side: critical energy, right side: synchrotron radiation power. The horizontal axis refers to the shift  $\Delta L^*$  of the position of the first proton superconducting magnet  $Q1A$ .

detector. Depending on the requirements for the actual detector geometry and shielding, the flexibility of the new IR layout allows us to optimise for either side.

The basic principle is—as before—based on the large ratio (approximately 140) of the proton to electron-beam momentum (or beam rigidity,  $B\rho = p/e$ ) that makes a magnetic-field-based separation scheme the straightforward solution to the problem, using effective dipole fields.

Boundary conditions are set, however, due to the limited longitudinal space resulting from the distance of the first focussing elements of the proton lattice, located at  $L^* = 15$  m, and the need for sufficient transverse separation, defined by the technical design of this first proton quadrupole. In addition, the sizes of the two beams, the power of the emitted synchrotron radiation  $P_{\text{syn}}$ , and the critical energy  $E_{\text{crit}}$  clearly have to be taken into account. The well-known dependencies of these two parameters on the beam energy  $E_e = m_e c^2 \gamma$  and the bending radius  $\rho$  are given by

$$P_{\text{syn}} = \frac{e^2 c}{6\pi\epsilon_0} \frac{\gamma^4}{\rho^2} \quad \text{and} \quad E_{\text{crit}} = \frac{3}{2} \frac{\hbar c \gamma^3}{\rho}. \quad (10.9)$$

The schematic layout of the original design of the electron interaction region shown in figure 176 is reproduced in figure 183(a). The long dipole magnet  $B$ , used to deflect the electron beam, is embedded inside the detector structure, which ranges from  $-6$  m to  $4$  m around the interaction point, extended by  $\pm 1.65$  m of muon chamber. Basic interaction region designs with and without chromaticity correction were presented [862, 863], but were not fully integrated into the ERL. The electron final quadrupoles were placed  $30$  m from the IP [864], which is compatible with the proton layout described above. While this approach is straightforward, the only parameter that can be used to minimise the power of the emitted synchrotron radiation is the length of the separator-dipole field [852]. In addition, the installation of the first focussing elements of the electron beam downstream from the triplet focussing the colliding proton beam leads to a considerable increase of the electron beam size in the separation plane.

Lattices that included chromaticity correction had a significant length of  $150$  m. However, the whole straight section between the linac and the arc is only  $290$  m long [1], and the IR design did not include a matching and splitting section, or a focus system for the spent, outgoing electron beam. Without chromaticity correction in the electron final focus, aberrations at the IP decrease luminosity by about  $20\%$  [865].

Investigations have been launched to minimise critical energy and emitted synchrotron radiation power by reducing the separation in two main steps:

- Introduce a compact mirror-plate half quadrupole (QNC) in front of Q1A (on the IP side) to focus the colliding proton beam and provide a field-free region for the electron and non-interacting proton beams. This reduces the required bending field of the separation dipole  $B$  for the same separation at Q1A. In addition, the normal conducting magnet QNC will act as a shield for the superconducting triplet magnets that would otherwise be subject to direct synchrotron radiation. Additional shielding is foreseen, to protect the SC magnets and avoid backshining to the detector as much as possible. In addition, sufficient space will be provided to correct the vertical orbit and coupling of the electrons coming from the solenoid.
- Reduce the beam size of the electron beam by very early beam focussing. As a positive side-effect this leads to a considerable reduction of the chromaticity of the electron lattice.

The first step is sketched in figure 183(b) and the corresponding electron beam trajectory is shown in figure 183(c).

The introduction of the mirror plate half quadrupole, QNC, allows us to reduce the length of the Q1A quadrupole while conserving the total integrated gradient, therefore leaving the overall focussing properties of the proton lattice quasi untouched. The entry of Q1A is therefore moved away from the IP to relax the separation fields.

Scanning the Q1A entry position leads to either an optimum of the critical energy or to a minimum of the emitted synchrotron power. Both cases are shown in figure 184, and for

each of them, the new Q1A entry position has been determined. The power of the emitted radiation is reduced by up to 28%. The colliding proton beam, passing through this half quadrupole with a certain offset to guarantee sufficient beam clearance, will receive a deflecting kick in the horizontal plane of about  $90 \mu\text{rad}$ . It supports the dipole-based beam separation provided by the so-called D1/D2 magnets in the LHC, and will be integral part of the LHC design orbit.

The resulting beam optics for the protons differ only marginally from the original version and only a slight re-match is needed. However, due to a careful choice of the gradient of the new magnet, the parameters of the superconducting proton quadrupoles are untouched, and the phase advance at the end of the interaction region lattice is conserved in both planes.

*10.7.3.1. Improved electron lattice* . A further improvement of the emitted synchrotron power and critical energy is obtained by introducing an early focussing scheme for the electrons, which leads to a reduced electron-beam size and thus to softer separation requirements.

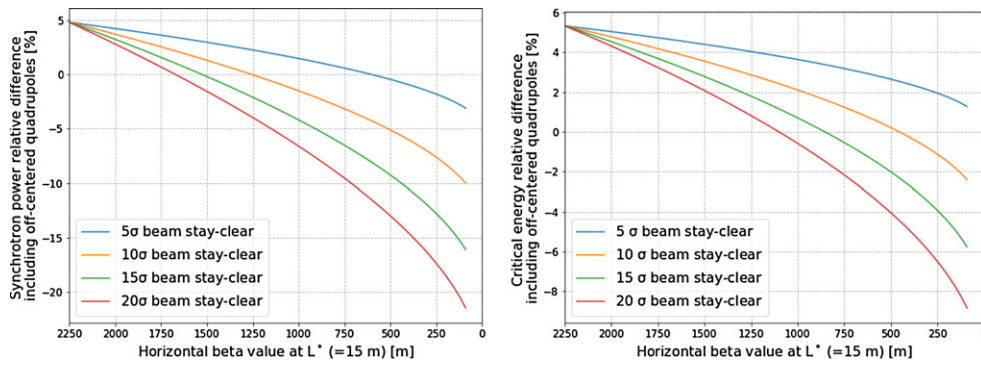
The reduction of the electron-beam size is obtained by installing a quadrupole doublet in the electron lattice between the separation dipole and the QNC (half-)quadrupole. A carefully matched focussing strength of this doublet minimises the  $\beta$  function of the electrons at the Q1A location. At the same time, an effective dipole field, which is needed to maintain the separation of the proton and electron beams, is provided by shifting the magnet centres of the doublet lenses off axis. The horizontal offset of these quadrupoles has been chosen to provide the same bending radius as that of the separation dipole, thus leading, to the first order, to the same critical energy of the emitted light in all separation fields. A detailed calculation of the divergence of the photons, the geometry of the radiation fan, and the positions of the absorbers and collimators will be one of the essential next steps within the so-called machine–detector-interface considerations.

Figure 183(d) shows the new layout compared to the previous version. The doublet that provides the early focussing of the electron beam is embedded in the separator dipole, i.e. it is positioned at  $s = 6.3 \text{ m}$  and acts in combination with the separation dipole. The quadrupole gradients have been chosen to provide optimum matching conditions for the electron beam, and the transverse shift of the field centres provides the same separation dipole effect as that used in the long dipole.

The early focussing of the electron beam allows for a softer separation of the beams, and therefore leads directly to a reduction in the critical energy  $E_{\text{crit}}$  and power  $P_{\text{syn}}$  of the emitted radiation. Figure 185 shows the dependence of  $E_{\text{crit}}$  and  $P_{\text{syn}}$  on the  $\beta$  function at  $s = L^*$  for the electron optics for different values of the required electron-beam clearance, expressed in units of the electron-beam size,  $\sigma$ . The beam separation has been re-calculated and the critical energy and radiation power are plotted. The graphs include different assumptions for the beam size considered. Including orbit tolerances, a beam clearance of  $20\sigma$  is considered as the most relevant case, indicated by the red curve in the graph.

In order to provide a complete study of the lattice featuring the off-centre quadrupoles, the new interaction region has been embedded in between the high-energy end of the acceleration part of the linac and arc six of the ERL, which marks the start of the energy-recovery lattice. An optimum has been found for beam optics with a beta function in the plane of the beam separation (i.e. horizontal) of  $\beta_x = 90 \text{ m}$  at  $L^* \approx 15 \text{ m}$ .

An improvement of about 9% for the critical energy and close to 25% of the radiated power is obtained, if electron-beam optics with  $\beta_x = 90 \text{ m}$  at the entrance of Q1A are used. For this most promising case the matched beam optics is shown in figure 186.



**Figure 185.** Relative difference with respect to the single-dipole separation scheme for different values of the required beam clearance expressed in  $\sigma$ . Left: for the power of the emitted radiation, as a function of the  $\beta$  function of the electron beam at the position  $s = 15$  m. Left: for the critical energy of the emitted radiation, as a function of the  $\beta$  function of the electron beam at the position  $s = 15$  m. The early focussing of the electron beam allows for a much-reduced separation field and thus to a reduction in the critical energy and power of the emitted radiation. The initial beta value is 2250 m.

**Table 49.** Chromaticity of the dipole-based separation scheme and the new lattice based on early focussing, off-axis quadrupole lenses.

	Dipole based separation	Early focussing scheme
$\xi_x$	-116	-15
$\xi_y$	-294	-32

The lower  $\beta$  function of the electron beam at the focussing elements has the additional positive feature of considerably reducing the chromaticity of the new lattice, which is a crucial parameter for the performance of the energy-recovery process (the details are described below in the chapter on tracking calculations). Compared to dipole-based separation and late focussing,  $Q'$  is reduced to a level of 13% horizontally and to a level of 11% in the vertical plane. The details are listed in table 49. Further studies will investigate the orbit-correction scheme of the new IR, and the eventual interplay of the solenoid fringe field and the quadrupoles.

The influence of the electron doublet magnets on the proton optics is marginal—as expected, due to the large difference in beam rigidity: if uncorrected, the electron doublet creates a distortion (a so-called *beta-beat*) of the proton optics of roughly 1%. Even so, it has been calculated and taken into account in the context of a re-match of the proton beam optics.

Combining the two improvement factors, namely the effective lengthening of  $L^*$  due to the use of a half quadrupole in front of the superconducting triplet, and the early focussing scheme in the electron lattice, leads to an overall improvement in the interaction region with respect to synchrotron radiation power and critical energy, as shown in figure 187. The overall improvement factor is plotted with reference to the baseline dipole separation design, which originally used  $\beta = 2250$  m at the separation point  $s = L^*$ . Using a normal conducting half quadrupole in combination with the early focussing scheme, the power of the emitted synchrotron radiation is reduced by 48% for an electron-beam clearance of  $20\sigma$ .

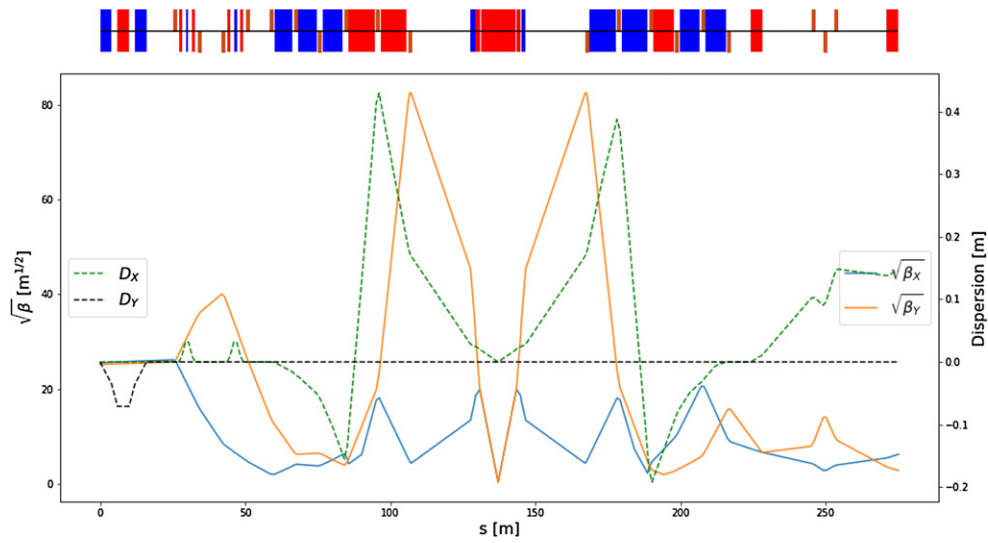


**Figure 186.** Electron-beam optics for the new lattice including the early focussing scheme. The offset of the new doublet quadrupoles is chosen to provide the same separation field as in the dipole. The new optics is matched to the end of the acceleration linac on the left side of the plot. The right-hand side is connected to arc six, the beginning of the ERL deceleration section. At the position of the first superconducting proton magnet the  $\beta$  function in the (horizontal) separation plane of the electron beam is reduced to 90 m to obtain the lowest possible synchrotron radiation load.

**Table 50.** Synchrotron radiation power and critical energy for the different optimised separation schemes.

Optimised scheme	Synchrotron radiation		Critical energy	
	Radiation power (kW)	Critical energy (keV)	Radiation power (kW)	Critical energy (keV)
Reference design	30.8	300	30.8	300
Dipole length optimum	26.8	336	30.8	300
Half quadrupole optimum	22.2	331	26.1	295
Off-centre quadrupole optimum	19.3	290	22.1	259
Half quad. + off-centered quad. opti.	16.2	265	17.4	255

The estimated synchrotron radiation power and critical energy for the different optimisations are plotted in figure 187 and the results are summarised in table 50. For a beam energy of 49.19 GeV and the design current of 20 mA, an overall power of 16.2 kW is emitted within one half of the interaction region.

Depending on the boundary conditions imposed by the integration of the particle detector, one of the two optimum layouts can be chosen—or a combination of both, i.e. an overall minimum defined by the critical energy and the radiated power.

The basic main parameters of the proton mirror-plate half quadrupole are summarised in table 51 for the two optimum scenarios explained above: the optimum found for the smallest synchrotron radiation power and the optimum for the smallest critical energy of the emitted

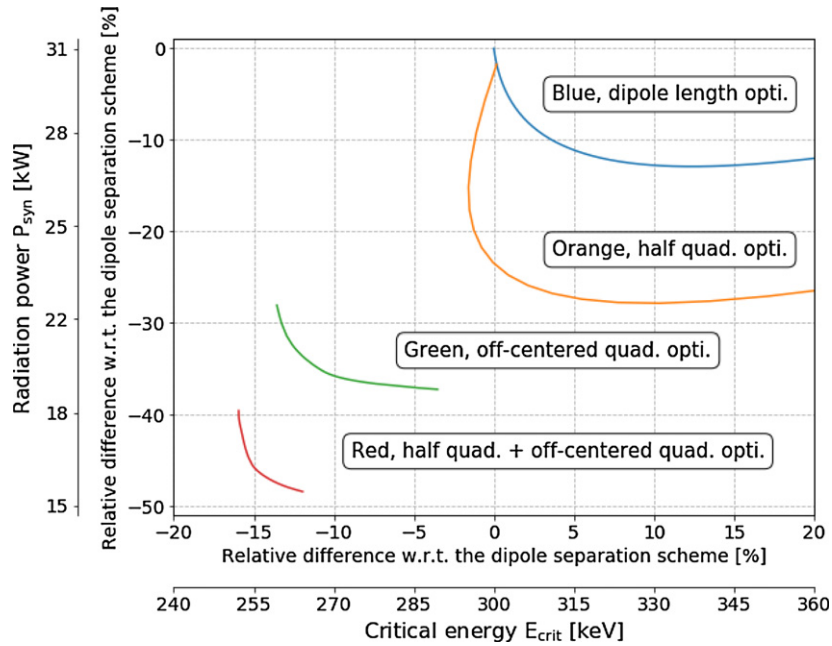


**Figure 187.** Relative differences with respect to the original single dipole separation scheme. The synchrotron radiated power is plotted as a function of the critical energy for different optimisation results: only optimising the dipole length (blue), only using a mirror quadrupole (orange), only using off-center quadrupoles (green), and combining the mirror quadrupole with earlier focussing (red).

**Table 51.** Magnetic gradient of the proposed half quadrupole for the lowest synchrotron radiaton power and the lowest critical energy. An aperture of  $15\sigma$  plus tolerances of 20% for beta beating and 2 mm for the orbit have been assumed.

Half quadrupole parameter	Unit	Minimum synchrotron	
		radiation power	Minimum critical energy
$\gamma\epsilon_p$	mm mrad	2.50	2.50
Gradient	$T m^{-1}$	48.2	50.7
Aperture radius	mm	27.0	25.6
Length	m	6.84	2.08

radiation. The values result from the optics studies of the previous sections. The presented gradients lead to a pole tip field of  $B_p \approx 1.3$  T.

In both cases, the proton aperture radius has been chosen to include an orbit tolerance of 2 mm, a 10% tolerance on the beam size due to optics imperfections (beta-beating) and a beam size that corresponds to  $n = 15\sigma$  for a proton-beam normalised emittance  $\epsilon_p = 2.50 \mu\text{m}$  (a value that is comfortably larger than the requirements of the HL-LHC standard lattice). The injection proton optics has been taken into account and although it features a larger emittance, it clearly fits in the aperture; see the red dashed line in figure 188. The electron beam and the non-colliding proton beam will pass through the field-free region delimited by the mirror plate.



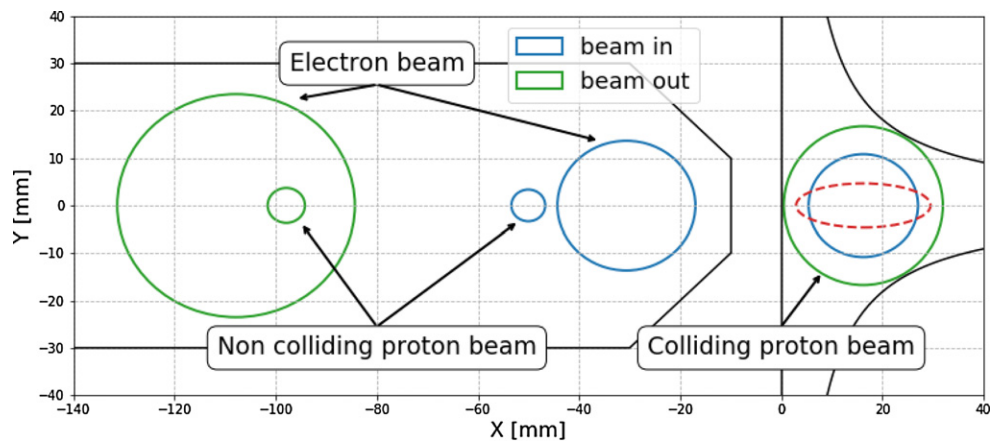


**Figure 188.** The positions of the three beams at the entrance (blue) and exit (green) of the half quadrupole. The colliding proton beam is centred inside the main magnet aperture, while the second proton beam and the electrons are located in the field-free region. The dashed red line represents the injection proton beam at the output of the half quadrupole.

The aperture requirements inside the half quadrupole are determined on one side by the colliding proton-beam optics in the main aperture of the magnet. The beam separation scheme and the optics of the electron and non-colliding proton beam on the other side have to fit into the field-free region beyond the midplane of the mirror plate. As described below, a crossing angle of 7 mrad is assumed for the noncolliding protons. These requirements are illustrated in figure 188. For the case of the smallest synchrotron radiation power, the three beams are plotted at the entrance and exit of the quadrupole lens. For both proton beams the beam size shown in the graph corresponds to  $15\sigma$  plus a 2 mm orbit tolerance and 10% for beam-size beating. Due to the mini-beta optics, the colliding proton beam nearly fills the given aperture of the magnet. The non-colliding proton beam follows a relaxed optical path with very limited aperture requirements. The envelope of the electron beam is shown for  $20\sigma$  beam size in both transverse planes.

In contrast to the proton half quadrupole, the doublet magnets of the early focussing scheme will house the three beams in a single aperture. In addition to the beam envelopes, the offset that has been chosen to provide the beam-separation effect has to be taken into account and included in the aperture considerations.

This situation is visualised in figure 189. The left side presents the first off-center quadrupole (powered as a focussing lens). Following the field direction, the electron beam is offset towards the outer side of the ring (right side of the plot), as defined by the proton beam's closed orbit. The right part of the figure shows the second quadrupole (powered as a defocusing lens) with the electron-beam offset shifted in the other direction. In order to provide a sufficient aperture for the three beams, an elliptical shape has been chosen for the vacuum chamber. It defines enough space for the beam envelopes and the off-centre design trajectories. The black ellipses correspond to the beams at the entrance of the magnet, while the red shapes represent the beams at the exit. From left to right, the three beams are, respectively, the non-colliding proton beam (tiny circles), the electron beam (squeezed ellipses), and the colliding proton beam. As defined before, we refer to a beam size of  $20\sigma$  in the case of the electrons and 15 sigma plus beta-beating plus a 2 mm orbit tolerance for the colliding and non-colliding proton beams.

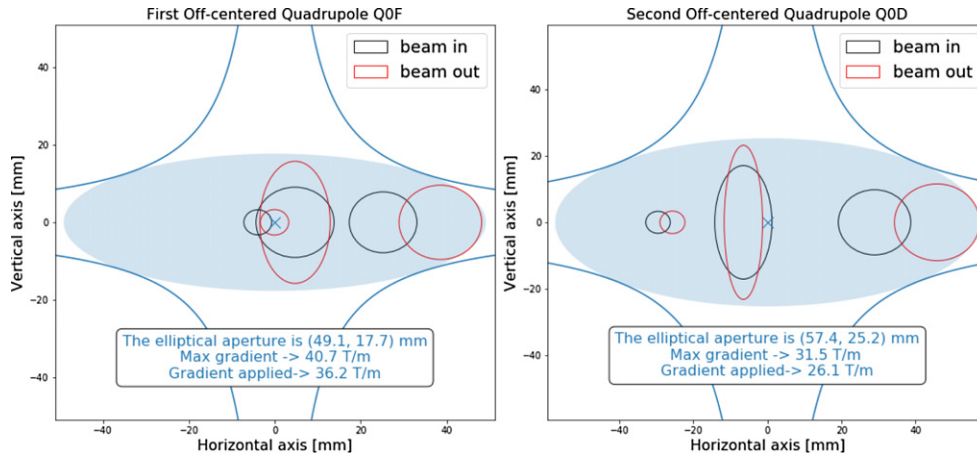


**Figure 189.** The positions of the three beams at the entrance (black) and exit (red) of the electron doublet magnets. Following the internal convention, beam envelopes of  $15\sigma$  plus a 20% beta beating tolerance plus a 2 mm orbit tolerance are chosen for the proton beams. The beam size of the electrons refers to  $20\sigma$ . From left to right, the three beams are, respectively, the non-colliding proton beam (tiny circles), the electron beam (squeezed ellipses), and the colliding proton beam.

**Table 52.** Magnetic gradients and pole tip apertures of the doublet quadrupoles for the synchrotron power optimum.

Parameter	Unit	Q0F	Q0D
$\gamma\epsilon_e$	mm mrad	50	50
$\gamma\epsilon_p$	mm mrad	2.50	2.50
Gradient	$\text{T m}^{-1}$	36.2	26.1
Min. pole tip radius	mm	28.9	38.1
Length	m	1.86	1.86

In this context, it should be pointed out that the non-colliding proton beam, travelling in the same direction as the electrons, is shifted in time by half the bunch spacing. While the projected beam envelopes in figures 189 and 188 seem to overlap in the transverse plane, they are well separated by 12.5 ns, corresponding to 3.75 m in the longitudinal direction.

The minimum required gradients and pole tip radii of the doublet quadrupoles are listed in table 52.

Following the increase in beam size after the IP, the two quadrupoles are optimised for a sufficient free aperture for the colliding beams and their design orbits. Accordingly, a different layout has been chosen for these magnets, to provide the best conditions for the radiation power and critical energy. An alternative approach has been studied, based on a single quadrupole design for both lenses of the doublet. While an optical solution is still possible, it does not, however, allow for the minimum radiation power, and it sets more stringent requirements on the shielding and absorption of the synchrotron light fan (figure 190).

The chromatic effect of the two lattice versions as a function of the momentum spread is shown in figure 191. The lattice based on a single dipole magnet and late focussing of the electron beam shows an increase of the  $\beta$  function of up to 40% in the vertical plane for particles

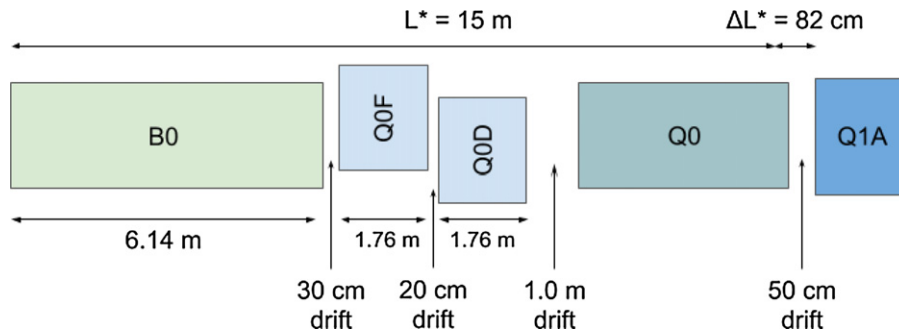


**Figure 190.** Possible optimised design featuring a 1.0 m drift between the off-centre quadrupoles and the half quadrupole in order to leave space for shielding material.

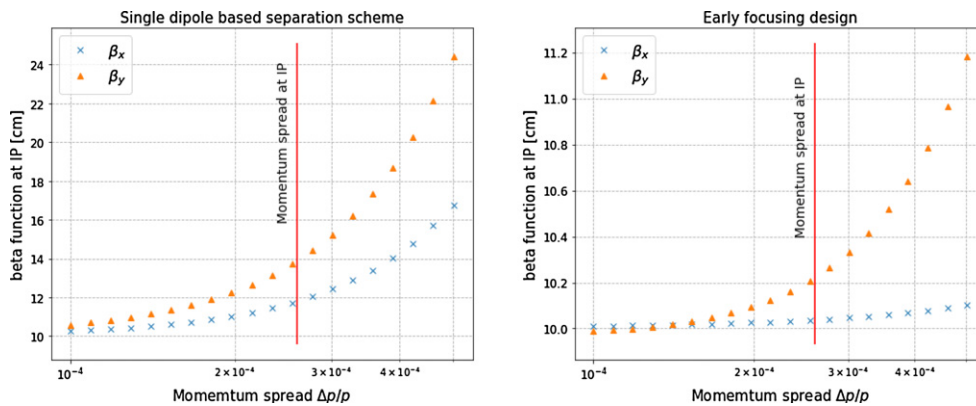


**Figure 191.** Beta function at the IP as a function of the momentum spread. Left: situation for the single-dipole-based separation scheme. Right: with the design featuring earlier focussing. The graphs show the increase of  $\beta^*$  due to the chromaticity of the lattice.

with a momentum deviation up to the design value of  $\frac{\Delta p}{p} = 2.6 \times 10^{-4}$  (vertical cursor line in the graph) and a corresponding luminosity loss of 20% for those particles (see figure 192). The optimised design, based on the early focussing scheme, shows a much-reduced chromatic effect and the resulting off-momentum beta beating at the IP is limited to a few percent. As a direct consequence, the luminosity loss is well below the 1.5% level. Therefore, a special local chromaticity correction scheme to address aberrations at the IP is not considered to be necessary. Further studies will include the recirculation of the post-collision beam and the energy-recovery performance and might nevertheless highlight the need for explicit sextupoles to mitigate the growing momentum spread through the deceleration process and to avoid beam losses.

10.7.4. Interaction-region magnet design.

10.7.4.1. Triplet magnet design . While the Q1 magnets remain in the range achievable with the well-proven Nb–Ti superconductors operated at 1.8 K, the Q2 magnets require Nb<sub>3</sub>Sn technology at an operating temperature of 4.2 K. The working points on the load line are given for both superconducting technologies in figure 193.

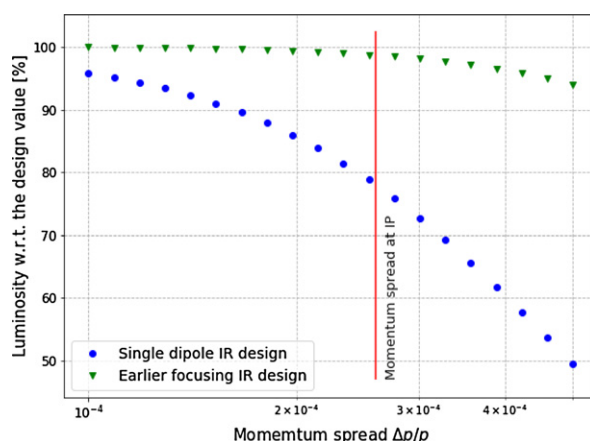


**Figure 192.** Luminosity as a function of the momentum spread for the single-dipole-based separation scheme (blue circles) and the design featuring earlier focussing (green triangles).

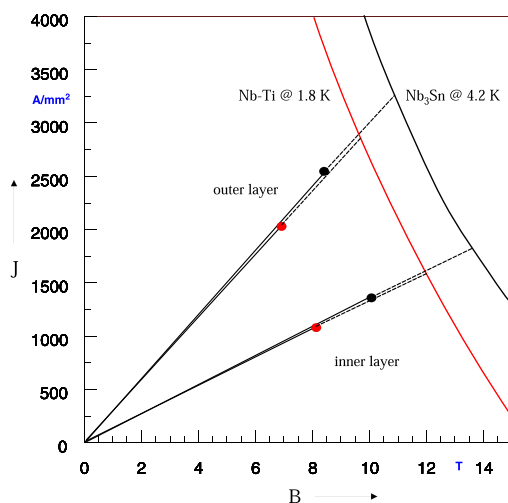


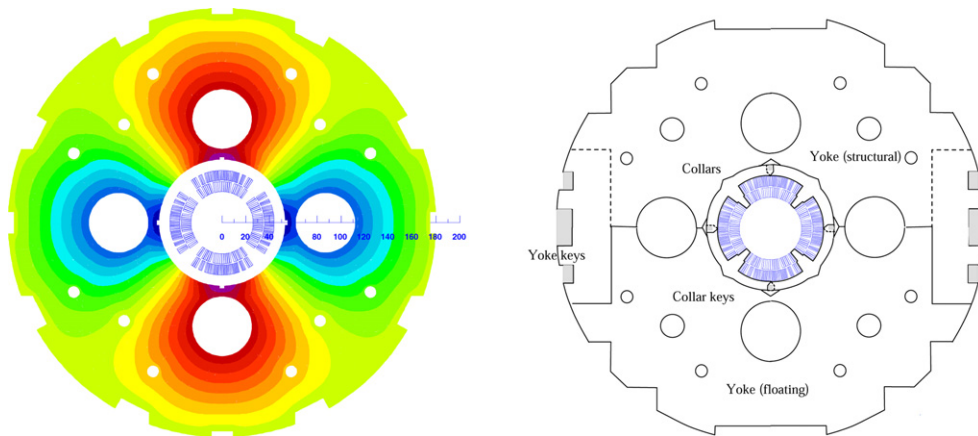
**Figure 193.** Working points on the load line for both Nb–Ti and Nb<sub>3</sub>Sn variants of Q1A.

The thickness of a coil layer is limited by the flexural rigidity of the cable, which will make the coil-end design difficult. Therefore, multilayer coils must be considered. However, a thicker, multilayer coil will increase the beam separation between the proton and the electron beams. The results of the field computation are given in table 53.

Unlike the design proposed in the CDR of 2012 [1], the increased beam separation distance between the colliding proton beam and the electron beam makes it possible to neglect the fringe fields in the electron beam pipe. For the Q2 and Q3 magnets, the electron beam is outside the quadrupole cold mass and consequently, an HL-LHC inner-triplet magnet design can be adapted.

**Table 53.** Main triplet magnet parameters.

Magnet parameter	Unit	Magnet type			
		Q1A	Q1B	Q2 type	Q3 type
Superconductor type		Nb–Ti	Nb–Ti	Nb <sub>3</sub> Sn	Nb <sub>3</sub> Sn
Coil aperture radius $R$	mm	20	32	40	45
Nominal current $I_{\text{nom}}$	A	7080	6260	7890	9260
Nominal gradient $g$	T m <sup>-1</sup>	252	164	186	175
Percentage on the load line	%	78	64	71	75
Beam separation distance $S_{\text{beam}}$	mm	106–143	148–180	233–272	414–452

**Figure 194.** Conceptual design of the final focus septa Q1. Left: magnetic vector potential (field lines). Right: sketch of the mechanical structure.

For the Nb<sub>3</sub>Sn material, we assume a composite wire produced with the internal Sn process (Nb rod extrusions) [866]. The non-Cu critical current density is 2900 A mm<sup>-2</sup> at 12 T and 4.2 K. The filament size of 46 μm in Nb<sub>3</sub>Sn strands gives rise to higher persistent current effects in the magnet. The choice of Nb<sub>3</sub>Sn would require a considerable research and development and engineering design effort, which is, however, no more challenging than other accelerator magnet projects, such as the HL-LHC.

The conceptual design of the mechanical structure of the Q1 magnets is shown in figure 194 (right). The necessary prestress in the coil-collar structure, which must be high enough to avoid unloading at full excitation, cannot be exerted by the stainless-steel collars alone. Two interleaved sets of yoke laminations (a large one comprising the area of the yoke keys and a smaller, floating lamination with no structural function) provide the necessary mechanical stability of the magnet during cooldown and excitation. Preassembled yoke packs are mounted around the collars and put into a hydraulic press, so that the keys can be inserted. The sizing of these keys and the amount of prestress before the cooldown will have to be calculated using mechanical FEM programs. This also depends on the elastic modulus of the coil, which has to be measured using a short model equipped with pressure gauges. Special care must be taken to avoid forbidden multipole harmonics, because the fourfold symmetry of the quadrupole will not be entirely maintained.

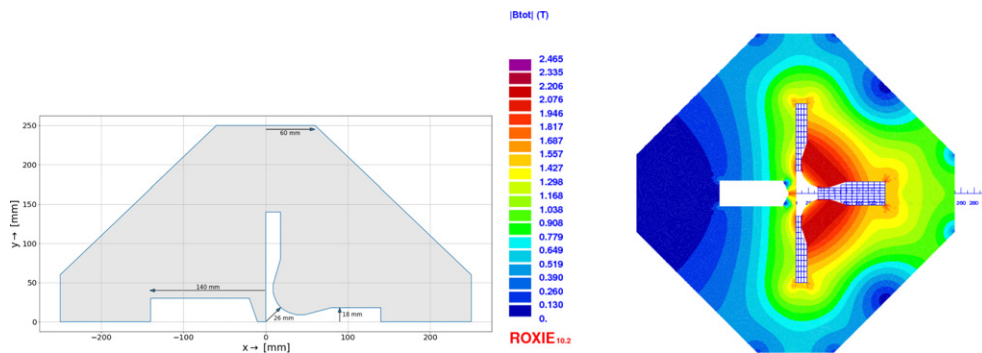


**Figure 195.** Left: mechanical layout of the new half quadrupole for the proton beam. Right: field distribution in the half quadrupole for the proton beam.

For the Q2 and Q3 magnets, an HL-LHC inner triplet design using a bladder and key mechanical structure can be adapted.

**10.74.2. Normal conducting magnet design** . The proposed mini-beta doublet of the electron lattice, which provides early focussing of the beam, and the normal conducting proton-half quadrupole are new magnet concepts. These have been conceptually studied to determine their technical feasibility. The geometry of the QNC magnet is shown in figure 195 (left). At the left of the mirror plate, the field-free region will provide space for the electron beam and the non-colliding proton beam. The thickness of the mirror plate at the magnet midplane is 20 mm, allowing for sufficient mechanical stability at the minimal beam separation between the electron and proton beams.

Field calculations made using the magnet design code Routine for the Optimisation of magnetic X-sections, Inverse field calculation and coil End design (ROXIE) [867] are presented in figure 195 (right). The achieved field gradient is  $50 \text{ T m}^{-1}$  for a current of 400 A, assuming a current density of  $21.14 \text{ A mm}^{-2}$ . This is in line with the conductor geometries used for normal conducting magnets installed in the CERN injector complex, for example, ID: PXMQNDD8WC, which is rated at 860 A corresponding to  $45.45 \text{ A mm}^{-2}$ . A more comprehensive design study must also include a further reduction of the multipole field components.

The geometries of the Q0F and Q0D quadrupoles are given in figure 189 and the main specifications are provided in table 52. A maximum magnetic field of 1.2 T at the pole tip is well within reach for a normal conducting quadrupole.

### 10.8. Civil engineering

Since the beginning of the LHeC study that proposed an electron–hadron collider, various shapes and sizes of the  $eh$  collider were studied in the context of the CERN region. Two main options were initially considered, namely the ring–ring and linac–ring configurations. The civil engineering implications of these options were studied, taking into account geology, construction risks, and land features as well as the technical constraints and operations of the LHC. The linac–ring configuration was selected, favouring a higher achievable luminosity. This chapter describes the civil engineering infrastructure required for an ERL injecting into the ALICE cavern at point two of the LHC. Figure 196 shows three options for different sizes of ERL, represented as fractions of the LHC circumference, namely,  $1/3$ ,  $1/4$ , and  $1/5$  of the LHC circumference.





**Figure 196.** Racetrack options proposed for the LHeC at point two of the LHC. The colour coding illustrates different options for 1/3, 1/4, and 1/5 of the LHC circumference, resulting in different electron-beam energies. Reproduced from [8]. © IOP Publishing Ltd. CC BY 3.0.

*10.8.1. Placement and geology.* The proposed site for the LHeC is in the northwestern part of the Geneva region at the existing CERN laboratory. The proposed interaction region is completely located within existing CERN land at LHC point two, close to the village of St. Genis, in France. The CERN area is extremely well suited to housing such a large project, with well-understood ground conditions, having accommodated several particle accelerators in the region for over 50 years. Extensive geological records exist from previous projects such as the LEP and the LHC and more recently, further ground investigations have been undertaken for the high-luminosity LHC project. Any new underground structures will be constructed in the stable molasse rock at a depth of 100–150 m in an area with low seismic activity.

The LHeC is situated within the Geneva basin, a sub-basin of the large molassic plateau (figure 197). The molasse is a weak sedimentary rock which resulted from the erosion of the Alps. It comprises alternating layers of marls and sandstones (and formations of intermediate composition), which show a high variety of strength parameters [868]. The molasse is overlaid by Quaternary glacial moraines. A simplified geological profile of the LHC is shown in figure 198. Although placed mainly within the molasse plateau, one sector of the LHC is situated in the Jura limestone.

The physical positioning of the LHeC has been developed based on the assumption that the maximum underground volume should be placed within the molasse rock and should, as far as possible, avoid any known geological faults or environmentally sensitive areas. As it is stable and dry, the molasse is considered a suitable rock type for tunnel boring machine (TBM) excavation. In comparison, CERN has experienced significant issues with the underground

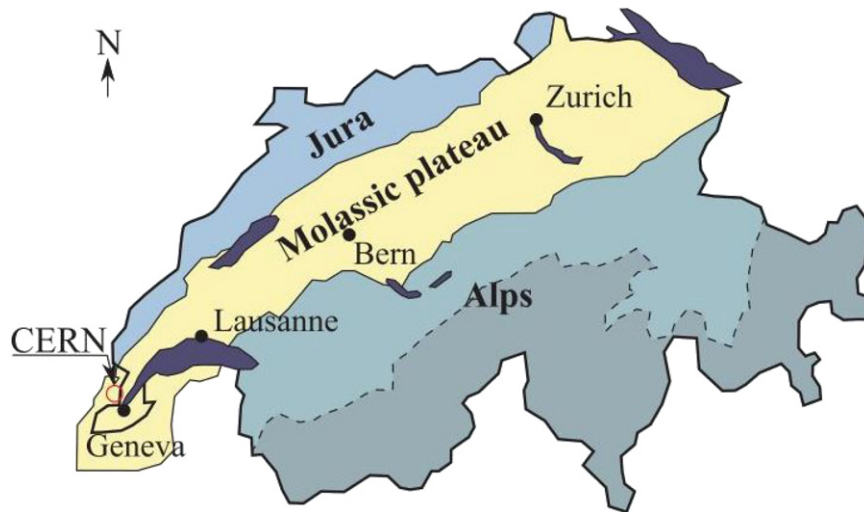


**Figure 197.** Simplified map of Swiss geology. Reprinted from [868], Copyright 2018, with permission from Elsevier.

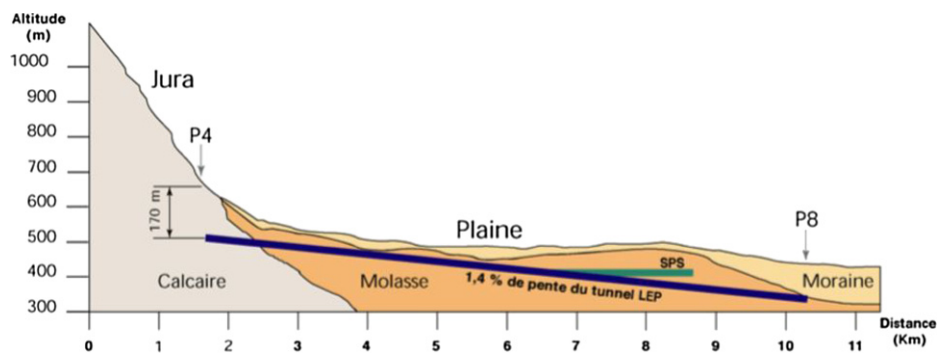


**Figure 198.** Geological profile of the LHC tunnel. Reproduced from [30]. CC BY 4.0.

construction of sectors three and four in the Jura limestone. There were major issues with water ingress at and behind the tunnel face [869]. Another challenging factor associated with limestone is the presence of karsts. These are formed by the chemical weathering of the rock, and they are often filled with water and sediment, which can lead to water infiltration and excavation instability.

The ERL will be positioned inside the LHC layout, in order to ensure that the new surface facilities are located on existing CERN land. The proposed underground structures for the LHeC with an electron beam energy of 60 GeV are shown in figure 199. The LHeC tunnel will be tilted similarly to the LHC at a slope of 1.4% to follow a suitable layer of molasse rock.

**10.8.2. Underground infrastructure.** The underground structures proposed for the LHeC option corresponding to 1/3 of the LHC require a 9 km-long tunnel and two LINACs. The internal diameter of the tunnel is 5.5 m. The RF galleries, each 1070 m long, are parallel to the

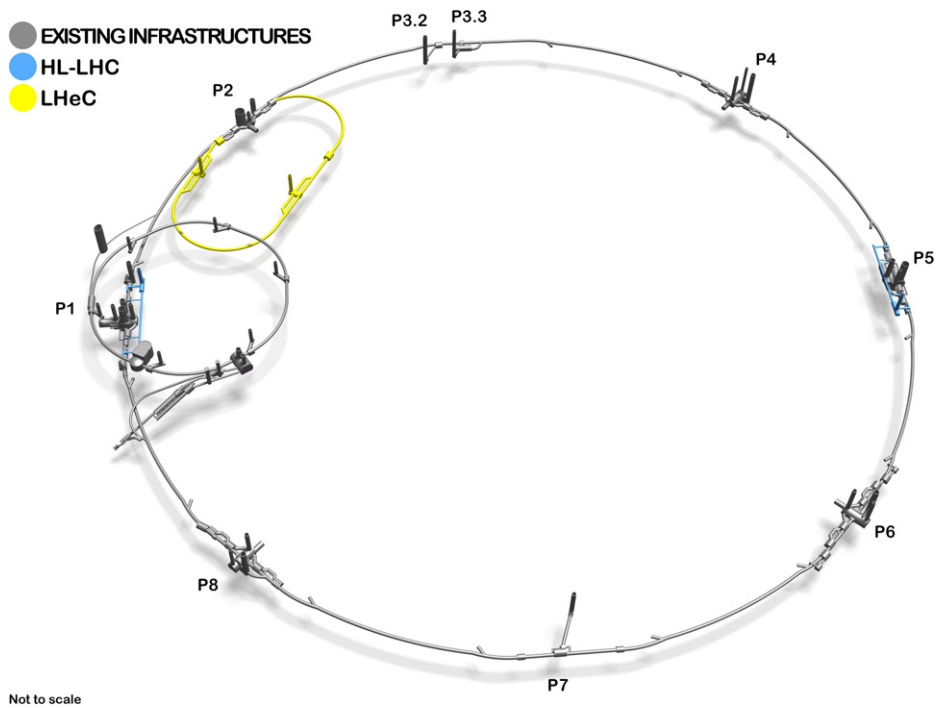


**Figure 199.** 3D schematic showing the proposed underground structures of the LHeC (shown in yellow). The HL-LHC structures are highlighted in blue. Reproduced from [1]. © IOP Publishing Ltd. CC BY 3.0.

**Table 54.** List of underground structures for LHeC for two different options with 1/3 or 1/5 of the LHC circumference.

Structure	Quantity	Span (m)	1/3 LHC	1/5 LHC
			Length (m)	Length (m)
Machine tunnels	—	5.5	9000	5400
Service caverns	2	25	50	50
Service shafts	2	9	80	80
Injection caverns	1	25	50	50
Dump caverns	1	16.8	90	90
Junction caverns	3	16.8	20	20
RF galleries	2	5.5	1070	830
Waveguide connections	50	1	10	10
Connection tunnels	4	3	10	10

LINACs at a distance of 10 m. Waveguides with a 1 m diameter and four connection tunnels connect the RF galleries and the LINACs. These structures are listed in table 54.

Two additional caverns, 25 m wide and 50 m long, are required for cryogenics and technical services. These are connected to the surface via two shafts 9 m in diameter, provided with lifts, to allow access for equipment and personnel. Additional caverns are needed to house the injection facilities and a beam dump. As shown in table 54, the underground structures

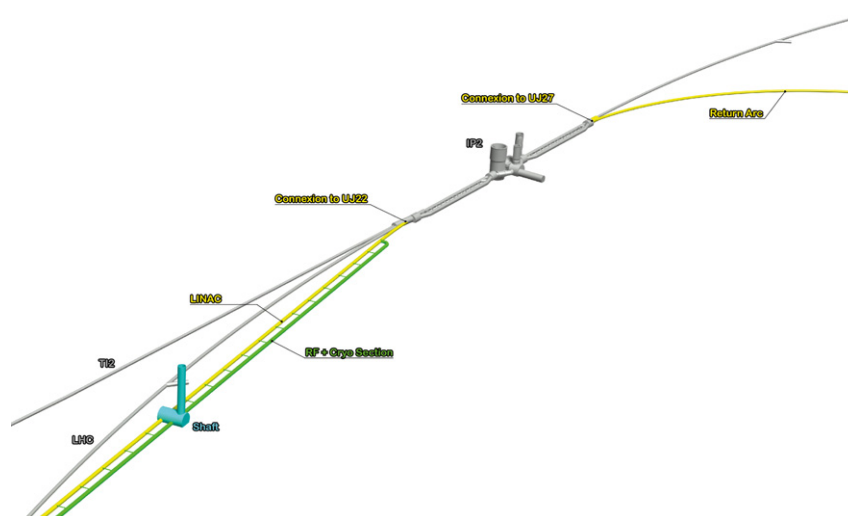


**Figure 200.** ERL injection area into IP2 and the junction cavern. Reproduced from [1].  
© IOP Publishing Ltd. CC BY 3.0.

proposed for the LHeC options corresponding to 1/5 of the LHC and 1/3 of the LHC are similar, with the exception of the main tunnel and the RF galleries, which have different lengths.

Shaft locations were chosen such that the surface facilities are located on CERN land. The scope of work for surface sites is still to be defined. New facilities are envisaged that will house technical services such as cooling and ventilation, cryogenics, and electrical distribution.

In addition to the new structures, the existing LHC infrastructure requires some modifications. To ensure a connection between the LHC and LHeC tunnels, the junction caverns UJ22 and UJ27 need to be enlarged. Figure 200 shows the location of these caverns. Localised parts of the cavern and tunnel lining will be broken out to facilitate the excavation of the new spaces and the new connections, requiring temporary support.

Infrastructure works for the LEP collider were completed in 1989, for which a design lifespan of 50 years was specified. If the LHC infrastructure is to be reused, refurbishment and maintenance works will be needed.

**10.8.3. Construction methods.** A TBM will be utilised for the excavation of the main tunnel to achieve the fastest construction. When ground conditions are good and the geology is consistent, TBMs can be two to four times faster than conventional methods. A double-shield TBM could be employed, installing pre-cast segments as the primary lining, and injecting grouting behind the lining.

For the excavation of the shafts, caverns, and connection tunnels, typical conventional techniques could be used. Similar construction methods to those used during the HL-LHC construction can be adopted for the LHeC, for example, the use of roadheaders and rockbreakers. This machinery is illustrated in figure 201, showing the excavation works at point one. One main constraint that dictated the choice of equipment used for the HL-LHC excavation was the vibration limit. Considering the sensitivity of the beamline, diesel excavators were modified and equipped with electric motors in order to reduce vibrations that could disrupt LHC operation. Similar equipment could be required for the LHeC, if construction works are carried out during the operation of the LHC.



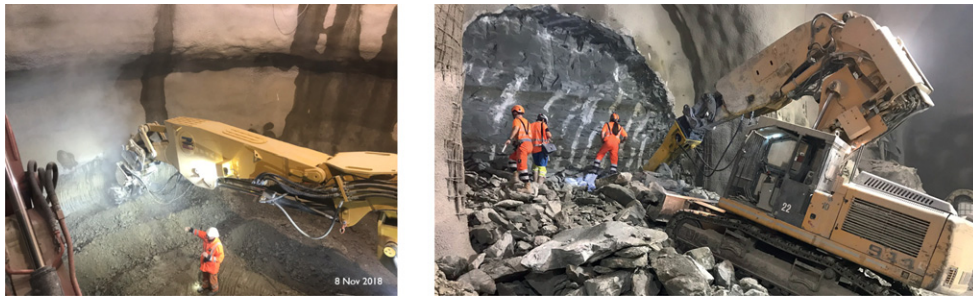


**Figure 201.** Left: roadheader being used for shaft excavation at HL-LHC point one. Right: rockbreaker used for new service tunnel excavation at HL-LHC point five. Reproduced with permission from [Z Arenas].

Existing borehole data for the area around IP2 show that the moraine layer is approximately 25–35 m thick above the molasse. Temporary support of the excavation, for example, using diaphragm walls, is recommended. Once stable ground under dry conditions is reached, common excavation methods can be adopted. The shaft lining will consist of a primary layer of shotcrete with rockbolts and an *in situ* reinforced concrete secondary lining, with a waterproofing membrane in between the two linings.

**10.8.4. Civil engineering for the FCC-eh.** A facility allowing collisions between protons and electrons was considered in the study for the FCC. Figure 202 shows the baseline position for the FCC and the lepton ring located at point *L*.

During the FCC feasibility stage, a bespoke geographical information system (GIS)-based tool (the tunnel optimisation tool (TOT)) was used to optimise the placement and layout of the FCC ring. The current baseline location was chosen such that the FCC tunnel is placed in preferable geology (90% of the tunnel is in molasse), the depth of the shafts and the overburden is minimised, and the tunnel under Lake Geneva goes through the lakebed, passing through reasonably stable ground. More investigations are needed to determine the feasibility of tunnelling under Lake Geneva. The baseline position also allows connections to the LHC. Figure 203 shows the geological profile of the tunnel in the baseline position. The TOT was used to evaluate different layouts and positions for the FCC ring and assess its impact on the location of the lepton ring. The candidate locations for the *eh* IR were the experimental points *A*, *B*, *G* and *L*. Point *L* was selected because it provides good geological conditions, being fully housed in the molasse layer at a depth of around 180 m. In comparison, point *G* is much deeper, point *A* is challenging due to proximity of the LHC, and point *B* is located in a congested urban area. Similarly to the LHeC, the lepton ring will be located inside the FCC ring, in this instance, to avoid the Jura limestone. The entire FCC-eh infrastructure is located in the molasse.

The geological data captured within the TOT tool were collected from various sources including previous underground projects at CERN, the French Bureau de Recherches Géologiques et Minières (BRGM), and existing geological maps and boreholes for geothermal and petroleum exploration. The data were processed to produce rock-head maps and to create the geological layers. No ground investigations have been conducted specifically for the FCC project [16]. In order to validate its baseline alignment and determine the geotechnical parameters required for the detailed design, site investigation campaigns will need to be carried out. Some boreholes exist in the region where the tunnel for the lepton ring will be built,

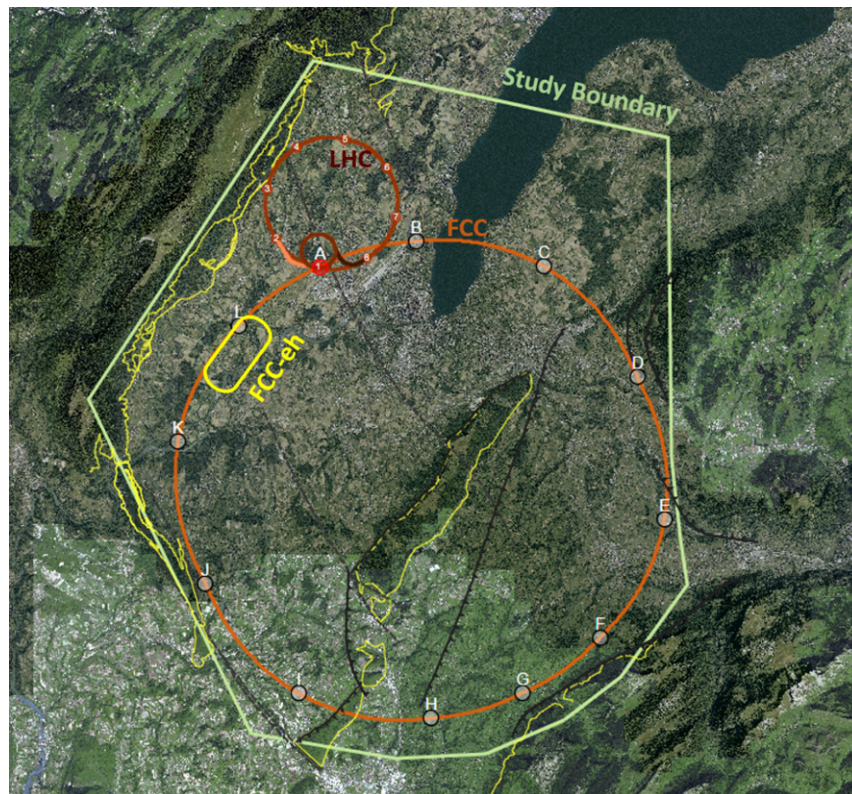


**Figure 202.** Baseline position and layout for the FCC. The leptonic ring location is shown at point *L*. Reproduced from [15]. CC BY 4.0.

reducing the uncertainty of the ground conditions. However, further ground investigations are needed in order to verify the boundaries between geological layers. The geological features of interest in this region are the Allondon fault and possible zones of poor rock and limestone content, which should be avoided.

The IP will be in the experimental cavern at point *L*, defined as an experimental point for FCC-hh. The layout of the ERL and the underground infrastructure for the FCC-eh are similar to those of the LHeC (see table 54), with the exception of the shafts, which are 180 m deep. The schematic layout and proposed civil engineering structures are shown in figure 204.

The upper excavation for each shaft will be through the moraines. Based on available geological data, the moraine layer should be approximately 30 m deep. Similar construction methods to those described in section 8.8.3 could be used. For the FCC, an alternative technology that has been considered for deep shafts is a vertical shaft-sinking machine. The junction caverns connecting the ERL tunnel with the FCC tunnel must be designed such that they meet the requirements for the new collider and the lepton machine. The junction caverns near point *L* will connect three tunnels: the FCC main tunnel, the ERL tunnel, and the RF galleries. These caverns will have a span of 25 m and a length of 50 m.

For the FCC TBM excavations, different lining designs have been developed, corresponding to the rock conditions [16]. Good ground conditions have been assumed, based on available



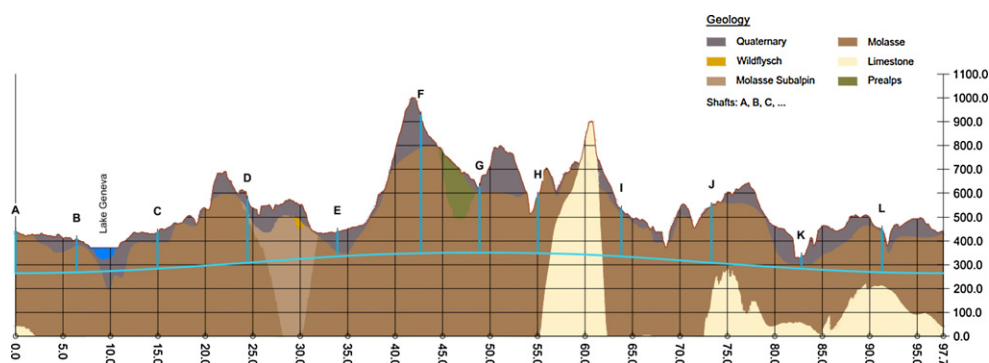


**Figure 203.** Geological profile along the FCC tunnel circumference. Reproduced from [15]. CC BY 4.0.

geological information in the area where the ERL tunnels are positioned, and a single-pass precast lining is proposed.

**10.8.5. Cost estimates.** The cost of the underground civil engineering for the FCC-eh facility was estimated to be approximately 430 MCHF. The construction programme for the lepton accelerator tunnels, caverns, and shafts is currently integrated into the overall FCC construction schedule.

A detailed cost estimate was prepared for a 9 km ERL located at point two of the LHC, using the same unit prices as for the FCC. More recently, for the LHeC, the cost figures were adapted to fit the smaller version, the 5.4 km racetrack at point two (the option corresponding to 1/5 of the LHC). The civil engineering costs amount to about 25% of the total project costs. For the 9 km ERL (the option corresponding to 1/3 of the LHC) the civil engineering costs were estimated to be 386 MCHF, and for a 5.4 km configuration (corresponding to 1/5 of the LHC) the costs would be 289 MCHF. These costs do not include the surface structures. Where possible, existing surface infrastructure will be reused.

The cost estimates include the fees for preliminary designs, approvals, and tender documents (12%), site investigations (2%), and contractor profits (3%). The accuracy range of the cost estimates at the feasibility stage is  $\pm 30\%$ .

**10.8.6. Spoil management.** As with all construction projects, environmental aspects play an important role. A detailed study is being conducted at CERN to find a potential reuse for the spoil that will be generated by the FCC underground excavations. The total amount of spoil is calculated to be approximately 10 million cubic metres, of which 778 000 cubic metres of spoil will be generated by the lepton ring tunnel construction.

## 11. The technology of ERL and PERLE

Energy recovery was proposed in 1965 [870] as a means for efficient colliding beam interactions. It has, indeed, been demonstrated to work at a number of laboratories, for example, the Budker Institute of Nuclear Physics (BINP) Novosibirsk, Daresbury, Jefferson Lab, and very recently at Cornell. The striking technology developments in high-quality superconducting cavities over the last decades and the need for high collider intensities at economic power levels have now led to a wider recognition of ERL applications as one of the most promising and fundamental developments of energy-frontier accelerator physics. For the

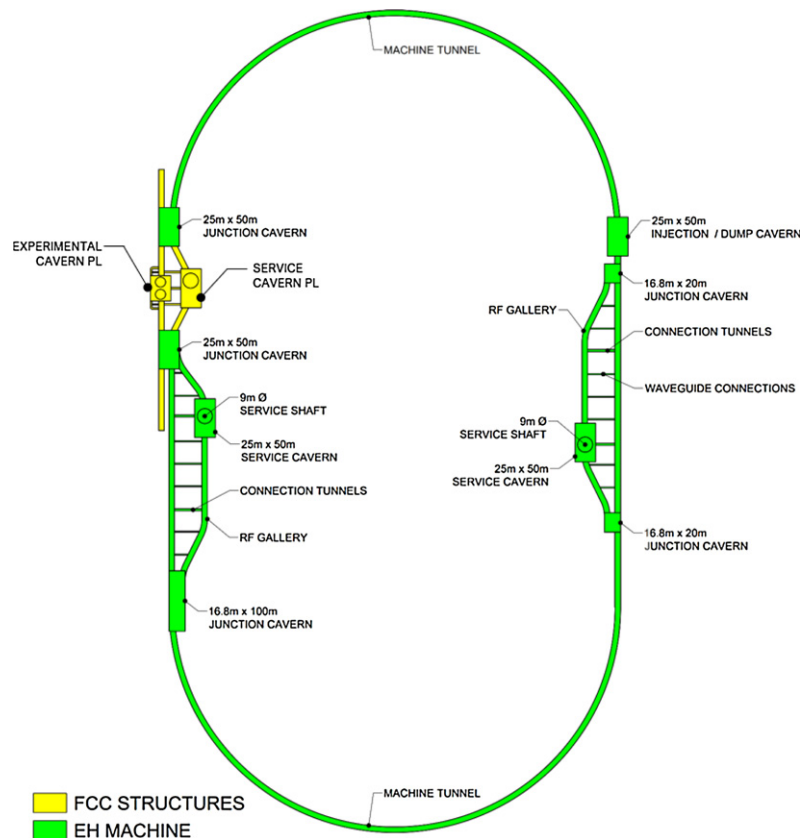


**Figure 204.** Schematic layout showing the proposed underground structures for FCC-eh.

LHeC, it had already become clear with, and before the CDR, that ERL technology was the only way to achieve high luminosity in  $ep$  within the given power limit of 100 MW at the wall plug for the linac–ring  $ep$  collider configuration. For FCC-ee, it has been promoted as an alternative to conventional synchrotron technology for extending the energy range and increasing the luminosity in the  $WW$  and top mass ranges [32]. A high-current electron ERL is designed to reach high luminosities with proton-beam cooling at the EIC [871]. High-energy particle and nuclear physics colliders are now waiting for high-current ERLs to become available.

Following the LHeC CDR, it became increasingly clear, and was much emphasised by the IAC of the LHeC that the basic concept of a high-current, multiturn ERL needed a smaller facility with which to gain experience and develop the technology. This led to the development of the PERLE concept, as described in a CDR published in 2017 [7]. PERLE imported the main characteristics of the LHeC, namely, the 802 MHz frequency and the three-turn racetrack configuration of two oppositely positioned linacs. With the 20 mA current goal and a 500 MeV beam, it represents the first ERL facility in the 10 MW power range. Its intensity, which exceeds that of ELI by two to three orders of magnitude, is the basis for novel low-energy experiments which are envisaged to follow the first years of dedicated accelerator design study and

technology development. PERLE therefore has a physics and technical programme that reaches beyond supporting the LHeC design and possible future operation.

An international collaboration has recently been established with the aim of realising PERLE in a few stages at the IJC Laboratory at Orsay near Paris within the next few years. The following chapter has two parts; the first describes the challenges and status of ERL developments, and the second briefly summarises PERLE. It should be noted that the crucial parts of PERLE are described above in the LHeC linac section, such as the choice of frequency, the electron source, and the successful design, construction, and test of the first five-cell SC niobium cavity, because all these characteristics are shared between the LHeC and its development facility.

### 11.1. Energy-recovery linac technology – status and prospects

In instances where a high beam power is required, the concept of energy recovery presents an attractive solution. ERLs constitute a class of novel accelerators which are uniquely qualified to meet the demands of a wide variety of applications by borrowing features from traditional architectures to generate linac-quality beams with near-storage-ring efficiency [872]. After acceleration through a linac section, the electrons in an ERL are returned 180° out of phase with respect to the RF accelerating field, which enables energy recovery. The beam deposits energy into cavity fields, which can then accelerate newly injected bunches, thereby effectively cancelling the beam-loading effects of the accelerated beam. Therefore, ERLs can accelerate very high average currents with only modest amounts of RF power. Because the beam is constantly being renewed, it never reaches an equilibrium state. Consequently, this provides flexibility to manipulate the phase space and tailor the beam properties for a specific application. Furthermore, since the energy of the decelerated beam is approximately equal to the injection energy, the dump design becomes considerably easier.

**11.1.1. ERL applications.** Historically, nearly all ERLs built and operated were used to drive an FEL. The requirement for high-peak-current bunches necessitated bunch compression and addressing the attendant beam dynamical challenges. In recent years, ERLs have changed from being drivers of light sources to being applied in nuclear physics experiments, as Compton backscattering sources, and for strong electron cooling. Unlike an FEL, these latter use cases require long, high-charge bunches with a small energy spread. While a short bunch length was once the key performance metric, there is now a premium on maintaining a small correlated energy spread (with a commensurately long bunch).

**11.1.2. Challenges.** ERLs are not without their own set of challenges. In the following sections, a brief survey is given of some of the most relevant. These include collective effects, such as space charge, the multipass BBU instability, CSR, and the microbunching instability ( $\mu$ BI), beam dynamic issues such as halo, the interaction of the beam with the RF system, and other environmental impedances as well as issues related to common transport lines.

**11.1.2.1. Space charge .** The role of space charge forces (both transverse and longitudinal) often dictates many operational aspects of the machine. Maintaining beam brightness during the low-energy injection stage is vitally important. In addition to the low energy, ERL injectors must also preserve beam quality through the merger system that directs the beam to the linac axis. Once injected into the linac, the beam energy at the front end is often still low enough that space charge forces cannot be neglected. Just as important is the longitudinal space charge (LSC) force, which manifests itself as an energy-spread asymmetry about the linac on-crest phase [873]. The LSC wake acts to accelerate the head of the bunch while decelerating the tail. Operating on the rising part of the waveform leads to a decrease

in the correlated energy spread, while acceleration of the falling side leads to an increase. These observations inform where acceleration is performed and how the longitudinal match is achieved.

**11.1.2.2. Beam breakup instability** . Beam breakup instability is initiated when a beam bunch passes through an RF cavity off-axis, thereby exciting dipole HOMs. The magnetic field of an excited mode deflects following bunches travelling through the cavity. Depending on the details of the machine optics, the deflection produced by the mode can translate into a transverse displacement at the cavity after recirculation. The recirculated beam in turn induces an HOM voltage which depends on the magnitude and direction of the beam displacement. Thus, the recirculated beam completes a feedback loop which can become unstable if the average beam current exceeds the threshold for stability [874]. Beam breakup is of particular concern in the design of high-average-current ERLs utilizing SRF technology. If not sufficiently damped by the HOM couplers, dipole modes can exist with quality factors several orders of magnitude higher than in normal conducting cavities, creating a risk that BBU will develop. For single-pass ERLs, beam optical-suppression techniques—namely, interchanging the horizontal and vertical phase spaces to break the feedback loop between the beam and the offending HOM—are effective at mitigating BBU [875].

**11.1.2.3. Coherent synchrotron radiation** . CSR poses a significant challenge for accelerators utilizing high-brightness beams. When a bunch travels along a curved orbit, fields radiated from the tail of the bunch can overtake and interact with the head. Rather than the more conventional class of head–tail instabilities, in which the tail is affected by the actions of the head, CSR is a tail–head instability. The net result is that the tail loses energy while the head gains energy, leading to an undesirable redistribution of particles in the bunch. Because the interaction takes place in a dispersion region, the energy redistribution is correlated with the transverse positions in the bend plane and can lead to projected emittance growth. While there has been much progress in recent years to undo the effects of CSR in the bend plane using an appropriate choice of beam optics [876], it is more difficult to undo the gross longitudinal distortion caused by the CSR wake. This is particularly true in applications in which the intrinsic energy spread is small and/or the effect can accumulate over multiple recirculations. One possible mitigation is to shield the CSR wake using an appropriately sized beam pipe [877].

**11.1.2.4. Microbunching instability** . Microbunching develops when an initial density modulation, either from shot noise or from the drive laser, is converted to energy modulations through short-range wakefields such as space charge and CSR. The energy modulations are then transformed back into density modulations through the momentum compaction of the lattice. Danger arises when positive feedback is formed and the initial modulations are enhanced. This phenomenon has been studied extensively, both theoretically and experimentally, in bunch-compressor chicanes [878, 879]. Only recently has there been a concerted effort to study microbunching instability in recirculating arcs [880–882]. Because the beam is subject to space charge and/or CSR throughout an ERL, density modulations can be converted to energy modulations, and because of the native momentum compaction of the lattice (in arcs, spreaders/recombiners, chicanes, etc), those energy modulations may be converted back into density modulations. Therefore, ERLs offer potentially favorable conditions for seeding microbunching instability, which requires careful attention in the early design stages.

**11.1.2.5. Halo** . ‘Halo’ is defined as the relatively diffuse and potentially irregularly distributed components of beam phase space, which can reach large amplitudes. It is of concern

because ERL beams are manifestly non-Gaussian and can have beam components of significant intensity beyond the beam core [883]. Although it samples large amplitudes, halo responds to the external focussing of the accelerator transport system in a predictable manner. It therefore does not always have a large spatial amplitude, but will instead, at some locations, be small in size but strongly divergent. Halo can therefore present itself as *hot spots* in a beam distribution, and thus may be thought of as a lower-intensity, co-propagating beam that is mismatched to the core beam focussing, timing, and energy. Beam loss due to halo scraping is perhaps the major operational challenge for higher-power ERLs. Megawatt-class systems must control losses at unshielded locations to better than 100 parts per million to stay within facility radiation envelopes. Scaling to 100 MW suggests that control must be at the part-per-million level. This has been demonstrated, but only at specific locations within an ERL [884].

**11.1.2.6. RF transients** . Dynamic loading due to incomplete energy recovery is an issue for all ERLs [885]. In some machines, this is due to unintentional errors imposed on the energy-recovered beam; for instance, path-length errors in large-scale systems. In other machines, such as high-power ERL-based FEL drivers, it is done intentionally. When there is a potential for rapid changes to occur in the relative phase of the energy-recovered beam, dynamic loading would be difficult to completely control using fast tuners. In such cases, adequate headroom in the RF power will have to be designed into the system. These transient beam-loading phenomena are widely unrecognized and/or neglected; however, studies have been exploring these issues and the dependence on factors such as the bunch injection pattern [886]. RF drive requirements for an ERL are often viewed as *minimal*, because in steady-state operation the recovered beam notionally provides RF power for acceleration. It has, however, been operationally established that RF drive requirements for ERLs are defined not by the steady state, but rather by beam transients and environmental/design factors such as microphonics [887]. As a result, the RF power required for stable ERL operation can differ dramatically from that derived from naïve expectations.

**11.1.2.7. Wakefields and the interaction of the beam with the environment** . As with other system architectures intended to handle high-brightness beams, the performance of ERLs can be limited by wakefield effects. Not only can beam quality be compromised by the interaction of the beam with environmental impedances, but there is also significant potential for localized power deposition in beamline components. Resistive wall and RF heating have proven problematic during ERL operation in the past [888]. Extrapolation of this experience to higher bunch charges and beam powers leads to serious concerns regarding heating effects. Careful analysis and management of system component impedances is required.

**11.1.2.8. Multiturn, common transport** . Future systems must evolve to utilize multiple turns; it is a natural cost-optimization method [889], and multiturn systems can, in principle, provide performance equal to that of one-pass up/down ERLs at significantly lower cost. In addition to the use of multiple turns, cost control motivates the use of extended lengths of common transport, in which both accelerated and recovered passes are handled simultaneously using the same beam lines. This presents unique challenges for high-energy ERLs, in particular, for the LHeC, in which energy loss due to synchrotron radiation cannot be ignored and causes an energy mismatch for the common transport lines. However, addressing these challenges will open up exciting new opportunities for ERLs. In addition to PERLE and the LHeC, a multiturn ERL design from Daresbury illustrates the manner in which the cost/complexity optimum favours shorter linacs, more turns, and multiple beams in fewer beamlines [802]. This

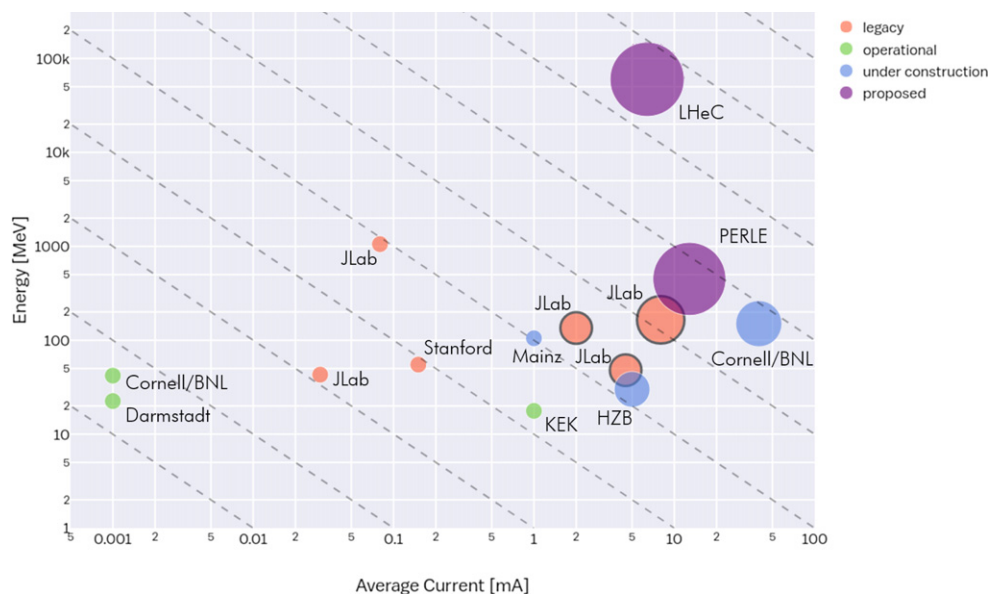


**Figure 205.** The *ERL landscape*; data points are restricted to CW, SRF-based ERLs. The dashed lines represent lines of constant beam power—starting from 10 W in the lower left and reaching 10 GW in the upper right. Note that both axes use a log scale.

also drives the use of multiple turns in stacking rings for hadron cooling; the more turns the cooling beam can utilize, the lower the current required from the driver ERL, which mitigates challenges associated with the source lifetime [890].

**11.1.3. ERL landscape.** One way to view the current state of ERLs globally is the so-called *ERL landscape* shown in figure 205 [891]. Every data point represents a machine that demonstrated energy recovery and is positioned in (maximum) energy and (average) current parameter space. For clarity, the plot is restricted to continuous-wave (CW), SRF-based ERLs only and includes legacy machines, those under construction and currently in operation, as well as the LHeC and PERLE (proposed). The size of the marker is indicative of the charge per bunch, while a black line around the marker indicates it was/is a *true ERL*, i.e. one in which the beam power exceeds the installed RF power (they are represented in the plot by the three FEL drivers that were designed, built, commissioned, and operated at the Jefferson Laboratory).

A cursory look at figure 205 illustrates several of the challenges facing the next generation of ERLs. While getting from the current state of the art to the LHeC requires only a modest increase in average current, it requires a significant increase in bunch charge and it also requires the consequent collective effects to be addressed [892]. Most significant, however, is the leap in energy from systems that have operated in the 100 MeV range to those that will operate at several tens of GeV. Note that PERLE is strategically positioned to address incremental changes in both the average current, bunch charge, and energy. As such, it provides a convenient test bed facility with which to address the issues described previously [893]. Several ERLs are still in the nascent stage and, as they ramp up beam power, will also be valuable for advancing the state of the art. For instance, though it uses a fixed-field alternating gradient arc, the CBETA will address multiturn energy recovery for the first time in an SRF system [5]. Note that with



**Table 55.** Summary of the main PERLE beam parameters.

Target parameter	Unit	Value
Injection energy	MeV	7
Electron beam energy	MeV	500
Norm. emittance $\gamma\epsilon_{x,y}$	mm mrad	6
Average beam current	mA	20
Bunch charge	pC	500
Bunch length	mm	3
Bunch spacing	ns	25
RF frequency	MHz	801.6
Duty factor		CW

only minor modifications, Jefferson Laboratory's CEBAF could be operated with multipass energy recovery at several GeV, using common transport with the same topology as that of the LHeC (i.e. bisected linacs of equal energy gain with arcs vertically separated by energy using spreaders and recombiners) [894].

### 11.2. The ERL facility, PERLE

PERLE is a compact three-pass ERL based on SRF technology, a new-generation machine uniquely covering the 10 MW power regime of beam current and energy. Its CDR was published recently [7]. Apart from low-energy experiments it could host, thanks to its beam characteristics, PERLE will serve as a hub for the validation of a broad range of accelerator phenomena and the development of ERL technology for future colliders, as introduced above. In particular, the basic three-turn configuration, design challenges, and beam parameters (see table 55) were chosen to enable PERLE to function as a testbed for the injection-line and SRF technology development, as well as multiturn and high-current ERL operation techniques for the LHeC. While the concept and promise of ERLs has been kick-started by demonstration machines based on existing accelerator technology, PERLE will be the first machine designed from the ground up to use fully optimised ERL-specific designs and hardware.<sup>194</sup>

The PERLE collaboration currently involves CERN, the Jefferson Laboratory, the Science and Technology Facilities Council (STFC) Daresbury (Accelerator Science & Technology Centre (ASTeC) with the Cockcroft Institute), the University of Liverpool, BINP-Novosibirsk, and the newly formed IJCLab at Orsay. Four of these international partners have been pioneering the development of ERL technology; the others are leading laboratories in the fields of SRF technology and accelerator physics. The Orsay lab, which belongs to Centre National de la Recherche Scientifique and Institut National de Physique Nucléaire et de Physiques des Particules, is leading the effort to develop and host PERLE at the Orsay campus in close collaboration with the LHeC coordinators.

The following PERLE summary focuses on the power challenge, the lattice, site, and time schedule. PERLE uses a cryomodule with four five-cell cavities, similar to those of the LHeC. The prototype cavity production and test are described in the LHeC linac chapter, along with the design status of the cryomodule. Above, one may also find a section on the source and

<sup>194</sup> During the year 2021, the field of ERLs has strongly developed further and a roadmap for its future is being worked out which will appear early 2022.

injector as well as the arc magnets, dipoles of a three-in-one design, and quadrupoles which are also expected to be used, *mutatis mutandis*, for PERLE.

**11.2.1. Configuration.** In the final PERLE configuration, a high-current electron beam (20 mA) is accelerated through three passes to a maximum energy of 500 MeV by superconducting RF CW linear accelerator cryocavity units. The three passes with increasing energy increase the energy spread and emittance, while the major part of the beam power remains. The beam is then sent back through the accelerators again, only this time, at roughly 180 degrees from the accelerating RF phase, such that the beam is decelerated through the same number of passes and may be sent to a beam dump at the injection energy. Several benefits arise from this configuration: the required RF power (and its capital cost and required electricity) is significantly reduced to that required to establish the cavity field; the beam power that must be dissipated in the dump is reduced by a large factor, and the electron-beam dump energy can often be reduced to less than the photo-neutron threshold, so that activation of the dump region can be reduced or eliminated.

**11.2.2. Importance of PERLE for the LHeC.** PERLE is an important and necessary step that accompanies the realisation of the LHeC. Together with the other ERL facilities, i.e. CBETA, hopefully bERLinPRO, and possibly others, it will bridge the power-level gap between the current maximum (CEBAF-ER at 1 MW) and the targeted performance of the LHeC (1 GW) by exploring the next higher operational power regime of around 10 MW. Moreover, as it shares the same conceptual design as the LHeC: a racetrack configuration with three acceleration and three deceleration passes, an identical injection line, the same SRF system, and the same beam current in the SRF cavities, it will allow us to acquire an enormous insight into multiple-pass operation and common transport from full energy, before and possibly during LHeC operation.

To date, existing SRF systems have only demonstrated stability at a modest fraction ( $\leq 20\%$ ) of the current envisaged for the LHeC. Although threshold currents have been indirectly measured at higher values, there is no direct evidence that multipass systems will be sufficiently resistant to BBU at higher currents, nor has the sensitivity of the instability threshold to linac length, dynamic range, and number of passes been directly or systematically measured as yet. PERLE will provide a single datum for linac length, and can directly measure the dependence on the number of passes and the turn-to-turn transfer matrix.

The dynamic range (which is the ratio of injected/extracted energy to the full energy) is a critical design parameter, inasmuch as it defines the sensitivity of the overall system to magnetic-field errors. Errors at the full-energy level drive phase or energy errors that are magnified by adiabatic anti-damping during recovery, which can exceed the dump acceptance should the errors be too large. Thus, the field quality needed is inversely proportional to the ratio of the full energy to the dump energy: that is, a very-high-energy machine (or one with a very low dump energy) needs very-high-quality magnets. For PERLE, the dynamic range is 70 : 1 (7 MeV of injected energy and 490 MeV of full energy). This implies a requirement for  $\Delta B/B_{\text{dipole}} \simeq 0.001\%$  field flatness (extrapolated from the JLab ERL requirements) to recover cleanly enough. This implies a tight constraint on magnet performance and also affects their cost, even when it is the SRF that drives the overall cost of the facility in the case of the LHeC. PERLE has a very large dynamic range and a transport system with considerable symmetry and flexibility. It is therefore a suitable tool with which to explore this issue and evaluate the cost implications for larger-scale systems.

Existing systems have operated at a maximum of 1 MW of full-beam power. This is too low for the precise understanding and control of beam halo. An extrapolation to 10 MW will

demand the suppression of localised losses to, or less than, parts per million. Higher power requires a lower fractional loss. The way to achieve this is not yet well understood—in particular, collimation systems require a more optimised control of CW losses at the rates observed in linacs. PERLE will provide a platform on which the next step in understanding can be taken. Other halo effects may only become visible at the higher CW powers under consideration for PERLE (including Touschek and intra-beam scattering, beam–gas scattering, and ion trapping). These lead to scattering events that adiabatically anti-damp and result in intolerable loss in the back end of the machine, limiting its dynamic range. There is no experience of these phenomena, although theoretical studies suggest they are problematic. PERLE will be the first system capable of directly exploring these issues.

There are many collective effects that have proven challenging at lower beam powers—including RF heating, resistive wall heating, THz emission heating, etc. which will have greater impacts at both higher powers and higher energies. There are, at present, no operational ERL systems that can study these. PERLE is the only system proposed or under construction that combines sufficient beam power with sufficient operational flexibility to study and test mitigation algorithms and methods. Without PERLE, higher energy/power machines will benefit from very little insight regarding these problems and will lack the ability to test solutions.

Beam quality preservation in the presence of collective effects is a significant challenge for modern machines. In particular, LSC, CSR, and the micro-bunching instability have very deleterious impacts on performance, and can prevent a machine from producing a beam consistent with user requirements—or, worse, from being able to operate at significant powers. PERLE will probe the regions of parameter space in which these effects are observable, and offer an opportunity to benchmark models and explore mitigation methods.

**11.2.3. PERLE layout and beam parameters.** The PERLE accelerator complex is arranged in a racetrack configuration hosting two cryomodules (containing four five-cell cavities operating at a frequency of 801.6 MHz), each located in one of two parallel straights completed by a vertical stack of three recirculating arcs on each side. The straights are 10 m long and the 180° arcs are 5.5 m across. Additional space is taken up by 4 m-long spreader/recombiners, including matching sections. As illustrated in figure 206, the PERLE footprint, excluding shielding and experiments, is:  $24 \times 5.5 \times 0.8 \text{ m}^3$ , accounting for a 40 cm vertical separation between arcs. Each of the two cryomodules provides up to 82 MeV of energy boost per path. Therefore, in three turns, a 492 MeV energy beam is generated. Adding the initial injection energy of 7 MeV yields a total energy of approximately 500 MeV. The main beam parameters of the PERLE facility are summarised in table 55.

As mentioned in the introduction, the essential PERLE parameters are the same as the corresponding parameters at the LHeC. The frequency choice, emittance, beam current, and the time structure are chosen by considering the requirements of the electron–proton collisions in the LHeC.

**11.2.4. PERLE lattice.** Multipass energy recovery in a racetrack topology explicitly requires that both the accelerating and decelerating beams share the individual return arcs (figure 206). Therefore, the Twiss functions at the linac ends have to be identical, for both the accelerating and decelerating linac passes that converge to the same energy and therefore enter the same arc.

Injection at 7 MeV into the first linac is performed using a fixed-field injection chicane, which has its last magnet (closing the chicane) placed at the beginning of the linac. It closes the orbit bump at the lowest-energy pass, the injection pass, but the magnet (physically located in the linac) will deflect the beam on all subsequent linac passes. In order to close the resulting higher-pass bumps, the so-called re-injection chicane is instrumented by placing two additional bends in front of the last chicane magnet. In this way, the re-injection chicane magnets

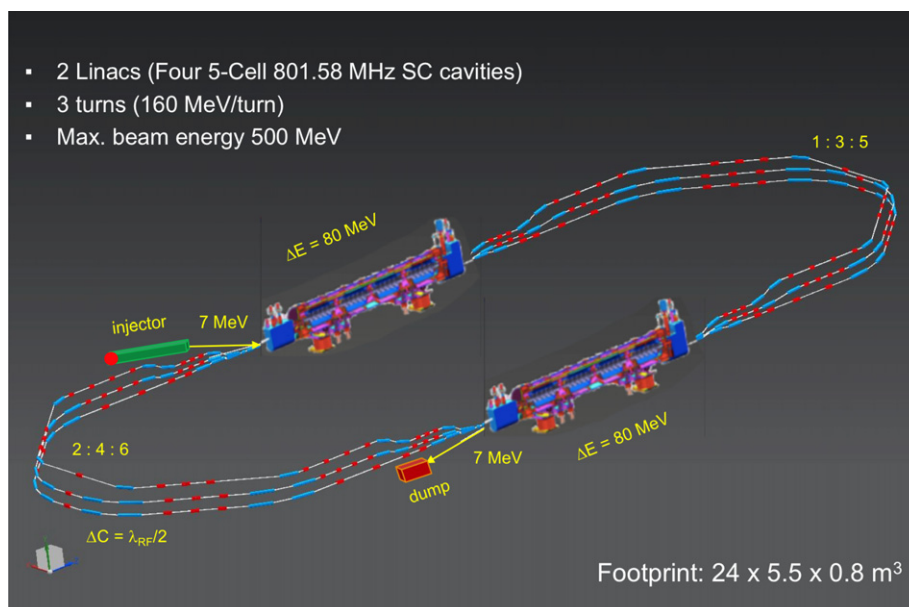


**Figure 206.** PERLE facility layout featuring two parallel linacs, each hosting a cryomodule housing four five-cell SC cavities, achieving 500 MeV in three passes; see the text.

are only visible to the higher-pass beams. The spreaders are placed directly after each linac to separate beams of different energies and to route them to the corresponding arcs. The recombiners facilitate just the opposite: merging beams of different energies into the same trajectory before they enter the next linac. The current spreader design (figure 207) consists of a vertical bending magnet, common to all three beams, that initiates the separation. The highest energy, at the bottom, is brought back to the horizontal plane using a chicane. The lower energies are captured with a two-step vertical deflection. The vertical dispersion introduced by the first step bends is suppressed by the three quadrupoles located appropriately between the two steps. The lowest energy spreader is configured with three curved bends following the common magnet, because of the large bending angle (45°) the spreader is configured with. This minimises the adverse effects of strong edge focussing on dispersion suppression in the spreader. Following the spreader, there are four matching quads to bridge the Twiss function between the spreader and the following 180° arc (two betas and two alphas). All six 180° horizontal arcs are configured with FMC optics to ease the individual adjustment of M56 in each arc (needed for longitudinal phase-space reshaping, which is essential for operation with energy recovery). The lower-energy arcs (arcs one, two, and three) are composed of four 45.6 cm-long curved 45° bends and of a series of quadrupoles (two triplets and one singlet), while the higher-energy arcs (arcs four, five, and six) use double-length, 91.2 cm-long, curved bends. The use of curved bends is dictated by the large bending angle (45°). If rectangular bends were used, their edge focussing would have caused a significant focussing imbalance, which, in turn, would have had an adverse effect on the overall arc optics. Another reason for using curved bends is to eliminate the problem of magnet sagitta, which would be especially significant for longer, 91.2 cm bends. Each arc is followed by a matching section and a recombiner (both are mirror symmetric to the previously described spreader and matching segments). As required in the case of

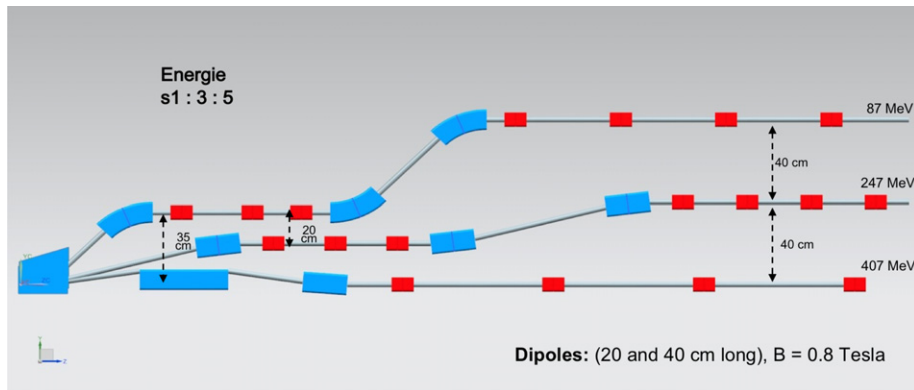


**Figure 207.** PERLE spreader design and matching to three circulating arcs.

identical linacs, the resulting arc features mirror-symmetric optics (identical betas and sign-reversed alphas at the arc ends).

The presented arc optics with modular functionality facilitate momentum compaction management (isochronicity), as well as orthogonal tunability for both beta functions and dispersion. The path length of each arc is chosen to be an integer number of RF wavelengths, except for the highest-energy pass, arc six, whose length is longer by half of the RF wavelength to shift the RF phase from acceleration to deceleration, switching to the energy-recovery mode.

**11.2.5. The site.** The IJCLab Orsay intends to host PERLE. The footprint of this facility occupies a rectangle of  $24 \times 5.5 \text{ m}^2$ . This area should be enclosed by shielding at a sufficient distance to allow passage and maintenance operations. We estimate the required passage and half thickness of the accelerator component to be 2 m. Concrete shielding is assumed here to stop photons and neutrons produced by halo electrons. A more detailed study of the radiation generated by the impinging electrons will be necessary at a subsequent stage. An requirement for an increase in the required shielding could be alleviated by the use of denser materials.

The operation of PERLE at the designed beam parameters (table 55) required an in-depth study of the machine failure scenario to estimate the power left in the machine during operation after beam losses and how to handle and control it. The study aimed at confirming whether the PERLE facility will be classified as INB (Infrastructure Nucleaire de Base) or not, with respect to the French radioprotection and nuclear safety rules. This conclusion is crucial for the decision to host PERLE at Orsay, since such INB facilities require heavy regulation procedures and a very high investment to fulfil the requirements and ensure the safety provisions are implemented. The outcome of the study concluded that PERLE shall not be considered as INB, even if the beam parameters are quite demanding, because in several failure scenarios, the energy of the beam is reduced to the injection energy and safely dumped in a few ten microseconds, due to the recovery mode. For the other scenarios, hard interlocks and the machine safety system are fast enough to manage the situation. The complete report of this study has been delivered by the Ingénierie, Radioprotection, Sûreté et Démantèlement team at Orsay.

Besides the central area required for machine implementation, space needs to be allocated for the auxiliary systems (power converters for magnets, septa and kickers, RF power, water cooling, cryogenics, electron source, and the sump). One has also to consider sufficient space

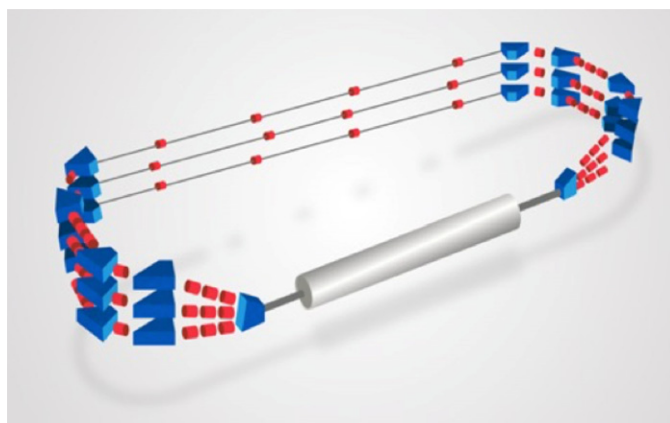


**Figure 208.** PERLE phase 1 layout featuring a single linac in the first straight and the beamline in the second straight, achieving 250 MeV in three passes.

for experiments that may use the PERLE beam. These have been sketched in the PERLE CDR [7]. As a rough estimate, one would need to triple the area of the accelerator itself to accommodate all services, with shielding included. The building that is foreseen to host this version of PERLE is a former experimental hall (Super ACO). It is equipped with cranes and electricity. The ground of the building is made of concrete slabs with variable ground resistance. More than half of the hall area has sufficient resistance to allow the installation of PERLE. Being next to the tunnel of the old Orsay linac and close to the *Igloo*, where new accelerators are currently being installed, the building is partially shielded and some equipment (water-cooling circuits, electrical transformer) can be shared with the other machines. The building offers the possibility of installing the RF source and the power supplies at a different level from the accelerator. An existing control room that overlooks the experimental hall may be used for PERLE. Since all the accelerators installed nearby are based on warm technology, a cryogenic plant will be built. All the support required for infrastructure could be assured by the Contrat Plan Etat Region programme. Altogether, this appears to be a very suitable site, which has the great advantage of being available.

**11.2.6. Building PERLE in stages.** The realisation of PERLE starts with a design and prototyping phase that ends with the PERLE TDR. This phase will include the design, simulation, and testing of the main component prototypes, allowing the definition of the technical choices and needs prior to the construction phases. The PERLE configuration (cf figure 206) allows the possibility of constructing PERLE in successive stages. Three phases of construction, commissioning, and exploitation are foreseen in order to achieve the final configuration. These are briefly characterised, as follows:

- **Phase 0:** installation of the injection line with a beam dump at its end: the injection line includes the DC gun, the load-lock photocathode system, solenoids, buncher, booster, merger, and beam instrumentation required to qualify the generated beam. The commissioning of the injection line will require the installation of the cryogenics, RF power source, power supplies for the optics, photocathode laser, beam dump, control-



command, vacuum systems, site shielding, safety control system, fluids, etc. Many of these installations must be already sized according to the final configuration of PERLE.

- **Phase 1:** 250 MeV version of PERLE, see figure 208: installation of a single linac in the first straight and installation of beam pipe and complete return arcs. The switchyards have to be chosen according to the beam energy at each end (energy acceptance ratio: 1:2:3 for the spreader and combiner). This version of the racetrack is connected to the injection line built in phase 0 via the merger. This particular stage is determined by the existence of the SPL cryomodule at CERN (see the discussion in section 10) which will permit a fairly rapid realisation of a 250 MeV machine, most likely still using the ALICE gun which already resides at the IJCLab. This will permit the first beam tests of the various SRF components in order to explore the multiturn ERL operation and to gain essential operational experience.
- **Phase 2:** 500 MeV version of PERLE: this phase is for the realisation of PERLE at its design parameters, as a 10 MW power machine which requires the nominal electron current, i.e. the upgraded electron gun and the completion of the production of a dedicated further cryomodule. Also, a second spreader and recombiner at the required acceptance ratio need to be installed on both sides of the second cryomodule.

The PERLE collaboration is currently developing a detailed time schedule for the project in its different phases, which depends on the possibility of using the SPL cryomodule adapted for PERLE and the availability of further essential components. In relation to the LHeC, it may be noted that PERLE allows us to gain the experience we would have had to gain with the LHeC, years before it starts. The LHeC cannot begin before the early 2030s, while PERLE will operate in the 2020s.

*11.2.7. Concluding remarks.* Currently, the focus of the planning for PERLE is on the development of ERL as a means for high-power, high-energy accelerator design, technology, and realisation. PERLE has considerable potential for low-energy particle and nuclear physics as well. Its intensity is orders of magnitude greater than that of ELI. This opens a huge field of physics and industrial applications for a user facility, once the machine has been understood and is operating in line with its design in a reliable manner. With the recent increased interest in energy-recovery technology applications at the LHeC, and also the FCC and the EIC, PERLE may become an important cornerstone for future high-energy and nuclear physics. The re-use of power is, *per se*, a green technology, which is an example of how science may react to the power reduction requirements of our time.

## 12. Experimentation at the LHeC

### 12.1. Introduction

The LHeC CDR [1] contained a very detailed description of a core detector concept for the LHeC. At the time of writing, the target luminosity was of the order of  $10^{33} \text{ cm}^{-2} \text{ s}^{-1}$  and, while the evidence for it was building, the Higgs boson had yet to be discovered. A detector design based on established technologies in use by either of the LHC general purpose detectors, i.e. ATLAS and CMS, or being developed for their upgrades, was thought to be adequate to realise the physics priorities of the project at the time and to be able to comply with the *ep* machine constraints at an affordable cost, provided the angular acceptance was sufficient (nominally to within  $1^\circ$  of the beamline). A salient feature of experimentation at the LHeC, as compared to

the LHC, is the complete absence of pile-up, which can be estimated<sup>195</sup> to be around 0.1 in  $ep$  at the LHeC, compared to  $\simeq 150$  in  $pp$  at the HL-LHC. Similarly, there is a reduced level of radiation in  $ep$ , i.e. orders of magnitude lower than in  $pp$ , which also enables us to consider novel technologies that are less radiation hardened than conventional ones, for example, HV CMOS silicon detectors.

This chapter provides a short overview of a partially revised LHeC detector design, with more detail on those aspects which have developed significantly since the 2012 version (notably the central tracking). To a large extent, the considerations in the CDR are still valid and are taken forward here. However, this update also profits from the evolution of the design in the subsequent years, the updated and long-term physics priorities, and the higher achievable luminosities. It also introduces new technologies that are becoming available. In more detail, the major considerations which motivate an update of the detector with respect to the 2012 baseline are:

- The increased luminosity and the confirmation of a Higgs boson discovery at a mass of around 125 GeV create the opportunity for the LHeC to provide a set of precision measurements of the Higgs properties, in particular, percent-level measurements of several of its couplings. The possibility of obtaining world-leading measurements of couplings to beauty and charm place a heavy emphasis on the inner tracking and vertexing. The tracking region has therefore been radially extended and also provided with increased segmentation. The requirement to maximise the acceptance for Higgs decays places an even stronger requirement on angular coverage than was the case in 2012; forward tracking and vertexing are of particular importance.
- The fast development of detector technologies and related infrastructure in some areas necessitates a fresh look at the optimum choices. Most notably, silicon detector technologies have advanced rapidly in response to both commercial and particle physics requirements. The low material budget, potential high granularity, and cost-effectiveness offered by monolithic active-pixel sensor (MAPS) solutions such as HV-CMOS are particularly attractive and can reasonably be assumed to be in widespread use in future particle physics collider detector contexts.
- The long-term, high-energy hadron collider physics programme, including the FCC and possibilities in Asia, as well as the ultimate use of the LHC for two more decades, require precise, independent, and comprehensive measurements to determine PDFs over a wider range of  $x$  and  $Q^2$  than has previously been possible. The implication for the LHeC is a need to further improve and extend the detector acceptance and overall performance.
- Options in which the  $ep$  centre-of-mass energy is increased, at the HE-LHC or the FCC-eh, require a further reinforcement of the detector design in the forward direction, increasing the overall size of the detector. In particular, the calorimeter depth scales logarithmically with  $E_p$  so as to fully contain particles from very high-energy forward-going hadronic showers and to allow for precise measurements of actual and missing energy. Using such

<sup>195</sup> The pile-up is given as the number of events per bunch crossing, which is obtained from the instantaneous luminosity  $L = 10^{34} \text{ cm}^{-2} \text{ s}^{-1}$ , the total cross-section  $\sigma_{\text{tot}} \simeq \sigma(\gamma p) \cdot \Phi_\gamma$ , and the bunch distance, 25 ns. The total photo-production cross-section, with a minimum of  $Q^2 = (M_e \cdot y)^2 / (1 - y)$ , is estimated to be 220(260)  $\mu\text{b}$  at the LHeC (FCC-eh) using the parameterisation given in reference [895]. Here,  $y$  is the inelasticity variable and  $M_e$  is the electron mass. The photon flux factor in the Weizsäcker–Williams approximation is calculated to be  $\Phi_\gamma = 1.03(1.25)$  for  $W = \sqrt{ys} > 1$  GeV. The hadronic final state at very small scattering angles,  $\theta_h \leq 0.7^\circ$  or  $|\eta| \geq 5$ , does not reach central detector acceptance, such that, at the LHeC,  $W_{\text{min}}$  would be larger, i.e., about 10 GeV, which reduces the flux factor to about 0.6. A conservative estimate is to use  $W > 1$  GeV. This translates to an estimated pile-up of 0.06 at the LHeC and 0.09 at the FCC-eh, which compares favourably with an estimated pile-up of 150 at HL-LHC.

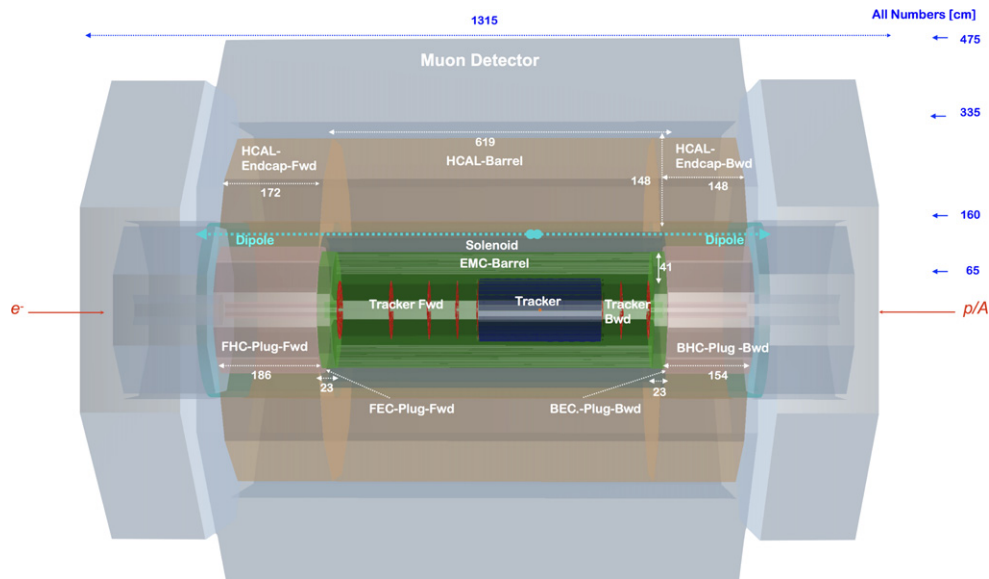


**Figure 209.** Side view of the updated baseline LHeC detector concept, providing an overview of the main detector components and their locations. The detector dimensions are about 13 m (length) and 9 m (diameter). The central detector is complemented by forward ( $p, n$ ) and backward ( $e, \gamma$ ) spectrometers, which are mainly used for diffractive physics and for photo-production and luminosity measurements, respectively. See the text for details.

scaling considerations, the LHeC design has also been applied to the post-LHC hadron beam configurations.

The design described in the following addresses the points above. The updated detector requirements in the tracking region point to the need for higher spatial resolution, improved precision in momentum measurements and enhanced primary and secondary vertexing capabilities. The most significant change, compared with 2012, is therefore a more ambitious tracking detector design. The detector must also provide accurate measurements of hadronic jets and missing transverse energy, as well as isolated electrons and photons. As an option compared to the CDR, the liquid argon (LAr) choice for the main electromagnetic barrel calorimeter sampling material is changed here to a scintillator-based solution. Both options are subsequently compared, and, as expected, long-term stability and resolution performance favour an LAr calorimeter, while the modularity and installation aspects are more easily solved using a warm crystal calorimeter.

Both the overall event kinematics (much larger proton- than electron-beam energy) and the specific acceptance requirements for the key Higgs production process imply an asymmetric design with enhanced hadronic final-state detection capabilities in the forward direction, where the deposited hadronic and electromagnetic energies are much higher than in the backward direction; see figure 5 in section 3.2.

A dipole magnet bends the electron beam into a head-on collision with the colliding proton beam, and after the interaction point, a further dipole with the opposite polarity separates the orbits of the electron and proton beams. These weak bending dipoles are placed outside the tracker and electromagnetic calorimeter regions. The total length is 10 m or  $2/3L^*$ , as explained

in the IR section. The resulting synchrotron radiation fan has to be given free space, and the beam pipe geometry is designed specifically to accommodate it. The residual synchrotron radiation background places a constraint on the inner detector components.

The 2012 and 2020 versions of the LHeC detector design are both realisable in terms of technology readiness. It has been a goal of this conceptual design to study the feasibility, performance, and integration of the detector, which will eventually be designed by a future  $ep/eA$  experiment collaboration. The two designs, while still similar, can be considered as two example solutions to the LHeC requirements, with differences in where the emphasis is placed in terms of performance and cost. The current design is produced using the DD4hep [903] software framework.

### 12.2. Overview of the main detector elements

A side projection overview of the current detector design is shown in figure 209, illustrating the main detector components. The overall size remains compact by recent standards, with overall dimensions of approximately 13 m in length and 9 m in diameter, which is small compared to ATLAS ( $45 \times 25 \text{ m}^2$ ) and even the CMS ( $21 \times 15 \text{ m}^2$ ). The inner silicon tracker contains a central barrel component ('tracker'), with additional disks in the forward and backward directions ('tracker Fwd' and 'tracker Bwd', respectively). It is surrounded at larger radii by the electromagnetic barrel ('EMC-barrel') and in the forward and backward directions by the electromagnetic forward and backward plug calorimeters ('FEC-plug-Fwd' and 'BEC-plug-Bwd', respectively). The solenoid magnet is placed at a radius immediately outside the EMC-barrel, and is housed in a cryostat, which it shares with the weak dipole magnet that ensures head-on collisions. The dipole and cost considerations suggest that the solenoid should be placed there, instead of surrounding the Hadron Calorimeter (HCAL), which, in terms of performance, would surely have been preferable.

The hadronic-barrel calorimeter ('HCAL-barrel') is located at radii beyond the solenoid and dipole, while the forward and backward hadronic plug detectors ('FHC-plug-Fwd' and 'BHC-plug-Bwd', respectively) lie beyond their electromagnetic counterparts in the longitudinal coordinate. The muon detector forms a near-hermetic envelope around all other parts of the main detector. It uses similar technologies to those employed by ATLAS, with a much smaller surface, see below.

A magnified view of the inner part of the detector, including the magnet elements, is shown in figure 210. The solenoid and steering dipoles completely enclose the electromagnetic calorimeters and the tracker setup, and the steering dipoles extend over the full 10 m length of the inner detector and the forward and backward plugs. If liquid argon is chosen as the sensitive material in the EMC, as in the 2012 design, the EMC will be mounted inside the cryostat, alongside the solenoid and dipoles. The hadronic calorimeter components remain outside the cryostat and magnet elements in all circumstances.

Exploiting the current state of the art, the beam pipe is constructed of beryllium 2.5–3 mm thick. As in the 2012 CDR, the beam pipe has an asymmetric shape in order to accommodate the synchrotron radiation fan from the dipole magnets. It is thus 2.2 cm distant from the interaction region, comparable to the HL-LHC beam pipes of the general purpose detectors, except in the direction of the synchrotron fan, where it is increased to 10.0 cm, giving rise to an overall circular-elliptical profile (see the illustration of the profile at the IP in figure 211). The beam pipe shape has implications for the design of the inner detector components, as illustrated in figure 212. The first layer of the barrel tracker follows the circular-elliptical beam pipe shape as closely as possible, while the profiles of subsequent layers revert to a circular geometry.

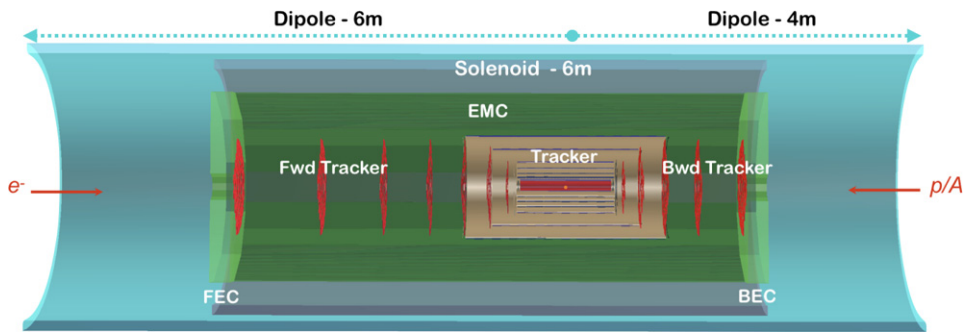


**Figure 210.** Side projection of the central part of the LHeC detector, which also illustrates the solenoid and electron-beam-steering dipoles. See the text for further details.

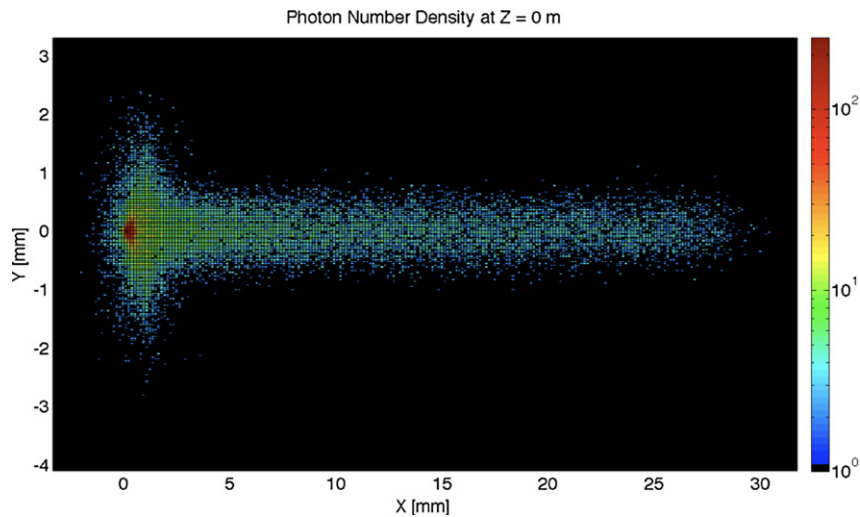


**Figure 211.** Simulation of the synchrotron radiation profile at the IP using GEANT4. Reproduced from [1]. IOP Publishing Ltd. [CC BY 3.0](#).

### 12.3. Inner tracking

**12.3.1. Overview and performance.** A schematic view of the updated tracking region is shown in figure 213. The layouts in the central, forward, and backward directions have been separately optimised using the tkLayout performance estimation tool for silicon trackers [904]. The result is seven concentric barrel layers with the innermost layer approximately 3 cm from the beam line at its closest distance and with approximately equal radial spacing thereafter. The tracker barrel is supplemented by seven forward disks and five backward disks, of which three in each direction comprise the central tracker end-cap, and four and two, respectively, are mounted beyond the central tracker enclosure.

For the reasons described in section 12.3.2, HV-CMOS MAPS sensors can be employed, restricting the material associated with the pixel sensors to just 0.1 mm per layer. The strip detector sensors have a larger thickness of 0.2 mm. The preferred active silicon solutions vary



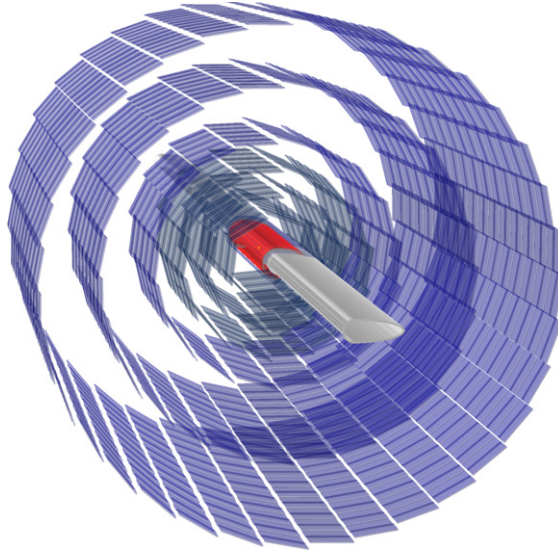


**Figure 212.** End-on view of the arrangement of the inner barrel tracker layers around the beam pipe.

with the radial distance from the interaction point, so as to provide the highest spatial resolution in the layers closest to the interaction point. The barrel is formed from one layer of pixel wafers, three layers of macropixels with radii between 10 cm and 30 cm, and three further layers of strip sensors beyond 30 cm. The end-cap disks and the forward tracker also contain combinations of the three types of sensor, while the backward tracker consists of macropixels and strips only.

Tables 56 and 57 summarise the overall basic properties of the tracker modules, including the total numbers of channels and the total area of silicon coverage, as well as spatial resolutions and material budgets. The inner barrel has a pseudorapidity coverage  $|\eta| < 3.3$  for hits in at least one layer, increasing to  $|\eta| < 4.1$  when the endcaps are also taken into account. The additional disks beyond the central tracker enclosure extend the coverage to  $\eta = 5.3$  and  $\eta = -4.6$  in the forward and backward directions, respectively. Figure 214 illustrates the coverage in more detail, displaying the numbers of layers that provide acceptance as a function of pseudorapidity in both the forward and backward directions, also broken down into different sensor types. Charged particles are sampled using between five and eight layers throughout the entire range  $-3.5 < \eta < 4$ , with sampling in at least two layers provided for  $-4.2 < \eta < 5$ .

Spatial resolutions in the  $r$ - $\phi$  plane, driven by the sensor pitches, reach  $7.5 \mu\text{m}$  for the pixel layers. The resolutions are propagated using tkLayout to produce simulated charged-particle transverse momentum resolutions, as shown in figure 215. Both active and passive material contributions are included, with a 2.5 mm Be beam pipe thickness. An excellent resolution ( $\delta p_{\text{T}}/p_{\text{T}}$ ) at the level of 1%–2% is achieved over a wide range of pseudorapidity and momentum. The precision degrades slowly in the forward direction, remaining at the sub-10% level up to very forward pseudorapidities  $\eta \sim 4.5$ . Central tracks with transverse momenta of up to 1 TeV are measured with a precision of 10%–20%. Similar results are achieved in the (negative  $\eta$ ) backward direction (not shown).



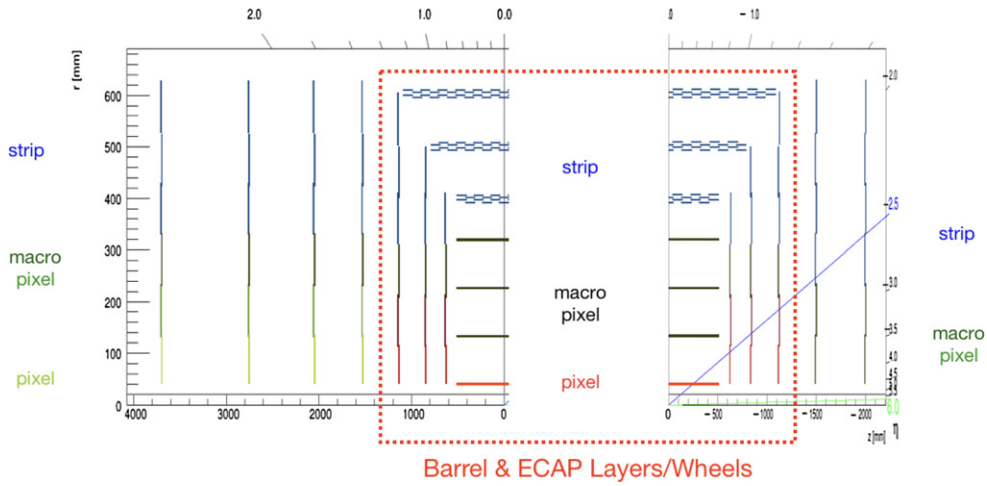


**Figure 213.** Schematic side view of the tracker, subdivided into forward and backward parts and including disks as well as barrel components. The layers/disks forming the barrel part are enclosed by the red-dotted box. The innermost pixel layers are coloured red, the macropixel layers are shown in black, and the strip detectors in blue. For the forward and backward disks, possibly formed with separate rings, (outside the dashed red box), the pixels, macropixels, and strip detectors are shown in light green, dark green, and blue, respectively.

**Table 56.** Summary of the main properties of the barrel and endcap tracker modules based on calculations performed using tkLayout [904]. For each module, the rows correspond to the pseudorapidity coverage, numbers of barrel and disk layers, number of sensors, total area covered by silicon sensors, number of readout channels, the hardware pitches affecting the  $(r-\phi)$  and the  $z$  resolution, respectively, and the average material budget in terms of radiation lengths and interaction lengths. Where appropriate, the numbers are broken down into the separate contributions made by the pixels, macropixels and strips. See table 57 for the sum of all tracker components.

Tracker (LHeC)	Inner barrel			ECAP		
	Pix	Pix <sub>macro</sub>	Strip	Pix	Pix <sub>macro</sub>	Strip
$\eta_{\max}, \eta_{\min}$	3.3, -3.3	2.1, -2.1	1.4, -1.4	$\pm[4.1, 1.8]$	$\pm[2.4, 1.5]$	$\pm[2.0, 0.9]$
Layers (barrel)	1	3	3			
Disks (ECAP)				2	1	1-3
Modules/sensors	320	4420	3352	192	192	552
Total Si area (m <sup>2</sup> )	0.3	4.6	17.6	0.8	5.6	3.3
Readout channels (10 <sup>6</sup> )	224.5	1738	20.6	322.4	73.3	17.0
Pitch <sup><math>r-\phi</math></sup> ( $\mu\text{m}$ )	25	100	100	25	100	100
Pitch <sup><math>z</math></sup> ( $\mu\text{m}$ )	50	400	50k	50	400	10k <sup>a</sup>
Average $X_0/\Delta_I$ (%)		7.2/2.2			2.2/0.7	

<sup>a</sup>Reaching the pitch <sup>$r-\phi$</sup>  using two wafer layers rotated by 20 mrad is achievable.

A major requirement of the tracking detectors will be the precise determination of vertex coordinates and track impact parameters relative to the primary vertex, in order to give the best possible sensitivity to secondary vertices from HF decays, for example for the study of the Higgs in its dominant  $b\bar{b}$  decay mode. The simulated results for longitudinal and transverse

**Table 57.** Summary of the main properties of the forward and backward tracker modules in the revised LHeC detector configuration based on calculations performed using tkLayout [904]. For each module, the rows correspond to the pseudorapidity coverage, number of disk layers, number of sensors, total area covered by silicon sensors, number of readout channels, the hardware pitches affecting ( $r$ - $\phi$ ) and the  $z$  resolution, respectively, and the average material budget in terms of radiation lengths and interaction lengths. The polar angle dependence and decomposition of  $X_0$  and  $\Lambda_I$  are shown in figure 217. Where appropriate, the numbers are broken down into the separate contributions made by the pixels, macropixels, and strips. The column *total* contains the sum of corresponding values in tables 56 and 57.

Tracker (LHeC)	Fwd tracker			Bwd tracker		Total (Incl. table 56)
	Pix	Pix <sub>macro</sub>	Strip	Pix <sub>macro</sub>	Strip	
$\eta_{\max}, \eta_{\min}$	5.3, 2.6	3.5, 2.2	3.1, 1.6	-4.6, -2.5	-2.9, -1.6	5.3, -4.6
Disks	2	1	3	2	4	
Modules/sensors	180	180	860	72	416	10 736
Total Si area (m <sup>2</sup> )	0.8	0.9	4.6	0.4	1.8	40.7
Readout channels (10 <sup>6</sup> )	404.9	68.9	26.4	27.6	10.6	2934.2
Pitch <sup><math>r</math>-<math>\phi</math></sup> ( $\mu$ m)	25	100	100	100	100	
Pitch <sup><math>z</math></sup> ( $\mu$ m)	50	400	50k	400	10k <sup>a</sup>	
Average $X_0/\Lambda_I$ (%)		6.7/2.1		6.1/1.9		
Incl. beam pipe (%)						40/25

<sup>a</sup>Reaching the pitch <sup>$r$ - $\phi$</sup>  using two wafer layers rotated by 20 mrad is achievable.

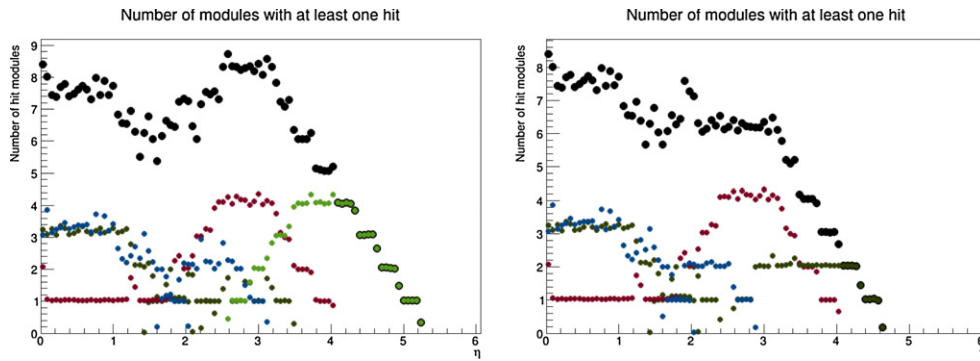


**Figure 214.** Numbers of silicon layers that provide acceptance for charged particles as a function of the absolute value of pseudorapidity in the forward (left) and backward (right) directions, summed across the central, forward, and backward trackers. The distributions are broken down according to sensor type, with a colour coding of red for pixels, light or dark green for macropixels, blue for strips, and black for the sum.

track impact parameter resolutions using the full new tracking layout are shown in figure 216. The transverse spatial resolutions are at a level of 10–50  $\mu$ m over a wide range of transverse momentum and pseudorapidity, extending well into the forward direction.

The material budget contributions from the sensors summed across all layers are given in table 56; the contribution is largest for the inner barrel, amounting to 7.2% of a radiation length. The sensors in the central tracker endcap and the forward and backward tracking rings contribute 2.2%, 6.7% and 6.1% of a radiation length, respectively. The material budget simulations, propagated for the full system and including passive contributions, are shown in

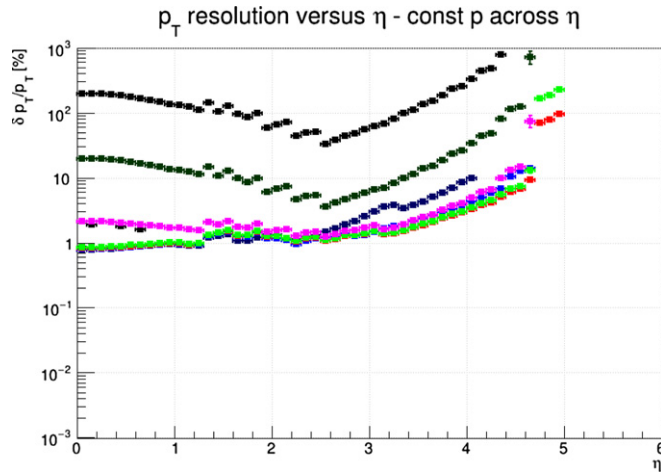


**Figure 215.** Simulated transverse momentum track resolution using all modules in the revised LHeC tracking system. The results are shown in terms of fractional  $p_T$  resolution as a function of pseudorapidity for several constant momenta,  $p = 100$  MeV (black, bottom, obscured), 1 GeV (dark blue, obscured), 2 GeV (light blue, obscured), 5 GeV (red), 10 GeV (light green), 100 GeV (magenta), 1 TeV (dark green), and 10 TeV (black, top).

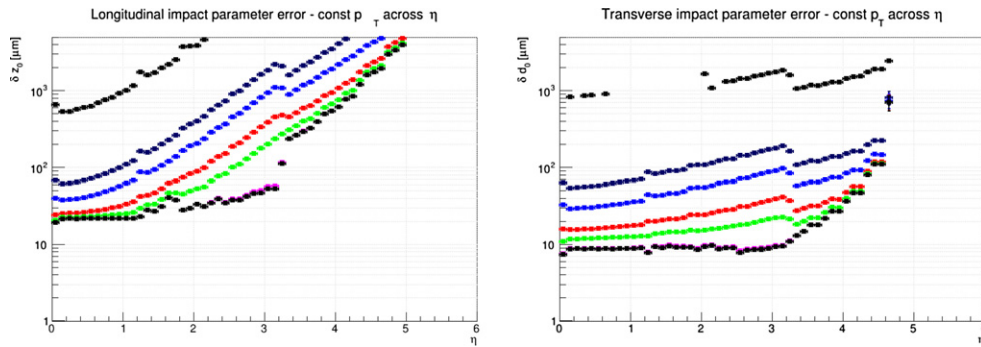


**Figure 216.** Simulated longitudinal (left) and transverse (right) impact parameter resolutions using all modules in the revised LHeC tracking system. Results are shown as a function of pseudorapidity for several constant momenta,  $p = 100$  MeV (black, top), 1 GeV (dark blue), 2 GeV (light blue), 5 GeV (red), 10 GeV (light green), 100 GeV (magenta, obscured), 1 TeV (dark green, obscured), and 10 TeV (black, bottom).

figure 217. The use of thin sensors keeps the total material to the level of  $0.2\text{--}0.4X_0$  throughout the entire tracking region up to  $\eta \sim 4.5$ . At the most forward (and backward) pseudorapidities, particles travel through a large effective thickness of material as they pass through the beam pipe; this becomes the dominant contribution for  $\eta > 3.5$ .

**12.3.2. Silicon technology choice.** Since they have been developed for several high-luminosity LHC (HL-LHC) upgrades and the proposed CLIC high-energy linear collider, we envisage that depleted CMOS sensor technology (also known as depleted monolithic active

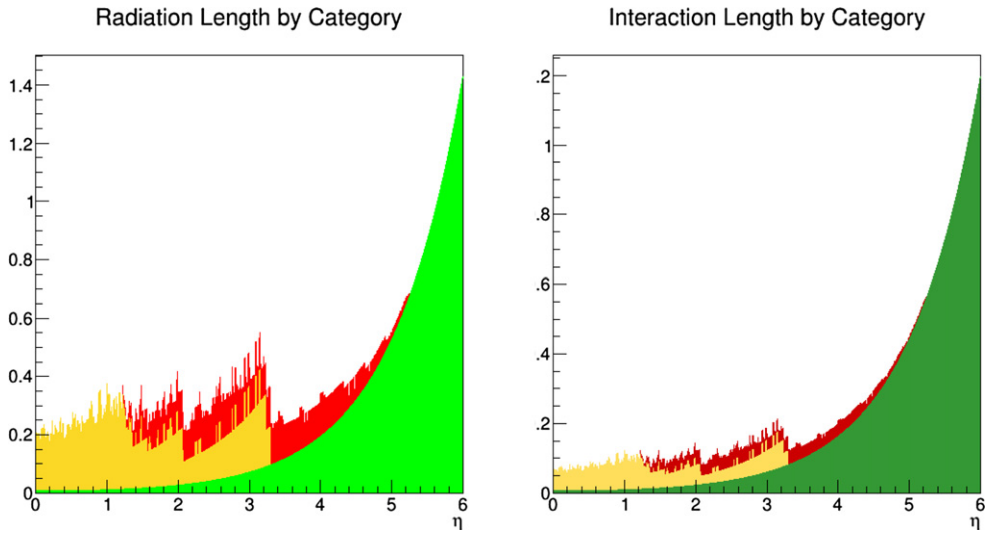


**Figure 217.** Material contributions from the tracking modules as a function of pseudorapidity. Results are given in terms of radiation lengths (left) and hadronic interaction lengths (right). The results are broken down into contributions from barrel modules (yellow) and endcap/additional disk modules (red) and are compared with the contribution from the 2.5 mm beam pipe (green).

pixel sensors (DMAPSs)), will be used as position-sensitive detectors in industry-standard CMOS processes or high-voltage-CMOS (HV-CMOS) processes [900]. These sensors are extremely attractive for experiments in particle physics, as they integrate the sensing element and the readout ASIC in a single layer of silicon, which removes the need for interconnections that use complex and expensive solder bump technology. Depleted CMOS sensors also benefit from faster turnaround times and lower production costs, compared to hybrid silicon sensors. To achieve fast charge collection and high radiation tolerance, DMAPS can be implemented using two different approaches known as low fill factor and large fill factor. Low-fill-factor DMAPSs benefit from high-resistivity (HR) substrates and thick epitaxial layers accessible by large-scale CMOS imaging processes, while large-fill-factor DMAPSs exploit the high-voltage (HV) option developed by commercial CMOS foundries for power electronics. Recently, HR wafers have become available in the production lines of foundries that manufacture HV-CMOS processes, thus DMAPSs in HR/HV-CMOS are also possible, which further improve the performance of the sensor. Today's most performant DMAPS detectors are  $50\ \mu\text{m}$  thick and have a  $50\ \mu\text{m} \times 50\ \mu\text{m}$  cell size with integrated mixed analogue and digital readout electronics, a 6 ns time resolution, and a  $2 \times 10^{15}\ \text{1 MeV n}_{\text{eq}}\ \text{cm}^{-2}$  radiation tolerance. The typical cross-section of a large-fill-factor DMAPS fabricated using an HV-CMOS process is shown in figure 218.

DMAPSs in HR/HV-CMOS have been adopted as a world first as the sensor technology of choice for the **Mu3e** experiment at the Paul Scherrer Institute (PSI) in Switzerland [902]. MuPix, the DMAPS detector for Mu3e, implements active pixels that amplify the collected charge in the collecting electrode and peripheral readout electronics that discriminate and process the amplified signals. The peripheral readout electronics of MuPix10 include readout buffers, a state machine, a phase-locked loop and voltage-controlled oscillator, 8/10-bit encoders and three serialisers for data transmission with a rate of up to  $1.6\ \text{Gbit s}^{-1}$ . Previous

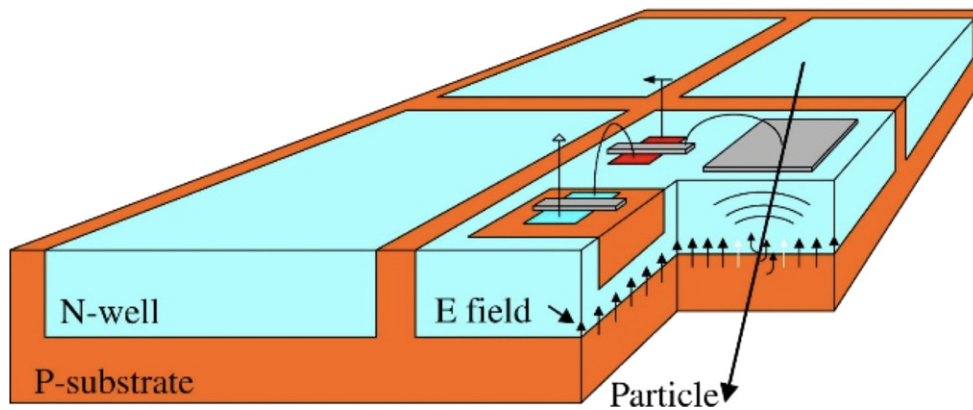


**Figure 218.** Typical cross-section of a depleted monolithic active-pixel sensor (DMAPS) detector in an HV-CMOS process. Reprinted from [900], Copyright 2018, with permission from Elsevier.

MuPix prototypes have successfully been thinned to  $50\ \mu\text{m}$  and tested to achieve a 6 ns time resolution after time-walk correction [903]. ATLASPix, the DMAPS development in HR/HV-CMOS that was originally aimed at providing an alternative sensor technology for the outermost pixel layer of the new ATLAS inner tracker (ITk) upgrade, has been confirmed to have an approximate  $150\ \text{mW cm}^{-2}$  power consumption and a radiation tolerance of up to  $2 \times 10^{15}$   $1\ \text{MeV n}_{\text{eq}}\ \text{cm}^{-2}$  fluences [904]. DMAPSs in HR-CMOS, such as the MALTA development [905], also originally aimed at the new ATLAS ITk upgrade, have achieved full efficiency after exposure to  $1 \times 10^{15}$   $1\ \text{MeV n}_{\text{eq}}\ \text{cm}^{-2}$  fluences [905]. However, further research is still needed to demonstrate reticle-sized DMAPSs in HR-CMOS. Research to further develop DMAPSs to meet the extreme requirements of future experiments in particle physics is ongoing.

The tracker design of the LHeC presented here utilises pixel detectors for high-resolution tracking in the inner barrel as well as the barrel endcaps and the forward tracker. The number of readout channels is close to  $10^9$ , with high transverse and longitudinal segmentation provided by a pitch of  $25 \times 50\ \mu\text{m}^2$ . One can expect that such fine segmentation will be in reach for a detector which is to be built a decade hence. The radiation level in electron–proton scattering is some orders of magnitude lower than in proton–proton interactions at the LHC and is, indeed, in a range of  $10^{15}$   $\text{MeV n}_{\text{eq}}\ \text{cm}^{-2}$ , for which radiation hardening has been proven, as indicated above. The monolithic CMOS detector technology leads to a significant simplification of the production of these detectors and a considerably reduced cost. We thus conclude that the LHeC pixel tracker represents a particularly suitable device for a large-scale implementation of HV CMOS silicon in a forthcoming collider detector.

#### 12.4. Calorimetry

The 2012 CDR detector design built on technologies employed by ATLAS for calorimetry in the barrel region, adopting a lead/liquid argon sampling electromagnetic calorimeter with an accordion geometry and a steel/scintillating tile and a scintillator-steel tile sampling calorimeter for the hadronic part. An alternative solution, namely, a lead/scintillator electromagnetic calorimeter was investigated for the version of the LHeC detector described here. This has the advantage of removing the need for cryogenics, while maintaining an acceptable performance level. In a comparison between the lead-scintillator design for the electromagnetic

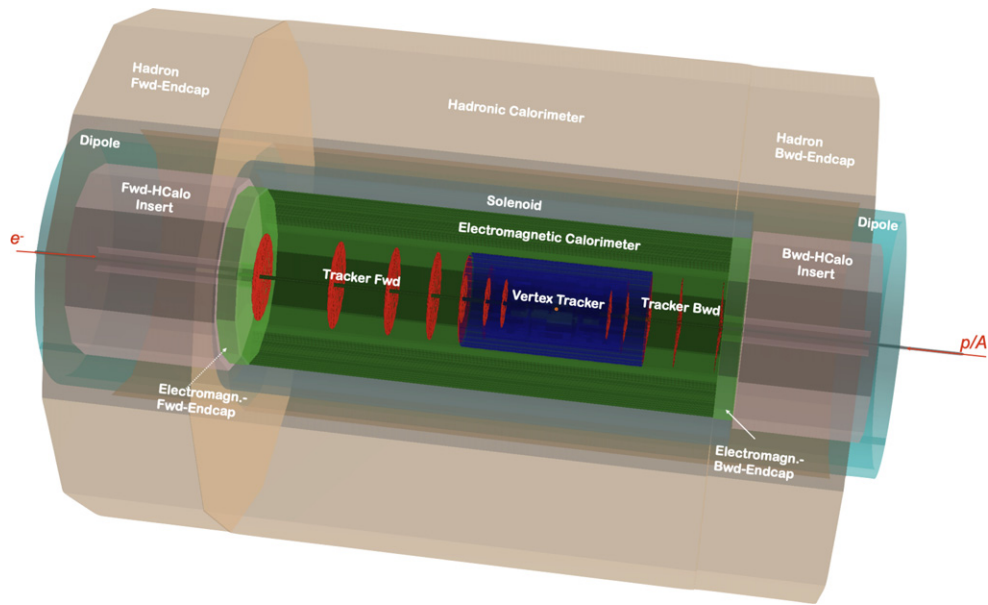


**Figure 219.** Three-dimensional view of the arrangement of the hadronic calorimeter, experimental magnets (solenoid and dipoles), the electromagnetic calorimeter, and tracking detector layers.

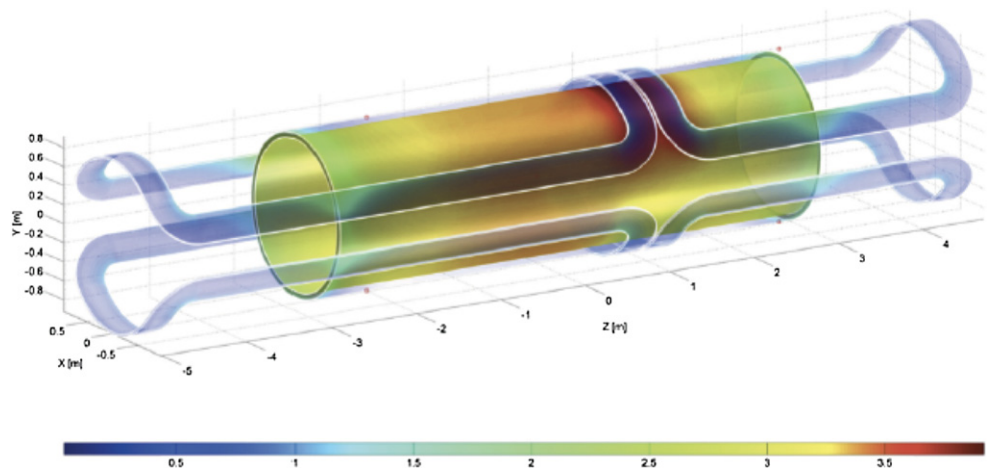


**Figure 220.** The coil arrangement of the solenoid and dipole systems housed in a common cryostat. Reproduced from [1]. © IOP Publishing Ltd. [CC BY 3.0](https://creativecommons.org/licenses/by/3.0/)

barrel calorimeter of the 2012 CDR and the updated setup, the resolution performance of the updated design is better ( $\mathbf{a} = 20\%$  and  $\mathbf{b} = 0.14\%$  in the 2012 CDR and  $\mathbf{a} = 12.4\%$  and  $\mathbf{b} = 1.9\%$  in the new design; the  $\mathbf{a}$ -term represents shower fluctuations and transverse leakages and the  $\mathbf{b}$ -term describes the back-leakages of the calorimeter). Although it is not discussed here, the liquid argon solution very much remains the favoured option, due to its high level of



**Table 58.** Basic properties and simulated resolutions of barrel calorimeter modules in the new LHeC detector configuration. For each of the modules, the rows indicate the absorber and sensitive materials, the number of layers, the total absorber thickness, the pseudorapidity coverage, the contributions to the simulated resolution made by the sampling ( $a$ ) and material ( $b$ ) terms in the form  $a/b$ , the depth in terms of radiation or interaction lengths and the total area covered by the sensitive material. Produced using GEANT4 [905] simulation-based fits using the crystal ball function [907–909].

Calo (LHeC)	EMC		HCAL	
	Barrel	Ecap Fwd	Barrel	Ecap Bwd
Readout, absorber	Sci, Pb	Sci, Fe	Sci, Fe	Sci, Fe
Layers	38	58	45	50
Integral absorber thickness (cm)	16.7	134.0	119.0	115.5
$\eta_{\max}, \eta_{\min}$	2.4, -1.9	1.9, 1.0	1.6, -1.1	-1.5, -0.6
$\sigma_E/E = a/\sqrt{E} \oplus b$ (%)	12.4/1.9	46.5/3.8	48.23/5.6	51.7/4.3
$\Lambda_I/X_0$	$X_0 = 30.2$	$\Lambda_I = 8.2$	$\Lambda_I = 8.3$	$\Lambda_I = 7.1$
Total area of Sci (m <sup>2</sup> )	1174	1403	3853	1209

performance and stability/radiation hardness. The fit results in the 2012 CDR for the LAr calorimeter option show a slightly better resolution performance than those of the lead-scintillator variant. Due to the accordion-shaped absorber, the LAr calorimeter forces more energy to be deposited in the calorimeter volume. The CDR values, for comparison, are:  $\mathbf{a} = 8.47\%$  and  $\mathbf{b} = 0.318\%$ . The hadronic calorimeter retains the steel and scintillating tile design, which is similar to that of ATLAS. As in the 2012 CDR, plug sampling calorimeters are also incorporated at large  $|\eta|$ ; the forward and backward components use tungsten and lead absorber materials, respectively, and both use silicon-based sensitive readout layers. The steel structures in the central and plug calorimetry close the outer field of the central solenoid. The solenoid and the dipoles are placed between the electromagnetic barrel and the hadronic calorimeter. The HCAL-barrel sampling calorimeter, which uses steel and scintillating tiles as the absorber and the active material, respectively, provides the mechanical stability for the magnet/dipole cryostat and the tracking system as shown in figure 219. The layout of the solenoid/dipole system is discussed in more detail in [1] and is illustrated by figure 220 (with the LAr cryostat in a cold EMC version) along with the iron required for the return flux of the solenoidal field. The main features of the new calorimeter layout are summarised in tables 58 and 59. The pseudorapidity coverage of the electromagnetic barrel is  $-1.4 < \eta < 2.4$ , while the hadronic barrel and its end cap cover  $-1.5 < \eta < 1.9$ . When the forward and backward plug modules are included, the total coverage is very close to hermetic, spanning  $-5.0 < \eta < 5.5$ . The total depth of the electromagnetic section is 30 radiation lengths in the barrel and backward regions, increasing to almost  $50X_0$  in the forward direction, where the particle and energy densities are highest. The hadronic calorimeter has a depth of between 7.1 and 9.6 interaction lengths, with the largest values in the forward plug region.

The performance of the new calorimeter layout has been simulated by evaluating the mean simulated response to electromagnetic (electron) and hadronic (pion) objects with various specific energies using GEANT4 [905] and interpreting the results as a function of energy in terms of sampling ( $a$ ) and material/leakage ( $b$ ) terms in the usual form:  $\sigma_E/E = a/\sqrt{E} \oplus b$ . Example results from fits are shown for the barrel electromagnetic and hadronic calorimeters in figure 221 and for the forward plug electromagnetic and hadronic calorimeters in figure 222. The results for the  $a$  and  $b$  parameters are summarised in tables 58 and 59. The response of

**Table 59.** Basic properties and simulated resolutions of forward and backward plug calorimeter modules in the new LHeC detector configuration. For each of the modules, the rows indicate the absorber and sensitive materials, the number of layers, the total absorber thickness, the pseudorapidity coverage, the contributions to the simulated resolution made by the sampling ( $a$ ) and material ( $b$ ) terms in the form  $a/b$ , the depth in terms of radiation or interaction lengths and the total area covered by the sensitive material. Produced using GEANT4 [905] simulation-based fits using the crystal ball function [907–909].

Calo (LHeC)	FHC plug Fwd	FEC plug Fwd	BEC plug Bwd	BHC plug Bwd
Readout, absorber	Si, W	Si, W	Si, Pb	Si, Cu
Layers	300	49	49	165
Integral absorber thickness (cm)	156.0	17.0	17.1	137.5
$\eta_{\max}, \eta_{\min}$	5.5, 1.9	5.1, 2.0	-1.4, -4.5	-1.4, -5.0
$\sigma_E/E = a/\sqrt{E} \oplus b$ (%)	51.8/5.4	17.8/1.4	14.4/2.8	49.5/7.9
$\Lambda_I/X_0$	$\Lambda_I = 9.6$	$X_0 = 48.8$	$X_0 = 30.9$	$\Lambda_I = 9.2$
Total area of Si (m <sup>2</sup> )	1354	187	187	745

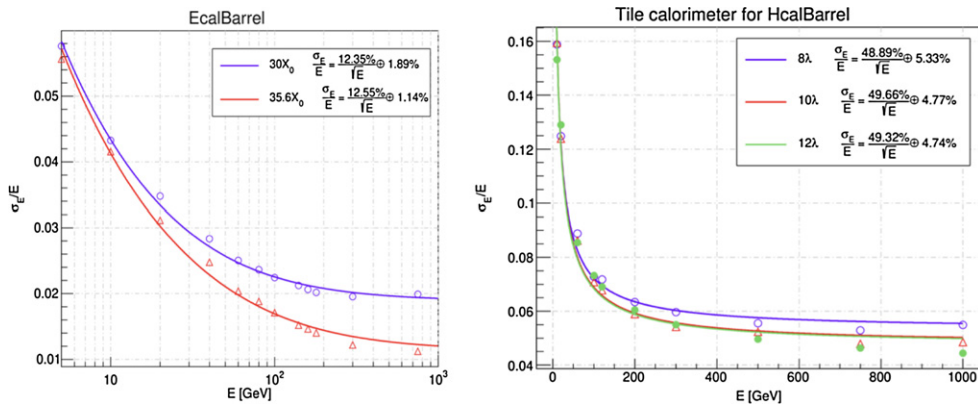


**Figure 221.** Crystal ball fitted energy-dependent resolutions of the barrel electromagnetic (left) and barrel hadronic (right) calorimeters, EMC and HCAL, respectively. The first ( $a$ ) term includes shower fluctuations and transverse leakages and the second ( $b$ ) term includes longitudinal leakages from the calorimeter volume.

the barrel electromagnetic calorimeter to electrons in terms of both sampling ( $a = 12.4\%$ ) and material ( $b = 1.9\%$ ) terms is only slightly worse than that achieved with the liquid argon sampling proposed in the 2012 CDR. The resolutions of the forward and backward electromagnetic plug calorimeters are comparable to those achieved in the 2012 design. A similar pattern holds for the hadronic response: the sampling terms are at the sub-50% level and the material terms are typically 5% throughout the barrel endcaps and forward and backward plugs.

### 12.5. Muon detector

Muon identification is an important aspect of any general-purpose high-energy physics experiment. At the LHeC, the muon detector can widen the scope and the spectrum of many measurements, of which only a few are listed here:

- Higgs decay;

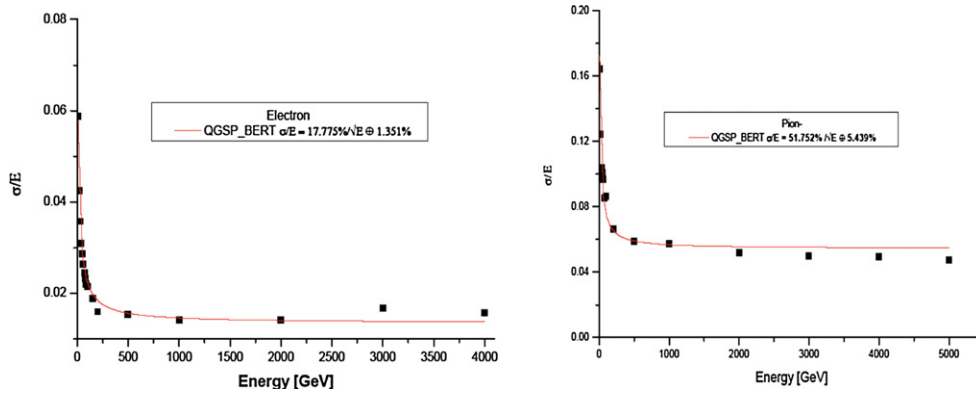


**Figure 222.** Crystal ball fitted energy-dependent resolutions of the forward electromagnetic (left) and forward hadronic (right) plug calorimeters, FEC and FHC, respectively. The first (a) term includes shower fluctuations and transverse leakages and the second (b) term includes longitudinal leakages from the calorimeter volume.

- semi-leptonic decays of heavy flavoured hadrons;
- vector meson production;
- direct  $W$  and  $Z$  production;
- di-muon production;
- LQs, lepton flavour violation, and other BSM phenomena.

The primary objective of the muon detector at the LHeC is to provide a reliable muon tag signature, which can be uniquely used in conjunction with the central detector for muon identification, triggering, and precision measurements. This specification is appropriate to the constraints of limited space<sup>196</sup> and the lack of a dedicated magnetic field, as in the baseline design. The muon chambers surround the central detector and cover the maximum possible solid angle. They have a compact multilayer structure, providing a pointing trigger and a precise timing measurement, which is used to separate muons coming from the interaction point from cosmic, beam halo, and nonprompt particles. This tagging feature does not include the muon momentum measurement, which is only performed in conjunction with the central detector. A trigger candidate in the muon detector is characterised by a time coincidence over a majority of the layers in a range of  $\eta$  and  $\phi$ , compatible with an  $ep$  interaction of interest in the main detector. The muon candidates are combined with the trigger information from the central detector (mainly the calorimetry at the level-one trigger) to reduce the fake rate or for more complex event topologies.

In terms of technology choices, the options in use in ATLAS and CMS and their planned upgrades are adequate for the LHeC. Generally, muon and background rates in the LHeC are expected to be lower than in  $pp$ . The option of an LHeC muon detector composed of layers of resistive plate chambers (RPC) providing the level-one trigger and a two-coordinate ( $\eta$ ,  $\phi$ ) measurement, possibly aided by monitored drift tubes (MDT) for additional precision measurements, as chosen for the 2012 CDR, is still valid. Recent developments, as presented in the LHC Phase-2 Upgrade Technical Design Reports [895, 897], further strengthen

<sup>196</sup> As in the 2012 CDR, the baseline LHeC detector (including the muon system and all of the services and supports), is expected to fit into the octagonal shape envelope of the L3 magnet (11.6 m minimum diameter).

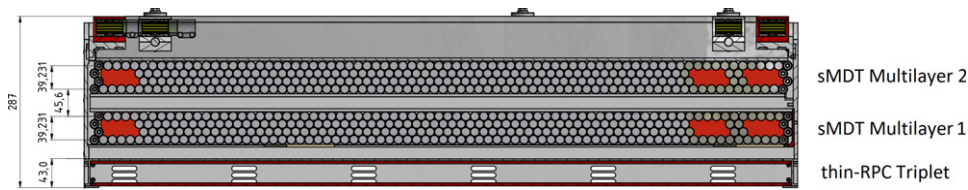


**Figure 223.** A transverse view of an RPC-MDT assembly as adapted from a drawing of the ATLAS phase-one muon upgrade. Reproduced from [895]. CC BY 4.0. In this case, a station is composed of an RPC triplet for trigger and two-coordinate readout and two MDT superlayers for precise track measurements.

this choice. A new thin RPC (with a 1 mm gas gap) operated at a reduced HV, provides a sharper time response (of the order of few ns), a higher rate capability (tens of  $\text{kHz cm}^{-2}$ ), and extends the already good ageing perspective. Advances in low-noise, high-bandwidth front-end electronics can improve the performance of older detectors. Similar arguments also hold for smaller MDTs (15 mm diameter) which provide lower occupancy and a higher rate capability.

Figure 223 shows an adaptation for the LHeC of an RPC-MDT assembly that will already be implemented for the inner muon layer of ATLAS during the Phase-1 upgrade as a pilot for Phase-2. A triplet of thin-gap RPCs, each with two-coordinate measurement, is combined with two superlayers of small MDTs. It is also important to note the reduced volume of this structure, in particular, that of the RPC part which would provide the muon tag. For the LHeC, a baseline would be to have one or two such stations forming a near-hermetic envelope around the central detector.

Finally, as already presented in the 2012 CDR, detector extensions with a dedicated magnetic field in the muon detector, either a second solenoid around the whole detector or an extra dipole or toroid in the forward region, are, at this stage, left open as possible developments for upgrade scenarios only.

### 12.6. Forward and backward detectors

In the 2012 CDR, initial plans for beamline instrumentation were provided for the LHeC. In the backward direction, low-angle electron and photon calorimeters were included, with the primary intention of measuring luminosity via the Bethe–Heitler process  $ep \rightarrow eXp$ ; an electron tagger was also provided to identify photoproduction ( $\gamma p \rightarrow X$ ) processes at intermediate  $y$  values. The current design carries forward the 2012 version of this backward instrumentation.

In the forward direction, Roman pot detectors were included in the region of  $z \sim 420$  m, which are capable of detecting scattered protons over a range of fractional energy loss,  $10^{-3} < \xi < 3 \times 10^{-2}$ , and which have a wide transverse momentum acceptance, based on previous extensive work in the LHC context by the FP420 group [898]. This also forms the basis of forward proton tagging in the revised design. However, as is the case at ATLAS and the TOTEM experiment at LHC, further Roman-pot detectors in the region of 200 m and (with HL-LHC optics) perhaps around 320 m would extend the acceptance towards higher  $\xi$  values up to around 0.2, allowing the study of diffractive processes  $ep \rightarrow eXp$  where the dissociation system  $X$  has a mass extending into the TeV regime. It is worth noting that Roman-pot technologies have come of age at the LHC; the TOTEM collaboration operated 14 separate stations at its peak. Silicon sensor designs borrowed from the innermost regions of the ATLAS

and CMS vertexing detectors have been used, providing high spatial resolution and radiation hardness well beyond the needs of the LHeC. Very precise timing detectors based on fast silicon or Cherenkov radiation signals from protons traversing quartz or diamond have also been deployed. It is natural that these advances and the lessons from their deployment at the LHC will be used to inform the next iteration of the LHeC design.

The forward beamline design also incorporates a zero-angle calorimeter, primarily designed to detect high-energy leading neutrons from semi-inclusive processes in  $ep$  scattering and to determine whether nuclei break up in  $eA$  events. This component of the detector was not considered in detail in 2012 and is therefore discussed here.

**12.6.1. Zero-degree (neutron) calorimeter.** The zero-degree calorimeter (ZDC) measures final-state neutral particles produced at angles close to the direction of the incoming hadron beam. They typically have large longitudinal momentum ( $x_F \gg 10^{-2}$ ), but a transverse momentum of the order of  $\Lambda_{\text{QCD}}$ . Such a calorimeter has been instrumented in experiments for  $ep$  collisions (H1 and ZEUS) and for  $pp$ ,  $pA$ , and  $AA$  collisions at the RHIC (STAR and PHENIX experiments) and at the LHC (ALICE, ATLAS, CMS and LHCf experiments). The detector's main focus is to study the soft-hard interplay in the QCD description of  $ep$  and  $eA$  collisions by studying the dependence of forward-travelling particles with small transverse momentum on variables such as  $Q^2$  and  $x$  that describe the hard scattering. The detector also allows the tagging of spectator neutrons to detect nuclear breakup in  $eA$  collisions and enables the precise study of the EMC effect by using neutron-tagged DIS on small systems, such as  $e^3\text{He} \rightarrow ed + n \rightarrow eX + n$ . For heavier ions, several tens of neutrons may enter the aperture of the ZDC. Inclusive  $\pi^0$  production has been measured by the LHCf experiments for  $pp$  collisions, and it is of great interest to compare this with DIS measurements at the same proton energies [902]. The precise understanding of the inclusive spectrum of the forward-going particles is a key ingredient in simulating air showers from ultra-high-energy cosmic rays.

**12.6.1.1. Physics requirement for forward neutron and  $\pi^0$  production measurement.** It is known from various HERA measurements that the slope parameter  $b$  is about  $8 \text{ GeV}^{-2}$  in the exponential parameterisation  $e^{bt}$  of the  $t$  distribution of leading neutrons. In order to precisely determine the slope parameter, it is necessary to measure the transverse momentum of the neutrons up to or beyond 1 GeV. The aperture for forward neutral particles does not have to be very large, thanks to the large energies of the proton and heavy ion beams. For example, collisions with  $E_p = 7 \text{ TeV}$  need 0.14 mrad for  $p_T = 1 \text{ GeV}$  neutrons at  $E_{\text{particle}}/E_{\text{beam}} \equiv x_F = 1.0$ , or 0.56 mrad for  $x_F = 0.25$ .

The energy or  $x_F$  resolution for neutrons will not be a dominant factor, thanks to the high energy of the produced particles. The energy resolution of a neutron with  $x_F = 0.1$  is about 2% for cutting-edge hadron calorimeters with  $\sigma_E/E = 50\%/\sqrt{E}$ , where the units of  $E$  are GeV. Such a resolution can be achieved if non-unity  $e/h$  can be compensated for, either by the construction of the calorimeter, or by software weighting, and if the size of the calorimeter is large enough that shower leakage is small.

On the other hand, the resolution requirement for the transverse momentum is rather stringent. For example, a 1 mm resolution for hadronic showers from the neutron measured 100 m downstream from the interaction point corresponds to 0.01 mrad or 70 MeV, which is rather a moderate ( $\leq 10\%$  resolution for large- $p_T$  hadrons with  $p_T > 700 \text{ MeV}$ ). For smaller  $p_T$ , it is more appropriate to evaluate the resolution in terms of  $t \simeq -(1 - x_F)p_T^2$  i.e.  $\Delta t \simeq 2(\Delta p_T)p_T$  at  $x_F = 1$ . At  $t = 0.1 \text{ GeV}^2$  or  $p_T \simeq 300 \text{ MeV}$ ,  $\Delta t$  is about 50%. A shower measurement with a positional resolution better than 1 mm would therefore significantly improve the  $t$ -distribution measurement.

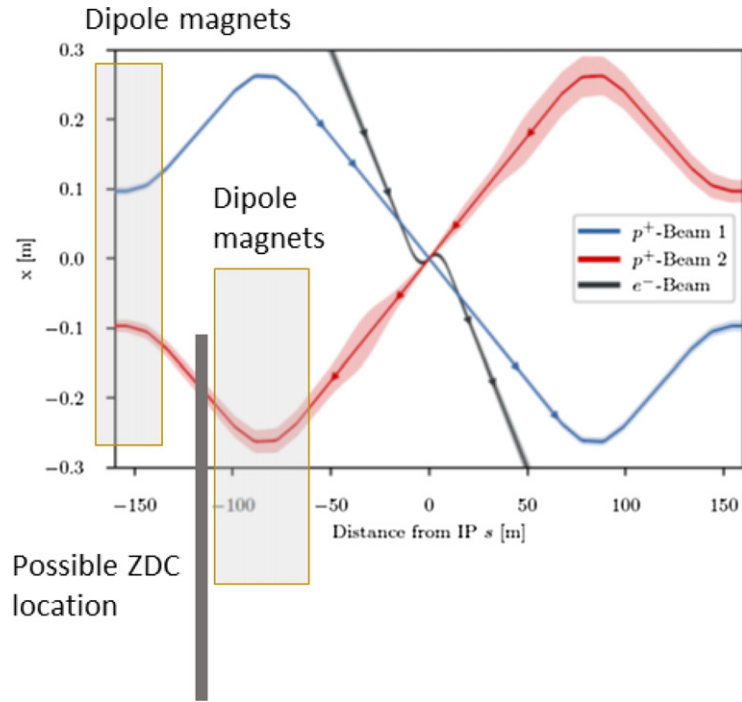


**Figure 224.** Possible location for a ZDC in the linac–ring IR design of the LHeC, as shown in figure 175. The solid rectangle represents the potential location and the magnet locations are also indicated.

According to the current LHC operational conditions with  $\beta^* = 5$  cm, the beam spread is  $8 \times 10^{-5}$  rad or 0.56 GeV. This is much larger than the resolution required in  $p_T$ . It is therefore neither possible to measure the particle flow nor to control the acceptance of the forward aperture. For a precise measurement of forward particles, it is necessary to have runs with  $\beta^* \geq 1$  m, corresponding to  $\sigma(p_T) < 70$  MeV.

The calorimeter should be able to measure more than 30 neutrons of 5 TeV to tag spectator neutrons from heavy-ion collisions. The dynamic range of the calorimeter should exceed 100 TeV with good linearity.

As for  $\pi^0$  measurements, the LHCf experiment has demonstrated that a positional resolution of  $200 \mu\text{m}$  for electromagnetic showers provides good performance for inclusive photon spectrum measurements [899]. This also calls for fine segmentation of the sampling layers.

**12.6.1.2. ZDC location** According to the IP design, a possible location for the ZDC is after the first deflection of the outgoing colliding proton beam at around  $Z = 110$  m, where no beam magnet is present (see figure 224). A neutral particle dump is planned at around this location, in order to protect accelerator components. A ZDC could serve as the first absorbing layer at zero degrees.

The aperture to the ZDC would be determined by the last quadrupole magnet at around  $z = 50$  m. Assuming a typical aperture for the LHC magnets of 35 mm, the aperture could be as large as 0.7 mrad. The horizontal apertures of the dipole magnets between 75 and 100 m would be larger, since otherwise, the magnets would receive significant radiation from neutral particles produced from the collisions at the IP. Even if the aperture is limited by the vertical



aperture of the last dipole at  $z = 100$  m, the aperture is 0.35 mrad, corresponding to 2.4 GeV in  $p_T$  for 7 GeV particles. This fulfils the physics requirement.

The space for the ZDC location in the transverse direction should be at least  $\pm 2\lambda_I$  to avoid a large leakage of hadronic showers. This can be achieved if the proton beam passes inside the calorimeter, about 20 cm from the centre of the calorimeter. The total size of the calorimeter could then be  $60 \times 60 \times 200$  cm<sup>3</sup> or larger, according to the eventual layout of the beam and accelerator components. This would provide about  $\pm 3\lambda_I$  in the transverse direction and about  $10\lambda_I$  in depth.

**12.6.1.3. Radiation requirement for the ZDC** It can safely be assumed that the energy spectra of the forward neutral particles produced in  $ep$  and  $pp$  events are very similar. According to a simulation, the LHCf tungsten–scintillator sandwich calorimeter receives about 30 Gy nb<sup>-1</sup> or  $10^8$  events nb<sup>-1</sup> assuming  $\sigma_{pp}^{\text{tot}} = 100$  mb, i.e.  $3 \times 10^{-7}$  J/event. This means that about 1/4 of the total proton beam energy (7 TeV  $\simeq 1.12 \times 10^{-6}$  J/event) is deposited in 1 kg of material in  $pp$  collisions. The  $ep$  total cross-section is expected to be approximately 68  $\mu\text{b}$  or 680 kHz at  $10^{34}$  cm<sup>2</sup> s<sup>-1</sup>. A 7 TeV beam or  $1.12 \times 10^{-6}$  J/event corresponds to  $0.76$  J s<sup>-1</sup> at this instantaneous luminosity. A quarter of the total dose is then about 0.2 Gy s<sup>-1</sup> or 0.02 Gy nb<sup>-1</sup>. The contribution from beam–gas interactions is estimated to be much smaller ( $\mathcal{O}(100$  kHz)).

Assuming that the ZDC is always operational during LHeC operation, one year of  $ep$  operation amounts to 2.5 MGy year<sup>-1</sup> assuming  $10^7$  s operation, or  $\mathcal{O}(10$  MGy) throughout the lifetime of the LHeC operation. This approximately corresponds to a  $10^{14}$  to  $10^{15}$  1 MeV neutron equivalent.

**12.6.1.4. Possible calorimeter design** The high dose of  $\mathcal{O}(10$  MGy) requires calorimeters based on modern crystals LYSO (Cerium doped Lutetium Yttrium Orthosilicate) or silicon as sampling layers, at least for the central part of the calorimeter where the dose is concentrated. Since we also need very fine segmentation for photons, it is desirable to use finely segmented silicon pads of the order of 1 mm. For the absorbers, tungsten should be used for good positional resolution of photons and the initial part of hadronic showers.

In the area outside the core of the shower i.e. well outside the aperture, the dose may be much smaller, and small scintillator tiles could be used as absorbers, which allows measurements with a good  $e/h$  ratio. If we choose a uniform design using silicon across the detector, the segmentation of the outer towers could be of the order of a few cm, which still allows the use of software compensation technology, as developed, for example, for the calorimeters in the ILC design. It may also be possible to use lead instead of tungsten for the outer towers to reduce the cost.

## 12.7. Detector installation and infrastructure

The usual constraints that apply to detector integration and assembly studies also apply to the LHeC. In places, they are even tighter, since the detector has to be installed in a relatively short time, as determined by the duration of an LHC machine shutdown, which is typically two years. For the purposes of this report, it is assumed that the LHeC detector will be installed at IP2, see figure 225. The magnet formerly used by L3 and now in use by ALICE is already present at IP2, and its support structure will be used once again for the LHeC. However, the time needed to remove the remainder of the existing detector and its services has to be included to the overall schedule. Thus, the only realistic possibility of accomplishing the timely dismantlement of the old detector and the installation of the new one is to complete as much as possible of the assembly and testing of the LHeC detector on the surface, where the construction can proceed without impacting the LHC physics runs. The prerequisite for doing this is the availability of



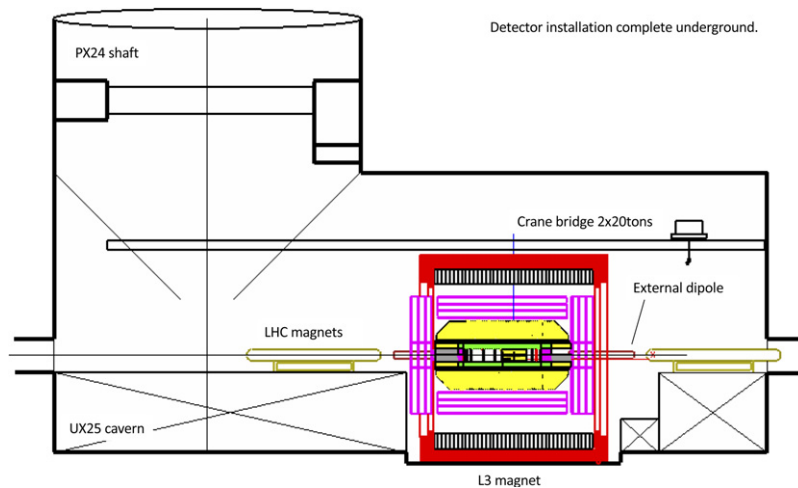


**Figure 227.** View of the LHeC detector, housed in the L3 magnet support structure, after installation at the interaction point.

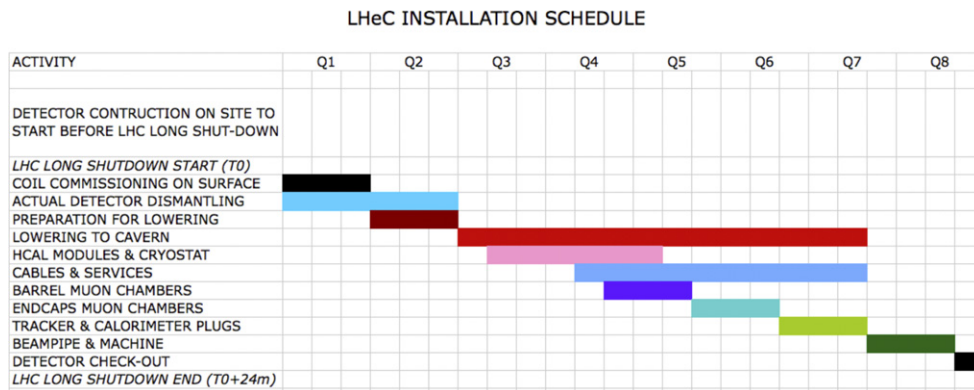


**Figure 228.** Time schedule of the sequential installation of the LHeC detector at Point 2, as described in the text.

for the time needed to lower the heaviest detector components, such as the HCal barrel and plug modules. A substantial amount of relevant experience will be acquired during LHC Long Shutdown 3, when a significant part of the ATLAS and CMS detectors will be replaced by new elements. At CMS, for instance, a new endcap calorimeter weighing about 220 tons will be lowered into the experimental cavern, a scenario very close to that envisaged for the LHeC detector assembly.

The detector has been split into the following main parts for assembly purposes:

- coil cryostat, including the superconducting coil, the two integrated dipoles and eventually the EMCAL;
- five HCal tile calorimeter barrel modules, fully instrumented and cabled (5);
- two HCal plugs modules, forward and backward (2);
- two EMCAL plugs, forward and backward (2);

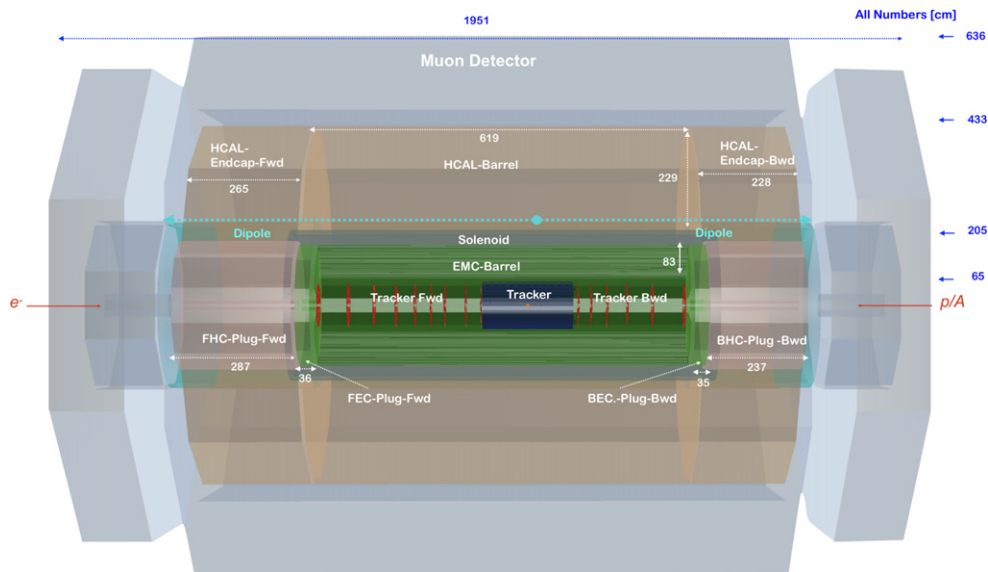


**Figure 229.** Side view of a low-energy FCCeh ( $E_p = 20$  TeV) concept detector, designed using the DD4hep framework [903], showing the essential features. The solenoid is again placed between the ECAL-barrel and hadronic-barrel calorimeters and is housed in a cryostat in common with the beam-steering dipoles that extend over the full length of the barrel and plug hadronic calorimeters. The sizes have been chosen such that the solenoid/dipoles and ECAL-barrel systems as well as the whole tracker are also suitable for operation after a beam-energy upgrade to  $E_p = 50$  TeV.

- inner tracking detector (1);
- beam pipe (1);
- central muon detector(s) (1 or 2); and
- endcap muon detectors (2).

The full detector, including the muon chambers, fits inside the former L3 detector magnet yoke once the four large doors are taken away. The goal is to prevent the loss of time caused by the dismantlement of the L3 magnet barrel yoke and to make use of its sturdy structure to hold the central part of the detector on a platform supported by the magnet's crown, while the muon chambers are inserted into lightweight structures (space-frames) attached to the inner surface of the octagonal L3 magnet.

The assembly of the main detector elements on the surface can start at any time, without a noticeable impact on the LHC run, provided that the surface facilities are available. The on-site coil system commissioning is estimated to require three months and the preparation for lowering, a further three months, including some contingency. In the same time window, the L3 magnet will be freed up and prepared for the new detector<sup>197</sup>. The lowering of the main

<sup>197</sup> The actual delay depends on the level of activation and the procedure adopted for dismantling the existing detector. Again, the experience acquired during the long shutdown (LS), LS2, due to the upgrades of ALICE and LHCb, and later with the ATLAS and CMS upgrades during LS3, will provide important insights for defining procedures and optimising the schedule.

**Table 60.** Summary of the main properties of the forward and backward tracker modules in the low-energy FCC-eh detector configuration, based on calculations performed using tkLayout. For each module, the rows correspond to the pseudorapidity coverage, the numbers of disk layers and sensors, the total area covered by silicon sensors, the number of readout channels, the hardware pitches affecting ( $r$ - $\phi$ ) and the  $z$  resolution, and the average material budget in terms of radiation lengths and interaction lengths. The numbers are broken down into the separate contributions of pixels, macropixels, and strips. The column *total* contains the sum of the corresponding values for barrel tracker modules (identical to the LHeC barrel layout, table 56) and the forward and backward trackers in this table.

Tracker (lowE-FCCeh) <sup>a</sup>	Fwd tracker			Bwd tracker		Total (Incl. table 56)
	Pix	Pix <sub>macro</sub>	Strip	Pix <sub>macro</sub>	Strip	
$\eta_{\max}, \eta_{\min}$	5.6, 2.6	3.8, 2.2	3.5, 1.6	-4.6, -2.6	-2.8, -1.6	5.3, -4.6
Disks	2	1	3	3	3	
Modules/sensors	288	288	1376	216	1248	12 444
Total Si area (m <sup>2</sup> )	1.35	1.45	7.35	1.0	6.5	49.85
Readout channels (10 <sup>6</sup> )	647.9	110.2	42.3	82.7	38.3	3317.2
Pitch <sup><math>r</math>-<math>\phi</math></sup> ( $\mu$ m)	25	100	100	100	100	
Pitch <sup><math>z</math></sup> ( $\mu$ m)	50	400	50k <sup>b</sup>	400	10k <sup>b</sup>	
Average $X_0/\Lambda_I$ (%)	6.7/2.1			6.1/1.9		
Incl. beam pipe (%)						40/25

<sup>a</sup>Based on tklayout calculations [904].

<sup>b</sup>Reaching the pitch  $r$ - $\phi$  using two wafer layers rotated by 20 mrad is achievable.

**Table 61.** Basic properties and simulated resolutions of barrel calorimeter modules in a scaled configuration, suitable for a low-energy FCC detector. For each module, the rows indicate the absorber and sensitive materials, the number of layers, the total absorber thickness, the pseudorapidity coverage, the contributions to the simulated resolution from the sampling ( $a$ ) and material ( $b$ ) terms in the form  $a/b$ , the depth in terms of radiation or interaction lengths and the total area covered by the sensitive material. The resolutions are obtained from a GEANT4 [905] simulation, with fits using a crystal ball function [907–909].

Calo (lowE-FCCeh)	EMC	HCAL		
	Barrel	Ecap Fwd	Barrel	Ecap Bwd
Readout, absorber	Sci, Pb	Sci, Fe	Sci, Fe	Sci, Fe
Layers	49	91	68	78
Integral absorber thickness (cm)	36.6	206.0	184.0	178.0
$\eta_{\max}, \eta_{\min}$	2.8, -2.5	2.0, 0.8	1.6, -1.4	-0.7, -1.8
$\sigma_E/E = a/\sqrt{E} \oplus b$ (%)	12.6/1.1	38.9/3.3	42.4/4.2	40.6/3.5
$\Lambda_I/X_0$	$X_0 = 66.2$	$\Lambda_I = 12.7$	$\Lambda_I = 11.3$	$\Lambda_I = 11.0$
Total area of Sci (m <sup>2</sup> )	2915	4554	12 298	3903

detector components into the cavern, illustrated in figure 226, is expected to take one week per piece (for a total of 15 pieces). Underground integration of the central detector elements inside the L3 magnet will require about six months, and cabling and connection to services will require some eight to ten months and will proceed in parallel with the installation of the muon chambers, the tracker, and the calorimeter plugs. Figure 227 shows the installed complete detector housed in the L3 magnet support.

**Table 62.** Basic properties and simulated resolutions of forward and backward plug calorimeter modules in a scaled configuration, suitable for a low-energy FCC detector. For each module, the rows indicate the absorber and sensitive materials, the number of layers, the total absorber thickness, the pseudorapidity coverage, the contributions to the simulated resolution from the sampling ( $a$ ) and material ( $b$ ) terms in the form  $a/b$ , the depth in terms of radiation or interaction lengths and the total area covered by the sensitive material. The resolutions are obtained from a GEANT4 [905] simulation, with fits using a crystal ball function [907–909].

Calo (lowE-FCCeh)	FHC plug Fwd	FEC plug Fwd	BEC plug Bwd	BHC plug Bwd
Readout, absorber	Si, W	Si, W	Si, Pb	Si, Cu
Layers	296	49	59	238
Integral absorber thickness (cm)	256.9	29.6	27.9	220.8
$\eta_{\max}, \eta_{\min}$	5.8, 1.8	5.4, 1.8	−1.5, −5.2	−1.5, −5.6
$\sigma_E/E = a/\sqrt{E} \oplus b$ (%)	61.9/0.5	26.5/0.4	24.7/0.4	46.7/4.4
$\Lambda_I/X_0$	$\Lambda_I = 15.5$	$X_0 = 84.7$	$X_0 = 50.2$	$\Lambda_I = 14.7$
Total area of Si (m <sup>2</sup> )	2479	364	438	1994

The total estimated time, from the start of the coil system testing on the surface, to the commissioning of the detector underground is thus 20 months. The beam-pipe bake out and vacuum pumping could take another three months and the final detector checks one additional month. Some contingency (two to three months in total) is foreseen at the beginning and the end of the installation period. A sketch of the installation schedule is provided in figure 228.

Concerning the detector infrastructure, not much can be said at this stage. The LHeC detector superconducting coil will need cryogenic services, and a choice has to be made between purchasing a dedicated liquid-helium refrigeration plant or leveraging the existing LHC cryogenic infrastructure to feed the detector magnet. The electrical and water-cooling networks present at LHC-P2 are already appropriately sized for the new detector, and only minor interventions are expected there.

### 12.8. Detector design for a low-energy FCC-eh

Although not the primary focus of this report, a full detector design has also been carried out for an  $ep$  facility based on an FCC tunnel with limited proton-ring magnet strengths, such that the proton energy is 20 TeV. For ease of comparison, the basic layout and the technology choices are currently similar to those of the LHeC detector. Similar or improved performance is obtained compared with the LHeC, provided that additional disks are included in the forward and backward trackers and the calorimeter depths are scaled logarithmically with the beam energies.

The basic layout is shown in figure 229. The barrel and end-caps of the central tracker are identical to those of the LHeC design, as given in table 56. The design parameters for the FCC-eh versions of the forward and backward trackers, the barrel calorimeters, and the plug calorimeters are given in tables 60–62, respectively. Comparing the performance of the ‘warm’ solution (Pb-scintillator) with the ‘cold’ variant (Pb-LAr) for the barrel electromagnetic calorimeter (EMC), the superior performance of the ‘cold’ calorimeter setup again favours the Pb-LAr option for the low-E FCCeh detector (see figure 230 and table 61).



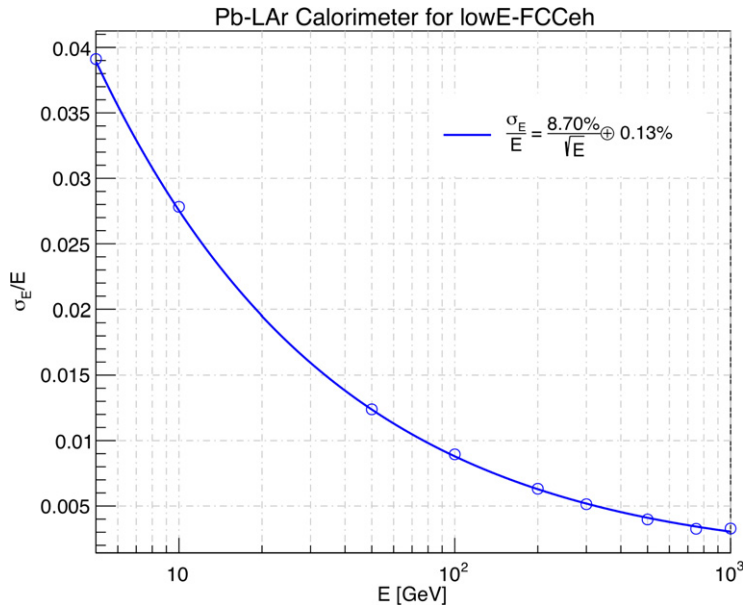


**Figure 230.** For comparison, the achievable resolution of a cold version of an EM-calorimeter stack is shown. The sampling calorimeter setup (ATLAS type) is characterised by lead as the absorber (2.2 mm thick), 3.8 mm gaps filled with liquid argon as the detecting medium, a Cartesian accordion geometry, and stack folds 40.1 mm long at an inclination angle of  $\pm 45^\circ$  to each other. The radiation length for the setup described is estimated from geantino scans using **GEANT4** [905]. The simulated calorimeter stack has a depth of 83.7 cm (approximately  $58X_0$ ). The fits were performed as for figure 221.

### 13. Conclusions

The Large Hadron Collider will determine the energy frontier of experimental collider physics for the next two decades. Following the current luminosity upgrade, the LHC can be further upgraded with a high-energy, intense electron beam, such that it becomes a twin-collider facility, in which  $ep$  collisions are registered concurrently with  $pp$ . A joint initiative by the European Committee for Future Accelerators (ECFA), CERN and the Nuclear Physics European Collaboration Committee (NuPECC) led to a detailed CDR [1] for the LHeC, published in 2012. The present paper represents an update of the original CDR in view of new physics and technology developments.

The LHeC uses a novel, energy-recovery linear electron accelerator which enables TeV-energy electron–proton collisions at a high luminosity of  $\mathcal{O}(10^{34}) \text{ cm}^{-2} \text{ s}^{-1}$ , exceeding that of HERA by nearly three orders of magnitude. The discovery of the Higgs boson and the surprising absence of BSM physics at the LHC demand an extension of the experimental basis of particle physics that is suitable for exploring the energy frontier beyond  $pp$  collisions at the LHC. The LHC infrastructure is the largest single investment the European and global particle physics community has ever assembled; the addition of an electron accelerator is a seminal opportunity to build on it and to sustain the HL-LHC programme by adding necessary elements that are provided by high-energy DIS. As has been shown in this paper, the external DIS input transforms the LHC into a much more powerful facility with a new level of matter substructure resolution, a more precise Higgs programme that challenges and complements

that of a next  $e^+e^-$  collider, and a hugely extended potential to discover physics beyond the SM.

The very high luminosity and the substantial extension of the kinematic range in DIS, compared to HERA, make the LHeC, on its own, a uniquely powerful TeV energy collider. Realising the *electrons for LHC* programme developed in the previous and present ‘white’ papers will create the cleanest high-resolution microscope accessible to the world, which one could call the ‘CERN Hubble telescope for the micro-universe’. It aims to unravel the substructure of matter encoded in the complex dynamics of the strong interaction, and to provide the necessary input for precision and discovery physics at the HL-LHC and for future hadron colliders.

This programme, as described in this paper, comprises the complete resolution of the partonic densities in an unexplored range of kinematics, the foundations for new, generalised views of proton structure, and the long-awaited clarification of QCD dynamics at high densities, as observed at small Bjorken  $x$ . New high-precision measurements of diffraction and vector mesons will shed new light on the puzzle of confinement. As a complement to the LHC and a possible future  $e^+e^-$  machine, the LHeC will scrutinise the SM more deeply than ever before, and possibly discover new physics in the electroweak and chromodynamic sectors, as outlined in this paper.

Through the extension of the kinematic range by about three orders of magnitude in lepton–nucleus ( $eA$ ) scattering, the LHeC is the most powerful electron–ion research facility that can be built in the forthcoming decades to clarify the partonic substructure and the dynamics inside nuclei for the first time and elucidate the chromodynamic origin of the quark–gluon plasma.

The Higgs programme at the LHeC is astonishing in its precision. It relies on CC and NC precision measurements, for which an inverse attobarn of integrated luminosity is desirable. The prospective results for the Higgs couplings to be obtained from the HL-LHC, combined with those presented here from the LHeC, will determine the couplings in the most frequent six Higgs decay channels to a one percent level of accuracy. This is as precise as one can expect from measurements made by linear  $e^+e^-$  colliders and dominantly obtained from  $gg$  and  $WW$  fusion, as compared to Higgs-strahlung in electron–positron scattering, which has the advantage of providing a Higgs width determination as well. The combined  $pp$  and  $ep$  LHC facility at CERN may therefore be expected to remain the centre of Higgs physics for two more decades.

Searches for BSM physics at the LHeC offer great complementarity to similar searches at the HL-LHC. The core advantage of the LHeC is the clean QCD background and pile-up-free environment of an electron–proton collider with a cms energy exceeding 1 TeV. This enables discoveries of signatures that could be lost in the hadronic noise in  $pp$  collisions or possibly inaccessible due to the limited cms energy of  $ee$  collisions. Prominent examples of discoveries enabled by  $ep$  collisions are heavy neutral leptons (or sterile neutrinos) that mix with the electron flavour, dark photons below the di-muon threshold, which are notoriously difficult to detect in other experiments, long-lived new particles in general, or new physics scenarios with a compressed mass spectrum, such as SUSY electrowinos and heavy scalar resonances with masses around and below 500 GeV, which may exist but would be buried in di-top backgrounds at the LHC.

The LHeC physics programme reaches far beyond any specialised goal, which underlines the unique opportunity for particle physics to build a novel laboratory for accelerator-based energy-frontier research at CERN. The project is fundable within the CERN budget, and does not prevent much more massive investments in the further future. It offers the possibility for the current generation of accelerator physicists to build a new collider using and developing

novel technology, while preparations proceed for the next grand step in particle physics for the generations ahead.

The main technical innovation of the LHeC is the first ever high-energy application of energy-recovery technology, based on high quality superconducting RF developments, representing a major contribution to the development of green collider technology, which is an appropriate response to the demands of our time. The ERL technique is increasingly seen to have major further applications beyond  $ep$  at the HE-LHC and the FCC-eh, such as the FCC-ee, a  $\gamma\gamma$  Higgs facility or, beyond particle physics, the highest-energy XFEL of hugely increased brightness.

This paper describes the plans and configuration of PERLE, the first 10 MW ERL facility, which is being prepared by an international collaboration to be built at Irène Joliot-Curie Laboratory at Orsay. PERLE has adopted the three-pass configuration, cavity and cryomodule technology, source and injector layout, and the frequency and electron-current parameters of the LHeC. This qualifies it to be the ideal machine to accompany the development of the LHeC. However, through its technology innovation and its challenging parameters, such as an intensity exceeding that of ELI by orders of magnitude, PERLE has an independent, far-reaching low-energy nuclear and particle physics programme with new and particularly precise measurements. It also has a possible programme of industrial applications, which has not been discussed in the present paper.

The LHeC provides an opportunity to build a novel collider detector, which is sought-after, as the design of the HL-LHC detector upgrades is approaching completion. A novel  $ep$  experiment will enable modern detection technology, such as HV CMOS silicon tracking, to be further developed and exploited in a new generation,  $4\pi$  acceptance, no-pile-up, high-precision collider detector in the decade(s) hence. This paper presented an update of the 2012 detector design in response to developments in physics, especially Higgs and BSM, and also of technology in the fields of detectors and analysis. The LHeC will have to be installed at IP2 at the LHC, because there is no other interaction region available while the heavy ion programme at the LHC is limited to the time until LS4. In the coming years it will have to be decided whether this or alternative proposals for the use of IP2 during the final years of LHC operation are considered attractive enough and realistic to be realised.

The next steps in this development are quite clear: the emphasis on ERLs, beyond the LHeC, requires the PERLE development to proceed rapidly. Limited funds are to be found for essential components, of which the challenging IR quadrupole is the main example. ECFA is about to establish a detector and physics series of workshops, including possible future Higgs facilities, and  $ep$ , which is a stimulus to further develop the organisational basis of the LHeC towards a detector proto-collaboration. These developments will include preparations for the FCC-eh and provide a necessary basis when, in a few years time, as recommended by the IAC, a decision on building the LHeC at CERN may be taken.

Recent history teaches us a lesson about the complementarity required for energy-frontier particle physics. In the seventies and eighties, CERN hosted the  $p\bar{p}$  energy frontier in the form of the UA1 and UA2 experiments and the most powerful DIS experiments with muons (the EMC, BCDMS and NMC experiments) and neutrinos (the CDHSW and CHARM experiments), while  $e^+e^-$  physics was pursued at the Positron–Electron Project (PEP) at SLAC, the Positron-Electron Tandem Ring Accelerator (PETRA) at DESY, and also the Transposable Ring Intersecting Storage Accelerator in Nippon (TRISTAN). Following this, the Fermi scale could be explored using the Tevatron, HERA, and the LEP collider. The next logical step proposed here is to complement the HL-LHC by a most powerful DIS facility, the LHeC, while preparations take shape for a next  $e^+e^-$  collider, currently at CERN and in Asia. A decision on

the LHeC can hardly be taken independently of how the grand future unfolds. Still, this scenario would give a realistic and yet exciting basis for completing the exploration of TeV-scale physics, which may not be achieved solely with the LHC.

The ERL concept and technology presented here have the potential to accompany the FCC in realising the FCC-eh machine when the time comes for the next, higher-energy hadron collider, and the search for new physics at the  $\mathcal{O}(10)$  TeV scale.

## Acknowledgments

The analyses and developments presented here would not have been possible without the CERN Directorate and other laboratories, universities, and groups that supported this study. We admire the skills of the technicians who successfully built the first 802 MHz SC cavity. We thank many of our colleagues for their interest in this work and a supportive attitude when time constraints could have resulted in reduced understanding. Special thanks are also due to the members and Chair of the International Advisory Committee for their attention to, and guidance of this project. From the beginning of the LHeC study, it has been supported by ECFA and its chairs, which was a great help and stimulus in the undertaking of this study, which was performed outside our usual duties. During this time, a number of students in master's and PhD courses have made essential contributions to this project, for which we are especially grateful. This also extends to colleagues with whom we have been working closely but who meanwhile left this development, perhaps temporarily, or who work at non-particle-physics institutions while wishing LHeC success. The current state of particle physics reminds us of the potential we have when resources and prospects are combined, to which this study is considered to be a contribution. The authors would like to thank the Institute of Particle Physics Phenomenology (IPPP) at Durham for the award of an IPPP Associateship to support this work, and gratefully acknowledge the support of the state of Baden-Württemberg through High Performance Computing in Baden-Württemberg (bwHPC) and the German Research Foundation (DFG) through Grant No. INST 39/963-1 FUGG. The financial support of the Ministerio de Ciencia e Innovación of Spain under project FPA2017-83814-P, the Unidad de Excelencia María de Maetzu under project MDM-2016-0692, the Xunta de Galicia (project ED431C 2017/07 and Centro singular de investigación de Galicia accreditation 2019–2022), and the European Union (European Regional Development Fund (ERDF)) is gratefully acknowledged. This study was performed within the framework of COST Action CA 15213 'Theory of hot matter and relativistic heavy-ion collisions' (THOR), MSCA RISE 823947 'Heavy ion collisions: collectivity and precision in saturation physics' (HIEIC), and has received funding from the European Union's Horizon 2020 research and innovation programme under Grant Agreement No. 824093.

## Appendix A. Statement of the International Advisory Committee

At the end of 2014, the CERN Directorate appointed an International Advisory Committee (IAC) to advise on the direction of energy-frontier electron-hadron scattering at CERN; for their mandate, see below. The committee and its chair, em. director general of CERN Herwig Schopper, were reconfirmed after a new director general was appointed. The IAC held regular sessions at the annual LHeC workshops, in which reports were heard by the co-coordinators of the project, Oliver Brüning and Max Klein. Its work and opinion shaped the project development considerably and it was pivotal for the foundation of the PERLE project. The committee was in close contact and advised, in particular, on the documents concerning the LHeC [8, 10]

and PERLE [11], submitted at end of 2018 to the update of the European strategy on particle physics. In line with the present updated LHeC design report and the strategy process, the IAC formulated a brief report to the CERN DG, in which its observations and recommendations were summarised. This report was also sent to the members of the European particle physics strategy group. It is reproduced here.

#### A.1. Report by the IAC on the LHeC to the DG of CERN

The development of the LHeC project was initiated by CERN and ECFA, in cooperation with NuPECC. It culminated in the publication of the CDR, arXiv:1206.2913 in 2012, which received by now about 500 citations. In 2014, the CERN Directorate invited our committee to advise the CERN Directorate, and the Coordination Group, on the directions of future energy frontier electron–hadron scattering as are enabled with the LHC and the future FCC (for the mandate see below). In 2016, Council endorsed the HL-LHC, which offers a higher LHC performance and strengthened the interest in exploring the Higgs phenomenon. In view of the imminent final discussions for the European road map for particle physics, a short summary report is here presented.

#### A.2. Main developments 2014–2019

A series of annual workshops on the LHeC and FCC-eh was held, and this report is given following the latest workshop <https://indico.cern.ch/event/835947>, October 24/25, 2019.

Based on recent developments concerning the development of the LHC accelerator and physics, and the progress in technology, a new default configuration of the LHeC and FCC-eh has been worked out with a tenfold increased peak luminosity goal, of  $10^{34} \text{ cm}^{-2} \text{ s}^{-1}$ , as compared to the CDR. A comprehensive paper, ‘The LHeC at the HL-LHC’, is being finalised for publication this year.

Within this work, it has been shown that the LHeC represents the cleanest, high resolution microscope the world can currently build, a seminal opportunity to develop and explore QCD, to study high precision Higgs and electroweak physics and to substantially extend the range and prospects for accessing BSM physics, on its own and in combination of  $pp$  with  $ep$ . The LHeC, in  $eA$  scattering mode, has a unique discovery potential on nuclear structure, dynamics and QGP physics.

Intense  $eh$  collisions with LHeC and FCC-eh are enabled through a special electron-beam racetrack arrangement with ERL technology. If LHeC were to be considered either on its own merits, or as a bridge project to FCC-eh, it seemed important to find a configuration, which could be realised within the existing CERN budget. Several options were studied and found.

Before a decision on such a project can be taken, the ERL technology has to be further developed. Considerable progress has been made in the USA, and a major effort is now necessary to develop it further in Europe. An international collaboration (ASTeC, BINP, CERN, Jefferson Lab, Liverpool, Orsay) has been formed to realise the first multiturn 10 MW ERL facility, PERLE at Orsay, with its main parameters set by the LHeC and producing the first encouraging results on 802 MHz cavity technology, for the CDR see arXiv:1705.08783.

This radically new accelerator technology, ERL, has an outstanding technical (SRF), physics (nuclear physics) and industrial (lithography, transmutations,...) impact, and offers possible applications beyond  $ep$  (such as a racetrack injector or ERL layout for FCC-ee, a high energy FEL or  $\gamma\gamma$  collider).

In conclusion it may be stated

- The installation and operation of the LHeC has been demonstrated to be commensurate with the currently projected HL-LHC programme, while the FCC-eh has been integrated into the FCC vision;
- The feasibility of the project as far as accelerator issues and detectors are concerned has been shown. It can only be realised at CERN and would fully exploit the massive LHC and HL-LHC investments;
- The sensitivity for discoveries of NP is comparable, and in some cases superior, to the other projects envisaged;
- The addition of an  $ep/A$  experiment to the LHC substantially reinforces the physics programme of the facility, especially in the areas of QCD, precision Higgs and electroweak as well as heavy ion physics;
- The operation of LHeC and FCC-eh is compatible with simultaneous  $pp$  operation; for LHeC the interaction point 2 would be the appropriate choice, which is currently used by ALICE;
- The development of the ERL technology needs to be intensified in Europe, in national laboratories but with the collaboration of CERN;
- A preparatory phase is still necessary to work out some time-sensitive key elements, especially the high power ERL technology (PERLE) and the prototyping of intersection region magnets.

Recommendations

- (a) It is recommended to further develop the ERL based  $ep/A$  scattering plans, both at LHC and FCC, as attractive options for the mid and long term programme of CERN, resp. Before a decision on such a project can be taken, further development work is necessary, and should be supported, possibly within existing CERN frameworks (e.g. development of SC cavities and high field IR magnets).
- (b) The development of the promising high-power beam-recovery technology ERL should be intensified in Europe. This could be done mainly in national laboratories, in particular with the PERLE project at Orsay. To facilitate such a collaboration, CERN should express its interest and continue to take part.
- (c) It is recommended to keep the LHeC option open until further decisions have been taken. An investigation should be started on the compatibility between the LHeC and a new heavy ion experiment in interaction point 2, which is currently under discussion.

After the final results of the European strategy process will be made known, the IAC considers its task to be completed. A new decision will then have to be taken for how to continue these activities.

Herwig Schopper, Chair of the Committee, Geneva, November 4, 2019

### A.3. Mandate of the International Advisory Committee

Advice to the LHeC Coordination Group and the CERN directorate by following the development of options of an  $ep/eA$  collider at the LHC and at FCC, especially with: provision of scientific and technical direction for the physics potential of the  $ep/eA$  collider, both at LHC and at FCC, as a function of the machine parameters and of a realistic detector design, as well as for the design and possible approval of an ERL test facility at CERN. Assistance in building the international case for the accelerator and detector developments as well



as guidance to the resource, infrastructure and science policy aspects of the  $ep/eA$  collider. (December 2014)

#### A.4. Members of the Committee

---

Sergio Bertolucci (U Bologna)	Max Klein (U Liverpool, Coordinator)
Nichola Bianchi (INFN, now Singapore)	Shin-Ichi Kurokawa (KEK)
Frederick Bordy (CERN)	Victor Matveev (JINR Dubna)
Stan Brodsky (SLAC)	Aleandro Nisati (Rome I)
Oliver Brüning (CERN, Coordinator)	Leonid Rivkin (PSI Villigen)
Hesheng Chen (IHEP Beijing)	Herwig Schopper (CERN, em.DG, chair)
Eckhard Elsen (CERN)	Jürgen Schukraft (CERN)
Stefano Forte (U Milano)	Achille Stocchi (IJCLab Orsay)
Andrew Hutton (Jefferson Lab)	John Womersley (ESS Lund)
Young-Kee Kim (U Chicago)	

---

## Appendix B. Membership of coordination

### B.1. Coordinating group

Gianluigi Arduini (CERN)  
 Néstor Armesto (University of Santiago de Compostela)  
 Oliver Brüning (CERN)—Co-Chair  
 Andrea Gaddi (CERN)  
 Erk Jensen (CERN)  
 Walid Kaabi (IJCLab Orsay)  
 Max Klein (University of Liverpool)—Co-Chair  
 Peter Kostka (University of Liverpool)  
 Bruce Mellado (University of Witwatersrand)  
 Paul R Newman (University of Birmingham)  
 Daniel Schulte (CERN)  
 Frank Zimmermann (CERN)

### B.2. Physics convenors

#### Parton distributions and QCD

Claire Gwenlan (University of Oxford)  
 Fred Olness (Texas University, Dallas)

#### Physics at small $x$

Paul R Newman (University of Birmingham)  
 Anna M Stasto (Pennsylvania State University)

#### Top and electroweak physics

Olaf Behnke (DESY Hamburg)  
 Daniel Britzger (MPI Munich)  
 Christian Schwanenberger (DESY Hamburg)

#### Electron–ion physics

Néstor Armesto (University of Santiago de Compostela)

#### Higgs physics

Uta Klein (University of Liverpool)  
Masahiro Kuze (Institute of Technology Tokyo)  
**BSM physics**  
Georges Azuelos (University of Montreal)  
Monica D’Onofrio (University of Liverpool)  
Oliver Fischer (MPIK Heidelberg)  
**Detector design**  
Peter Kostka (University of Liverpool)  
Alessandro Polini (INFN Bologna)

## ORCID iDs

D Britzger  <https://orcid.org/0000-0002-9246-7366>

M Klein  <https://orcid.org/0000-0002-8527-964X>

## References

- [1] Abelleira Fernandez J L *et al* (LHeC Study Group) 2012 *J. Phys. G: Nucl. Part. Phys.* **39** 075001
- [2] Burkhardt H 2012 *ICFA Beam Dyn. Newslett.* **58** 76 (<http://cds.cern.ch/record/1559765>)
- [3] Apollinari G, Béjar Alonso I, Brüning O, Fessia P, Lamont M, Rossi L and Tavian L (ed) 2017 High-luminosity large hadron collider (HL-LHC) *CERN Yellow Rep. Monogr., CERN-2017-007-M* vol 4
- [4] Rossi L and Brüning O 2019 Progress with the high luminosity LHC project at CERN *Proc., 10th Int. Particle Accelerator Conf. (IPAC2019)* (Melbourne, Australia May 19–24, 2019)
- [5] Hoffstaetter G *et al* 2017 arXiv:1706.04245
- [6] Bartnik A *et al* 2020 *Phys. Rev. Lett.* **125** 044803
- [7] Angal-Kalinin D *et al* 2018 *J. Phys. G: Nucl. Part. Phys.* **45** 065003
- [8] Brüning O *et al* (LHeC Study Group) 2018 Exploring the energy frontier with deep inelastic scattering at the LHC *A Contribution to the Update of the European Strategy on Particle Physics, CERN-ACC-NOTE-2018-0084* (<http://cds.cern.ch/record/2652313>)
- [9] Brüning O and Klein M *et al* (LHeC and PERLE Collaborations) 2019 *J. Phys. G: Nucl. Part. Phys.* **46** 123001
- [10] Brüning O *et al* (LHeC Study Group) 2018 Addendum: exploring the energy frontier with deep inelastic scattering at the LHC *A Contribution to the Update of the European Strategy on Particle Physics, CERN-ACC-NOTE-2018-0085*
- [11] Klein M and Stocchi A *et al* (PERLE Collaboration) 2018 PERLE: a high power energy recovery facility for Europe *A Contribution to the Update of the European Strategy on Particle Physics, CERN-ACC-NOTE-2018-0086* (<https://cds.cern.ch/record/2652336>)
- [12] Altarelli G 2014 *Frascati Phys. Ser.* **58** 102 (arXiv:1407.2122)
- [13] De Hondt J 2019 *Talk on the Future of Particle Physics and on ECFA Matters, Plenary Session, ECFA, CERN*
- [14] Abada A *et al* (FCC Collaboration) 2019 *Eur. Phys. J. C* **79** 474
- [15] Abada A *et al* (FCC Collaboration) 2019 *Eur. Phys. J. Spec. Top.* **228** 261
- [16] Abada A *et al* (FCC Collaboration) 2019 *Eur. Phys. J. Spec. Top.* **228** 755
- [17] Ahmad M *et al* (CEPC-SPPC Study Group) 2015 *CEPC-SPPC Preliminary Conceptual Design Report: 2. Accelerator, IHEP-CEPC-DR-2015-01, IHEP-AC-2015-01*
- [18] Dong M *et al* (CEPC Study Group) 2018 CEPC conceptual design report: volume 2—physics & detector (arXiv:1811.10545)
- [19] Feynman R P 1972 *Photon–Hadron Interactions* (Reading, MA: Westview Press)
- [20] Bloom E D *et al* 1969 *Phys. Rev. Lett.* **23** 930
- [21] Breidenbach M, Friedman J I, Kendall H W, Bloom E D, Coward D H, DeStaebler H, Drees J, Mo L W and Taylor R E 1969 *Phys. Rev. Lett.* **23** 935
- [22] Feynman R P 1969 *Phys. Rev. Lett.* **23** 1415

- [23] Bjorken J D and Paschos E A 1969 *Phys. Rev.* **185** 1975
- [24] Prescott C Y *et al* 1978 *Phys. Lett. B* **77** 347
- [25] Weinberg S 1967 *Phys. Rev. Lett.* **19** 1264
- [26] Wiik B H 1985 *Acta Phys. Pol. B* **16** 127
- [27] Klein M and Yoshida R 2008 *Prog. Part. Nucl. Phys.* **61** 343
- [28] De Rújula A, Glashow S L, Politzer H D, Treiman S B, Wilczek F and Zee A 1974 *Phys. Rev. D* **10** 1649
- [29] Dainton J B, Klein M, Newman P, Perez E and Willeke F 2006 *J. Inst.* **1** P10001
- [30] Abada A *et al* (FCC Collaboration) 2019 *Eur. Phys. J. Spec. Top.* **228** 1109
- [31] Marhauser F *et al* 2018 802 MHz ERL cavity design and development *Proc., 9th Int. Particle Accelerator Conf. (IPAC 2018)* (Vancouver, BC Canada April 29–May 4, 2018)
- [32] Litvinenko V N, Roser T and Chamizo-Llatas M 2020 *Phys. Lett. B* **804** 135394
- [33] Telnov V I 2021 A high-luminosity superconducting twin  $e^+e^-$  linear collider with energy recovery (arXiv:2105.11015)
- [34] Brüning O 2018 *FCC-eh Cost Estimate, CERN-ACC-NOTE-2018-0061*
- [35] Bogacz A 2019 *The LHeC ERL—Optics and Performance Optimisation, Talk Given at ERL Workshop* (Berlin)
- [36] Brüning O, Jowett J, Klein M, Pellegrini D, Schulte D and Zimmermann F 2017 *Future Circular Collider Study FCC-eh Baseline Parameters, CERN FCC-ACC-RPT-012*
- [37] Bordry F *et al* 2018 Machine parameters and projected luminosity performance of proposed future colliders at CERN (arXiv:1810.13022)
- [38] Quigg C 2013 *Proc. Sci.* **DIS2013** 034
- [39] Collins J C, Soper D E and Sterman G 1989 Factorization of hard processes in QCD *Adv. Ser. Direct. High Energy Phys.* **5** 1
- [40] Abelleira J L *et al* (LHeC Study Group) 2012 On the relation of the LHeC and the LHC (arXiv:1211.5102)
- [41] Boroun G R 2015 *Phys. Lett. B* **744** 142
- [42] Hobbs T J, Londregan J T, Murdock D P and Thomas A W 2011 *Phys. Lett. B* **698** 123
- [43] Klein M 2010 The structure of the proton and HERA *Int. Conf. on the Structure and Interactions of the Photon and 18th Int. Workshop on Photon–Photon Collisions and Int. Workshop on High Energy Photon Linear Colliders*
- [44] Aaron F *et al* (H1 and ZEUS Collaborations) 2010 *J. High Energy Phys.* **JHEP01(2010)109**
- [45] Abramowicz H *et al* (H1 and ZEUS Collaborations) 2015 *Eur. Phys. J. C* **75** 580
- [46] Alekhin S *et al* (HERAFitter Group) 2015 *Eur. Phys. J. C* **75** 304
- [47] Aaron F *et al* (H1 Collaboration) 2009 *Eur. Phys. J. C* **64** 561
- [48] Botje M 2011 *Comput. Phys. Commun.* **182** 490  
Botje M 2016 Erratum for the time-like evolution in QCDNUM (arXiv:1602.08383)
- [49] Thorne R 2006 *Phys. Rev. D* **73** 054019
- [50] Thorne R 2012 *Phys. Rev. D* **86** 074017
- [51] Alekhin S, Blümlein J and Moch S 2012 *Phys. Rev. D* **86** 054009
- [52] Alekhin S, Blümlein J, Moch S-O and Placakyte R 2017 *Phys. Rev. D* **96** 014011
- [53] Klein M 2019 Future deep inelastic scattering with the LHeC *From My Vast Repertoire . . . : Guido Altarelli's Legacy* ed A Levy, S Forte and G Ridolfi (Singapore: WSP) p 303
- [54] Klein M and Radescu V 2013 *Partons from the LHeC, CERN-LHeC-Note-2013-002* (<https://cds.cern.ch/record/1564929>)
- [55] Bentvelsen S, Engelen J and Kooijman P 1992 Reconstruction of  $(x, Q^2)$  and extraction of structure functions in neutral current scattering at HERA *Workshop on Physics at HERA Hamburg* (Germany October 29–30, 1991)
- [56] Bassler U and Bernardi G 1995 *Nucl. Instrum. Methods Phys. Res. A* **361** 197
- [57] Bassler U and Bernardi G 1999 *Nucl. Instrum. Methods Phys. Res. A* **426** 583
- [58] Blümlein J and Klein M 1990 Kinematics and resolution at future  $e p$  colliders 1990 *DPF Summer Study on High-Energy Physics: Research Directions for the Decade (Snowmass 90)* (Snowmass, Colorado June 25–July 13, 1990)
- [59] Abdul Khalek R, Bailey S, Gao J, Harland-Lang L and Rojo J 2019 *SciPost Phys.* **7** 051
- [60] Brodsky S J and Farrar G R 1973 *Phys. Rev. Lett.* **31** 1153
- [61] Brodsky S J and Farrar G R 1975 *Phys. Rev. D* **11** 1309
- [62] Matveev V A, Muradyan R M and Tavkhelidze A N 1973 *Lett. Nuovo Cimento* **7** 719
- [63] Klein M 2016 *EPJ Web Conf.* **112** 03002

- [64] Aad G *et al* (ATLAS Collaboration) 2019 *Eur. Phys. J. C* **79** 970
- [65] Abramowicz H *et al* (H1 and ZEUS Collaborations) 2018 *Eur. Phys. J. C* **78** 473
- [66] Kuti J and Weisskopf V F 1971 *Phys. Rev. D* **4** 3418
- [67] Hou T-J *et al* 2021 *Phys. Rev. D* **103** 014013
- [68] Seligman W G *et al* 1997 *Phys. Rev. Lett.* **79** 1213
- [69] Tzanov M *et al* (NuTeV Collaboration) 2006 *Phys. Rev. D* **74** 012008
- [70] Onengut G *et al* (CHORUS Collaboration) 2006 *Phys. Lett. B* **632** 65
- [71] Berge J P *et al* 1991 *Z. Phys. C* **49** 187
- [72] Samoylov O *et al* (NOMAD Collaboration) 2013 *Nucl. Phys. B* **876** 339
- [73] Aad G *et al* (ATLAS Collaboration) 2012 *Phys. Rev. Lett.* **109** 012001
- [74] Chatrchyan S *et al* (CMS Collaboration) 2014 *J. High Energy Phys.* **JHEP02(2014)013**
- [75] Aad G *et al* (ATLAS Collaboration) 2014 *J. High Energy Phys.* **JHEP05(2014)068**
- [76] Aaboud M *et al* (ATLAS Collaboration) 2017 *Eur. Phys. J. C* **77** 367
- [77] Alekhin S, Blümlein J and Moch S 2018 *Phys. Lett. B* **777** 134
- [78] Cooper-Sarkar A M and Wichmann K 2018 *Phys. Rev. D* **98** 014027
- [79] Alekhin S, Blumlein J, Kulagin S, Moch S-O and Petti R 2018 *Proc. Sci.* **DIS2018** 008
- [80] Abdolmaleki H *et al* (xFitter Developers' Team Collaboration) 2019 *Eur. Phys. J. C* **79** 864
- [81] Behnke O, Geiser A and Lisovsky M 2015 *Prog. Part. Nucl. Phys.* **84** 1
- [82] Zenaiev O 2017 *Eur. Phys. J. C* **77** 151
- [83] Aivazis M A G, Olness F I and Tung W-K 1990 *Phys. Rev. Lett.* **65** 2339
- [84] Aivazis M A G, Olness F I and Tung W-K 1994 *Phys. Rev. D* **50** 3085
- [85] Aivazis M A G, Collins J C, Olness F I and Tung W-K 1994 *Phys. Rev. D* **50** 3102
- [86] Thorne R S and Roberts R G 2001 *Eur. Phys. J. C* **19** 339
- [87] Alekhin S, Blümlein J and Moch S 2014 *Phys. Rev. D* **89** 054028
- [88] Alekhin S, Blümlein J, Klein S and Moch S 2010 *Phys. Rev. D* **81** 014032
- [89] Forte S, Laenen E, Nason P and Rojo J 2010 *Nucl. Phys. B* **834** 116
- [90] Martin A D, Stirling W J, Thorne R S and Watt G 2010 *Eur. Phys. J. C* **70** 51
- [91] Ball R D, Bertone V, Cerutti F, Del Debbio L, Forte S, Guffanti A, Latorre J I, Rojo J and Ubiali M 2011 *Nucl. Phys. B* **849** 296
- [92] Ball R D, Bonvini M and Rottoli L 2015 *J. High Energy Phys.* **JHEP11(2015)122**
- [93] Moch S, Ruijl B, Ueda T, Vermaseren J A M and Vogt A 2017 *J. High Energy Phys.* **JHEP10(2017)041**
- [94] Herzog F, Moch S, Ruijl B, Ueda T, Vermaseren J A M and Vogt A 2019 *Phys. Lett. B* **790** 436
- [95] Das G, Moch S-O and Vogt A 2020 *JHEP* **3** 116
- [96] Ball R D 2017 *AIP Conf. Proc.* **1819** 030002
- [97] Klein M and Riemann T 1984 *Z. Phys. C* **24** 151
- [98] Argento A *et al* 1984 *Phys. Lett. B* **140** 142
- [99] Drell S D and Yan T-M 1970 *Phys. Rev. Lett.* **25** 316  
Drell S D and Yan T-M 1970 *Phys. Rev. Lett.* **25** 902 (erratum)
- [100] Kubar J, Le Bellac M, Meunier J L and Plaut G 1980 *Nucl. Phys. B* **175** 251
- [101] Accardi A *et al* 2016 *Eur. Phys. J. A* **52** 268
- [102] Lomnitz M and Klein S 2019 *Phys. Rev. C* **99** 015203
- [103] Belitsky A V, Ji X-d and Yuan F 2004 *Phys. Rev. D* **69** 074014
- [104] Nikolaev N N and Zakharov B G 1991 *Z. Phys. C* **49** 607
- [105] Nikolaev N N and Zakharov B G 1992 *Z. Phys. C* **53** 331
- [106] Nikolaev N N and Zakharov B G 1994 *J. Exp. Theor. Phys.* **78** 598  
Nikolaev N N and Zakharov B G 1994 *Zh. Eksp. Teor. Fiz.* **105** 1117
- [107] Nikolaev N N, Zakharov B G and Zoller V R 1995 *Z. Phys. A* **351** 435
- [108] Mueller A H 1994 *Nucl. Phys. B* **415** 373
- [109] Mueller A H and Patel B 1994 *Nucl. Phys. B* **425** 471
- [110] Berger J and Stasto A M 2013 *J. High Energy Phys.* **JHEP01(2013)001**
- [111] Amaldi U and Schubert K R 1980 *Nucl. Phys. B* **166** 301
- [112] Munier S, Stašto A M and Mueller A H 2001 *Nucl. Phys. B* **603** 427
- [113] Armesto N and Rezaeian A H 2014 *Phys. Rev. D* **90** 054003
- [114] Kowalski H and Teaney D 2003 *Phys. Rev. D* **68** 114005
- [115] Kowalski H, Motyka L and Watt G 2006 *Phys. Rev. D* **74** 074016
- [116] Watt G and Kowalski H 2008 *Phys. Rev. D* **78** 014016
- [117] Lipatov L N 1986 *Sov. Phys. - JETP* **63** 904

- Lipatov L N 1986 *Zh. Eksp. Teor. Fiz.* **90** 1536
- [118] Hatta Y, Xiao B-W and Yuan F 2016 *Phys. Rev. Lett.* **116** 202301
- [119] Altinoluk T, Armesto N, Beuf G and Rezaeian A H 2016 *Phys. Lett. B* **758** 373
- [120] Mäntysaari H, Muller N and Schenke B 2019 *Phys. Rev. D* **99** 074004
- [121] Salazar F and Schenke B 2019 *Phys. Rev. D* **100** 034007
- [122] Mäntysaari H and Schenke B 2016 *Phys. Rev. Lett.* **117** 052301
- [123] Mäntysaari H and Schenke B 2016 *Phys. Rev. D* **94** 034042
- [124] Mäntysaari H and Schenke B 2017 *Phys. Lett. B* **772** 832
- [125] Mäntysaari H and Schenke B 2018 *Phys. Rev. D* **98** 034013
- [126] Cepila J, Contreras J G and Tapia Takaki J D 2017 *Phys. Lett. B* **766** 186
- [127] Bendova D, Cepila J and Contreras J G 2019 *Phys. Rev. D* **99** 034025
- [128] Krelina M, Goncalves V P and Cepila J 2019 *Nucl. Phys. A* **989** 187
- [129] Baltz A J 2008 *Phys. Rep.* **458** 1
- [130] Klein S R 2017 *Nucl. Phys. A* **967** 249
- [131] Zweig G 1964 An  $SU(3)$  model for strong interaction symmetry and its breaking. Version 1 *CERN-TH-401*
- [132] Fritzsche H, Gell-Mann M and Leutwyler H 1973 *Phys. Lett. B* **47** 365
- [133] Gross D J and Wilczek F 1973 *Phys. Rev. Lett.* **30** 1343
- [134] Politzer H D 1973 *Phys. Rev. Lett.* **30** 1346
- [135] Dissertori G 2016 *Adv. Ser. Direct. High Energy Phys.* **26** 113
- [136] Tanabashi M *et al* (Particle Data Group) 2018 *Phys. Rev. D* **98** 030001
- [137] d'Enterria D *et al* 2019 *Workshop on Precision Measurements of the QCD Coupling Constant ALPHAS2019* 001
- [138] Streng K H, Walsh T F and Zerwas P M 1979 *Z. Phys. C* **2** 237
- [139] Aaron F D *et al* (H1 Collaboration) 2010 *Eur. Phys. J. C* **67** 1
- [140] Ellis S D and Soper D E 1993 *Phys. Rev. D* **48** 3160
- [141] Adloff C *et al* (H1 Collaboration) 2000 *Eur. Phys. J. C* **13** 397
- [142] Adloff C *et al* (H1 Collaboration) 2001 *Eur. Phys. J. C* **19** 289
- [143] Adloff C *et al* (H1 Collaboration) 2002 *Phys. Lett. B* **542** 193
- [144] Aktas A *et al* (H1 Collaboration) 2004 *Eur. Phys. J. C* **33** 477
- [145] Aktas A *et al* (H1 Collaboration) 2004 *Eur. Phys. J. C* **37** 141
- [146] Aktas A *et al* (H1 Collaboration) 2007 *Phys. Lett. B* **653** 134
- [147] Aaron F D *et al* (H1 Collaboration) 2010 *Eur. Phys. J. C* **65** 363
- [148] Andreev V *et al* (H1 Collaboration) 2015 *Eur. Phys. J. C* **75** 65
- [149] Andreev V *et al* (H1 Collaboration) 2017 *Eur. Phys. J. C* **77** 215
- [150] Breitweg J *et al* (ZEUS Collaboration) 2000 *Phys. Lett. B* **479** 37
- [151] Chekanov S *et al* (ZEUS Collaboration) 2002 *Eur. Phys. J. C* **23** 13
- [152] Chekanov S *et al* (ZEUS Collaboration) 2002 *Phys. Lett. B* **547** 164
- [153] Chekanov S *et al* (ZEUS Collaboration) 2004 *Eur. Phys. J. C* **35** 487
- [154] Chekanov S *et al* (ZEUS Collaboration) 2007 *Nucl. Phys. B* **765** 1
- [155] Chekanov S *et al* (ZEUS Collaboration) 2007 *Phys. Lett. B* **649** 12
- [156] Abramowicz H *et al* (ZEUS Collaboration) 2010 *Eur. Phys. J. C* **70** 965
- [157] Abramowicz H *et al* (ZEUS Collaboration) 2010 *Phys. Lett. B* **691** 127
- [158] Khachatryan V *et al* (CMS Collaboration) 2017 *J. High Energy Phys.* **JHEP03(2017)156**
- [159] Rabbertz K 2017 *Springer Tracts Mod. Phys.* **268** 1
- [160] Aaboud M *et al* (ATLAS Collaboration) 2017 *J. High Energy Phys.* **JHEP09(2017)020**
- [161] Aaboud M *et al* (ATLAS Collaboration) 2018 *J. High Energy Phys.* **JHEP05(2018)195**
- [162] Currie J, Gehrman T and Niehues J 2016 *Phys. Rev. Lett.* **117** 042001
- [163] Currie J, Gehrman T, Huss A and Niehues J 2017 *J. High Energy Phys.* **JHEP07(2017)018**  
Currie J, Gehrman T, Huss A and Niehues J 2017 *J. High Energy Phys.* **JHEP12(2020)042**  
(erratum)
- [164] Gehrman T *et al* 2018 *Proc. Sci.* **RADCOR2017** 074
- [165] Andersen J R *et al* 2018 Les houches 2017: physics at TeV colliders standard model working group report (arXiv:1803.07977)
- [166] Amoroso S *et al* 2020 Les houches 2019: physics at TeV colliders: standard model working group report *11th Les Houches Workshop on Physics at TeV Colliders: PhysTeV Les Houches* (arXiv:2003.01700)
- [167] Britzger D *et al* 2019 *Eur. Phys. J. C* **79** 845



- [168] Carli T, Salam G P and Siebert F 2005 *A posteriori* inclusion of PDFs in NLO QCD final-state calculations *HERA and the LHC: A Workshop on the Implications of HERA for LHC Physics* CERN (Geneva, Switzerland October 11–13, 2004)
- [169] Carli T, Clements D, Cooper-Sarkar A, Gwenlan C, Salam G P, Siebert F, Starovoitov P and Sutton M 2010 *Eur. Phys. J. C* **66** 503
- [170] Kluge T, Rabbertz K and Wobisch M 2006 FastNLO: fast pQCD calculations for PDF fits *Proc., 14th Int. Workshop of Deep Inelastic Scattering (DIS2006)* (Tsukuba, Japan April 20–24, 2006)
- [171] Britzger D, Rabbertz K, Stober F and Wobisch M 2012 New features in version 2 of the fastNLO project *Proc., 20th Int. Workshop on Deep-Inelastic Scattering and Related Subjects (DIS2012)* (Bonn, Germany March 26–30, 2012)
- [172] Andreev V *et al* (H1 Collaboration) 2017 *Eur. Phys. J. C* **77** 791  
Andreev V *et al* (H1 Collaboration) 2021 *Eur. Phys. J. C* **81** 738 (erratum)
- [173] Khachatryan V *et al* (CMS Collaboration) 2017 *J. Inst.* **12** P02014
- [174] Aaboud M *et al* (ATLAS Collaboration) 2019 Determination of jet calibration and energy resolution in proton–proton collisions at  $\sqrt{s} = 8$  TeV using the ATLAS detector *Eur. Phys. J. C* **80** 1104
- [175] Kogler R 2011 Measurement of jet production in deep-inelastic e p scattering at HERA *PhD Thesis* Hamburg University
- [176] Ellis J, Gardi E, Karliner M and Samuel M A 1996 *Phys. Lett. B* **366** 268
- [177] Brodsky S J and Wu X-G 2012 *Phys. Rev. D* **85** 034038  
Brodsky S J and Wu X-G 2012 *Phys. Rev. D* **86** 079903 (erratum)
- [178] Brodsky S J and Wu X-G 2012 *Phys. Rev. Lett.* **109** 042002
- [179] Brodsky S J and Di Giustino L 2012 *Phys. Rev. D* **86** 085026
- [180] Mojaza M, Brodsky S J and Wu X-G 2013 *Phys. Rev. Lett.* **110** 192001
- [181] Brodsky S J, Mojaza M and Wu X-G 2014 *Phys. Rev. D* **89** 014027
- [182] Wang S-Q, Brodsky S J, Wu X-G, Shen J-M and Di Giustino L 2019 *Phys. Rev. D* **100** 094010
- [183] Tanabashi M *et al* (Particle Data Group) 2019 Update of the review of particle physics *Prog. Theor. Exp. Phys.* **2020** 083C01
- [184] Aoki S *et al* (Flavour Lattice Averaging Group) 2020 *Eur. Phys. J. C* **80** 113
- [185] Boito D, Golterman M, Maltman K, Osborne J and Peris S 2015 *Phys. Rev. D* **91** 034003
- [186] Baak M *et al* (Gfitter Group) 2014 *Eur. Phys. J. C* **74** 3046
- [187] Azzi P *et al* 2019 *CERN Yellow Rep. Monogr.* **7** 1
- [188] Abt I, Cooper-Sarkar A M, Foster B, Myronenko V, Wichmann K and Wing M 2017 *Phys. Rev. D* **96** 014001
- [189] Ablinger J, Blümlein J, Klein S, Schneider C and Wissbrock F 2011 *Nucl. Phys. B* **844** 26
- [190] Ablinger J, Blümlein J, De Freitas A, Hasselhuhn A, von Manteuffel A, Round M, Schneider C and Wissbrock F 2014 *Nucl. Phys. B* **882** 263
- [191] Ablinger J, Behring A, Blümlein J, De Freitas A, von Manteuffel A and Schneider C 2014 *Nucl. Phys. B* **890** 48
- [192] Behring A, Bierenbaum I, Blümlein J, De Freitas A, Klein S and Wißbrock F 2014 *Eur. Phys. J. C* **74** 3033
- [193] Ablinger J, Blümlein J, De Freitas A, Schneider C and Schönwald K 2018 *Nucl. Phys. B* **927** 339
- [194] Ablinger J, Blümlein J, De Freitas A, Goedicke A, Schneider C and Schönwald K 2018 *Nucl. Phys. B* **932** 129
- [195] Dasgupta M and Salam G P 2004 *J. Phys. G: Nucl. Part. Phys.* **30** R143
- [196] Aktas A *et al* (H1 Collaboration) 2006 *Eur. Phys. J. C* **46** 343
- [197] Chekanov S *et al* (ZEUS Collaboration) 2007 *Nucl. Phys. B* **767** 1
- [198] Kang D, Lee C and Stewart I W 2013 *Phys. Rev. D* **88** 054004
- [199] Kang Z-B, Liu X and Mantry S 2014 *Phys. Rev. D* **90** 014041
- [200] Kang D, Lee C and Stewart I W 2015 *Proc. Soc. DIS2015* 142
- [201] Abelof G, Boughezal R, Liu X and Petriello F 2016 *Phys. Lett. B* **763** 52
- [202] Höche S, Kuttimalai S and Li Y 2018 *Phys. Rev. D* **98** 114013
- [203] Currie J, Gehrmann T, Glover E W N, Huss A, Niehues J and Vogt A 2018 *J. High Energy Phys.* **JHEP05(2018)209**
- [204] Gehrmann T, Huss A, Mo J and Niehues J 2019 *Eur. Phys. J. C* **79** 1022
- [205] Adloff C *et al* (H1 Collaboration) 2003 *Eur. Phys. J. C* **29** 497
- [206] Aktas A *et al* (H1 Collaboration) 2006 *Phys. Lett. B* **639** 21
- [207] Chekanov S *et al* (ZEUS Collaboration) 2007 *Phys. Rev. D* **76** 072011



- [208] Abramowicz H *et al* (ZEUS Collaboration) 2012 *Nucl. Phys. B* **864** 1
- [209] Klasen M 2002 *Rev. Mod. Phys.* **74** 1221
- [210] Glück M, Reya E and Vogt A 1992 *Phys. Rev. D* **46** 1973
- [211] Sasaki K, Ueda T and Uematsu T 2018 *CERN Proc.* **1** 7
- [212] Abramowicz H *et al* (H1 and ZEUS Collaborations) 2015 *J. High Energy Phys.* **JHEP09(2015)149**
- [213] Larkoski A J, Moult I and Nachman B 2020 *Phys. Rep.* **841** 1–63
- [214] Ringer F 2019 *Proc. Sci.* **ALPHAS2019** 010
- [215] Balitsky I I and Lipatov L N 1978 *Sov. J. Nucl. Phys.* **28** 822  
Balitsky I I and Lipatov L N 1978 *Yad. Fiz.* **28** 1597
- [216] Kuraev E A, Lipatov L N and Fadin V S 1977 *Sov. Phys. - JETP* **45** 199  
Kuraev E A, Lipatov L N and Fadin V S 1977 *Zh. Eksp. Teor. Fiz.* **72** 377
- [217] Fadin V S and Lipatov L N 1998 *Phys. Lett. B* **429** 127
- [218] Ciafaloni M and Camici G 1998 *Phys. Lett. B* **430** 349
- [219] Ross D A 1998 *Phys. Lett. B* **431** 161
- [220] Kovchegov Y V and Mueller A H 1998 *Phys. Lett. B* **439** 428
- [221] Levin E 1999 *Nucl. Phys. B* **545** 481
- [222] Armesto N, Bartels J and Braun M A 1998 *Phys. Lett. B* **442** 459
- [223] Blümlein J and Vogt A 1996 *Phys. Lett. B* **370** 149
- [224] Blümlein J and Vogt A 1998 *Phys. Rev. D* **58** 014020
- [225] Ciafaloni M 1988 *Nucl. Phys. B* **296** 49
- [226] Andersson B, Gustafson G and Samuelsson J 1996 *Nucl. Phys. B* **467** 443
- [227] Kwiecinski J, Martin A D and Sutton P J 1996 *Z. Phys. C* **71** 585
- [228] Ellis R K, Kunszt Z and Levin E M 1994 *Nucl. Phys. B* **420** 517  
Ellis R, Kunszt Z and Levin E 1995 *Nucl. Phys. B* **433** 498 (erratum)
- [229] Ellis R K, Hautmann F and Webber B R 1995 *Phys. Lett. B* **348** 582
- [230] Kwiecinski J, Martin A D and Stasto A M 1997 *Phys. Rev. D* **56** 3991
- [231] Catani S, Ciafaloni M and Hautmann F 1993 *Phys. Lett. B* **307** 147
- [232] Catani S and Hautmann F 1993 *Phys. Lett. B* **315** 157
- [233] Catani S and Hautmann F 1994 *Nucl. Phys. B* **427** 475
- [234] Salam G P 1998 *J. High Energy Phys.* **JHEP07(1998)019**
- [235] Ciafaloni M, Colferai D and Salam G P 1999 *J. High Energy Phys.* **JHEP10(1999)017**
- [236] Ciafaloni M, Colferai D and Salam G P 1999 *Phys. Rev. D* **60** 114036
- [237] Ciafaloni M, Colferai D, Salam G P and Staśto A M 2003 *Phys. Lett. B* **576** 143
- [238] Ciafaloni M, Colferai D, Salam G P and Staśto A M 2004 *Phys. Lett. B* **587** 87
- [239] Ciafaloni M, Colferai D, Salam G P and Staśto A M 2003 *Phys. Rev. D* **68** 114003
- [240] Ciafaloni M, Colferai D, Salam G P and Staśto A M 2007 *J. High Energy Phys.* **JHEP08(2007)046**
- [241] Altarelli G, Ball R D and Forte S 2000 *Nucl. Phys. B* **575** 313
- [242] Altarelli G, Ball R D and Forte S 2001 *Nucl. Phys. B* **599** 383
- [243] Altarelli G, Ball R D and Forte S 2002 *Nucl. Phys. B* **621** 359
- [244] Altarelli G, Ball R D and Forte S 2003 *Nucl. Phys. B* **674** 459
- [245] Altarelli G, Ball R D and Forte S 2008 *Nucl. Phys. B* **799** 199
- [246] Thorne R S 2001 *Phys. Rev. D* **64** 074005
- [247] Sabio Vera A 2005 *Nucl. Phys. B* **722** 65
- [248] Bonvini M, Marzani S and Peraro T 2016 *Eur. Phys. J. C* **76** 597
- [249] Bertone V, Carrazza S and Rojo J 2014 *Comput. Phys. Commun.* **185** 1647
- [250] Bonvini M, Marzani S and Muselli C 2017 *J. High Energy Phys.* **JHEP12(2017)117**
- [251] Müller A H 1990 *Nucl. Phys. B* **335** 115
- [252] Ball R D, Bertone V, Bonvini M, Marzani S, Rojo J and Rottoli L 2018 *Eur. Phys. J. C* **78** 321
- [253] Abdolmaleki H *et al* 2018 *Eur. Phys. J. C* **78** 621
- [254] Butterworth J *et al* 2016 *J. Phys. G: Nucl. Part. Phys.* **43** 023001
- [255] Carrazza S, Forte S, Kassabov Z, Latorre J I and Rojo J 2015 *Eur. Phys. J. C* **75** 369
- [256] Paukkunen H and Zurita P 2014 *J. High Energy Phys.* **JHEP12(2014)100**
- [257] Rojo J and Caola F 2009 Parton distributions and small- $x$  QCD at the large hadron electron collider  
*17th Int. Workshop on Deep-Inelastic Scattering and Related Subjects (DIS 2009)* (Madrid, Spain April 26–30, 2009) (Berlin)
- [258] Abdul Khalek R, Bailey S, Gao J, Harland-Lang L and Rojo J 2018 *Eur. Phys. J. C* **78** 962
- [259] Bartels J, Golec-Biernat K J and Kowalski H 2002 *Phys. Rev. D* **66** 014001
- [260] Golec-Biernat K J and Sapeta S 2006 *Phys. Rev. D* **74** 054032

- [261] Golec-Biernat K J and Sapeta S 2018 *J. High Energy Phys.* **JHEP03(2018)102**
- [262] Gao J, Harland-Lang L and Rojo J 2018 *Phys. Rep.* **742 1**
- [263] Bertone V, Gauld R and Rojo J 2019 *J. High Energy Phys.* **JHEP01(2019)217**
- [264] Hand L N, Miller D G and Wilson R 1963 *Rev. Mod. Phys.* **35 335**
- [265] Miller G *et al* 1972 *Phys. Rev. D* **5 528**
- [266] Riordan E M *et al* 1974 *Phys. Rev. Lett.* **33 561**
- [267] Aaron F D *et al* (H1 Collaboration) 2011 *Eur. Phys. J. C* **71 1579**
- [268] Altarelli G and Martinelli G 1978 *Phys. Lett. B* **76 89**
- [269] Glück M, Hoffmann E and Reya E 1982 *Z. Phys. C* **13 119**
- [270] Ewerz C and Nachtmann O 2007 *Ann. Phys., NY* **322 1670**
- [271] Hautmann F 2002 *Phys. Lett. B* **535 159**
- [272] Marzani S, Ball R D, Del Duca V, Forte S and Vicini A 2008 *Nucl. Phys. B* **800 127**
- [273] Bonvini M and Marzani S 2018 *Phys. Rev. Lett.* **120 202003**
- [274] Andreev V *et al* (H1 Collaboration) 2014 *Eur. Phys. J. C* **74 2814**
- [275] Aad G *et al* (ATLAS Collaboration) 2012 *Phys. Rev. D* **85 072004**
- [276] Altarelli G 2012 *Nuovo Cimento* **1 C035N1**
- [277] Blümlein J and Klein M 1993 *Nucl. Instrum. Methods Phys. Res. A* **329 112**
- [278] Gehrmann T, Huss A, Niehues J, Vogt A and Walker D M 2019 *Phys. Lett. B* **792 182**
- [279] Catani S, Fiorani F and Marchesini G 1990 *Nucl. Phys. B* **336 18**
- [280] Marchesini G and Webber B R 1992 *Nucl. Phys. B* **386 215**
- [281] Hautmann F and Jung H 2008 *J. High Energy Phys.* **JHEP10(2008)113**
- [282] Mueller A H 1991 *J. Phys. G: Nucl. Part. Phys.* **17 1443**
- [283] Forshaw J R, Vera A S and Webber B R 1999 *J. Phys. G: Nucl. Part. Phys.* **25 1511**
- [284] Hautmann F 2009 *Acta Phys. Pol. B* **40 2139**
- [285] Bartels J, Del Duca V, De Roeck A, Graudenz D and Wüsthoff M 1996 *Phys. Lett. B* **384 300**
- [286] Kwiecinski J, Martin A D and Stasto A M 1999 *Phys. Lett. B* **459 644**
- [287] Andersson B, Gustafson G, Kharraziha H and Samuelsson J 1996 *Z. Phys. C* **71 613**
- [288] Jung H *et al* 2010 *Eur. Phys. J. C* **70 1237**
- [289] Hautmann F, Jung H and Monfared S T 2014 *Eur. Phys. J. C* **74 3082**
- [290] van Hameren A 2018 *Comput. Phys. Commun.* **224 371**
- [291] van Hameren A 2019 *Proc. Sci.* **DIS2019 139**
- [292] Chachamis G and Sabio Vera A 2016 *Phys. Rev. D* **93 074004**
- [293] Hoeche S, Krauss F and Teubner T 2008 *Eur. Phys. J. C* **58 17**
- [294] Andersen J R, Brooks H M and Lönnblad L 2018 *J. High Energy Phys.* **JHEP09(2018)074**
- [295] Chekanov S *et al* (ZEUS Collaboration) 2007 *Nucl. Phys. B* **786 152**
- [296] Hautmann F and Jung H 2014 *Nucl. Phys. B* **883 1**
- [297] Hautmann F, Jung H, Lelek A, Radescu V and Žlebčik R 2017 *Phys. Lett. B* **772 446**
- [298] Hautmann F, Jung H, Lelek A, Radescu V and Zlebck R 2018 *J. High Energy Phys.* **JHEP01(2018)070**
- [299] Bermudez Martinez A, Connor P, Jung H, Lelek A, Zlebčik R, Hautmann F and Radescu V 2019 *Phys. Rev. D* **99 074008**
- [300] Höche S, Krauss F and Prestel S 2017 *J. High Energy Phys.* **JHEP10(2017)093**
- [301] Höche S and Prestel S 2017 *Phys. Rev. D* **96 074017**
- [302] Bermudez Martinez A *et al* 2020 *Eur. Phys. J. C* **80 598**
- [303] Webb J *et al* (NuSea Collaboration) 2003 arXiv:[hep-ex/0302019](https://arxiv.org/abs/hep-ex/0302019)
- [304] Aidala C *et al* (PHENIX Collaboration) 2019 *Phys. Rev. D* **99 072003**
- [305] Gandhi R, Quigg C, Reno M H and Sarcevic I 1998 *Phys. Rev. D* **58 093009**
- [306] Aartsen M G *et al* (IceCube Collaboration) 2017 *J. Inst.* **12 P03012**
- [307] Kwiecinski J, Martin A D and Stasto A M 1999 *Phys. Rev. D* **59 093002**
- [308] Aartsen M G *et al* (IceCube Collaboration) 2017 *Nature* **551 596**
- [309] Gaisser T K 1990 Cosmic rays and particle physics <http://cambridge.org/uk/catalogue/catalogue.asp?isbn=0521326672>
- [310] Aartsen M G *et al* (IceCube Collaboration) 2014 *Phys. Rev. Lett.* **113 101101**
- [311] Gelmini G, Gondolo P and Varieschi G 2000 *Phys. Rev. D* **61 056011**
- [312] Bhattacharya A, Enberg R, Jeong Y S, Kim C S, Reno M H, Sarcevic I and Stasto A 2016 *J. High Energy Phys.* **JHEP11(2016)167**
- [313] Aab A *et al* (Pierre Auger Collaboration) 2014 *Phys. Rev. D* **90 122006**
- [314] Aab A *et al* (Pierre Auger Collaboration) 2014 *Phys. Rev. D* **90 122005**

- [315] Drescher H, Dumitru A and Strikman M 2005 *Phys. Rev. Lett.* **94** 231801
- [316] Klein S R and Mäntysaari H 2019 *Nat. Rev. Phys.* **1** 662
- [317] Derrick M *et al* (ZEUS Collaboration) 1993 *Phys. Lett. B* **315** 481
- [318] Ahmed T *et al* (H1 Collaboration) 1994 *Nucl. Phys. B* **429** 477
- [319] Adloff C *et al* (H1 Collaboration) 1997 *Z. Phys. C* **76** 613
- [320] Breitweg J *et al* (ZEUS Collaboration) 1998 *Eur. Phys. J. C* **1** 81
- [321] Collins J C 1998 *Phys. Rev. D* **57** 3051  
Collins J C 2000 *Phys. Rev. D* **61** 019902 (erratum)
- [322] Berera A and Soper D E 1996 *Phys. Rev. D* **53** 6162
- [323] Trentadue L and Veneziano G 1994 *Phys. Lett. B* **323** 201
- [324] Chekanov S *et al* (ZEUS Collaboration) 2005 *Nucl. Phys. B* **713** 3
- [325] Aktas A *et al* (H1 Collaboration) 2006 *Eur. Phys. J. C* **48** 749
- [326] Aktas A *et al* (H1 Collaboration) 2006 *Eur. Phys. J. C* **48** 715
- [327] Chekanov S *et al* (ZEUS Collaboration) 2009 *Nucl. Phys. B* **816** 1
- [328] Chekanov S *et al* (ZEUS Collaboration) 2010 *Nucl. Phys. B* **831** 1
- [329] Aaron F *et al* (H1 Collaboration) 2011 *Eur. Phys. J. C* **71** 1578
- [330] Aaron F *et al* (H1 Collaboration) 2012 *Eur. Phys. J. C* **72** 2074
- [331] Newman P R and Wing M 2014 *Rev. Mod. Phys.* **86** 1037
- [332] Ingelman G and Schlein P E 1985 *Phys. Lett. B* **152** 256
- [333] Buchmüller W, Gehrmann T and Hebecker A 1999 *Nucl. Phys. B* **537** 477
- [334] Hautmann F, Kunszt Z and Soper D E 1998 *Phys. Rev. Lett.* **81** 3333
- [335] Hautmann F, Kunszt Z and Soper D E 1999 *Nucl. Phys. B* **563** 153
- [336] Brodsky S J, Enberg R, Hoyer P and Ingelman G 2005 *Phys. Rev. D* **71** 074020
- [337] Ingelman G, Pasechnik R and Werder D 2016 *Phys. Rev. D* **93** 094016
- [338] Rasmussen C O and Sjöstrand T 2016 *J. High Energy Phys.* **JHEP02(2016)142**
- [339] Bjorken J D 1993 *Phys. Rev. D* **47** 101
- [340] Bartels J, Ellis J, Kowalski H and Wüsthoff M 1999 *Eur. Phys. J. C* **7** 443
- [341] Hautmann F and Soper D 2001 *Phys. Rev. D* **63** 011501
- [342] Hautmann F and Soper D E 2007 *Phys. Rev. D* **75** 074020
- [343] Gribov V N 1969 *Sov. Phys. - JETP* **29** 483  
Gribov V N 1969 *Zh. Eksp. Teor. Fiz.* **56** 892
- [344] Frankfurt L, Guzey V and Strikman M 2012 *Phys. Rep.* **512** 255
- [345] Guzey V and Zhalov M 2013 *J. High Energy Phys.* **JHEP10(2013)207**
- [346] Armesto N, Newman P R, Slominski W and Stasto A M 2019 *Phys. Rev. D* **100** 074022
- [347] Khanpour H 2019 *Phys. Rev. D* **99** 054007
- [348] Aaron F D *et al* (H1 and ZEUS Collaborations) 2012 *Eur. Phys. J. C* **72** 2175
- [349] Gribov V N and Lipatov L N 1972 *Sov. J. Nucl. Phys.* **15** 675  
Gribov V N and Lipatov L N 1972 *Yad. Fiz.* **15** 1218
- [350] Gribov V N and Lipatov L N 1972 *Sov. J. Nucl. Phys.* **15** 438  
Gribov V N and Lipatov L N 1972 *Yad. Fiz.* **15** 781
- [351] Altarelli G and Parisi G 1977 *Nucl. Phys. B* **126** 298
- [352] Dokshitzer Y L 1977 *Sov. Phys. - JETP* **46** 641  
Dokshitzer Y L 1977 *Zh. Eksp. Teor. Fiz.* **73** 1216
- [353] Collins J C and Tung W-K 1986 *Nucl. Phys. B* **278** 934
- [354] Thorne R S and Tung W K 2008 *HERA and the LHC: 4th Workshop on the Implications of HERA for LHC Physics* **C08-05-26.4** 332
- [355] Owens J F 1984 *Phys. Rev. D* **30** 943
- [356] Glück M, Reya E and Vogt A 1992 *Z. Phys. C* **53** 651
- [357] Thorne R S and Roberts R G 1998 *Phys. Rev. D* **57** 6871
- [358] Aaron F *et al* (H1 Collaboration) 2011 *Eur. Phys. J. C* **71** 1836
- [359] Motyka L, Sadzikowski M and Slominski W 2012 *Phys. Rev. D* **86** 111501
- [360] Aad G *et al* (ATLAS Collaboration) 2016 *Phys. Lett. B* **754** 214
- [361] Britzger D, Currie J, Gehrmann T, Huss A, Niehues J and Žlebčik R 2018 *Eur. Phys. J. C* **78** 538
- [362] Nagy Z 2003 *Phys. Rev. D* **68** 094002
- [363] Moch S, Vermaseren J A M and Vogt A 2004 *Nucl. Phys. B* **688** 101
- [364] Vogt A, Moch S and Vermaseren J A M 2004 *Nucl. Phys. B* **691** 129
- [365] de Florian D, Sborlini G F and Rodrigo G 2016 *J. High Energy Phys.* **JHEP10(2016)056**
- [366] Vermaseren J A M, Vogt A and Moch S 2005 *Nucl. Phys. B* **724** 3

- [367] Ablinger J, Behring A, Blümlein J, De Freitas A, Hasselhuhn A, von Manteuffel A, Round M, Schneider C and Wißbrock F 2014 *Nucl. Phys. B* **886** 733
- [368] Ablinger J, Blümlein J, De Freitas A, Hasselhuhn A, Schneider C and Wißbrock F 2017 *Nucl. Phys. B* **921** 585
- [369] Niehues J and Walker D M 2019 *Phys. Lett. B* **788** 243
- [370] Hirschi V, Frederix R, Frixione S, Garzelli M V, Maltoni F and Pittau R 2011 *J. High Energy Phys.* **JHEP05(2011)044**
- [371] Cascioli F, Maierhofer P and Pozzorini S 2012 *Phys. Rev. Lett.* **108** 111601
- [372] Cullen G *et al* 2014 *Eur. Phys. J. C* **74** 3001
- [373] Frederix R, Frixione S, Hirschi V, Pagani D, Shao H-S and Zaro M 2018 *J. High Energy Phys.* **JHEP07(2018)185**
- [374] Buccioni F, Lang J-N, Lindert J M, Maierhöfer P, Pozzorini S, Zhang H and Zoller M F 2019 *Eur. Phys. J. C* **79** 866
- [375] Alwall J *et al* 2014 *J. High Energy Phys.* **JHEP07(2014)079**
- [376] Bellm J *et al* 2016 *Eur. Phys. J. C* **76** 196
- [377] Bothmann E *et al* (Sherpa Collaboration) 2019 *SciPost Phys.* **7** 034
- [378] Dasgupta M and Salam G P 2002 *J. High Energy Phys.* **JHEP08(2002)032**
- [379] Brodsky S J, Hoyer P, Peterson C and Sakai N 1980 *Phys. Lett. B* **93** 451
- [380] Brodsky S J, Kusina A, Lyonnet F, Schienbein I, Spiesberger H and Vogt R 2015 *Adv. High Energy Phys.* **2015** 231547
- [381] Brodsky S J and Gardner S 2016 *Phys. Rev. Lett.* **116** 019101
- [382] de Téramond G F and Brodsky S J 2009 *Phys. Rev. Lett.* **102** 081601
- [383] Ocherashvili A *et al* (SELEX Collaboration) 2005 *Phys. Lett. B* **628** 18
- [384] Bland L C *et al* (ANDY Collaboration) 2019 arXiv:1909.03124
- [385] Brodsky S J, de Téramond G F, Dosch H G and Erlich J 2015 *Phys. Rep.* **584** 1
- [386] de Téramond G F, Dosch H G and Brodsky S J 2013 *Phys. Rev. D* **87** 075005
- [387] de Alfaro V, Fubini S and Furlan G 1976 *Nuovo Cimento A* **34** 569
- [388] Veneziano G 1968 *Nuovo Cimento A* **57** 190
- [389] Deur A, Brodsky S J and de Téramond G F 2016 *Prog. Part. Nucl. Phys.* **90** 1
- [390] Grunberg G 1980 *Phys. Lett. B* **95** 70  
Grunberg G 1982 *Phys. Lett. B* **110** 501 (erratum)
- [391] Bjorken J D 1966 *Phys. Rev.* **148** 1467
- [392] Deur A *et al* 2004 *Phys. Rev. Lett.* **93** 212001
- [393] Deur A, Prok Y, Burkert V, Crabb D, Girod F X, Griffioen K A, Guler N, Kuhn S E and Kvaltine N 2014 *Phys. Rev. D* **90** 012009
- [394] Deur A *et al* 2008 *Phys. Rev. D* **78** 032001
- [395] Brodsky S J and Lu H J 1995 *Phys. Rev. D* **51** 3652
- [396] Brodsky S J, de Téramond G F and Deur A 2010 *Phys. Rev. D* **81** 096010
- [397] Deur A, Brodsky S J and de Téramond G F 2015 *Phys. Lett. B* **750** 528
- [398] Brodsky S J, de Téramond G F, Deur A and Dosch H G 2015 *Few-Body Syst.* **56** 621
- [399] Deur A, Burkert V, Chen J P and Korsch W 2007 *Phys. Lett. B* **650** 244
- [400] Deur A, Burkert V, Chen J P and Korsch W 2008 *Phys. Lett. B* **665** 349
- [401] Brodsky S J 2019 *J. Phys.: Conf. Ser.* **1137** 012027
- [402] Lepage G P and Brodsky S J 1979 *Phys. Lett. B* **87** 359
- [403] Efremov A V and Radyushkin A V 1980 *Phys. Lett. B* **94** 245
- [404] Brodsky S J, de Téramond G F and Dosch H G 2014 *Phys. Lett. B* **729** 3
- [405] Brodsky S J 2016 *Few-Body Syst.* **57** 703
- [406] Sufian R S, de Téramond G F, Brodsky S J, Deur A and Dosch H G 2017 *Phys. Rev. D* **95** 014011
- [407] de Téramond G F, Liu T, Sufian R S, Dosch H G, Brodsky S J and Deur A (HLFHS Collaboration) 2018 *Phys. Rev. Lett.* **120** 182001
- [408] Gutsche T, Lyubovitskij V E, Schmidt I and Vega A 2015 *Phys. Rev. D* **91** 114001
- [409] Gutsche T, Lyubovitskij V E and Schmidt I 2016 *Phys. Rev. D* **94** 116006
- [410] Dosch H G, de Téramond G F and Brodsky S J 2015 *Phys. Rev. D* **91** 085016
- [411] Brodsky S J, de Téramond G F, Dosch H G and Lorcé C 2016 *Int. J. Mod. Phys. A* **31** 1630029
- [412] Nielsen M, Brodsky S J, de Téramond G F, Dosch H G, Navarra F S and Zou L 2018 *Phys. Rev. D* **98** 034002
- [413] de Téramond G F, Dosch H G and Brodsky S J 2015 *Phys. Rev. D* **91** 045040
- [414] Glashow S L 1961 *Nucl. Phys.* **22** 579



- [415] Weinberg S 1971 *Phys. Rev. Lett.* **27** 1688
- [416] Weinberg S 1972 *Phys. Rev. D* **5** 1412
- [417] Salam A and Ward J C 1964 *Phys. Lett.* **13** 168
- [418] Higgs P W 1964 *Phys. Lett.* **12** 132
- [419] Higgs P W 1964 *Phys. Rev. Lett.* **13** 508
- [420] Englert F and Brout R 1964 *Phys. Rev. Lett.* **13** 321
- [421] Aktas A *et al* (H1 Collaboration) 2006 *Phys. Lett. B* **632** 35
- [422] Abramowicz H *et al* (ZEUS Collaboration) 2016 *Phys. Rev. D* **93** 092002
- [423] Andreev V *et al* (H1 Collaboration) 2018 *Eur. Phys. J. C* **78** 777
- [424] Britzger D, Klein M and Spiesberger H 2020 *Eur. Phys. J. C* **80** 831
- [425] Böhm M and Spiesberger H 1987 *Nucl. Phys. B* **294** 1081
- [426] Bardin D Y, Burdík Č, Christova P C and Riemann T 1989 *Z. Phys. C* **42** 679
- [427] Hollik W, Bardin D Y, Blümlein J, Kniehl B A, Riemann T and Spiesberger H 1992 Electroweak parameters at HERA: theoretical aspects *Workshop on Physics at HERA Hamburg* (Germany October 29–30, 1991)
- [428] Böhm M and Spiesberger H 1988 *Nucl. Phys. B* **304** 749
- [429] Bardin D Y, Burdík C, Christova P C and Riemann T 1989 *Z. Phys. C* **44** 149
- [430] Sirlin A 1980 *Phys. Rev. D* **22** 971
- [431] Böhm M, Spiesberger H and Hollik W 1986 *Fortschr. Phys.* **34** 687
- [432] Hollik W F L 1990 *Fortschr. Phys.* **38** 165
- [433] Aaron F D *et al* (H1 Collaboration) 2012 *J. High Energy Phys.* [JHEP09\(2012\)061](#)
- [434] Britzger D and Klein M 2018 *Proc. Sci.* [DIS2017 105](#)
- [435] Spiesberger H 1995 EPRC: a program package for electroweak physics at HERA *Future Physics at HERA Proc., Workshop* (Hamburg, Germany September 25, 1995–May 31, 1996) vol 1–2
- [436] Cowan G, Cranmer K, Gross E and Vitells O 2011 *Eur. Phys. J. C* **71** 1554  
Cowan G, Cranmer K, Gross E and Vitells O 2013 *Eur. Phys. J. C* **73** 2501 (erratum)
- [437] CDF and D0 Collaborations 2012 2012 update of the combination of CDF and D0 results for the mass of the  $W$  boson (arXiv:[1204.0042](#))
- [438] Schael S *et al* (ALEPH, DELPHI, L3, OPAL, LEP Electroweak Collaboration) 2013 *Phys. Rep.* **532** 119
- [439] Aaboud M *et al* (ATLAS Collaboration) 2018 *Eur. Phys. J. C* **78** 110  
Aaboud M *et al* (ATLAS Collaboration) 2018 *Eur. Phys. J. C* **78** 898 (erratum)
- [440] de Blas J, Ciuchini M, Franco E, Mishima S, Pierini M, Reina L and Silvestrini L 2016 *J. High Energy Phys.* [JHEP12\(2016\)135](#)
- [441] Haller J, Höcker A, Kogler R, Peiffer T and Stelzer J 2018 *Eur. Phys. J. C* **78** 675
- [442] Tishchenko V *et al* (MuLan Collaboration) 2013 *Phys. Rev. D* **87** 052003
- [443] Schott M 2019 Global EW fits: experimental and theoretical issues *Talk Presented at the Ultimate Precision at Hadron Colliders* (Sarclay, France)
- [444] Schael S *et al* (ALEPH, DELPHI, L3, OPAL, SLD Collaborations, LEP Electroweak Working Group, SLD Electroweak Heavy Flavour Groups) 2006 *Phys. Rep.* **427** 257
- [445] Abazov V M *et al* (D0 Collaboration) 2011 *Phys. Rev. D* **84** 012007
- [446] Aaltonen T A *et al* (CDF and D0 Collaborations) 2018 *Phys. Rev. D* **97** 112007
- [447] Aaij R *et al* (LHCb Collaboration) 2015 *J. High Energy Phys.* [JHEP11\(2015\)190](#)
- [448] ATLAS Collaboration 2018 Measurement of the effective leptonic weak mixing angle using electron and muon pairs from  $Z$ -boson decay in the ATLAS experiment at  $\sqrt{s} = 8$  TeV *ATLAS-CONF-2018-037*
- [449] Sirunyan A M *et al* (CMS Collaboration) 2018 *Eur. Phys. J. C* **78** 701
- [450] Erler J 2019 Global fits of the SM parameters *7th Large Hadron Collider Physics Conf. (LHCP 2019)* (Puebla, Mexico May 20–25, 2019)
- [451] Erler J and Schott M 2019 *Prog. Part. Nucl. Phys.* **106** 68
- [452] Accomando E *et al* 2019 *J. High Energy Phys.* [JHEP10\(2019\)176](#)
- [453] Accomando E, Fiaschi J, Hautmann F and Moretti S 2018 *Eur. Phys. J. C* **78** 663  
Accomando E, Fiaschi J, Hautmann F and Moretti S 2019 *Eur. Phys. J. C* **79** 453 (erratum)
- [454] Accomando E, Fiaschi J, Hautmann F and Moretti S 2018 *Phys. Rev. D* **98** 013003  
Accomando E, Fiaschi J, Hautmann F and Moretti S 2019 *Phys. Rev. D* **99** 079902 (erratum)
- [455] Chekanov S *et al* (ZEUS Collaboration) 2009 *Phys. Lett. B* **672** 106
- [456] Aaron F D *et al* (H1 Collaboration) 2009 *Eur. Phys. J. C* **64** 251
- [457] Aaron F D *et al* (H1 and ZEUS Collaboration) 2010 *J. High Energy Phys.* [JHEP03\(2010\)035](#)

- [458] Baur U and Zeppenfeld D 1989 *Nucl. Phys. B* **325** 253
- [459] Baur U, Kniehl B A, Vermaseren J A M and Zeppenfeld D 1990 Single W and Z Production at LEP/LHC *ECFA Large Hadron Collider Workshop* (Aachen, Germany 4–9 Oct 1990)
- [460] Baur U, Vermaseren J A M and Zeppenfeld D 1992 *Nucl. Phys. B* **375** 3
- [461] Ball R D *et al* (NNPDF Collaboration) 2013 *Nucl. Phys. B* **877** 290
- [462] Hagiwara K, Ishihara S, Szalapski R and Zeppenfeld D 1993 *Phys. Rev. D* **48** 2182
- [463] Hagiwara K, Ishihara S, Szalapski R and Zeppenfeld D 1992 *Phys. Lett. B* **283** 353
- [464] De Rújula A, Gavela M B, Hernandez P and Massó E 1992 *Nucl. Phys. B* **384** 3
- [465] Biswal S S, Patra M and Raychaudhuri S 2014 arXiv:1405.6056
- [466] Cakir I T, Cakir O, Senol A and Tasci A T 2014 *Acta Phys. Pol. B* **45** 1947
- [467] Li R, Shen X-M, Wang K, Xu T, Zhang L and Zhu G 2018 *Phys. Rev. D* **97** 075043
- [468] Köksal M, Billur A A, Gutiérrez-Rodríguez A and Hernández-Ruiz M A 2020 *Phys. Lett. B* **808** 135661
- [469] Gutiérrez-Rodríguez A, Köksal M, Billur A A and Hernández-Ruiz M A 2020 *J. Phys. G* **47** 055005
- [470] Sirunyan A M *et al* (CMS Collaboration) 2017 *Phys. Lett. B* **772** 21
- [471] Sirunyan A M *et al* (CMS Collaboration) 2019 *JHEP* **12** 62
- [472] Villa S 2005 *Nucl. Phys. B* **142** 391
- [473] Dutta S, Goyal A, Kumar M and Mellado B 2015 *Eur. Phys. J. C* **75** 577
- [474] Bouzas A O and Larios F 2013 *Phys. Rev. D* **88** 094007
- [475] Ovin S, Rouby X and Lemaître V 2009 DELPHES, a framework for fast simulation of a generic collider experiment (arXiv:0903.2225)
- [476] Khachatryan V *et al* (CMS Collaboration) 2014 *J. High Energy Phys. JHEP06(2014)090*
- [477] Sarmiento-Alvarado I A, Bouzas A O and Larios F 2015 *J. Phys. G: Nucl. Part. Phys.* **42** 085001
- [478] Sun H 2018 *Proc. Sci.* **DIS2018** 167
- [479] Khachatryan V *et al* (CMS Collaboration) 2014 *Phys. Lett. B* **736** 33
- [480] Aguilar-Saavedra J A 2004 *Acta Phys. Pol. B* **35** 2695
- [481] Charles J *et al* 2015 *Phys. Rev. D* **91** 073007
- [482] Atag S and Sahin B 2006 *Phys. Rev. D* **73** 074001
- [483] Bouzas A O and Larios F 2013 *Phys. Rev. D* **87** 074015
- [484] Coleppa B, Kumar M, Kumar S and Mellado B 2017 *Phys. Lett. B* **770** 335
- [485] Ball R D *et al* (NNPDF Collaboration) 2017 *Eur. Phys. J. C* **77** 663
- [486] Demartin F, Forte S, Mariani E, Rojo J and Vicini A 2010 *Phys. Rev. D* **82** 014002
- [487] Turk Cakir I, Yilmaz A, Denizli H, Senol A, Karadeniz H and Cakir O 2017 *Adv. High Energy Phys.* **2017** 1572053
- [488] Cakir O, Yilmaz A, Turk Cakir I, Senol A and Denizli H 2019 *Nucl. Phys. B* **944** 114640
- [489] Aguilar-Saavedra J A and Riemann T 2001 Probing top flavor changing neutral couplings at TESLA *5th Workshop of the 2nd ECFA* (Obernai, France October 16–19, 1999)
- [490] Agashe K *et al* (Top Quark Working Group) 2013 Working group report: top quark *Community Summer Study on the Future of U.S. Particle Physics* (Minneapolis, MN July 29–August 6, 2013)
- [491] Behera S, Islam R, Kumar M, Poullose P and Rahaman R 2019 *Phys. Rev. D* **100** 015006
- [492] Sun H and Wang X 2018 *Eur. Phys. J. C* **78** 281
- [493] Aubert J J *et al* (European Muon Collaboration) 1983 *Phys. Lett. B* **123** 275
- [494] Gomez J *et al* 1994 *Phys. Rev. D* **49** 4348
- [495] Amaudruz P *et al* (New Muon Collaboration) 1995 *Nucl. Phys. B* **441** 3
- [496] Arneodo M *et al* (New Muon Collaboration) 1995 *Nucl. Phys. B* **441** 12
- [497] Arneodo M *et al* (New Muon Collaboration) 1996 *Nucl. Phys. B* **481** 3
- [498] Ashman J *et al* (European Muon Collaboration) 1993 *Z. Phys. C* **57** 211
- [499] Arneodo M *et al* (New Muon Collaboration) 1996 *Nucl. Phys. B* **481** 23
- [500] Amaudruz P *et al* (New Muon Collaboration) 1992 *Nucl. Phys. B* **371** 3
- [501] Arneodo M 1994 *Phys. Rep.* **240** 301
- [502] Geesaman D F, Saito K and Thomas A W 1995 *Annu. Rev. Nucl. Part. Sci.* **45** 337
- [503] Eskola K J, Paakkinen P, Paukkunen H and Salgado C A 2017 *Eur. Phys. J. C* **77** 163
- [504] Salgado C A *et al* 2012 *J. Phys. G: Nucl. Part. Phys.* **39** 015010
- [505] Golec-Biernat K J and Wusthoff M 1998 *Phys. Rev. D* **59** 014017
- [506] Gelis F, Iancu E, Jalilian-Marian J and Venugopalan R 2010 *Annu. Rev. Nucl. Part. Sci.* **60** 463
- [507] Kovchegov Y V and Levin E 2012 *Camb. Monogr. Part. Phys. Nucl. Phys. Cosmol.* **33** 1



- [508] Citron Z *et al* 2018 Future physics opportunities for high-density QCD at the LHC with heavy-ion and proton beams *HL/HE-LHC Workshop: Workshop on the Physics of HL-LHC, and Perspectives at HE-LHC* (Geneva, Switzerland June 18–20, 2018)
- [509] Ioffe B L, Fadin V S and Lipatov L N 2010 *Quantum Chromodynamics: Perturbative and Nonperturbative Aspects* vol 30 (Cambridge: Cambridge University Press)
- [510] Collins J 2013 *Foundations of Perturbative QCD* vol 32 (Cambridge: Cambridge University Press)
- [511] Paukkunen H 2017 *Nucl. Phys. A* **967** 241
- [512] Paukkunen H 2018 *Proc. Sci. HardProbes2018* 014
- [513] Eskola K J, Paukkunen H and Salgado C A 2009 *J. High Energy Phys.* **JHEP04(2009)065**
- [514] de Florian D, Sassot R, Zurita P and Stratmann M 2012 *Phys. Rev. D* **85** 074028
- [515] Kovarik K *et al* 2016 *Phys. Rev. D* **93** 085037
- [516] Khanpour H and Atashbar Tehrani S 2016 *Phys. Rev. D* **93** 014026
- [517] Abdul Khalek R, Ethier J J and Rojo J (NNPDF Collaboration) 2019 *Eur. Phys. J. C* **79** 471
- [518] Paukkunen H and Salgado C A 2010 *J. High Energy Phys.* **JHEP07(2010)032**
- [519] Kovarik K, Schienbein I, Olness F I *et al* 2011 *Phys. Rev. Lett.* **106** 122301
- [520] Paukkunen H and Salgado C A 2013 *Phys. Rev. Lett.* **110** 212301
- [521] Armesto N 2006 *J. Phys. G: Nucl. Part. Phys.* **32** R367
- [522] Eskola K J, Paakkinen P and Paukkunen H 2019 *Eur. Phys. J. C* **79** 511
- [523] Armesto N, Paukkunen H, Penín J M, Salgado C A and Zurita P 2016 *Eur. Phys. J. C* **76** 218
- [524] Kusina A, Lyonnet F, Clark D B, Godat E *et al* 2017 *Eur. Phys. J. C* **77** 488
- [525] Armesto N, Capella A, Kaidalov A B, López-Albacete J and Salgado C A 2003 *Eur. Phys. J. C* **29** 531
- [526] Armesto N, Kaidalov A B, Salgado C A and Tywoniuk K 2010 *Eur. Phys. J. C* **68** 447
- [527] Krelina M and Nemchik J 2020 *Eur. Phys. J. Plus* **135** 444
- [528] Brodsky S J, Schmidt I and Yang J-J 2004 *Phys. Rev. D* **70** 116003
- [529] Paukkunen H (LHeC Study Group) 2018 *Proc. Sci. DIS2017* 109
- [530] Aschenauer E C, Fazio S, Lamont M A C, Paukkunen H and Zurita P 2017 *Phys. Rev. D* **96** 114005
- [531] Aaij R *et al* (LHCb Collaboration) 2017 *J. High Energy Phys.* **JHEP10(2017)090**
- [532] Aaij R *et al* (LHCb Collaboration) 2019 *Phys. Rev. D* **99** 052011
- [533] Eskola K J, Helenius I, Paakkinen P and Paukkunen H 2020 *J. High Energy Phys.* **JHEP05(2020)037**
- [534] Helenius I, Eskola K J and Paukkunen H 2014 *J. High Energy Phys.* **JHEP09(2014)138**
- [535] Pumplin J, Stump D, Brock R *et al* 2001 *Phys. Rev. D* **65** 014013
- [536] Armesto N 2018 Nuclear pdfs *2nd FCC Physics Workshop* (CERN, January 15–19 2018)
- [537] Armesto N 2019 *Proc. Sci. HardProbes2018* 123
- [538] Alekhin S *et al* (HERAFitter Group) 2015 *Eur. Phys. J. C* **75** 304
- [539] Lappi T and Mäntysaari H 2013 *Phys. Rev. C* **87** 032201
- [540] Adamczyk L *et al* (STAR Collaboration) 2017 *Phys. Rev. C* **96** 054904
- [541] Toll T and Ullrich T 2013 *Phys. Rev. C* **87** 024913
- [542] Mäntysaari H 2020 arXiv:2001.10705
- [543] Gribov V N and Migdal A A 1969 *Sov. J. Nucl. Phys.* **8** 583  
Gribov V N and Migdal A A 1968 *Yad. Fiz.* **8** 1002
- [544] Frankfurt L L, Miller G A and Strikman M 1994 *Annu. Rev. Nucl. Part. Sci.* **44** 501
- [545] Marquet C, Moldes M R and Zurita P 2017 *Phys. Lett. B* **772** 607
- [546] Frankfurt L L and Strikman M I 1996 *Phys. Lett. B* **382** 6
- [547] Kowalski H, Lappi T, Marquet C and Venugopalan R 2008 *Phys. Rev. C* **78** 045201
- [548] Müller A H and Navelet H 1987 *Nucl. Phys. B* **282** 727
- [549] Deak M, Hautmann F, Jung H and Kutak K 2012 *Eur. Phys. J. C* **72** 1982
- [550] Albacete J L and Marquet C 2010 *Phys. Rev. Lett.* **105** 162301
- [551] Lappi T and Mäntysaari H 2013 *Nucl. Phys. A* **908** 51
- [552] Stasto A, Wei S-Y, Xiao B-W and Yuan F 2018 *Phys. Lett. B* **784** 301
- [553] van Hameren A, Kotko P, Kutak K, Marquet C, Petreska E and Sapeta S 2016 *J. High Energy Phys.* **JHEP12(2016)034**  
van Hameren A, Kotko P, Kutak K, Marquet C, Petreska E and Sapeta S 2019 *J. High Energy Phys.* **JHEP02(2019)158** (erratum)
- [554] Khachatryan V *et al* (CMS Collaboration) 2010 *J. High Energy Phys.* **JHEP09(2010)091**
- [555] Schlichting S and Tribedy P 2016 *Adv. High Energy Phys.* **2016** 8460349
- [556] Loizides C 2016 *Nucl. Phys. A* **956** 200

- [557] Schenke B 2017 *Nucl. Phys. A* **967** 105
- [558] Romatschke P 2017 *Eur. Phys. J. C* **77** 21
- [559] ATLAS Collaboration 2019 Two-particle azimuthal correlations in photo-nuclear ultra-peripheral Pb + Pb collisions at 5.02 TeV with ATLAS *ATLAS-CONF-2019-022*
- [560] Badea A *et al* 2019 *Phys. Rev. Lett.* **123** 212002
- [561] ZEUS Collaboration 2020 Two-particle azimuthal correlations as a probe of collective behaviour in deep inelastic *ep* scattering at HERA *JHEP* **4** 70
- [562] Chatrchyan S *et al* (CMS Collaboration) 2013 *Phys. Lett. B* **724** 213
- [563] Khachatryan V *et al* (CMS Collaboration) 2017 *Phys. Lett. B* **765** 193
- [564] Glazek S D, Brodsky S J, Goldhaber A S and Brown R W 2018 *Phys. Rev. D* **97** 114021
- [565] Bjorken J D, Brodsky S J and Scharff Goldhaber A 2013 *Phys. Lett. B* **726** 344
- [566] Brodsky S, Pauli H-C and Pinsky S S 1998 *Phys. Rep.* **301** 299
- [567] Dirac P A M 1949 *Rev. Mod. Phys.* **21** 392
- [568] Ashery D 2006 *Nucl. Phys. B* **161** 8
- [569] Bertsch G, Brodsky S J, Goldhaber A S and Gunion J G 1981 *Phys. Rev. Lett.* **47** 297
- [570] Frankfurt L, Miller G A and Strikman M 2002 *Phys. Rev. D* **65** 094015
- [571] Brodsky S J, Ji C-R and Lepage G P 1983 *Phys. Rev. Lett.* **51** 83
- [572] Brodsky S J and Mueller A H 1988 *Phys. Lett. B* **206** 685
- [573] Brodsky S, Schmidt I and de Téramond G 1990 *Phys. Rev. Lett.* **64** 1011
- [574] Brodsky S J and Lu H J 1990 *Phys. Rev. Lett.* **64** 1342
- [575] Brodsky S J, Schmidt I and Liuti S 2019 arXiv:1908.06317
- [576] Aad G *et al* (ATLAS Collaboration) 2012 *Phys. Lett. B* **716** 1
- [577] Chatrchyan S *et al* (CMS Collaboration) 2012 *Phys. Lett. B* **716** 30
- [578] Guralnik G S, Hagen C R and Kibble T W B 1964 *Phys. Rev. Lett.* **13** 585
- [579] Migdal A A and Polyakov A M 1967 *Sov. Phys. - JETP* **24** 91  
Migdal A A and Polyakov A M 1966 *Zh. Eksp. Teor. Fiz.* **51** 135
- [580] Gori S, Grojean C, Juste A and Paul A 2018 *J. High Energy Phys.* **JHEP01(2018)108**
- [581] Cohen T, Craig N, Giudice G F and McCullough M 2018 *J. High Energy Phys.* **JHEP05(2018)091**
- [582] Blümlein J, van Oldenborgh G J and Rückl R 1993 *Nucl. Phys. B* **395** 35
- [583] Pumplin J, Stump D R, Huston J, Lai H-L, Nadolsky P and Tung W-K 2002 *J. High Energy Phys.* **JHEP07(2002)012**
- [584] Kumar M, Ruan X, Islam R, Cornell A S, Klein M, Klein U and Mellado B 2017 *Phys. Lett. B* **764** 247
- [585] de Florian D *et al* (LHC Higgs Cross Section Working Group) 2016 CERN-2017-002
- [586] Asner D M *et al* 2013 ILC Higgs white paper *Proc., 2013 Community Summer Study on the Future of U.S. Particle Physics: Snowmass on the Mississippi (CSS2013)* (Minneapolis, MN July 29–August 6, 2013) (<http://slac.stanford.edu/econf/C1307292/docs/submittedArxivFiles/1310.0763.pdf>)
- [587] Abramowicz H *et al* 2017 *Eur. Phys. J. C* **77** 475
- [588] Higgs Cross Section Working Group <https://twiki.cern.ch/twiki/bin/view/LHCPhysics/CERNYellowReportPageBR>
- [589] Han T and Mellado B 2010 *Phys. Rev. D* **82** 016009
- [590] Tanaka M 2014 Study of the Higgs measurements at the LHeC *BSc Thesis* Tokyo Institute of Technology (talk at DIS Workshop 2017 <https://indico.cern.ch/event/568360/contributions/2523555/>)
- [591] Kay E 2014 Higgs studies at a high luminosity LHeC *MSc Thesis* University of Liverpool
- [592] Klein U 2014 *Poster at 37th Int. Conf. on High Energy Physics (ICHEP)* (Valencia) (<https://indico.ific.uv.es/event/2025/contributions/937/>)
- [593] Klein U 2015 *Talk at LHeC Workshop* (CERN, Chavannes-De-Bogis) (<https://indico.cern.ch/event/356714/contributions/844946/>)
- [594] Hampson D 2016 Precision Higgs coupling measurements at a high luminosity LHeC *MSc Thesis* University of Liverpool
- [595] Harris I 2017 Finding Higgs to charm decays in electron–proton collisions *BSc Thesis* University of Liverpool
- [596] Aaboud M *et al* (ATLAS Collaboration) 2018 *Phys. Lett. B* **786** 59
- [597] Sirunyan A M *et al* (CMS Collaboration) 2018 *Phys. Rev. Lett.* **121** 121801
- [598] ATLAS and CMS Collaborations 2019 *CERN Yellow Rep. Monogr.* **7** addendum
- [599] Sjöstrand T, Mrenna S and Skands P 2006 *J. High Energy Phys.* **JHEP05(2006)026**

- [600] Klein U 2014 *Talk at Workshop on the LHeC* (Chavannes-de-Bogis) (<https://indico.cern.ch/event/278903/contributions/631181>)
- [601] de Favereau J, Delaere C, Demin P, Giammanco A, Lematre V, Mertens A and Selvaggi M 2014 *J. High Energy Phys.* **JHEP02(2014)057**
- [602] Höcker A *et al* 2007 TMVA—toolkit for multivariate data analysis *CERN-OPEN-2007-007*
- [603] Greder S 2004 *b* quark tagging and cross-section measurement in quark pair production at D0 *PhD Thesis* Louis Pasteur University, Strasbourg
- [604] Banda Y, Lastovicka T and Nomerotski A 2009 Measurement of the Higgs boson decay branching ratio to charm quarks at the ILC (arXiv:0909.1052)
- [605] Aad G *et al* (ATLAS Collaboration) 2019 *Phys. Rev. D* **100** 032007
- [606] Aaboud M *et al* (ATLAS Collaboration) 2017 *Eur. Phys. J. C* **77** 361
- [607] Englert C, Kogler R, Schulz H and Spannowsky M 2016 *Eur. Phys. J. C* **76** 393
- [608] Dittmaier S *et al* (LHC Higgs Cross Section Working Group Collaboration) 2011 arXiv:1101.0593
- [609] Barklow T, Fujii K, Jung S, Karl R, List J, Ogawa T, Peskin M E and Tian J 2018 *Phys. Rev. D* **97** 053003
- [610] Trott M 2014 *Invited Talk at the LHeC Workshop* (Chavannes) (<https://indico.cern.ch/event/278903/contributions/631177/>)
- [611] Rindani S D, Sharma P and Shivaji A 2016 *Phys. Lett. B* **761** 25
- [612] Biswal S S, Godbole R M, Mellado B and Raychaudhuri S 2012 *Phys. Rev. Lett.* **109** 261801
- [613] Alloul A, Christensen N D, Degrande C, Duhr C and Fuks B 2014 *Comput. Phys. Commun.* **185** 2250
- [614] Ball R D *et al* 2013 *Nucl. Phys. B* **867** 244
- [615] Tang Y-L, Zhang C and Zhu S-h 2016 *Phys. Rev. D* **94** 011702
- [616] Bernaciak C, Plehn T, Schichtel P and Tattersall J 2015 *Phys. Rev. D* **91** 035024
- [617] Cashmore R *et al* 1985 *Phys. Rep.* **122** 275
- [618] Buddenbrock S, Cornell A S, Fang Y, Fadol Mohammed A, Kumar M, Mellado B and Tomiwa K G 2019 *J. High Energy Phys.* **JHEP10(2019)157**
- [619] Liu W, Sun H, Wang X and Luo X 2015 *Phys. Rev. D* **92** 074015
- [620] Wang X, Sun H and Luo X 2017 *Adv. High Energy Phys.* **2017** 4693213
- [621] Aaboud M *et al* (ATLAS Collaboration) 2018 *Phys. Rev. D* **98** 032002
- [622] Khachatryan V *et al* (CMS Collaboration) 2017 *J. High Energy Phys.* **JHEP02(2017)079**
- [623] Hernandez-Sanchez J, Flores-Sanchez O, Honorato C G, Moretti S and Rosado S 2017 *Proc. Sci. CHARGED2016* 032
- [624] Sirunyan A M *et al* (CMS Collaboration) 2018 *J. High Energy Phys.* **JHEP11(2018)115**
- [625] Khachatryan V *et al* (CMS Collaboration) 2015 *J. High Energy Phys.* **JHEP12(2015)178**
- [626] Das S P, Hernandez-Sanchez J, Moretti S and Rosado A 2018 arXiv:1806.08361
- [627] Sun H, Luo X, Wei W and Liu T 2017 *Phys. Rev. D* **96** 095003
- [628] Azuelos G, Sun H and Wang K 2018 *Phys. Rev. D* **97** 116005
- [629] Sirunyan A M *et al* (CMS Collaboration) 2017 *Phys. Rev. Lett.* **119** 141802
- [630] Sirunyan A M *et al* (CMS Collaboration) 2018 *Phys. Rev. Lett.* **120** 081801
- [631] Mosomane C, Kumar M, Cornell A S and Mellado B 2017 *J. Phys.: Conf. Ser.* **889** 012004
- [632] Rose L D, Fischer O and Hammad A 2019 *Int. J. Mod. Phys. A* **34** 1950127
- [633] Sirunyan A M *et al* (CMS Collaboration) 2018 *J. High Energy Phys.* **JHEP06(2018)127**  
Sirunyan A M *et al* (CMS Collaboration) 2019 *J. High Energy Phys.* **JHEP03(2019)128** (erratum)
- [634] CMS Collaboration 2019 Search for a new scalar resonance decaying to a pair of Z bosons at the high-luminosity LHC *CMS-PAS-FTR-18-040*
- [635] Das S P, Hernández-Sánchez J, Moretti S, Rosado A and Xoxocotzi R 2016 *Phys. Rev. D* **94** 055003
- [636] Das S P and Nowakowski M 2017 *Phys. Rev. D* **96** 055014
- [637] Senol A 2013 *Nucl. Phys. B* **873** 293
- [638] Çakir I T, Çakir O, Senol A and Tasci A T 2013 *Mod. Phys. Lett. A* **28** 1350142
- [639] Hesari H, Khanpour H and Mohammadi Najafabadi M 2018 *Phys. Rev. D* **97** 095041
- [640] Liu S, Tang Y-L, Zhang C and Zhu S-h 2017 *Eur. Phys. J. C* **77** 457
- [641] Curtin D, Deshpande K, Fischer O and Zurita J 2018 *J. High Energy Phys.* **JHEP07(2018)024**
- [642] Azuelos G, D’Onofrio M, Iwamoto S and Wang K 2020 *Phys. Rev. D* **101** 095015
- [643] ATLAS Collaboration 2019 SUSY July 2019 summary plot update <http://cds.cern.ch/record/2682063>
- [644] Han C, Li R, Pan R-Q and Wang K 2018 *Phys. Rev. D* **98** 115003
- [645] Kuday S 2014 *J. Korean Phys. Soc.* **64** 1783

- [646] Zhang R-Y, Wei H, Han L and Ma W-G 2014 *Mod. Phys. Lett. A* **29** 1450029
- [647] Li X-P, Guo L, Ma W-G, Zhang R-Y, Han L and Song M 2013 *Phys. Rev. D* **88** 014023
- [648] Evans J A and Mckeen D 2018 The light gluino gap (arXiv:1803.01880)
- [649] Curtin D, Deshpande K, Fischer O and Zurita J 2019 *Phys. Rev. D* **99** 055011
- [650] Antusch S and Fischer O 2015 *J. High Energy Phys.* **JHEP05(2015)053**
- [651] Antusch S, Cazzato E and Fischer O 2017 *Int. J. Mod. Phys. A* **32** 1750078
- [652] Antusch S, Fischer O and Hammad A 2020 *J. High Energy Phys.* **JHEP03(2020)110**
- [653] Das A, Jana S, Mandal S and Nandi S 2019 *Phys. Rev. D* **99** 055030
- [654] Aad G *et al* (ATLAS Collaboration) 2019 arXiv:1905.09787
- [655] Antusch S, Cazzato E and Fischer O 2017 *Phys. Lett. B* **774** 114
- [656] Abreu P *et al* (DELPHI Collaboration) 1997 *Z. Phys. C* **74** 57  
Abreu P *et al* (DELPHI Collaboration) 1997 *Z. Phys. C* **75** 580 (erratum)
- [657] Adam J *et al* (MEG Collaboration) 2013 *Phys. Rev. Lett.* **110** 201801
- [658] Duarte L, González-Sprinberg G A and Sampayo O A 2015 *Phys. Rev. D* **91** 053007
- [659] Duarte L, Zapata G and Sampayo O A 2018 *Eur. Phys. J. C* **78** 352
- [660] Mondal S and Rai S K 2016 *Phys. Rev. D* **93** 011702
- [661] Lindner M, Queiroz F S, Rodejohann W and Yaguna C E 2016 *J. High Energy Phys.* **JHEP06(2016)140**
- [662] Mondal S and Rai S K 2016 *Phys. Rev. D* **94** 033008
- [663] Das A and Mandal S 2020 arXiv:2006.04123
- [664] Aghanim N *et al* (Planck Collaboration) 2020 *Astron. Astrophys.* **641** A6
- [665] Jana S, Okada N and Raut D 2019 arXiv:1911.09037
- [666] Das A, Mandal S and Modak T 2020 *Phys. Rev. D* **102** 033001
- [667] Holdom B 1986 *Phys. Lett. B* **166** 196
- [668] D’Onofrio M, Fischer O and Wang Z S 2020 *Phys. Rev. D* **101** 015020
- [669] Aaij R *et al* (LHCb Collaboration) 2018 *Phys. Rev. Lett.* **120** 061801
- [670] Heeba S and Kahlhoefer F 2019 Probing the freeze-in mechanism in dark matter models with  $U(1)$  gauge extensions (arXiv:1908.09834)
- [671] Yue C-X, Liu M-Z and Guo Y-C 2019 *Phys. Rev. D* **100** 015020
- [672] Mikaelian K O, Samuel M A and Sahdev D 1979 *Phys. Rev. Lett.* **43** 746
- [673] Brodsky S J and Brown R W 1982 *Phys. Rev. Lett.* **49** 966
- [674] Brown R W, Kowalski K L and Brodsky S J 1983 *Phys. Rev. D* **28** 624  
Brown R W, Kowalski K L and Brodsky S J 1984 *Phys. Rev. D* **29** 2100–4
- [675] Samuel M A and Reid J H 1986 *Prog. Theor. Phys.* **76** 184
- [676] Amhis Y S *et al* (HFLAV Collaboration) 2019 arXiv:1909.12524
- [677] Pati J C and Salam A 1974 *Phys. Rev. D* **10** 275  
Pati J C and Salam A 1975 *Phys. Rev. D* **11** 703
- [678] Buchmüller W, Rückl R and Wyler D 1987 *Phys. Lett. B* **191** 442  
Buchmüller W, Rückl R and Wyler D 1999 *Phys. Lett. B* **448** 320 (erratum)
- [679] Doršner I, Fajfer S, Greljo A, Kamenik J F and Košnik N 2016 *Phys. Rep.* **641** 1
- [680] ATLAS Collaboration 2019 ATLAS exotics searches [https://atlas.web.cern.ch/Atlas/GROUPS/PHYSICS/CombinedSummaryPlots/EXOTICS/ATLAS\\_Exotics\\_Summary/ATLAS\\_Exotics\\_Summary.pdf](https://atlas.web.cern.ch/Atlas/GROUPS/PHYSICS/CombinedSummaryPlots/EXOTICS/ATLAS_Exotics_Summary/ATLAS_Exotics_Summary.pdf)
- [681] CMS Collaboration 2019 Overview of CMS exo results <http://cms-results.web.cern.ch/cms-results/public-results/publications/EXO/index.html>
- [682] Zhang J, Yue C-X and Liu Z-C 2018 *Mod. Phys. Lett. A* **33** 1850039
- [683] Doršner I and Greljo A 2018 *J. High Energy Phys.* **JHEP05(2018)126**
- [684] Bähr M *et al* 2008 *Eur. Phys. J. C* **58** 639
- [685] Mandal S, Mitra M and Sinha N 2018 *Phys. Rev. D* **98** 095004
- [686] Padhan R, Mandal S, Mitra M and Sinha N 2019 arXiv:1912.07236
- [687] Antusch S, Hammad A and Rashed A 2020 *Phys. Lett. B* **810** 135796
- [688] Aaboud M *et al* (ATLAS Collaboration) 2018 *Phys. Rev. D* **98** 092008
- [689] Aad G *et al* (ATLAS Collaboration) 2019 *Phys. Lett. B* **796** 68
- [690] Aubert B *et al* (BaBar Collaboration) 2010 *Phys. Rev. Lett.* **104** 021802
- [691] Hayasaka K *et al* 2010 *Phys. Lett. B* **687** 139
- [692] Zhang Y-J, Han L and Liu Y-B 2017 *Phys. Lett. B* **768** 241
- [693] Liu Y-B 2017 *Nucl. Phys. B* **923** 312
- [694] Han L, Zhang Y-J and Liu Y-B 2017 *Phys. Lett. B* **771** 106



- [695] Ozansoy A, Ari V and Çetinkaya V 2016 *Adv. High Energy Phys.* **2016** 1739027
- [696] Caliskan A 2017 *Adv. High Energy Phys.* **2017** 4726050
- [697] Caliskan A and Kara S O 2018 *Int. J. Mod. Phys. A* **33** 1850141
- [698] Günaydin Y O, Sahin M and Sultansoy S 2018 *Acta Phys. Pol. B* **49** 1763
- [699] Sahin M 2014 *Acta Phys. Pol. B* **45** 1811
- [700] Acar Y C, Kaya U, Oner B B and Sultansoy S 2017 *J. Phys. G: Nucl. Part. Phys.* **44** 045005
- [701] Abramowicz H *et al* (ZEUS Collaboration) 2016 *Phys. Lett. B* **757** 468
- [702] Zarnecki A F 2008 Leptoquarks and contact interactions at LHeC *Proc., 16th Int. Workshop on Deep Inelastic Scattering and Related Subjects (DIS 2008)* (London, UK 7–11 April 2008)
- [703] Yock P C M 1969 *Int. J. Theor. Phys.* **2** 247
- [704] Schwinger J 1969 *Science* **165** 757
- [705] Aad G *et al* (ATLAS Collaboration) 2020 *Phys. Rev. Lett.* **124** 031802
- [706] Hofstadter R 1956 *Rev. Mod. Phys.* **28** 214
- [707] Zarnecki A F 1999 *Eur. Phys. J. C* **11** 539
- [708] Aaboud M *et al* (ATLAS Collaboration) 2017 *J. High Energy Phys.* **JHEP10(2017)182**
- [709] Sirunyan A M *et al* (CMS Collaboration) 2019 *J. High Energy Phys.* **JHEP04(2019)114**
- [710] Michel A and Sher M 2019 *Phys. Rev. D* **100** 095011
- [711] Boroun G R 2017 *Chin. Phys. C* **41** 013104
- [712] Boroun G R, Rezaei B and Heidari S 2017 *Int. J. Mod. Phys. A* **32** 1750197
- [713] Bi H-Y, Zhang R-Y, Han H-Y, Jiang Y and Wu X-G 2017 *Phys. Rev. D* **95** 034019
- [714] He K, Bi H-Y, Zhang R-Y, Li X-Z and Ma W-G 2018 *J. Phys. G: Nucl. Part. Phys.* **45** 055005
- [715] Bi H-Y, Zhang R-Y, Wu X-G, Ma W-G, Li X-Z and Owusu S 2017 *Phys. Rev. D* **95** 074020
- [716] ATLAS Collaboration 2018 Prospect for a measurement of the weak mixing angle in  $pp \rightarrow Z/\gamma^* \rightarrow e^+e^-$  events with the ATLAS detector at the high luminosity large hadron collider *ATL-PHYS-PUB-2018-037* (Geneva: CERN) (<https://cds.cern.ch/record/2649330>)
- [717] CMS Collaboration 2017 A proposal for the measurement of the weak mixing angle at the HL-LHC *CMS-PAS-FTR-17-001* (Geneva: CERN) (<https://cds.cern.ch/record/2294888>)
- [718] Barter W J 2018 Prospects for measurement of the weak mixing angle at LHCb *LHCb-PUB-2018-013. CERN-LHCb-PUB-2018-013* (Geneva: CERN) (<https://cds.cern.ch/record/2647836>)
- [719] Harland-Lang L A, Martin A D, Motylinski P and Thorne R S 2015 *Eur. Phys. J. C* **75** 204
- [720] Dulat S *et al* 2016 *Phys. Rev. D* **93** 033006
- [721] Aad G *et al* (ATLAS Collaboration) 2015 *J. High Energy Phys.* **JHEP09(2015)049**
- [722] ATLAS Collaboration 2018 Prospects for the measurement of the W-boson mass at the HL- and HE-LHC *ATL-PHYS-PUB-2018-026* (Geneva: CERN) (<http://cds.cern.ch/record/2645431>)
- [723] Zimmermann F 2017 *ICFA Beam Dyn. Newslett.* **72** 138 (<http://cds.cern.ch/record/2315725>)
- [724] Peskin M E and Takeuchi T 1992 *Phys. Rev. D* **46** 381
- [725] De Blas J *et al* 2020 *Eur. Phys. J. C* **80** 456
- [726] Cepeda M *et al* 2019 *CERN Yellow Rep. Monogr.* **7** 221
- [727] Campbell J and Neumann T 2019 *J. High Energy Phys.* **JHEP12(2019)034**
- [728] Mistlberger B 2018 *J. High Energy Phys.* **JHEP05(2018)028**
- [729] Dulat F, Lazopoulos A and Mistlberger B 2018 *Comput. Phys. Commun.* **233** 243
- [730] David A *et al* (LHC Higgs Cross Section Working Group Collaboration) 2012 LHC HXSWG interim recommendations to explore the coupling structure of a Higgs-like particle (arXiv:1209.0040)
- [731] Aad G *et al* (ATLAS Collaboration) 2020 *Phys. Rev. D* **101** 012002
- [732] de Blas J *et al* 2020 *J. High Energy Phys.* **JHEP01(2020)139**
- [733] ATLAS Collaboration 2015 Study of correlation of PDF uncertainty in single top and top pair production at the LHC *ATL-PHYS-PUB-2015-010* (Geneva) (<http://cds.cern.ch/record/2020601>)
- [734] Khachatryan V *et al* (CMS Collaboration) 2016 *Phys. Rev. D* **94** 072002
- [735] Aaltonen T *et al* (Tevatron Electroweak Working Group) 2016 Combination of CDF and D0 results on the mass of the top quark using up  $9.7 \text{ fb}^{-1}$  at the Tevatron (arXiv:1608.01881)
- [736] Khachatryan V *et al* (CMS Collaboration) 2016 *Phys. Rev. D* **93** 072004
- [737] Aaboud M *et al* (ATLAS Collaboration) 2016 *Phys. Lett. B* **761** 350
- [738] Sirunyan A M *et al* (CMS Collaboration) 2017 *Eur. Phys. J. C* **77** 354
- [739] Sirunyan A M *et al* (CMS Collaboration) 2018 *Eur. Phys. J. C* **78** 891

- [740] ATLAS Collaboration 2018 Prospects for measurement of the top quark mass using  $t\bar{t}$  events with  $J/\psi \rightarrow \mu^+ \mu^-$  decays with the upgraded ATLAS detector at the high luminosity LHC *ATL-PHYS-PUB-2018-042* (Geneva) (<http://cds.cern.ch/record/2649882>)
- [741] Britzger D, Rabbertz K, Savoie D, Sieber G and Wobisch M 2019 *Eur. Phys. J. C* **79** 68
- [742] Aaboud M *et al* (ATLAS Collaboration) 2018 *Phys. Rev. D* **98** 092004
- [743] Aaboud M *et al* (ATLAS Collaboration) 2017 *Eur. Phys. J. C* **77** 872
- [744] Johnson M and Maître D 2018 *Phys. Rev. D* **97** 054013
- [745] Klijnsma T, Bethke S, Dissertori G and Salam G P 2017 *Eur. Phys. J. C* **77** 778
- [746] Sirunyan A M *et al* (CMS Collaboration) 2019 *Eur. Phys. J. C* **80** 658
- [747] Sirunyan A M *et al* (CMS Collaboration) 2020 *J. High Energy Phys.* **JHEP06(2020)018**
- [748] d'Enterria D and Poldaru A 2020 *J. High Energy Phys.* **JHEP06(2020)016**
- [749] Bouzid B, Iddir F and Semlala L 2017 arXiv:1703.03959
- [750] Grazzini M, Kallweit S, Rathlev D and Wiesemann M 2016 *Phys. Lett. B* **761** 179
- [751] Grazzini M, Kallweit S and Wiesemann M 2018 *Eur. Phys. J. C* **78** 537
- [752] Aaboud M *et al* (ATLAS Collaboration) 2019 *Eur. Phys. J. C* **79** 535
- [753] Sirunyan A M *et al* (CMS Collaboration) 2019 *J. High Energy Phys.* **JHEP04(2019)122**
- [754] Cid Vidal X *et al* 2019 *CERN Yellow Rep. Monogr.* **7** 585
- [755] Aaboud M *et al* (ATLAS Collaboration) 2018 *Phys. Rev. D* **97** 112001
- [756] Sirunyan A M *et al* (CMS Collaboration) 2018 *J. High Energy Phys.* **JHEP05(2018)025**
- [757] Ball R D *et al* (NNPDF Collaboration) 2015 *J. High Energy Phys.* **JHEP04(2015)040**
- [758] Schmidt C, Pumplin J, Yuan C P and Yuan P 2018 *Phys. Rev. D* **98** 094005
- [759] Wang B-T, Hobbs T J, Doyle S, Gao J, Hou T-J, Nadolsky P M and Olness F I 2018 *Phys. Rev. D* **98** 094030
- [760] Hobbs T J, Wang B-T, Nadolsky P M and Olness F I 2019 *Proc. Sci.* **DIS2019** 247
- [761] Brenner Mariotto C and Machado M 2012 *Phys. Rev. D* **86** 033009
- [762] Coelho R and Goncalves V 2020 arXiv:2002.10713
- [763] Coelho R O and Goncalves V P 2020 *Nucl. Phys. B* **956** 115013
- [764] Bonvini M 2018 *Eur. Phys. J. C* **78** 834
- [765] Bonvini M, Gauld R, Giani T and Marzani S in preparation
- [766] Bonvini M and Silveti F in preparation
- [767] Collins J C, Soper D E and Sterman G 1985 *Nucl. Phys. B* **250** 199
- [768] Angeles-Martinez R *et al* 2015 *Acta Phys. Pol. B* **46** 2501
- [769] Diehl M 2016 *Eur. Phys. J. A* **52** 149
- [770] Rogers T C 2016 *Eur. Phys. J. A* **52** 153
- [771] Balitsky I and Tarasov A 2016 *J. High Energy Phys.* **JHEP06(2016)164**
- [772] Catani S, Ciafaloni M and Hautmann F 1990 *Phys. Lett. B* **242** 97
- [773] Catani S, Ciafaloni M and Hautmann F 1991 *Nucl. Phys. B* **366** 135
- [774] Collins J C and Ellis R K 1991 *Nucl. Phys. B* **360** 3
- [775] Levin E, Ryskin M, Shabelski Y and Shuvaev A 1991 *Sov. J. Nucl. Phys.* **53** 657
- [776] Altinoluk T and Boussarie R 2019 *J. High Energy Phys.* **JHEP10(2019)208**
- [777] Armesto N and Scomarini E 2016 *Eur. Phys. J. Plus* **131** 52
- [778] Busza W, Rajagopal K and van der Schee W 2018 *Annu. Rev. Nucl. Part. Sci.* **68** 339
- [779] Romatschke P and Romatschke U 2019 *Relativistic Fluid Dynamics in and Out of Equilibrium (Cambridge Monographs on Mathematical Physics)* (Cambridge: Cambridge University Press)
- [780] Mehtar-Tani Y, Milhano J G and Tywoniuk K 2013 *Int. J. Mod. Phys. A* **28** 1340013
- [781] Andronic A *et al* 2016 *Eur. Phys. J. C* **76** 107
- [782] SISSA 2018 *Proc., 9th Int. Conf. on Hard and Electromagnetic Probes of High-Energy Nuclear Collisions: Hard Probes 2018 (HP2018)* (SISSA) (<https://pos.sissa.it/345>)
- [783] Andrews H A *et al* 2020 *J. Phys. G* **47** 065102
- [784] Abelev B B *et al* (ALICE Collaboration) 2014 *Phys. Lett. B* **734** 314
- [785] Song H, Bass S A, Heinz U, Hirano T and Shen C 2011 *Phys. Rev. Lett.* **106** 192301  
Song H, Bass S A, Heinz U, Hirano T and Shen C 2012 *Phys. Rev. Lett.* **109** 139904 (erratum)
- [786] Niemi H, Eskola K J and Paatelainen R 2016 *Phys. Rev. C* **93** 024907
- [787] Liu J, Shen C and Heinz U 2015 *Phys. Rev. C* **91** 064906  
Liu J, Shen C and Heinz U 2015 *Phys. Rev. C* **92** 049904 erratum
- [788] Schenke B, Tribedy P and Venugopalan R 2012 *Phys. Rev. Lett.* **108** 252301
- [789] Ollitrault J-Y, Poskanzer A M and Voloshin S A 2009 *Phys. Rev. C* **80** 014904
- [790] Adams J *et al* (STAR Collaboration) 2005 *Phys. Rev. C* **72** 014904



- [791] Abelev B I *et al* (STAR Collaboration) 2009 *Phys. Rev. C* **79** 034909
- [792] Sirunyan A M *et al* (CMS Collaboration) 2020 *Phys. Lett. B* **800** 135048
- [793] Contreras J G 2017 *Phys. Rev. C* **96** 015203
- [794] Guzey V and Klasen M 2019 *Eur. Phys. J. C* **79** 396
- [795] Aaboud M *et al* (ATLAS Collaboration) 2018 *Phys. Rev. Lett.* **121** 212301
- [796] Aaboud M *et al* (ATLAS Collaboration) 2019 *Phys. Rev. C* **100** 034903
- [797] Aaij R *et al* 2017 Expression of interest for a phase-II LHCb upgrade: opportunities in flavour physics, and beyond *The HL-LHC Era, CERN-LHCC-2017-003* (Geneva: CERN)
- [798] Brüning O 2015 Accelerator design Presented at the *lhcc Workshop* <https://indico.cern.ch/event/356714/contributions/844912/>
- [799] Brandt D, Burkhardt H, Lamont M, Myers S and Wenninger J 2000 *Rep. Prog. Phys.* **63** 939
- [800] Pellegrini D, Latina A, Schulte D and Bogacz S A 2015 *Phys. Rev. ST Accel. Beams* **18** 121004
- [801] Bogacz S A *et al* 2017 *ICFA Beam Dyn. Newslett.* **71** 135 (<http://cds.cern.ch/record/2316013>)
- [802] Williams P 2018 A staged, multi-user x-ray free electron laser and nuclear physics facility based on a multi-pass recirculating superconducting CW linac *Proc., Future Light Sources 2018* (Shanghai)
- [803] Jefferson Lab 2012 12 GeV CEBAF upgrade, reference design [www.jlab.org/physics/GeV/accelerator](http://www.jlab.org/physics/GeV/accelerator)
- [804] Hoffstaetter G H and Bazarov I V 2004 *Phys. Rev. ST Accel. Beams* **7** 054401
- [805] Schwinger J S 1946 *Phys. Rev.* **70** 798
- [806] Pellegrini D 2016 *PhD Thesis* EPFL, Switzerland
- [807] Milanese A 2014 *Talk Presented at the LHeC Workshop at CERN*
- [808] Jowett J *et al* 2019 The 2018 heavy-ion run of the LHC *Proc., 10th Int. Particle Accelerator Conf. (IPAC2019)* (Melbourne, Australia 19–24 May 2019)
- [809] Argyropoulos T, Bohl T, Lasheen A, Papotti G, Quartullo D and Shaposhnikova E 2019 Momentum slip-stacking in CERN SPS for the ion beams *Proc., 10th Int. Particle Accelerator Conf. (IPAC2019)* (Melbourne, Australia 19–24 May 2019)
- [810] Schaumann M 2015 *Phys. Rev. ST Accel. Beams* **18** 091002
- [811] Brüning O *et al* 2015 *ICFA Beam Dyn. Newslett.* **68** 46 (<http://cds.cern.ch/record/2153752>)
- [812] Calaga R and Jensen E 2013 A proposal for an ERL test facility at CERN *Proc., 4th Int. Particle Accelerator Conf. (IPAC 2013)* (Shanghai, China 12–17 May 2013) <http://JACoW.org/IPAC2013/papers/wepwo049.pdf>
- [813] Marhauser F 2014 Cost rationales for an SRF proton linac *Proc., 5th Int. Particle Accelerator Conf. (IPAC 2014)* (Dresden, Germany 15–20 June 2014)
- [814] Marhauser F 2018 Recent results on a multi-cell 802 mhz bulk nb cavity *FCC Week 2018* [https://indico.cern.ch/event/656491/contributions/2932251/attachments/1629681/2597650/5\\_cell\\_Cavity\\_Marhauser.pdf](https://indico.cern.ch/event/656491/contributions/2932251/attachments/1629681/2597650/5_cell_Cavity_Marhauser.pdf)
- [815] Schneider W *et al* 2001 Design of the sns cryomodule *Proc., the 2001 Particle Accelerator Conf. (PACS2001)*
- [816] Parma V *et al* 2011 Conceptual design of the superconducting proton linac short cryo-module *Proc. of the SRF2011* (Chicago)
- [817] Olivier G, Thermeau J and Bosland P 2013 Ess cryomodules for elliptical cavities *Proc. of the 2013 Superconducting Radio Frequency Conf.*
- [818] Bluem H, Dowell D, Todd A and Young L 2011 High brightness thermionic electron gun performance *Proc., 50th Advanced ICFA Beam Dynamics Workshop on Energy Recovery Linacs (ERL'11)* (Tsukuba, Japan October 2011)
- [819] Sannibale F *et al* 2016 The VHF-gun, the LBNL high-brightness electron photo-injector for MHz-class repetition-rate applications *High-Brightness Sources and Light-Driven Interactions* (Optical Society of America)
- [820] Wang Z, Gu Q, Wang G and Zhao M 2019 Injector physics design at SHINE *Proc., 10th Int. Particle Accelerator Conf. (IPAC'19)* (Melbourne, Australia 19–24 May 2019) (Geneva: JACoW Publishing)
- [821] Shu G, Chen Y, Lal S, Qian H, Shaker H and Stephan F 2019 First design studies OF a NC CW RF gun for EUROPEAN XFEL *Proc., 10th Int. Particle Accelerator Conf. (IPAC'19)* (Melbourne, Australia 19–24 May 2019) (Geneva: JACoW Publishing)
- [822] Teichert J *et al* 2014 *Nucl. Instrum. Methods Phys. Res. A* **743** 114

- [823] Bisognano J *et al* 2013 Wisconsin srf electron gun commissioning *Proc., North American Particle Accelerator Conf. (NAPAC'13)* (Pasadena, CA, USA September–October 2013) <http://accelconf.web.cern.ch/AccelConf/PAC2013/papers/tupma19.pdf>
- [824] Vogel E *et al* 2018 *SRF Gun Development at DESY* (Geneva: JACoW)
- [825] Neumann A *et al* 2019 Status of SRF gun for bERLinPro *Proc., ERL'19* (Berlin, Germany September 2019)
- [826] Belomestnykh S A *et al* 2015 Commissioning of the 112 MHz SRF gun *Proc., 17th Int. Conf. RF Superconductivity, Whistler* (Canada September 2015)
- [827] Hernandez-Garcia C *et al* 2009 JLab FEL DC gun *Proc., 45th ICFA Advanced Beam Dynamics Workshop on Energy Recovery LINAC Workshop (ERL'09)* (Ithaca, NY, USA June 2009)
- [828] Jones L B, McKenzie J W, Middleman K J, Militsyn B L, Saveliev Y M and Smith S L 2011 *J. Phys.: Conf. Ser.* **298** 012007
- [829] Kato R, Honda Y, Kawata H, Miyajima T, Nakamura N, Sakai H, Shimada M, Tanimoto Y and Tsuchiya K 2019 Ir-fel project at the cerl and future euv-fel lithography *39th Int. Free Electron Laser Conf. (FEL'19)* (Hamburg, Germany August 2019)
- [830] Hoffstaetter G H *et al* 2016 CBETA: the Cornell/BNL 4-turn ERL with FFAG return arcs for eRHIC prototyping *Proc., 28th Linear Accelerator Conf. (LINAC'16)* (East Lansing, MI, USA)
- [831] Hounsell B, Kaabi W, Klein M, Militsyn B and Welsch C 2019 Optimisation of the PERLE injector *Proc., ERL'19* (Berlin, Germany September 2019)
- [832] Suleiman R, Adderley P, Grames J, Hansknecht J, Poelker M and Stutzman M 2018 *AIP Conf. Proc.* **1970** 050007
- [833] Sinclair C K *et al* 2007 Performance of a very high voltage photoemission electron gun for a high brightness, high average current ERL injector *Proc., 22nd Particle Accelerator Conf. (PAC'07)* (Albuquerque, NM, USA) <https://accelconf.web.cern.ch/AccelConf/p07/PAPERS/TUPMS021.PDF>
- [834] Nishimori N *et al* 2013 *Appl. Phys. Lett.* **102** 234103
- [835] Nishimori N, Nagai R, Hajima R, Yamamoto M, Honda Y, Miyajima T and Uchiyama T 2019 *Phys. Rev. Accel. Beams* **22** 053402
- [836] Liu W, Chen Y, Lu W, Moy A, Poelker M, Stutzman M and Zhang S 2016 *Appl. Phys. Lett.* **109** 252104
- [837] Wang E 2018 *AIP Conf. Proc.* **1970** 050008
- [838] Sokolov A and Ternov I 1964 *Sov. Phys. - Dokl.* **8** 1203
- [839] Zimmermann F, Brüning O and Klein M 2013 The LHeC as a Higgs boson factory *4th Int. Particle Accelerator Conf.*
- [840] Antonelli M, Boscolo M, Di Nardo R and Raimondi P 2016 *Nucl. Instrum. Methods Phys. Res. A* **807** 101
- [841] Boscolo M, Antonelli M, Blanco-Garcia O, Guiducci S, Liuzzo S, Raimondi P and Collamati F 2018 *Phys. Rev. Accel. Beams* **21** 061005
- [842] Aicheler M *et al* 2012 *A Multi-TeV Linear Collider Based on CLIC Technology: CLIC Conceptual Design Report, CERN-2012-007*
- [843] Adolphsen C *et al* 2013 *The International Linear Collider Technical Design Report—Volume 3.II: Accelerator Baseline Design*
- [844] Bambade P *et al* 2019 The international linear collider: a global project (arXiv:1903.01629)
- [845] Krasny M W 2015 The gamma factory proposal for CERN, an executive summary of the gamma factory proposal addressed to the CERN management (arXiv:1511.07794)
- [846] Zimmermann F 2018 *J. Phys.: Conf. Ser.* **1067** 022017
- [847] Zimmermann F, Aksakal H, Aksoy A and Nergiz Z 2019 Free electron laser driven by a high-energy high-current energy-recovery Linac *10th Int. Particle Accelerator Conf.*
- [848] Zaltsman A and Lambiase R 2011 *Proc. of the 24th Particle Accelerator Conf., PAC-2011, TUP125*
- [849] Parker B 2017 Latest developments and progress on the IR magnet design *LHeC and FCC-Eh Workshop*
- [850] Parker B 2018 Superconducting magnet concepts for electron hadron collider IRs *Electrons for the LHC—LHeC/FCCEH and Perle Workshop*
- [851] Cruz-Alaniz E, Newton D, Tomás R and Korostelev M 2015 *Phys. Rev. ST Accel. Beams* **18** 111001
- [852] Martin R and Tomás Garcia R 2018 Length optimization of the detector region dipoles in LHeC and FCC-eh *CERN-ACC-2018-0042, CERN* (Geneva) (<http://cds.cern.ch/record/2644892>)
- [853] Fartoukh S 2013 *Phys. Rev. ST Accel. Beams* **16** 111002
- [854] LHeC Lattice Group 2019 Lattice repository <https://gitlab.cern.ch/lhec-optics/lhec-lattice>

- [855] Gaddi A 2017 Installation issues of eh detectors (LHC and FCC) *Talk Presented at the LHeC and FCC-Eh Workshop* (CERN)
- [856] Gaddi A 2019 private communication
- [857] Bruce R, Bracco C, De Maria R, Giovannozzi M, Redaelli S, Tomás Garcia R, Velotti F M and Wenninger J 2017 Updated parameters for HL-LHC aperture calculations for proton beams *CERN-ACC-2017-0051* (Geneva: CERN) <https://cds.cern.ch/record/2274330>
- [858] De Maria R *et al* 2020 HLLHCv1.3 optics repository <http://lhc-optics.web.cern.ch/lhc-optics/HLLHCv1.3/>
- [859] Cruz-Alaniz E, Martin R and Tomás R 2019 LHeC optics with  $\beta^* = 10$  cm and  $L^* = 15$  m *CERN-ACC-NOTE-2019-0049* (Geneva: CERN) <https://cds.cern.ch/record/2701426>
- [860] CERN – BE/ABP Accelerator Beam Physics Group 2021 <http://sixtrack.web.cern.ch/SixTrack/>
- [861] Cruz-Alaniz E, Abelleira J L, van Riesen-Haupt L, Seryi A, Martin R and Tomás R May 2018 Methods to increase the dynamic aperture of the FCC-hh lattice *Proc. Int. Particle Accelerator Conf. (IPAC'18)* (Vancouver, Canada 2018) (Geneva, Switzerland: JACoW) <https://accelconf.web.cern.ch/AccelConf/ipac2018/papers/thpak145.pdf>
- [862] Zimmermann F *et al* 2010 Interaction-region design options for a linac–ring LHeC *Proc., Int. Particle Accelerator Conf. (IPAC'10)* (Kyoto, Japan 23–28 May 2010) (Geneva, Switzerland: JACoW)
- [863] Abelleira J L, Garcia H, Tomás R and Zimmermann F 2012 Final-focus optics for the LHeC electron beam line *Proc., Int. Particle Accelerator Conf. (IPAC'12)* (New Orleans, Louisiana, USA 20–25 May 2012) (Geneva, Switzerland: JACoW)
- [864] Arduini G, Brüning O and Klein M (LHeC Study Group, FCC-eh Study Group, PERLE Collaboration) 2018 *Proc. Sci.* **2018** 183
- [865] Tomás R 2012 LHeC interaction region *Talk Presented at DIS 2012 Workshop* (Bonn)
- [866] Parrell J A, Field M B, Zhang Y and Hong S 2004 *AIP Conf. Proc.* **711** 369–75
- [867] Russenschuck S 2010 *Field Computation for Accelerator Magnets: Analytical and Numerical Methods for Electromagnetic design and Optimization* (New York: Wiley)
- [868] Fern E J, Di Murro V, Soga K, Li Z, Scibile L and Osborne J A 2018 *Tunnelling and Underground Space Technology* **77** 249
- [869] Laughton C 1988 *Int. J. Min. Geol. Eng.* **6** 353
- [870] Tigner M 1965 *Nuovo Cimento* **37** 1228
- [871] Litvinenko V *et al* 2019 Coherent electron cooling experiment at RHIC: status and plans *12th Int. Workshop on Beam Cooling and Related Topics*
- [872] Tennant C 2016 Energy recovery linacs *Challenges and Goals for Accelerators in the XXI Century* ed O Brüning and S Myers (Singapore: World Scientific)
- [873] Tennant C 2010 Progress at the Jefferson laboratory FEL *Particle Accelerator. Proc., 23rd Conf., PAC'09* (Vancouver, Canada May 4–8, 2009) ([http://1.jlab.org/UI/publications/view\\_pub.cfm?pub\\_id=8641](http://1.jlab.org/UI/publications/view_pub.cfm?pub_id=8641))
- [874] Hoffstaetter G H and Bazarov I V 2004 *Phys. Rev. Spec. Top. Accel. Beams* **7** 054401
- [875] Douglas D R *et al* 2006 *Phys. Rev. Spec. Top. Accel. Beams* **9** 064403
- [876] Di Mitri S, Cornacchia M and Spampinati S 2013 *Phys. Rev. Lett.* **110** 014801
- [877] Fedurin M G, Kayran D, Yakimenko V, Fedotov A V, Litvinenko V and Muggli P 2011 *Proc.: Particle accelerator. 24th Conference, PAC'11 (New York, March 28-April 1, 2011)* **C110328** 1677
- [878] Heifets S, Stupakov G and Krinsky S 2002 *Phys. Rev. Spec. Top. Accel. Beams* **5** 064401
- [879] Huang Z and Kim K-J 2002 *Phys. Rev. Spec. Top. Accel. Beams* **5** 074401
- [880] Di Mitri S and Cornacchia M 2015 *Europhys. Lett.* **109** 62002
- [881] Tsai C-Y, Douglas D, Li R and Tennant C 2016 *Phys. Rev. Accel. Beams* **19** 114401
- [882] Tsai C-Y, Di Mitri S, Douglas D, Li R and Tennant C 2017 *Phys. Rev. Accel. Beams* **20** 024401
- [883] Douglas D *et al* 2012 *Jefferson Laboratory Technical Note 12-017*
- [884] Alarcon R *et al* 2013 *Phys. Rev. Lett.* **111** 164801
- [885] Powers T and Tennant C 2007 Implications of incomplete energy recovery in srf-based energy recovery linacs *Proc. of the 2007 ICFA Workshop on Energy Recovery Linacs* (Daresbury, UK)
- [886] Setiniyaz S, Apsimon R and Williams P 2020 *Phys. Rev. Accel. Beams* **23** 072002
- [887] Powers T 2017 Control of microphonics for narrow control bandwidth cavities *Talk Presented at the 2017 Int. Conf. on RF Superconductivity* (Lanzhou, China)
- [888] Benson S *et al* 2007 *Conf. Proc.* **C070625** 79

- [889] Powers T 2013 Optimization of SRF linacs *Proc. of the 2013 Int. Conf. on RF Superconductivity* (Paris, France)
- [890] Benson S *et al* 2018 Development of a bunched-beam electron cooler for the Jefferson lab electron-ion collider *Proc., 9th Int. Particle Accelerator Conf. (IPAC 2018)* (Vancouver, BC Canada)
- [891] Tennant C 2019 ERL Landscape plot <https://userweb.jlab.org/~tennant/>
- [892] Tennant C 2018 Analysis of the baseline PERLE lattice *Jefferson Laboratory Technical Note 18-031*
- [893] Douglas D *et al* 2018 Why PERLE? Historical context and technological motivation *Jefferson Laboratory Technical Note 18-014*
- [894] Satogata T *et al* 2016 ER@CEBAF: a test of five-pass energy recovery at CEBAF *Program Advisory Committee Proposal*
- [895] Donnachie A and Landshoff P V 1992 *Phys. Lett. B* **296** 227–32
- [896] ATLAS Collaboration 2017 *Technical Design Report for the Phase-II Upgrade of the ATLAS Muon Spectrometer* (<http://cds.cern.ch/record/2285580>)
- [897] CMS Collaboration 2017 *The Phase-2 Upgrade of the CMS Muon Detectors*
- [898] Albrow M G *et al* (FP420 R & D Collaboration) 2009 *J. Inst.* **4** T10001
- [899] Adriani O *et al* (LHCf Collaboration) 2018 *Phys. Lett. B* **780** 233
- [900] Adriani O *et al* 2018 Measurement of inclusive forward neutron production cross section in proton-proton collisions at  $\sqrt{s} = 13$  TeV with the LHCf Arm2 detector *J. High Energy Phys. JHEP11(2018)073*
- [901] CERN 2019 Screenshot from MapCERN <http://maps.web.cern.ch>
- [902] Dellacasa G *et al* (ALICE Collaboration) 2000 *ALICE Technical Design Report of the Time-of-flight System (TOF)* (<https://cds.cern.ch/record/430132>)
- [903] Frank M, Gaede F, Petric M and Sailer A 2018 *Aidasoft/dd4hep*
- [904] Bianchi G (CMS Collaboration) 2014 *J. Inst.* **9** C03054
- [905] Hiti B *et al* 2019 *Proc. Sci TWEPP2018* 155
- [906] Agostinelli S *et al* (GEANT4 Collaboration) 2003 *Nucl. Instrum. Methods Phys. Res. A* **506** 250
- [907] Oreglia M 1983 A study of the reactions  $\psi' \rightarrow \gamma\gamma\psi$  *PhD Thesis* (<https://search.proquest.com/docview/303269954>)
- [908] Gaiser J E 1980 Charmonium spectroscopy from radiative decays of the  $J/\psi$  and  $\psi'$  *PhD Thesis* (<https://search.proquest.com/docview/303269954>)
- [909] Skwarnicki T 1986 A study of the radiative CASCADE transitions between the upsilon-prime and upsilon resonances *PhD Thesis* Institute of Nuclear Physics, Cracow (<http://library.desy.de/cgi-bin/showprep.pl?DESY-F31-86-02>)